MODELLING AND PASSIVE CORRECTION INVESTIGATION OF VIBRATION INDUCED MACHINING ERRORS ON CNC MACHINE TOOLS

MUHAMMAD HELMI NUR WIDIYARTO

A thesis submitted to the University of Huddersfield in partial fulfilment of the requirements for the degree of Doctor of Philosophy

The University of Huddersfield

July 2006

Abstract

Machine tool vibration is a complex subject requiring a multi-disciplinary approach involving the identification and analysis of the vibration sources and characteristics, as well as its direct and indirect effects. Machine tool vibration is influenced and can be characterised by the machine's structural dynamics, the drive system performance and the cutting force generation. Its effect materialises in the form of poor surface finish of the workpiece, accelerated cutting-tool wear, and chatter during the machining process.

This research project investigates vibration-induced errors on a Cincinnati Arrow 500 CNC vertical machining centre under dynamic conditions. Analyses and identifications of suitable experimental configurations for modal analysis and cutting process investigations are carried out to determine the most appropriate techniques for the aforementioned processes. The results are compiled into recommended metrology practices for determining the vibration modes.

State-of-the-art practices are employed in the study to formulate and validate a machine tool axis drive model to examine the drive's individual element effects on the overall dynamic performance. The feasibility of an active control vibration technique employing the drive is also investigated. The hybrid modelling technique incorporating a new digital current control loop developed using the power system blockset and field-oriented control strategy was employed to construct the model. Analytical and experimental techniques for the validation of the digital drive system's position, velocity and current control loops utilising deterministic and non-deterministic signals from the internal machine drive system functions are also devised.

The majority of machine tool vibration is generated while the machining process is taking place. Thus, the analysis and in-depth study of the machining process plays an important role in the investigation of machine tool vibration. In this study, vibration models of the cutting tool and workpiece are formulated and incorporated with an advanced cutting force generation model to create a machining process model constructed as part of an EPSRC project collaboration. The model is validated using various machining process conditions and correlated with the workpiece surface finish analysed using state-of-the-art 3D surface topography technique to identify salient vibration effects.

In this study, a model of the machine structural dynamics is constructed using the Finite Element Method (FEM) for the comprehensive analytical investigation of the machine

vibration behaviour accurately. The analytical model is validated against the measured results from the experimental modal analysis investigation obtained using the appropriate technique. Correlation analysis of the simulated and experimental modal analysis results is performed in order to improve the accuracy of the model and minimise modelling practice errors. The resulting optimised model then undergoes sensitivity analysis through parametric structural analysis and characterisation technique in order to identify potential vibration reduction technique by the passive methods.

Acknowledgment

I wish to thank my supervisors Professor Derek Ford, Dr. Andrew Longstaff and Dr. Stephen Lockwood for their expert advice throughout the research programme. Also thank you to Mr Alan Myers for the specialist advice relating to the FEA practices and Dr. Crinela Pislaru for the drive modelling investigation.

I am also grateful to the EPSRC and industrial collaborators Siemens Automation UK Ltd, Cincinnati UK Ltd and Kistler Instruments Ltd for the financial, equipment and technical support in allowing me to work on a major research grant [3]. The experience gained of being able to work as part of a team was most rewarding where my specialised content was appreciated by my more experienced colleagues. This opportunity has given me the chance to develop my skills for my challenge ahead in my future career.

Finally, I wish to acknowledge the patience and understanding of my parents, wife, son and the rest of the family for their support and encouragement throughout the period of study.

Table of Content

List of Figures

List of Tables

Glossary of Terms

2CR	-	Surface roughness filter representing an analogue circuit with two sets of capacitor and resistor pairs in series
2D	-	Two-dimensional
3D	-	Three-dimensional
ABAQUS	-	Finite element analysis software suite produced by ABAQUS, Inc.
ABAQUS/Standard	-	General finite element analysis software using the implicit method produced by ABAQUS, Inc.
AC	-	Alternating Current
ADC	-	Analogue to Digital Converter
AMD	-	Active Mass Damper
AMTRI	-	Advanced Manufacturing Technology Research Institute
ANSYS	-	Finite element analysis software suite produced by ANSYS, Inc.
ASCII	-	American Standard Code for Information Interchange
AutoCAD	-	Computer aided design software produced by Autodesk, Inc.
BE2-SPRINGA	-	Beam element with 2 points and stiffness property finite element analysis using ABAQUS
BED	-	Machine bed
BJT	-	Bipolar Junction Transistor
BS	-	British Standard
BS1	-	Ballscrew 1
BS2	-	Ballscrew 2
BSE	-	Ballscrew end
BSF	-	Ballscrew front
BSM	-	Ballscrew middle
BSN	-	Ballscrew nut
C3D4	-	First-order tetrahedral element with four nodes for finite element analysis using ABAQUS
CAD	-	Computer Aided Design
CAE	-	Computer Aided Engineering
CATIA	-	Computer Aided Three-dimensional Interactive Application software suite produced by Dassault Systèmes S.A.
CCABS	-	Weighted Absolute Relative Difference
CCDISP	-	Weighted Absolute Modal Displacement Difference
CCMAC	-	Weighted MAC values
CCMASS	-	Weighted Absolute Modal Mass Difference
CCMEAN	-	Weighted Relative Difference
CCTOTAL	-	Total Weighted Difference
CMIF	-	Complex Mode Indicator Function
CMM	-	Co-ordinate Measuring Machine
CNC	-	Computer Numerically Controlled
CRAFT	-	Cooperative Research Award For Technology
CWT	-	Continuous Wavelet Transform
DAC	-	Digital to Analogue Converter
DC	-	Direct Current
DDR SDRAM	-	Dual Data Rate Synchronous Dynamic Random Access Memory
DFT	-	Discrete Fourier Transform
DIN	-	Deutsches Institut für Normung

DOF	-	Degree Of Freedom
DSA	-	Dynamic Signal Analyser
DSP	-	Digital Signal Processing
DUT	-	Device Under Test
EMA	-	Experimental Modal Analysis
EPSRC	-	Engineering and Physical Science Research Council
ERA	-	Eigensystem Realisation Algorithm
ESP	-	Error Simulation Program
FEA	-	Finite Element Analysis
FEM	-	Finite Element Method
FEMGEN	-	Pre-processing module of the FEMGV software
FEMGV	-	General purpose finite element analysis pre- and post-processing software by Femsys Ltd.
FEMLAB	-	Finite element analysis software suite produced by COMSOL, Inc.
FEMtools	-	Computer aided engineering software for analytical and experimental structural analysis produced by Dynamic Design Solutions N.V.
FFT	-	Fast Fourier Transform
FOC	-	Field Oriented Control
Form Talysurf PGI	-	Contact measurement solution for form & surface finish applications produced by Taylor Hobson Ltd.
FRF	-	Frequency Response Function
GRFP	-	Global Rational Fractional Polynomial
GTO	-	Gate Turn Off
GUI	-	Graphical User Interface
HE20-C3D20	-	Second-order tetrahedral element with twenty nodes for finite element model development using FEMGEN
HMD	-	Hybrid Mass Damper
HSM	-	High Speed Machining
ICP	-	Integrated Circuit Piezoelectric
idinput	-	MATLAB function to generate various input signals utilised for system identification purposes
IGBT	-	Insulated Gate Bipolar Transistor
IGES	-	Initial Graphics Exchange Specification
IRF	-	Impulse Response Function
ISO	-	International Organization for Standardization
LDV	-	Laser Doppler Vibrometer
LVDT	-	Linear Variable Differential Transducer
MAC	-	Modal Assurance Criterion
MACMEAN	-	Average MAC values
MATLAB	-	Mathematical computation, analysis, visualisation, and algorithm development software by The Mathworks, Inc.
MDOF	-	Multi-Degree Of Freedom
Microloc	-	Workpiece holding system for vertical and horizontal milling machines and vertical machining centres
MIF	-	Mode Indicator Function
MIMO	-	Multi-Input Multi-Output
MOOZ	-	Source frequency range control function as opposed to zoom
MOS	-	Metal Oxide Semiconductor
MRR	-	Metal Removal Rate

MShaft	-	Motor shaft
Nastran	-	Finite element analysis software suite produced by MSC.Software Corporation
NC	-	Numerical Controller
NLLS	-	Non-Linear Least Squares
ode23tb	-	Ordinary differential equation with second order trapezoidal backward differential rule (TR-BDF2)
PDE	-	Partial Differential Equation
PI	-	Proportional Integral
PID	-	Proportional Integral Differential
PMSM	-	Permanent Magnet Synchronous Motor
PRBS	-	Pseudo Random Binary Signal
Pro/ENGINEER	-	Solid modelling computer aided design software produced by Parametric Technology Corporation (PTC)
Pro/MECHANICA	-	Structural analysis software produced by Parametric Technology Corporation (PTC)
PSD	-	Power Spectral Density
PVDF	-	Poly-Vinylidene Fluoride
PWM	-	Pulse Width Modulation
RADRAT	-	Radius ratio number for finite element compliance
RCSA	-	Receptance Coupling Substructure Analysis
RFP	-	Rational Fractional Polynomial
RMS	-	Root Mean Square
S85R	-	Second-order plate element with eight nodes and five degree-of-freedom for FEA model development in FEMGEN
SDL	-	Saddle
SDM	-	Structural Dynamic Modification
SDOF	-	Single Degree Of Freedom
SDRAM	-	Synchronous Dynamic Random Access Memory
SF	-	Spindle Frequency
SIMO	-	Single-Input Multi-Output
Simulink	-	Simulation software module for the MATLAB software
SISO	-	Single-Input Single-Output
SNR	-	Signal to Noise Ratio
SolidWorks	-	Solid modelling computer aided design software produced by Dassault Systèmes S.A.
STARStruct	-	Structural modal analysis software produced by Spectral Dynamics, Inc.
SVD	-	Singular Value Decomposition
TBL	-	Table
TIRAvib	-	Shaker/exciter model produced by TIRA GmbH
TLM	-	Transmission Line Matrix
TMD	-	Tuned Mass Damper
TPF	-	Tooth Passing Frequency
UFF	-	Universal File Format
VMC	-	Vertical Machining Centre

Nomenclature

Greek symbols

$\alpha(\omega)$ - Receptance ($m \cdot N^{-1}$)
α_e - Effective rake angle (°)
α_{e0} - Initial effective rake angle (°)
α_n - Normal rake angle (°)
α_r - Rake angle of tool (°)
β - Helix angle of end mill (°)
β_a - Average friction angle (°)
$\gamma(\omega)$ - Coherence
δ - Mass proportional damping ($N \cdot s \cdot m^{-1}$)
δ_e - Cutter run-out (m)
δX - Dimensional error of the 2D surface profile (m)
∂T - Kinetic energy variation (W)
∂U - Internal strain energy variation (W)
∂W_d - Mechanical work variation due to damping (J)
∂W_e - Mechanical work variation due to external forces (J)
∂q_i - Virtual displacement variation (m)
η - Damping loss factor (%) (Chapter 3)
η - Chip flow angle (°) (0)
η_r - Hysteretic damping of the r^{th} mode
ι - Cutting edge inclination angle (°)
λ - Permanent magnet flux linkage (Wb)
μ - Coefficient of friction (no unit) (Chapter 5)
μ - Eigenvalue ($rad \cdot s^{-1}$) (Chapter 7)
μ_l - Bearing coefficient of friction (no unit)
μ_a - Average coefficient of friction (no unit)
φ - Torsional angle (°) (Chapter 5)
φ - Helix lag angle (°) (Chapter 6)
φ_e - Helix lag angular location of the end point of contact (°)
φ_{e0} - Initial location angle of the cutter centre relative to spindle centre (°)
φ_i - Position angle of a point on the cutting edge of the i^{th} helical flute (°)
φ_i' - Position angle of a point on the cutting edge of the i^{th} helical flute considering the cutter run-out(°)
φ_s - Helix lag angular location of the starting point of contact (°)
ϕ_c - Shear angle (°)
ϕ_c - Shear angle (°)
ϕ_i - Oblique shear angle (°)
ϕ_n - Normal shear angle (°)
ϕ_{ik} - Mode shape i of the k^{th} mode
Φ - Mass normalisation (no unit)
ψ - Eigenvector (no unit) (Chapters 3, 7, 8)
ψ - Eigenvector value (no unit) (Chapter 3)
ψ - Axial immersion angle of a tooth (°) (Chapter 6)
θ - Rotor angular position (rad)
θ_i - Oblique force angle (°)
θ_{h1} - Coupling Hub1 angular position (rad)
θ_{h2} - Coupling Hub2 angular position (rad)
θ_n - Normal force angle (°)
θ_{BSN} - Ballscrew nut angular displacement (rad)
$\dot{\theta}$ - Angular velocity ($rad \cdot s^{-1}$)
$\dot{\theta}_{h1}$ - Coupling hub1 angular velocity ($rad \cdot s^{-1}$)
$\dot{\theta}_{h2}$ - Coupling hub2 angular velocity ($rad \cdot s^{-1}$)
$\ddot{\theta}$ - Angular acceleration ($rad \cdot s^{-2}$)
σ_k - Modal damping of the k^{th} mode
σ_s - Normal stress ($N \cdot m^{-2}$)
Σ - Singular value matrix
τ_s - Shear stress ($N \cdot m^{-2}$)
ω - Frequency ($rad \cdot s^{-1}$) (Chapter 5)
ω - Spindle rotational speed ($rad \cdot s^{-1}$) (Chapter 6)
ω_d - Damped natural frequency ($rad \cdot s^{-1}$)
ω_i - Frequency at point i ($rad \cdot s^{-1}$)
ω_n - Natural frequency ($rad \cdot s^{-1}$)
ω_k - Resonant frequency of the k^{th} mode
ω_r - Frequency of the r^{th} mode ($rad \cdot s^{-1}$) (Chapter 3)
ω_r - Rotor angular velocity ($rad \cdot s^{-1}$) (Chapter 5)
Ω_i - Measured frequency (Hz)
ζ - Damping ratio (no unit)

ζ_r - Damping ratio of the r[th] mode (no unit)

Small Latin letters

a_o - Output acceleration (m/s^2)
a_b - Base acceleration (m/s^2)
b - Width of cut (m)
b_a - Axial depth of cut (m)
c - Viscous damping (N·s·m^{-1})
c_0 - Hysteretic damping (N·s·m^{-1})
c_1 - Radial cutting force ratio (no unit)
c_2 - Axial cutting force ratio (no unit)
c_c - Coupling damping (N·s·m^{-1})
c_{cr} - Critical damping (N·s·m^{-1})
c_k - Polynomial coefficient (no unit)
c_s - Workpiece material specific heat constant (N·m·kg^{-1}°C^{-1})
d - Ballscrew root diameter (mm)
d-q - Direct-Quadrature (no unit)
e - Voltage (V)
e_{back} - Back electromotive force (V)
e_x - Position error signal/following error (mm)
e_n - Velocity error signal (rpm)
e_{iq} - Quadrature current error signal (A)
e_{id} - Direct current error signal (A)
f - Frequency (Hz) (Chapter 3)
f - Force (N) (Chapter 5)
$\mathbf{f}$ - Force vector (N)
f_0 - Bearing directional coefficient of the load-free part (No unit)
f_1 - Bearing directional coefficient of the load-dependent part (No unit)
f_c - Damping force (N)
f_n - Natural frequency (Hz)
f_t - Feedrate per tooth per revolution (mm/tooth)
f_s - Sampling rate (Hz)
g_i - Weighing function for GRFP parameter estimation
h - Hysteretic damping (N·s·m^{-1}) (Chapter 3)
h - Depth of cut (m) (Chapter 6)
$\mathbf{h}$ - Transfer vector (m·N^{-1})
h_i - Global FRF for the i^{th} point (m·N^{-1})
i - Current (A) (Chapter 5)
i - Tooth number (no unit) (Chapter 6)
i_α - Stator current in the α-axis (A)
i_β - Stator current in the β-axis (A)

ζ_r - Damping ratio of the r[th] mode (no unit)

i_a - Stator current in the a-axis (A)
i_b - Stator current in the b-axis (A)
i_c - Stator current in the c-axis (A)
i_d - Direct current (A)
i_q - Quadrature current (A)
i_{d_set} - Direct current setpoint (A)
i_{q_set} - Quadrature current setpoint (A)
j - Imaginary operator
k - Stiffness (N·m^{-1})
k_1 - Shaker constant 1 (N·A^{-1})
k_2 - Shaker constant 2 (V·s·m^{-1})
k_c - Coupling stiffness (N·m^{-1})
l - Length (m)
ℓ_p - Ballscrew pitch (mm)
m - Mass (kg)
m - Number of cutter flutes (no unit) (Chapter 6)
m_c - Metal removal rate (k·g·s^{-1})
n - Speed (rpm)
p - Pole pair number (pair)
p_k - Pole of the k^{th} mode
p_k* - Conjugate of the k^{th} mode's pole
q - Charge (Coulomb)
r_k - Complex residue of the k^{th} mode
r_k* - Conjugate of the k^{th} mode complex residue
$r_{nj}(k)$ - Complex residue at n point in the k^{th} mode
s - Operator for the s-domain
t - Time (s)
t_0 - Initial un-deformed chip thickness (m)
t_i - Un-deformed chip thickness of the i^{th} tooth (m)
u - Mode shape vector
u' - Total cutting energy per unit volume (J·m^{-3})
u_0 - Initial total cutting energy per unit volume (J·m^{-3})
u_k - Mode shape vector the k^{th} mode
u_{nk} - Mode shape vector at point n in the k^{th} mode
v - Operational viscosity (mm^2·s^{-1})
v_a - Stator voltage in the a-axis (V)
v_b - Stator voltage in the b-axis (V)

v_c - Stator voltage in the c-axis (V) (Chapter 5)
v_c - Chip flow velocity ($m \cdot s^{-1}$) (Chapter 6)
v_f - Feed velocity ($m \cdot s^{-1}$)
v_{ic} - Dynamic cutter displacement of the i^{th} flute (m)
$v_{ic(-T)}$ - Dynamic cutter displacement of the $(i-1)^{th}$ flute (m)
v_{iw} - Dynamic workpiece displacement of the i^{th} flute (m)
$v_{ic(-T)}$ - Dynamic workpiece displacement of the $(i-1)^{th}$ flute (m)
v_d - Direct voltage (V)
v_q - Quadrature voltages (V)
v_{d_set} - Direct voltage setpoint (V)
v_{q_set} - Quadrature voltage setpoint (V)
v_{bsm} - Ballscrew middle velocity ($m \cdot s^{-1}$)
v_{bsn} - Ballscrew nut velocity ($m \cdot s^{-1}$)
v_{Table} - Table velocity ($m \cdot s^{-1}$)
v_s - Shear velocity ($m \cdot s^{-1}$)
x_b - Ball position (m)
x_c - Regenerative cutting tool displacement in the X-direction (m)
x_{bsm} - Ballscrew middle displacement (m)
x_{bsn} - Ballscrew nut displacement (m)
x_n - Nut position (m)
x_w - Regenerative workpiece displacement in the X-direction (m)
x_{Table} - Table displacement (m)
x - Displacement (m)
$\mathbf{x}$ - Displacement vector (m)
$\dot{x}$ - Velocity ($m \cdot s^{-1}$)
$\dot{\mathbf{x}}$ - Velocity vector ($m \cdot s^{-1}$)
$\ddot{x}$ - Acceleration ($m \cdot s^{-2}$)
$\ddot{\mathbf{x}}$ - Acceleration vector ($m \cdot s^{-2}$)
y_c - Regenerative cutting tool displacement in the Y-direction (m)
y_w - Regenerative workpiece displacement in the Y-direction (m)
z_{ik} - Theoretical model for the k^{th} mode at point i

Capital Latin letters

A - Open loop gain
$A(\omega)$ - Accelerance (kg^{-1})
A - Cross-sectional area (m^2)
A_0, A_1, A_2 - Residual function coefficients
A_k - Modal constant of the k^{th} mode
${}_rA_{jk}$ - Modal constant of the r^{th} mode relating two points j and k
$\mathbf{B}$ - System matrix ($N \cdot m^{-1}$)
C_B - Shaker body damping ($N \cdot s \cdot m^{-1}$)
C_C - Shaker coil damping ($N \cdot s \cdot m^{-1}$)
C_S - Shaker support damping ($N \cdot s \cdot m^{-1}$)
C_T - Coupling torsional stiffness ($m \cdot rad^{-1}$)
C_t - Sensor capacitance (F)
C_c - Cable capacitance (F)
C_f - Feedback capacitance (F)
$\mathbf{C}$ - Viscous damping matrix ($N \cdot s \cdot m^{-1}$)
D - Mean diameter (m)
E - Young's modulus ($N \cdot m^{-2}$)
F - Force (N)
$\mathbf{F}$ - Force matrix (N)
$F(j)$ - Fourier transform at frequency j (no unit)
$F_k(j\omega)$ - k^{th} force vector (N)
F_a - Bearing load axial force (N)
F_{ai} - Axial cutting force of the i^{th} helical flute (N)
F_{ix} - Cutting force of the i^{th} helical flute in the X-direction (N)
F_{iy} - Cutting force of the i^{th} helical flute in the Y-direction (N)
F_r - Bearing load radial force (N) (Chapter 5)
F_r - Radial cutting force (N) (Chapter 6)
F_{ri} - Radial cutting force of the i^{th} helical flute (N)
F_{bs} - Ballscrew axial force (N)
F_{bsn} - Ballscrew nut axial force (N)
F_c - Cutting force (N)
F_f - Feed cutting force (N)
F_n - Normal cutting force (N)
F_{vf} - Rotor and load viscous friction ($N \cdot m \cdot s$)
F_s - Shear cutting force (N)
F_t - Tangential cutting force (N)
F_{ti} - Tangential cutting force of the i^{th} helical flute(N)
F_u - Friction force between the chip and the tool's rake face (N)
F_v - Normal force acting on the tool's rake face (N)

F_x - Total cutting force component in the X-direction (N)

F_y - Total cutting force component in the X-direction (N)

F_z - Total cutting force component in the Z-direction (N)

$F(\omega)$ - Force input in frequency domain (N)

G - Shear modulus of rigidity ($N \cdot m^{-2}$)

G_{xx}^{c} - Transfer function of the cutting tool in the X-direction ($m \cdot N^{-1}$)

G_{yy}^{c} - Transfer function of the cutting tool in the Y-direction ($m \cdot N^{-1}$)

G_{xx}^{w} - Transfer function of the workpiece in the X-direction ($m \cdot N^{-1}$)

G_{yy}^{w} - Transfer function of the workpiece in the Y-direction ($m \cdot N^{-1}$)

$\hat{G}_{FF}$ - Auto power spectrum (Watt)

$\hat{G}_{FX}$ - Cross power spectrum (Watt)

$H(\omega)$ - Transfer function ($m \cdot N^{-1}$)

$H_k(s)$ - Transfer function of the k^{th} mode ($m \cdot N^{-1}$)

$\mathbf{H}$ - Hysteretic damping matrix ($N \cdot s \cdot m^{-1}$)

$\mathbf{H}(s)$ - Transfer matrix ($m \cdot N^{-1}$)

H_{Cq} - Quadrature current controller transfer function ($V \cdot A^{-1}$)

H_{Cd} - Direct current controller transfer function ($V \cdot A^{-1}$)

H_{jk} - Transfer function element between point k and j ($m \cdot N^{-1}$)

H_t - Theoretical transfer function ($m \cdot N^{-1}$)

H_V - Velocity controller transfer function ($N \cdot m \cdot s \cdot rad^{-1}$)

H_P - Position controller transfer function ($rad \cdot s^{-1} \cdot m^{-1}$)

H_t^m - Measured transfer function ($m \cdot N^{-1}$)

J - Inertia ($kg \cdot m^2$)

J_1 - Front hub and coupling load inertia ($kg \cdot m^2$)

J_2 - Back hub and coupling load inertia ($kg \cdot m^2$)

J_3 - Ballscrew middle load inertia ($kg \cdot m^2$)

J_4 - Ballscrew end load inertia ($kg \cdot m^2$)

J_τ - Polar moment of inertia (m^4)

$\mathbf{K}$ - Stiffness matrix ($N \cdot m^{-1}$)

$K(\omega)$ - Dynamic stiffness ($N \cdot m^{-1}$)

K_1 - Motor shaft torsional stiffness ($N \cdot m \cdot rad^{-1}$)

K_2 - Coupling torsional stiffness ($N \cdot m \cdot rad^{-1}$)

K_3 - Ballscrew 1 torsional stiffness ($N \cdot m \cdot rad^{-1}$)

K_4 - Ballscrew 2 torsional stiffness ($N \cdot m \cdot rad^{-1}$)

K_5 - Ballscrew nut axial stiffness ($N \cdot m^{-1}$)

K_6 - Table axial stiffness ($N \cdot m^{-1}$)

K_{bs} - Ballscrew axial stiffness ($N \cdot m^{-1}$)

K_f - Coefficient of feed cutting force ($N \cdot mm^{-2}$)

K_{iC} - Current controller integral constant ($V \cdot A^{-1}$)

K_{iV} - Velocity controller integral constant ($N \cdot m \cdot s \cdot rad^{-1}$)

K_{pC} - Current controller proportional constant ($V \cdot A^{-1}$)

K_{pV} - Velocity controller proportional constant ($N \cdot m \cdot s \cdot rad^{-1}$)

K_s - Ballscrew axial stiffness ($N \cdot m^{-1}$) (Chapter 5)

K_s - Tangential cutting force coefficient ($J \cdot m^{-3}$) (Chapter 6)

K_t - Coefficient of tangential cutting force ($N \cdot mm^{-2}$)

K_v - Velocity gain factor ($m \cdot min^{-1} \cdot mm^{-1}$)

K_B - Shaker body stiffness ($N \cdot m^{-1}$)

K_C - Shaker coil stiffness ($N \cdot m^{-1}$)

K_S - Shaker support stiffness ($N \cdot m^{-1}$)

K_{jk}^{r} - Modal stiffness of the r^{th} mode

L - Inductance (H) (Chapter 3)

L - Distance between thrust bearing and nut centre of gravity (m) (Chapter 5)

L_q - q-axis inductance (H)

L_d - d-axis inductance (H)

M_{jk}^{r} - Modal mass of the r^{th} mode

M - Spectrum amplitude (no unit)

M_B - Shaker body mass (kg)

M_C - Shaker coil mass (kg)

M_D - Test device mass (kg)

M_T - Shaker table mass (kg)

N - Number of samples (no unit)

$\mathbf{M}$ - Mass matrix (kg)

$M(\omega)$ - Apparent mass (kg)

$P_{AN/LN}$ - Maximum generated power (kW)

P - Parameter (no unit) (Chapter 8)

$\mathbf{P}$ - Parameter matrix (no unit) (Chapter 8)

P - Power (Watt)
P_s - Power dissipated on the primary shear area (Watt)
P_t - Total energy dissipated in the cutting process (Watt)
P_u - Power dissipated in the secondary shear area (Watt)
Q - Amplitude increase factor
R - Resistance (Ohm) (Chapter 5)
R - Tool radius (m) (Chapter 6)
R - Response (no unit) (Chapter 8)
$\mathbf{R}$ - Response matrix (no unit) (Chapter 8)
R_t - Time constant resistance (Ohm)
R_i - Insulation resistance (Ohm) (Chapter 5)
R_i - Actual cutting radius of the i^{th} tooth (m) (Chapter 6)
R_i' - Cutting radius of the i^{th} tooth considering the run-out (m)
$\mathbf{S}$ - Sensitivity matrix (no unit)
$\hat{S}_{FF}$ - Power spectrum of the excitation point
$\hat{S}_{FX}$ - Power spectrum of the excitation and response points
S - Sensitivity (no unit)
S_R - Reference accelerometer sensitivity (Volt·s^2·m^{-1})
S_T - Sensitivity of accelerometer under test (Volt·s^2·m^{-1})
T_{0f} - Load-free frictional torque (N·mm)
T_{1f} - Load-dependent frictional torque (N·mm)
T - Torque (N·m)
T_c - Coupling torque (N·m)
T_e - Electromagnetic torque (N·m)
T_f - Friction torque (N·m)
T_m - Shaft mechanical Torque (N·m)
T_{max} - Ballscrew maximum torque (N·m)
T_N - Motor rated torque (N·m)
T_{Saddle} - Saddle reaction torque (N·m)
T_{MShaft} - Motor shaft reaction torque (N·m)
T_{bs2} - Ballscrew 2 reaction torque (N·m)
T_{bsm} - Ballscrew Middle reaction torque (N·m)
T_{bsn} - Ballscrew Nut reaction torque (N·m)
ΔT_u - Heat generated by the cutting in the secondary shear area (°C)
V - Workpiece feed velocity (m·s^{-1})
V_c - Chip velocity on the rake face (m·s^{-1})
V_s - Workpiece shear velocity (m·s^{-1})
V_o - Output voltage (Volt)
V_R - Reference voltage (Volt)
V_T - Readout device voltage (Volt)
V_x - Displacement due to cutting force in the X-direction (μm)
V_y - Displacement due to cutting force in the Y-direction (μm)
G_{FF} - Auto power spectrum
$W(n)$ - Windowing weight
$\mathbf{X}$ - Displacement matrix (m)
X - Axial load factor (No unit) (Chapter 5)
X - 2D surface profile (m) (Chapter 6)
X_k - k^{th} displacement vector (m)
X_B - Shaker body displacement (m)
X_C - Shaker coil displacement (m)
X_T - Shaker table displacement (m)
$X(\omega)$ - Displacement response in frequency domain (m)
$\dot{X}_B$ - Shaker body velocity (m·s^{-1})
$\dot{X}_C$ - Shaker coil velocity (m·s^{-1})
$\dot{X}_T$ - Shaker table velocity (m·s^{-1})
$\ddot{X}_B$ - Shaker body acceleration (m·s^{-2})
$\ddot{X}_C$ - Shaker coil acceleration (m·s^{-2})
$\ddot{X}_T$ - Shaker table acceleration (m·s^{-2})
$\mathbf{Y}$ - Vector of measurement data
Y - 2D surface profile (Chapter 6)
Y_i - 2D surface profile for the i^{th} flute
$Y(\omega)$ - Mobility (s·kg^{-1})
$Z_m(\omega)$ - Mechanical impedance (kg·s^{-1})

Chapter 1. INTRODUCTION

The modern manufacturing industry characterised by competitiveness and profitability calls for a realignment of businesses, involving comprehensive process optimisation and short turnaround time without compromising product quality. A recent survey [1] reveals that modern Computer Numerically Controlled (CNC) machine tools have been increasingly utilised in the manufacture of high accuracy components and zero defect production. The report shows that the production of CNC machines tools by the top 31 producing countries in 2004 has increased by 23%.

Excess vibration during machining processes has been known to generate negative effects including dimensional inaccuracy, poor surface finish, accelerated cutting tool wear and even tool breakage. Therefore, supervising techniques for fault detection, vibration monitoring, and acoustic emission are essential for effective preventive maintenance strategies, which contribute to the development of high-speed applications to inspect the condition and performance of the equipment.

The research on automated, faster and more accurate systems for vibration monitoring and analysis is an ongoing process and the existing systems are still less reliable than human analysts. The systems accuracy depends on how well the rules are defined and there are always exceptions that defy the rules. Consequently, the tendency is to build automatic expert systems that combine the data analysed by various modules with case-based reasoning and start after a pre-defined condition has been reached. In addition, a more integrated machine control and monitoring system can be developed by consolidating the recent findings from various domains, such as condition based maintenance with costing, control engineering and instrumentation, energy management, computer modelling, and design of advanced mechanics.

Unwanted vibration in a machining process originates from various internal and external sources: inferior drive performance, unsound structural dynamic properties, inadequate machine support, unsuitable cutting tool selection, excessive cutting speed, and inappropriate workpiece material. The vibration can manifest in cutting and non-cutting conditions as chatter, unusual noise or other abnormal machining process behaviour. Various standards (such as ISO 10816-1 [2]) assess the extent of the phenomenon, although the specifications are generally intended for machine health monitoring with respect to machine reliability and safety. Other related standards, such as for machined surface finish, can also be combined to reveal and quantify the source and effect of unwanted vibration in more detail.

1.1. Drive system performance

Greater flexibility, reduced wear and maintenance, shortened design, commissioning and changeover times are obtained by implementing the mechatronics concept, which is a discipline involving the integration of mechanical, electrical and software engineering. Modern digital drives are built on this concept and combine intelligent motion control with simple functionality incorporating advanced features (space vector modulation, high-resolution synchronous serial interface, incremental encoder feedback interfaces etc.) to improve motor speed and smoothness of motion. The drives performance is boosted by faster speeds with lower switching losses and harmonics, high-resolution absolute position data while trimming costs.

The actual trends in servo drives are decentralised drives (located next to the motor, more flexible and reliable) and smart drives (intelligent servo drives with integrated position control capabilities). These are easy to set up, cost effective (eliminate the need for separate motion controllers or Programmable Logic Controllers), offering good performance, and fitting well into modular motion control systems.

The increasing complexity of machines with growing numbers of axes and capability of high-speed machining processes encourage interest and investment in the technology. Academic and industrial researchers have used computer modelling and analysis to overcome previous technical difficulties (keeping the drive cool, avoiding the transfer of heat and vibration from the motor or other rotating components, etc.). The modelling of a machine tool drive system describes the behaviour of various control loops as a set of mathematical equations for the investigation and, ultimately, improvement of its dynamic performance. It plays an important part in the investigation of machine tool vibration due to the presence of rotational / traverse accelerations and velocities of mechanical components. The vibration generated in these components coupled with the machine's structural dynamics defines the machine tool dynamic behaviour.

The CNC machine tools are ***hybrid systems*** comprising continuous and discrete elements. Therefore, the energy conversion and dissipating elements (motors, gears, bearings etc.) are represented by lumped models, while energy–transporting elements (ball-screws) are analysed as distributed realisations. The model contains explicit damping factors, non-linearities (backlash and Coulomb friction) and the effects of moving mass, velocity and positional gains, and control loop time constants. The combination of these dynamic elements and parameters over the distributed load achieves a more realistic dynamic performance compared

to the previous models. The model allows the identification of the vibration error sources within the machine and the various elements influence on the drive performance.

1.2. Structural dynamics properties

The ***structural dynamics*** of the machine tool elements is a major factor affecting the machine vibration characteristics. The material choice for structural elements influences significantly the machine damping characteristics. The use of polymer concrete materials for the machine base and smart materials for mechanical structures are examples of techniques utilised to improve the machine vibration characteristics by structural dynamic enhancements. The vibration isolation capabilities of the machine support influence the transmissibility of external vibration to cutting components, thus indirectly affecting the workpiece quality. Therefore, the study of the machine tool structural dynamic characteristics through modelling and experiments becomes an essential analytical tool.

The ***Finite Element Method*** (FEM) is generally employed for modelling the structural dynamic properties by utilising specialised software (ABAQUS, ANSYS, Nastran, FEMLAB, etc.). Various algorithms are available to perform the meshing process (the division of a structure into a finite number of smaller elements with individual mass, stiffness, and other relevant properties), such as DeLaunay triangulation, paving and mapped methods. The generated elements are checked for conformity to certain requirements (aspect ratio, minimum and maximum angle, etc.) to produce robust and accurate solutions.

The FEM has been progressing significantly in recent years due to the advancement of computational hardware and software technologies. The advent of 32- and 64-bit computer processors and the development of FEM software to exploit the instruction sets enable faster analysis of more complex and accurate models. The inter-operability between FEM and solid modelling software (Pro/ENGINEER, CATIA, SolidWorks, AutoCAD, etc.) has also improved, increasing the FEM analysis flexibility and accuracy.

The analytical results of structural dynamic models are normally validated using the ***experimental modal analysis*** technique (modal testing). The dynamic forces introduced to the machine structure are applied via electro-mechanical shakers and / or instrumented hammers. The dynamic response is then measured by piezoelectric accelerometers or Laser Doppler Vibrometer (LDV) and converted into Frequency Response Function (FRF) data. A dynamic signal analyser is employed to control the disturbance forces, measure the dynamic response of the structure, and process the experimental data. Single- or Multi-Degree-of-Freedom (SDOF or MDOF) curve-fitting algorithms are then employed to extract the structural modal

parameters (natural frequencies, damping factors and mode shapes) from the measured data. Multiple data from one or more experiments (Single-Input Multi-Output (SIMO) or Multi-Input Multi-Output (MIMO) analysis) can be analysed simultaneously using the global curve fitting techniques in order to produce more accurate modal parameter estimations.

Accurate experimental modal analysis results are paramount in order to produce good estimations of the modal parameters. To obtain such results, comprehensive knowledge of the appropriate equipment selection, experimental configurations and signal conditioning is required. The measurement devices must be able to prevent both signal aliasing and leakage as well as yield high signal-to-noise ratio and frequency resolution. The driving point (excitation location) selection in the experimental setup influences the frequency bandwidth significantly. In addition, the placement of a heavy excitation device can alter the measured results considerably as described in this report by comparing suspended and machine-tool-worktable-supported shaker configurations. As a result, a good practice guideline for experimental modal analysis is compiled in this report.

1.3. Machining process modelling

The ***cutting forces*** of the machining process introduce disturbances to both the drive system and structural elements and may lead to excessive vibration and poor surface finish. Academic and industrial researchers have paid a special attention to the development of accurate and reliable machining process models in recent years. The techniques used traditionally in industry are based on past experience, extensive experimentation, and trial-and-error. Thus, they are time consuming, expensive and lack a rigorous scientific basis. In addition, modern industry calls for simultaneous engineering of products and the machining process, and, thus, more comprehensive models have to be developed. The models should be capable of reliably predicting a wide range of performance measures (cutting forces, dimensional and form errors, surface finish, cutting process stability, the occurrence of chatter, etc.) for various machining processes such as turning, face milling, boring, end milling, drilling, etc.

Several fundamental mechanics of machining processes should be included in the dimensional cutting process models, such as:

- Analytical relationship between the fundamental parameters governing the cutting process (flank wear geometry, material shear flow stress, shear angle, friction coefficients, tool geometry, basic force system defined on the shear plane and flank wear land, etc.);

- Quantitative effects of the wearing of metal-cutting tools by cutting forces – considering hardness of cutting tool material and tool wear geometry aiding in the selection of processes, fixtures, and product dimensions;
- Material constitutive models – containing strain, strain rate and temperature from orthogonal machining tests based a new shear zone model;
- Thermo-mechanical models of machining processes – generate coupled solutions of plastic deformation and thermal field based on temperature dependent material properties and adaptive meshing;
- Tool-chip interface temperature analysis and its relationship with machining parameters, workpiece temperature analysis by finite difference models and other methods, etc.

These validated mathematical models could contribute to the enhancement of machining process design and analysis in different ways:

- Establish optimal cutting conditions;
- Design efficient tooling, fixtures and select the appropriate cutting tools;
- Enable automatic generation and verification of NC programs.

Cutting forces can be modelled with sufficient accuracy by using the ***orthogonal cutting*** theory where the cutting edge is assumed as perpendicular to the tool-workpiece motion direction. The simplified solution regarding the formation of a two-dimensional plane strain deformation process does not take into account the side spreading of the cut material. Thus, the equations determining the constituent forces in the primary, secondary and tertiary deformation zones are simplified. The more accurate and complex modelling technique of the cutting forces is the ***oblique cutting*** approach when the presence of the cutting edge angle is considered. The strain deformation process is represented in three-dimensional plane (shear, normal and velocity plane). Various methods (minimum energy, maximum shear stress principles) are employed to predict the shear angle magnitude used for the cutting force modelling.

The theoretical and experimental studies use two approaches to determine the cutting force models for various cutting processes (orthogonal / oblique milling, turning, drilling):

1. ***Mechanistic force models*** – assume that the cutting forces are proportional to the uncut chip area. The specific cutting energy (relates the proportionality between cutting geometry and conditions under the given tool-workpiece materials combination) is determined by calibration. However, additional calibration tests or new methodologies to account for the ***change*** in rake face geometry are necessary due to effects on the cutting coefficients. The additional calibration tests are undesirable so the mechanistic approach

must be extended to include the chip-control tools without the need of additional calibration tests.

2. ***Finite element based models*** – based on experimental results obtained when clamping force and cutting force along tool path are loaded. This could be included in a mathematical optimisation model which shows promise of improving the quality of machined products based on the optimised fixture design and set-up. Various techniques (Eulerian, Lagrangian or Arbitrary Eulerian Lagrangian) with implicit or dynamic explicit solutions are used in conjunction with adaptive meshing or automatic re-meshing to simulate continuous, serrated or shear localized and segmented chip formation observed when cutting metals. The cutting tools always could have round and/or chamfered edges to represent realistic tool geometry.

The metal cutting process variables have an enormous influence on the integrity and quality of the machined workpiece. An accurate determination of temperature, strain, strain rate and residual stress fields during metal machining necessitates an investigation into the formation of residual stresses, micro-hardness and microstructure in the machined workpiece surfaces during orthogonal metal cutting. The deduction of the resultant hardness field, microstructure distribution and surface properties should consider the underlying physics of thermo-mechanical processing of the machined layer at multiple length scales.

Information on the influence of machine tool vibration on the surface finish can be extracted from the surface measurement data through the appropriate selections of the surface parameters. The advance in ***3D surface topography*** measurement and parameter extraction techniques greatly improves the analysis of machine tool vibration effect on the surface finish. The impact of the cutting forces on the workpiece creates a new surface whose characteristics depend on the forces and various dynamic and static factors, such as the cutting tool-workpiece vibration, structural vibration and tool wear. The machined surface analysis with appropriate wavelength filtering and parameterisation techniques will reveal the influence of these factors on the surface finish quality. Measurement methods of the surface finish have improved dramatically over the years from the manual technique of running a fingernail across the surface to fully automatic 3D surface topography. It is also the same in the surface measurement analysis methods, where the development of ***wavelet technology*** has matured and the standardisation of new parameters for surface characteristics is aggressively pursued [201].

1.4. Vibration control techniques

A successful investigation of a machine tool ***vibration minimisation technique*** must consider all those aforementioned factors. The differences in the drive system and structural dynamics will determine whether the vibration of the system can be minimised, unaffected or even magnified by a particular compensation system. The investigation into cutting force modelling and 3D surface characterisation of the machined surface further assists the determination of the required strategy. Vibration error reduction techniques can be broadly divided into ***passive*** and ***active*** methods. The ***passive methods*** reduce the vibration through the modification of the structural properties using various methods such as additions or removals of structural elements and modifications of the structural support. This change either shifts the natural frequencies of the structure out of the operating ranges, or dissipates more kinetic energy lowering the vibration level at the particular frequencies. The technique is normally achieved through the investigations of FEM models utilising the Structural Dynamic Modification (SDM) analysis of the structure's material properties. On the other hand, ***active vibration correction techniques*** apply an opposite force or displacement using an actuator attached to the structure against the vibration measured by sensors. The correcting action can be achieved externally, such as by employing piezo-electric actuators to apply the compensation force, or internally, for example by utilising the machine tool drives to offset the workpiece displacement.

Recent investigations have produced vibration reduction techniques which are the combination of the passive and active methods:

- ***Semi-active vibration control*** techniques - the compensation is transmitted from the active vibration control system to the structure through a passive system attached to the structure;
- ***Hybrid vibration control*** techniques - the active vibration control system applies the compensation directly into the structure and into the passive vibration control system simultaneously.

The modifications of machine tool damping, mass and stiffness properties by a passive vibration control system can be performed through structural design change or by the application of passive energy dissipation device (PED) into systems difficult to be structurally modified. The second method uses the tuned mass damper (TMD) system for large structures such as buildings and bridges. The method is applied to turning machines by adding mass to the structure or by changing its stiffness through the application of force using piezoelectric

actuators. The introduction of smart structures (magneto- and electro-rheological fluid, magneto-strictive materials and visco-elastic polymer, etc.) has also opened an avenue into the implementation of structural vibration suppression techniques through active mechanical property control.

1.5. Aim

The aim of this research project is to investigate the vibration induced errors of a vertical machining centre under dynamic conditions. The investigation will involve detailed practical and analytical studies as listed in the objectives.

1.6. Objectives

To achieve the aim of the project, the methodology was defined by dividing the tasks into a set of objectives as follows:

- Familiarisation with a wide range of metrology and vibration assessment equipment and the analysis of measured data;
- Structural dynamics investigation of the machine tool in order to identify its vibration modes using experimental modal analysis;
- Machine tool axis modelling allowing the study of the various drive element contribution to machine vibration using a MATLAB/Simulink package;
- Identification of the machining conditions under which vibrations can develop and grow based on measured data during cutting tests;
- Use of 3D surface topography measurements to correlate measured machine vibration with surface finish and to predict excitation modes;
- Analytical modelling of the machine structural dynamics using Finite Element Analysis (FEA);
- Investigation of a passive technique that may be used to widen non-vibrational machining envelopes by employing parametric structural analysis, surface characterisation, including a review of other possible methods.

1.7. Research strategies and thesis organisation

The investigation of machine tool vibration is a complex subject requiring a multi-disciplinary approach. It involves the identification and analysis of both the vibration sources and characteristics (structural dynamics, drive system performance and cutting force generation) as well as its effects (surface finish, tool wear, chatter, etc). An experimental modal analysis

study is required to measure the dynamic properties of the machine structure. The results are then employed to validate and update an FEA model of the machine tool structure.

The ***passive vibration correction technique*** developed in this study is based on a parametric study of the validated model to determine possible structural modifications which could improve the machine vibration characteristics. The best possible vibration correction scenario is determined by various simulation exercises employing a wide range of damping, stiffness or mass properties for the machine structure. The availability and suitability of existing experimental methods for this process are also reviewed and examined.

The dynamic behaviour of the digital feed drives employed in the machine tool under the investigation is represented by hybrid models with distributed load, explicit damping coefficients, backlash and friction. The use of digital filters and other additional functions in the controller is also modelled to determine the dynamic response of the drive system with respect to the mechanical load. The vibration characteristics of the closed loop for the current, velocity and position control and their influence on the overall machine vibration are examined. The hybrid models are implemented in Simulink and validated against the experimental results. The possibilities of including the digital drives in closed loop for ***active vibration control*** are also explored.

The study of the relationship between the cutting forces, machine vibration, structural dynamics and workpiece surface finish represents a significant part of this investigation. The research into the cutting process modelling and its associated parameters is an on-going process in an EPSRC project to develop "Novel Metrology-Based Control Algorithm for Precision Manufacture" [3], in which the author was also involved. One academic collaborator (Leeds Metropolitan University) developed a dynamic model for the cutting process taking into consideration the cutting forces, chip thickness, cutting energy, surface topography, surface roughness and tool wear.

The author examines the behaviour of the machine tool during various machining processes and employs the experimental modal analysis to determine the cutting component vibration modes and transfer functions. These modes (especially at low frequencies) considerably influence the surface finish of the machined workpiece. Therefore, the author worked closely with the Surface Characterisation research group within the University of Huddersfield, in order to determine the theoretical and practical approaches of identifying the parameters from the surface characterisation. The morphological features of the workpiece surface produced by the cutting process are accurately examined by the second generation of bi-orthogonal wavelet (lifting scheme) developed by the Surface characterisation group.

The surface analysis based on the 3D surface topography employing the wavelet techniques is performed to measure and quantify the surface profile with respect to the dynamic behaviour of the machine structure, the servo drives and the dynamic cutting process model. The main conclusions of the EPSRC project are included in this thesis.

The main contribution to knowledge of this study is the production of a comprehensive analysis on the different contributing factors affecting the machine vibration behaviour, which include the ***machine tool structural dynamic properties***, the ***drive system performance***, and the ***machining process effects***. The machine tool ***structural dynamic investigation*** covers both experimental and analytical studies, and aims to determine the suitable vibration control methods through the passive technique. The produced outcomes include the identification of various experimental configurations and their applications through the compilation of a report on the good practice of machine tool structural dynamic measurements. The analytical study contributes into the creation of an accurate dynamic model of the machine structure by employing solid design, FEA analysis, and multi-functional CAE software for correlation analyses. In addition, a sensitivity analysis of the machine structural dynamic behaviour using the CAE software produces a parametric map of the structural element vibration characteristics to changes in the mechanical properties. This result can be utilised as the basis for the development of a vibration control technique via the passive method.

A ***computer model of the machine tool drive*** based on the hybrid technique is formulated in this study and contributes to knowledge with the introduction of a new method of representing the digital current control loop utilising the power system blockset and field-oriented control strategy. Analytical and experimental techniques are devised to validate the drive system's position, velocity and current control loops utilising the deterministic and non-deterministic signals sourced from the internal machine drive system functions. This single axis model is employed to investigate the proof-of-concept of utilising the drive system as the means of applying an active vibration control technique.

Vibration models of the cutting tool and workpiece were formulated in this study and contribute into the development of a machining dynamics model with a collaborating institution. The completed model encompasses the cutting tool and workpiece vibration transfer functions, cutting force generation and surface finish prediction. The model represents the mechanistic forces and displacement of the workpiece and cutting tool in a machining process and is, therefore, useful for this study to predict the level of generated vibrations. A series of machining trials are assembled to validate the model where the predicted cutting force are compared against measured data obtained using dynamometer and

the predicted displacements are evaluated against the measured vibrations measured using the accelerometers. In addition, the predicted surface finish is validated against the machined surface 3D topography characterisation utilising the lifting wavelet scheme.

The remainder of the thesis is divided into the following chapters.

Chapter 2 contains a critical review of the literature pertaining to the relevant and up-to-date investigations into machine tool accuracy, vibration analysis, feed drive modelling and identification techniques, experimental modal analysis, metal cutting process modelling, 3D surface topography, and vibration reduction techniques.

Chapter 3 discusses the theoretical fundamentals and existing measurement techniques for the experimental modal analysis. An in-depth review of the existing equipment is carried out, including the principle of operations and the calibration techniques. The chapter also discusses the strengths and weaknesses of the current techniques for the basis of improving the experimental method adopted in the investigation.

Chapter 4 presents the experimental modal analysis by the application of two methods (shaker placed on the worktable and suspended on a crane) are analysed. The benefits and pitfalls of each method for determining the machine's structural dynamic properties are reviewed. Several guidelines for accurate practical applications of these techniques are presented.

Chapter 5 focuses on the development of hybrid models for the digital drives of the machine tool under investigation. The models of the closed loops for the current, velocity and position control contain lumped parameter representations of the digital controller, power converter and permanent magnet synchronous motor. The mechanical load is modelled as distributed elements, which consider the damping coefficients, backlash and friction. The hybrid models are implemented in Simulink and the simulated results for step and Pseudo Random Binary Signal (PRBS) inputs compare well with the measured machine responses.

Chapter 6 analyses the correlation between the dynamic cutting forces, vibration and surface waviness. The development of cutting process models (encompassing cutting forces, vibration, thermal and wear models) is presented with the emphasis on orthogonal and oblique cutting theories. The machining dynamic models contain the parameters determined by an experimental modal analysis investigation of the machine's cutting components. Various cutting trial results (including three-dimensional surface topography and cutting force measurements) are employed to verify the predicted outputs of the models.

Chapter 7 presents the investigation into the modelling of the machine's structural dynamic behaviour using the FEA technique. The optimal structural model was developed and updated

by employing the parametric exercise of the measured results obtained from the experimental modal analysis. The geometrical model development using the Pro/ENGINEER package and the meshing type selections in the FEA pre-processor software (FEMGV) are also discussed.

Chapter 8 contains a comprehensive analysis of the vibration control techniques investigated in the study. The SDM technique applied in order to establish an optimum passive vibration correction solution is discussed. The possibilities of applying an active passive vibration reduction technique by utilising the machine's control loops via the investigation of the hybrid models is also presented.

Finally, ***Chapter 9*** summarises the most important points achieved in the investigation and presents the conclusions obtained the study. In addition, suggestions for further work based on the findings are presented.

The next chapter contains a critical review of various references in research areas associated with the vibration investigation, underlining the strong points and limitations of the previous and up-to-date studies.

Chapter 2. LITERATURE REVIEW

2.1. Machine tool accuracy

Ford [4] expressed that machine tool accuracy depends on various internal and external factors, including the structural static and dynamic properties, drive system performance, environmental influence and user expertise. The ever-increasing demand for machine tool accuracy and the potential cost benefit could only be achieved through the combined application of ***error avoidance, error measurement*** and ***error compensation techniques***. The error avoidance practice was normally undertaken by machine tool builders during the machine design, manufacture and assembly. The effort was carried out in order to minimise the constituent errors at source and to increase both the general positioning accuracy and repeatability of the machine tool. The error measurement and error compensation techniques come into action to quantify and minimise further the repeatable residual errors in order to produce accuracy values unachievable previously using the error avoidance technique only.

The ***error avoidance technique*** is exemplified in a report by AMTRI [5] which provides suggestions of high performance materials for machine tool structural elements (bed, column, head, saddle, and table) in order to increase machine accuracy. Various types of material (ferrous metals and alloys, hydraulic and epoxy concretes, ceramics, plastics, fibre and reinforced composites) were presented, including the conformities to specific criteria, such as high damping and stiffness properties. The error avoidance technique by the utilisation of linear motion guideways for machine tools was demonstrated by Furukawa and Moronuki [6]. It was shown that the friction at the slide-base interface for machine tool linear axes was greatly reduced and that common problems existing in the conventional slide designs, such as the low friction liner deformation, could be eliminated. Likewise, the error avoidance practice can be extended to other machine tool elements and properties, such as motion control performance, kinematic design and thermal stability for increased accuracy, reduced vibration level and higher machining speed.

Machine tool accuracy is determined from the machine tool's constituent errors which can be obtained using various ***error measurement techniques***. Chatterjee [7] summarised these constituent errors into two groups: quasi-static and dynamic. ***Quasi-static errors***, which account for 70% of the total machine tool errors, occur very slowly with time and are related to the machine's structure and configuration. They consist of the geometric errors, static loading and thermal effects. Based on the analysis of an extensive amount of thermal data, Bryan [8] stated that the thermal effect itself might account for 40-70% of the machining

error. ***Dynamic error*** occurrences, on the other hand, depend greatly on the machine's operating conditions and include machine tool vibration, chatter, spindle deflection, thermal effects and controller errors.

Okafor and Ertekin [9] stated that one of the most important aspects of modern machine tool performance is the ***volumetric accuracy*** which is defined as the maximum value of the ***volumetric errors*** in the working volume of the machine. The volumetric error at any point in the working volume is defined as the vector sum of the total axial geometric displacement error of the three reference axes at that point. The volumetric error in a working space of a machine tool can be ***measured directly*** using artefacts with known dimensions or by ***synthesis*** from the measured constituent errors. The direct measurement technique of volumetric error was demonstrated by Silva and Burdekin [10] employing a modular space frame as the artefact. It was performed on a Co-ordinate Measuring Machine (CMM) but could be extended easily to machine tools employed with touch-trigger probes. Another direct measurement technique was the triangulation and single socket methods shown by Wang and Ehmann [11, 12]. The technique employed telescoping ball-bars to measure a number of points in the working volume and determine the associated volumetric errors. The direct volumetric error measurement technique is simple to perform but time-consuming and prone to the thermal error. On the other hand, the alternative method of volumetric error synthesis has been carried out by employing mathematical calculations exclusively or as combinations with other measurement techniques. The Precision Engineering Centre at The University of Huddersfield [13] developed the Error Simulation Program (ESP) software to synthesise the volumetric errors of a given machine tool from its constituent elements. It was developed as part of two European CRAFT projects [14, 15] and capable of evaluating the volumetric errors of various different machine configurations (3 –axis vertical milling centre and gantry machines, 5–axis machine tools). Okafor and Ertekin [9] presented a synthesis method to calculate the volumetric errors of a vertical milling machine from its constituent errors by employing the rigid body kinematics and small angle approximation. The developed error model synthesises both the geometric and thermal errors using homogeneous matrix transformations of the axis slides and is utilised to derive the resultant volumetric error vectors at the tool-workpiece interface. Lei and Hsu [16, 17] developed a volumetric error measurement technique using the combined technique of a volumetric error measurement device (3D probe-ball) and a reduced error model. The device was utilised to measure the overall position errors of 5-axis machine tools, whereas the model was employed to identify

the link errors (rotary axis block, main spindle block and tool holder) normally immeasurable using the laser interferometry.

The construction of very accurate machines through the error avoidance technique alone can be very expensive. The achievable accuracy is also limited by some factors which cannot be completely accounted for in the detailed design stage, such as the thermal and cutting force deformations. Therefore, the application of the ***error compensation*** practice in addition to the error avoidance technique can provide the solution of delivering the expected accuracy but with considerable cost benefit. The error compensation technique is designed to supplement the error avoidance technique and not to replace it. Error compensation systems can be grouped into the ***active method***, where the error measurement, calculation and correction are performed online during the machining process, and the ***pre-calibrated method***, where the correction values are calculated off-line from the measured data and then applied on-line.

Carlisle and Edson [18] described the design of an ***active compensation system*** in an advanced diamond turning machine which can also be used for the grinding process. It utilises capacitance sensors within the metrology frame to actively measure the axial or tilt movements of the face plate. The measurement data is then fed to an automatic compensation system in the CNC controller to perform any necessary correction. Fung and Yang [19] proposed a new system for on-line straightness motion error measurement and compensation of a precision linear slide. Multiple capacitive sensors were employed to provide an ideal model datum for the compensation system by separating the motion error from the slide's linear straightness profile.

Active compensation systems, while being able to provide very accurate and real-time correction, suffer from the high implementation cost and, hence, prohibitive for volume implementation. Ford [20] proposed a real-time ***pre-calibrated compensation system*** for the correction of non-random or systematic position error, residual after utilising the error avoidance technique. The author presented that pre-calibrated compensation systems, combined with good machine tool design practices could provide high accuracy as well as substantial cost benefits. A generic mathematical model of the error for a 2-axis lathe considering the effects of the geometric, thermal and load error constituents was constructed in the investigation to assist the development of the compensation algorithm. The compensation system applied the correction values to the control signals from the controller. The developed model and compensation algorithm were shown to be generic and could be implemented into all machine tool types and configurations, such as 3-axis machining centres. Postlethwaite [21] successfully developed a universal pre-calibrated electronic-based

geometric error compensation system which applied the correction on the feedback signal received by the controller from the linear position measuring devices of the translating axes. The method was shown to be very effective especially when the controller is inaccessible or incompatible with the compensation system. The compensation system was expanded by including a novel practical thermal compensation system through the development of temperature distribution and structural distortion models [22, 23]. The system was developed further by White et. al. [24] through the application of thermal sensor strips for online machine temperature measurement and the construction of the position independent and dependent thermal error compensation systems. Blake [25] improved the compensation system further by considering the non-rigid body effect and Ford et. al. [26] showed that the complete system used on a machining centre produced a geometric and thermal accuracy improvement of 10:1 and 9.3:1 respectively.

Yuan and Ni [27] outlined the development of another software-based pre-calibrated compensation implemented using a separate external computer from the machine controller. The investigation produced synthesis and mapping of the machine geometric and thermal errors, cutting force induced errors and workpiece thermal errors. The compensation control system sent the compensation signals to the controller which adjusted the cutting tool position. The compensation system on various machines was shown to achieve between a 3:1 and 10:1 accuracy improvement.

An EPSRC funded research [28] was undertaken to investigate the benefit of ***combined error avoidance and error compensation techniques*** to improve machine tool accuracy. Studies were carried out into advanced methodology in the design, assembly, error measurement and error correction practices of CNC machine tool. The obtained results provided the collaborating machine tool builders and users an advanced and generic guide to improve performance of the machine using error avoidance and error correction techniques respectively. Another research project was performed in parallel to investigate a "novel metrology-based control algorithm for precision manufacture" [3]. It was looking into the ***direct implementation*** of the geometric and thermal pre-calibrated compensation system ***into the controller*** to enable the high-speed real-time communication between the controller and the compensation system. Geometric and thermal volumetric accuracy of the machine was shown to increase by 30:1 and 10:1 respectively [29].

2.2. Machine tool vibration analysis

Vibration is a repetitive motion of an object relative to a stationary frame of reference or nominal position involving the interplay between the stored potential energy and released kinetic energy. Excessive machine tool vibration can accelerate tool wear and chipping, resulting in poor workpiece surface finish quality and even bearing damage [30]. On the other hand, excessive vibration may indicate that there is an impending failure of the machine. The typical values for the maximum vibration level of machine tool drives and mechanical elements are about 2.5 and 6.3 mm/s respectively [31].

A vibrating system can be modelled by either SDOF or MDOF method (although only a few structures could be realistically represented by an SDOF system) and is categorised into the free and forced vibration [32]. The ***free vibration*** is produced by a small displacement from the steady-state, such as by shock impulses from the ground, an axis rapid transverse or the initial engagement of the cutting tool, causing the machine to vibrate at its natural frequency. The ***forced vibration*** occurs when the system is continually displaced from its equilibrium state, such as by the floor vibration, intermittent engagement of the cutting teeth or unbalanced rotating mass, forcing the system to vibrate at the source frequency. The vibration characteristics of a machine tool depend on various aspects, such as the system's stiffness and damping factors, workpiece material and machine tool kinematic behaviour [33].

Damping is one of the most important parameters in the study of vibration and represents the dissipation of the potential and kinetic energy from the vibrating system, enabling the vibration to diminish or die out. Dimarogonas [34] presented several modelling methods for the damping effect, including viscous, hysteretic (structural), coulomb (friction) and proportional damping. The ***viscous damping model*** represents the dissipative force as proportional to the instantaneous generalised velocity, whereas the ***hysteretic damping*** simulate the energy dissipation process through internal structural deformations. The ***coulomb damping model*** depicts the energy dissipation process by the friction of two surfaces, while the ***proportional damping model*** considers the dissipated energy as directly proportional to the stiffness and/or mass of the structure.

Adhikari and Woodhouse [35] presented a method to identify non-proportional equivalent viscous damping in a structure with non-viscous damping. The damping values were obtained from the complex modes and natural frequencies produced by the conventional modal testing theory. The validity of this method was explored by applying it to measured data and it was found to be relatively successful when the damping in the structure was reasonably light.

However, when heavy damping is present in the system, other non-viscous damping models are necessary, one of which is outlined by the same authors, which is based on an exponentially decaying relaxation function [36].

Chen and You [37] proposed a time-domain based method to model hysteretic damping in MDOF and continuous systems as an extension of an earlier SDOF model [38]. Hysteresis loops initially constructed using the SDOF model were compared to those from the frequency domain and found to be equivalent as expected. The results obtained also showed that the dissipation energy for various loss factors did not depend on the excitation frequency. The same conclusions were also produced in the SDOF and continuous systems.

Kumabe and Taniguchi [39] emphasised that the vibration generated in a machining process is generally unwanted, except in ***vibration cutting*** where the cutting tool is intentionally excited at a certain frequency. This technique was proven to increase the Metal Removal Rate (MRR) and lower the cutting force. Ruud et. al. [40] presented that a dynamic instability of the machining process can lead to another type of vibration, known as ***self-excited vibration*** or ***chatter***. It occurred from the build up of structural oscillation at one its natural frequencies and could result in poor machining results, cutting tool damage and uncharacteristic noise.

A study by Lee et. al. [41] shows that the ***dynamic performance*** of a machine tool drive system greatly affects the accuracy of the finished workpiece. The high traverse speed and acceleration generated by the drive system was identified to have caused unwanted structural vibration, which subsequently affected the machining results. A practical tuning method to obtain the optimum controller parameters without sacrificing the control bandwidth was proposed and validated. The method was demonstrated to improve the contouring accuracy by the reduction of structural vibration and validated on a high-speed machine tool.

Machining errors can also be generated due to ***excessive spindle drive system vibration*** as investigated by Vafaei et. al. [42]. It was concluded that the vibration was bearing induced and generated by inherent geometric characteristics, out-of-balance assembly and interactions between rolling mating members having surface irregularities. The authors proposed a new method using autocorrelation analysis in the frequency domain with good resolution combined with windowing capability to monitor and isolate the significant causes. Another investigation into pre-process determination of optimum spindle speed was performed by Schmitz et. al. [43] to improve the material removal rates by minimising vibration at the tool point. Combined with Receptance Coupling Substructure Analysis (RCSA) and sampled audio signal analysis, a rapid identification of tool point frequency response was proposed and

validated to enable high speed machining and efficiently produce accurate workpieces. It was also demonstrated by the author that the analysis of the audio signal emitted from the machining process could be employed to determine whether excessive vibration in the form of chatter was occurring [44].

Vibration occurring in a machining process can affect the quality of the ***surface finish*** as shown by Jang et. al. [45]. The authors developed an algorithm to correlate the surface roughness and cutting vibration between the tool and workpiece in a turning process. The vibration component was obtained through relative displacement measurement using an inductance pickup device and an analogue band-pass filtering. The surface simulated from the proposed algorithm was correlated successfully against the machined surface analysis using a surface profilometer. Luo et. al. [46] reversed the principle by investigating the vibration of a cutting process to monitor the surface quality of the workpiece under a machining process. The proposed algorithm used an adaptive spline wavelet, based on the time-frequency localisation of B-spline wavelets, to extract the correlation between amplitude variation at relevant vibration frequency and surface quality. The results showed a strong correlation between the amplitude variation and measured surface quality and the algorithm was proven to be sufficiently fast for an on-line vibration analysis.

Machine tool vibration can also be influenced by the ***workpiece material properties*** as investigated by Lee et. al. [47]. A micro-plasticity model was developed in the study to predict the effect of crystallographic orientation on the shear angle, chip formation and variation of micro-cutting forces. The varying substrate crystallography of the material was shown to affect the generated micro-cutting force which led to the vibration between the cutting tool and workpiece. The simulated surface finish affected by the vibration was shown as a 3D surface topography plot and validated using measured results of a surface produced by an ultra precision machine.

Vibration due to ***environmental factors*** also influences the machining accuracy and surface finish quality, especially in ultra precision machining processes or light structures. One of the most well known types of environmentally induced vibration is the ***micro-vibration***, which occurs at frequencies below 1 kHz and at a low amplitude, as described by Aglietti et. al. [48]. A state-space formulation was developed in this study to model a prototype system subject to micro-vibration. A Lagrange-Rayleigh-Ritz (LRR) approach was then utilised to design a feedback control system using piezoelectric actuators for this scheme. Tagawa et. al. [49] developed an accurate measurement system for micro vibration by utilising the control system of a micro-vibration testing device. The equipment used air

actuators to deploy the correction with three different controller types: dual model matching, on-line feed-forward and off-line feed-forward.

The machine tool structural dynamic behaviour contributes very significantly towards its vibration performance when subjected to either external or internal excitation. Various methods exist to identify the structural dynamic properties of mechanical system, such as one presented by Ramsey [50]. This method was markedly advantageous because it is based on the Laplace domain analysis of the frequency response, which can be readily acquired using modern dynamic signal analysers. The method was applied on a structure to identify its dynamic properties, which were subsequently utilised in the verification and updating of its mathematical model, the identification of the weak structural locations, and the investigation of the vibration sources and paths.

2.3. Experimental and theoretical modal analysis

Experimental modal analysis is a technique to identify the dynamic behaviour of a structure in terms of the modal parameters, *i.e.* the natural frequencies, damping ratios and mode shapes, by using experiments. It consists of two distinct steps, *i.e.* ***data acquisition*** and ***analysis***, which must conform to certain rules and principles in order to obtain accurate parameters. They include the proper experimental procedures, such as structural support, excitation technique, signal conditioning and sensor placement [51, 52], as well as the appropriate data analysis, such as data filtering, model size determination and curve-fitting algorithm selection [53].

Experimental modal analysis can be performed using a single reference (SIMO) or multiple references (MIMO) method. The single reference method uses a single fixed input, such as an electro-mechanical shaker, to excite the structure and measures its response on various locations. The multiple reference method employs more than one excitation input into the structure and obtains its measurement response at various points on the structure. Schwarz and Richardson [54] presented that the SIMO methods have been so far one of the most widely used methods in experimental modal analysis as the balance between accuracy and required test period was fulfilled.

The simplest and least time consuming method is the ***instrumented hammer testing*** as described by Pavic et. al. [55], who applied it on very heavy structures with low natural frequencies, closely spaced vibration modes and relatively high damping. This method employs a hammer equipped with force sensor at its tip to record the impact force and one or more accelerometers to measure the response of the structure. The response and input signals

are transmitted to a dynamic signal analyser, where Fast Fourier Transform (FFT) is performed to obtain the FRF. For heavy structures, where the response of the system is very short, a soft-tipped hammer should be used to concentrate the excitation energy in the low frequency region. The impact force magnitude should not be too strong or too weak and an appropriate measurement bandwidth should be selected to produce good resolution FRF, essential for identification of closely spaced vibration modes.

Although hammer testing is very fast to perform, it should be carried out carefully to avoid an incomplete FRF data matrix, especially when performing three-dimensional modal analysis as pointed out by Avitabile [56]. This situation can appear when a roving hammer hitting the measurement points at a single direction is used to excite the structure and a fixed tri-axial accelerometer is used to measure the response. This will result in blank spaces in the data rows and creates a diagonal response matrix instead, which prevents the modal parameters estimation process to be performed. The best alternative method to this is by hitting the structure at a single point and by moving the tri-axial accelerometer along the measurement points instead. This will produce a row matrix from which the modal parameters can be extracted.

Døssing [57] explained fully the experimental requirements for a successful ***single shaker excitation*** method. Several aspects need to be satisfied for a successful data acquisition, including the selection on the number of degree of freedom (DOF), suspension of the structure, choice of excitation, position/connection of exciter to the structure, and mounting of the transducers. The detailed requirements for these aspects are as follows:

- The number of DOF points selected should be able to represent the structure adequately.
- The structure should be suspended elastically to establish a free-free condition and to obtain high-quality results. However, some compromises are acceptable as long as the structure support does not affect the results greatly.
- Random excitation signal should be used to cover the low frequency range and linearise any non-linear behaviour.
- The excitation location should be at the corner where both symmetric and asymmetric modes exhibit the maximum motion in order to obtain the best response of the structure. The force transducer should be stud mounted on the structure and the excitation force should be transferred via a stinger to minimise unwanted force direction.
- A suitable technique for mounting the response transducers should be selected according to the frequency range. For a test with a bandwidth of 0 – 1 kHz, a magnetic mount is sufficient to obtain respectable results.

Ramsey [58] outlined several additional techniques to excite a structure and measure the response to obtain its dynamic properties by using the experimental modal analysis technique with FFT dynamic signal analysers. ***Random***, ***transient*** and ***sinusoidal excitation techniques*** with their variants were discussed in-depth and a comparison of the modal parameter accuracies obtained by using these stimuli was made. The variants of the random excitation techniques discussed were the pure-random, pseudo-random and periodic-random whereas the transient excitations included impact testing and step relaxation methods. It was concluded that pure-random and periodic-random stimuli would give the best result, especially for non-linear systems, due to the use of the averaging technique.

The most advanced and complex method of experimental modal analysis is the ***multi-shaker excitation test***, or MIMO method, as demonstrated by Shye et. al. [59]. The advantages of modal testing using multiple references were presented in the study using both theoretical and experimental approaches. These include the effective removal of non-linearities for testing large structures, producing a more consistent set of modal parameters. Multiple reference impact testing is also more effective to treat local modes and structures with uni-directional modes as well as reducing the likelihood of missed modes. In the theoretical approach, a frequency-domain multi-reference curve fitter, with added terms to account for out-of-band modes, was shown to correctly identify repeated modes. This case could not be solved successfully, either theoretically or practically, with single reference methods.

Phillips and Allemang [60] provided an overview into the availability and merit of several excitation, averaging and signal processing techniques for MIMO experimental modal analyses. The excitation sources for this method were almost exclusively shakers and the study gave an in-depth comparison of various input signals to drive the shakers. They included traditional signal types such as pure-random, periodic-random, pseudo-random, and burst-random, as well as ***more advanced excitation signals***, such as burst-cyclic random, slow-random, MOOZ (Source Frequency Range Control) random, and periodic chirps. The study considered the merit of these excitation and averaging methods as well as taking into account the damping, non-linearities, FRF models, peak to RMS (crest factor), and signal-to-noise ratio (SNR) issues. Experimental results were used to establish the important issues affecting the accuracy of the modal parameters obtained.

A number of investigations have been focussed in increasing the accuracy of modal parameters by better excitation methods for both SIMO and MIMO methods, especially for structures with non-linearities, as performed by Nessler and Deel [61]. The proposed method

utilised closed-loop proportional integral (PI) controller to regulate the RMS structural response level resulting from electromagnetic shaker excitation. It was shown that this method gave less frequency shift due to the structural non-linearities when compared to regulating the excitation force directly through the PI controller. The variation of the modal frequencies, damping and response amplitudes resulted from varying excitation force level was also minimised.

Recently, a new technique using the laser as the vibration sensor emerged rapidly for both SIMO and MIMO methods as described by Stanbridge and Ewins [62]. This technique is gaining popularity because it is non-contact and fast to perform, thus hot and unfriendly surface measurement is now a possibility. The study described a number of mode shape measurement techniques where a point over the surface of a sinusoidally excited structure was continuously scanned using a Laser Doppler Vibrometer (LDV). Its output, which was in the form of an amplitude-modulated sine wave and mode shapes, was then established in the time domain by demodulation. The LDV output was also analysed in the frequency domain producing a line spectrum with sidebands centred on the excitation frequency and spaced at the scan frequency. The sideband amplitudes gave series coefficients for the mode shape defined along the scan line. These are the Fourier coefficients for a circular scan or polynomial coefficients for a sinusoidal straight-line or area scans.

In the machine tool industry, various studies have been conducted to investigate the structural dynamic behaviour, such as by AMTRI [63]. The study involved a cutting trial to examine the cutting stability of the machine and the frequency response analysis of the structure to determine the dynamic properties by using a shaker. It was shown that the machine cutting performance was stable, thus a structural dynamic analysis could then be performed. It was carried out by securing the shaker to the worktable and the spindle, then exciting it using a random signal to simulate machine vibration due to the cutting forces measured at the tool point. The resonant frequencies were subsequently determined from the observed peaks in the response measurement graphs. The structure was further excited using sinusoidal signals at the resonant frequencies to obtain the mode shapes. It was shown that the mode shapes obtained using this method were quite accurate, which was deemed as due to the force concentration at the resonant frequencies. However, the structural parameter identification results are considered not satisfactory because the excitation force input to the table was not measured. The weight of the shaker also significantly affects the structural dynamics due to the additional mass on the structure. Ewins [64] expressed that by utilising an alternative method of suspending the shaker would produce more satisfactory results, due

to the elimination of unwanted input force sources. Another suggested method is by mounting the shaker on the structure via spring elements to absorb these forces, although this will not remove the unwanted input completely. These test procedures, where the resonant frequencies are identified and later excited using sinusoidal signals, are generally known as the ***normal testing*** as outlined by Hutin [65].

From all the experimental methods described above, Stroud [66] described that the most popular modal testing method for real structures so far is the MIMO random-excitation method, which is then followed by the SIMO random technique. The next most popular method is the normal mode, which uses multi-input tuned-sinusoidal excitation, followed by modal testing using natural ambient excitation forces, such as wind and ocean waves.

To achieve the goal of experimental modal analysis, the measurement data needs to be analysed to obtain the modal parameters through a process known as the ***modal parameter extraction*** (also called as the ***modal parameter estimation*** process). It involves curve fitting of the measured responses to an analytical model with known parameters. When a best fit is obtained, the measured system parameters are approximated to be equal to those of the analytical model. Modal parameter estimation methods are divided into two main groups, time and frequency domain, depending on the type of FRF data used in the analysis. Both methods will produce the same results, but Døssing [67] outlined that the frequency domain method is the most widely adopted technique due to several crucial factors (such as the ease of use, availability of equipment and software).

The most widely used algorithm in modal parameter extraction process is the rational fraction polynomial (RFP), with over twenty years of development behind it as described by Formenti and Richardson [68]. This algorithm was introduced initially to overcome the problems associated with least squared error parameter estimation technique. This enabled the implementation of reliable curve-fitting technique on a mini computer to obtain accurate modal parameters as implemented by the same authors [69]. The development of more advanced computing equipment raised an expectation for the development of new algorithms capable of producing more accurate results from more measurement data. Thus, the same authors [70] introduced the global rational fraction polynomial (GRFP) method to fulfil this challenge. The technique divides the curve fitting process into two steps: the estimation of the natural frequency and damping parameters from all measurement data and the calculation of the mode shape parameter for each measurement point.

Recent research has attempted to combine both methods to find more accurate modal parameter estimation as performed by Peterson and Alvin [71]. Over-determined parameters

previously obtained using the time domain Eigensystem Realisation Algorithm (ERA) model were filtered subsequently using a frequency domain curve fit algorithm to remove computational modes. The method was also shown to very tightly converge onto the poles of the structure when there is a significant increase of data. The model vectors, including the residual terms, are then determined using a linear least squares curve fit to the FRF data to determine the mode shapes.

As a summary, the experimental procedures, equipment and methods in experimental modal analysis have been changing and will continually change over the years. Essentially, all of these methods work well on simple structures, but care must be taken when performing experiments on complex structures to obtain acceptable results. The methods widely used today are those which have repeatedly demonstrated their tolerance to the complexities of real data and provided fast and accurate data acquisition as expressed by Juang [72]. The use of the experimental modal analysis technique, along with their industrial applications, trends and challenges, were outlined by Van Der Auweraer [73]. The discussion includes the utilisation of the technique in the aerospace, civil, process and automotive industries as well the main advances and practical obstacles of its applications. These comprise the issues of smart instrumentation, pre-test definition, optical transducers, in-operation modal analysis, vibro-acoustic testing, measurement principles, and parameter estimation.

The results from experimental modal analysis are usually correlated to those from finite element analysis as discussed by Taleghani and Pappa [74]. The study evaluated the use of rubber layer to reduce the vibration of rocket motor tubes made of graphite epoxy composites. The produced report compared the results obtained by experimental modal analyses using impact testing and those from an analytical model developed using Nastran FEA software. Mixed comparison results were produced in the investigation prompting further research to improve the analytical model.

A ***finite element model*** to design and build a three-axis ultra precision grinding machine was developed by Kim et. al. [75]. The machine design required the use of a high damping resin concrete bed, air spindle, high performance AC servomotor and CNC controller. The study proposed a new method to calculate the stiffness of the machine by modelling the linear motion guides and ballscrew stiffness using the three-dimensional finite-element method. A prototype machine was built based on the model and a comparison was made between the calculated results and the experimental results. It was found that the modelling method gives accurate prediction of the machine tool stiffness. An experimental modal analysis was also performed to find the first natural frequency mode shape of the machine tool worktable to

validate with the calculated results. The FEA model was subsequently updated to match the measured results.

2.4. Cutting force modelling and surface characterisation

Cutting forces can sometimes be modelled sufficiently accurately by using the simple orthogonal approach, where the cutting edge is assumed to be perpendicular to the cutting direction. Merchant [76] proposed a mechanistic force method to solve this approach by assuming the shear zone as a thin plate. Palmer and Oxley [77] and Lee and Shaffer [78] gave a different solution by representing the deformation zone as a thick plane. All methods produce sufficiently accurate solutions when careful consideration is paid to the type of cutting process.

Rubenstein [79, 80] proposed an improved approach to Merchant's shear zone concept by calculating the stress distribution at the lower boundary of the deformation zone. This approach solves the limitation of the previous concept by removing the requirement for prior knowledge of the chip-tool friction. The proposed analysis was supported by the cutting data obtained by using carbon tetrachloride as a cutting fluid.

A recent investigation by Toropov and Ko [81] proposed a new slip-line solution with unrestricted rake face to enhance the accuracy of orthogonal cutting theory. The theory of plasticity was utilised to analyse the metal chip formation and the slip-line solution was selected specifically as the metal deformation process was considered as a special case of plastic flow. The theoretical results obtained with the suggested method was verified with experimental data and showed good correspondence.

A more accurate cutting model is produced when the acute cutting angle is considered as explained by Shamoto and Altintas [82]. This approach uses the same principle of mechanistic force decomposition as the orthogonal cutting approach, with the addition of the cutting edge angle. Three reference planes are required to describe the force components, generating various angles for the analysis purpose, such as the normal and oblique shear angle, the chip flow angle, the normal rake and force angle and the oblique force angle.

Venuvinod and Jin [83] proposed an extension to Merchant's deformation zone concept by applying the 'no friction prior knowledge' solution suggested by Rubenstein in orthogonal metal cutting processes. The proposed method was able to predict the thrust force component when the force-velocity collinearity principle between the tangential force was satisfied at the contact surface, although such an event is rarely observed in empirical data. The model also

demonstrated that the non-uniformity of the normal stress distribution on the true lower boundary was significant.

Liu et. al. [84] proposed a new cutting model with improved dynamic characteristics for peripheral milling with helical end mills. This model is based on the oblique cutting theory and accounts for the chip thickness to enable accurate representation of the cutting forces generated in the machining process. The coefficients used in this investigation were estimated from the cutting trial results performed on a previous investigation. This approach was successfully verified for general peripheral milling processes when the feed rate is higher than the equivalent linear speed of the rotational velocity between adjacent cutting teeth.

Li et. al. [85] developed a machining simulation system, which was based on the hybrid-machining model utilising the predictive machining theory and neural network models. The system employed the machining theory to predict the cutting characteristics including generated force components, temperature, chip geometry, tool wear, surface roughness and chip breakability. The neural network model was used to predict difficult-to-model machining characteristics as well as to provide a bridge from the machining theory to the required predictions of tool wear, surface roughness and chip breakability. The whole system was validated using the results from experimental machining tests to verify all the component models in the system.

The effect of the cutting force on the surface contour as part of a complete machining system was discussed by Cheng and Chin [86]. The system consisted of the effects of the trajectory planning by the controller, the machine structural dynamic and the cutting process itself. Several cutting parameters were analysed including surface curvature, feed-rate and cutting depth, and it was found that the contour error was most affected by the machining feed-rate.

Shirase and Altintas [87] presented a cutting force mechanistic model and its effect on dimensional surface error generation. It was demonstrated that the variable pitch cutters reduce the dimensional surface errors due to different chip loads on each of the flutes, where the excess surface errors generated by larger chip load flutes were removed by the following smaller flutes. The model also considered the stiffness of the spindle, tool holder, collet and cutter and it was verified by experimental studies.

A dynamic model of the surface roughness generated by a face milling process was proposed by Baek et. al. [88]. The mathematical model considered the static and dynamic components of the cutting process, including the edge profile, cutter run-out, cutting forces and structural vibration. These factors were taken into account to calculate the relative

displacement of the workpiece and cutting tool in order to predict the surface roughness. The model was validated by employing experimental findings which showed vibration marks due to the forced vibration caused by the cutting process.

The 3D surface characterisation of the machined surface can be utilised to investigate micro-fractures, residual damage, and surface roughness as presented by Yin et. al. [89]. A Silicon Carbide substrate was placed under a grinding process and the optical micrographs of the surface finish obtained was able to show the investigated surface characteristics. In another study, Cheung et. al. [90] proposed a data dependent systems analysis method to perform surface characterisation of Aluminium-Silicon Carbide metal matrix composites in ultra-precision machining process. The method was validated using a series of machining processes and the measured surface finish indicated good correlation between the characteristics of the wavelength components produced by the method and the surface generation mechanisms. This method provided an approach to resolve the shortcomings of the current spectrum analysis method in the characterisation of surface properties such as pits and cracks.

Jiang et. al. [91] proposed a new technique to perform 3D surface characterisation by using the ***lifting wavelet***. This method utilised filtering and lifting factors using a cubic spline interpolation in three stages with no destruction to the filtering boundary. A series of experiments was performed to demonstrate the feasibility and applicability of this method to determine the roughness, waviness and the multi-scalar topographical features of the produced surfaces.

A study into areal surface characterisation utilising the ***bi-orthogonal spline wavelet*** was performed by Xiao et. al. [92]. This method was constructed using the lifting algorithm and it was shown to be capable of producing linear phase shift, finite pulse response and perfect reconstruction of various bio-engineering surfaces produced in a series of experimental studies.

2.5. Machine tool feed drive modelling and system identification

To describe the behaviour of the system under different conditions, an accurate mathematical model is required. The modelling of CNC machine tool feed drives is therefore an important step to develop a vibration control system and in designing high performance CNC machine tools as expressed by Altintas [94]. The model should accurately represent the feed drive system which consists of three cascaded closed loops for acceleration, velocity and position control. This model can be used to accurately describe the response of the system under

various conditions, which might be different from the original design. A successful development of a machine tool drive model must also include accurate dynamic parameter identification as well as the identification of non-linear behaviour of the system.

Ford [95] presented a ***lumped parameter modelling method*** of a machine tool, where the load inertia is referred to the motor and obtained from the sum of all component inertia in the mechanical load of a machine tool, including the table, saddle, ballscrew and frictional load. The model describes the system behaviour as a set of ordinary differential equations over the considered bandwidth, including a detailed example of mathematical block diagrams built for Pulse Width Modulation (PWM) fed brush and brush-less DC drive systems.

A ***modular approach*** into drive system modelling was investigated by Pislaru et. al. [96], where the system's mechanical and electrical components are modelled as modules interacting with each other. This enables the mathematical representation of the force producing interaction between the modules to be described, thus producing more accurate model. The model component modification is also more practical due to the ability to exchange its components easily without altering the whole model.

An extension of this approach was investigated by the same author to model an analogue machine tool drive system by employing the ***hybrid modelling technique*** with distributed load, explicit damping coefficient, backlash and friction [97]. The developed model was shown to be capable of simulating the influence of ***non-linear effects*** as well as representing the interaction between the ***continuous*** and ***discrete elements***. The non-linearities incorporated into the model include the resistance of the motor and ballscrew bearings and seals, the damping in the motor shaft and ballscrew, and the friction and damping of the drive belt. The ballscrew was modelled as nine modular units with apportioned rigidity whereas the load is assumed to be in the centre of the ballscrew length. The developed model also considers the effect of the moving mass, velocity and positional gains, and control loop time constants to achieve a more realistic dynamic performance.

The parameters of the hybrid model were obtained from the manufacturer's catalogue as well as from the measurement results. The natural frequencies, damping coefficients and mode shapes of the drive system were calculated based on a parameter identification technique developed by Holroyd et. al. [98]. It is based on the eigenvalue method by the quadratic form approximation of the kinetic and potential energies to determine the undamped natural frequencies and vibration modes. A ***generalised eigenvalue method*** is then employed to determine the damping of the system, which is assumed to be viscous. The same authors [99] have previously developed a parameter identification technique and Simulink model of

the coulomb friction in addition to the viscous damping. It was found that the friction tended to generate vibration as well as dissipating the energy and that the simulation results compared fairly well to the measurement data.

The hybrid modelling of the ballscrew as modular units was based on the investigation by Bartlett and Whalley [100] on the power transmission dynamic performance of long drive shafts, including the clutch and load. A model of the torsional system was developed using the hybrid distributed-lumped method to account for the expected apportioned dynamic behaviour. It represents the shaft as a distributed element whereas the clutch and load as lumped components. The simulation results containing the radial and torsional oscillation were compared to existing clutch judder measurement results.

Various other machine tool dynamic models have also been developed, such as the ***Transmission Line Matrix*** (TLM) method, which was investigated by Castaneda [101]. This technique represents the interaction between the machine components using their electrical equivalents operating on an electrical transmission line. This interaction between machine tool drive elements is represented using the wave propagation between the various components in the equivalent electrical circuit.

Holroyd [102] developed a ballscrew dynamic model by representing the system as a set of smaller mass, spring and damper elements with moving nut between the masses. A set of matrices containing these variables are then implemented into equations expressing the interaction between the various sections of the ballscrew and the nuts. The behaviour of the system is defined using the eigenvalues and eigenvectors produced from the model.

Ebrahimi and Whalley [103] presented a lumped modelling technique of a machine tool feed drive which included the inertia of the rotary parts and table, plus the friction reaction torques and forces acting on these elements. The effects of non-linearities, such as coulomb friction and backlash were included in the model by utilising the measured values. A comparison between the linear and non-linear models is made and it shows that the effect of the non-linearities in the model is significant. This model is used to study the performance of a system when one or more of its parameters are adjusted.

In another approach to create a model of the feed drive system of a CNC machine tool, Erkorkmaz and Altintas [104] presented a method to identify the dynamic parameters and the friction characteristics. The dynamic parameters were obtained using a classical servo model together with the estimation of inertia and viscous friction through an unbiased least squares scheme. This is performed by observing the disturbance torque through a Kalman filter while simultaneously jogging the axes under closed loop control at various speeds.

Using an open-architecture controller, Rober and Shin [105] developed two milling machine models for single- and 3-axis systems. Identification methods were performed on the single axis system by injecting sinusoidal inputs to obtain the frequency response of the systems. The results were then used to develop an adaptive model to maintain a constant cutting force. Another model was built for the three-axis system to minimise the position and contour error of a two-dimension milled workpiece. The model algorithms were implemented through the open architecture controller and were successfully interfaced to the drive systems.

Blaszkowski et. al. [106] introduced a new identification technique for the servo drives of machine tools and robots using a time domain matrix approach in which the models of the system dynamics were estimated by ***deconvolution*** in discrete time. This identification technique was shown to be applicable for deterministic non-linear and time-varying systems as well as stochastic systems. The method was validated using a DC servomotor of a machine tool moving its table and found to be accurate and useful.

Pislaru et. al. [107] presented a novel use of the ***continuous wavelet transform*** (CWT) to identify the resonance frequencies and damping ratios of CNC machine tool drives. The transform employs the Morlet wavelet as the mother wavelet to obtain the best performance in the frequency and time measurement as determined by Heizenberg's uncertainty principle. A comparison to the classical method of the transmissibility relation at resonance was made in identifying the modal parameters of simulated data. It was found that the technique was able to accurately detect the parameter values of the weak components in the presence of strong noise and non-stationary processes. The technique, however, still requires a manual intervention to determine the amplitude peaks from the CWT graph. Thus, further work to automatically detect these occurrences is necessary to enable the practical implementations of the technique in industrial environment, such as for condition monitoring purposes.

2.6. Correction of vibration induced errors

To resolve vibration problems in machining, two main techniques are available: ***active*** and ***passive vibration control.*** In active vibration control, energy is fed into the machining process via actuators to control the vibration level by opposing the force or displacement. On the other hand, a passive vibration control system draws energy from the system by using damping components or prevents any external vibration from entering by isolating the system. Spencer and Soong [108] described these vibration reduction techniques as well as the more recent developments of advanced vibration compensation techniques utilising a combination of the passive and active methods. These techniques are known as the semi-active and hybrid

vibration reduction techniques, which differ in the attachment of the active vibration compensation system to the structure. The most widely utilised technique amongst the hybrid vibration control systems is the Hybrid Mass Damper (HMD), where an active control actuator is used to control the natural motion of a passive Tuned Mass Damper (TMD). Other types of techniques discussed by the author were the Active Mass Damper (AMD), which is used when the available space was constrained, and the semi-active damper systems, which include variable orifice fluid damper and magneto/electro-rheological fluid systems.

Garg and Anderson [109] described thoroughly the recent advances in the research of innovative vibration control techniques for civilian and armed force applications by employing effective and economical active structural damping methods. These include sophisticated techniques such as ***smart structures***, ***surface damping treatments*** and ***passive energy dissipation circuits***. The smart structural vibration control was implemented using an active-passive piezoelectric network and active constrained layer approaches, whereas the surface damping methods were implemented by using micro-cellular foams and active standoff constrained layer. The passive energy dissipation circuit was assembled from a number of state-switchable vibration absorbers, so that its stiffness can be altered to enable ***adaptive vibration control*** of multiple disturbance frequencies. These methods are mostly fragmented and based on the linearity principle, thus further investigations are required to create an integrated solution, capable of solving system non-linearities.

The results of system identification using the modal analysis technique can also be used for the purpose of vibration control as shown for example by Stöbener et. al. [110]. The mode shapes obtained from an experimental modal analysis were transformed into a closed analytical formulation and the modal input and output factors were extracted for the sensors and actuators. These factors were implemented into a modal state-space formulation, which results in a modal filter for the point sensor array and a re-transformation filter for the segmented actuator patches. In this study, Poly-Vinylidene fluoride (PVDF) foil was used for sensors and actuators. The modal controller was implemented on a digital controller board and the proposed concept was validated using a series of experimental tests.

Ramsey et. al. [111] outlined that the modal parameters obtained from an experimental study can also be utilised for an analytical work using the structural dynamic modification (SDM) technique to study the structure's behaviour under different configurations. In addition, the parameters could also be used in a finite element analysis investigation for the same purpose. Using the new and optimum set of parameters and FEA model, a structural change could then be simulated to study the new structural behaviour, without having to

perform an expensive and unnecessary work. An optimum solution of passive vibration control by modifying the structure could thus be achieved.

Ismail and Ziaei [112] proposed a new method of controlling vibration in a machining process by implementing an on-line spindle speed ramping controller combined with an off-line adjustment of the feed rate. The controller continually adjusts the spindle speed and monitors the acoustic intensity of the cutting process to detect any sign on chatter vibration with respect to a prepared stability chart.

One type of active vibration control was implemented by Martinez et. al. [113] to suppress self-excited chatter in a milling machine and to damp vibration caused by rigid body stepping in a photolithography platen. It uses structurally embedded piezoelectric actuators to provide high frequency, force and stiffness along with reasonable stroke limit. Finite element modelling and analysis of the structures were used to locate and size the actuators as well as to perform further simulations of the system response.

Choudhury et. al. [114] developed another system of ***on-line active vibration control*** for a turning machine by using piezoelectric actuators. It uses bifurcated optical fibre assemblies to measure the relative vibration between the workpiece and the cutting tool, which is then phase shifted, amplified and fed back to the piezoelectric actuators supporting the tool. These actuators then generate an equal and opposite force to stabilise the vibration. Prior to the implementation of the system, a mathematical modelling of the system was performed to simulate the relationship between the feedback parameter and the control system output. It was also used to establish the relationship between the cutting parameters and the response of the system and its stability. The experimental results and mathematical model indicate a significant improvement in the dynamic characteristics of the machine.

An on-line monitoring and active suppression of chatter vibration in end milling was proposed by Tarng and Li [115]. It uses the spectrum of the cutting force obtained from a table type dynamometer through a data acquisition board to identify the self-excited vibration. It is detected when the peak of the spectrum does not correspond to the cutter rotation frequency or the tooth frequency. A control algorithm based on the dynamics of the cutting process and the machine's structure then calculates the necessary adjustment of the spindle speed to reduce the vibration.

Stammers and Sireteanu [116] proposed a semi-active vibration control of machines using dry friction damping. It is called semi-active because it uses active damper employing the dry friction and a passive spring. A mathematical model was built to simulate the system containing the dry friction, the spring and sequential damping used to minimise the force

transmitted. Sequential damping, which is dependent on the displacement and velocity, is used to oppose the spring force and thus reduce the acceleration, possibly to zero, of the body compared to the passive case. It is only possible to balance the spring and damper forces when relative displacement and relative velocity have opposite sign.

In ***passive vibration control***, Marsh and Slocum [117] presented a damping method applicable to a wide range of structural geometries including machine tool bases and components. It uses viscoelastic materials embedded within the structure as opposed to being externally implemented. Modal strain energy approach was used to provide an analytical solution to the amount of damping bending modes. The experimental results of the passive vibration control system showed that energy dissipation covered a range of frequencies and amplitudes and that its implementation did not compromise the structural stiffness. It was also shown that the system could be manufactured and placed inside the structure robustly, so that its theory could predict the performance of the system accurately.

An investigation into the feasibility of polymer concrete for machine tool beds was investigated by Orak [118]. The materials investigated consisted of polyester resin and quartz filler with different ratios. Samples of the material were investigated to determine the damping characteristics and a comparison with cast iron samples was also made. It was observed that the critical damping ratio of the polymer concrete was approximately four to seven times of that of cast iron. However, the difference in ratios between the polyester resin and quartz filler of the polymer concrete showed no effect on the critical damping of the materials.

Rivin [119] presented a systematic analysis of vibratory environments along with the principles and criteria for vibration isolation. They were then used to determine the requirements for vibration isolation of four high-precision components used in precision machine tools. It was found out that the vibration isolation could be satisfied in most of the cases by properly selecting passive isolators with high damping characteristics. Only in exceptional cases where a very high standard was required were active isolation systems required. Enhanced damping of the isolators increased the natural frequencies, hence the stiffness, and consequently improved the performance of the isolators.

2.7. Summary

The machining errors induced by machine tool vibration have been shown in the studied literature to be highly influenced by the structural, drive system element and cutting process dynamics. Therefore, the accurate identification of the structural properties, the development

of a proper drive system model, and the thorough knowledge of the machining process are required in order to obtain the optimum vibration control solutions. In addition, it was shown that an accurate identification of the workpiece surface finish parameters can assist the determination of the relationship between the cutting process dynamic, machine vibration and workpiece surface finish generation. This knowledge is valuable in order to identify the machining error sources correctly from the associated measured surface parameters.

It was shown in the review that the experimental modal analysis is one of the most advanced and established methods to investigate the structural dynamic properties. The SIMO technique was shown as one of the most widely adopted since it can provide sufficiently accurate data in a reasonable length of experimental time. However, the technique can be limiting, especially if the structure is more rigid in one direction in comparison with the other directions. The input force introduced may not be sufficient in exciting structural modes in the aforementioned direction and, thus, only MIMO technique can be employed.

The study also found that the experimental modal analysis technique normally implemented in the machine tool industry was by positioning the shaker on the worktable. The configuration was found to be susceptible to error as it might introduce unmeasured force (the formation of force loop in the structure under investigation). The study also identified that one of the ideal configurations by suspending the shaker might provide a better measurement technique since the excitation force was only introduced at a single, measurable location.

The investigation into the various methods to extract the modal parameters from the measured data was also carried out. The global rational fraction polynomial (GRFP) method was identified as the most suitable for this investigation since the statistical properties of the measured data enabled an accurate estimation of the global properties of the structure (i.e. the natural frequencies). Accurate estimations of the natural frequencies would yield better estimation of the other global and local properties (the damping ratio and mode shapes). It was also found that the quality of the extracted parameters relied heavily on the measured data quality. Thus, various techniques from different literature were investigated, compiled and tested to acquire the optimum experimental practices in the field.

The investigation revealed that the FEM technique is a valuable tool in the investigation, modelling and improvement of a machine tool structural dynamic behaviour. The FEA model, validated with the experimental method, combined with structural analysis software, such as FEMtools, provided a powerful instrument into the structural dynamic behaviour

optimisation. The technique minimises the vibration-induced error by relocating the critical behaviour (such as natural frequencies) out of the operating frequencies.

The development of FEA models were investigated through numerous literature sources to combine the state of the art techniques of solid modelling, FEA pre/post-processing and numerical analysis in order to develop a very accurate FEA model. This involved the development of geometrically accurate solid model of the machine structure (using Pro/ENGINEER) and both pre- and post-processing of the FEA model (by the FEMGV) in order to generate a representative FEM analysis results. Various pre-processing techniques with fully- and semi-automatic mesh generation were researched to obtain the most optimum structural meshes and appropriate physical property assignments. The post-processing involves the extraction of the natural frequencies and mode shapes from the calculated eigenvalues and eigenvectors respectively.

The study also identified several modelling methods capable of representing the drive element dynamics where the traditional lumped parameter technique is not sufficient. It was found that the hybrid modelling technique with distributed load, explicit damping coefficient, backlash and friction was the most suitable as it was shown to represent the resonant states of the drive system accurately. The model was also shown to successfully simulate the effect of system's non-linearities as well as the interaction between the continuous and discrete elements of the drive system. A single axis model employing the technique is to be developed to demonstrate the principle of drive system element influence on the machine's resonant states.

Various machining process models based on the oblique and orthogonal cutting theories have been reviewed in this investigation. It was found that a model based on the oblique cutting theory which considers the chip thickness was sufficient to represent the cutting process dynamics. However, it was found that a machining dynamic model considering the cutting element structural dynamic effects and surface generation profiling provided better representation of the cutting and overall vibration effect. In addition, several comparison methods of simulated and measured workpiece surface finishes were studied in order to find the best technique for identification of machine's structural dynamic effect on the cutting process. It was found that the lifting wavelet technique was one of the most successful identification methods in identifying the roughness, waviness and multi-scalar topographical features of a surface.

The study of the various references also recognised that a comprehensive investigation involving various related disciplines is required in order to successfully minimise vibration-

induced errors. A combination of error measurement, avoidance and compensation was the most cost-effective solution in improving machine tool accuracy. This investigation attempts the aforementioned techniques in order to identify both the source and effect of the unwanted vibration and proposes a passive vibration reduction technique through the machine structure and drive dynamic studies. Analytical and experimental dynamic analyses are presented using the FEA study and experimental modal analysis respectively in order to identify the machine's vibrational behaviour. The proposed passive vibration reduction technique is investigated by employing a parametric study of the FEA model in order to find the optimum structural configuration. The study into the active method is performed by the investigation of a single-axis digital drive model employing the hybrid technique with distributed load, explicit damping, backlash and friction technique. Both deterministic and non-deterministic time-domain signals and frequency response analysis are utilised to validate the model and derive a precedent on the possibilities of utilising an active vibration control via the control system (digital filters) or an external device.

Having critically reviewed the relevant "state of the art" references, a comprehensive investigation into the experimental modal analysis technique to identify the structural dynamic behaviour of a machine tool is pursued in Chapter 3.

Chapter 3. THEORETICAL BACKGROUND OF MODAL ANALYSIS

Modal analysis is the study of a linear time-invariant dynamic system in terms of the natural frequencies of vibration, damping factors and structural dynamic deformation (mode shapes). These properties, also called vibration modes, can be formulated mathematically over a frequency bandwidth for a certain structure to obtain the modal model. This model can be employed to predict the behaviour of a structure as a response to an external force as well as to re-construct its structural dynamic properties (mass, stiffness and damping) from a set of measured response data. The modal analysis of a structure can be performed by two methods:

1. Computational Method

This method (also known as the ***analytical*** or ***theoretical*** modal analysis) obtains the modal model through the numerical analysis of the structural mechanical property matrices (spatial model) and is employed to predict the dynamic behaviour of the structure (see Figure 3.1.a). The finite element method (FEM) is normally employed to develop the modal model and simulate the dynamic behaviour of the structure with the response model.

2. Experimental Method

This approach (also called ***Modal Testing***) is carried out by exciting the structure appropriately, measuring its responses, and extracting the modal parameters from the measured data to obtain the modal model. Figure 3.1.b outlines the procedures involved, including the structural model development in order to reconstruct the structure's mechanical properties.

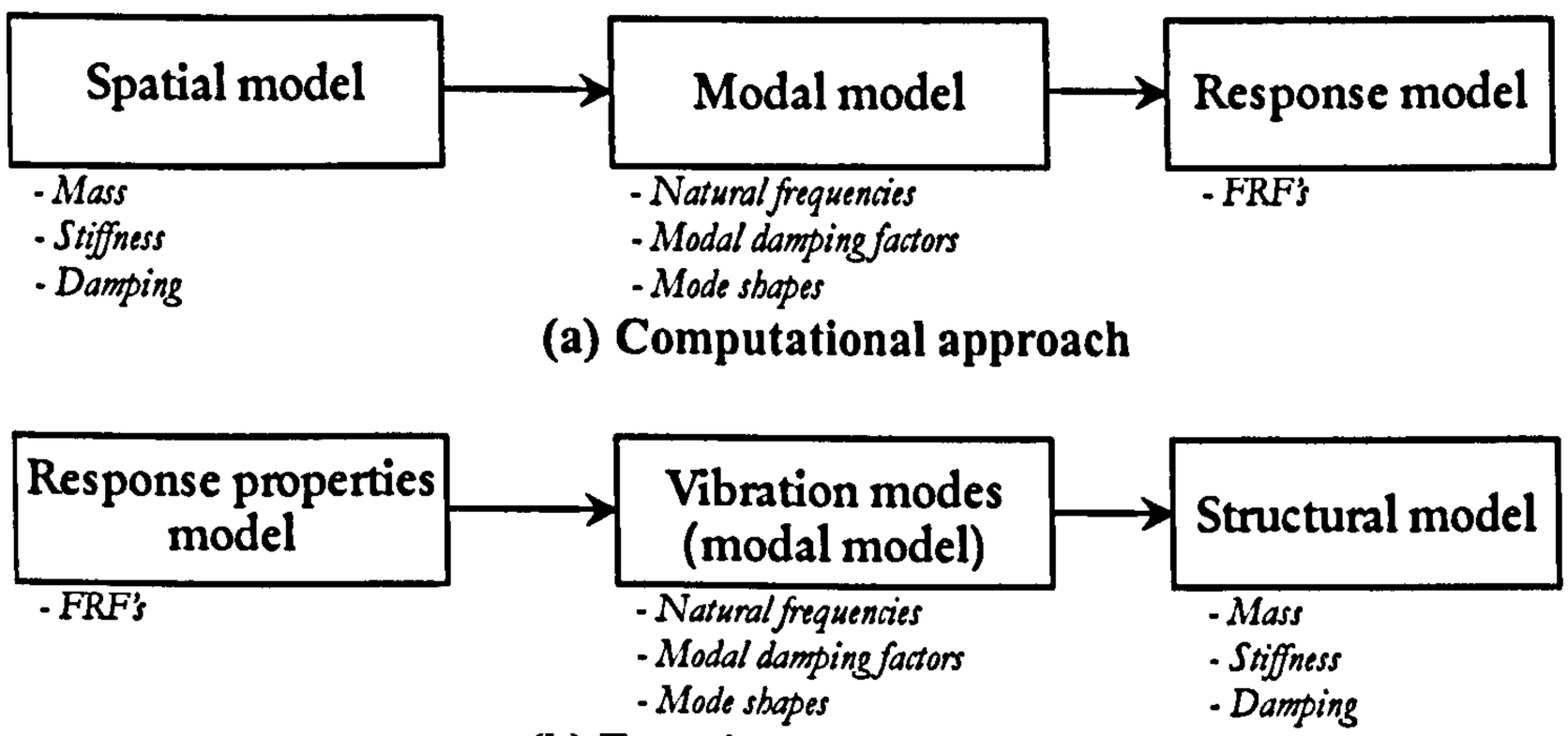

Figure 3.1. Diagram of modal analysis approaches [64]

The procedures for the computational and experimental methods are the reverse of each other. Thus, the results from a computational modal analysis should be theoretically the same as the measured FRF response of the experimental method. However, structural non-linearities,

measurement uncertainties and environmental noise are several of the factors preventing the ideal conditions to be achieved. Despite the aforementioned shortcomings, both experimental and computational methods contribute significantly towards a detailed understanding of the dynamic properties of a structure. The experimental modal analysis results provide the measured dynamic properties of the structure which can be employed to validate and update an FEA model. The model can then be utilised subsequently to predict out-of-band modes which cannot be measured directly due to various limitations, such as structural integrity, measurement device capabilities, etc. In addition, the model can be employed to aid the design, development, and evaluation of both active and passive structural vibration control systems by simulating the structural response to external or internal disturbances.

This chapter presents the mathematical formulation for modal analysis with the emphasis on the experimental method. The benefits and pitfalls of the experimental procedures to obtain the measurement data are discussed in order to obtain the most accurate data possible in the presence of non-linearities, measurement uncertainties and environmental factors. The various methods for extracting the modal parameters from the measured data with their strengths and weaknesses are also presented. The computational modal analysis application to model and simulate the structural dynamic behaviour of the machine tool under investigation is presented in more details later in Chapter 7.

3.1. Mechanical system modelling

The modelling of a mechanical system provides the necessary analytical tool to analyse the system behaviour using a set of mathematical relationships based on the system properties and applicable physics theories. The known properties of an FEA model, for instance, are the mass, stiffness, damping and geometrical definitions of the structure, whereas the system behaviour (response) includes displacement, velocity and acceleration.

The most fundamental mechanical system representation is the ***single-degree of freedom*** (SDOF) model, which consists of a mass, a spring and a damper (see Figure 3.2.a). The dynamic behaviour of this model can be mathematically represented as a second order equation by applying D'Alambert's dynamic equilibrium principle and Newton's second law of motion:

$$m\ddot{x}(t) + c\dot{x}(t) + kx(t) = f(t) \tag{3.1}$$

The behaviour of most real systems cannot be described sufficiently and accurately using this method and, thus, must employ the ***multi-degree of freedom*** (MDOF) model, which is constructed by the application of linear superposition principle of two or more SDOF models

(see Figure 3.2.b). The model's mathematical representation extends equation (3.1) by including the matrices and vectors of the sub-systems' collective properties in order to obtain the following matrix equation:

$$\mathbf{M}\ddot{\mathbf{x}} + \mathbf{C}\dot{\mathbf{x}} + \mathbf{K}\mathbf{x} = \mathbf{F} \tag{3.2}$$

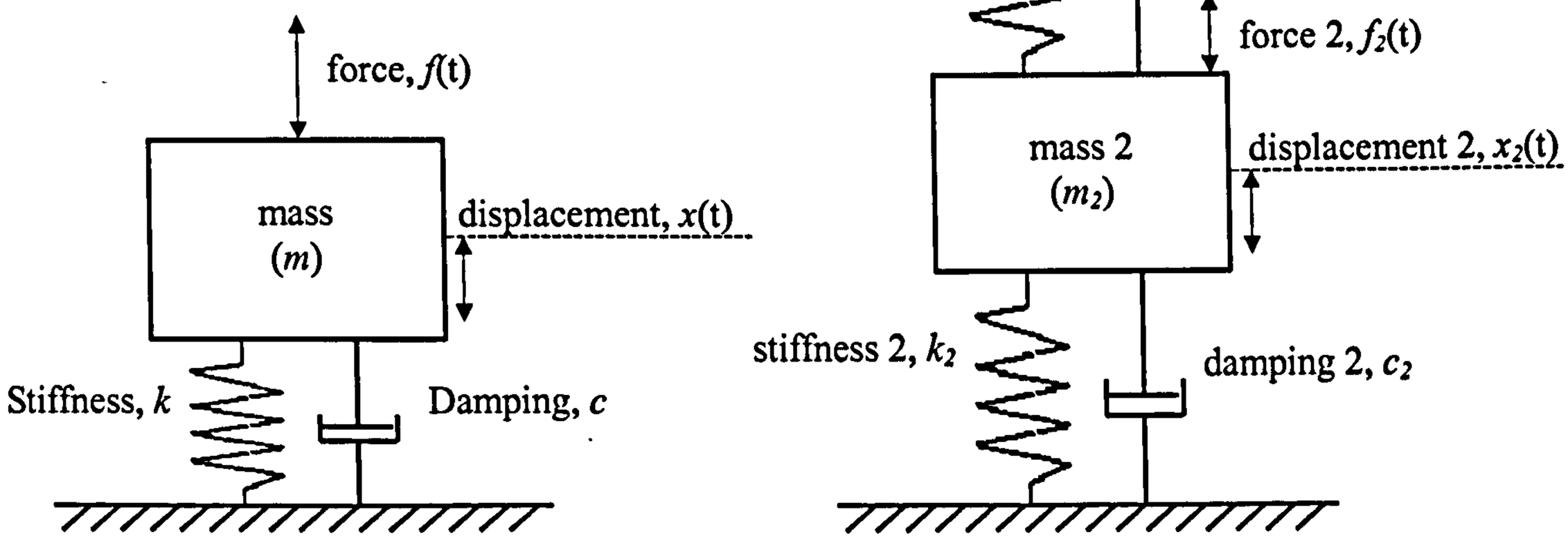

(a) Single Degree of Freedom (SDOF) Model

(b) Two Degree of Freedom Model

Figure 3.2. Diagram of single- and multi-degree of freedom models [32]

In the modelling of mechanical systems, the damping property, which describes the energy dissipation function, is the most mathematically complex parameter to model as its function varies from one system to another and can be non-linear. One of the most widely adopted models is the ***viscous damping*** where the dissipation force is directly proportional to the velocity of the system (see equation (3.3)).

$$f_c = c\dot{x} \tag{3.3}$$

This model has a fundamental shortcoming in that the damping function is influenced by the frequency, which is not always the case in real structures as suggested by Wilson [120]. This influences the modelling accuracy of certain systems whose behaviour is very sensitive to the presence of damping. Various research efforts have been undertaken to address this drawback employing different representations such as the ***hysteretic*** [37] and ***non-viscous proportional*** [121] damping models (see Table 3.1). They represent the inherent material property-induced

and mass and/or stiffness proportional energy dissipation methods respectively. These models can remove the frequency dependency of the energy dissipation method but introduce other modelling weaknesses inevitably. These include the inadequacy of the hysteretic damping to describe the transients in the structure and the remote likelihood of the proportional damping occurrence in real systems.

Damping Model	Energy Dissipation Equation
Viscous	$c\pi x^2 \omega_d$
Coulomb	$4\mu N x$
Hysteretic	$\pi k c_0 x^2$
Proportional	$(\eta m + \delta k)\ \pi x^2 \omega_d$

Table 3.1. Examples of damping models and their energy dissipation representations

An investigation by Richardson and Potter [122] shows that the damping force generated in a vibrating structure was the result of combined viscous, Coulomb and hysteretic mechanisms. However, the energy loss is attributed only by the viscous damping mechanism, whereas the other damping types only account for the system's non-linearities. Since experimental modal analysis assumes system linearity, the viscous damping model is thus considered as adequate to describe the damping mechanism in the system over a limited bandwidth. This notion is used in most experimental modal analysis studies, including this investigation, to build the structural model for the modal parameter extraction process.

The following terms are widely employed to describe the dynamic behaviour of a viscously damped system: the undamped natural frequency, the damped natural frequency, the critical damping and the damping ratio. The ***undamped natural frequency*** can be defined as the rate at which an undamped structure oscillates when it is allowed to vibrate freely following a disturbance from its normal state. When damping is present, the oscillation rate is called the ***damped natural frequency***. The ***critical damping*** is defined as the lowest value of damping required to return the system to its equilibrium without any oscillation. Finally, the ***damping ratio*** can be described as the ratio of the actual system damping to its critical damping. The mathematical representations of these properties can be described respectively as follows:

$$\omega_n = \sqrt{\frac{k}{m}} \tag{3.4}$$

$$\omega_d = \omega_n \sqrt{1-\zeta^2} \tag{3.5}$$

$$c_{cr} = 2m\omega_n = 2\sqrt{km} \tag{3.6}$$

$$\zeta = \frac{c}{c_{cr}} = \frac{c}{2m\omega_n} = \frac{c}{2\sqrt{km}} \tag{3.7}$$

For a structure where the number of DOF is huge (for instance in FEA), the use the mathematical analysis using equation (3.2) becomes very impractical and difficult to manage. Therefore, the analytical formulation is normally derived using the ***Lagrange's equation*** (3.8) which can be rapidly deployed into a computer program as demonstrated by Fertis [33] as investigated further in Chapter 7.

$$\frac{d}{dt}\frac{\partial T}{\partial q_i} - \frac{\partial T}{\partial q_i} + \frac{\partial U}{\partial q_i} - \frac{\partial W_d}{\partial q_i} = \frac{\partial W_e}{\partial q_i} \tag{3.8}$$

3.2. Theoretical basis of experimental modal analysis

Experimental modal analysis plays a very important part in the structural dynamic property studies since the ***damping parameter*** can only be accurately obtained from measured data. An approximate damping factor value can be obtained by the computational method, but only when the system is lightly damped or when the damping value does not affect the other dynamic parameters significantly. The experimental method calculates the natural frequency parameters from the measured ***resonance frequencies***, which occur when the excitation rates of the external force match the damped natural frequencies producing maximum dynamic displacement. The kinetic energy of the structure at these frequencies is at maximum and manifested in the form of structural motions known as the ***mode shapes***.

The experimental modal analysis calculates the modal parameters by employing the frequency analysis of the response and excitation force. The experimental procedures are normally carried out under closely controlled conditions to prevent damage as the measurement range can often be outside the normal operating conditions. The approach is essentially ***a system identification*** technique where the structural properties of the system can be treated as a 'black box' and determined from the measured ***transfer function*** (or ***inverse transfer function***). The technique is developed from previous types of testing such as 'Resonance Testing' and 'Mechanical Impedance Methods' and the principle behind it is summarised by Ewins [64] as follows:

$$Properties = \frac{Response}{Input} \tag{3.9}$$

One of the most important and extensively used measurands in the experimental modal analysis is the ***Frequency Response Function*** (FRF) which is defined as the ratio between the gain and phase response and a given input in the frequency domain [123]. The FRF data can

represent both the transfer function and inverse transfer function as shown in Table 3.2 as some applications can be solved more efficiently using the inverse transfer functions rather than the 'direct' transfer function.

Transfer Function		Inverse Transfer Function	
Terminology	Definition	Terminology	Definition
Accelerance, $A(\omega)$	$\frac{acceleration\,(\ddot{x})}{force\,(f)}$	Apparent mass, $M(\omega)$	$\frac{force\,(f)}{acceleration\,(\ddot{x})}$
Mobility, $Y(\omega)$	$\frac{velocity\,(\dot{x})}{force\,(f)}$	Mechanical impedance, $Z_m(\omega)$	$\frac{force\,(f)}{velocity\,(\dot{x})}$
Receptance, $\alpha(\omega)$	$\frac{displacement\,(x)}{force\,(f)}$	Dynamic stiffness, $K(\omega)$	$\frac{force\,(f)}{displacement\,(x)}$

Table 3.2. Various representations of Frequency Response Function (FRF)

The modal parameters are extracted (or estimated) from the experimental results through the ***least-squared error minimisation*** of the frequency responses of a theoretical model to the measured FRF data. The theoretical model is constructed generally using the MDOF Newtonian approach, and when a best fit is obtained, the modal parameters of the measured system and the model are considered identical. The natural frequencies and damping ratios are then calculated from the measured damped resonant frequencies which are indicated by the peaks on the FRF amplitude data. The ***residues*** from the calculation are employed subsequently to determine the mode shapes at each measurement point. The modal parameter extraction process is normally semi or fully automated using computer software, although for some very simple cases, manual graphical calculations can be more efficient.

The theoretical model for the modal parameter extraction is developed in the frequency domain based on the mathematical expressions shown in equation (3.2) considering the initial conditions (see equation (3.10)). Each vector component represents a motion at a particular point in a specific direction characterised by up to six DOF motion. This consists of the translational and rotational motions in and about the three orthogonal axes respectively.

$$s^2\mathbf{M}\mathbf{x}(s) - s\mathbf{M}\mathbf{x}(0) - \mathbf{M}\dot{\mathbf{x}}(0) + s\mathbf{C}\mathbf{x}(s) - \mathbf{C}\mathbf{x}(0) + \mathbf{K}\mathbf{x}(s) = \mathbf{F}(s) \tag{3.10}$$

Setting the initial conditions to zero:

$$\mathbf{B}(s)\mathbf{X}(s) = \mathbf{F}(s) \tag{3.11}$$

where $\mathbf{B}(s)$ is the system matrix:

$$\mathbf{B}(s) = s^2\mathbf{M} + s\mathbf{C} + \mathbf{K} \tag{3.12}$$

To find the system dynamics, the System matrix is inversed to obtain the Transfer matrix $\{\mathbf{H}(s)\}$ in order to calculate the relationship between the response and the applied forces. Thus, equation (3.11) can then be rewritten using the transfer matrix as:

$$\mathbf{X}(s) = \mathbf{H}(s)\mathbf{F}(s) \tag{3.13}$$

or in expanded form:

$$\begin{Bmatrix} x_1(j\omega) \\ x_2(j\omega) \\ x_3(j\omega) \\ \bullet \\ \bullet \end{Bmatrix} = \begin{bmatrix} \bullet & \bullet & H_{17}(j\omega) & \bullet & \bullet \\ \bullet & & H_{27}(j\omega) & & \\ \bullet & & H_{37}(j\omega) & & \\ & & \bullet & \bullet & \\ & & \bullet & & \bullet \end{bmatrix} \begin{Bmatrix} \bullet \\ \bullet \\ f_7(j\omega) \\ \bullet \\ \bullet \end{Bmatrix} \tag{3.14}$$

The transfer function elements in the Transfer matrix can be expressed as the ratio of two polynomial functions, which describe the complete dynamic properties between an input and the corresponding response DOF [124]:

$$H_k(s) = \frac{r_k}{2j(s-p_k)} + \frac{r_k^*}{2j(s-p_k^*)} \tag{3.15}$$

$$p_k = \sigma_k + j\omega_k \tag{3.16}$$

$$r_k = A_k u_k u_k^T \tag{3.17}$$

3.3. Experimental considerations

Careful considerations are required for successful experimental modal analysis, starting from the data acquisition stage up to the modal parameter extraction. The required steps for a successful experimental modal analysis are summarised as follows:

- Preparation of the structure to prevent or minimise any external influence
- Selection of the excitation system best suited to the structure
- Measurement using FFT based spectrum analyser
- Measured data post-processing to extract the modal parameters by a curve-fitting method

In addition to the requirements above, a sound theoretical basis is required to obtain accurate measurement results despite the straightforward concept shown in equation (3.9). The knowledge of some complexities frequently assumed as negligible in the theory is needed to minimise its influence and enhance the measured data quality.

(a) Non-linearities

The presence of non-linearities in a structure can be postulated if the response is not proportional to the applied force or when the addition of two excitation patterns do not follow

the superposition theory. Gloth and Sinapius [125] performed a thorough investigation into the identification procedures and the influence of non-linearities by employing swept-sine experimental modal analysis. The use of swept-sine input force produced concentrated excitation power and increased oscillation amplitude at the investigated frequencies, which is unachievable using the random signals due its broadband nature (wide frequency spread). Schoukens et. al. [126] further investigated the effects of non-linearities in the measurement results by comparing various excitation signal types. The authors found that the inverse repeated periodic random signals and the random-phase multi-sine provided the best linearised system provided that the necessary steps to minimise signal leakage was taken.

Detailed structural dynamic studies, which are largely outside of the scope of this study, find that the non-linearities can be represented by different mathematical descriptions, such as those mentioned by Dimitriadis and Cooper [127]:

- Cubic stiffness, where the spring force is proportional to the cube of displacement
- Coulomb friction, where some of damping is provided by dry friction
- Bilinear stiffness, where stiffness varies with the direction of force
- Micro-slip friction damping, where elastic and plastic deformation occur when a frictional load applied is less than that necessary to produce sliding action
- Quadratic damping, where the damping force is proportional to the square of velocity
- Backlash, where a discontinuity occurs in the displacement of a reversing motion

(b) Complex mode

Complex modes occur when phase variations are observed on the measured point DOF's as opposed to only in- and out-of-phase motions (the case with normal modes). The phenomenon is seen as travelling wave behaviour and happens predominantly on rotating structures. Non-rotational structures may also exhibit this behaviour provided the following points occur:

- Non-proportional damping distribution, which mostly occurs in systems with mechanical joints
- Two or more closely coupled modes
- Very high damping
- Repeated roots, i.e. two or more identical natural frequencies

(c) Subsequent use of the analysis results

Clear follow-up applications of the modal analysis results can assist the optimisation of the experimental procedures while still obtaining high quality data. The optimisation can include measurement point number reductions to minimise the experiment time, increased frequency

resolution to maximise the data quality and lower frequency bandwidth to accelerate the analysis speed.

Several subsequent applications of the modal testing results are:

- ***Validation and updating of a theoretical model (FEA, etc)***

Theoretical (such as FEA) models are normally validated using the experimental modal analysis results enabling further analysis of more intricate cases unsuitable for experimental techniques, such as the prediction of the structure's response to a complex excitation pattern. Accurate estimates of the natural frequencies and sufficiently detailed mode shape descriptions are required to ensure a satisfactory validation. Modal parameters with these accuracies can be achieved by covering all the frequency bandwidth of interest and measuring a sufficient number of points on the structure.

- ***Sub-structuring process***

A sub-structuring is the construction of a complex structural model from the simpler mathematical models representing its elements (sub-structures) for simplified and faster numerical analysis. The method is the most appropriate tool for the analysis of a complex structure with repeatable elements by the multiple use of the element's model. Accurate estimates of the natural frequencies, mode shape descriptions and damping factors of the repeatable element from the measured data are necessary for a successful sub-structuring process. The results must also be obtained simultaneously to consider the out-of-range modes which may be amplified when the complex structure (super-structure) is assembled.

However, the data accuracy requirements can be slightly relaxed for a variant of the process where the element models are modified slightly during the integration procedure. The modification is generally required to fine-tune the element's modal parameters to closely match pre-determined dynamic properties of the super-structure.

- ***Indirect force determination***

This method is employed to determine the input force vector where the direct measurement is impractical. It is a variation of the experimental modal analysis concept shown in equation (3.9) where the input force is the unknown variable and estimated from the modal model and the measured response. An accurate mathematical model and measured response of the structure are thus required to produce an accurate estimation of the input force.

3.4. Measurement methods

Three main functions are involved the data acquisition stage of an experimental modal analysis: structural excitation, response measurement and signal analysis. Two experimental

techniques, based on the number of the excitation and measurement points (and thus the transfer matrix size), can be employed:

1. ***Multi reference testing*** (MIMO)

The structure excitations and response measurements are performed at more than one point. This produces an m×n transfer matrix where m corresponds to the number of input points and n the number of output points. The FRF for each output-input combination is calculated to obtain the transfer function matrix as shown in equation (3.14). This method is best used if the structure or its modes of interest cannot be adequately excited from a single point, or if the structure exhibits repeated roots (very closely coupled modes).

2. ***Single reference testing*** (SIMO)

The response measurement or excitation of the structure is performed at a single reference point. An m×1 transfer matrix is generated for a single measurement point and m number of excitation points, whereas a 1×n transfer matrix is produced for a single excitation point and n number of measured output points. An example of a single reference measurement is the roving hammer technique, whereas a single reference excitation is best illustrated by single shaker excitation method. The SIMO technique generally produces better FRF quality because it is calculated directly between two points, which is not the case in the MIMO technique despite the higher oscillation amplitude. An additional advantage of the SIMO technique is a number of FRF data with different reference points can be assembled to form a MIMO data series.

The accuracy of the modal parameters obtained in the parameter extraction process entirely depends on the measured data quality. The curve-fitting algorithm always produces an estimation of the modal parameters regardless of the supplied data quality. Therefore, several aspects must be observed in the experiments to obtain high quality measurement data. They include, but not limited to, the correct data collating techniques, suitable mechanical aspects of the structure support, excitation and the appropriate signal processing of data as outlined by Døssing [57].

3.4.1. Support of the measured structure

The support of the structure under test affects directly its dynamic behaviour and the appropriate experimental procedures must be followed to obtain the accurate modal parameter estimations. Its combined mass and stiffness with the main structure govern the measured response across the frequency bandwidth. Its selection must also be reflected in the boundary

condition selection of the theoretical (FEA) model for its accurate validation using the obtained experimental results.

Two structural support methods can be utilised for an experimental modal analysis: ***free*** and ***grounded*** support. However, no experimental condition perfectly complies with the full definition for both methods and only a close approximation can be achieved as shown in Figure 3.3.

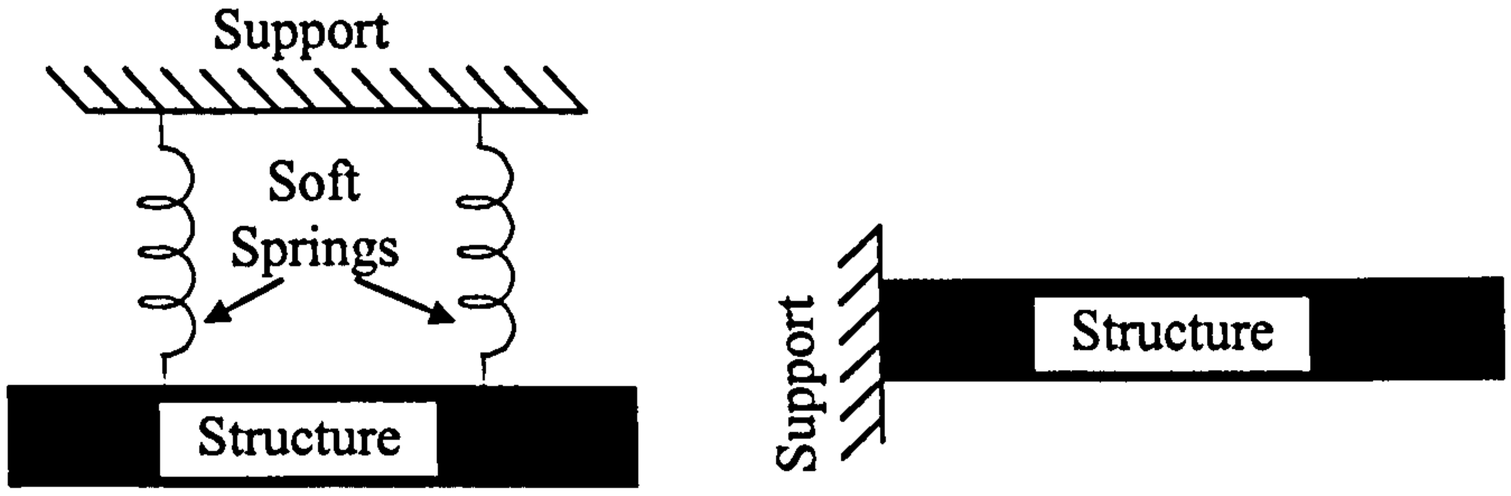

(a) Free Support Approximation (b) Grounded Support

Figure 3.3. Two types of experimental structural supports

(a) Free Support

This arrangement is achieved when the structure is not attached to the ground at any of its co-ordinates and thus is the most ideal support condition since the structure is isolated from any external influence. It can be closely approximated by supporting the structure with very soft materials or by suspending it with very soft springs as shown in Figure 3.3 (a). The supported locations on the structure should be as close as possible to its nodal points and in the normal direction to the primary vibration path in order to minimise any interference to the structure's dynamic properties. The support mechanical properties and locations must be accurately selected because they substantially affect the measured natural frequencies as highlighted by Munsi et. al. [128].

(b) Grounded Support

This condition is achieved when one or more points of the structure are rigidly attached to the ground (see Figure 3.3 (b)). Although this is the most commonly used method for real systems, it cannot be fully achieved in practice because all the bases of all structures have some degree of impedance due to their finite rigidity. Hence, the ground mobility effect should be measured over the frequency bandwidth of interest and should be much lower than the measured results at the structure. In addition, the local stiffening effect due to the grounding must be avoided because this will introduce distortion to the measurement results. This can be checked with the repeatability of the measurements by dismantling and reassembling the structure and ground construction.

3.4.2. Excitation system

This system provides an input force into the structure with a sufficient frequency bandwidth and amplitude level in order to excite the structural vibration modes of interest. Its setup must satisfy certain requirements, such as the ***connection*** to the structure, the ***driving point*** location and the ***type of excitation signals*** employed. Two main types of experimental modal analysis excitation systems:

(a) Instrumented impact hammer

The impact of this device produces an impulse force which causes the structure to vibrate. It provides a simple and fast excitation technique although repeatable results are rather difficult to obtain (especially for complex structures) due to the manual application of the force. The device usually has an interchangeable ***impact tip*** and a removable ***extra mass*** secured on the other side to increase the input force magnitude. The impact tip hardness and hammer head mass influence the excitation frequency bandwidth given by the following relationship:

$$frequency = \sqrt{\frac{contact\ stiffness}{impactor\ mass}} \tag{3.18}$$

The impulse force and the corresponding frequency bandwidth of the excitation can be seen in Figure 3.4. A soft-tipped hammer produces concentrated excitation energy in the low frequency region suitable for the measurement of heavy and short response structures, whereas a hard-tipped hammer can excite a wider frequency spectrum bandwidth. Avitabile [129] warned against using a hard-tipped hammer on every measurement because an excessively hard tip could excite the modes outside of the required frequency bandwidth and might distort the vibration modes of interest.

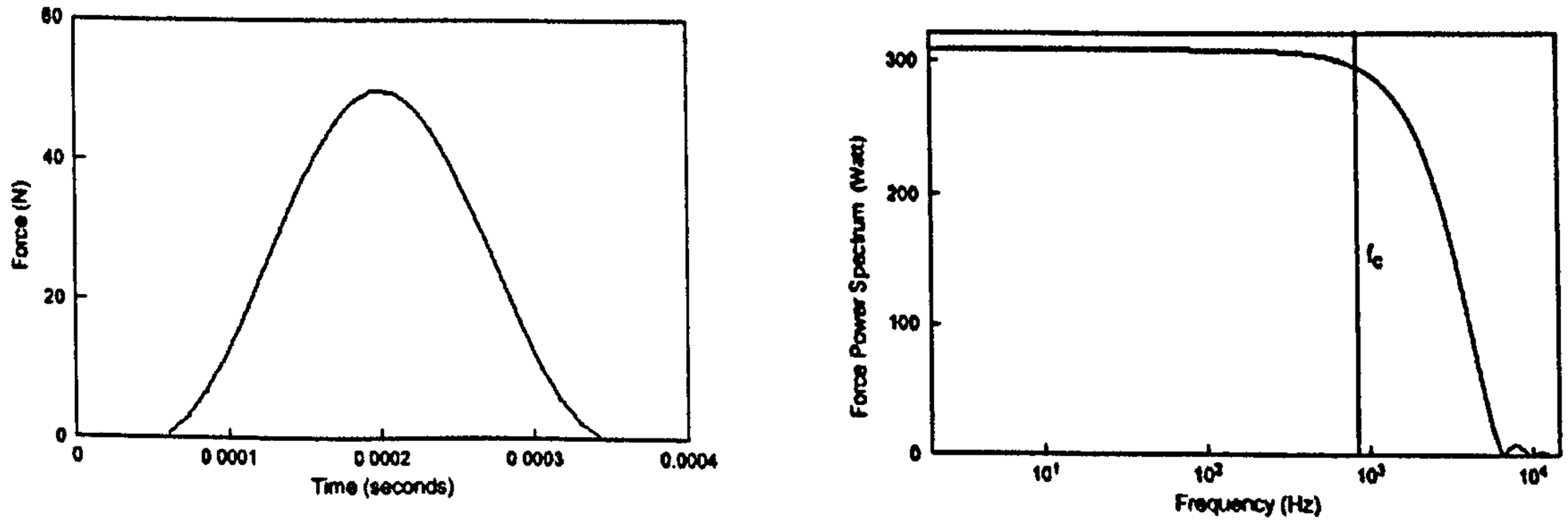

Figure 3.4. Typical force- time history and frequency spectrum of a hammer excitation [130]

Forest [131] highlighted several key points for successful experimental modal analysis using the impact testing, which include the clear definition of the test objectives, the right selection of impact tips and accelerometers, and the careful consideration of unwanted structural noise,

such as rattles, buzzes, etc. The appropriate impact force magnitude and measurement bandwidth should also be employed to produce FRF data with satisfactory resolution and to avoid any damage to the hammer and structure. The ***previewing*** of captured signals can be performed by the dynamic analyser before the frequency analysis to improve the data quality. Any signal distortion, mostly due to manual errors such as double impacts (also known as double bounce) inputs can thus be rejected.

(b) Shaker

This device is normally connected to the driving point on the structure and activated by converting the electrical or hydraulic input power to a mechanical vibration. Its vibration excites the structure at a certain frequency bandwidth depending on the signal generator input and shaker capability. The most widely adopted type is the electro-mechanical shaker and the complete system normally consists of the signal generator (mostly integrated within a modern signal analyser), power amplifiers and shaker as seen on Figure 3.5.

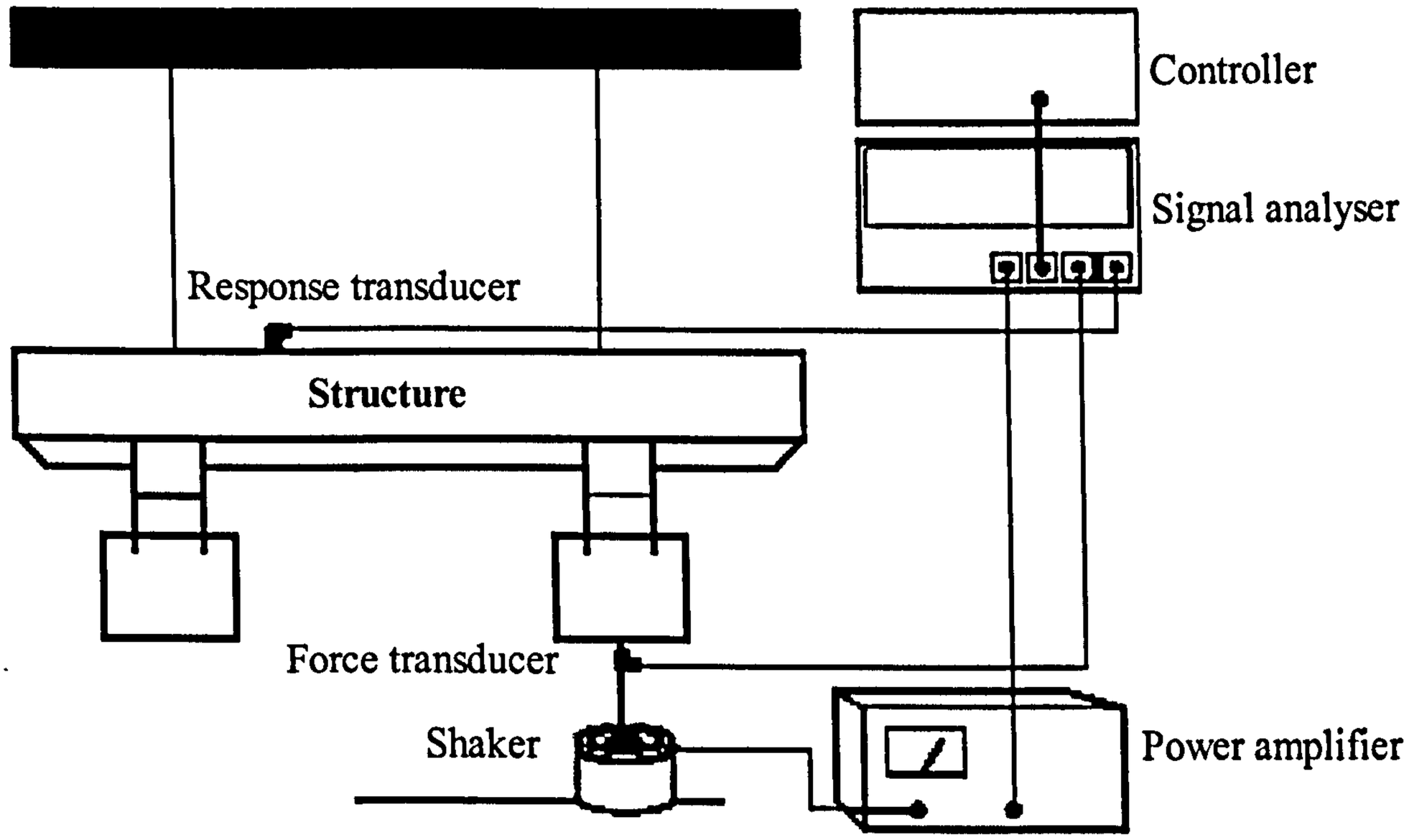

Figure 3.5. General modal testing setup [51]

The analytical model of an electromagnetic shaker showing the interaction between the electrical circuitry and mechanical components can be seen in Figure 3.6 and represented by equation (3.19).

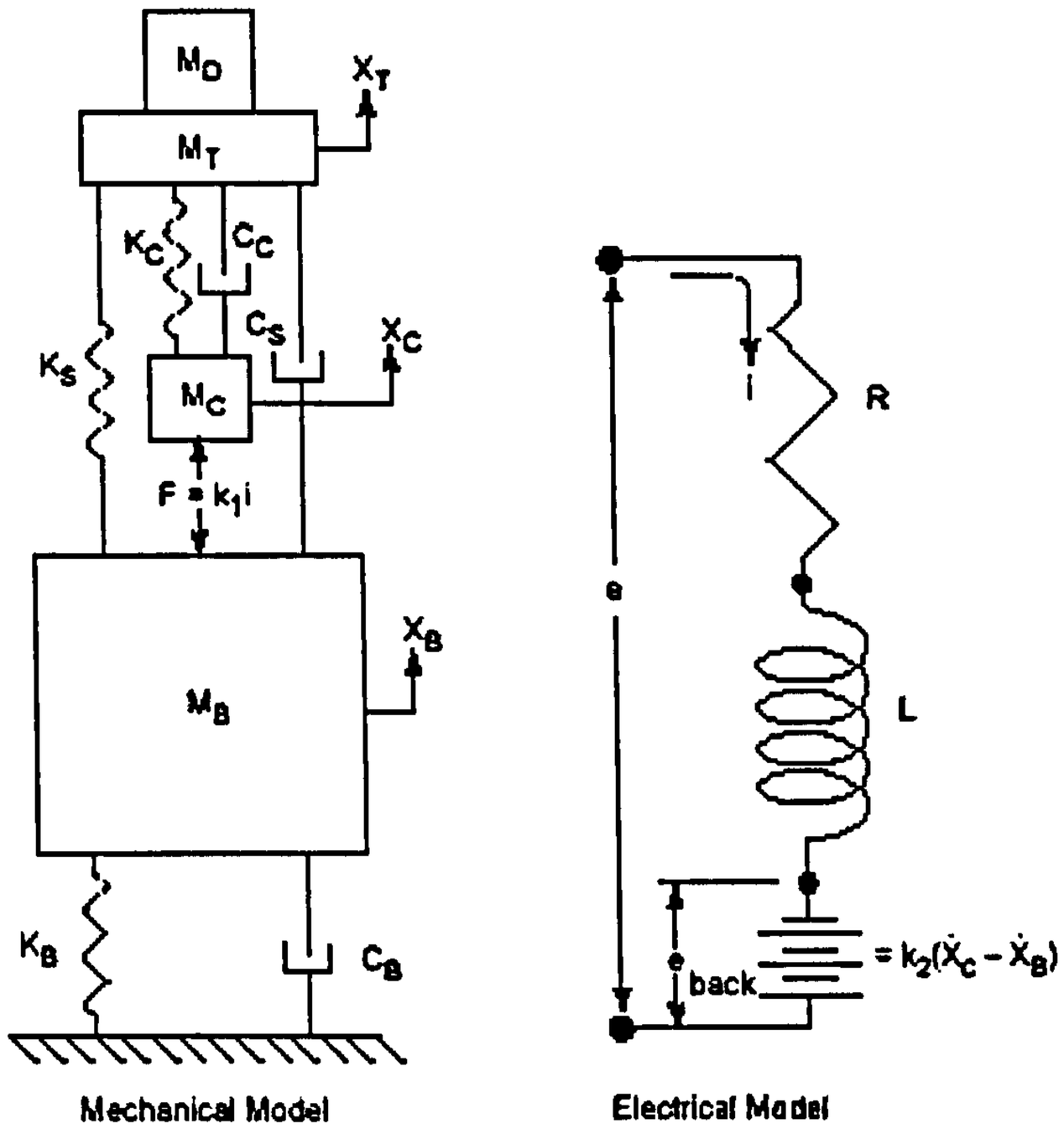

Figure 3.6. Analytical model of an electro-mechanical shaker [52]

$$\begin{bmatrix} M_C & 0 & 0 & 0 \\ 0 & M_T + M_D & 0 & 0 \\ 0 & 0 & M_B & 0 \\ 0 & 0 & 0 & 0 \end{bmatrix} \begin{Bmatrix} \ddot{X}_C \\ \ddot{X}_T \\ \ddot{X}_B \\ 0 \end{Bmatrix} + \begin{bmatrix} C_C & -C_C & 0 & 0 \\ -C_C & C_S + C_C & -C_S & 0 \\ 0 & -C_S & C_B + C_S & 0 \\ k_2 & 0 & -k_2 & L \end{bmatrix} \begin{Bmatrix} \dot{X}_C \\ \dot{X}_T \\ \dot{X}_B \\ \dfrac{di}{dt} \end{Bmatrix} +$$

$$\begin{bmatrix} K_C & -K_C & 0 & -k_1 \\ -K_C & K_S + K_C & -K_S & 0 \\ 0 & -K_S & K_B + K_S & k_1 \\ 0 & 0 & 0 & R \end{bmatrix} \begin{Bmatrix} X_C \\ X_T \\ X_B \\ i \end{Bmatrix} = \begin{Bmatrix} 0 \\ 0 \\ 0 \\ e \end{Bmatrix} \tag{3.19}$$

The typical acceleration generation performance of an electromagnetic shaker over the effective frequency bandwidth with and without device under test (DUT) is shown in Figure 3.7. The shaker produces constant displacement output at the first segment (A-D), constant velocity on the second part (D-E) and constant acceleration at the last section (E-C).

The shaker is normally connected to the structure using a '***stinger***' (thin metal rod stiff only in the direction of excitation) to ensure that the force is only injected in the intended direction. It also functions to safeguard both the shaker and the structure from any damage due to possible excessive input force or displacement. It should not be too long or too flexible because it will introduce its own resonance to the measured system and affect the measurement data.

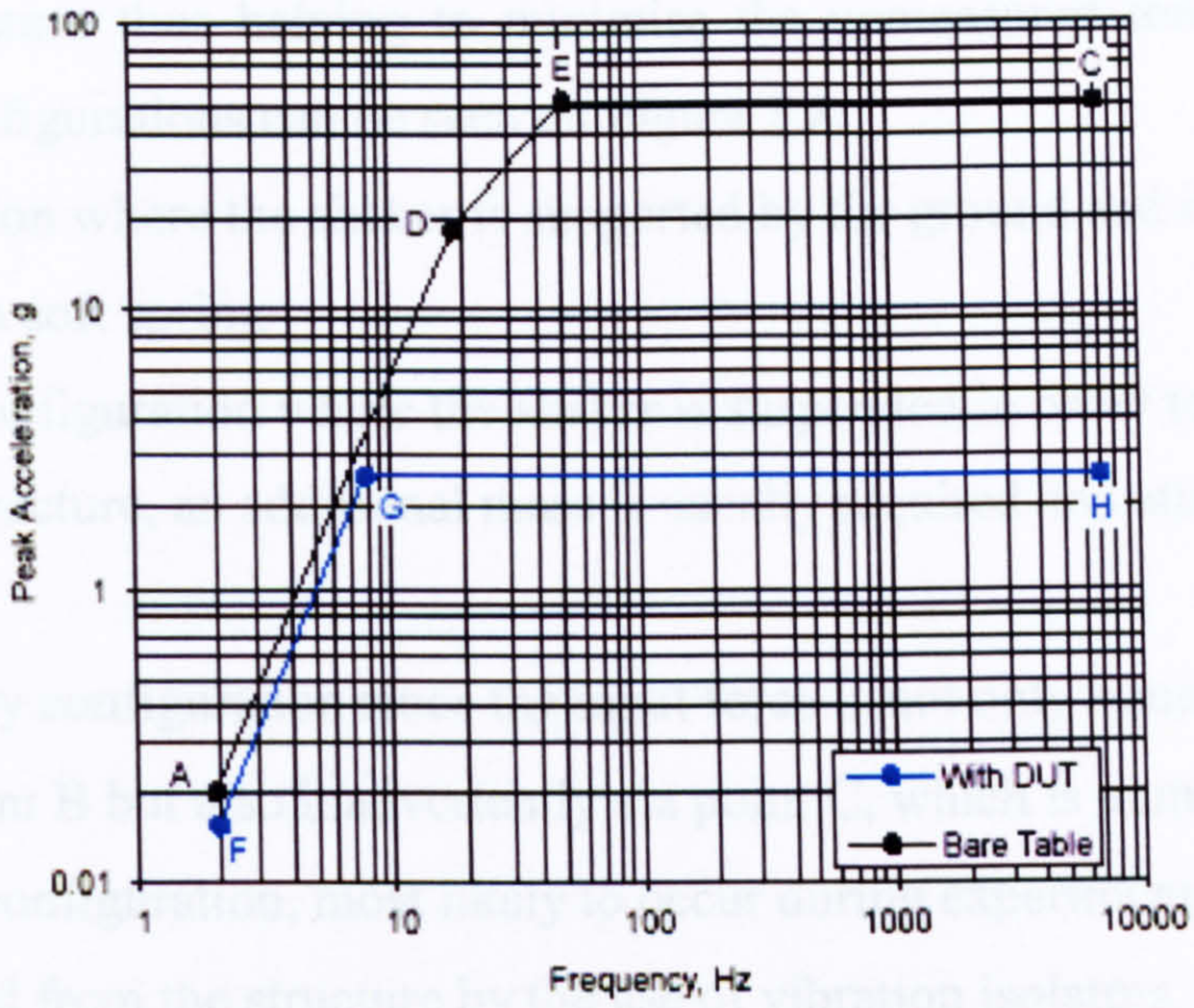

Figure 3.7 Typical performance curve of an electro-mechanical shaker [52]

The ***driving point*** of an experimental modal analysis configuration should not be located on or close to one of the structure's nodal points. Re-writing equation (3.17) for each mode for the j^{th} column, the residue matrix can be calculated as:

$$\begin{Bmatrix} r_{1j}(k) \\ r_{2j}(k) \\ \vdots \\ r_{jj}(k) \\ \vdots \\ r_{nj}(k) \end{Bmatrix} = A_k \begin{Bmatrix} u_{1k}u_{jk} \\ u_{2k}u_{jk} \\ \vdots \\ (u_{jk})^2 \\ \vdots \\ u_{nk}u_{jk} \end{Bmatrix} = A_k u_{jk} \begin{Bmatrix} u_{1k} \\ u_{2k} \\ \vdots \\ u_{jk} \\ \vdots \\ u_{nk} \end{Bmatrix} \qquad \text{k} = 1, \ldots, \text{n} \tag{3.20}$$

Inversing the equation and substituting A^k with $\frac{1}{\omega_k}$ to obtain the mode shape:

$$\begin{Bmatrix} u_{1k} \\ u_{2k} \\ \vdots \\ u_{nk} \end{Bmatrix} = \frac{1}{A_k u_{jk}} \begin{Bmatrix} r_{1j}(k) \\ r_{2j}(k) \\ \vdots \\ r_{nj}(k) \end{Bmatrix} = \sqrt{\frac{\omega_k}{r_{jj}(k)}} \begin{Bmatrix} r_{1j}(k) \\ r_{2j}(k) \\ \vdots \\ r_{nj}(k) \end{Bmatrix} \qquad \text{k} = 1, \ldots, \text{n} \tag{3.21}$$

Thus, zero or very low residue at the driving point ($r_{jj}(k)$) due to the proximity to a nodal point produces very large modal displacements on the other structural DOF's [124].

The shaker should not be in contact with the structure other than at the point where the input force is located to avoid any unmeasured force entering the structure inadvertently and invalidating the basic concept of the experimental modal analysis (see equation (3.9)). However, if this is not possible, a vibration isolation device must be used to separate the

shaker and the structure thus helping to minimise the unmeasured force. Several possible shaker-mounting configurations can be seen on Figure 3.8:

(a) The ideal condition where the shaker is supported by the ground and the structure is suspended with a soft spring

(b) An alternative configuration where the shaker is suspended in order to increase the force applied to the structure, an additional mass is usually required and attached at the back of the shaker

(c) An unsatisfactory configuration since the input force is not only transmitted to the structure via point B but also inadvertently via point C, which is unmeasured.

(d) A compromise configuration, most likely to occur during experimental works, where the shaker is isolated from the structure by the use of vibration isolators

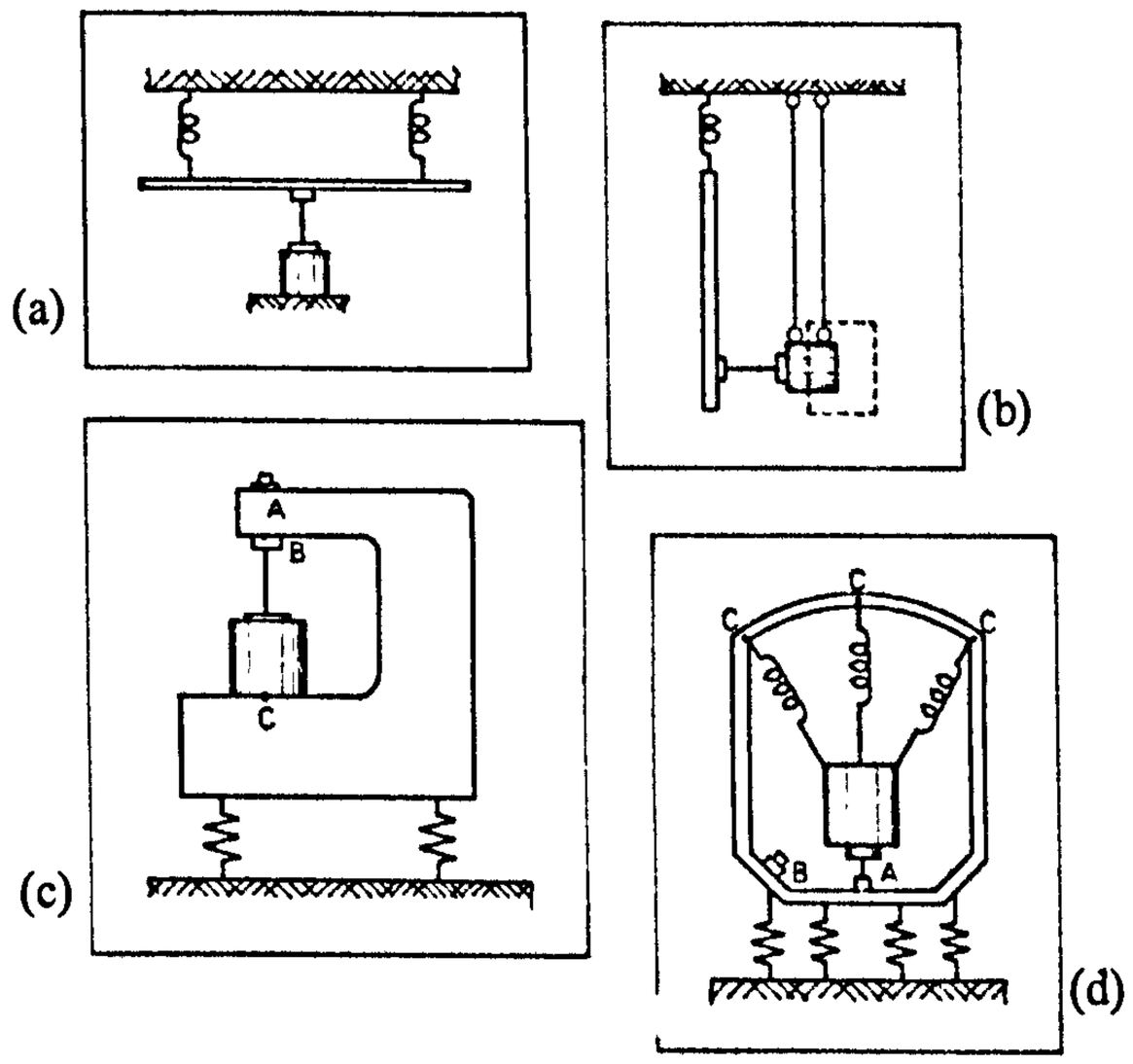

Figure 3.8. Shaker attachment configuration [64]

In addition, the ***force sensor placement*** also requires careful consideration in order to correctly measure all of the input force entering the structure. The sensor must always be attached between the structure and the stinger, and not between the shaker and stinger to enable the measurement of the net force going into the structure and not the gross force produced by the shaker.

3.4.3. Measurement system

The FRF data is obtained from the measured excitation force and response at different DOF's on the structure. The excitation input is normally measured using a force transducer, which is placed between the stinger and the structure in a shaker arrangement or integrated into the impacting end of an instrumented hammer.

The structure's response can be measured in three forms: displacement, velocity or acceleration. LVDT's (Linear Variable Differential Transducers) [132] are usually employed to measure the structural displacement, whereas PiezoVelocity transducers [133] can be used to measure the response velocity. The most common type, however, are the acceleration transducers (accelerometers) due to their wide availability, portability, price competitiveness and ease of installation.

The most commonly adopted acceleration transducers nowadays are the ***piezoelectric*** type due to its high material stress limit, rigidity, insulation, temperature resistance, natural frequency, measuring range and its almost constant sensitivity over a wide temperature range. This type of transducer employs a quartz crystal which produces a proportional electrical charge to the applied mechanical load. The typical frequency response of this transducer can be seen on Figure 3.9 and can be modelled using a second order system as shown on equation (3.22).

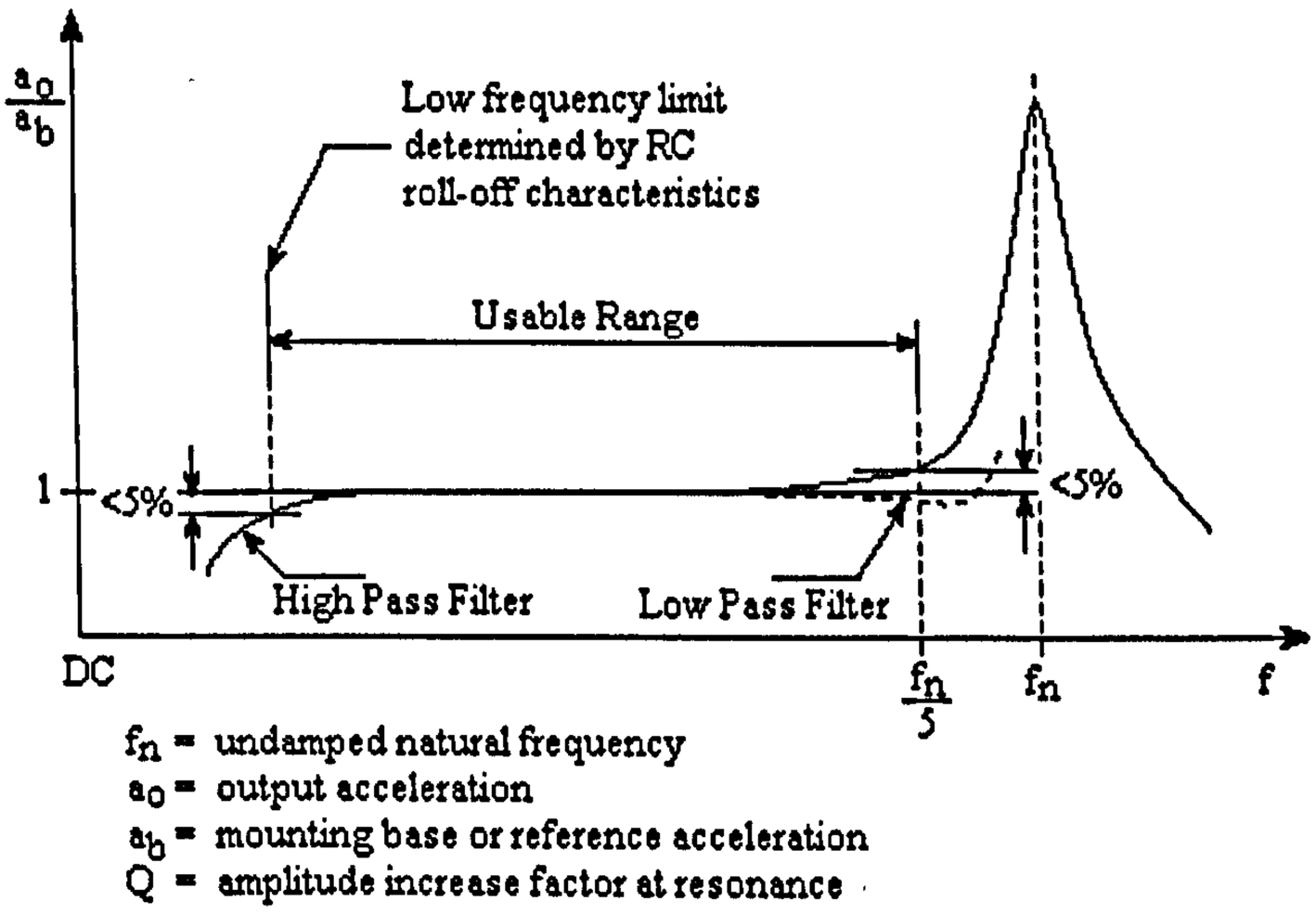

Figure 3.9. Typical frequency response of a piezoelectric sensor [134]

$$\frac{a_o}{a_b} \cong \frac{1}{\sqrt{\left[1-\left(\frac{f}{f_n}\right)^2\right]^2+\left(\frac{1}{Q^2}\right)\left(\frac{f}{f_n}\right)^2}} \tag{3.22}$$

The output charge of the piezoelectric transducer requires a signal conditioning unit to convert it to low impedance voltage signal so that it can readily be measured by a dynamic signal analyser (discussed further in section 3.4.4). The low impedance signal also allows a longer cable to be used in the experiment since it is less sensitive to electrical noise pick-up. This function can usually be realised by using a charge amplifier, which can be illustrated with a simplified electronic model on Figure 3.10.

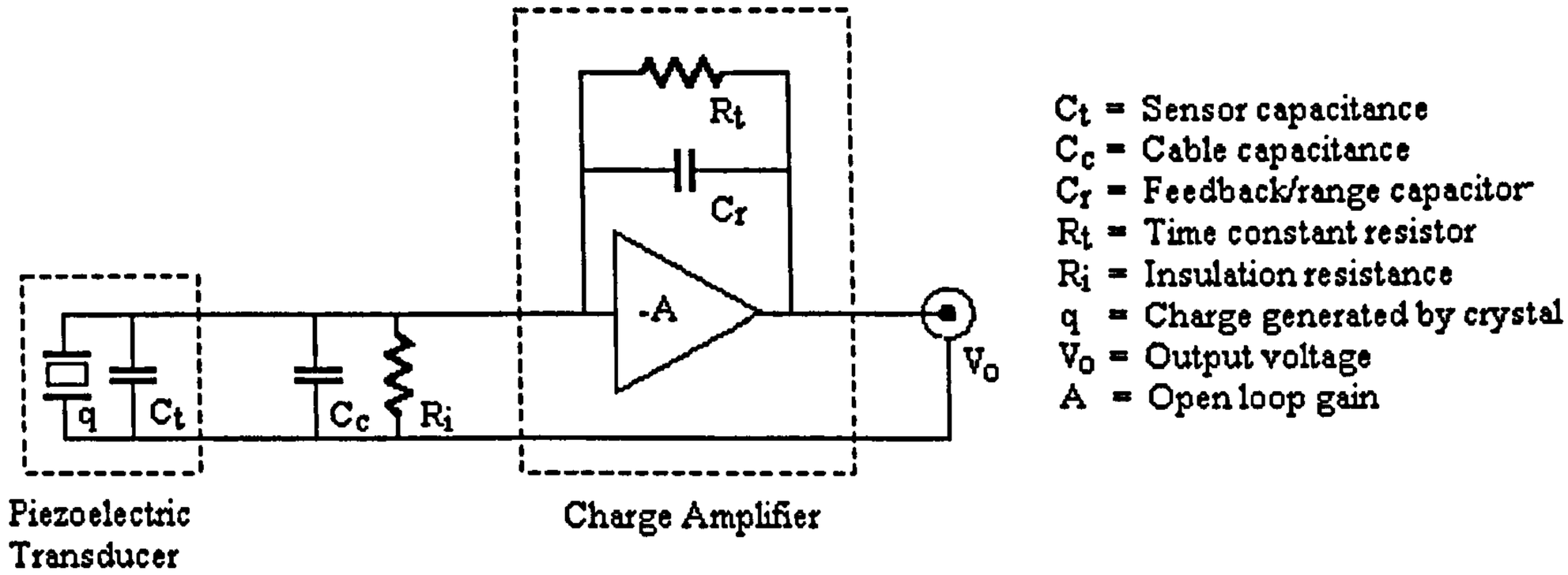

Figure 3.10. Typical configuration of a charge amplifier [134]

The output voltage from the charge amplifier can be calculated as follows:

$$V_o = \frac{-q}{C_r} \times \frac{1}{1 + \frac{1}{AC_r}(C_t + C_r + C_c)} \tag{3.23}$$

whereas its time constant can be represented as:

$$T_c = R_t C_r \tag{3.24}$$

When the open loop gain is sufficiently high the effect of the cable and transducer capacitance can be neglected, thus the output voltage only depends on the generated charge and feedback capacitor:

$$V_o = \frac{-q}{C_r} \tag{3.25}$$

The rapid advance of electronic technology, especially in component miniaturisation, enables the integration of charge amplifiers into the transducers. This development allows the possibility of rapid measurement deployment as well as provides a considerable cost benefit. The integrated amplifier is powered by small constant current from the signal analyser to which it is connected. This system is called Piezotron technology [135] by one manufacturer while another calls it an ICP transducer [136].

Several experimental factors with regard to the transducer utilisation must be considered carefully in order to obtain high-quality measurement data. They apply to both the input force and response transducers and include the attachment methods, measurement locations and external effect considerations. In addition to the considerations described previously in section 3.4.2, if a large mass difference exists between the sides of the force transducer in a shaker excitation setup, the heavier end should be connected to the stinger and the lighter end to the structure. The argument also applies to the hammer testing where the point of impact of the hammer should contain the least mass.

The response transducer attachment methods to the structure significantly affect the usable measurement frequency bandwidth. The typical effective frequency bandwidth of handheld accelerometers is from DC level to circa 500 Hz. The bandwidth increases to around 1 kHz when a magnetic base is used and to about 4 kHz when a cemented stud is utilised. It rises even further to approximately 7.5 kHz when a stud mounting is employed and to about 7.9 kHz when wax is used [137].

Similar to force transducers, the selection of the accelerometer measurement locations should not be situated at or close to the nodal points of the structure (see equation (3.9)). However, if the locations are already pre-determined, then the measurements still need to be carried out, even if the results are less than ideal. The location selection should also be done with care by evaluating the possibility of the cantilever effect since this will distort the measurement results.

Despite the high stability of piezoelectric transducers, they still require periodic calibrations in order to maintain the measurement accuracy. Some degree of deviations might occur due to the harsh environment or other conditions experienced by the transducers. The deviations can manifest themselves in various ways, including a shift of the resonant frequency due to a cracked crystal, a temporary loss of low frequency measurement due to diminishing resistance insulation, or even a total electronic circuitry failure due to extreme mechanical impact. The most widely adopted technique to calibrate accelerometers is the ***back-to-back method***, where a previously calibrated accelerometer is used as the reference (see Figure 3.11).

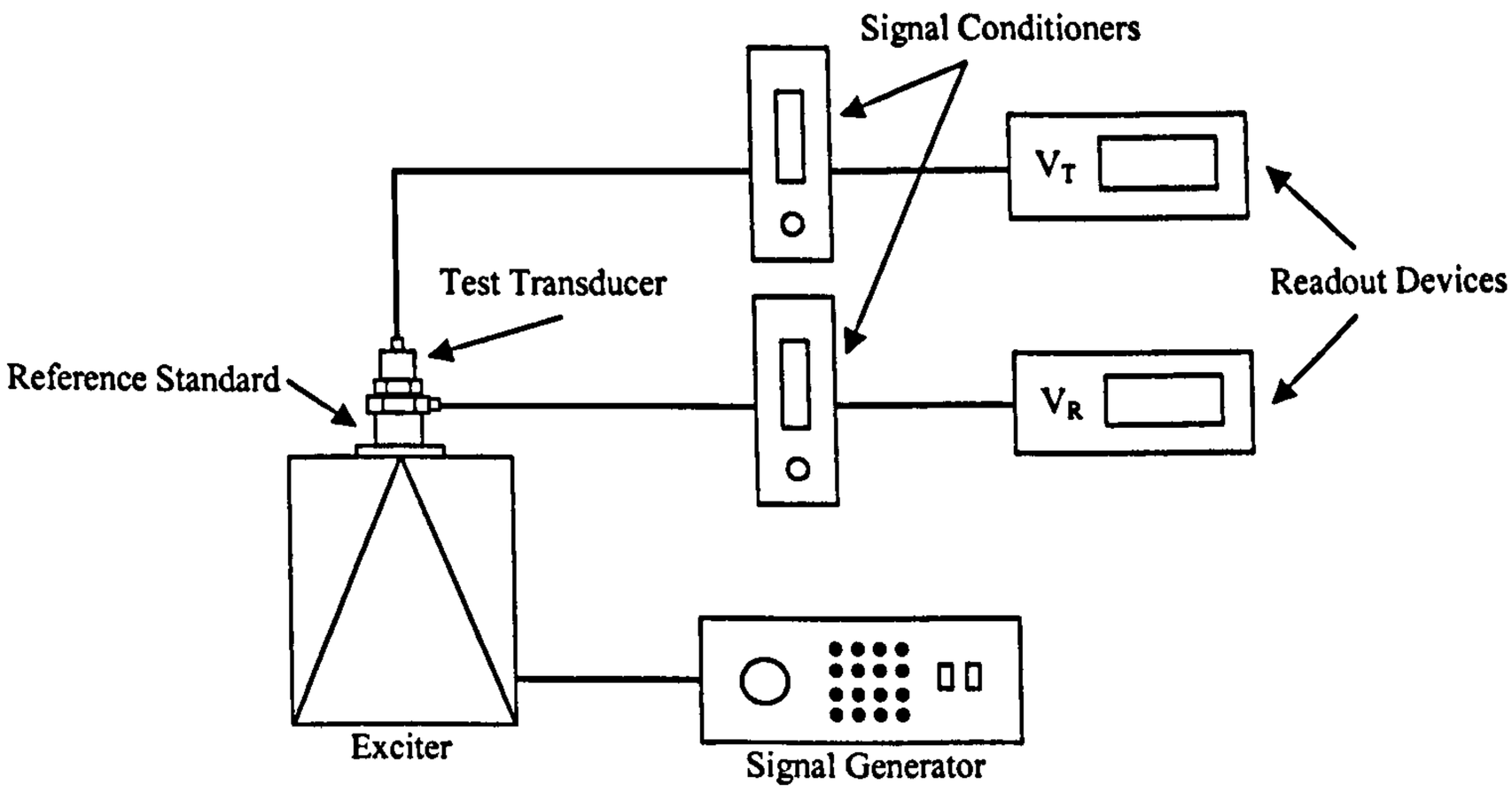

Figure 3.11. Typical back-to-back calibration setup [138]

The sensitivity value of the accelerometer under test can be calculated from the reference accelerometer sensitivity using the voltage readouts of the test accelerometer and the reference as follows:

$$S_T = \frac{V_T}{V_R} S_R \tag{3.26}$$

Force sensor calibrations are usually performed using a hydraulic jack stand with a traceable reference proving ring as seen on Figure 3.12. The gradient of the best-fit line on the voltage output versus force graphs represents the sensitivity of the force transducer.

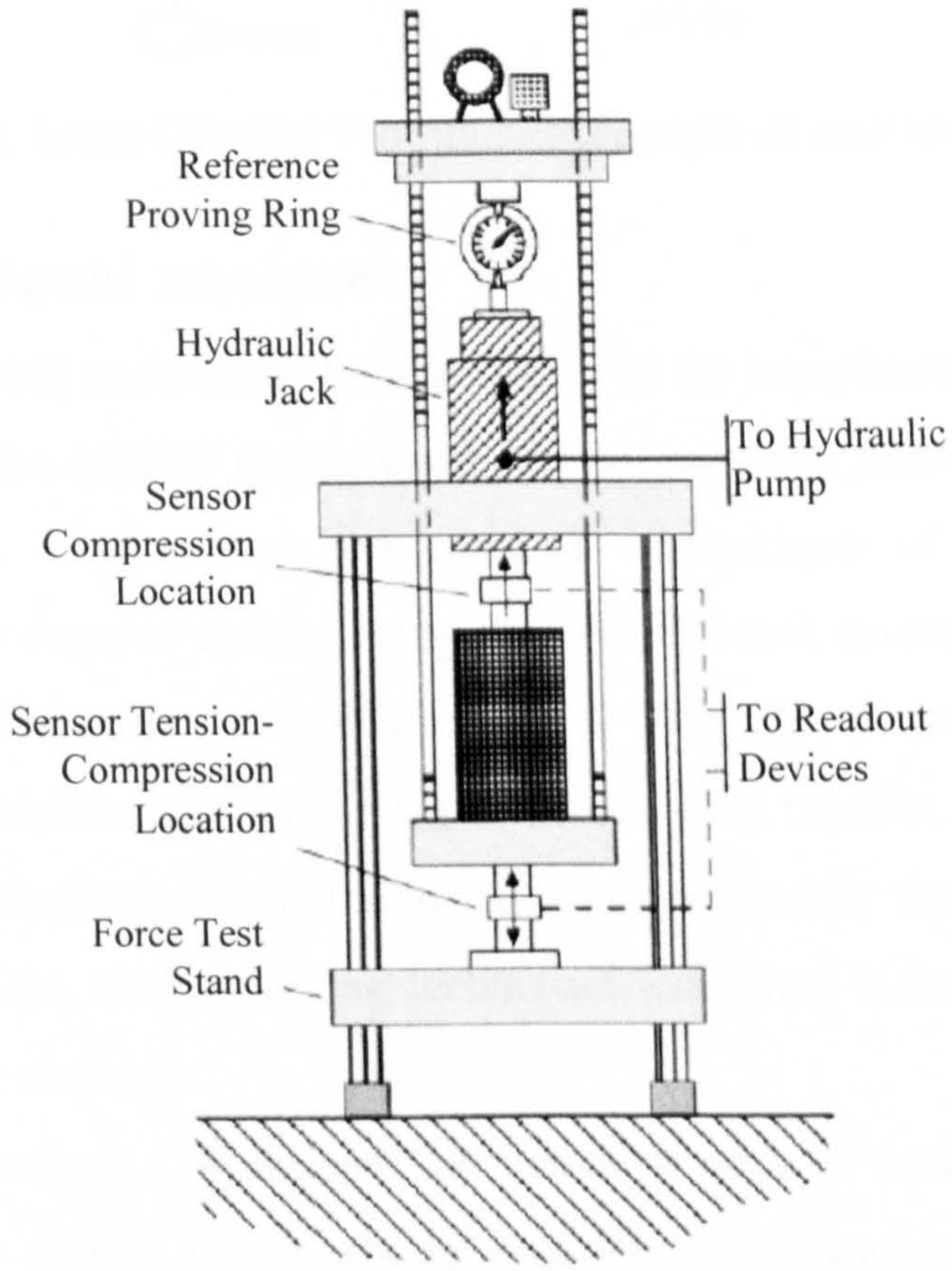

Figure 3.12. Typical force sensor calibration system [139]

A new type of response transducer utilising the ***laser technology*** is emerging [140, 141]. These devices are suitable in applications where the conventional methods are very difficult to employ, such as the measurement of liquid surfaces, hazardous materials, and very small and light objects. The most commonly used type is the Laser Doppler Vibrometer (LDV), which works on the Doppler shift principle by mixing two reflected coherent laser beams: the reference and the reflection from the targeted object. The device measures the beat frequency of the mixed beam obtained by the detector to calculate the relative velocity of the object. A Bragg cell acousto-optic modulator is usually employed to determine the velocity direction by calculating the carrier frequency shift. The measurement principle and basic configuration of an LDV is illustrated in Figure 3.13.

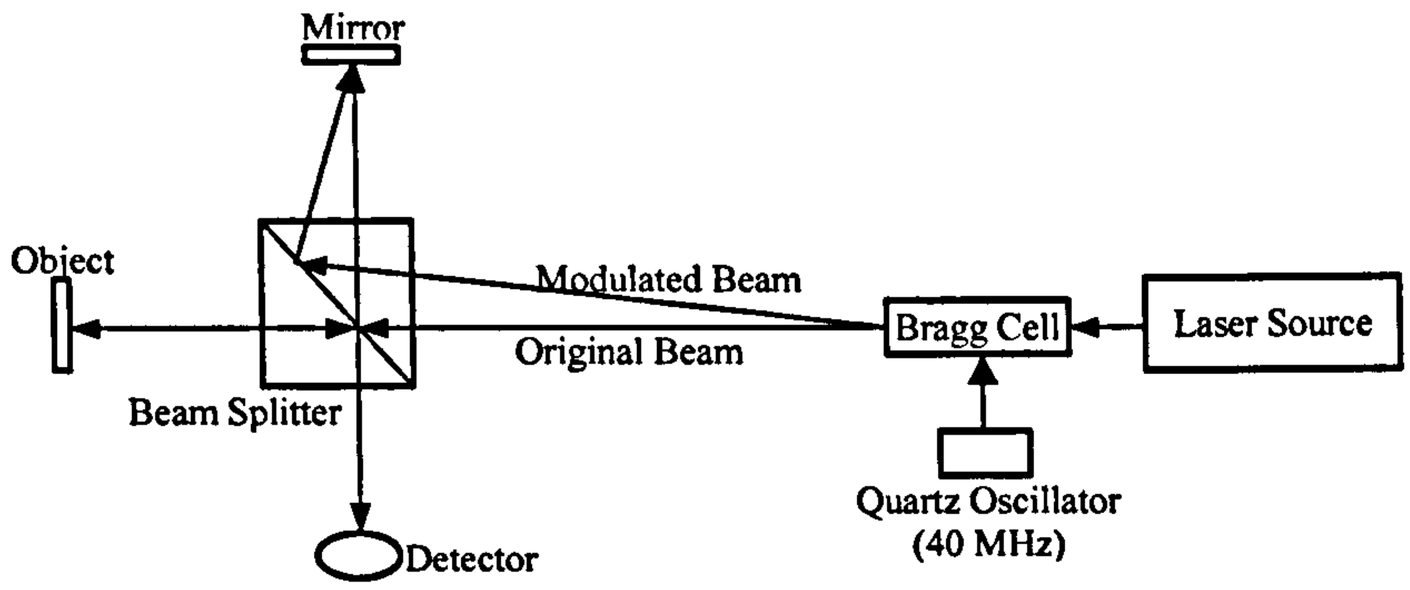

Figure 3.13. Laser Doppler Vibrometer principle of operation [140]

3.4.4. Dynamic signal analyser

Phillips and Allemang [60] underlined that the quality of the experimental modal analysis data is directly affected by the applied ***measurement techniques*** and indirectly influenced by the ***averaging techniques***. The authors presented a comparison of several measurement techniques on a lightly damped system using the conventional excitation methods (random, periodic-random, pseudo-random and burst-random). They also discussed the application of the more advanced excitation methods, such as burst-cyclic random, slow-random, MOOZ-random (slow-random excitation signal adjusted to accommodate the frequencies of a zoom FFT), and periodic chirps. The averaging techniques examined including the asynchronous, synchronous and cyclic methods.

Schwarz and Richardson [54] argued that the most popular excitation signal for shaker testing is the ***random signal***. It was shown that the non-linearities in the structure were excited by the random vibration but then removed by the spectrum averaging. This can produce a set of almost noise-free FRF measurement data with no distortion, which is very important for obtaining accurate modal parameter estimation.

Figure 3.14 shows the diagram of a two-channel dynamic signal analyser which discretely captures the continuous real-time data and transforms it into the frequency domain to obtain the ***FRF*** and ***coherence*** data. The signals are conditioned through the windowing process and the noise reduction system using the ***averaging*** method. A dynamic signal analyser usually also provides the means to store or transfer the data to an external computer module for archiving or further analysis. It can also produce excitation signals, which can be employed to drive a shaker after a suitable amplification as previously discussed in section 3.4.2. It is also capable of providing a power supply to sensors with integrated charge amplifiers to enable faster measurements by removing the requirement for an external charge amplifier as discussed earlier in section 3.4.3.

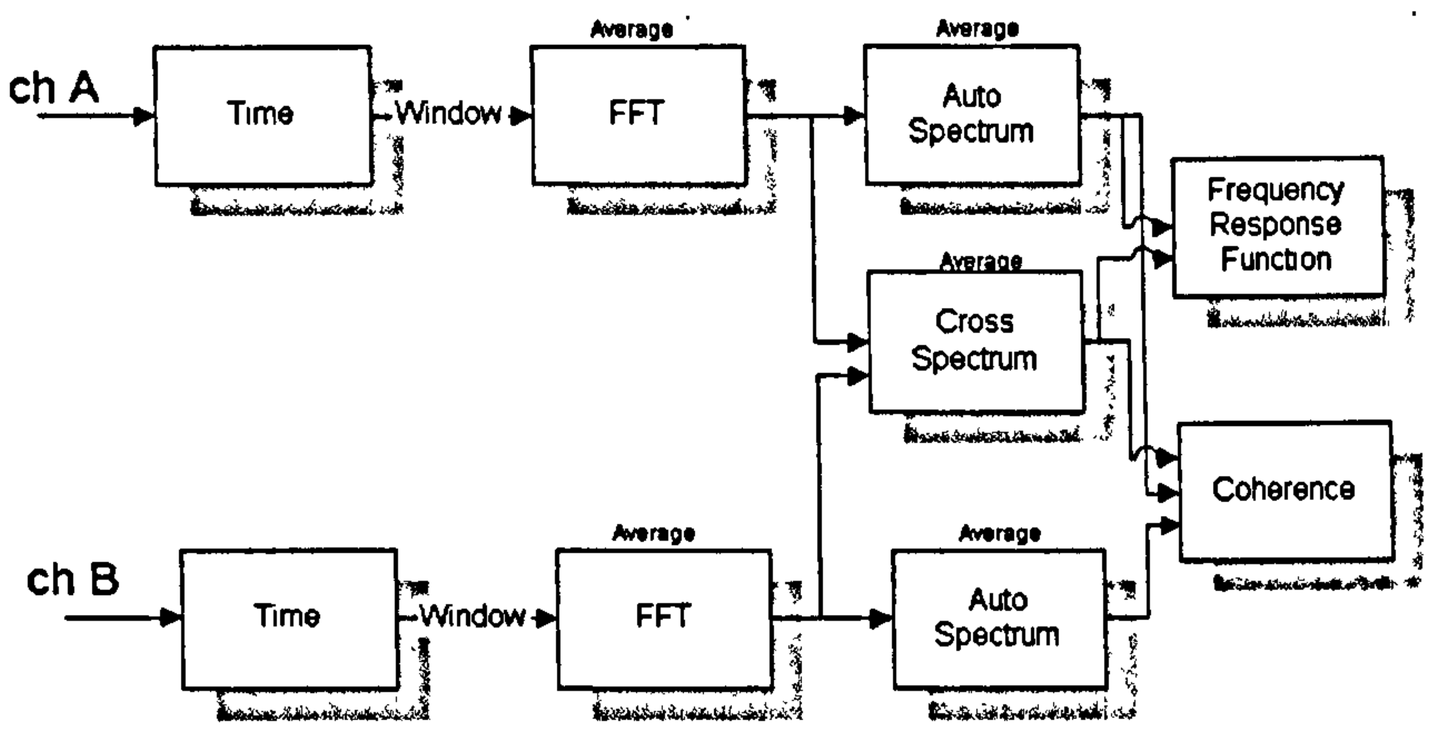

Figure 3.14. The schematic of a signal analyser [142]

The relationship between the excitation and response inputs and the structural properties is described previously in equation (3.9) and can be rearranged as a complex ratio in the frequency domain as follows:

$$H(\omega)=\frac{X(\omega)}{F(\omega)} \tag{3.27}$$

The transformation of the discretely captured data into the frequency domain is performed using the FFT algorithm established by Cooley and Tukey [143]. It is based on the Discrete Fourier Transform (DFT) theory, with an additional requirement that the number of points in the series must be a power of two (see equation (3.28)). This enables much faster data processing, which allows rapid deployment of the algorithm into digital signal processing equipment. The Fourier transform value can be calculated as follows:

$$F(j)=\sum_{k=0}^{N-1}A(k)e^{\frac{2\pi ijk}{N}} \qquad j=0,\ldots,N-1 \tag{3.28}$$

where k is the index for the calculated data A, $log_2 N$ is an integer and N is not equal to zero.

A direct calculation of the FRF from the frequency domain input and response data does not produce satisfactory results due to the presence of mechanical and electrical noise in the measurement data as well as the limited resolution of the data. A statistical approach is therefore required in the forms of ***auto*** and ***cross spectra*** as described in equations (3.29) and (3.30) respectively:

$$\hat{G}_{FF}(\omega)=2\hat{S}_{FF}(\omega)=2\left[F^{*}(\omega)F(\omega)\right] \tag{3.29}$$

$$\hat{G}_{FX}(\omega)=2\hat{S}_{FX}(\omega)=2\left[F^{*}(\omega)X(\omega)\right] \tag{3.30}$$

The spectrum estimation procedures also include the averaging process to remove noise. This step is exemplified in equation (3.31) where this process is applied onto the excitation input auto-spectrum.

$$\hat{G}_{FF} = \frac{1}{K}\sum_{k=1}^{K} F_k^*(\omega) F_k(\omega) \tag{3.31}$$

The ***FRF*** can then calculated from the averaged cross and auto spectra data as follows:

$$H(\omega) = \frac{\hat{G}_{FX}(\omega)}{\hat{G}_{FF}(\omega)} \tag{3.32}$$

The ***coherence*** value can also be calculated from these spectra as shown on equation (3.33) to indicate the measurement quality. It represents the correlation of the measured response to the excitation input and has a maximum quantity of unity, which means that all of the measured response is directly generated by the excitation force and not from any external source. The coherence value is only meaningful if it is averaged from a number of measurement data to indicate the consistency of the relationship between the output and input data.

$$\gamma(\omega) = \sqrt{\frac{\left|\hat{G}_{FX}(\omega)\right|^2}{\hat{G}_{FF}(\omega) \cdot \hat{G}_{FF}(\omega)}} \tag{3.33}$$

There are several data acquisition and FFT related aspects which require special attention of the user to obtain sufficiently accurate frequency domain results. These factors include aliasing, leakage, signal resolution and averaging methods [51].

(a) Aliasing

Welaratna [144] defined aliasing as the creation of an erroneously low frequency digital signal as the result of an analogue signal conversion because of too low a sampling rate. Figure 3.15 illustrates this phenomenon where the high frequency analogue signal shown by (a) is wrongly converted to a much lower frequency digital signal (b) due to the low sampling rate, the points of which are shown as the black dots. The frequency of the digital signal as the result of the conversion can be calculated from the sampling rate f_s as follows:

$$f = (n \pm 0.25) \times f_s \qquad n = \text{integer} \tag{3.34}$$

This problem can be theoretically avoided when the ***sampling rate of the conversion is at least twice the maximum frequency of interest*** and by applying a low-pass anti-aliasing filter with a very sharp cut-off frequency. However, this type of filter is difficult to realise in practice and can lead to the generation of undesired phase shift. A practical solution to this is to increase the sampling rate so that the ***Nyquist*** frequency, which is defined one half of the sampling frequency, is well above the frequency of interest. The cut-off frequency of the low pass filter is also usually designed to be less sharp to reduce the phase shift effect, thus improving the data quality.

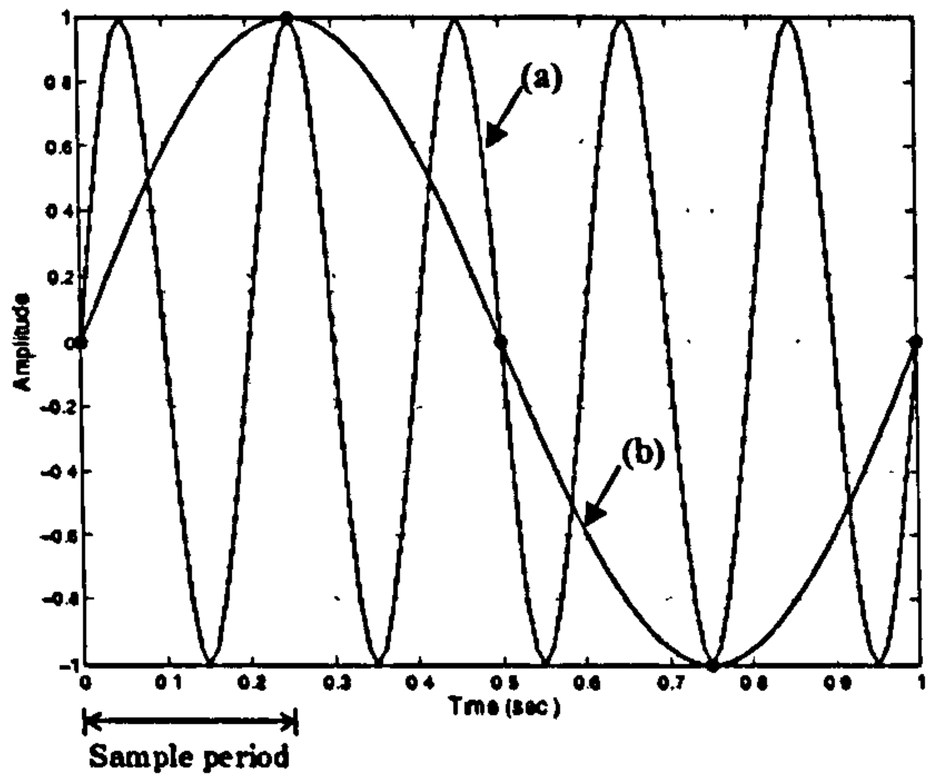

Figure 3.15. An example of the aliasing effect [145]

(b) Leakage

This phenomenon occurs when the energy from a frequency in a spectrum leaks to the adjacent frequency range as seen on Figure 3.16. It occurs when the signal requirement for a fixed length of time history and a periodicity by the FFT algorithm are not satisfied [146]. Graph (a) shows that when the measurement duration period, *T*, matches the periods of the sine wave, a spectrum at the sine wave frequency can be clearly observed. When this is not the case, as seen on graph (b), the spectrum of the remainder signal 'leaks' to the adjacent spectral frequencies. This effect can be minimised by employing several methods:

- Changing the duration of the test to match the underlying periodicity in the signal if a periodic signal is used.
- Increasing the measurement period so that the leakage becomes negligible.
- Padding the signal with zeroes to match the underlying periodicity of the signal.
- Using the 'windowing' technique to modify the signal to reduce the severity of leakage.

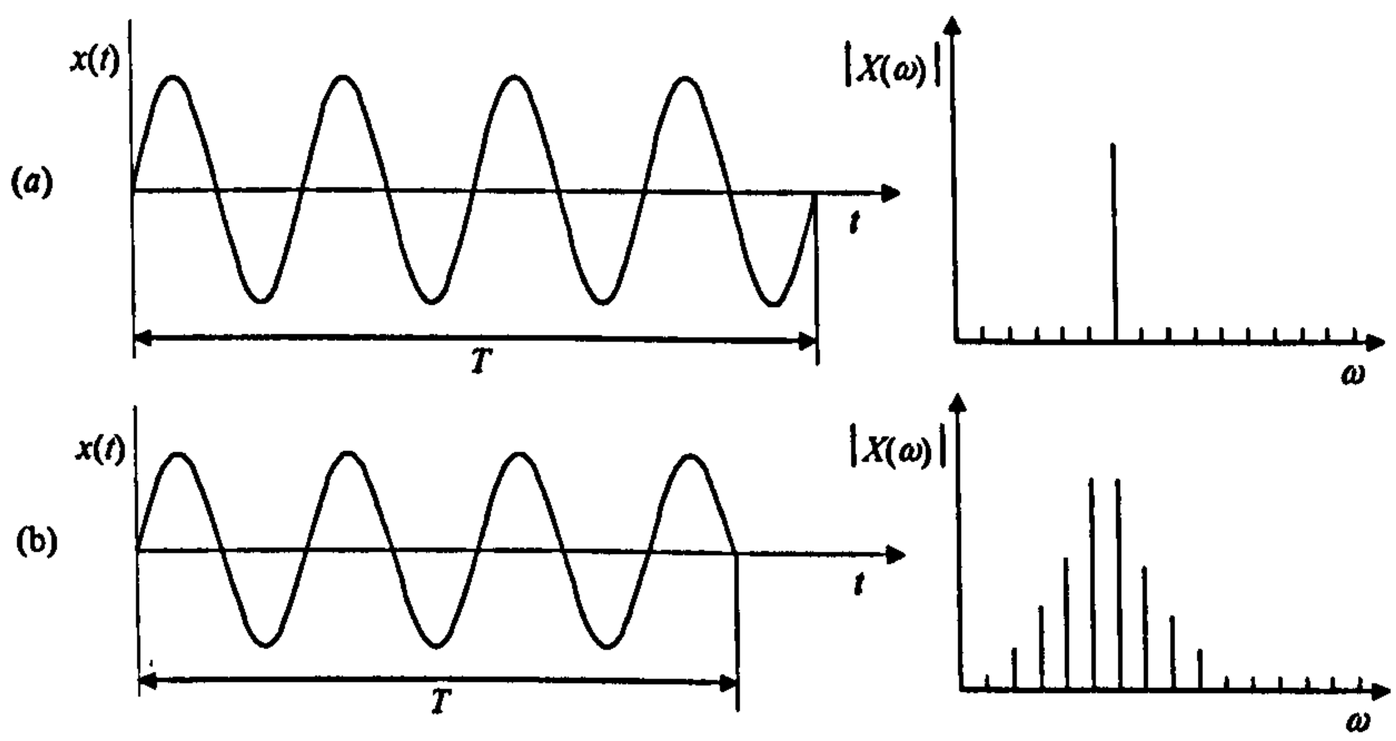

Figure 3.16. Leakage

Among these solutions, the most widely adopted experimental method to reduce the effect of leakage is the 'windowing' technique, mainly due to the unpredictability of most real signals. This method multiplies the signal to a weighing function to simulate the periodicity in order

to reduce the leakage. Various windowing techniques are available but a single method is normally only applicable for one type of signal. One of the most commonly used techniques to reduce leakage on periodic or random vibration continuous signal is the Hanning window, the weighting function of which is described mathematically in equation (3.35). Some other common techniques include the rectangle, hamming, cosine taper, kaiser and exponential windowing methods [147-149].

$$W(n)=\begin{cases}0.5+0.5\cos\left(\dfrac{2n\pi}{N}\right) & -\mathrm{N}\langle n\langle \mathrm{N} \\ 0 & \text{elsewhere}\end{cases} \tag{3.35}$$

(c) Signal resolution

High-resolution measurement data allows a good analysis to be performed although it requires long acquisition time and high processing power to obtain and evaluate the data. The signal resolution over a frequency bandwidth is usually a function of power of two. Therefore, one step increase in the data resolution usually means twice the data acquisition and computing time required. The resolution of the data must therefore be balanced between the need for fast measurement time and data quality.

When high-resolution data is required, modern systems have a new feature called the '***zoom***' function which will aid in the data acquisition time and analysis as seen on Figure 3.17. This utility will perform high-resolution analysis centred on a certain frequency and is most useful where a more detailed analysis of one or more frequencies of interest is required. It enables the same data resolution at a narrower frequency bandwidth to be obtained, hence avoid increasing the analysis time and resource required.

However, care should be taken when using 'zoom' in an experimental analysis using a shaker at the lower frequencies. The output power from the shaker is usually maintained at a constant level, so at this bandwidth it will produce a longer shaker displacement. This might cause damage to the test object or the shaker itself when the investigation is performed on a high inertia object.

In addition, the input range of the Analogue to Digital Converter (ADC) for the analyser should be utilised as fully as possible without overloading. This is to enhance the quality of the measurement data by increasing the signal-to-noise ratio (SNR), which is defined as:

$$SNR=\frac{P_S}{P_N} \tag{3.36}$$

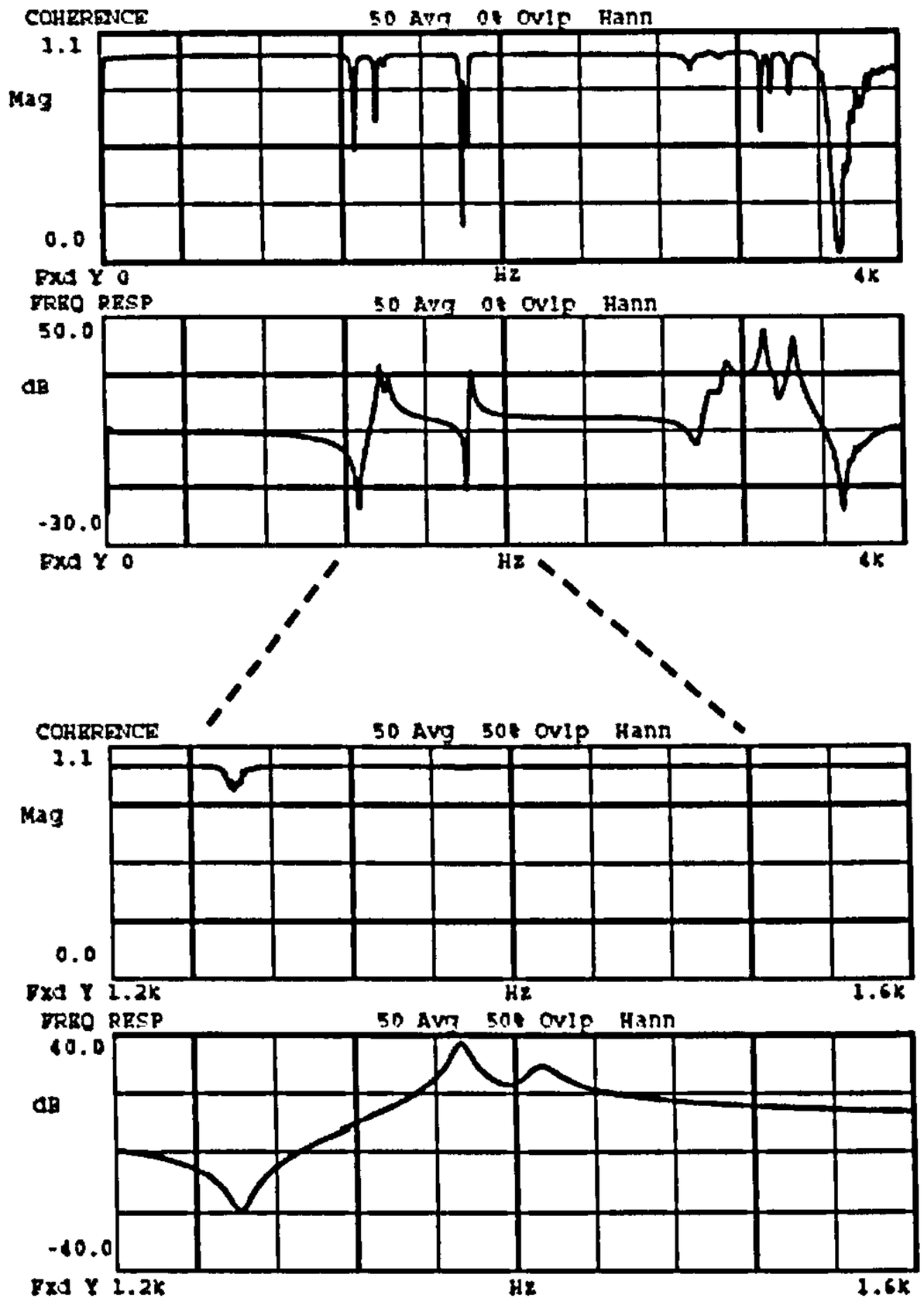

Figure 3.17. Zoom feature of a dynamic signal analyser [51]

(d) Averaging

The averaging process is required to improve the accuracy, consistency and statistical reliability of the measurement data by reducing the effect of noise [150]. This process involves the summing of the measurement results and averaging them as previously illustrated in equation (3.31). The averaging process is required even more when the measurement is performed using the impulse hammer due to the manual control of the input force. Previewing of the averaging process enables the rejection of poor data, such as a double bounced hit, to improve the analysis data.

Various types of averaging can be applied during an experimental modal analysis to improve the quality of the measurement data, either on the frequency or on time domain data. The frequency domain averaging techniques include RMS, vector and peak hold, which can be performed either in linear or exponential averaging mode [151]. The linear averaging mode is performed by adding a number of spectra and then dividing the result by the added number to obtain the true arithmetic average. On the other hand, the exponential averaging technique generates a continuously running averaging calculation where the most recent spectra are weighted more compared to the earlier data.

Time domain averaging (also known as waveform averaging) is normally performed on rotating machinery where the captured signal is averaged before its FFT is calculated. It is performed to remove any background noise by employing a reference trigger pulse to synchronise the sampling process. This trigger is typically sourced from an element of the machine under the test [152].

3.4.5. Frequency Response Function (FRF) data quality

The quality of the data obtained in the experiment needs to be checked before performing any modal parameter estimation. This process can also be used to produce an estimate of the number of modes contained in the measurement data. Several methods are available to check the quality of FRF data ranging from the simple visual check to the more sophisticated and detailed software based calculation.

(a) Visual checks

The features that need to be analysed in a visual check are the number of peaks and the low and high frequency asymptotes in a log-log plot of magnitude against frequency as shown in Figure 3.18. The number of peaks gives an estimate of the number of modes that can be found in the structure whereas the asymptotes can be used to determine the data quality. At low frequency below the first resonance, the measurement result will reflect the support condition of the structure under test. At high frequency, the measurement result may exhibit the dominant local effect, which can affect the effectiveness of the modal parameter extraction. The asymptote at low frequency will exhibit stiffness-like characteristic if the structure under test is grounded as illustrated by the dashed line on Figure 3.18 (a). The magnitude of the asymptote at the lowest frequency should correspond to the static stiffness of the structure at the measurement point. Conversely, a mass-like characteristic as seen on the dashed line on Figure 3.18 (b) will appear if the structure under test is freely suspended. The magnitude of the response asymptote at the lowest frequency should match the mass deducted from rigid body considerations.

If some deviations occur against the expected behaviour, they may indicate that the measurement data does not contain sufficiently low frequency information. They could also indicate that the appropriate support condition is not fully achieved by the applied technique.

The measurement curve may also tend to be asymptotic at high frequencies, either mass-like or stiffness-like. This indicates that the excitation is applied at a point of very high mass or flexibility. This does not necessarily mean that the data is not accurate, but it will present difficulties in analysing the data because local dominant effects will overwhelm the data.

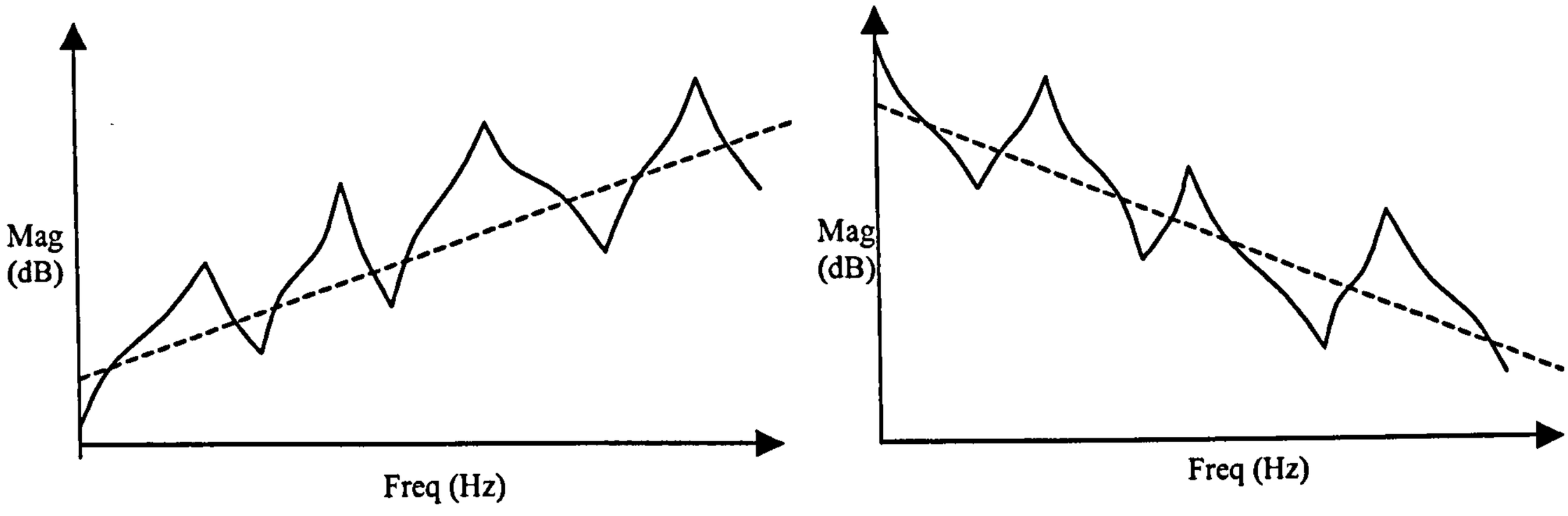

(a) Stiffness-like behaviour (b) Mass-like behaviour

Figure 3.18. Typical FRF measurement data from an experimental modal analysis

(b) Detailed checks

These types of checks are aimed more towards SIMO or MIMO measurements where much more measurement data is obtained. They are based on the Singular Value Decomposition (SVD) method of the FRF matrix **S** as shown in equation (3.37) [153].

$$\mathbf{S} = \mathbf{U}\boldsymbol{\Sigma}\mathbf{V}^{T} \tag{3.37}$$

By applying SVD to the measurement data matrices, there will be three parameters found:

1. The singular values, σ_ω, as elements of $\boldsymbol{\Sigma}$ which represents the order of the system
2. A column matrix **U** of the frequency distribution of σ_ω
3. A column matrix **V** of the spatial distribution of σ_ω

Further calculation on the results can produce a set of functions which can indicate the quality of the measurement data and estimate the number of modes present in the structure. This data is usually presented in a ***stability diagram*** to help the user determine the modes and modal parameters. These functions include the Principal Response Function matrix, MIF (Mode Indicator Functions) and CMIF (Complex Mode Indicator Functions).

3.5. Modal parameter extraction

The modal parameter extraction step obtains or estimates the structure's modal parameters by the examinations of the measurement results, by using either manual or computer assisted methods. Two fundamental methods of modal parameter extraction are available: ***frequency*** and ***time domain*** methods. The majority of modern modal parameter extraction studies employ the frequency domain method by examining the FRF data. The invention of modern dynamic signal analysers which can easily produce the frequency domain data and the advance of modal analysis software and computing technology are responsible for this trend. The time domain method, where the IRF (Impulse Response Function) data is investigated, is

only utilised for a number of specialised applications, such as the modal analysis of structures with very low natural frequencies.

The modal parameter estimation method in the frequency domain using the numerical technique involves two phases of analysis: suitable theoretical model synthesis and modal parameter extraction using a curve fitting technique. The order of the theoretical model is normally estimated to be at least the number of peaks observed in the measurements, whereas the curve-fitting algorithm can be selected from a number of available techniques discussed later in this section.

The frequency domain modal parameter extraction methods can be classified into three main groups which themselves contain several sub-methods:

(a) SDOF Modal Analysis

This approach is useful to perform the curve fitting of FRF measurement data with clear and separated peaks indicating the presence of resonant frequencies. It is the most basic method and most suitable for the modal parameter extraction of simple structures as presented by Gade et. al. [154]. The author described both the manual techniques, where no theoretical SDOF model was constructed, and a more advanced method, which employs the inverse FRF line-fit method. The manual method involves the peak picking of the measurement data to determine the natural frequencies and the half power points to calculate the damping factor. In addition to the two methods, there are other SDOF modal parameter extraction techniques including the circle-fit and least square methods.

The SDOF modal analysis techniques are normally time consuming and thus not suitable for analysing data obtained by SIMO or MIMO methods due to the large amount of data. However, the simplicity of this approach is valuable for preliminary checks on the data obtained using any experimental method. This technique also assumes that there are no other modes in the vicinity of the mode under analysis and, hence, it is not suitable for repeated and closely coupled modes normally associated with highly damped structures.

(b) MDOF modal analysis

A more suitable approach in a modal parameter extraction task is by employing an MDOF curve fit method which estimates several modes using one theoretical model. This approach will therefore account for closely coupled resonant frequencies and out-of-band modes to produce more accurate modal parameter estimates. It is suitable for the FRF data obtained from the SISO, SIMO and MIMO measurement methods over a frequency bandwidth.

Most computational MDOF modal parameter extraction methods are devised to permit user intervention to carefully consider some data which might be less accurate. This feature is

essential to balance the need of fast data extraction against the data quality despite the development of faster computing hardware and fully automated software. Modal parameter extraction of FRF measurement data using the MDOF approach can be performed using several methods:

- ***Non-linear least squares (NLLS) method*** [64]

This method is a general curve fitting approach of a theoretical curve obtained using the partial fraction equations, H_ℓ (see equation (3.38)), to the measured transfer function data, H_ℓ^m.

$$H_\ell = H_{jk}(\Omega_\ell) = \sum_{r=m_1}^{m_2} \frac{{}_rA_{jk}}{\omega_r^2 - \Omega_\ell^2 + i\eta_r\omega_r^2} + \frac{1}{K_{jk}^r} - \frac{1}{\Omega_\ell^2 M_{jk}^r} \tag{3.38}$$

This technique attempts to minimise the difference between the theoretical and measured curves ($H_\ell^m - H_\ell$) by differentiating the error equations which produces a set of non-linear equations. An iterative calculation process is then normally required to solve the equations and extract the modal parameters.

- ***Rational fractional polynomial (RFP) method*** [69]

This method is based on the NLLS curve fitting approach but using rational fractional equations instead of partial fraction equations to produce the theoretical curve as shown in equation (3.39). This approach will produce a set of linear equations and hence a direct matrix solution can be created. This enables the use of numerical solution using computer and thus this method has become one of the most established standards in MDOF modal analysis.

$$H_\ell = H_{jk}(\omega) = \sum_{r=1}^{N} \frac{A_r}{\omega_r^2 - \omega^2 + 2i\omega\omega_r\zeta_r} \tag{3.39}$$

- ***Lightly damped structures method*** [64]

This method is designed to estimate the modal parameters from the measurement data with inferior quality at the resonant frequencies. This case is mostly true for structures with very light damping such as automotive components when tested individually. This method is based on equation (3.40) and only the natural frequencies and mode shapes are obtained.

$$H_\ell = H_{jk}(\omega) = \sum_{r=1}^{N} \frac{{}_rA_{jk}}{\omega_r^2 - \omega^2} \tag{3.40}$$

(c) Global and poly-reference modal analysis

This modal parameter extraction method is a further development of the MDOF methods to produce better estimates of the modal parameters from a series of measurement data. It is

different from the 'local' SDOF and MDOF approaches discussed in sections 3.5.(a) and 3.5.(b) because the parameter estimation process is performed using all of the measurement data instead of one by one.

This approach is based on the theoretical assumption that the modal parameter is a global property of a structure. The modal parameters obtained from this approach are expected to be more accurate due to the use of all available data. The multi-curve fit process will also produce a single composite curve as a summation of the FRF series, from which the modal parameters of the structure can be derived.

There are several methods of global modal analysis methods:

- ***Global rational fraction polynomial method (GRFP) method*** [70]

This method is based on the MDOF Rational Fraction Polynomial technique and can be applied to both SIMO and MIMO measurement data. The process modal parameter estimation is divided into the estimation of the natural frequencies and damping factors, and the calculation of mode shapes from the estimated frequencies and damping factors.

The estimation of frequencies and damping factors in this method are obtained from all of the measurement data as shown in equation (3.41).

$$h_i = \sum_{k=0}^{m} z_{ik} c_k \qquad i = 1, \ldots, \mathrm{L} \tag{3.41}$$

The theoretical model represented by z_{ik} for all of the modes is developed using orthogonal polynomials from the natural frequencies and damping factors in the following equation:

$$z_{ik} = \frac{\phi_{ik}}{\sum_{k=1}^{m} (\omega_k^2 - \omega_i^2 + j2\sigma_k\omega_i)} \tag{3.42}$$

This can be simplified further as follows:

$$z_{ik} = \frac{\phi_{ik}}{g_i} \tag{3.43}$$

where for all points

$$\sum_{i=1}^{\mathrm{L}} \frac{\phi_{ik}\phi_{ij}}{|g_i|^2} = \begin{cases} 0.5 & k = j \\ 0 & k \neq j \end{cases} \tag{3.44}$$

Equation (3.41) can be represented in a matrix format as follows:

$$\mathbf{H} = \mathbf{ZC} \tag{3.45}$$

This can be used to perform the curve fitting calculation using the least squared error methods as follows:

$$C = \mathrm{Re}\left(\left[Z^{*}\right]^{t} Y\right) \tag{3.46}$$

The mode shapes can be calculated subsequently from the estimated residues on each individual measurement data as shown in equations using a partial fraction expansion process.

- ***Global singular value decomposition (SVD) method*** [153]

This method is a global method based on the SVD technique discussed in section 3.4.5.(b). Although the SVD technique is used to determine the quality of the FRF's as shown in the corresponding section, it can also be utilised to estimate the modal parameters. This global method is only applicable for a set of FRF data with a single reference (SIMO). It is based on the assumption of viscous damping in the structure.

3.6. Summary

The theoretical background for the experimental modal analysis and parameter extraction methods has been studied in this chapter. Robust knowledge basis in the experimental techniques are quintessential because the accuracy of the extracted parameters depend on the measured data quality. The fundamental principle of experimental modal analysis states that all input force into the system must be measured. Otherwise, the measured data will be contaminated and inaccuracies are introduced resulting in incorrect modal parameters. Various techniques of modal parameter extraction from the measured data have also been investigated. The global method was found to be the most suitable for the type of investigation to be carried out. The natural frequencies are global dynamic properties of the structure, so that almost all the measured data (except on measurement nodes) reflects their existence and magnitudes. Based on the findings, the rest of the structural dynamic properties can be derived from each or a group of measured data.

The next chapter discusses the implementation of the different experimental configurations discussed in this chapter on the Cincinnati Arrow 500 vertical machining centre, including the modal parameter estimation from the measured data using the GRFP method.

Chapter 4. EXPERIMENTAL MODAL ANALYSIS OF CINCINNATI ARROW 500 VERTICAL MACHINING CENTRE

Accurate experimental modal analysis requires the appropriate experimental configurations, signal conditioning and parameter extraction methods. The measurement devices must be able to prevent aliasing and leakage of the measured signal as well as providing sufficient SNR and frequency resolution. Following the discussion of the theoretical background, experimental setup, and modal parameter extraction process described in the previous chapter, a SIMO experimental modal analysis investigations are undertaken on the Cincinnati Arrow 500 machine tool structure illustrated by Figure 4.1.

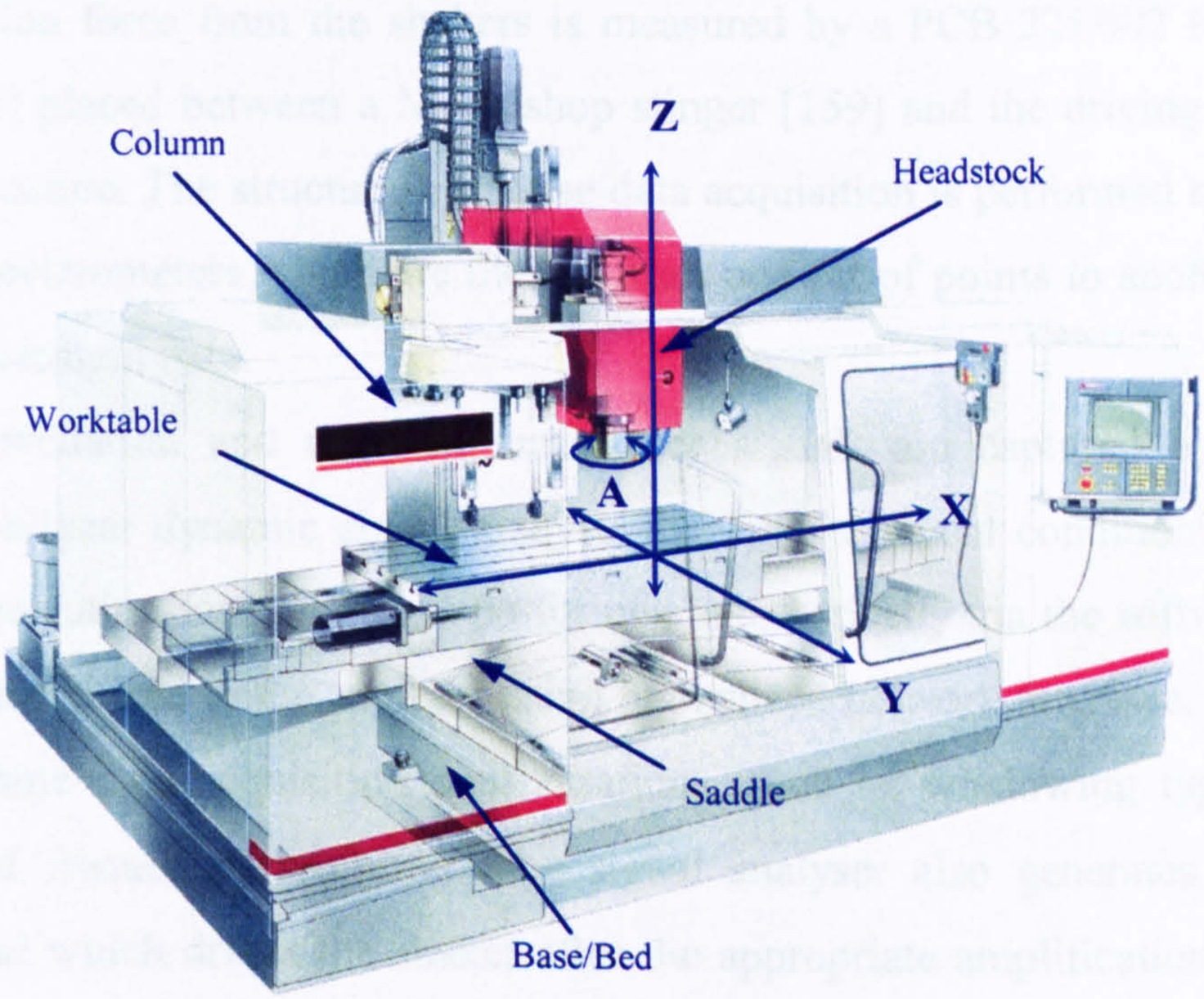

Figure 4.1. Machine tool configuration [155]

The investigation examines the effects of different experimental configurations on the measured modal parameters with two main methods presented: shaker placed on the machine tool worktable and suspended shaker. The benefits and pitfalls of the investigated method are reviewed showing the suitability of each technique for different type of structural dynamic analysis (cutting and non-cutting conditions). The investigation begins with an initial experimental modal analysis in one axial direction to validate the methodology before the full SIMO studies in three orthogonal directions are carried out. The modal parameters are extracted from the measurement data using the global rational fraction polynomial method using a commercial software package (STARStruct). A set of guidelines covering basic as well as more complex experimental practices is developed to provide generic procedures for

obtaining high quality measurement data. The modal parameters obtained in the investigation are utilised to validate an analytical model of the machine structure developed using the FEA technique further discussed in Chapter 8.

4.1. Experimental equipment

Medium- and heavy-weight TIRAvib [156] and Brüel & Kjær [157] electro-mechanical shakers are employed to provide the excitation input force for the relatively heavy machine structure. Both devices are employed for the suspended shaker configuration, whereas only the TIRAvib shaker is utilised when the shaker is placed on the worktable due to the workspace restriction.

The excitation force from the shakers is measured by a PCB 221B02 ICP piezoelectric transducer [158] placed between a Modalshop stinger [159] and the driving point located at the machine structure. The structural response data acquisition is performed by PCB ICP Uni- and tri-axial accelerometers which are moved from one set of points to another to obtain the complete measurement data.

Both the excitation and response transducer signals are captured by a DataPhysics SignalCalc Mobilyzer dynamic signal analyser [160]. The signal conditioning (anti-leakage and aliasing, resolution setting, etc) is performed automatically via the software interface on the host computer linked to the analyser using high-speed network interface. User settings are required for some data acquisition configurations, such as windowing type, measurement bandwidth, and frequency resolution. The signal analyser also generates the low-voltage excitation signal which drives the shaker after the appropriate amplifications. A single stage power amplifier is required for the TIRAvib shaker, whereas the Brüel & Kjær exciter needs two-stage amplification due to the higher output. The analyser also produces the small DC current necessary to energise the transducers' built-in charge amplifiers (ICP).

The analyser performs the conditioning of the measurement signals including the windowing, averaging and, optionally, zooming. The Hanning windowing technique reduces any spectrum leakage generated by the random signals, whereas the normal averaging method minimises any noise presence in the measured signals. The signal analyser also features some additional software functions to assist the data acquisition, such as file exporting and sensor management. The detailed specifications for the shakers, transducers, and the related devices can be seen in Appendix A.1.

4.2. Applied modal parameter extraction technique

STARStruct software [161] from Spectral Dynamics Inc. is employed to extract the modal parameters from the experimental data. The software is widely adopted in the experimental modal analysis field and capable of performing modal parameter estimation using the SDOF, MDOF and GRFP methods. It also allows interfacing to external FEA software packages to perform structural dynamic modification analysis. A utility software (*Measurement File Exchange*) [124] is additionally supplied for rectifying measurement data with incorrect assignments of the point number, direction, file format, etc. This capability eliminates the need to repeat the experiments if the data configuration is incorrectly set up. However, the quality of the measurement data can only be determined during the experiments.

The modal parameter extraction from the measurement data involves the following steps:

(a) The development of a 3-D representation of the machine structure

The 3D geometrical representation of the machine structure is created by assembling the measurement point (DOF) locations obtained from direct dimensional measurements or machine drawing interpretation. The main purpose of this representation is to enable the animation of the mode shapes to study the directions, sources and characteristics of the vibration. It can then be used as a preliminary investigation for possible method of reducing the machine vibration.

(b) Modal parameter extraction

The employed technique is called as the 'advanced method' in the software and based on the GRFP method (see section 3.5.(c)). Two stages are involved in the estimation of the parameters:

1. Frequency and damping parameters estimation

The software employs the GRFP algorithm and the model size estimated by the user to produce a stability diagram (see Figure 4.2). It shows the possible occurrence of vibration modes and the associated damping ratios over the selected frequency bandwidth and model size. The estimated modes are indicated by greyscale coded small circles explained in Table 4.1, whereas the superimposed graph shows the averaged FRF data. The values of the associated frequencies and damping ratios are tabularised below the graph. Unstable modes may indicate the presence of non-linearities, whereas mathematical modes are non-existent physically and only employed to assist the calculation of 'real' vibration modes.

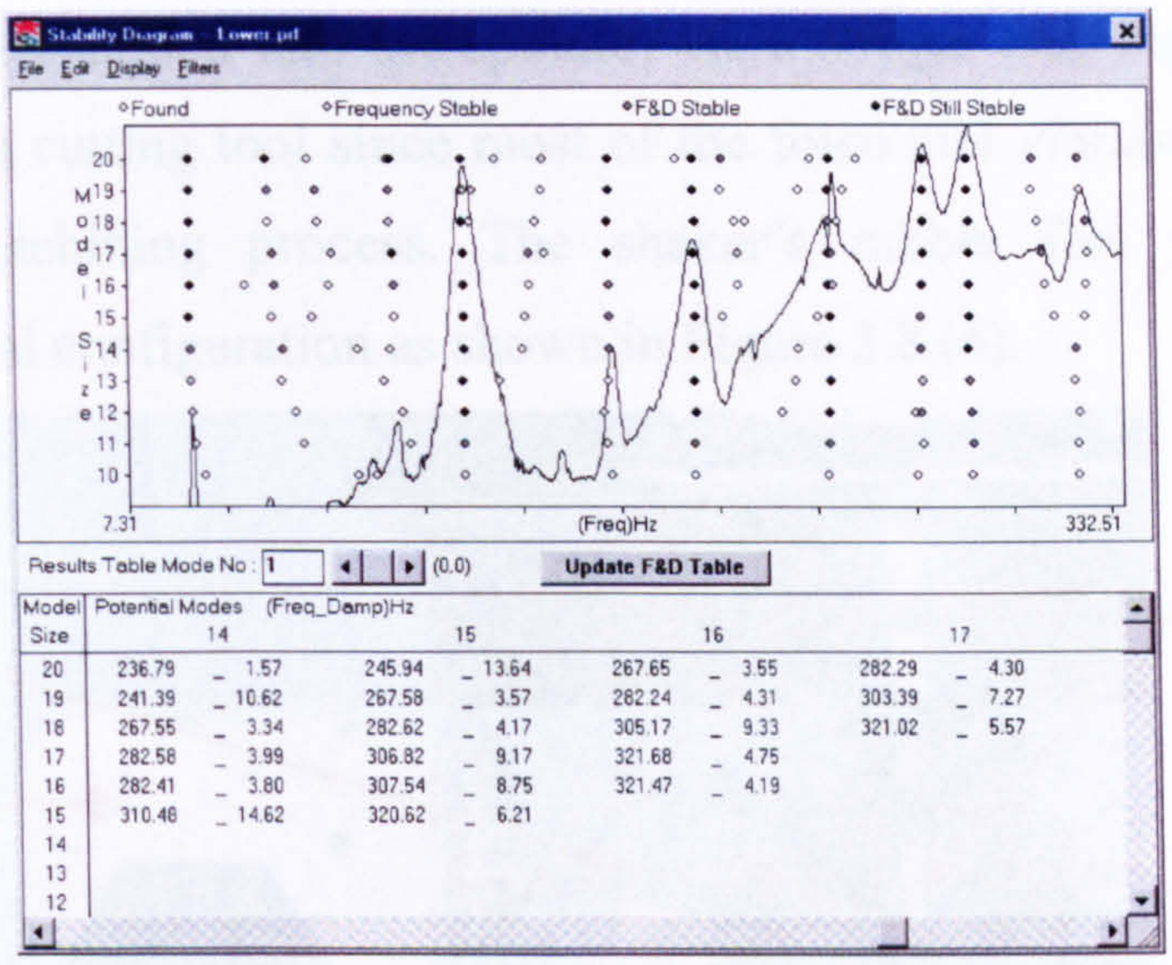

Figure 4.2. Stability diagram (MIF log imaginary^2)

The software also provides a means to deselect some of DOF's data in order to remove the influence of poor measurement FRF in the estimation process. In addition, the frequency bandwidth of the analysis can be altered in order to obtain more accurate parameter estimation by minimising the effects of out-of-band modes.

2. Mode shape parameter estimation

The software can calculate both normal and complex mode shapes by using the frequency, damping and residue values obtained in the first stage. The complex mode option generally suffices for most conditions since a normal mode is a special case of complex modes. An option to select a different DOF as the normalisation reference to calculate the mode shapes instead of the driving point is also available. This feature avoids excessive mode shape displacement generation due to a low driving point excitation level.

Greyscale code	Indication
Black	Fixed frequency between model sizes and stable damping ratios
Dark grey	Varying frequencies between model sizes but stable damping ratios
Light grey	Stable frequency between model sizes but varying damping ratios
White	Modal frequency detected (mathematical mode)

Table 4.1. Greyscale coding of estimated mode stability

4.3. Initial investigation in one orthogonal direction

This investigation is performed to validate the fundamental experimental methods and considerations discussed in section 3.4. It assesses the machine's structural dynamic properties in the X-axis direction by simulating the cutting force excitation commonly associated with this machine type. The TIRAvib shaker (supported by four rubber feet) is placed on the worktable without being clamped. It is then connected to the machine structure

(a dummy cutting tool clamped into the spindle) via a stinger (see Figure 4.3). The driving point is selected at the cutting tool since most of the force and vibration is generated at this location during a machining process. The shaker's rubber feet provide the practical compromise to the ideal configuration as shown in Figure 3.8.(d).

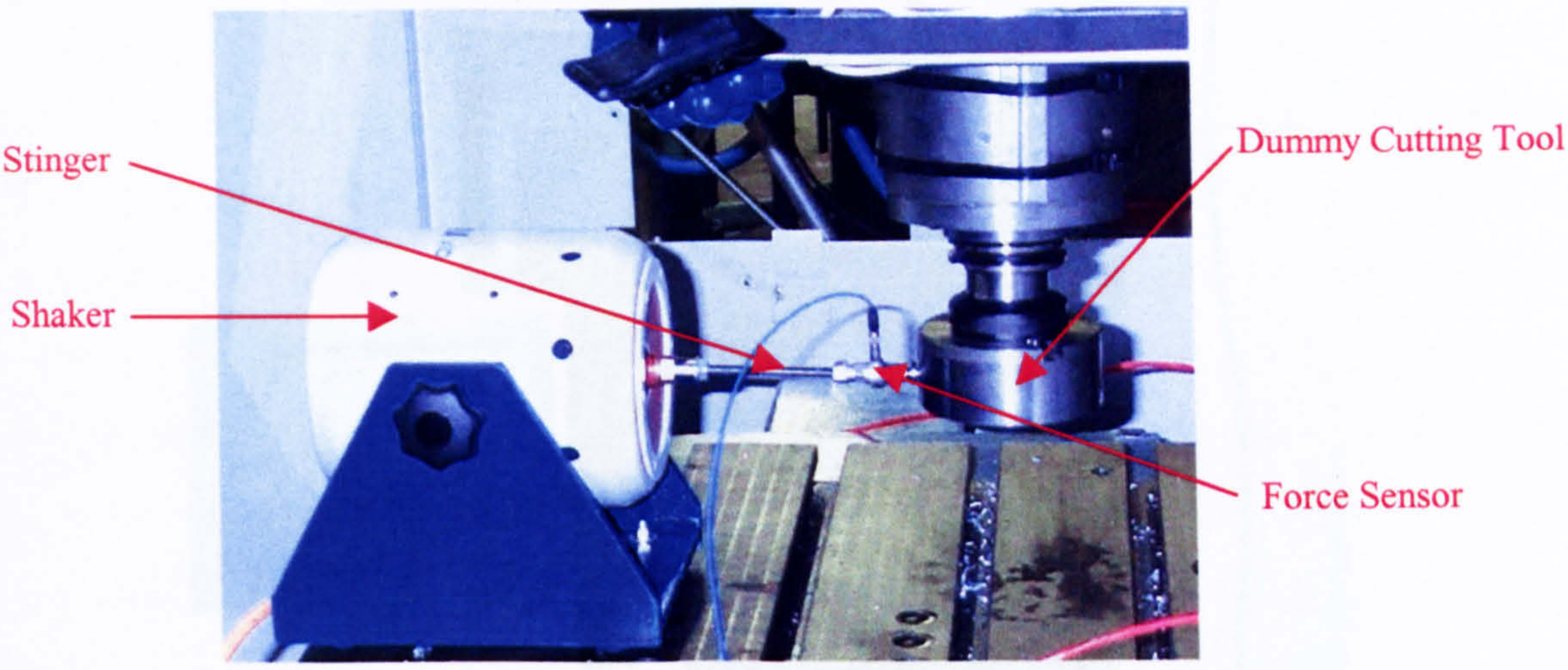

Figure 4.3. Experimental configuration of the excitation force application

Uni-axial accelerometers are employed to measure the structure's responses in parallel with the shaker excitation direction. The accelerometers are moved from one set of measurement locations to another in order to measure the response of the entire machine structure. The mass-loading effect of the accelerometers on lighter parts of the structure (such as the spindle), which might alter the natural frequencies, is minimised by utilising two lightweight PCB 353B03 ICP accelerometers [162]. The response of the other structural members is measured using three PCB 629A11 industrial grade ICP accelerometers [138]. The lightweight and industrial accelerometers are attached to the structure using wax and magnetic bases respectively in order to obtain a sufficient frequency bandwidth covering the vibration modes of interest. Figure 4.4 shows the implemented experimental configuration showing the excitation system (shaker, stinger and force sensor), accelerometers and the dynamic signal analyser unit.

The measurement frequency bandwidth is from 0 to 320 Hz, which covers most of the machine's operating frequency. The data quality is observed by measuring the coherence values across the frequency bandwidth of interest (see equation (3.33)). They should be as close as possible to unity to indicate that the measured response is directly attributed to the input force and is repeatable. The measurements are performed on 114 points on the structure with the driving point denoted as number 1. The measurement data obtained is stored as SignalCalc native format files to examine the software functionality. It is then exported into

the UFF (Universal File Format) files and subsequently converted into the STAR format using the '*Measurement File Exchange*' software.

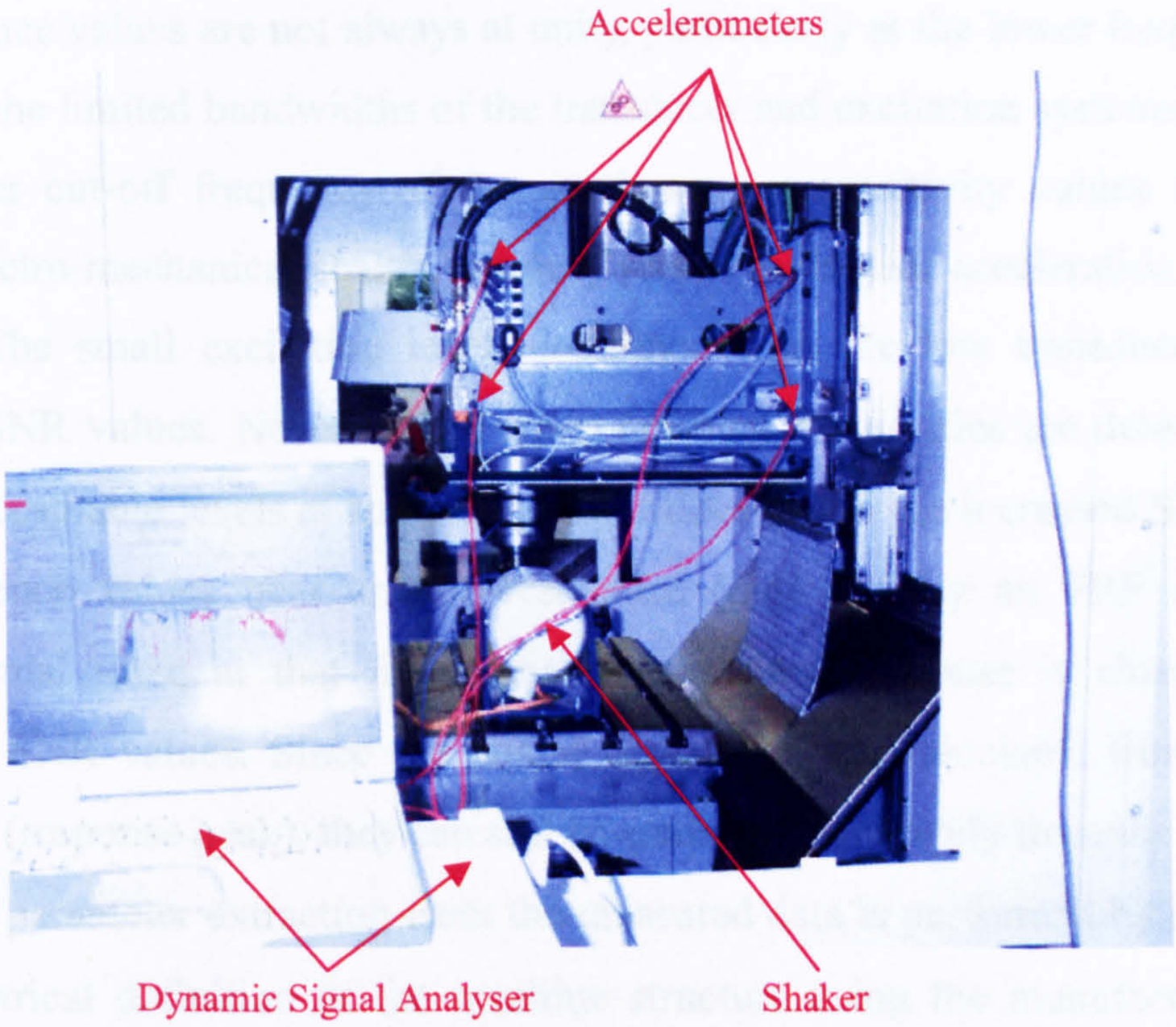

Figure 4.4. Test layout

The typical FRF and coherence data measured by the signal analyser is shown in Figure 4.5. Channel 3, 4 and 5 of the analyser represent the measurement from the driving point (point number 1), whereas Channel 6, 7 and 8 show the data of a location at the front of the machine headstock (point number 2). The FRF data is all referenced to Channel 1 where the excitation force signal is measured.

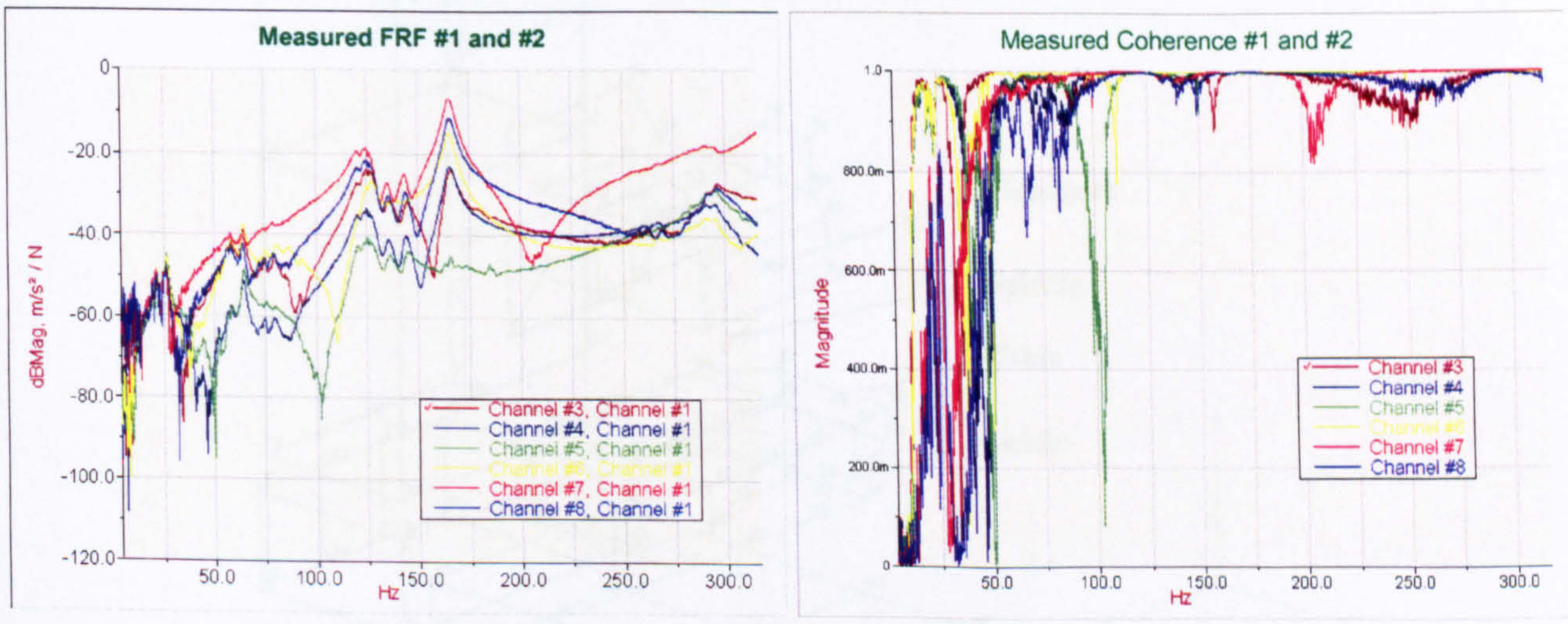

Figure 4.5. Measured FRF and coherence data of point number 1 and 2

The use of the random signal excitation technique successfully minimises the effects of the structural non-linearities to about 1% of the total bandwidth technique but not completely. This is shown by the slight shifts of the resonant frequencies indicated by the curve peaks of

measured FRF data between the channels. This emphasises the necessity to use the global method to accurately estimate the modal parameters.

The coherence values are not always at unity, particularly at the lower frequencies, which is attributed to the limited bandwidths of the transducer and excitation systems (see Appendix A.1). The lower cut-off frequency of the accelerometer sensitivity values is about 5 Hz, whereas the electro-mechanical shaker can only produce constant acceleration output starting from 50 Hz. The small excitation level, combined with the low transducer sensitivities, produces low SNR values. Nevertheless, when resonant frequencies are detected, coherence values rise to acceptable levels at and around the values due to the increased SNR values. The drop of coherence values near an anti-resonance (indicated by an FRF data trough) is considered normal since at that frequency the structural response is close to zero, thus producing low SNR values. Since the modal parameters are calculated from the measured FRF resonance (response peak), they can still be estimated accurately from the measured data.

The modal parameter extraction from the measured data is performed by initially creating the full geometrical definition of the machine structure using the manufacturer's technical drawings and the measured point coordinates (see Figure 4.6) [155]. With each point having three degree of freedom of movement and, 342 measurement files are produced and analysed in the investigation.

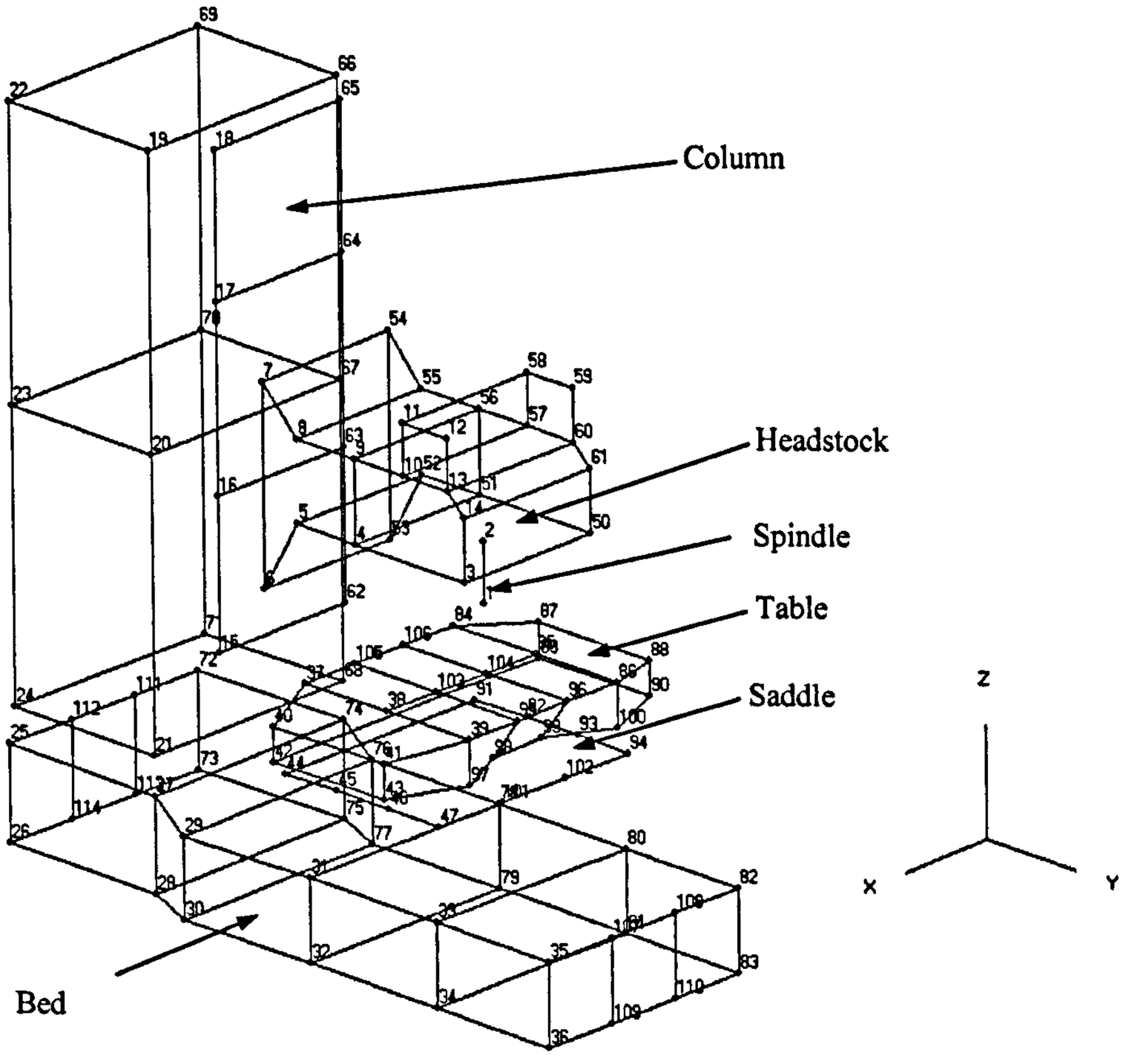

Figure 4.6. The machine structure geometrical definition for the uni-axial investigation

The modal parameter estimation using the advanced analysis option (global method) analyses the measured data on three overlapping frequency bandwidths. This is necessary because of the discrete data resolution that the software can handle (multiple of 128 data blocks up to 2048).

- 3.76 – 84.98 Hz
- 84.34 – 246.94 Hz
- 231.37 – 312.59 Hz

Thus, splitting the analysis into three enables the analysis of all measured data and allows an improvement in the parameter estimation accuracy. The model size is selected as 10 to 20 since the visual inspection of the magnitude plots shows approximately 8 to 10 potential modes. The minimum model number is generally equal to the number of observed peaks and the maximum is two to three times the minimum number.

One stability diagram is produced for each frequency bandwidth showing the averaged FRF data, the potential modes and the associated damping ratios. Figure 4.7 shows the stability diagram of the middle frequency band whereas the rest can be seen in Appendix A.2. The small red circles indicate the selected modes manually selected from the stable and still potential modes which correspond to the peaks of the averaged response curve. The frequency and damping values of the selected modes are transferred into a result table and subsequently used to calculate the residues of the response matrix to produce the mode shapes. The modal parameters results containing the summary of the mode shapes are presented in Table 4.2 and the illustration can be seen in Appendix A.2.

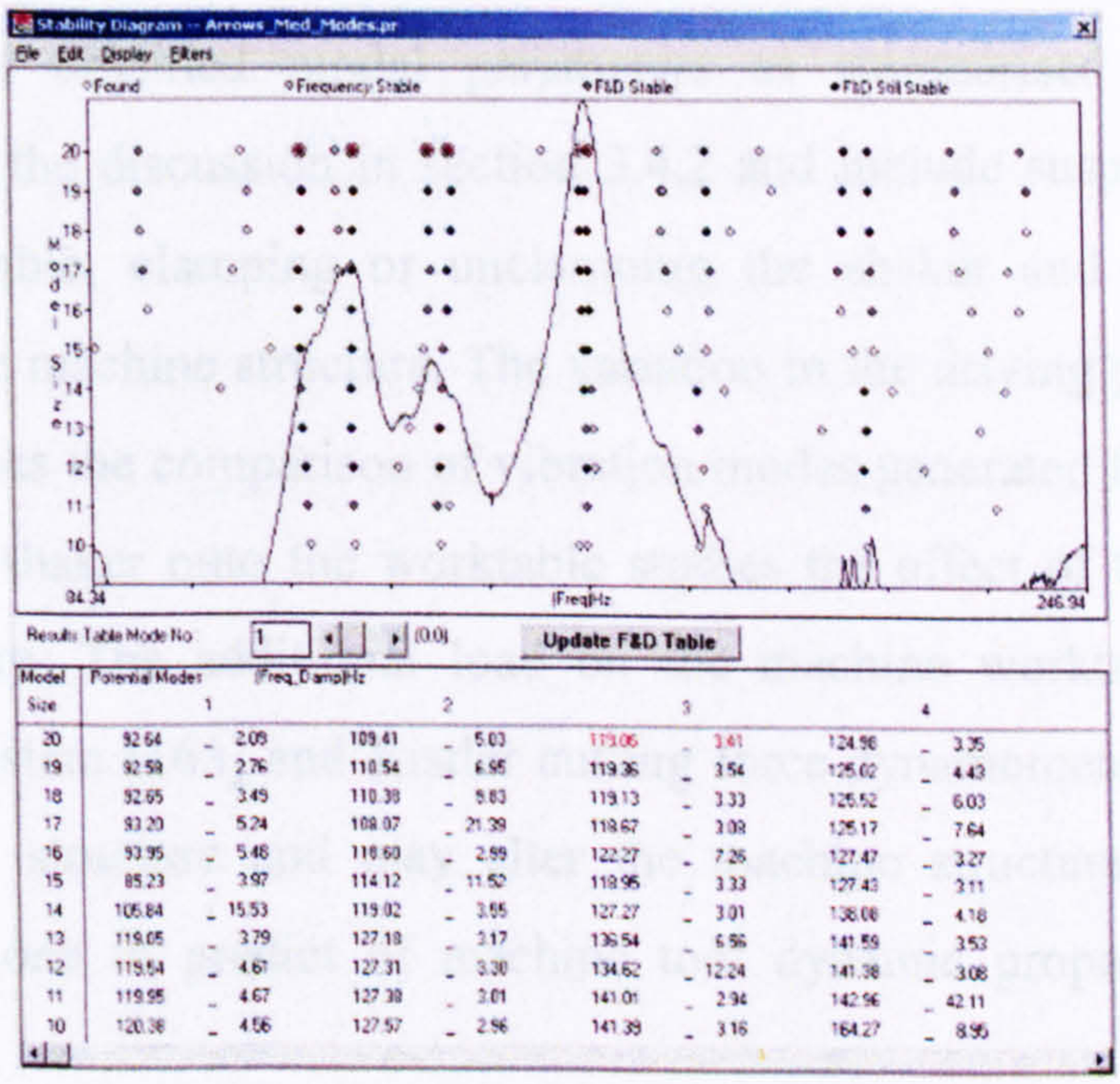

Model Size	Potential Modes Freq_Damp Hz 1		2		3		4	
20	92.64	2.09	109.41	5.03	119.06	3.41	124.96	3.35
19	92.58	2.76	110.54	6.95	119.36	3.54	125.02	4.43
18	92.65	3.49	110.38	9.83	119.13	3.33	125.52	6.03
17	93.20	5.24	109.07	21.39	118.67	3.08	125.17	7.64
16	93.95	5.48	116.60	2.99	122.27	7.26	127.47	3.27
15	85.23	3.97	114.12	11.52	118.96	3.33	127.43	3.11
14	105.84	15.53	119.02	3.55	127.27	3.01	136.08	4.18
13	119.05	3.79	127.18	3.17	136.54	6.56	141.59	3.53
12	119.54	4.67	127.31	3.30	134.62	12.24	141.38	3.08
11	119.95	4.67	127.38	3.01	141.01	2.94	142.96	42.11
10	120.38	4.56	127.57	2.96	141.39	3.16	164.27	8.95

Figure 4.7. STAR Modal stability diagram for the middle frequency range

Mode	Frequency	Damping	Mode Shape Summary
1	21.14 Hz	3.16 %	Dynamic bending of the column in the XZ plane with in-phase headstock and table rocking in the X-axis
2	59.03 Hz	4.20 %	Dynamic bending of the column in the XZ plane with out-of-phase headstock and in-phase table movements in the X-axis
3	64.44 Hz	1.54 %	Dynamic bending of the column in the XZ plane with out-of-phase headstock and in-phase table movements in the X-axis
4	74.96 Hz	2.05 %	Column and headstock bending in the XZ plane, table out of phase movement with relatively big amplitude and headstock bending
5	79.71 Hz	2.77 %	Column and headstock bending, table out of phase movement with relatively big amplitude and bending of headstock
6	119.06 Hz	2.87 %	Rocking of the headstock in the X-axis and slight dynamic bending of the column in the XZ plane
7	127.79 Hz	2.39 %	Small-amplitude dynamic bending of the table and headstock in the XZ and XY planes respectively
8	140.03 Hz	2.24 %	Column and headstock bending and slight bending on table
9	143.42 Hz	3.24 %	Column and headstock bending and slight bending on table with relatively big amplitude
10	165.01 Hz	1.54 %	Twisting of headstock

Table 4.2. Modal parameter results

4.4. Structural dynamic study in three orthogonal directions

This study compares the effects of the various possible experimental modal analysis configurations on the obtained modal parameters as summarised in Figure 4.8. The configurations extend the discussion in section 3.4.2 and include suspending or placing the shaker on the worktable, clamping or unclamping the shaker and placing or removing additional mass on the machine structure. The variation in the driving point from the tool tip to the worktable enables the comparison of vibration modes generated for each configuration. The clamping of the shaker onto the worktable studies the effect of the force transmission path into the structure. The additional load on the machine worktable (in the forms of Microloc clamping system [163] and Kistler cutting force dynamometer [164]) puts an extra 81 kg mass into the structure and may alter the machine structural dynamic properties. However, it enables one to predict of machine tool dynamic properties during a normal machining process.

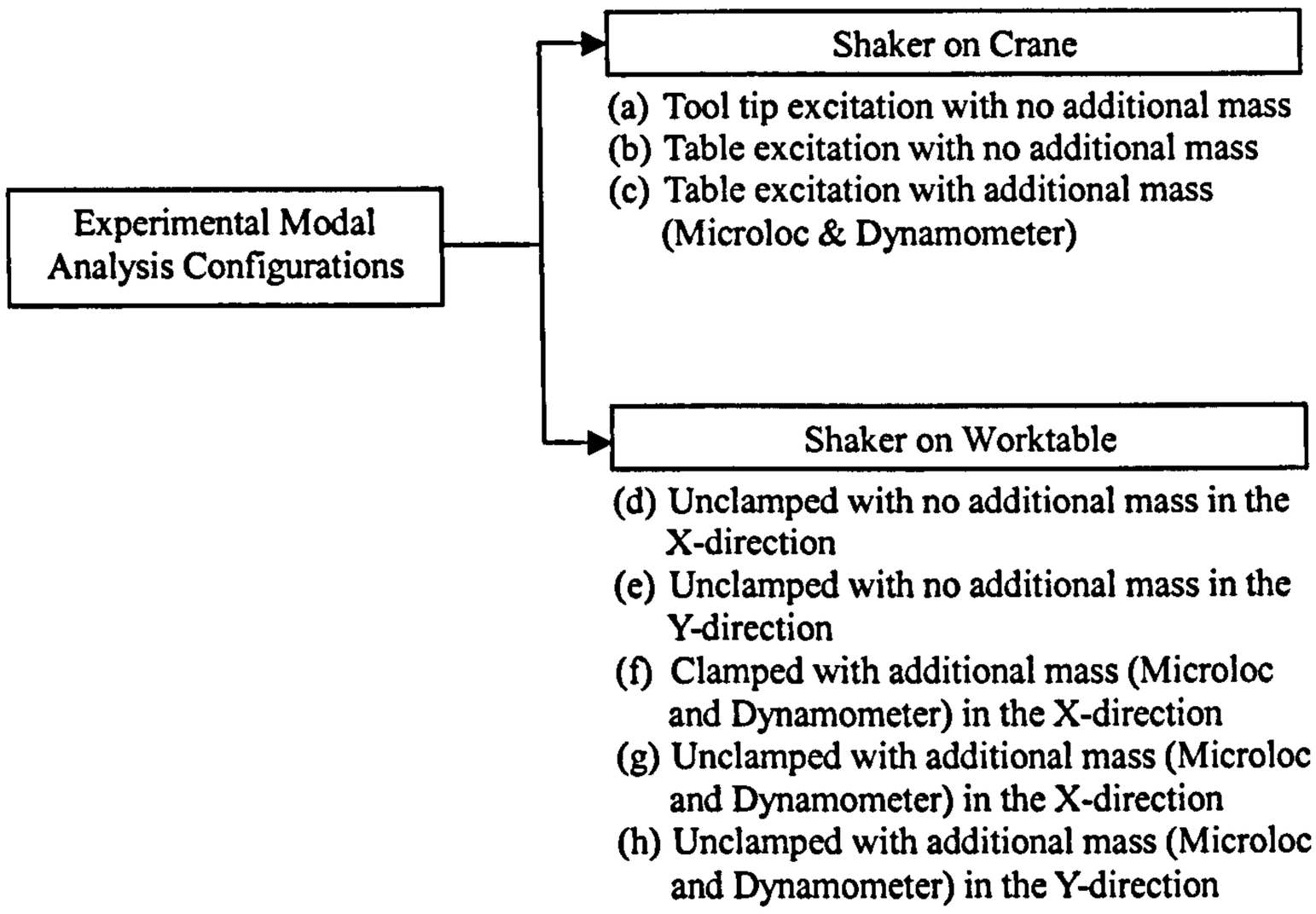

Figure 4.8. Diagram of the investigated experimental configurations

4.4.1. Electrical drive consideration

An opposing force generated by the machine drives due to the control loop disturbances may have an influence on the structural dynamic properties. A series of quick tests are performed to quantify and to determine the effect of energising the control loops during the experiments. Figure 4.9 shows the measured FRF data for the controller state enabled (left column) and disabled (right column) in a shaker-on-the-table-unclamped configuration.

A close inspection on the graphs shows that there is no obvious difference in the resonant frequencies and amplitudes between FRF's at the same DOF. However, the noise content varies between the controller states although there is no clear distinctive pattern. This most probably comes from the electrical circuitry, especially the power electronic devices, because the mains power is supplied to the machine during the experiments. By considering the results and the fact that headstock position shifts during the electrical powering off, all experiments in the investigations are performed with the controller switched off. It also simplifies the mechanical load position displacement for different experimental configurations.

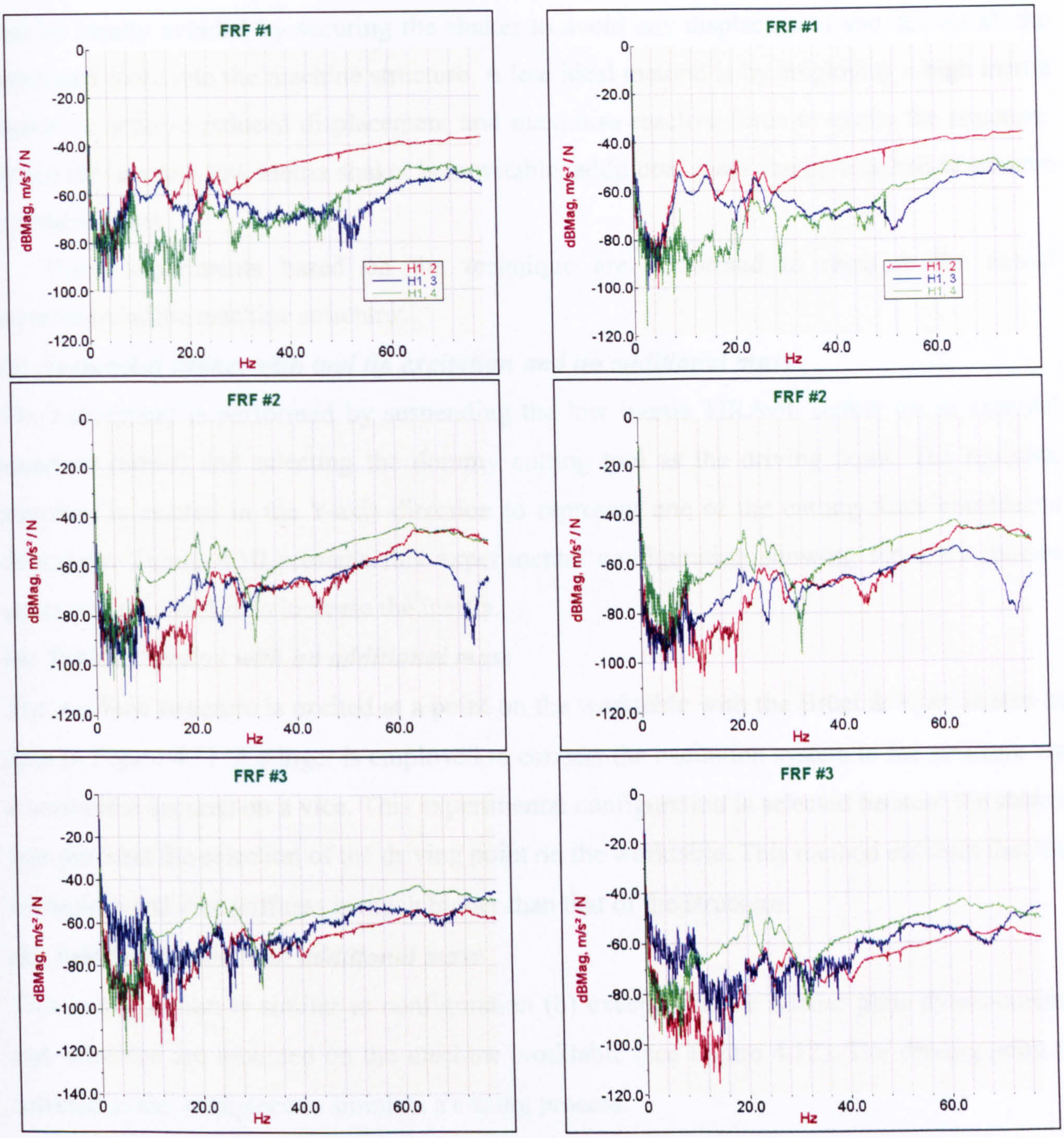

Controller On

Controller Off

Figure 4.9. Graphs of the CNC controller state effects on the measured FRF

4.4.2. Suspended shaker experiments

Suspending the shaker on an external platform confines the introduction of the excitation force only at the driving point. This technique produces more accurate transfer functions (FRF's) due to the measurement of only the net excitation force entering the machine tool structure. It also breaks any force loop linking the machine worktable and the cutting tool which is the case in a shaker-on-worktable configuration.

The high mass of the machine structure may force the shaker to recoil if the mass ratio of the shaker to the machine is relatively small, reducing the excitation force magnitude. This

can be ideally avoided by securing the shaker to avoid any displacement and deliver all the generated force into the machine structure. A less ideal method is by employing a high inertia shaker to achieve reduced displacement and maximise reactive force to excite the structure. When the use of a low inertia shaker is inevitable, additional mass can be attached to achieve a similar effect.

Three experiments based on the technique are performed to measure the modal parameters of the machine structure:

(a) Suspended shaker with tool tip excitation and no additional mass

The experiment is performed by suspending the low inertia TIRAvib shaker on an external structure (crane) and selecting the dummy cutting tool as the driving point. The machine structure is excited in the Y-axis direction to represent one of the cutting force constituent directions. Figure 4.10 presents this experimental configuration showing the extra masses attached to the shaker to increase the inertia.

(b) Table excitation with no additional mass

The machine structure is excited at a point on the worktable with the Brüel & Kjær shaker as seen in Figure 4.11. A stinger is employed to connect the excitation system to the structure via a workpiece secured on a vice. This experimental configuration is selected because the shaker size prevents the selection of the driving point on the worktable. This method assumes that the workpiece and vice stiffness is much higher than that of the structure.

(c) Table excitation with additional mass

This configuration is similar to configuration (b) except that the Kistler plate dynamometer and Microloc are mounted on the machine worktable (see Figure 4.12). The driving point is selected at the workpiece to simulate a cutting process.

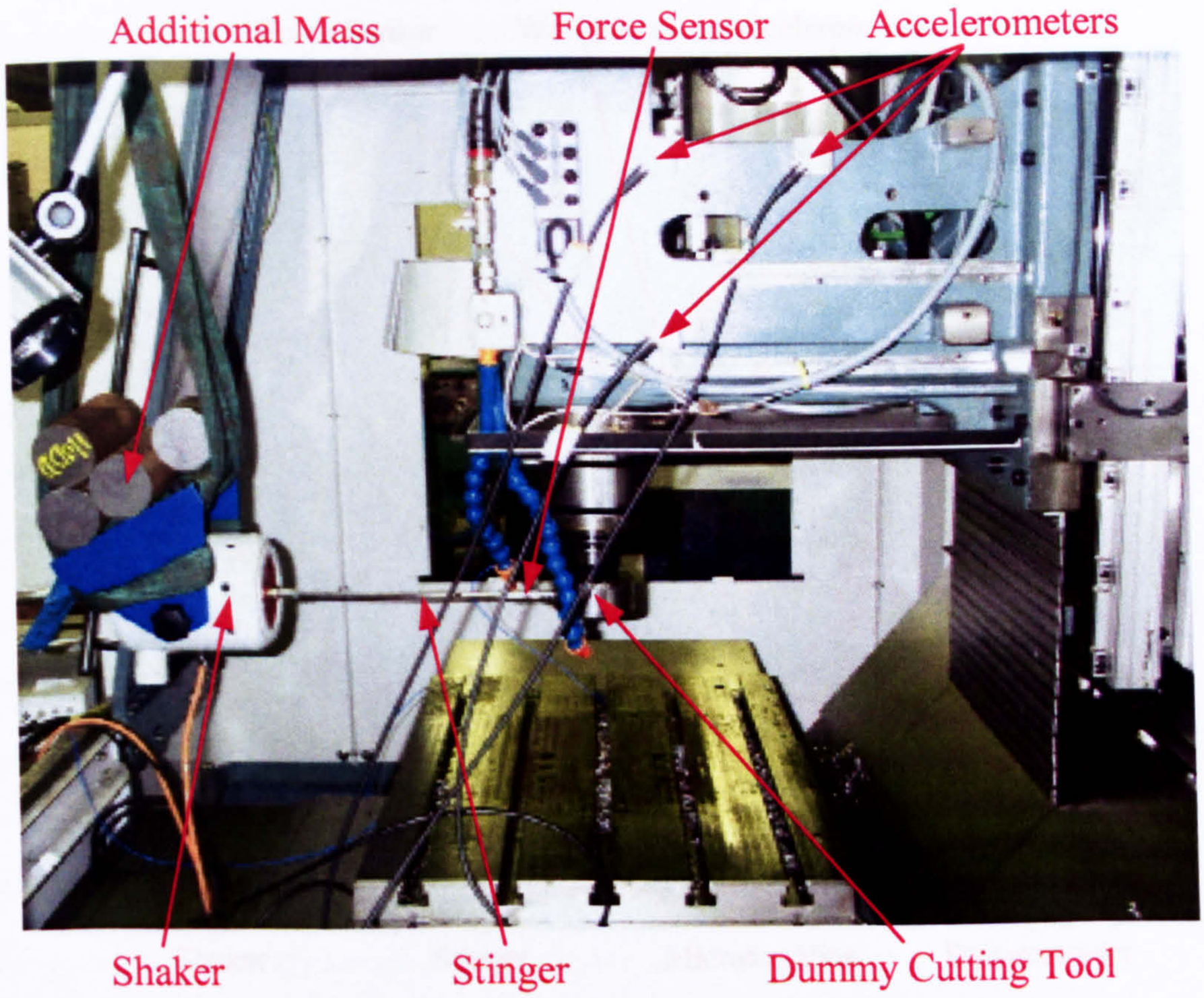

Figure 4.10. Test layout for tool tip excitation with no additional mass

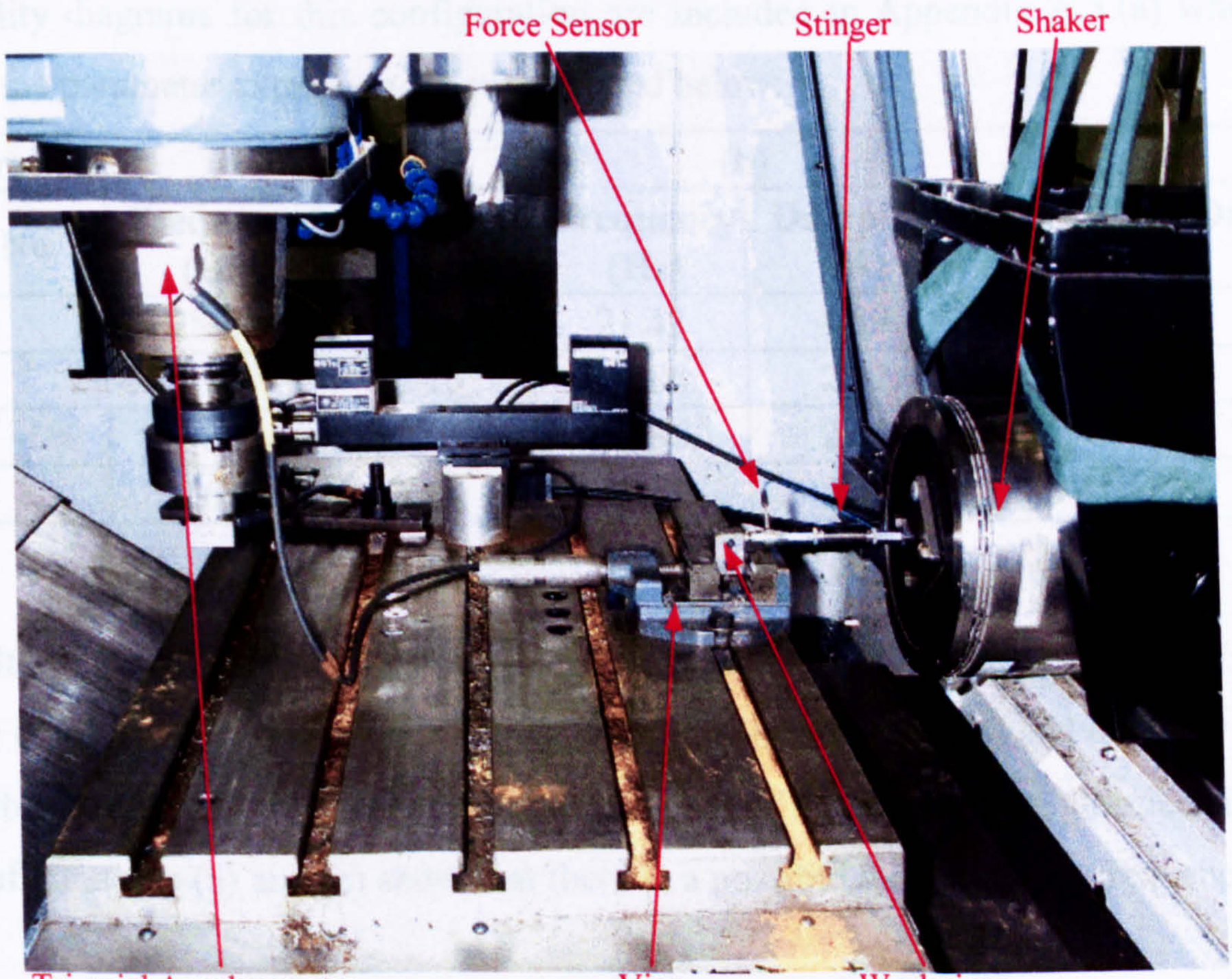

Figure 4.11. Test layout for worktable excitation with no additional mass

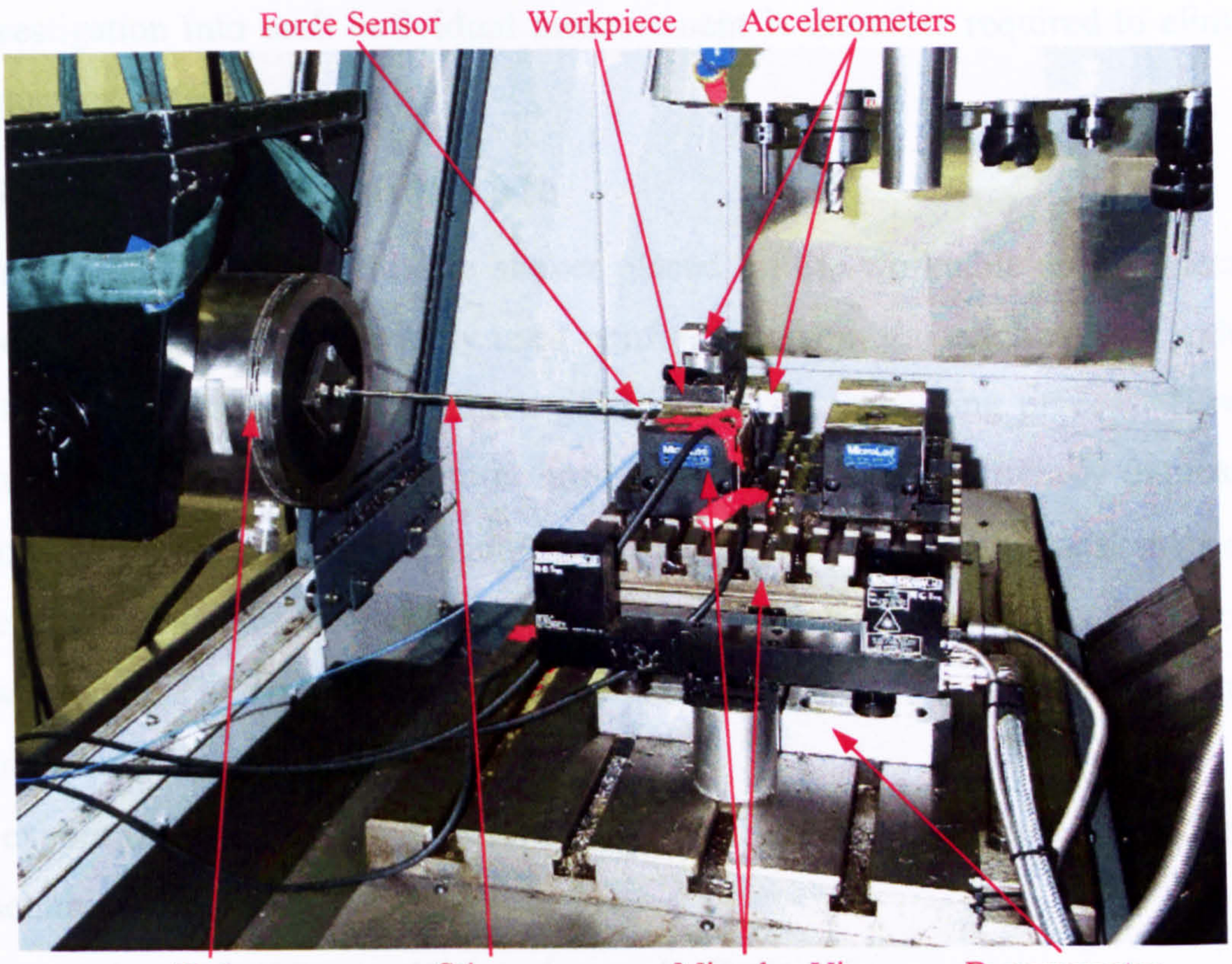

Figure 4.12. Test layout for worktable excitation with no additional mass

The stability diagrams for this configuration are included in Appendix A.3.(a) whereas the results of the parameter extraction are summarised below:

Configuration	(a)		(b)		(c)	
Mode No.	Frequency (Hz)	Damping (%)	Frequency (Hz)	Damping (%)	Frequency (Hz)	Damping (%)
1	28.28	2.80	21.42	4.59	26.72	2.50
2	52.99	6.16	28.86	2.22	46.39	6.00
3	94.09	2.85	38.86	2.65	70.41	10.43
4	116.69	2.50	49.34	2.39	83.31	6.90

Table 4.3. Summary of results for suspended shaker experiments

The results show that definite resonant frequencies occur at around 28 Hz and 49 Hz, varying from one configuration to another. The results from configurations (b) and (c) show that there are possibly two closely coupled modes around each of the resonant frequencies. The results from configurations (a) and (c) show that there is a possible third resonant frequency at about 83 Hz.

This shows that the variation in the driving point produces different modal parameter results, which is very much against the theory. It indicates that the machine tool structure is not linear. The non-linearities also manifest in the occurrence of the closely coupled modes. A

further investigation into each individual measurement is therefore required to eliminate this effect as much as possible.

4.4.3. Shaker on the worktable

Experimental modal analysis with the shaker placed on the worktable and connected to the cutting tool is one of the most widely used configurations in the machine tool industry [63] because it can simulate the cutting force generation of a machining process. However, the constituent forces entering the structure through the worktable is generally unmeasured and may distort the measured modal parameters. The clamping of the shaker body to the worktable can increase the excitation force on the driving point as well as the reaction force into the worktable. The configuration enables the excitation of the machine structure in both the X- and Y-direction.

Five experiments based on this technique are performed to measure the modal parameters of the machine structure:

(a) Shaker unclamped with no additional mass in X-direction

The TIRAvib shaker is placed on the worktable on its rubber feet and connected via a stinger to the dummy cutting tool. The excitation is generated in the machine's X-axis direction (see Figure 4.13).

(b) Shaker unclamped with no additional mass in Y-direction

This is a repeat of the previous experiment (configuration (a)) except that the machine structure is excited in the Y- direction as illustrated in Figure 4.14.

(c) Shaker clamped with additional mass in X-direction

The additional mass (cutting force dynamometer and Microloc) is secured on the worktable and the shaker body is clamped on the vice. (see Figure 4.15). The worktable and headstock positions are adjusted slightly to accommodate the additional mass and raised shaker.

(d) Shaker unclamped with additional mass in X-direction

This experimental configuration is similar to the previous one (configuration (c)) with the shaker clamping removed and replaced with rubber legs (see Figure 4.16).

(e) Shaker unclamped with additional mass in Y-direction

Figure 4.17 shows the experimental configuration for this particular investigation, which is similar to the previous one but in Y-direction.

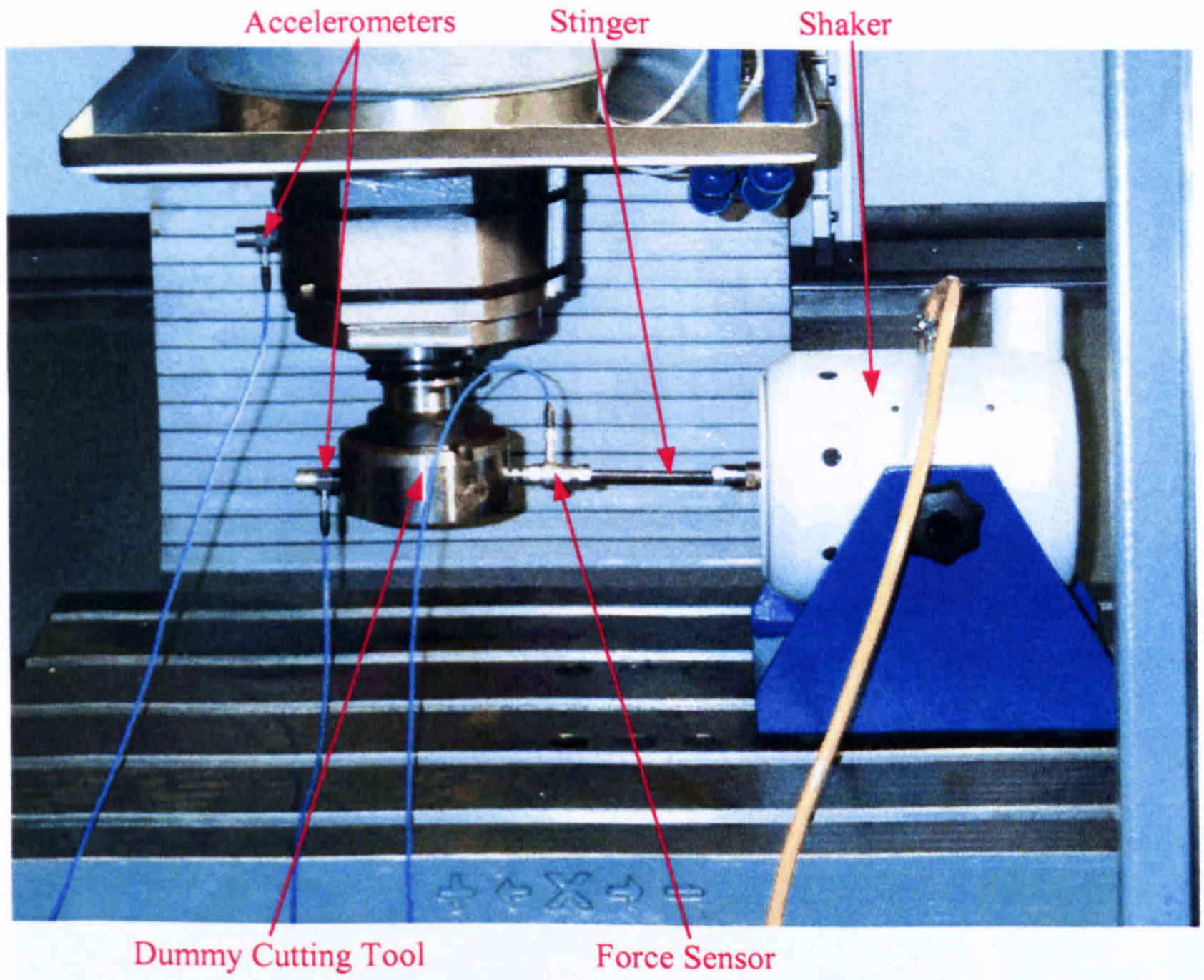

Figure 4.13. Shaker-on-table excitation test layout with no added mass in X-direction

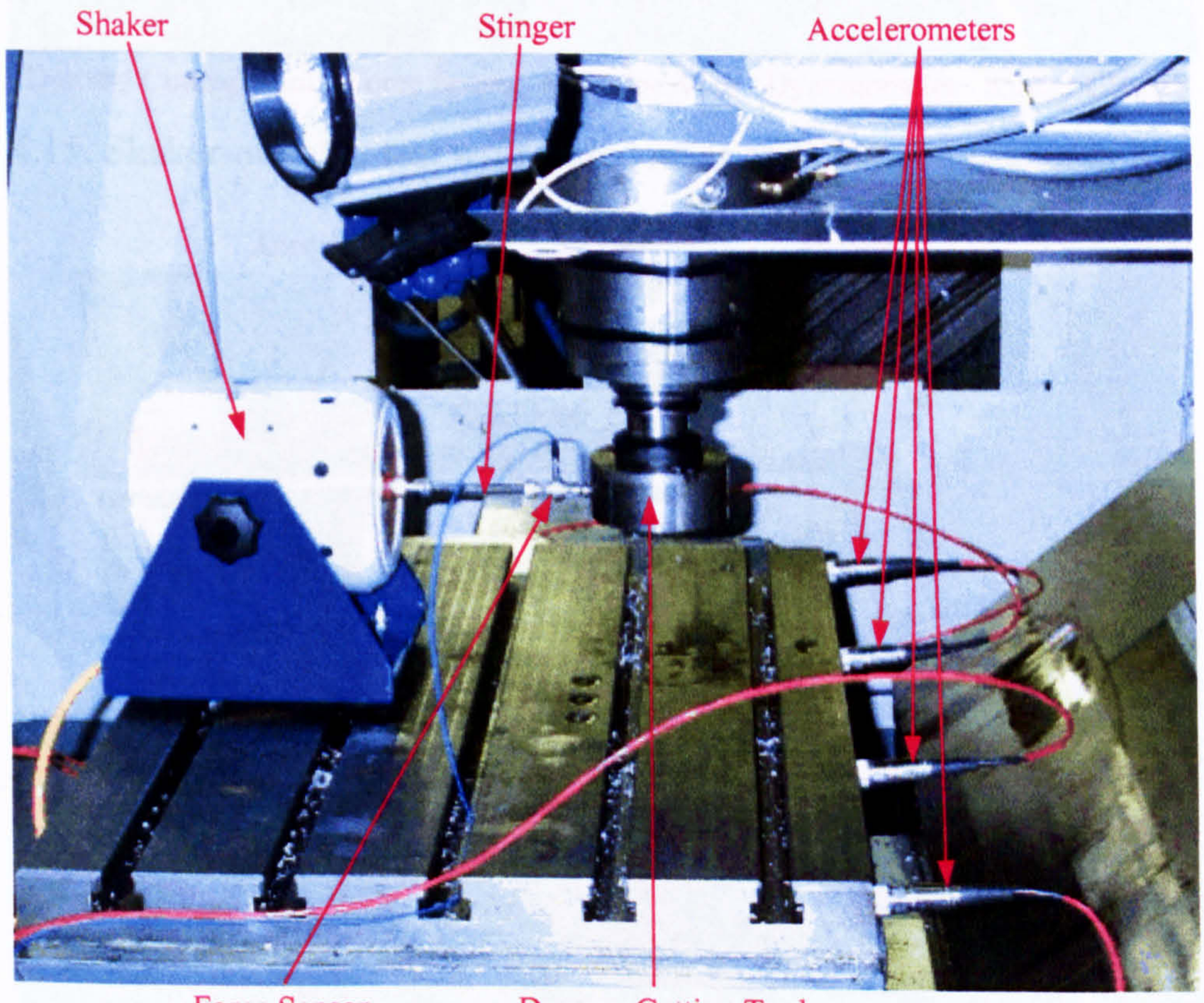

Figure 4.14. Shaker-on-table excitation test layout with no added mass in Y-direction

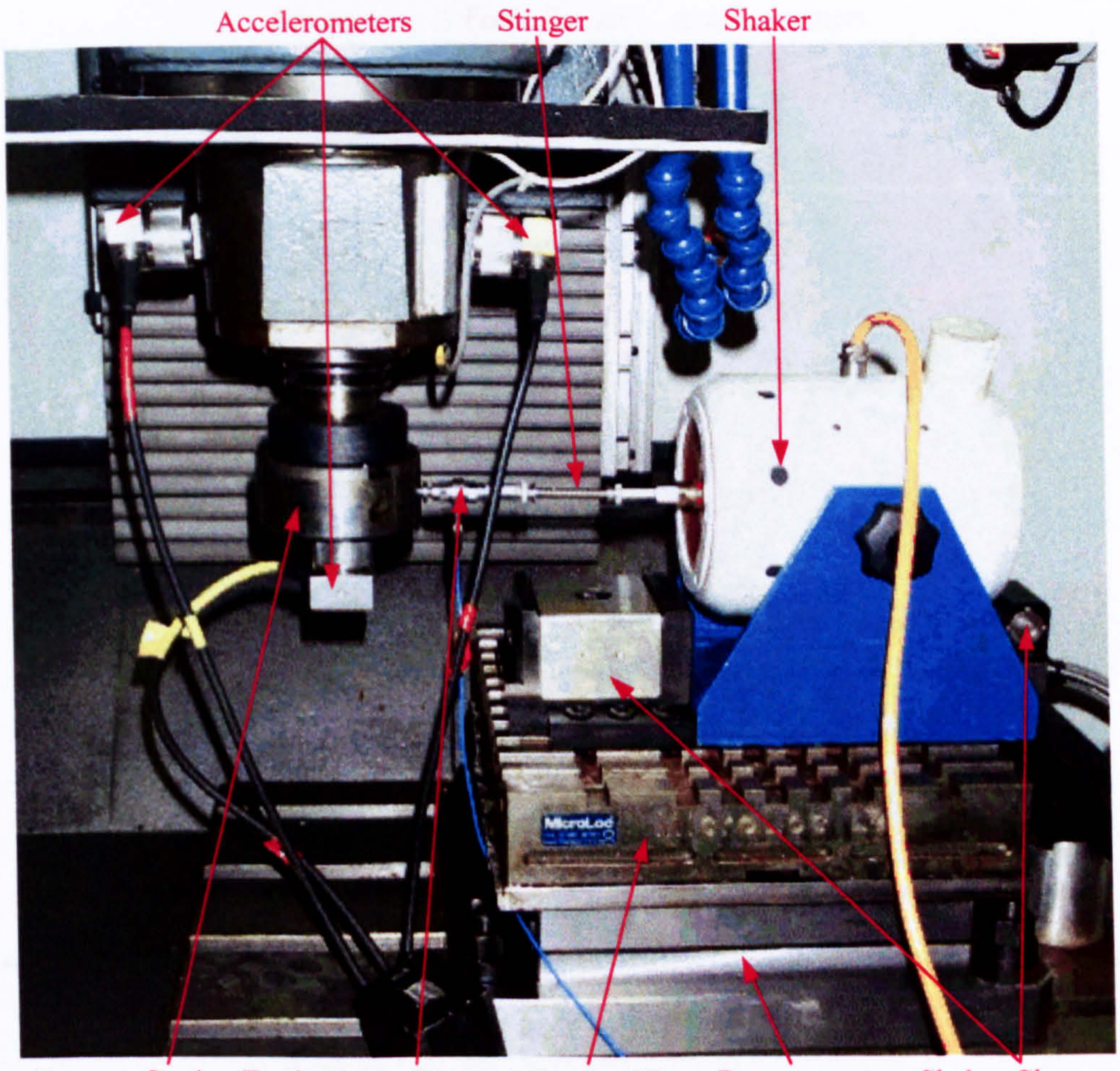

Figure 4.15. Shaker-on-table test with added mass and clamped shaker in X-direction

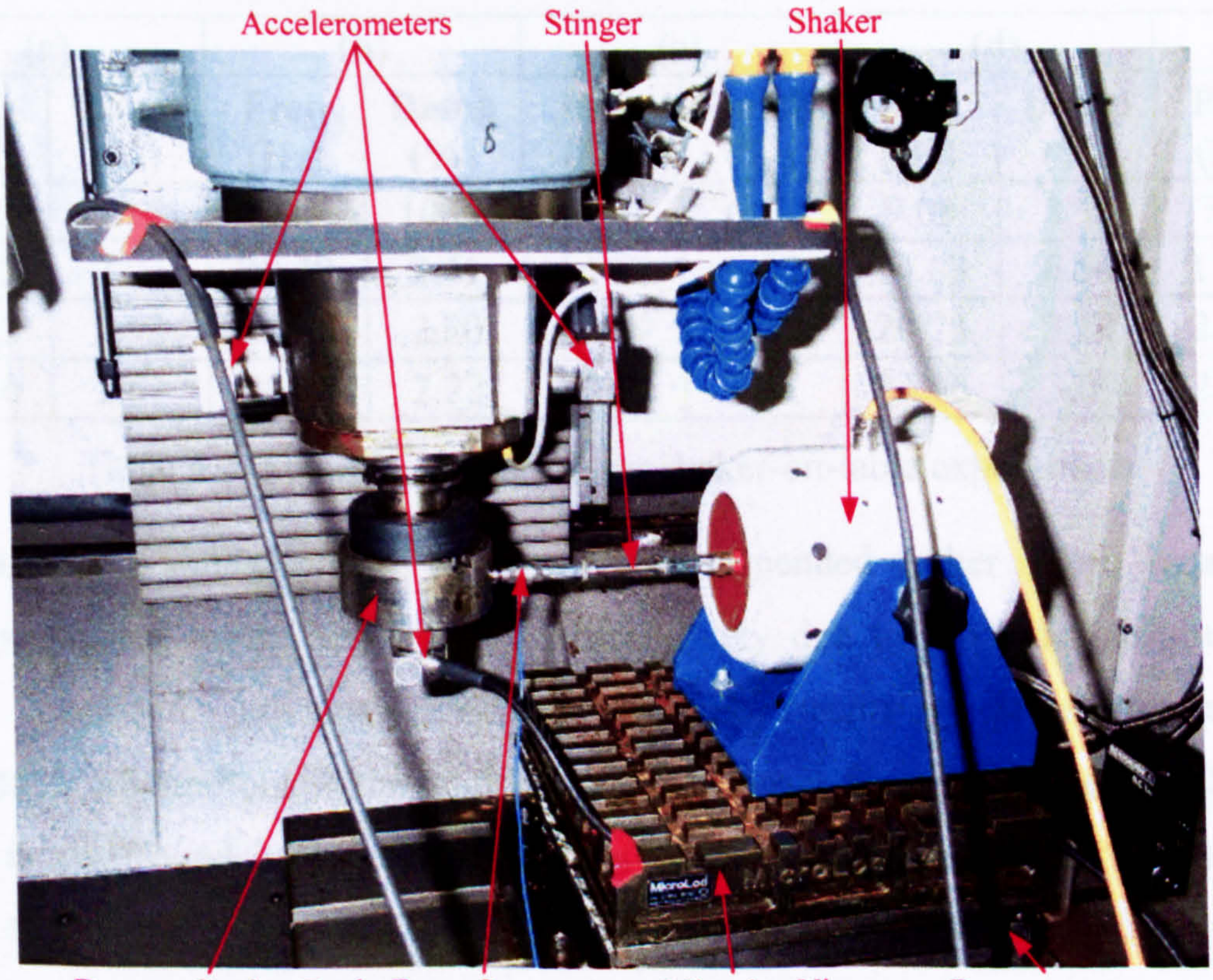

Figure 4.16. Shaker-on-table excitation test layout with additional mass and unclamped shaker in X-direction

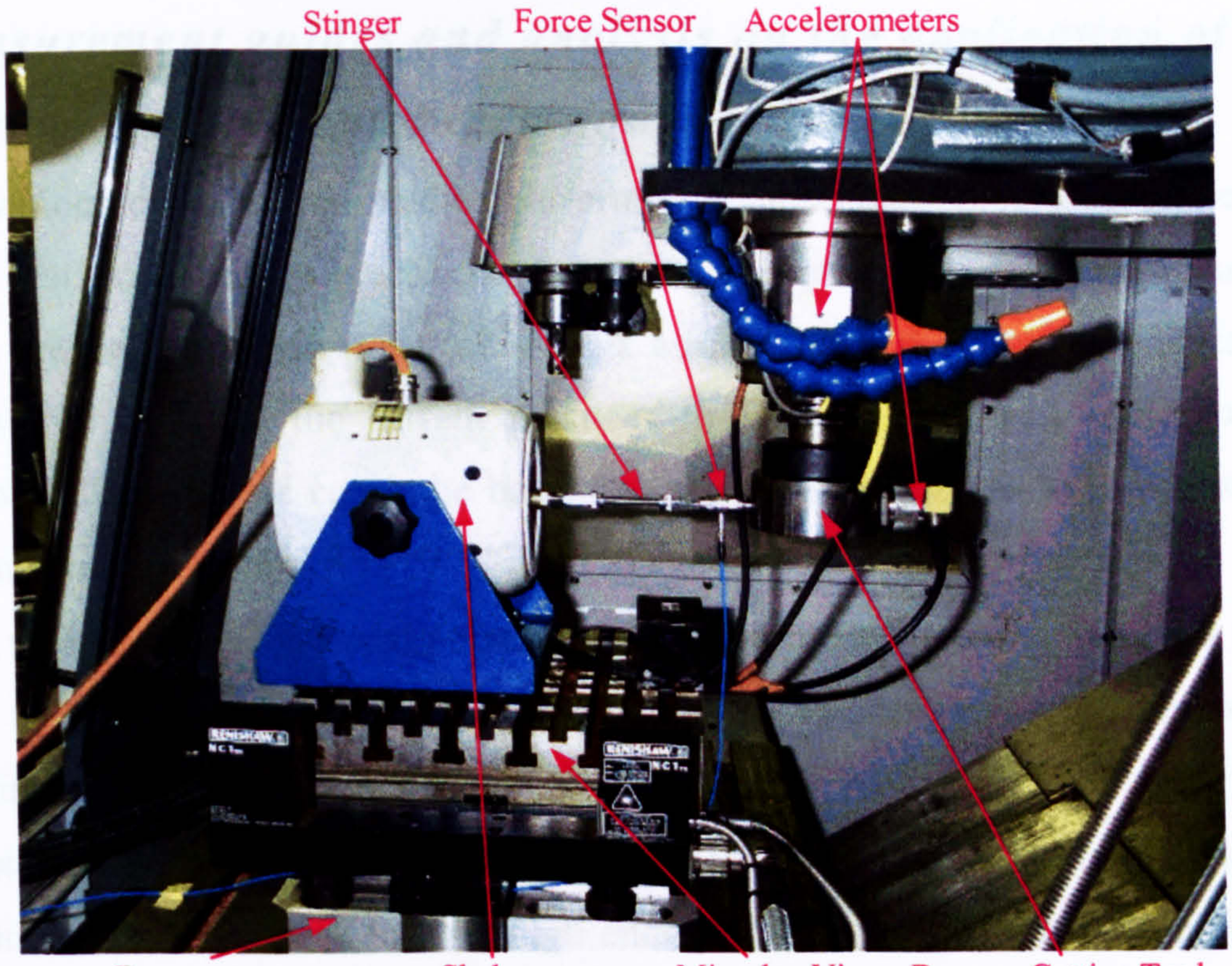

Figure 4.17. Shaker-on-table excitation test layout with additional mass and unclamped shaker in Y-direction

The stability diagrams for this configuration are included in Appendix A.3(b), and the modal parameters obtained are summarised below:

	(a)		(b)		(c)		(d)		(e)	
Mode No.	**Freq (Hz)**	**Damp (%)**	**Freq (Hz)**	**Damp (%)**	**Freq (Hz)**	**Damp (%)**	**Freq (Hz)**	**Damp (%)**	**Freq (Hz)**	**Damp (%)**
1	20.75	5.15	9.06	10.31	9.14	6.77	9.08	3.99	7.99	6.48
2	23.75	2.07	28.49	2.41	14.61	6.00	14.63	6.54	13.47	13.35
3	26.12	1.92	38.40	2.80	19.89	2.41	20.73	3.10	23.20	9.00
4	50.16	2.61	50.07	2.22	39.15	2.01	24.06	3.09	27.46	3.87

Table 4.4. Summary of results for shaker-on-table experiments

The results show a similar pattern to those of the suspended shaker where frequency shifts and closely coupled mode occur. This is most likely due to the machine structure non-linearities discussed previously. Another feature occurring at shaker-on-worktable experimental configurations is the additional low resonant frequency at around 10 Hz. This indication is also found in the cutting process experiments discussed further in Chapter 6. Therefore, this configuration is shown to be suitable for simulating the machining process, but not the study of the structure's modal parameters.

4.5. Measurement guides and analysis on the application of various experimental techniques

From the various experimental studies performed in this investigation, several conclusions containing best measurement practices of machine tool structures to obtain accurate modal parameters are drawn. These practical aspects comply with the basic principles of modal analysis as well as allow the current practices to be continued with some configuration modifications. These points cover the basic measurement practice as well as more complex experimental configurations:

- Taking measurements on nodal points should be avoided. More importantly, a nodal point should never be used as the driving point since all measurements will be normalised to this point in the modal analysis stage.
- The determination of nodal points can be done by performing an initial measurement and determine if the coherence level is high enough. It can also be done during the analysis step by performing a global modal analysis after the measurements, so that measurements can be performed quickly.
- The number of points that needs to be taken depends on the structure. If the movement of parts of the structure is an important issue due to vibration then more points need to be taken to represent the movement of those parts. On the other hand, if the movement of certain parts of the structure is not very important for the performance of the machine then less number of points should be measured.
- Ideally, measurements should be performed using a fine resolution. It means that the measurement bandwidth may need to be split into several smaller bandwidths using the zoom function. However, normally zoom analysis is not necessary. The bandwidth of measurement usually depends on the operating frequency of the machine up to the third or fourth harmonics.
- In exciting the structure, the amount of force introduced to the structure should be less than the maximum force that the shaker and structure can receive. However, this should not sacrifice the coherence of the measurements.
- Measurements should be measured only on the structure of the machine. Guarding that prevent access to those points might need to be removed.
- To optimise the signal strength, 'auto range' and final tweaks on the input signal range may be required. Acoustic signal may also indicate that unwanted vibration is occurring in addition to the structural vibration to be measured.

4.6. Conclusions

The investigation results for the experimental modal analysis of the Cincinnati vertical machining centre has been presented in this chapter. An initial investigation of SIMO experimental modal analysis in the X-direction was carried out to provide proofs for the theoretical concepts discussed in the earlier chapter and to obtain the optimum methods available in the modal parameter extraction software. Further SIMO experimental modal analyses were carried out in the main investigations by exciting the structure in a single direction and measuring the responses in tri-axial directions. Different suspended shaker and shaker-on-worktable experimental configurations were explored to determine the benefits and pitfalls of the selected configuration.

The modal parameters extracted from the measured data for different experimental configurations vary from one another to a small degree. This indicates that the presence of non-linearities in the structure and care must be taken not to aggravate their influence during the measurement process. The experimental results show that the lowest mode shape obtained in all configurations involves the bending of the column and the head in the Y-direction. Thus, it can be deduced that the column's structural properties limit the performance of the machine.

The investigation has also produced several guidelines for performing reliable experimental modal analysis in order to obtain accurate FRF data and maximised SNR. It was also found that the suspended shaker configurations generated more accurate data due to the better input force measurement. However, the measured FRF from shaker-on-table configuration produced higher SNR because most excitation force was delivered into the structure rather than dissipated by the recoiling of the shaker.

Having performed this investigation on the structural vibration, the modelling of the machine tool feed drives, where further vibration can be generated by the axis motions, is investigated in the following chapter.

Chapter 5. HYBRID MODELLING OF THE DIGITAL DRIVES APPLIED ON CINCINNATI ARROW 500 MACHINE TOOL

Modern industry requires high acceleration, fast response and small tracking errors from high-speed machine tools in order to reduce cutting and non-cutting times and improve productivity. The positions and velocities of machine tool slides or axes are controlled by the machine feed drives in accordance with the commands generated by the CNC interpolator. Therefore, improving the feed drive performances represent an important factor in the process of enhancing the machine tool accuracy by reducing/eliminating the machining errors.

The modelling approach to machine tool feed drive system plays an important part in the above-mentioned process because the essential elements in machine tool dynamics can be studied and their influence on the overall machining precision can be evaluated without wasting workpieces for practical operations. The modelling and simulation techniques are used by the machine producers (during the design stage) and users (to improve the machine performance) in order to predict and study the machine behaviour under various operating conditions, at much lower costs, while enhancing performance and efficiency.

The CNC machine tools are hybrid systems, therefore the hybrid modelling approach developed by Pislaru et. al. [97] is applied to model the feed drives within Arrow 500 vertical machining centre. The hybrid models with distributed load, explicit damping factors, non-linearities (backlash and Coulomb friction) are implemented in Simulink. The simulated results are compared with the dynamic behaviour of the machine tool feed drive to verify the accuracy and performance of simulation models. These modelling and simulation techniques have the potential to reduce experimentation, optimise cutting parameters, and improve the quality of the machining process reflected on the machined surfaces.

The development of an accurate Simulink model for the Sinumerik 840D controller fitted on the machine represents an important contribution to the study of motion control for high-performance drive systems. The CNC control is a complete digital system where microprocessors command and control the axis drive motors with high precision.

The hybrid models of the digital feed drives implemented in the Cincinnati Arrow 500 machine tool are used for the study of the vibration error sources within the machine and the various elements influence on the drive performance.

5.1. Drive system configuration

The studied feed drive has two main parts: control (electrical) part and mechanical load (see Figure 5.1). The latest state-of-the-art digital controller (Sinumerik 840D) controls the permanent magnet synchronous AC motors by the vector control method.

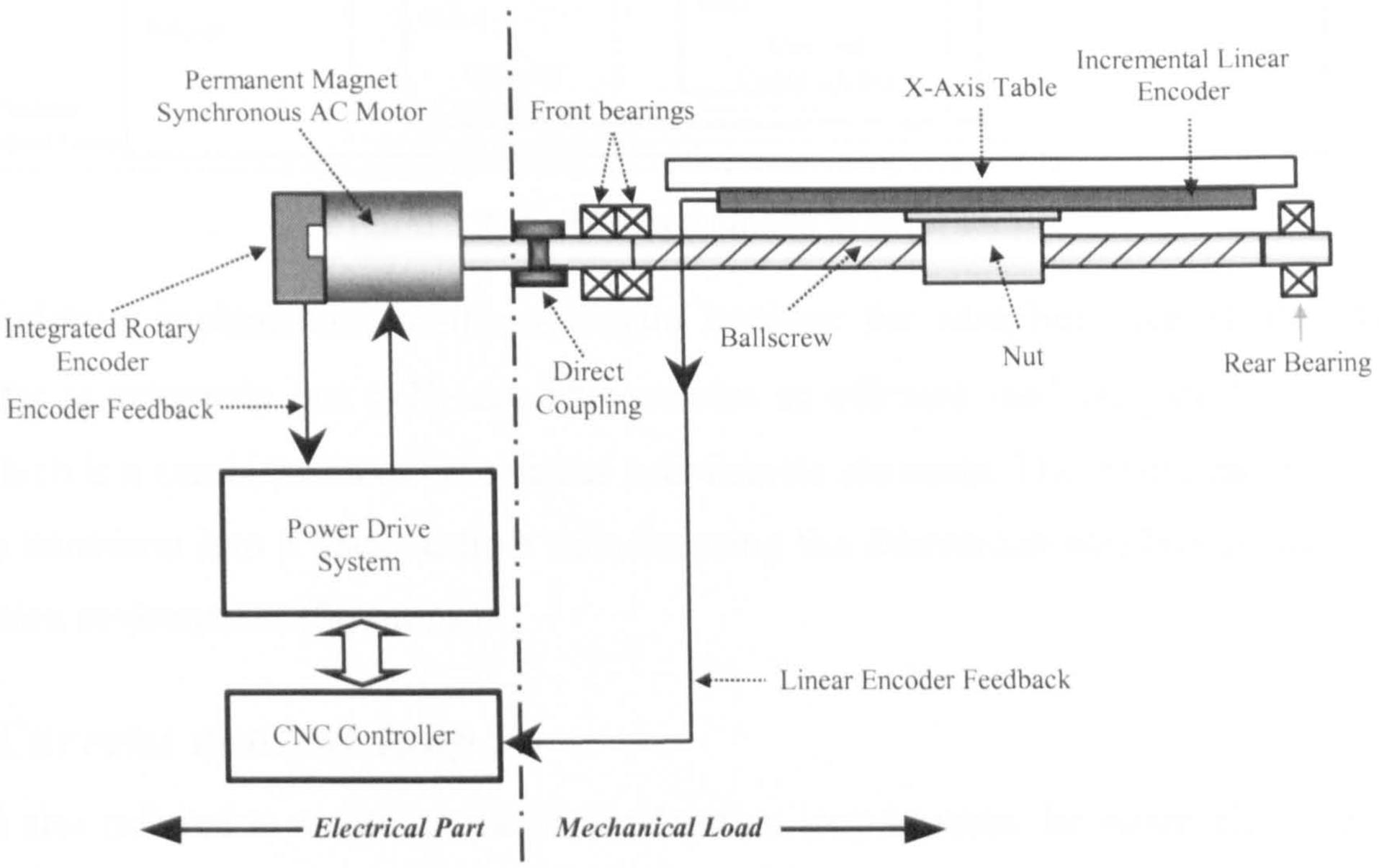

Figure 5.1. X-axis feed drive configuration

The linear movement of the machine worktable is generated by converting the rotary motion of the AC motor through a ballscrew system. However, friction between the moving components of the machine (ballscrew – nut, guideways – worktable, etc.) can cause significant errors in precision machining. The dominant friction of this setup is the complex kinematics of the ball nut which is sometimes desirable to provide high damping, although in the majority of cases, it is unwanted due to the introduction of the steady state or static error.

An accurate model of the feed drive should contain values for the various damping coefficients and non-linearities (backlash, Coulomb friction) influencing the performance of the CNC machine tool.

The studied feed drives have feedback signals generated by incremental linear encoders and feed-forward paths to enable fast and an accurate positioning. Three loops for position, velocity and current control are connected in cascade (see Figure 5.2). The technical data of the Arrow 500 machine tool is listed in Appendix B.

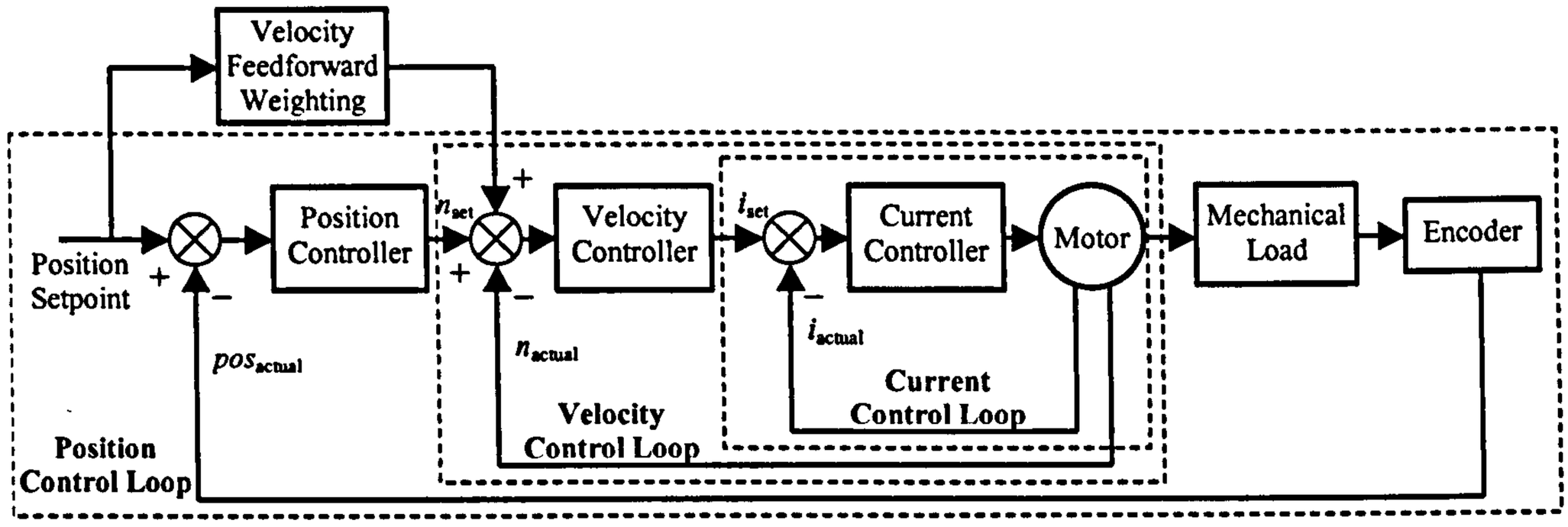

Figure 5.2. Feed drive closed control loop

The model is implemented in the s-domain because the sampling-time of the machine controller is extremely fast (125 μs). This enables an efficient modelling of the mechanical load which is a combination of continuous and discrete elements. The model can be relatively easy to transform into a discrete time domain using the ***Discretiser blockset*** available in the simulation environment (Simulink).

5.2. Current control loop

This is also referred to as the torque or acceleration loop because the motor electrical torque and the machine acceleration by the feed drive are proportional to the motor current. The controllers compare the set point with the measured currents and produces the voltage values required by the power electronic system to minimise the error signal (see Figure 5.3).

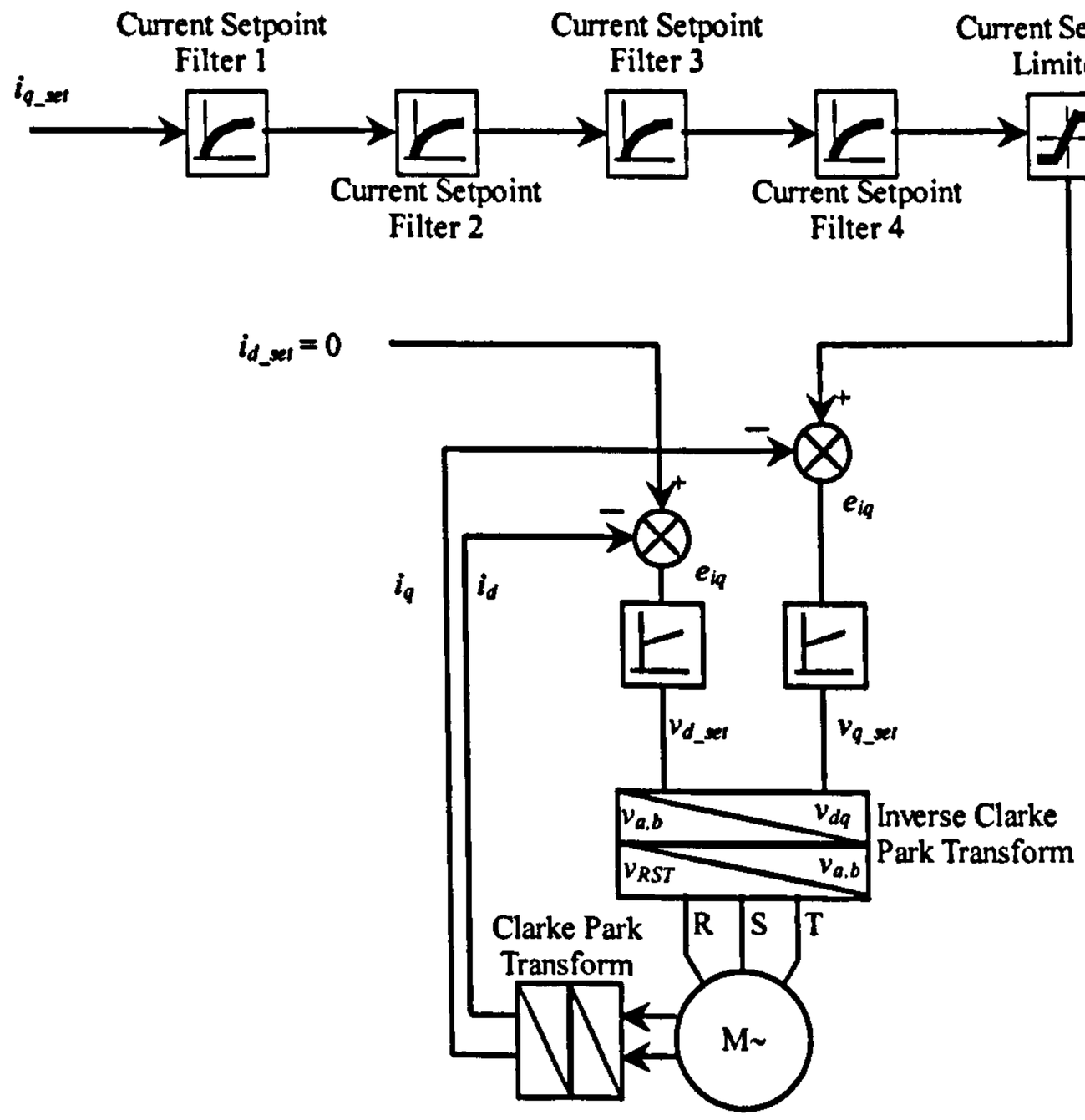

Figure 5.3. Current control loop diagram [165]

There are two control loops in the system regulating the ***quadrature*** (torque generating) and ***direct*** (magnetic flux producing) currents. This control loop architecture is based on the ***field oriented control*** (FOC) method [166], which regulates the magnitude and phase of the motor current (***vector control***). This technique generally requires the Digital Signal Processor (DSP) technology to accurately and quickly performs the complex mathematical calculations.

The conversion of the three-phase into two-phase current (***direct*** (d) and ***quadrature*** (q) components) for the control purpose is performed with the ***Clarke-Park transformation***. The ***Clarke*** transformation (illustrated by Figure 5.4) translates the three-phase variables (R-S-T or a-b-c) into two-phase time varying parameters with a static reference (a-b or α-β).

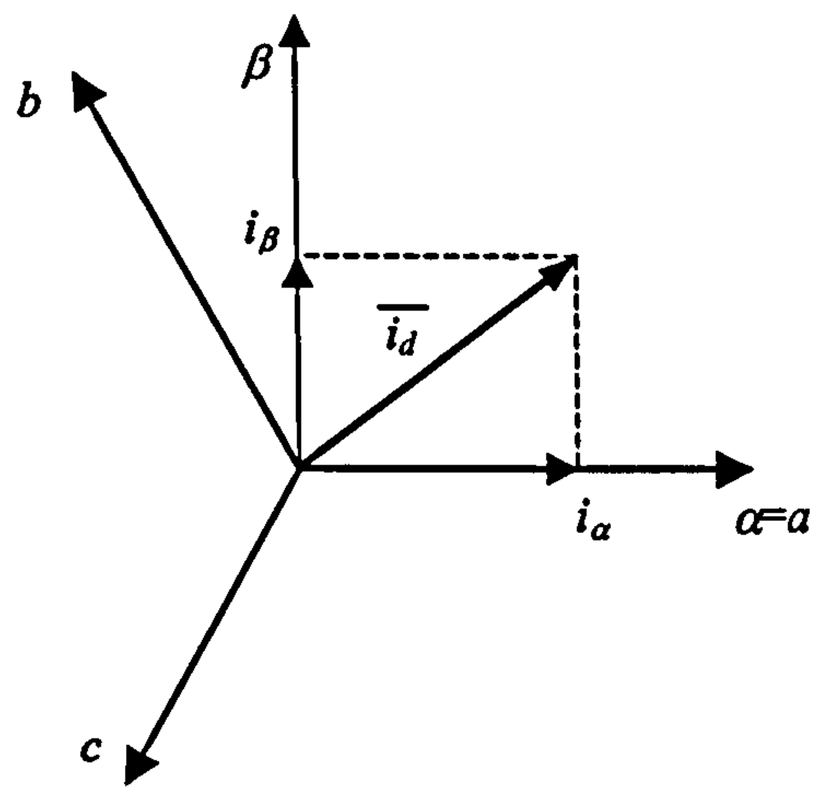

Figure 5.4. Clarke transformation

When the *a*-axis is superimposed with the static reference α, the transformation algorithm can be represented by the following equation:

$$i_\alpha = i_a;\ i_\beta = \frac{1}{\sqrt{3}} i_a + \frac{2}{\sqrt{3}} i_b \text{ where } i_a + i_b + i_c = 0 \qquad (5.1)$$

The ***Park*** transformation (Figure 5.5) converts the two-phase time varying parameters with a static reference into two-phase time invariant parameters with a rotating reference and direct-quadrature (d-q) axes. They are also called the ***rotor torque axes*** because the directions correspond to the rotor shaft and magnetic flux generated by the stator. Park transformation can be performed only when the rotor angular position, θ, is known. Its value is usually obtained from an integrated rotary position sensor or from a theoretical prediction in a sensor-less strategy using the high speed DSP technology. This transformation is represented using the following algorithm:

$$i_d = i_\alpha \cos(\theta) + i_\beta \sin(\theta);\ i_q = -i_\alpha \sin(\theta) + i_\beta \cos(\theta) \qquad (5.2)$$

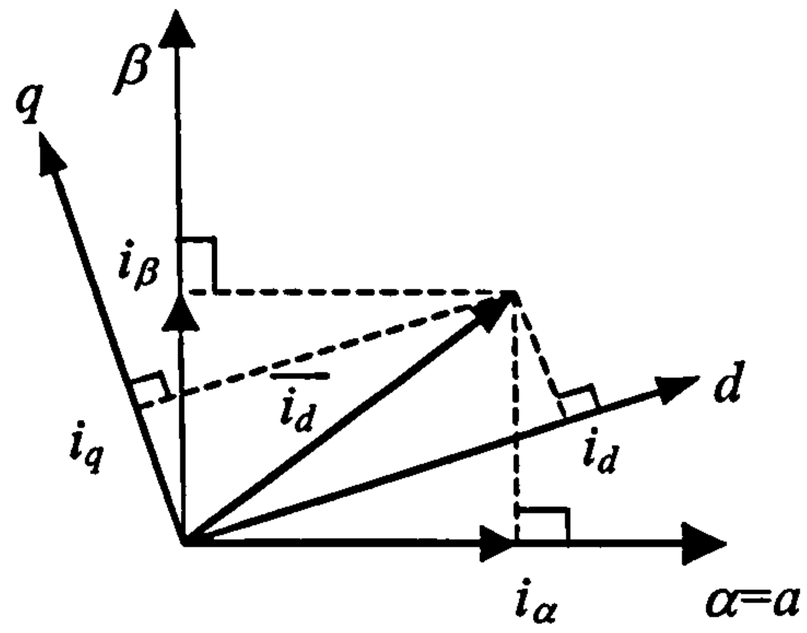

Figure 5.5. Park transformation

Since the FOC method implements the current control algorithm in the d-q reference frame, an inverse of the Clarke-Park transformation is necessary to calculate the required three-phase voltages applied to the power electronic system. The following mathematical equations are employed:

$$v_a = v_d \cos(\theta) - v_q \sin(\theta) \tag{5.3}$$

$$v_b = v_d \cos\left(\theta - \frac{2}{3}\pi\right) - v_q \sin\left(\theta - \frac{2}{3}\pi\right) \tag{5.4}$$

$$v_c = v_d \cos\left(\theta + \frac{2}{3}\pi\right) - v_q \sin\left(\theta + \frac{2}{3}\pi\right) \tag{5.5}$$

In addition, low-pass or band-stop filters are normally employed to dampen the resonance frequency peaks (resonance) contained in the current setpoint received from the velocity control loop. The notch (narrow band-stop) filter can reduce a needle-shaped spike located at a fixed frequency, whereas a low-pass filter can minimise moving spikes up to a certain frequency. The value of the filtered current setpoint is normally limited to avoid any damage to the motor or power drive unit. The direct and quadrature voltage setpoints from the PI controller feed a power electronic inverter based on the ***pulse width modulation*** (PWM) technique to energise the motor.

An indirect AC power electronic converter (consisting of rectifier, DC link and inverter) (see Figure 5.6) provides the current and voltage for the PMSM. The converter transforms the three-phase AC mains to a high voltage power supply of the DC link unit through power diodes arranged in a bridge rectifier configuration. The generated DC voltage level is approximately 1.35 times of the line-to-line mains voltage, which is further smoothed by the use of the inductor and capacitor.

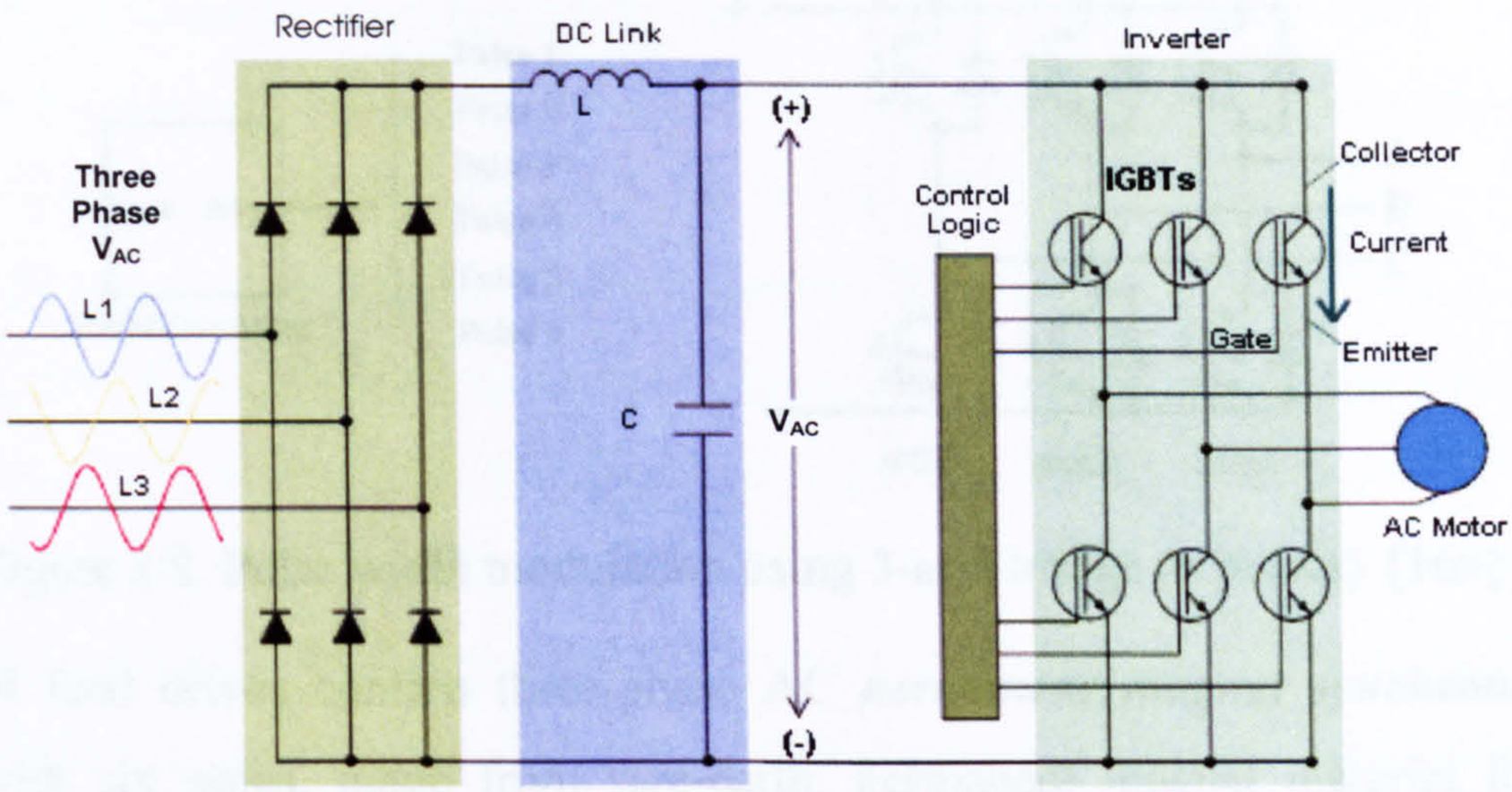

Figure 5.6. Diagram of the power electronic system [167]

The DC link voltage is used by the inverter to drive the motor by switching on and off the power electronic devices at a rate controlled by the PWM control logic unit, creating an impressed sinusoidal AC current. The principle of PWM technique is illustrated in Figure 5.7, where the power-on period of the electronic devices is varied to obtain the required output voltage or current (for both DC and AC applications). The phase of output voltage of AC drive applications can also normally be controlled in addition to its amplitude. In addition to IGBT, the inverter elements could use thyristors, gate turn off thyristors (GTO), bipolar junction transistor (BJT) or Metal Oxide Semiconductor (MOS) transistors or insulated gate bipolar transistor (IGBT). Some systems can also contain a re-generating inverter unit to feed back the voltage from the motor to the DC link to save mains power consumption.

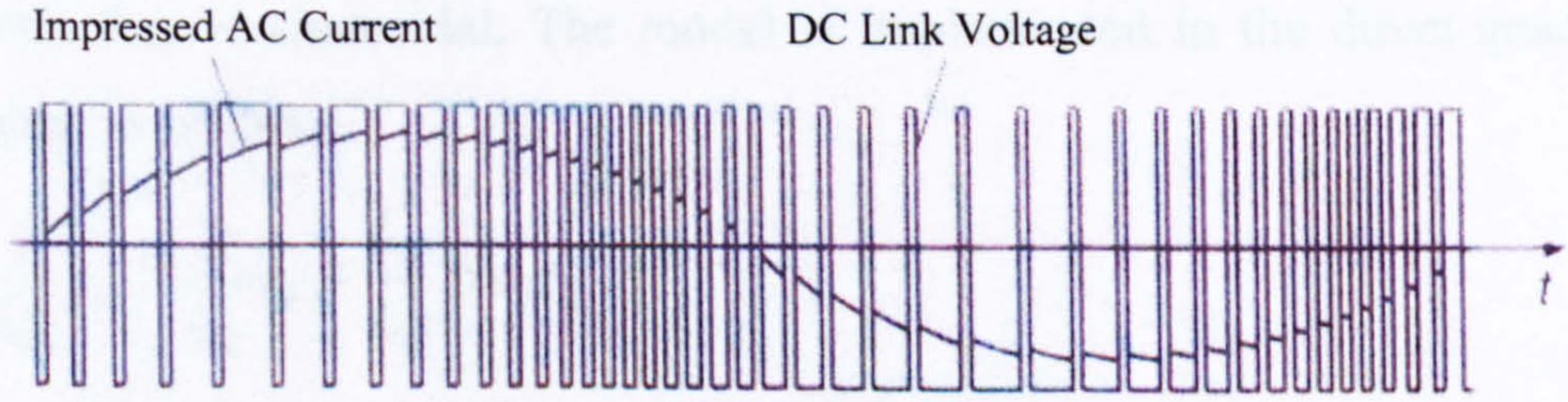

Figure 5.7. Principle of pulse width modulation from DC to AC [168]

The power electronic converter under investigation employs a 3-arm bridge (6 pulses) PWM technique inverter with 8 kHz carrier frequency (see Figure 5.8). Pulses 1, 3 and 5 power on the upper power electronic devices (IGBTs) of arm 1, 3 and 5 respectively for a certain period, whereas pulses 2, 4, and 6 enable the lower devices in the same fashion. The power on period varies the impressed sinusoidal current generated from the ± 300 V DC link.

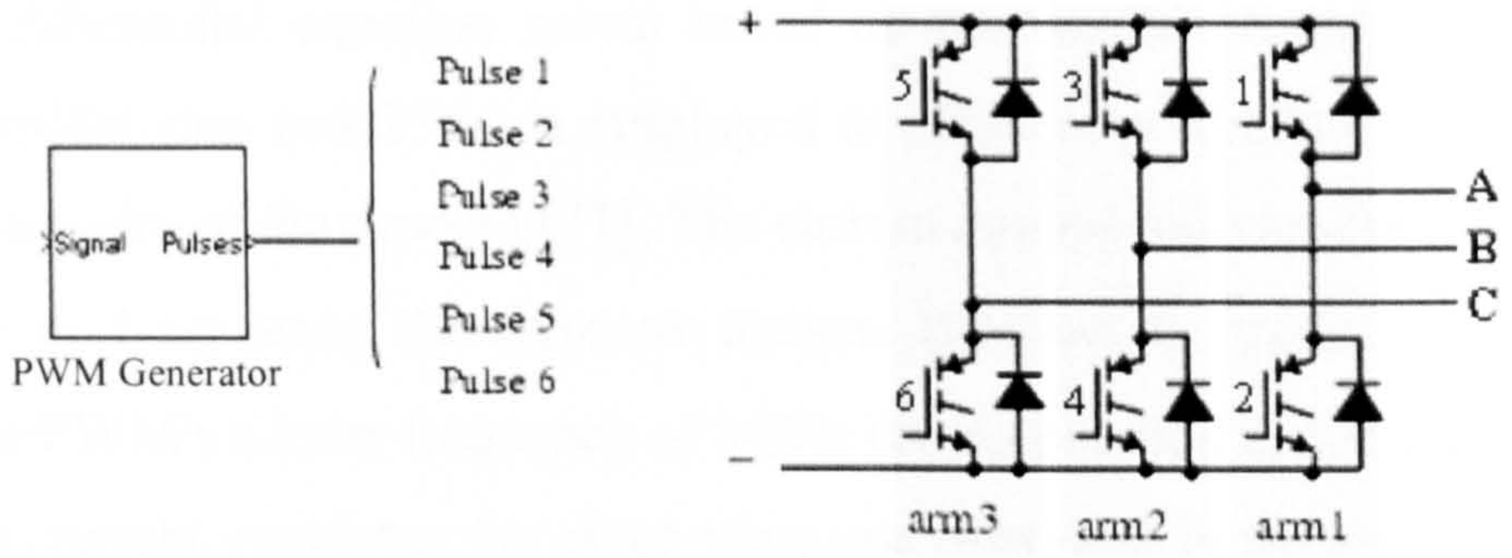

Figure 5.8. Pulse width modulation using 3-arm bridge (6 pulses) [169]

The studied feed drives contain three-phase AC ***permanent magnet synchronous motors*** (PMSM) with six poles, made from rare-earth, permanent magnet material for the rotor (Figure 5.9) and a built-in incremental encoder producing a sinusoidal output signal.

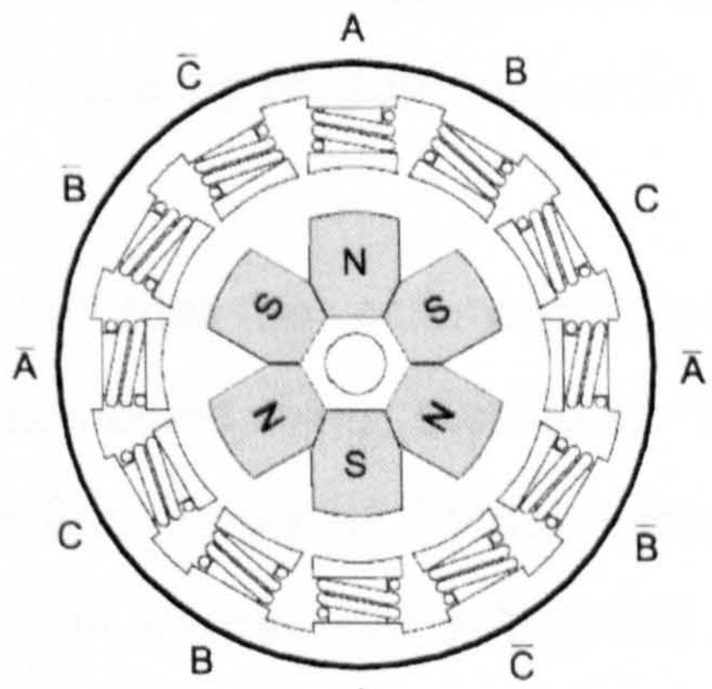

Figure 5.9. Diagram of six-pole permanent magnet synchronous AC motor [170]

The PMSM model is represented as a second-order state-space system by assuming that the rotor magnetic flux is sinusoidal. The model is implemented in the direct-quadrature (*d-q*) reference frame as follows:

$$\frac{d}{dt}i_d = \frac{1}{L_d}v_d - \frac{R}{L_d}i_d + \frac{L_q}{L_d}p\omega_r i_q \tag{5.6}$$

$$\frac{d}{dt}i_q = \frac{1}{L_q}v_q - \frac{R}{L_q}i_q - \frac{L_d}{L_q}p\omega_r i_d - \frac{\lambda p\omega_r}{L_q} \tag{5.7}$$

$$T_e = 1.5p\left[\lambda i_q + (L_d - L_q)i_d i_q\right] \tag{5.8}$$

The mechanical equations of the system describing the rotor rotational acceleration and velocity are:

$$\frac{d}{dt}\omega_r = \frac{1}{J}\left(T_e - F\omega_r - T_m\right) \tag{5.9}$$

$$\frac{d\theta}{dt} = \omega_r \tag{5.10}$$

Stiff ordinary differential equation solver based on the implicit Runge-Kutta formula with variable trapezoidal step (ode23tb) is employed to efficiently simulate the power electronic system's non-linearity of the model [171]. The current control loop model is discretised with a sampling time of 1 μs using the ***Discrete System*** Blockset to produce accurate results by considering the PWM's carrier frequency of 8 kHz (corresponding to 125 μs sampling time).

The direct current regulates the rotor magnetic flux and is normally set to zero for a PMSM because the magnetic flux is already present from the permanent magnet material. However, the field weakening technique can be used to set it to a non-zero value to extend the motor velocity range beyond its rated value. An excessive use of this feature might impair the magnetic material of the rotor in the longer term.

The quadrature current controls the motor electrical torque. The PMSM magnetic flux is constant so the generated torque is directly proportional to the quadrature current:

$$T_e \propto \lambda i_q \tag{5.11}$$

The hybrid mathematical model includes the vector control of PMSM which uses the Clarke-Park transformation and is implemented using the blocks from a recent Simulink toolbox (***Power System Blockset***). The four inputs of PMSM subsystem represent the three-phase voltages and the motor mechanical torque. The subsystem is connected to the rest of the Simulink model through a *demultiplexer* (Machine Measurement Demux) which converts its outputs (motor current, rotary velocity, rotary displacement, electrical torque) into signals compatible with Simulink. The Simulink model of the current control loop is shown in Figure 5.10.

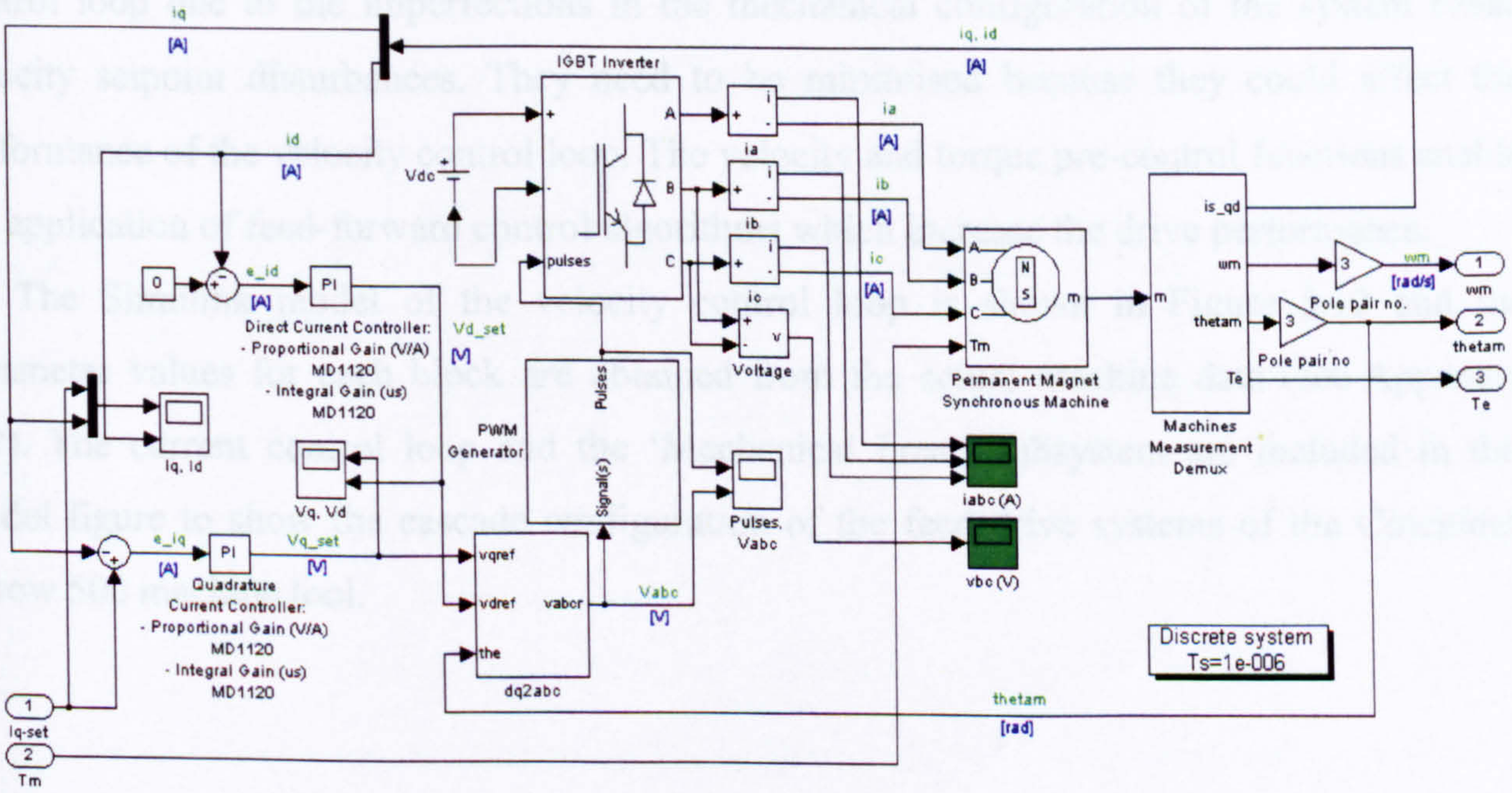

Figure 5.10. Simulink model of the current control loop

5.3. Velocity control loop

The velocity setpoint (filtered and limited) is compared with the motor angular velocity (measured by the rotary incremental encoder attached to PMSM). The velocity feedforward value generated by the position control loop can be added through the velocity pre-control setpoint input. The velocity error generated is applied to the ***proportional-integral*** (PI) velocity controller which is part of the studied Sinumerik 840D controller (see Figure 5.11).

The actual value of the motor angular velocity can also be obtained using several types of sensors (such as resolvers, tachometers, rotary encoders). Rotary encoders (as employed by the motor under study) are normally chosen when very accurate measurements and large velocity range are required. Resolvers work well in applications within very harsh environments due to the ruggedness of the rotating magnetic field equipment [172, 173]. In addition, tachometer is used for general-purpose applications where less accurate measurement of rotational movement is required.

The torque setpoint value generated by the velocity controller can be modified by activating the acceleration feedforward control which adds a calculated value to the weight equalisation/pre-control torque input. This is normally enabled where large acceleration feed is required, such as in High Speed Machining (HSM) environment. The torque setpoint is constrained within a range by a limiter and converted to a quadrature current value which is applied as demand for the current control loop based on FOC algorithm.

Notch and low-pass filters are used in the velocity control loop to smooth out the velocity setpoint received from the position control loop. The resonance frequencies in the position control loop due to the imperfections in the mechanical configuration of the system cause velocity setpoint disturbances. They need to be minimised because they could affect the performance of the velocity control loop. The velocity and torque pre-control functions enable the application of feed-forward control algorithms which increase the drive performance.

The Simulink model of the velocity control loop is shown in Figure 5.12 and the parameter values for each block are obtained from the actual machine data (see Appendix B.2). The current control loop and the 'Mechanical Load' subsystem are included in this model figure to show the cascade configuration of the feed drive systems of the Cincinnati Arrow 500 machine tool.

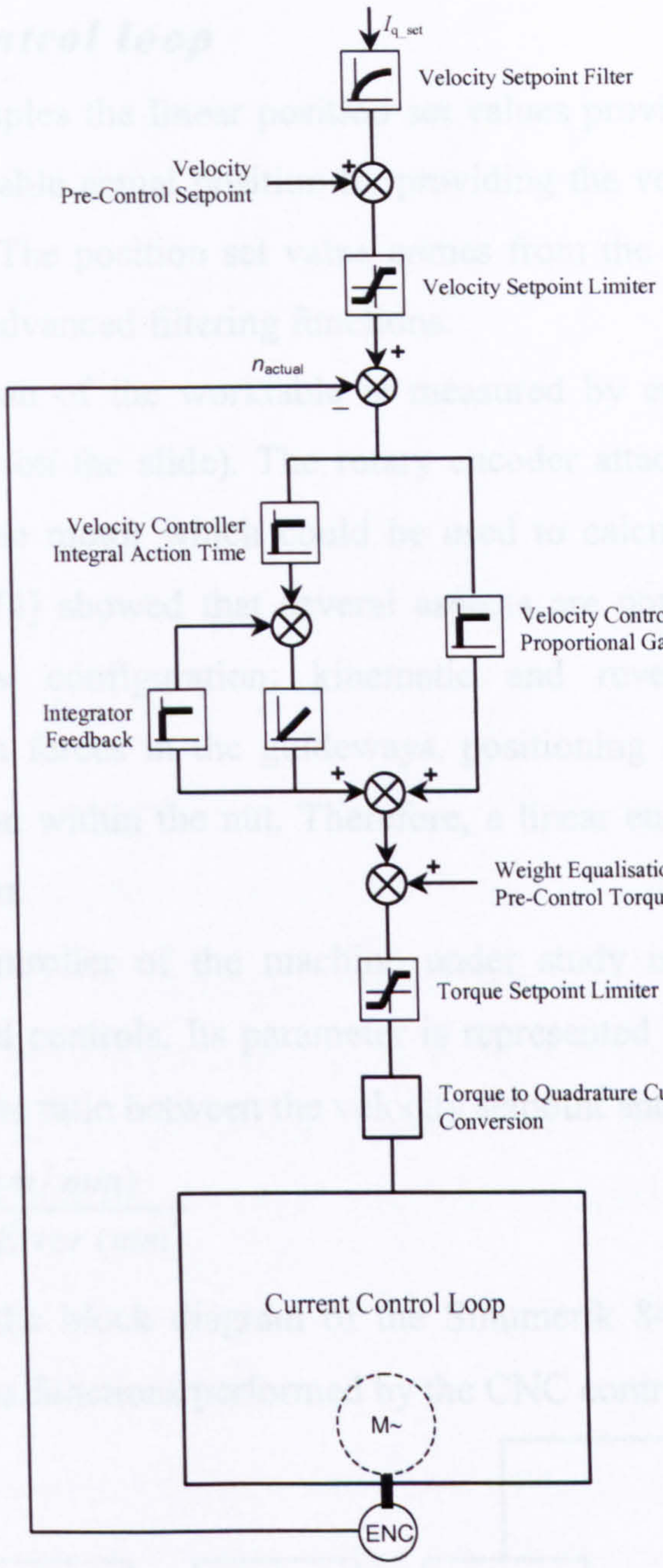

Figure 5.11. Diagram of the velocity control loop [165]

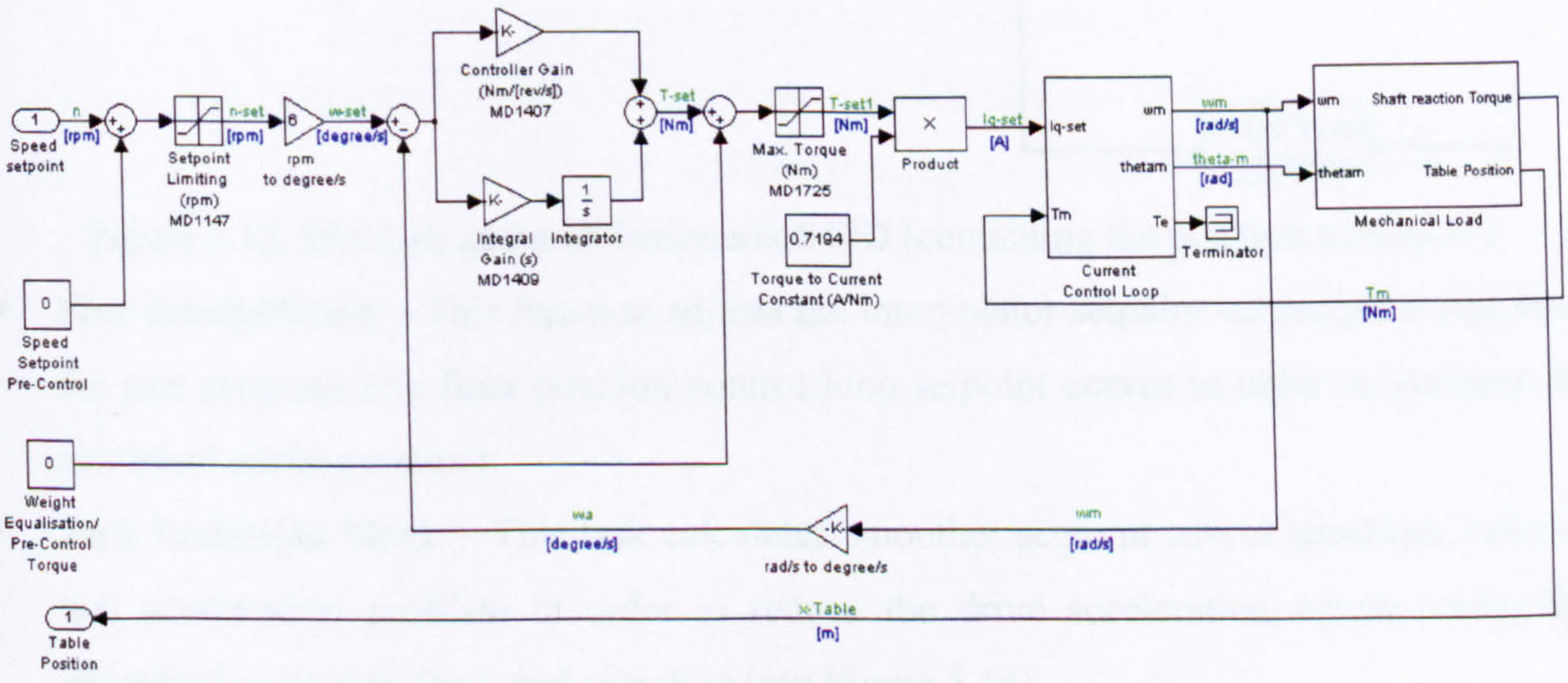

Figure 5.12. Simulink model of the velocity control loop

5.4. Position control loop

This control loop samples the linear position set values provided by the user (part program) and adjusts the worktable actual position by providing the velocity setpoint to minimise the position signal error. The position set value comes from the controller interpolator, optional fine interpolator and advanced filtering functions.

The actual position of the worktable is measured by encoders (attached to the motor and/or linear encoder on the slide). The rotary encoder attached to the motor evaluates the angular velocity of the motor which could be used to calculate theoretically the worktable position. Braasch [174] showed that several aspects are not included in the case of rotary encoder – ballscrew configuration: kinematic and reversal errors, drive mechanism deformations, friction forces in the guideways, positioning errors due to ballscrew thermal expansion and friction within the nut. Therefore, a linear encoder measures more accurately the worktable position.

The position controller of the machine under study is a ***proportional (P)*** type with optional feed forward controls. Its parameter is represented by the ***Velocity Gain*** (K_v ***factor***) which is defined as the ratio between the velocity setpoint and the deviation in the position:

$$K_v = \frac{Velocity\,(m/min)}{Following\ Error\,(mm)} \tag{5.12}$$

Figure 5.13 shows the block diagram of the Sinumerik 840D, which include the position controller and various functions performed by the CNC controller.

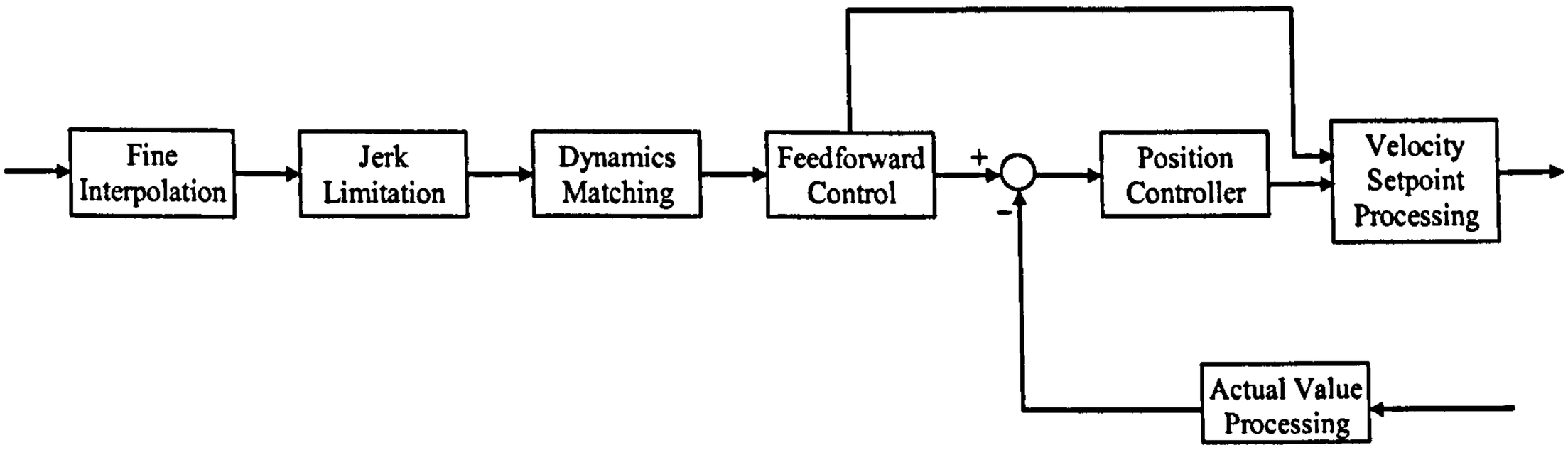

Figure 5.13. Block diagram of Sinumerik 840D (containing the position controller)

- **Fine interpolation** – This function adjusts the interpolator setpoint values generated from the part program into finer position control loop setpoint curves in order to improve the machined surface contour.
- **Jerk limitation block** – This task calculates smoother setpoint curves (position, velocity and acceleration profiles) in order to reduce the drive acceleration which lowers the generated excitation force and vibration (see Figure 5.14).

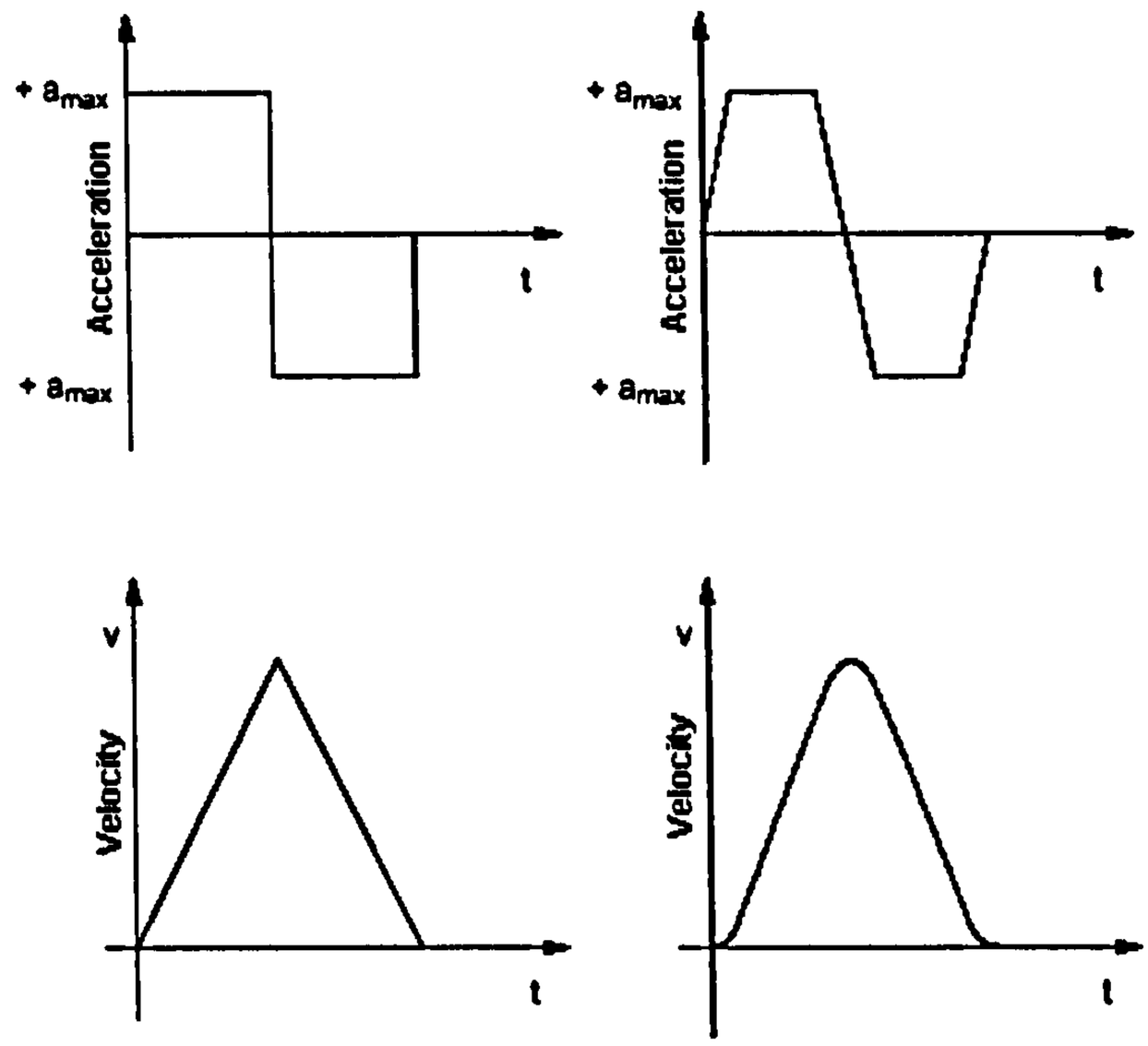

(a) Without Jerk Limitation (b) With Jerk Limitation

Figure 5.14. Acceleration and velocity profiles without and with jerk limitation function [175]

- **Dynamics matching** – This technique matches the dynamic response of two or more axes with different position control loop gains in order to achieve optimum contour accuracy. This is achieved by actively reducing position loop gain of the faster axes to match the time constants of the slowest axis. The equivalent of position control loop time constant of an axis can be estimated as follows:

$$T_{equivalent} \approx \frac{1}{K_v} \tag{5.13}$$

- **Velocity Feed forward control** – This control strategy feeds the position command to the velocity control loop in order to reduce the following error (lag) and obtain high drive velocity without any positioning overshoot (see Figure 5.15). The lag is inversely proportional to the gain and directly proportional to the feed rate so it is possible to have near infinite gain with zero lag. Increasing feed forward gain reduces the lag, allowing machine tools to cut more accurate circles and sharper corners with minimal input on the machine. The equivalent velocity control loop time constant is used to build a balancing filter to simulate the equivalent velocity control loop time delay. The value is measured from the response of closed velocity control loop and the filter is used to ensure that the lag value approaches zero.

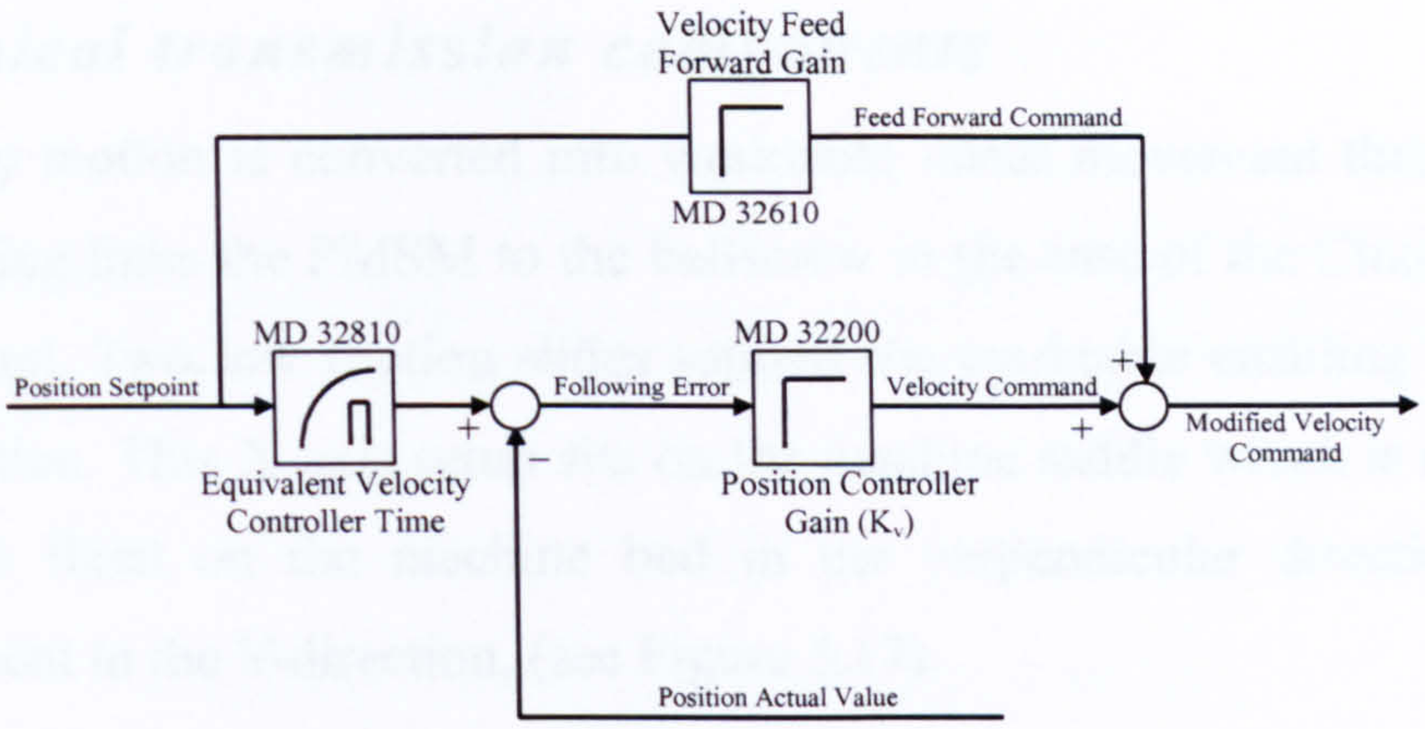

Figure 5.15. Velocity feed forward control

- **Velocity setpoint processing** – This method adjusts the velocity command to comply with restrictions imposed by the machine drive configurations, i.e. maximum motor speed, linear to rotary conversion and velocity controller cycle. In addition, the controller can also apply static friction compensation by injecting an additional velocity pulse setpoint in the reversing travel direction.
- **Actual value processing** – This function performs the calculation or extrapolation necessary to determine the actual position of the worktable from the measured data.

The primary function of the position control loop is represented in the model as the proportional controller which calculates the following error (see Figure 5.16 and equation (5.12)). The calculation unit of the model is in the machine controller to enable close correlation of the measured data to the simulated results. This is represented by the proportional software block which converts the worktable actual position from the SI unit (m) to the position controller unit (mm). In addition, the velocity command of the position controller is translated from a linear (m/min) to rotary unit (rpm) using the ballscrew pitch constant. The command value is limited to avoid any system damage (mechanical/electrical) and fed into the velocity control loop.

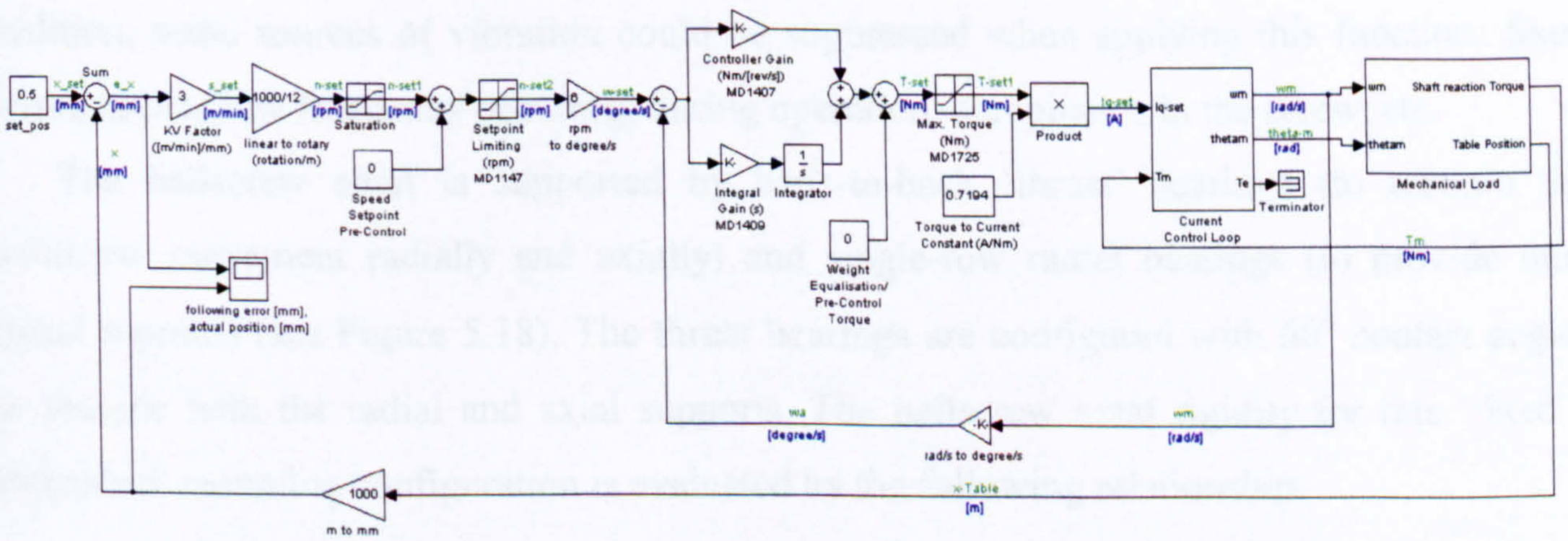

Figure 5.16. Simulink model of the position control loop

5.5. Mechanical transmission components

The motor rotary motion is converted into worktable linear movement through a ballscrew. An elastic coupling links the PMSM to the ballscrew in the case of the Cincinnati Arrow 500 CNC machine tool. Two low friction slides support the worktable enabling the movement in the X-axis direction. This X-axis setup sits on the machine saddle which is supported by two other guideways fixed on the machine bed in the perpendicular direction, enabling the machine movement in the Y-direction. (see Figure 5.17).

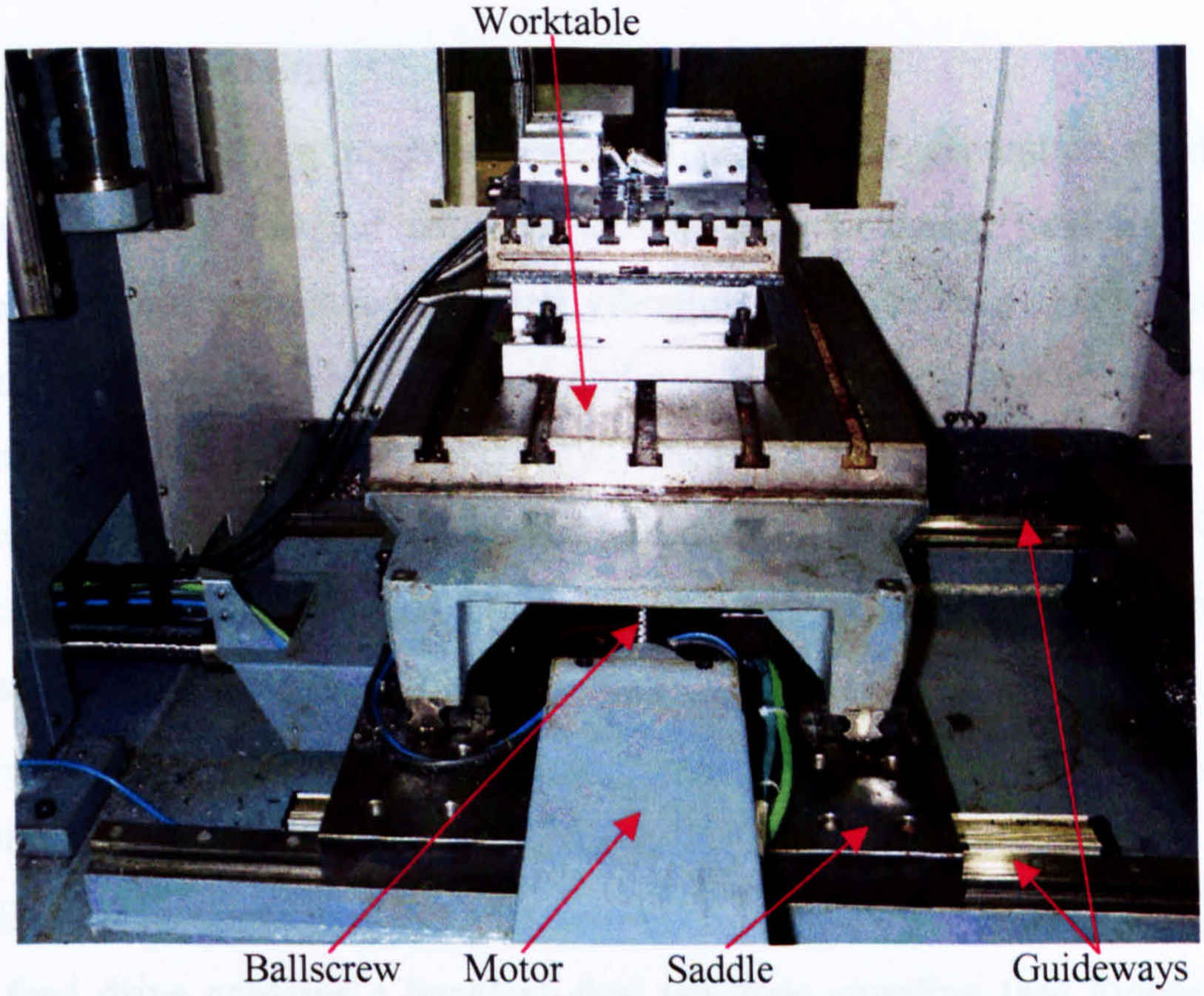

Figure 5.17. Mechanical load of the X-axis drive for Arrow 500 CNC machine tool

Modern industrial controllers comprise ***friction compensation*** for sticky slides, backlash and time delays within feed drives. The imperfections occurring when the worktable has to reverse direction are corrected in this way and the machine performance improved. In addition, some sources of vibration could be suppressed when applying this function: fixed resonances at low frequency occurring during operation, compliance in the screw, etc.

The ballscrew shaft is supported by back-to-back 'thrust' bearings (to restrain the ballscrew movement radially and axially) and single-row radial bearings (to provide only radial support) (see Figure 5.18). The thrust bearings are configured with 60° contact angles to provide both the radial and axial supports. The ballscrew axial rigidity for this 'fixed – supported' mounting configuration is evaluated by the following relationship:

$$K_s = \frac{\pi d^2 E}{4L} \tag{5.14}$$

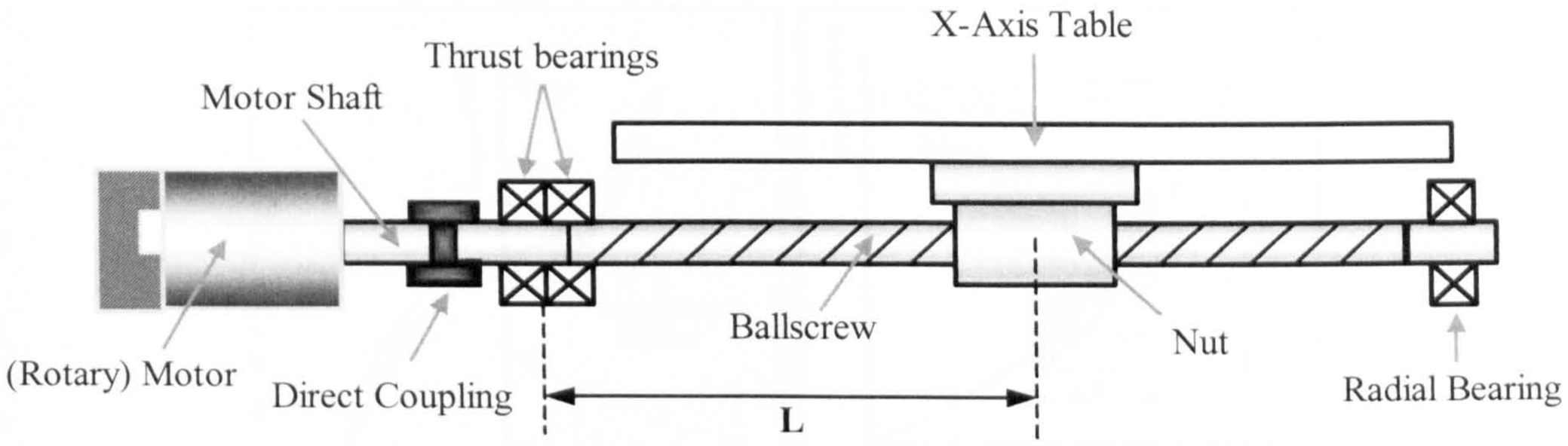

Figure 5.18. Block diagram of the feed drive

5.5.1. Coupling system

The motor-ballscrew coupling plays an essential part in the generation of drive system vibration. An incorrectly selected coupling system with excessive torsional stiffness and rotational inertia values generates unwanted vibration in the driving system (motor and its shaft) and the driven system (ballscrew unit and mechanical load). In contrast, too flexible a material reduces the drive positioning accuracy [176, 177].

High machine accuracy can be achieved when using a direct coupling with increased transmission rigidity. Banemann and Deister [178] present three types of direct coupling which increase the drive torsional stiffness:

- Backlash-free jaw-type coupling
- Steel lamina coupling
- Metal bellow-type coupling.

The studied feed drive contains a backlash-free jaw-type coupling (see Figure 5.19) which provides typically 200 to 400 percent torsional stiffness of a belt-driven system.

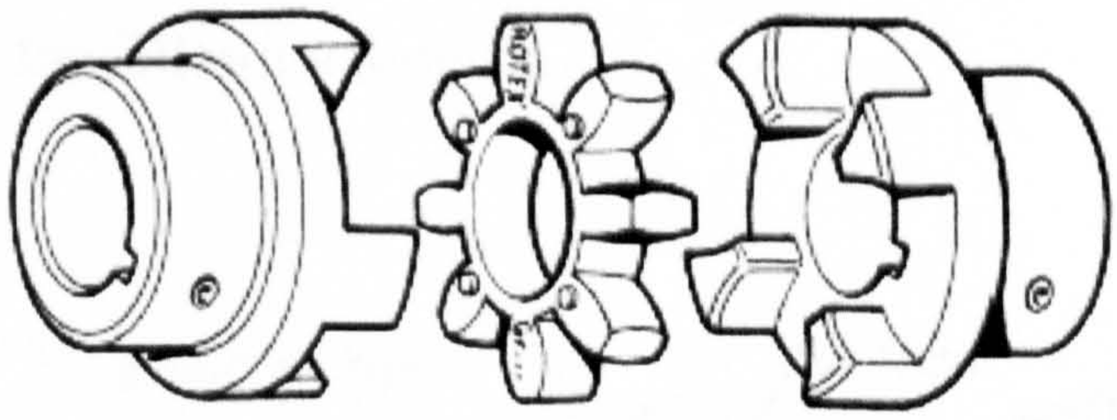

Figure 5.19. Ballscrew and motor coupling system [179]

The middle piece called spider is made from elastomer material capable of transmitting high torque and dampening vibration (see Figure 5.20). Other advantages of this type of spider are the relative easy installation and coupling tolerance against radial and axial displacements.

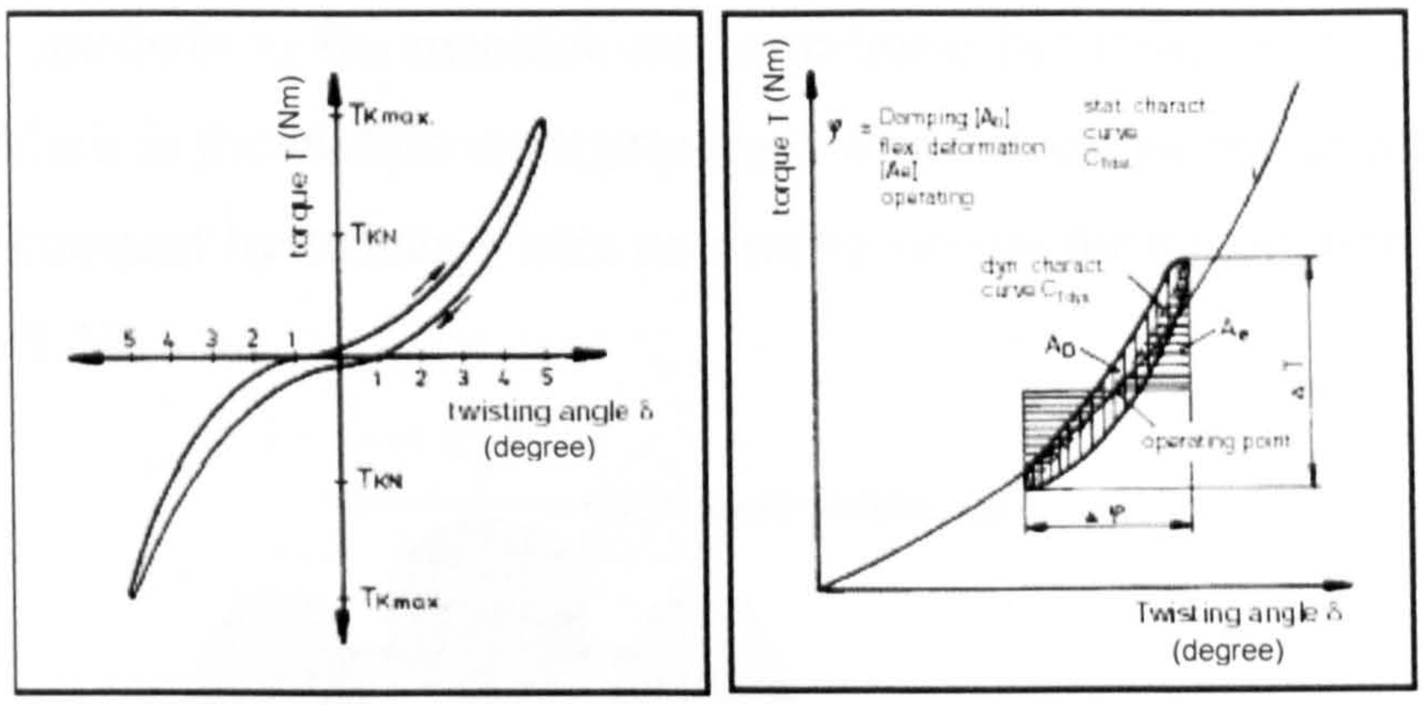

Figure 5.20. Torque and damping characteristic of the spider [179]

The torque characteristics of the coupling can be calculated from the motor specifications by:

$$T_N = 9550 \cdot \frac{P_{AN/LN}}{n} \tag{5.15}$$

Whereas the transmission error due to the torsional strain is:

$$\varphi = \frac{180}{\pi} \frac{T_N}{C_T} \tag{5.16}$$

5.5.2. Ballscrew unit

The ballscrew device is commonly used in machine tools (especially for relatively short travel) due to its high efficiency, durability and accuracy. In addition, a pre-loaded ballscrew can provide extremely beneficial damping characteristics due to the acquired high rigidity minimising the chatter during machining operations.

The typical elements of a ballscrew unit are shown in Figure 5.21. The ballscrew rotational motion drives the balls to roll into the return pipe, deflector and end pipe generating the linear movement of the nut. The generated linear displacement per unit ballscrew rotation can be calculated using the following formula:

$$Ratio = \frac{\ell_p}{2 \times \pi} \tag{5.17}$$

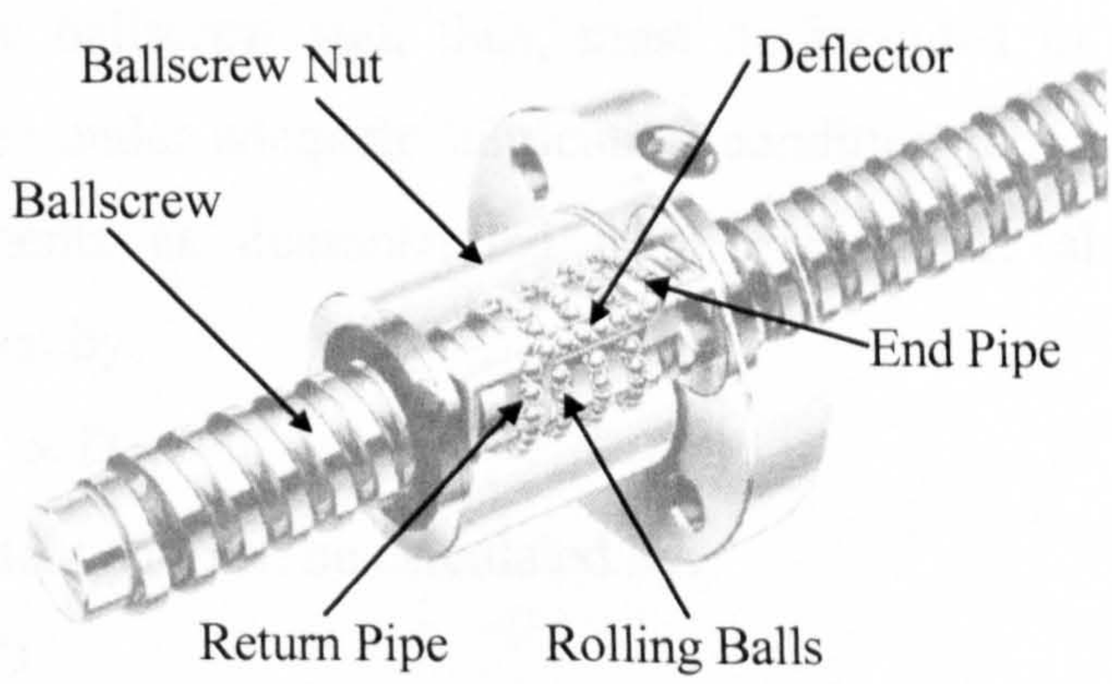

Figure 5.21. Rotary to linear movement conversion of a ballscrew nut [180]

Ballscrews also contribute to the machine tool non-linear behaviour in the form of backlash and friction. Backlash is the motion error produced when reversing the direction of motion. It is presented as a constant hysteresis where no motion occurs for a predetermined range (dead zone) (see Figure 5.22).

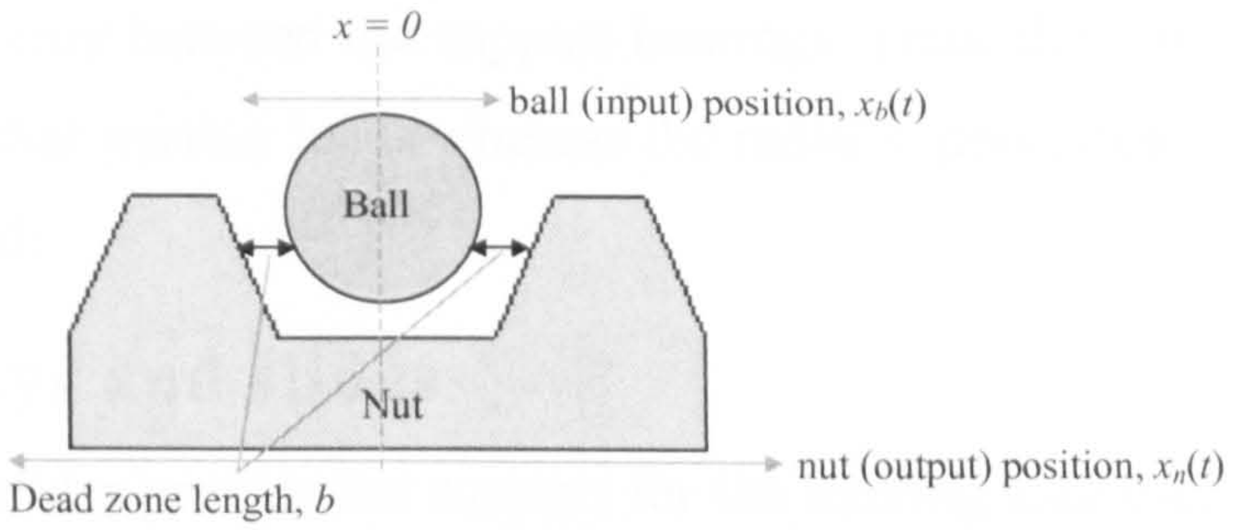

Figure 5.22. Diagram of backlash

Assuming that the reference and ball positions are in the middle, the output position of the nut along the axis at a given time can be calculated with respect to the ball position as follows:

$$\begin{aligned} x_n(t) &= x_b(t) - b \quad \text{if} \quad x_b(t) - x_n(t) > b \\ &= x_b(t) + b \quad \text{if} \quad x_b(t) - x_n(t) < -b \\ &= x_b(t) \quad \text{otherwise} \end{aligned} \tag{5.18}$$

Backlash is normally caused by the mechanical play between the mechanical elements (the rolling balls and nut) and can be minimised by applying preload in the nut assembly (see Figure 5.23).

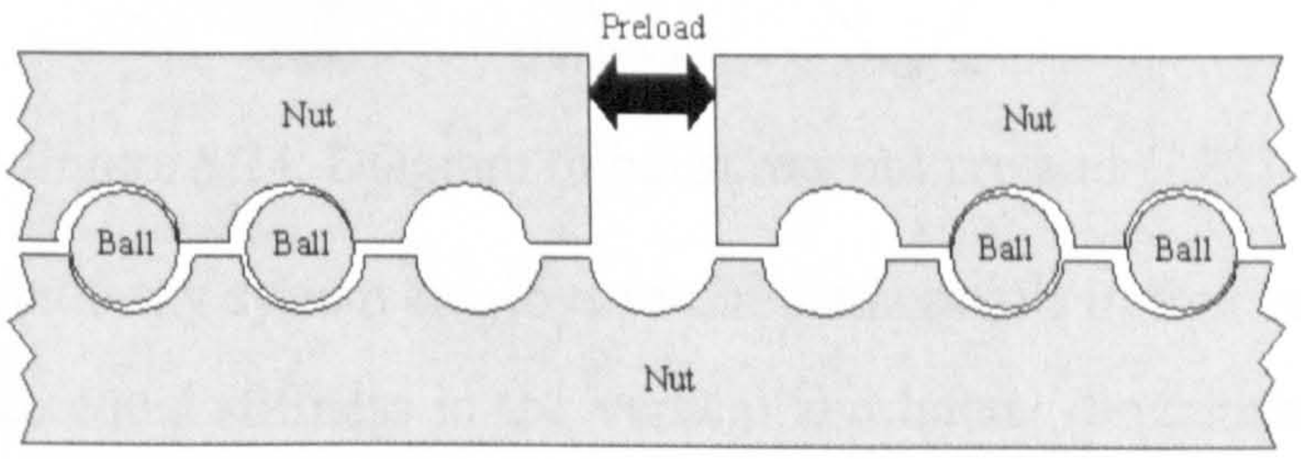

Figure 5.23. Diagram of ballscrew nut preload

The thrust and radial support bearings introduce friction torque opposing the axial and rotational motion of the ballscrew and, thus, must be included in the investigation. The applicable bearing torque under adequate lubrication condition is made of the load-free and load-dependent components as demonstrated by Eschmann et al [181]. The load-free component torque is given by:

$$T_{0f} = f_0 \times 10^{-7} \times (\nu n)^{2/3} \times D \tag{5.19}$$

whereas the load-dependent part can be calculated by:

$$T_{1f} = \mu_1 \times f_1 \times F \times \frac{D}{2} \tag{5.20}$$

The resultant bearing load can be calculated from its axial and radial components by assuming negligible tangential load as follows:

$$F = X \times F_r + Y \times F_a \tag{5.21}$$

The axial load is considered only as the result of the nut motion reaction whereas the radial load is distributed evenly between the support bearings. Thus, the thrust bearings experience both the axial and radial friction loads whereas the radial support bearing is only subjected to the radial friction load.

5.5.3. Guideways and slides

The guideways and slides provide the support for the moving load-carrying elements and are designed to provide high positioning accuracy, rigidity and load rating. The Cincinnati Arrow 500 machine employs one set of four-way equal-load-rating guideways for the worktable and saddle in the X- and Y-axis drives respectively (see Figure 5.24) to achieve the required performance.

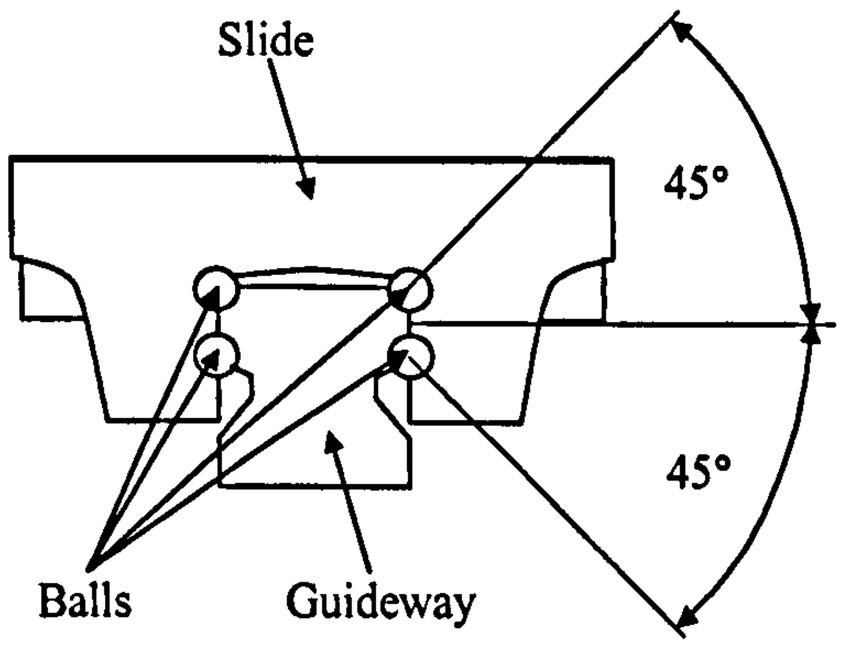

Figure 5.24. Diagram of ballscrew nut preload [182]

The linear motion guideway system employs re-circulating balls in four raceways separated at 45° angle to produce equal stiffness in the vertical and lateral directions. This configuration also reduces the rolling ball differential slip value, i.e. the difference of distance between the inner and outer surfaces touching the guideway and slide respectively. This minimises the friction force of the contact surfaces and subsequently produces smooth linear movement and positioning accuracy.

Another factor affecting the load positioning accuracy is the guideway parallelism. Non-compliance of parallelism produces non-continuous friction force along the load path causing uneven movement which can affect the positioning accuracy. Guideway non-parallelism also affects directly the uniformity of air gap between the encoder head and the scale on which the encoder's working principle is based. Non-uniform air gap may corrupt the measurement signal and may produce data corruption or deviation.

5.5.4. Simulink implementation of the mechanical load

The various elements of CNC machine tools present oscillations during machining processes therefore they can be considered as mass-spring combinations of second order. Their resonant frequencies result from rigidity or stiffness of the components and limit the maximum acceleration rate of the machine and the maximum position loop gain. The designers are continually trying to obtain "more dynamic" machines with high resonant frequencies by increasing the rigidity or reducing the masses of various elements. The limitations are not removed, but rather shifted to higher frequencies which are not normally reached during machining processes.

The feed drive system (excluding the industrial controller) is represented as series of mass-spring combinations as performed by Pislaru [183] (see Figure 5.25). The numerical values of the variables are discussed in Appendix B.4.

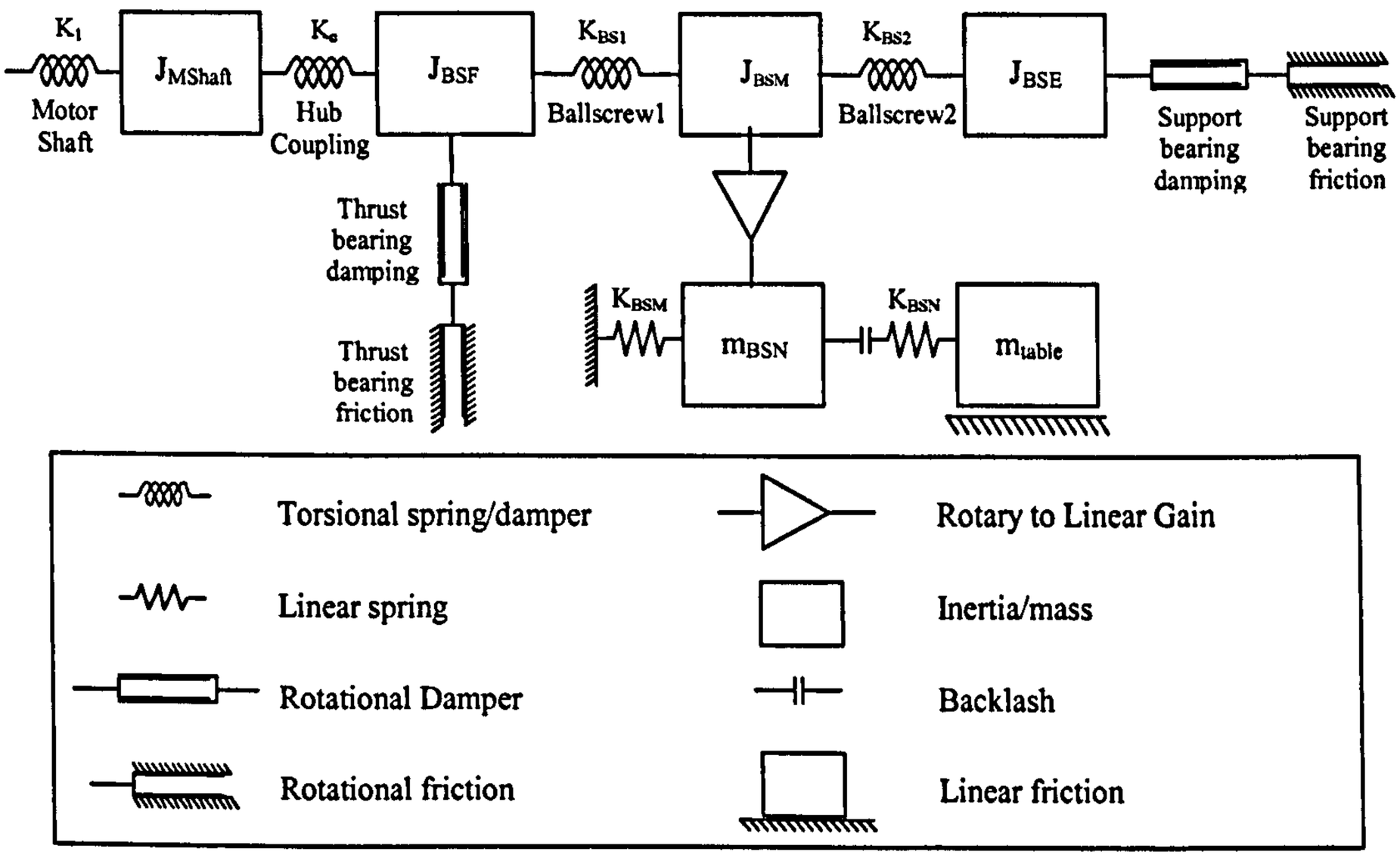

Figure 5.25. Block diagram containing the representations of mechanical transmission components

The mechanical transmission components are represented in Simulink (see Figure 5.26) as lumped subsystems (motor shaft, elastic coupling, worktable) and the ballscrew as distributed element (7 subsystems with total ballscrew flexibility apportioned between each). The explicit damping coefficients are included to simulate the resonant states of the feed drive system and the nut is assumed to be at the middle of travel. The values of model coefficients are obtained and calculated from manufacturers' catalogues and can be found in details in Appendix B.4.

The mathematical models of various subsystems are developed accordingly to the method presented by Pislaru [183] and are included in Table 5.1. The details of functional blocks comprised in the Simulink subsystems are presented in Appendix C.

Subsystem	Modelling element	Equation
Motor shaft	Inertia element	$\ddot{\theta} = \frac{T_{MShaft}}{J_{MShaft}}$
	Rotational frictional element	$T_{MShaft} = T_e$ when $T \le \mu \times T_{\max}$ $T_{MShaft} = \mu_{MShaft} \cdot T_{\max}$ when $T > \mu \times T_{\max}$
Elastic coupling	Torsional spring / damper	$T_c = k_c \cdot (\theta_{h2} - \theta_{h1}) + c_c (\dot{\theta}_{h2} - \dot{\theta}_{h1})$
Ballscrew Front	Inertia element	$\ddot{\theta}_{BSF} = \frac{T_{BSF}}{J_{BSF}}$
Ballscrew 1	Torsional spring / damper	$T_{BS1} = k_{BS1} \cdot (\theta_{BSM} - \theta_{h2}) + c_{BS1} (\dot{\theta}_{BSM} - \dot{\theta}_{h2})$
Ballscrew Middle	Inertia element	$\ddot{\theta}_{BSM} = \frac{T_{BSM}}{J_{BSM}}$
	Mass element	$\ddot{x}_{BSM} = \frac{F_{BSM}}{m_{BSM}}$
Ballscrew 2	Inertia element	$\ddot{\theta}_{BS2} = \frac{T_{BS2}}{J_{BS2}}$
Ballscrew End	Inertia element	$\ddot{\theta}_{BSE} = \frac{T_{BSE}}{J_{BSE}}$
	Rotational frictional element	$T_{BSE} = T_{BS2}$ when $T_{BS2} \le \mu \times T_{\max}$ $T_{BSE} = \mu_{BSE} \cdot T_{\max}$ when $T_{BS2} > \mu \times T_{\max}$
Ballscrew Nut	Linear spring / damper	$F_{BSN} = c_{BSN} \cdot (\dot{x}_{BSN} - \dot{x}_{BSM}) + k_{BSN} (x_{BSN} - x_{BSM})$
BS linear stiffness	Linear spring / damper	$F_{BSM} = c_{BSM} \cdot (\dot{x}_{TBL} - \dot{x}_{BSM}) + k_{BSM} (x_{TBL} - x_{BSM})$
Table	Coulomb friction	$F_{TBL} = 0$, when $F_{BSN} \le \mu \times F_n$ $F_{TBL} = F_{TBL} - \mu_{TBL} \cdot F_n$,when $F_{BSN} > \mu \times F_n$
	Mass element	$\ddot{x}_{TBL} = \frac{F_{TBL}}{m_{TBL}}$
Bed stiffness	Inertia element	$\ddot{\theta} = \frac{T}{J}$
	Rotational frictional element	$T_b = T$ when $T \le \mu \times T_{\max}$ $T_b = \mu T_{\max}$ when $T > \mu \times T_{\max}$

Table 5.1. Mathematical models of Simulink subsystems

Figure 5.27 shows the transfer function diagram for one axis feed drive showing the mechanical load as well as the current, velocity and position controls loop. The transfer

functions are solved numerically in Simulink and derived from the equations contained in sections 5.2 to 5.4 using the data provided by the manufacturer (Siemens) as follows:

- Current control loop

Quadrature current control gain and integrator:

$$H_{Cq} = \frac{K_{iC}}{s} + K_{pC} = \frac{0.002}{s} + 15.7311 = \frac{0.002 + 15.7311s}{s} \tag{5.22}$$

Direct current control gain and integrator:

$$H_{Cd} = \frac{K_{iC}}{s} + K_{pC} = \frac{0.002}{s} + 15.7311 = \frac{0.002 + 15.7311s}{s} \tag{5.23}$$

Permanent motor synchronous motor electrical circuit (see equations (5.7) – (5.8)):

Direct current:

$$si_d = \frac{1}{L_d} v_d - \frac{R_i}{L_d} i_d + \frac{L_q}{L_d} p\omega_r i_q \tag{5.24}$$

$$(sL_d + R_i) i_d = v_d + pLq\omega_r i_q \tag{5.25}$$

$$(0.0065s + 0.83) i_d = v_d + 0.0292\omega_r i_q \tag{5.26}$$

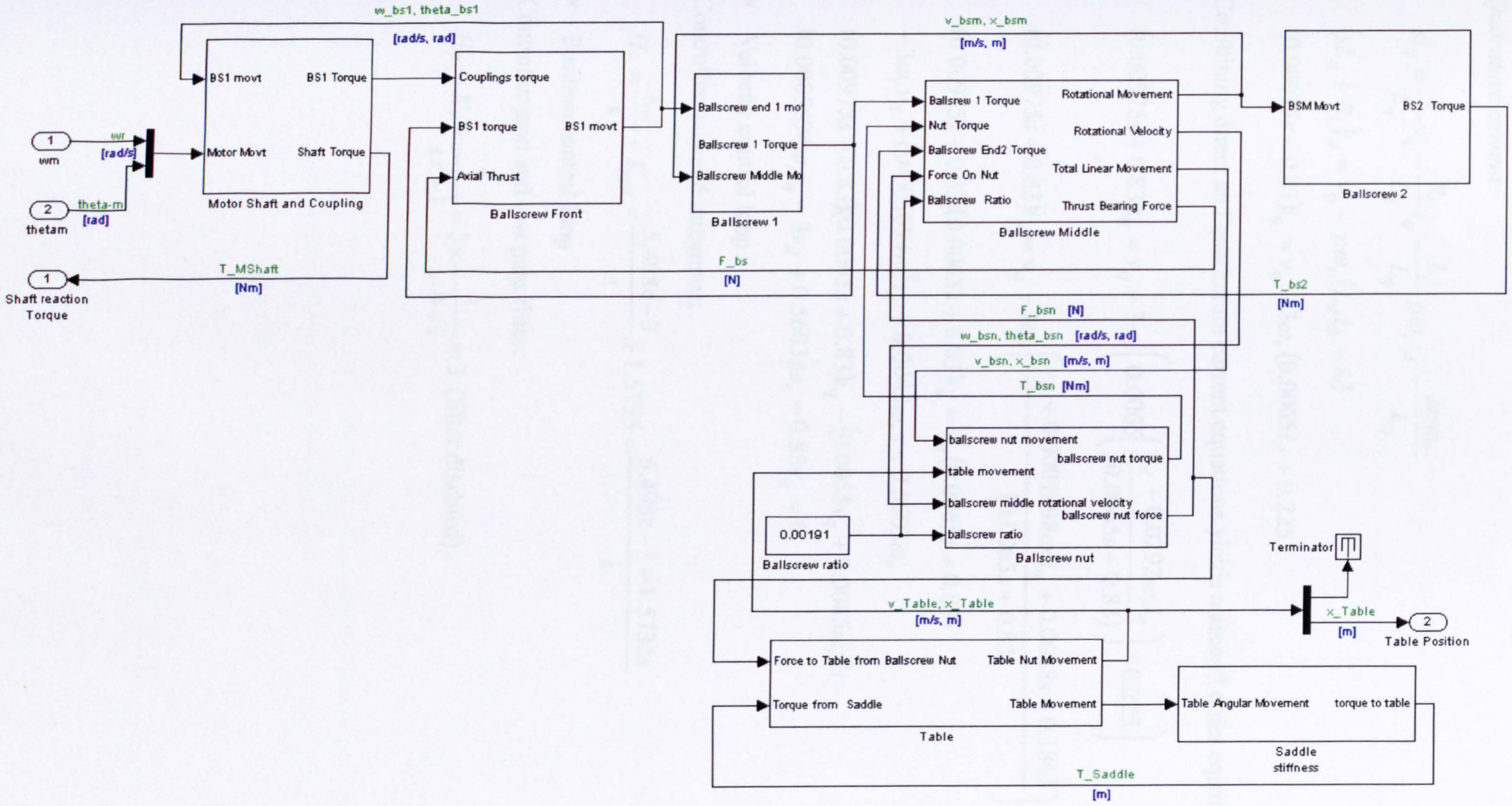

Figure 5.26. Simulink model of mechanical transmission components

Qudrature current:

$$si_q = \frac{1}{L_q}v_q - \frac{R_i}{L_q}i_q - \frac{L_d}{L_q}p\omega_r i_d - \frac{\lambda p\omega_r}{L_q} \tag{5.27}$$

$$(sL_q + R_i)i_q = v_q - p\omega_r(L_d i_d + \lambda) \tag{5.28}$$

$$(0.00975s + 0.83)i_q = v_q - 3\omega_r(0.0065i_d + 0.225) \tag{5.29}$$

Combining direct and quadrature current equations yields a second order equation:

$$(0.00975s + 0.83)i_q = v_q - 3\omega_r\left(0.0065\left(\frac{v_d + 0.0292\omega_r i_q}{(0.0065s + 0.83)}\right) + 0.225\right) \tag{5.30}$$

$$(0.00975s + 0.83)i_q = v_q - 3\omega_r\left(\frac{v_d + 0.0001898\omega_r i_q + 0.0015s + 0.1868}{(0.0065s + 0.83)}\right) \tag{5.31}$$

$$\begin{aligned}&(0.00975s + 0.83)(0.0065s + 0.83)i_q = v_q(0.0065s + 0.83)\\ &-3\omega_r v_d + 0.0005694\omega_r^2 i_q + 0.0045\omega_r s + 0.5603\omega_r\end{aligned} \tag{5.32}$$

$$\begin{aligned}&(0.00975s + 0.83)(0.0065s + 0.83)i_q - (0.0065v_q + 0.0045\omega_r)s -\\ &(0.0005694\omega_r i_q - 3v_d + 0.5603)\omega_r - 0.83v_q = 0\end{aligned} \tag{5.33}$$

- Velocity control loop

Controller gain and integrator:

$$H_V = \frac{K_{iV}}{s} + K_{pV} = \frac{5.498e-3}{s} + 1.5735 = \frac{5.498e-3 + 1.5735s}{s} \tag{5.34}$$

- Position control loop

Controller gain and low pass filter:

$$H_P = K_V \times \frac{1}{s\tau + 1} = 3 \times \frac{1}{s \cdot 0 + 1} = 3 \text{ (filter disabled)} \tag{5.35}$$

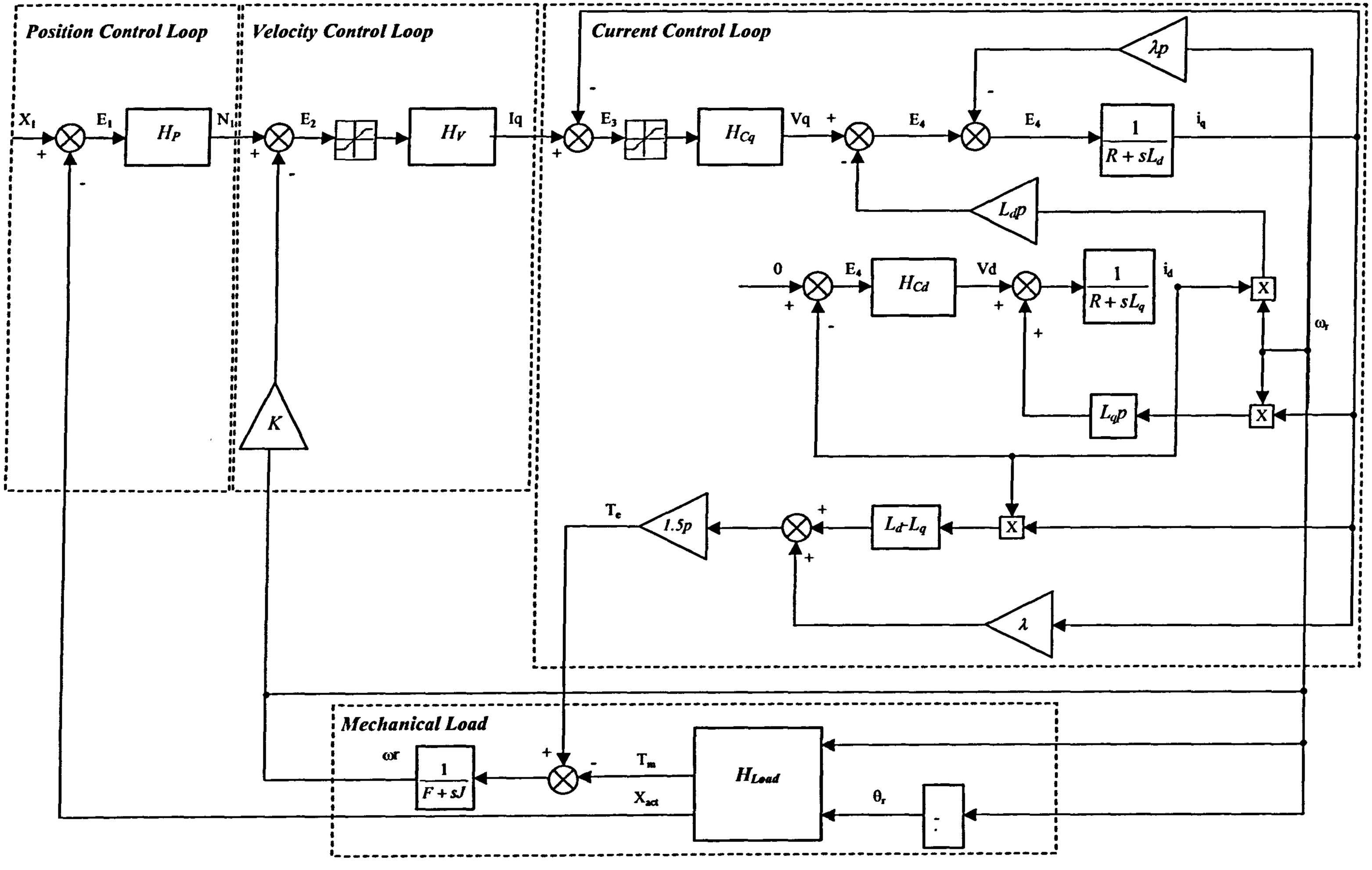

Figure 5.27. Transfer function diagram of the drive system

5.6. Comparison between simulated and measured results

The developed models are validated by comparing the simulated results against the measured data. The measurements are performed on the machine drive using some of the built-in functions used for the diagnostic and optimisation routines for the control loops (see Figure 5.28). The ***closed position controller loop*** function evaluates the response of the actual positions measured by the linear encoder against the demand values. The ***closed speed controller loop*** measures the measured rotational velocities of the motor against the commanded values. The measurement data is captured by the controller, viewable as graphs and exportable as ASCII files.

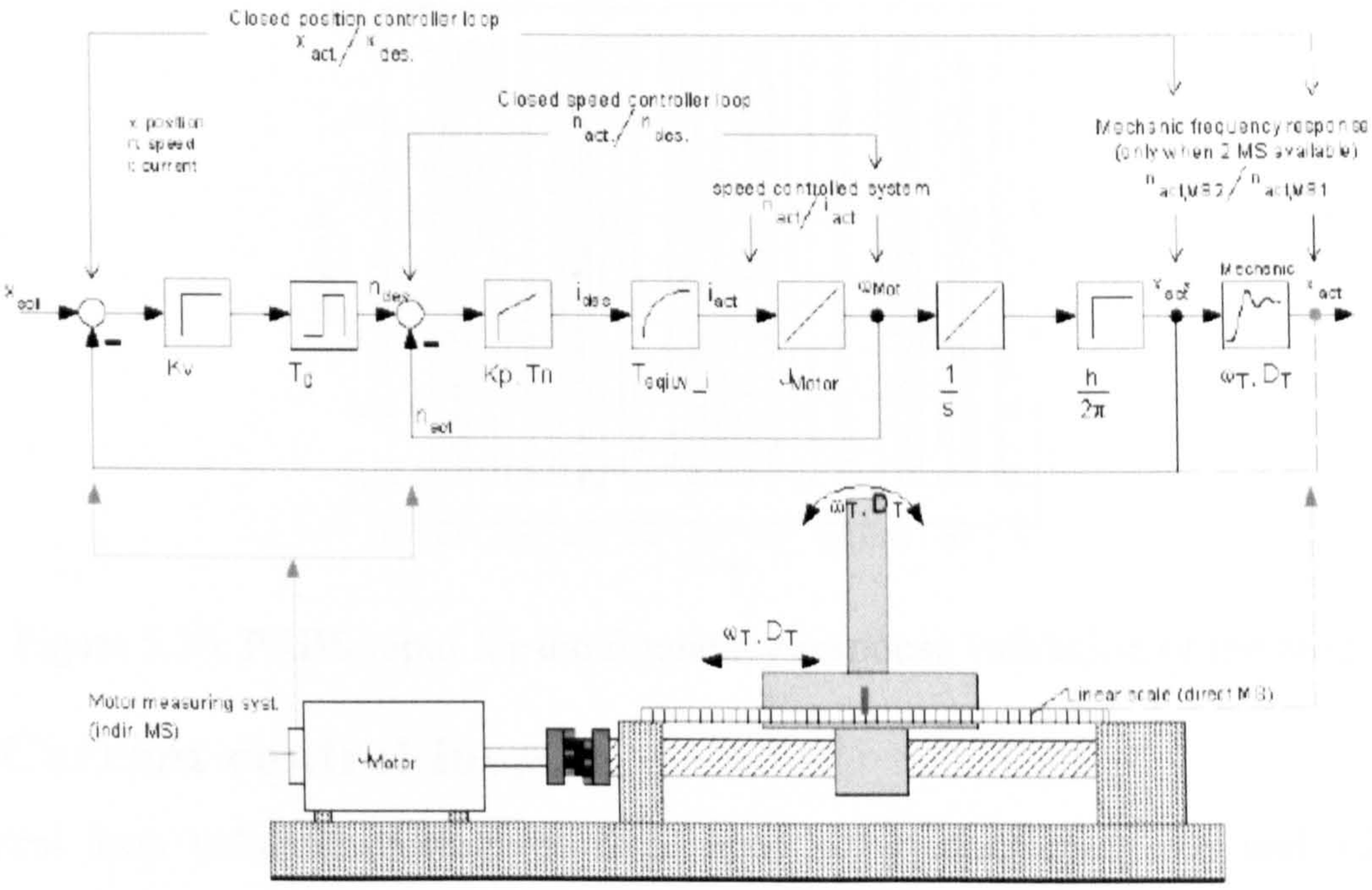

Figure 5.28. Diagram of the controller's built-in diagnostic and optimisation functions [184]

The simulated and actual systems are evaluated using deterministic and random signals to analyse the response (Step and Pseudo Random Binary Signal (PRBS) inputs). The step input test is performed to analyse the time response of the systems whereas the PRBS disturbance is utilised to appraise the frequency response. The step input signal employed to analyse the model is performed using the ***signal builder*** block, is which parameterised for time delay and ramping experienced by the measured input signal of the feed drive system (see Figure 5.29).

The PRBS input generated by the signal generator in the CNC feed drive system is simulated using ***idinput*** function in MATLAB. The generated signal is stored in software's workspace and imported by Simulink to feed the model. The random nature of the signal prevents a replication in the simulation environment but the amplitude, bandwidth and sampling time parameters are maintained to generate the simulated data (see Figure 5.30).

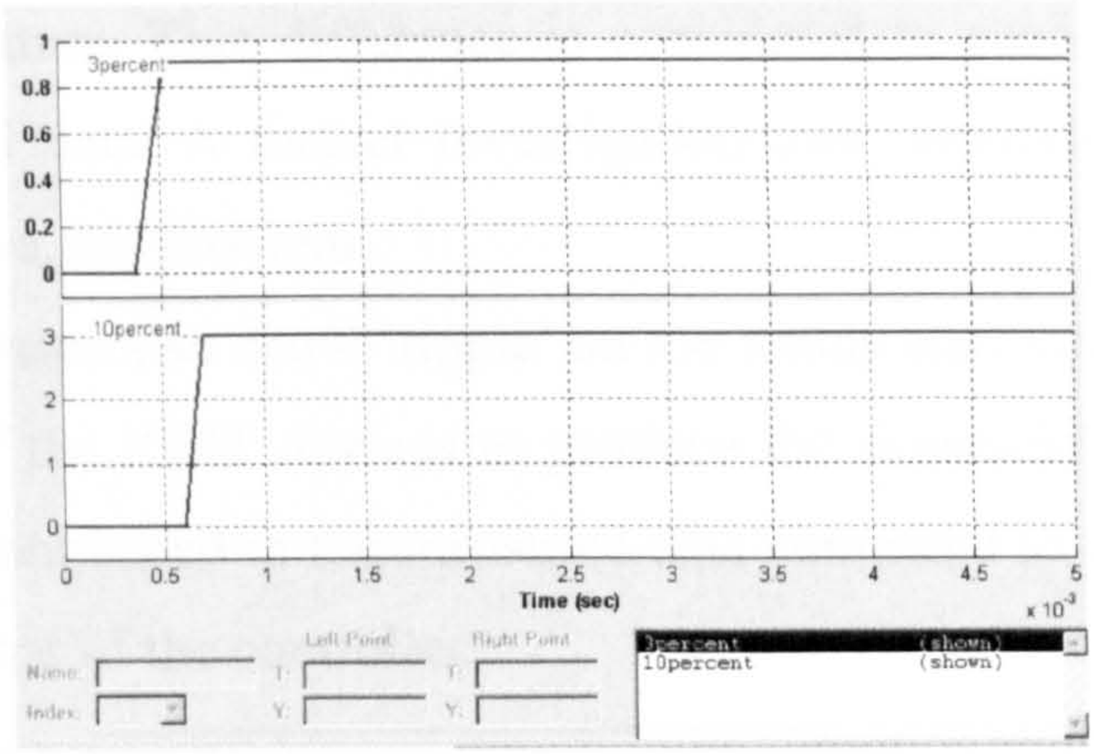

Figure 5.29. Signal builder function for the step input model validation

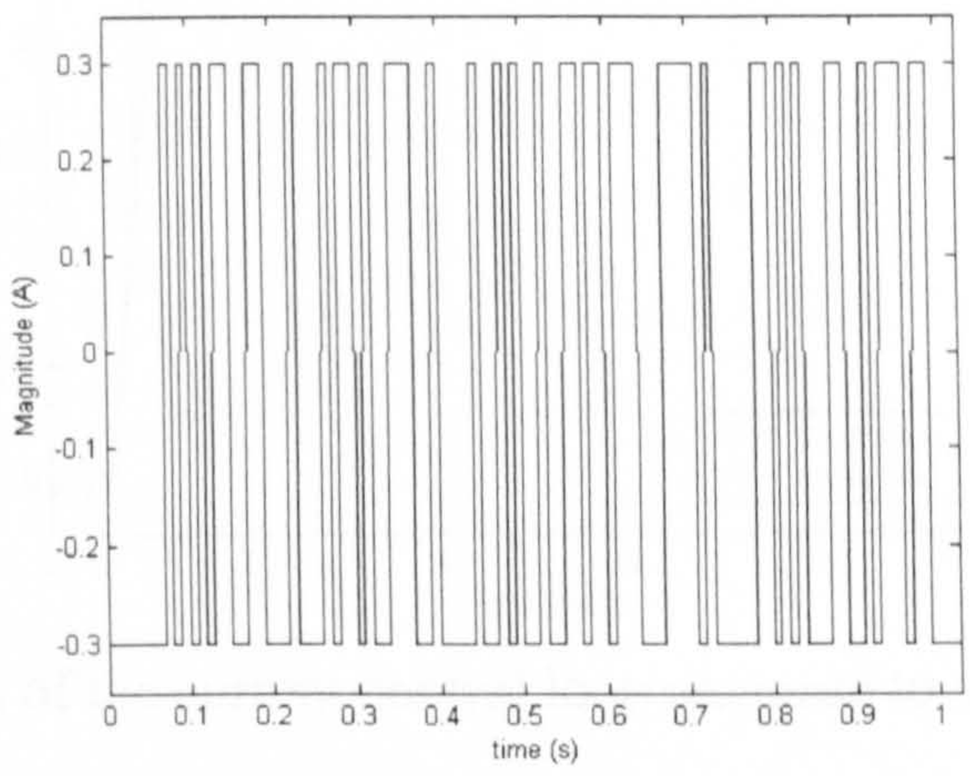

Figure 5.30. PRBS input for the frequency response validation of the model

5.6.1. Current control loop

The control loop validation using the step input is by introducing 3% and 10% current setpoint increase of the maximum motor current representing 0.84 A and 2.8 A respectively. The model responses show good agreement to the measured data at both input values (see Figure 5.31 and Figure 5.32). The simulated value graph at 3% input indicates an overshoot of around 3% and a lead-time of approximately 0.2 ms. Both the simulated and measured responses at the higher input level (10%) show overshoots of about 2% but the simulated result shows a lag time of approximately 1 ms.

A parametric investigation into the power electronic circuits reveals that it strongly influences the system behaviour as well as exhibits non-linear properties. The developed model includes a linear snubber circuit which is not in the actual power electronic system. This is utilised by Simulink to simulate the protection circuit (consisting of resistive and capacitive elements) which dissipates heat from the high current commutation. The system under investigation utilises power electronic devices manufactured using a new type of material known as the High Voltage (HV) IGBT's, which provides better performance and

lower operating temperature. This difference is considered to produce the deviation of the simulated and measured data. A further investigation into improving the power electronic system model will resolve this problem.

The measured responses also show 'ripple' on the steady state current response due to the voltage commutation of the IGBT devices to produce the sinusoidally impressed quadrature current. This is more pronounced in the measured data compared to the simulated results due to the lower sampling time of the controller.

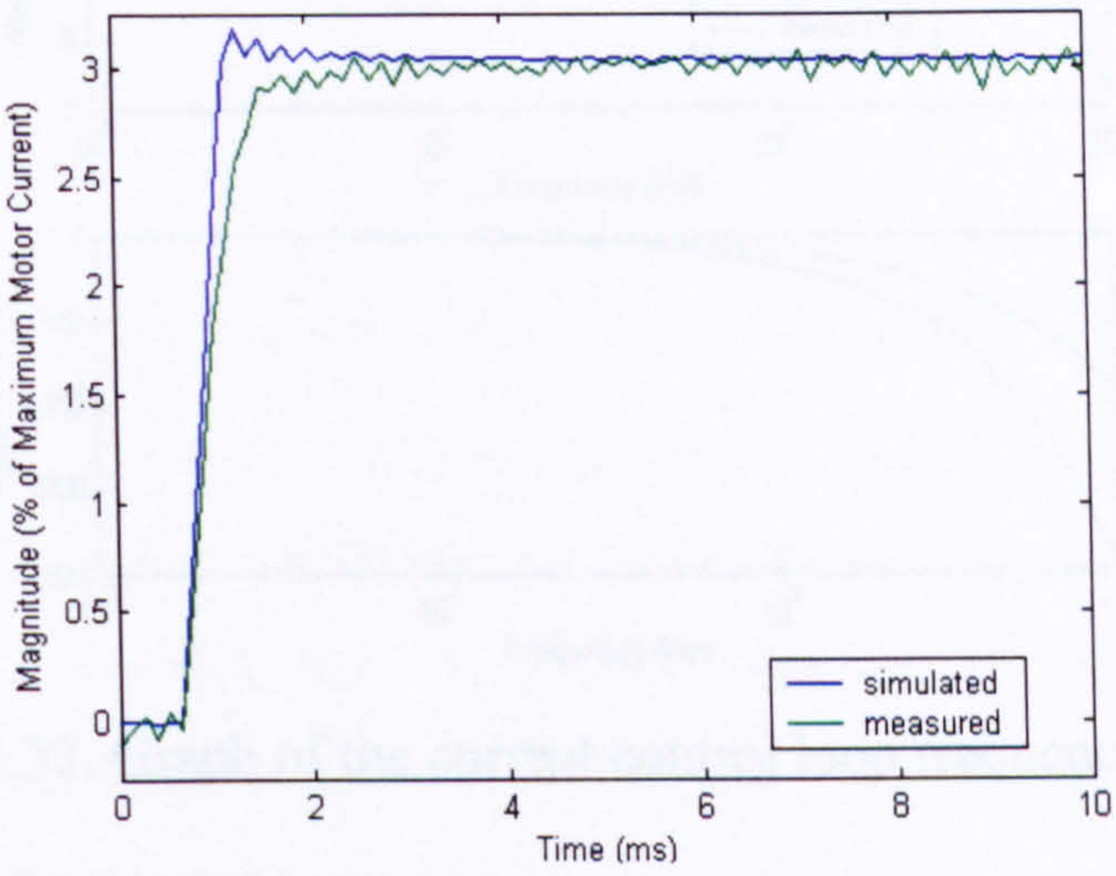

Figure 5.31. Graph of the current control loop response to a 3% setpoint increase

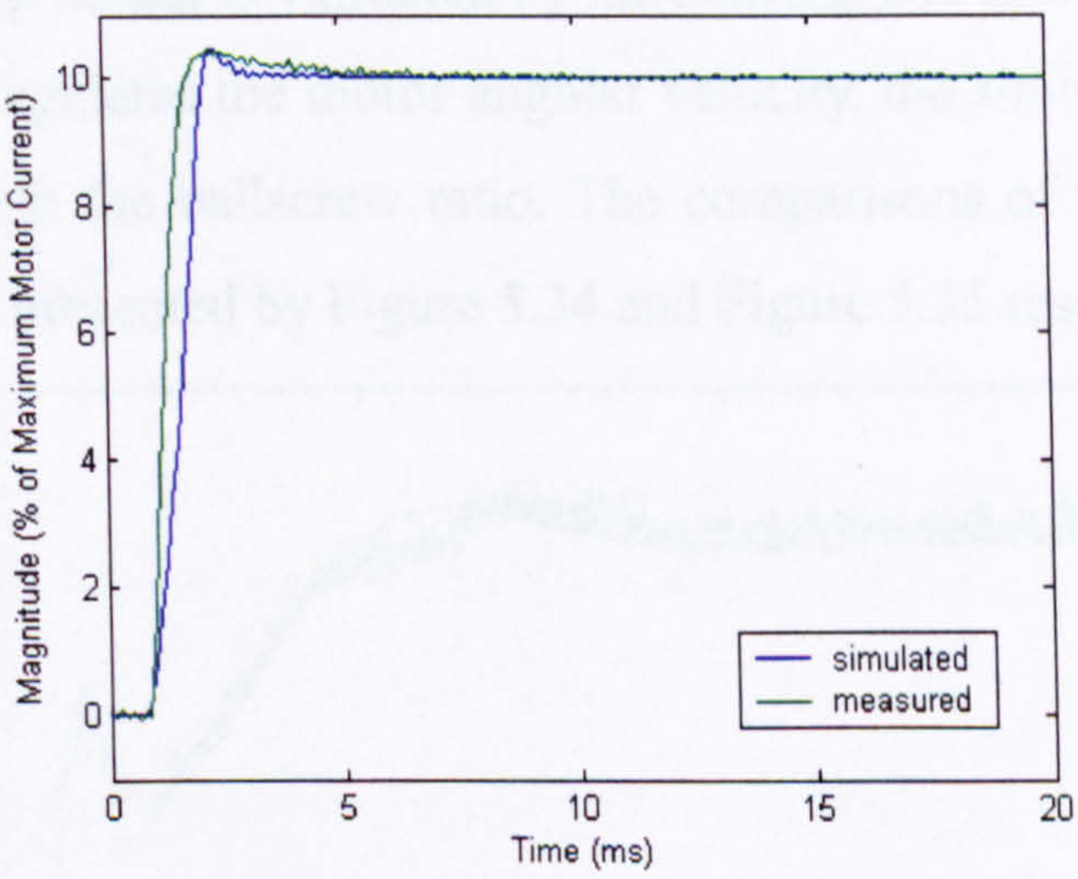

Figure 5.32. Graph of the current control loop response to a 10% setpoint increase

The frequency response of the control loop obtained using the PRBS input is shown in Figure 5.35. The response magnitude of the simulated result matches the measured data up to 800 Hz after which the gain decreases down to –7.5 dB compared to the measured results at about -5 dB. This indicates that the response of the power electronic device is not as fast as the actual system. The notch at about 400 Hz and the subsequent frequency gain drop at 800 Hz indicate that there is a resonance of the power electronic system about 400 Hz that needs to be investigated further. The phase of the simulated system drops to –400 degree compared to the

actual system of –200 degree. This effect could originate from the time delay introduced by the resistive and capacitive components of the snubber circuit which do not present in the actual system. The sampling time difference between the simulated and measured results may also contribute to the differences.

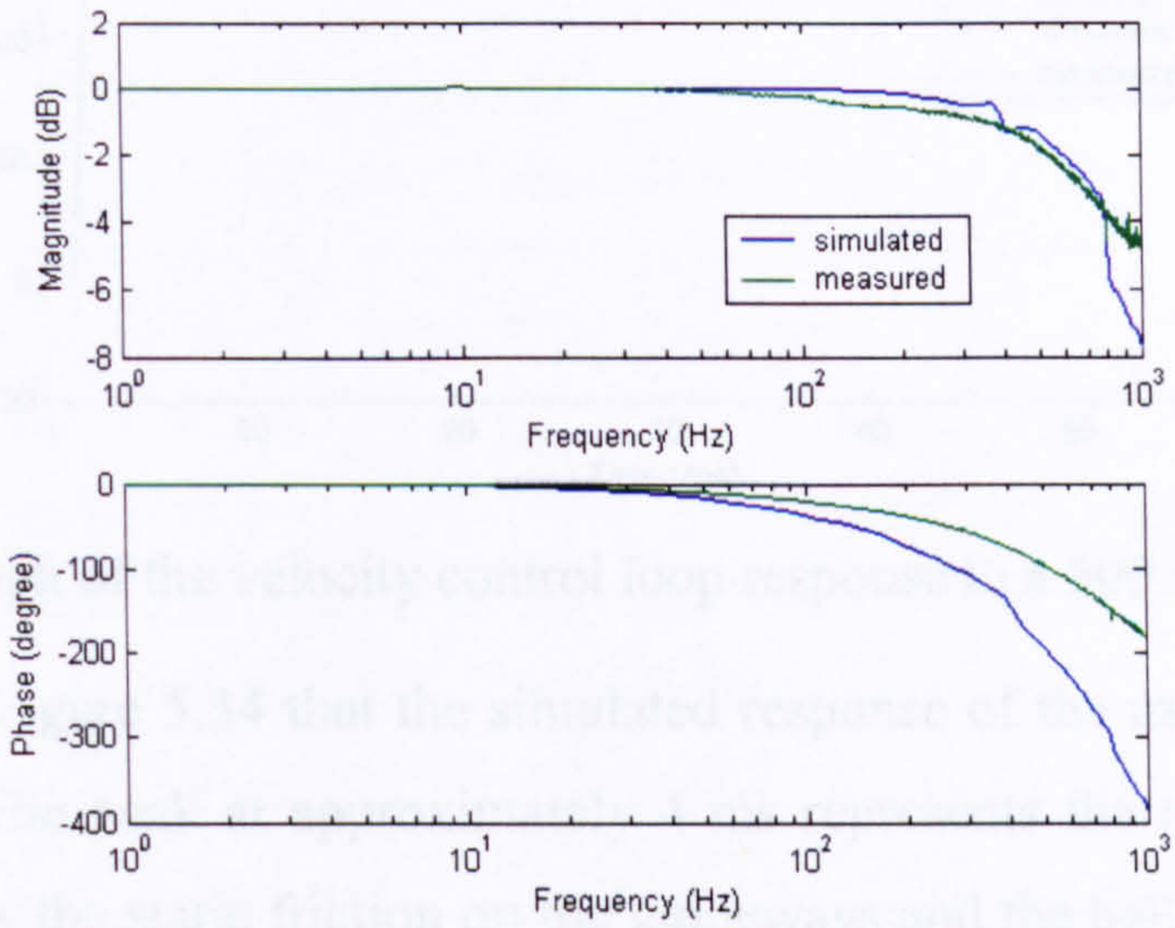

Figure 5.33. Graph of the current control loop frequency response

5.6.2. Velocity control loop

The velocity control loop model is validated by introducing 200 and 500 mm/min step inputs. Since the control loop regulates the motor angular velocity, the simulated values are obtained by multiplying them with the ballscrew ratio. The comparisons of the simulated against the measured responses are presented by Figure 5.34 and Figure 5.35 respectively.

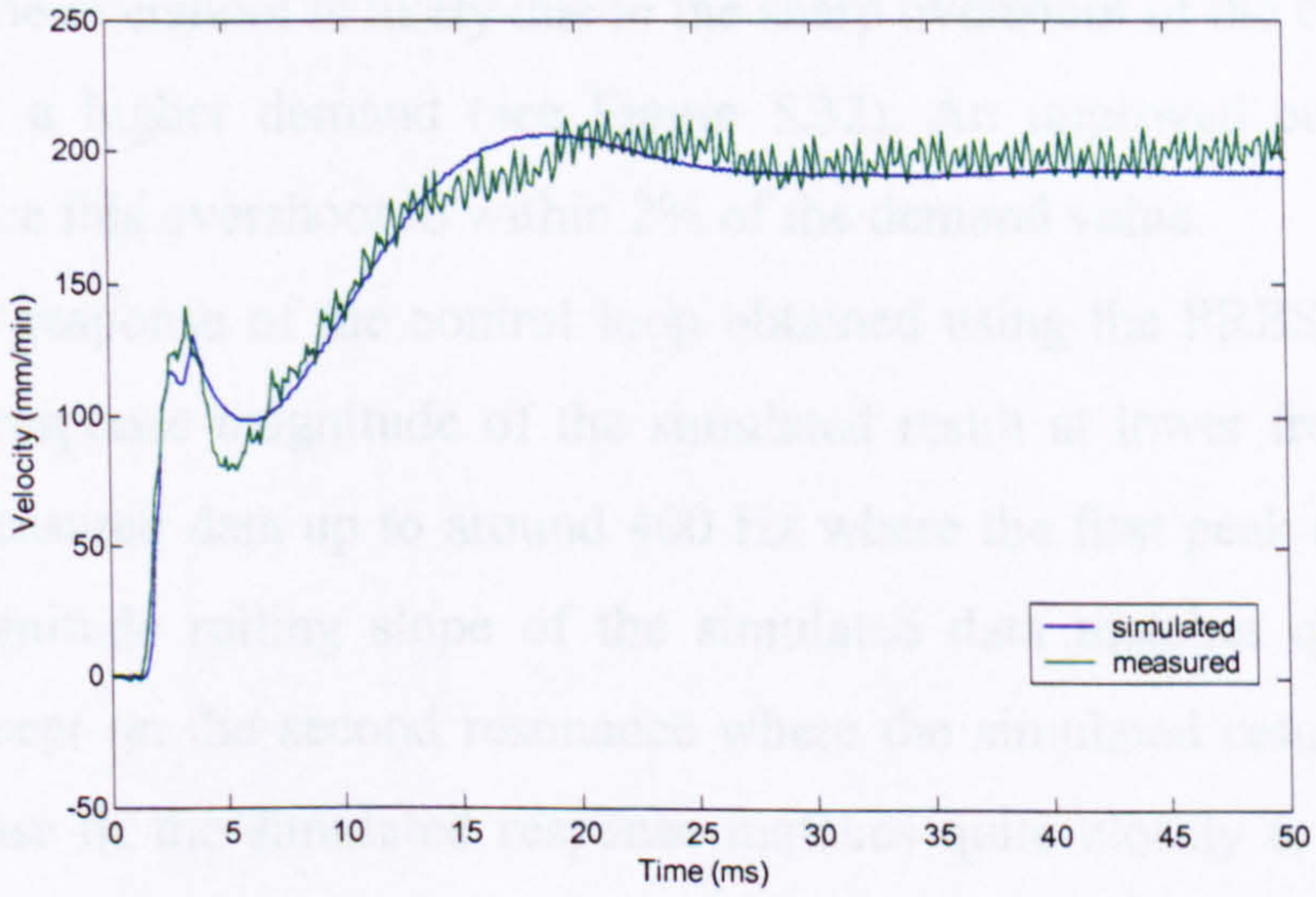

Figure 5.34. Graph of the velocity control loop response to a 200 mm/min step input

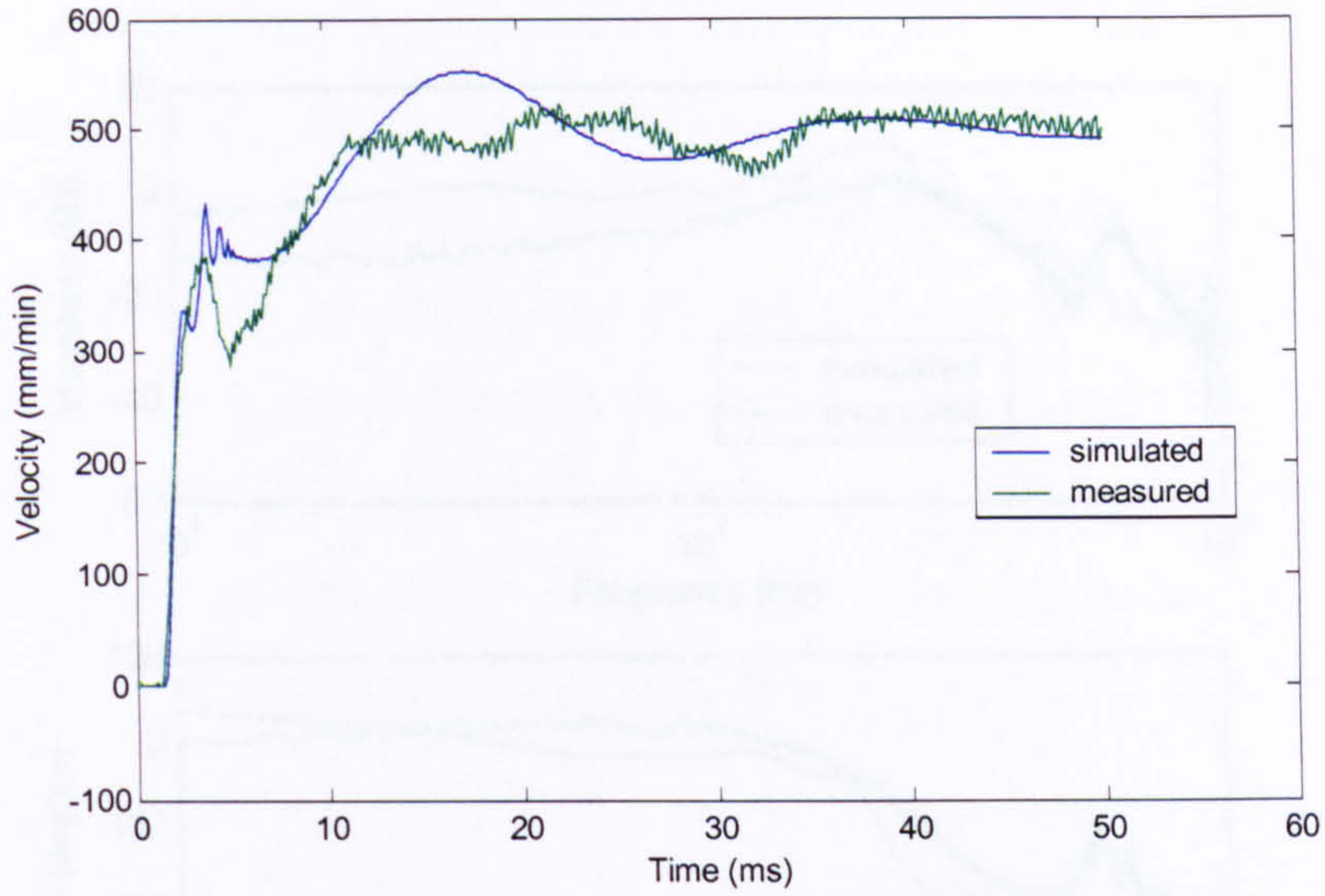

Figure 5.35. Graph of the velocity control loop response to a 500 mm/min step input

It can be seen from Figure 5.34 that the simulated response of the model matches closely to the measured data. The peak at approximately 4 ms represents the mechanical system jerk, most likely caused by the static friction on the guideways and the ballscrew support bearings. The simulated jerk changes less rapidly on the reversing velocity due to the simplified friction model utilised in the model.

When the demand is increased to 500 mm/min (Figure 5.35), the simulated response does not correspond as well to the measured data. The peak representing the mechanical non-linearities at about 4 ms is still present on both responses. However, the simulated response overshoots by approximately 10% although less oscillation is observed compared to the measured result. The overshoot is likely due to the sharp overshoot of the current control loop response where at a higher demand (see Figure 5.32). An improved current control loop model should reduce this overshoot to within 2% of the demand value.

The frequency response of the control loop obtained using the PRBS input is shown in Figure 5.36. The response magnitude of the simulated result at lower frequencies is 10 dB higher than the measured data up to around 400 Hz where the first peak (resonance) occurs. The response magnitude rolling slope of the simulated data matches quite closely to the measured data except on the second resonance where the simulated result does not show a presence. The phase of the simulated response matches quite closely to the measured data except for the second resonance where the simulated response does not show any peak in the response phase. The absence of the higher resonance is normally due to the difference in the mass of the simulated and actual mechanical systems, and thus a further investigation is required.

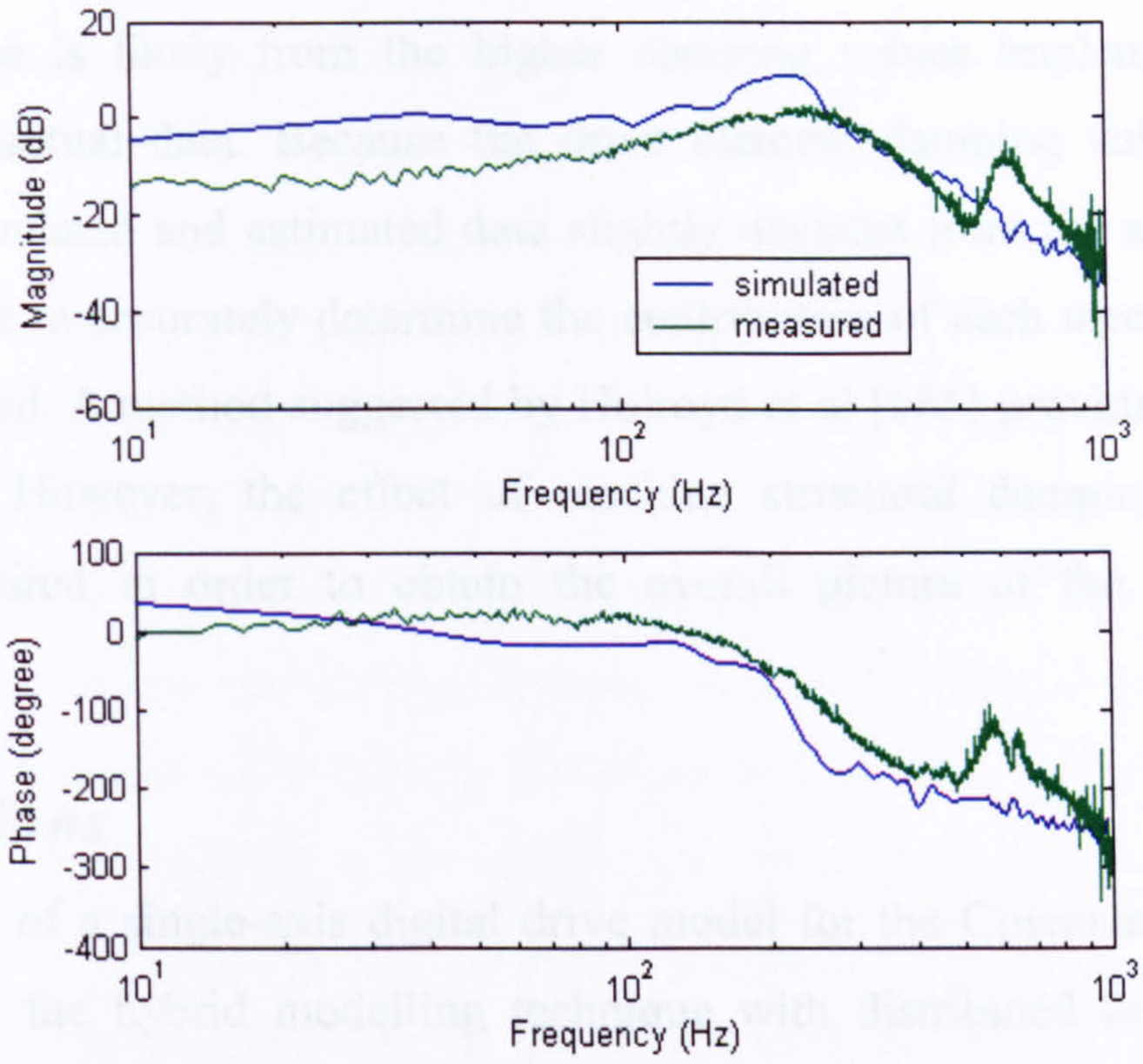

Figure 5.36. Graph of the velocity control loop frequency response to a PRBS input

5.6.3. Position control loop

The validation of the position control loop by a deterministic signal is performed by introducing a 0.5 mm step demand. Figure 5.37 shows the graph of the absolute position of the simulated and measured responses with an initial position of 250 mm. The measured response shows an overshoot indicating that the actual system is lightly damped and not critically damped, as it should be. Both responses are of a second order system with heavier damping characteristic in the model.

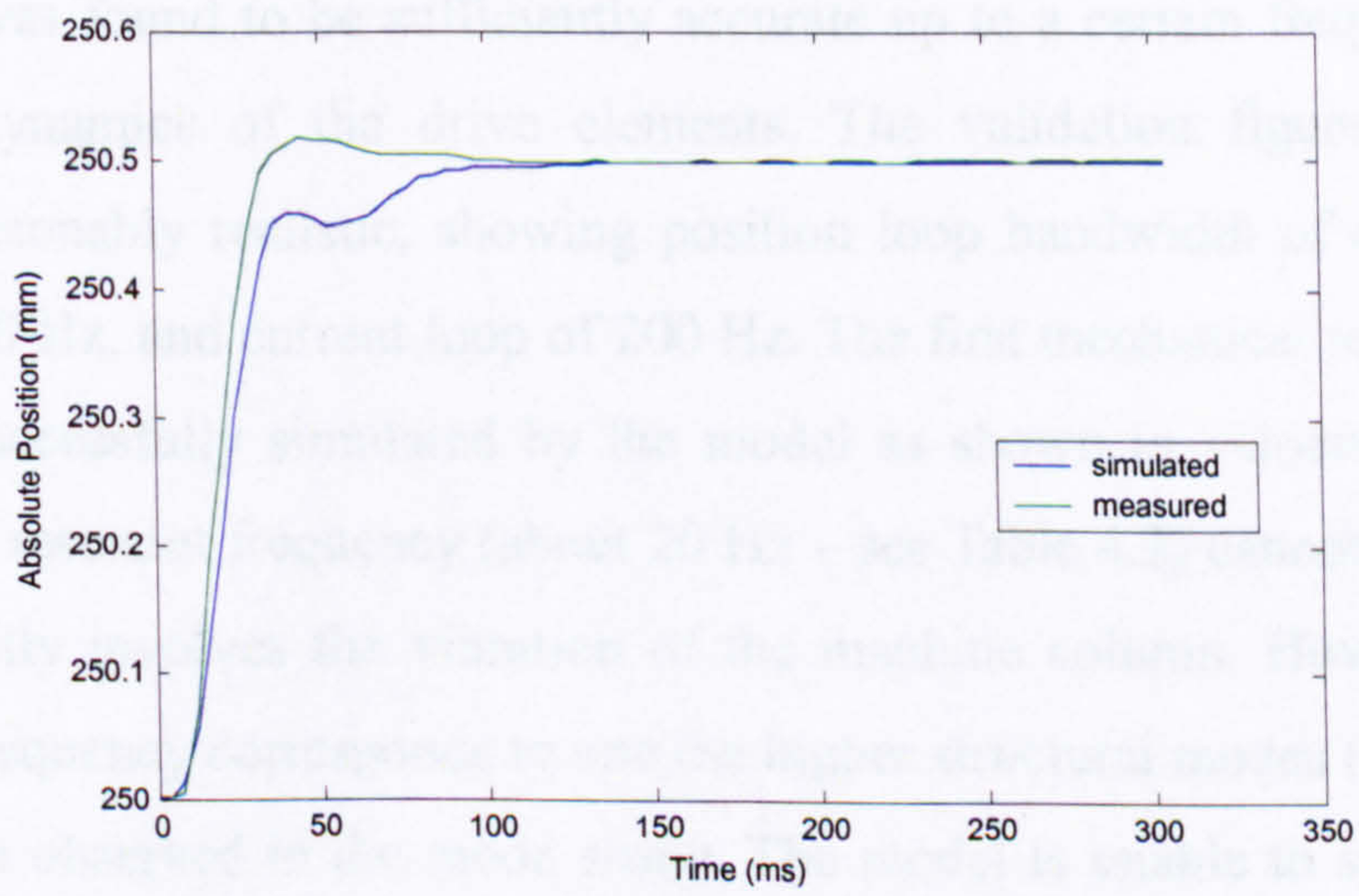

Figure 5.37. Graph of the position control loop response to a 0.5 mm step input

The position control loop response is largely influenced by the mechanical load. The simulated response lag from the actual system is most likely due to mass and stiffness

parameter tolerances of the data supplied by the manufacturer. The undershoot response of the simulated response is likely from the higher damping values implemented in the model compared to the actual data. Because the drive element damping values are not directly measured, the calculated and estimated data slightly deviates from the actual values. Thus, a sensitivity analysis to accurately determine the contribution of each mechanical load element damping is required. A method suggested by Holroyd et al [185] provides a possible solution to this problem. However, the effect of machine structural damping and an optimised algorithm is required in order to obtain the overall picture of the feed drive damping behaviour.

5.7. Conclusions

The development of a single-axis digital drive model for the Cincinnati vertical machining centre employing the hybrid modelling technique with distributed load, explicit damping coefficients, backlash and friction technique has been presented in this chapter. The model was validated using measured signals from the machine drive by employing time-domain deterministic and non-deterministic signals including the frequency response analysis. The development of a single-axis model was intended as a proof of concept for the possibility of employing the drive system as a method of active vibration control. The models for the other axes can be developed relatively easily from the current model as they utilise similar drive configurations. However, more effort might be required for modelling the Z-axis drive as it has a vertical configuration and, thus, requires consideration for headstock mass balancing to compensate for the gravitational force (via motor brake and quadrature current offset).

The model was found to be sufficiently accurate up to a certain frequency bandwidth in modelling the dynamics of the drive elements. The validation figures indicate that the simulation is reasonably realistic, showing position loop bandwidth of circa 5 Hz, velocity loop of about 100 Hz, and current loop of 200 Hz. The first mechanical resonant frequency of the drive was successfully simulated by the model as shown in velocity control loop. The lowest structural resonant frequency (about 20 Hz – see Table 4.2) cannot be simulated by the model as it mostly involves the vibration of the machine column. However, the simulated drive resonant frequency corresponds to one the higher structural modes (circa 120 Hz) where table vibration is observed in the mode shape. The model is unable to simulate other higher resonant frequencies as the modelling technique of dividing the ballscrew into three sections is considered as limited in the number of degree of freedom. A hybrid model with higher

number of ballscrew sections might be able to overcome the problem. Alternatively, other techniques, such as transmission line matrix modelling can be employed for the purpose.

The model's capability to simulate one of the structural resonant frequencies provides a possibility of developing an active vibration compensation technique via the drive system. However, a difficulty might be encountered as this frequency is very close the limit of the drive system's bandwidth. Thus, further work is required to increase the model bandwidth in order to represent the drive system and its performance more accurately. A sensitivity analysis on the drive elements might be required to determine the closest parametric values to the actual figures as manufacturer-supplied data were extensively used in the modelling process. In addition, a direct access to the velocity and other control loops is required (e.g. via compile cycles) in order to implement the active vibration control algorithm into the drive system. The drive's capability of delivering the necessary dynamic stiffness to compensate for the vibration needs to be assessed as well. At the present time, this method can be performed with a limited stiffness range via an external system [186] although this is not practical for normal machining processes. A passive vibration control system is considered as more practical in delivering the necessary vibration reduction.

The next chapter presents the investigation and analytical modelling of the machining process using both theoretical and experimental results to find the relationship between the cutting force generation, surface topography prediction and structural dynamic properties.

Chapter 6. CUTTING PROCESS MODELLING AND SURFACE FINISH ANALYSIS

A typical VMC milling process removes a predetermined amount of material from a workpiece progressively by feeding a rotating cutting tool to its surface in order to achieve a desired shape and dimension. It is one of the most common forms of cutting processes along with turning and drilling, followed up by special operations such as boring, broaching, shaping, form cutting and grinding. The cutting processes, also known as the machining processes, are the most commonly used method to obtain the final shapes of mechanical components with improving accuracy and productivity over the years [94].

The cutting process generates most of the dynamic forces in a machine tool and subsequently induces vibration on both the machine and workpiece, which may affect the quality of the finished product. Other large force-generating occurrences include the rapid travelling of the machine's moving elements such as the table and saddle. However, it does not usually happen in the cutting process and its characteristics and modelling have already been discussed in Chapter 5. The shaping of the workpiece with a machining process also creates new surfaces on the workpiece which are influenced by various aspects such as the cutting tool condition, machining parameters, generated cutting forces and cutting tool-workpiece vibration. Thus, the characterisation of the machined surface can reciprocally reveal a wealth of information regarding the machining process and machine conditions including the cutting tool and machine structural dynamic properties (see Chapter 4).

This chapter discusses a proposed relationship between the metal cutting process, machined surface topography and structural dynamic properties of a vertical CNC machine tool (see Figure 4.1) as part of an EPSRC funded project [3]. The author contributes to the measurement, evaluation and analysis of the generated cutting force, machine vibration as well as the structural dynamic properties of the machine tool and its cutting elements. The measured structural dynamic properties is integrated into a proposed vibration model in order to further improve the mechanistic machining process model of the Computer Aided Manufacturing Group from Leeds Metropolitan University (see Figure 6.1). The investigation into the physical model focuses on the dynamic peripheral milling force and includes a study into the ball-end milling process.

The machining process model also produces simulated 3D surface by calculating the cutting tool displacement relative to the workpiece by considering the measured dynamic properties. The simulated surface is validated against 3D characterisation of the machined

workpiece by the Surface Characterisation Group at the University of Huddersfield. Form Talysurf PGI and data filtering using the lifting wavelet technique are employed to measure and analyse the results, which are subsequently correlated against the machining parameters used to produce the workpiece.

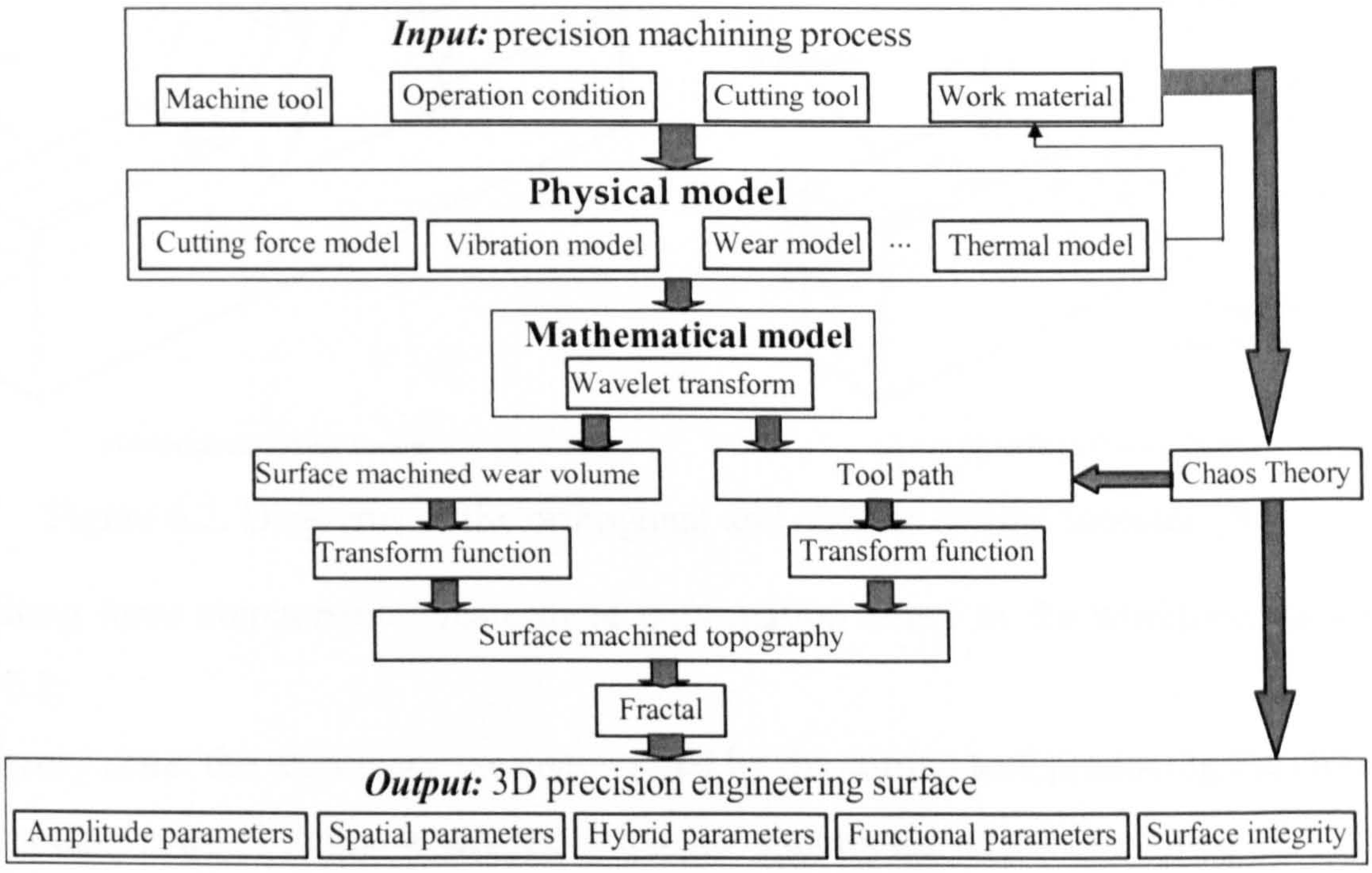

Figure 6.1. Diagram of the proposed machining process model [3]

6.1. Cutting process theories

Investigations into the metal cutting process are mostly performed with either the FEA or the mechanistic force approach. The most recent finite element investigations are able to simulate cutting chip formation and separation using various criteria including the distance tolerance, strain energy density and fracture mechanics algorithms as shown by Hashemi et al [187]. The meshing problem generated by the chip separation from the workpiece can be solved by various methods such as the re-zoning technique demonstrated by Shih and Yang [188] or by removing elements below a critical value as studied by Ceretti [189].

The investigation into the cutting process in this study is performed using the mechanistic force modelling technique. This technique can be generally grouped into two approaches: two-dimensional orthogonal and three-dimensional oblique theories. The orthogonal cutting theory assumes that the cutting tool edge is normal to the cutting and chip flow direction, whereas the oblique approach simulates inclined acute angles of cutting edge and chip flow directions (see Figure 6.2). The material flow and the cutting edge motion of an orthogonal cutting produce a two-dimensional plane strain deformation process formed by the tangential force (parallel with the cutting direction) and the feed force (from the uncut chip thickness)

(see Figure 6.2.(a)). The oblique cutting approach includes an additional deformation plane to represent the rake forces which acts normal to the other force components (see Figure 6.2.(b)).

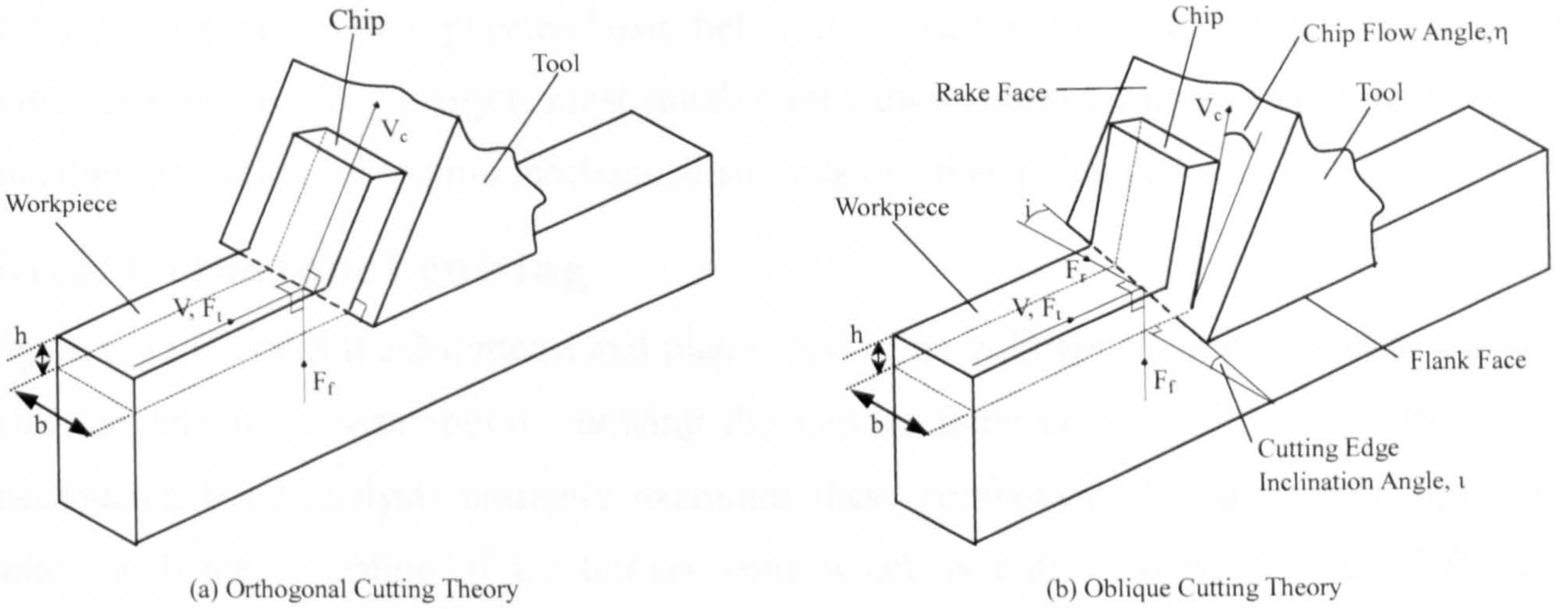

Figure 6.2. Diagrams of the orthogonal and oblique cutting theories [94]

The cutting force components create three deformation zones in the workpiece as shown in Figure 6.3:

1. ***Primary zone***: the workpiece area penetrated by the cutting tool producing the chips.
2. ***Secondary zone***: the zone where the chips move along the rake face of the tool
3. ***Tertiary zone***: the workpiece area where the friction with the flank face of the tool occurs

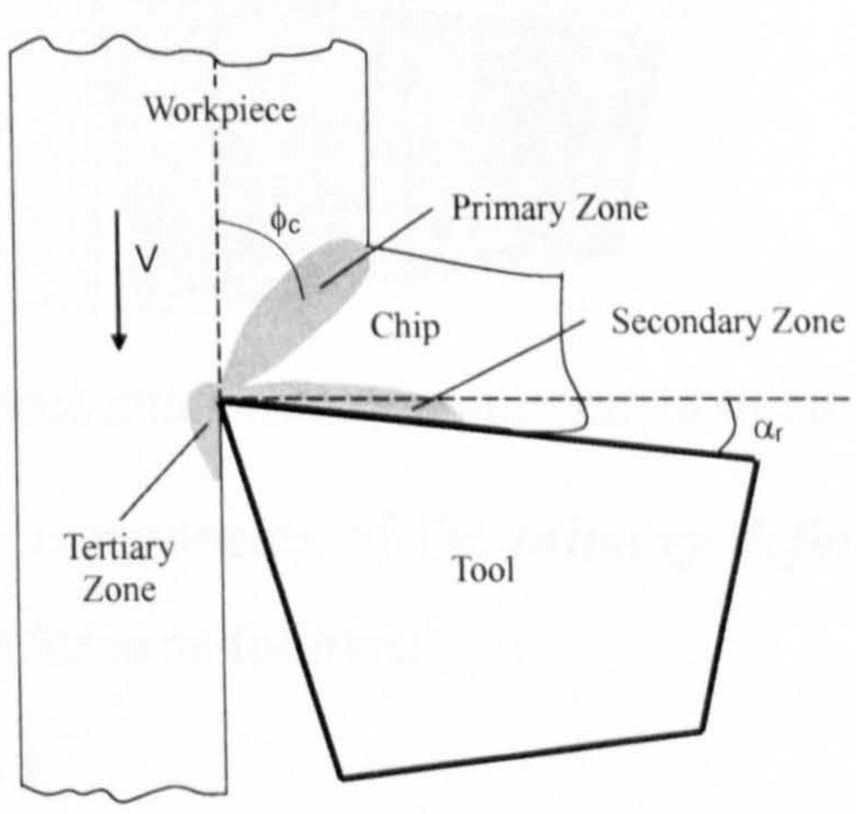

Figure 6.3. Deformation zones of a cutting process [94]

The mechanistic analysis of the component forces is dependent on the chip formation postulation of the primary deformation zone. The first approach as proposed by Merchant [76] assumes that the deformation occurs on a thin plane and the material is sheared as the cutting edge glided in the primary zone. This theory is widely used where higher cutting speed or low depth of cut is employed, thus highly appropriate for extensive range of practical applications. The theory also leads to a simpler mathematical treatment which is also beneficial in analysing more complex metal cutting configurations, including the subject of this investigation.

The other more complex theory assumes that the chip is formed from a thick plane as proposed by Palmer and Oxley [77] and Lee and Shaffer [78]. It postulates that the thick deformation zone exhibits plastic-elastic behaviour, thus the plasticity theory is required to solve the problem. This theory is most suitable for slowly rotating cutting tool or deep cutting situations as well as for thermo mechanical analysis of a machining process.

6.1.2. Orthogonal cutting

Figure 6.4 illustrates the 2-dimensional plane view of an orthogonal cutting process analysed with the thin plate assumption, showing the cutting force and velocity components. The mechanistic force analysis normally examines these components based on their operating zones, with the exception of the tertiary zone which is only used when detailed thermo-mechanical treatment is required.

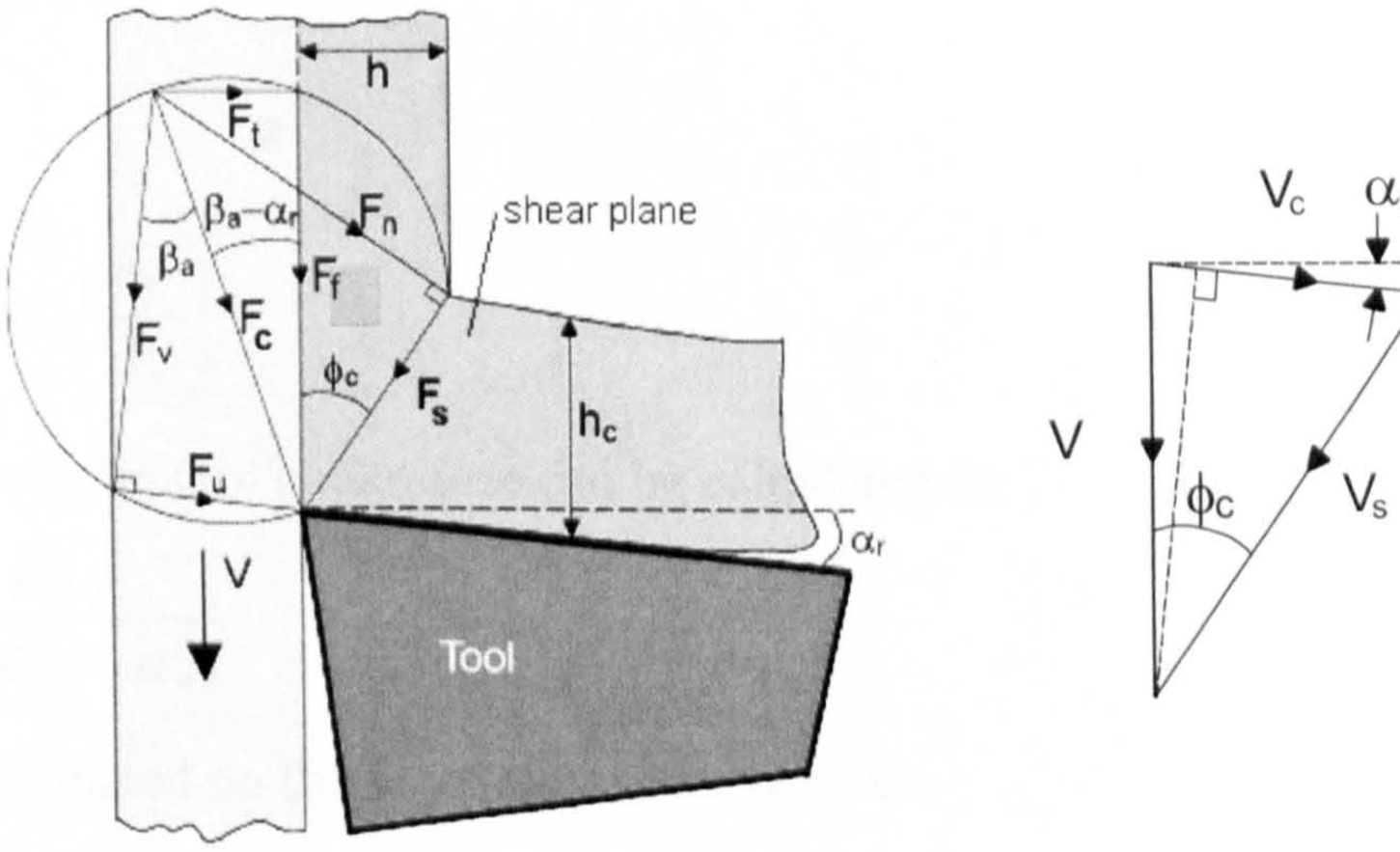

Figure 6.4. Diagram of the force and velocity components of an orthogonal cutting process [94]

The shear and normal force components of the ***primary deformation zone*** can be analysed respectively from the cutting force as follows:

$$F_s = F_c \cos(\phi_c + \beta_\alpha - \alpha_r) \tag{6.1}$$

$$F_n = F_c \sin(\phi_c + \beta_\alpha - \alpha_r) \tag{6.2}$$

They can also be represented respectively as functions of the feed and tangential cutting forces as:

$$F_s = F_f \cos\phi_c - F_t \sin\phi_c \tag{6.3}$$

$$F_n = F_f \sin\phi_c + F_t \cos\phi_c \tag{6.4}$$

The shear velocity of the workpiece can be found from the feed velocity:

$$V_s = V \frac{\cos\alpha_r}{\cos(\phi_c - \alpha_r)} \tag{6.5}$$

The values of the shear velocity and force can be used to calculate the dissipated power (heat) in the primary shear area as follows:

$$P_s = F_s \cdot V_s \tag{6.6}$$

The cutting force components acting in the ***secondary shear zone*** are the normal force acting on the tool's rake face and the friction force between the chip and the tool's rake face (see Figure 6.4). Using the assumption of a constant and averaged friction coefficient, these forces can be calculated using the following equations:

$$F_v = F_t \cos\alpha_r - F_f \sin\alpha_r \tag{6.7}$$

$$F_u = F_t \sin\alpha_r + F_f \cos\alpha_r \tag{6.8}$$

The constant and averaged friction coefficient can be found as:

$$\mu_a = \tan\beta_a = \frac{F_u}{F_v} \tag{6.9}$$

or, alternatively

$$\mu_a = \tan\left(\alpha_r + \tan^{-1}\frac{F_f}{F_t}\right) \tag{6.10}$$

The chip velocity over the tool's rake face can be calculated as:

$$V_c = Vr_c = V\frac{\sin\phi_c}{\cos(\phi_c - \alpha_r)} \tag{6.11}$$

Hence the power dissipated on the secondary shear zone is:

$$P_u = F_u \cdot V_c \tag{6.12}$$

When the ***resultant cutting force*** acting on the workpiece is unknown, it can be calculated from the predicted feed and tangential cutting forces using the ideal condition where the shear and normal stresses of the shear plane are constant:

$$F_c = \sqrt{{F_t}^2 + {F_f}^2} \tag{6.13}$$

$$F_t = bh\left(\tau_s \frac{\sin(\beta_a - \alpha_r)}{\sin\phi_c \cos(\phi_c + \beta_a - \alpha_r)}\right) \tag{6.14}$$

$$F_f = bh\left(\tau_s \frac{\cos(\beta_a - \alpha_r)}{\sin\phi_c \cos(\phi_c + \beta_a - \alpha_r)}\right) \tag{6.15}$$

The expressions in the brackets are normally described as the tangential cutting force coefficient and the feed force constant respectively.

The cutting force produced can be also predicted from the formulation of the shear force, which is obtained as a function of the shear stress and angle:

$$F_s = \tau_s b \frac{h}{\sin \phi_c} \tag{6.16}$$

$$F_c = \frac{F_s}{\cos(\phi_c + \beta_a - \alpha_r)} = \tau_s bh \frac{1}{\sin \phi_c \cos(\phi_c + \beta_a - \alpha_r)} \tag{6.17}$$

Another important consideration in a machining process analysis is the total energy dissipation and cooling. Heat build-up at the workpiece and cutting tool can affect the accuracy, surface finish, cutting tool life and safety. The energy dissipated in the tertiary zone is minimal compared to the other zones and, therefore, the total energy dissipation can be found by summing the energy dissipated in the primary and secondary shear zones:

$$P_t = P_s + P_u \tag{6.18}$$

According to the force and velocity equilibrium principle, the energy is also equal to the power drawn from the spindle motor:

$$P_t = F_t V \tag{6.19}$$

The heat generated by the cutting process, both on the primary and secondary shear zones can be estimated respectively by:

$$\Delta T_s = \frac{P_s}{\mathrm{m_c c_s}} \tag{6.20}$$

$$\Delta T_u = \frac{P_u}{\mathrm{m_c c_s}} \tag{6.21}$$

6.1.3. Oblique cutting

The inclined tool edge of an oblique cutting model produces a tilting cutting velocity with respect to the plane normal to the cutting edge, requiring additional planes to be defined (see Figure 6.5). The ***cut surface*** is formed in the X- and Y-coordinates, which are perpendicular and parallel to the tool edge directions respectively. In addition, the ***normal plane*** is formed in the *x* and *z* coordinates, and arranged normal to the tool edge. The ***velocity plane*** (not shown in the figure), parallel with the cutting velocity and feed direction, is further added for the analysis purpose.

The inclination angle of the cutting tool generates three cutting force and velocity vectors in the three Cartesian coordinates. The projection of these vectors onto the normal plane produces several analytical angles: the normal shear angle, the oblique shear angle, the chip flow angle, the normal rake angle, the normal force angle and the oblique force angle. The cutting force vector can then be separated into its components: the friction and normal force on the rake face.

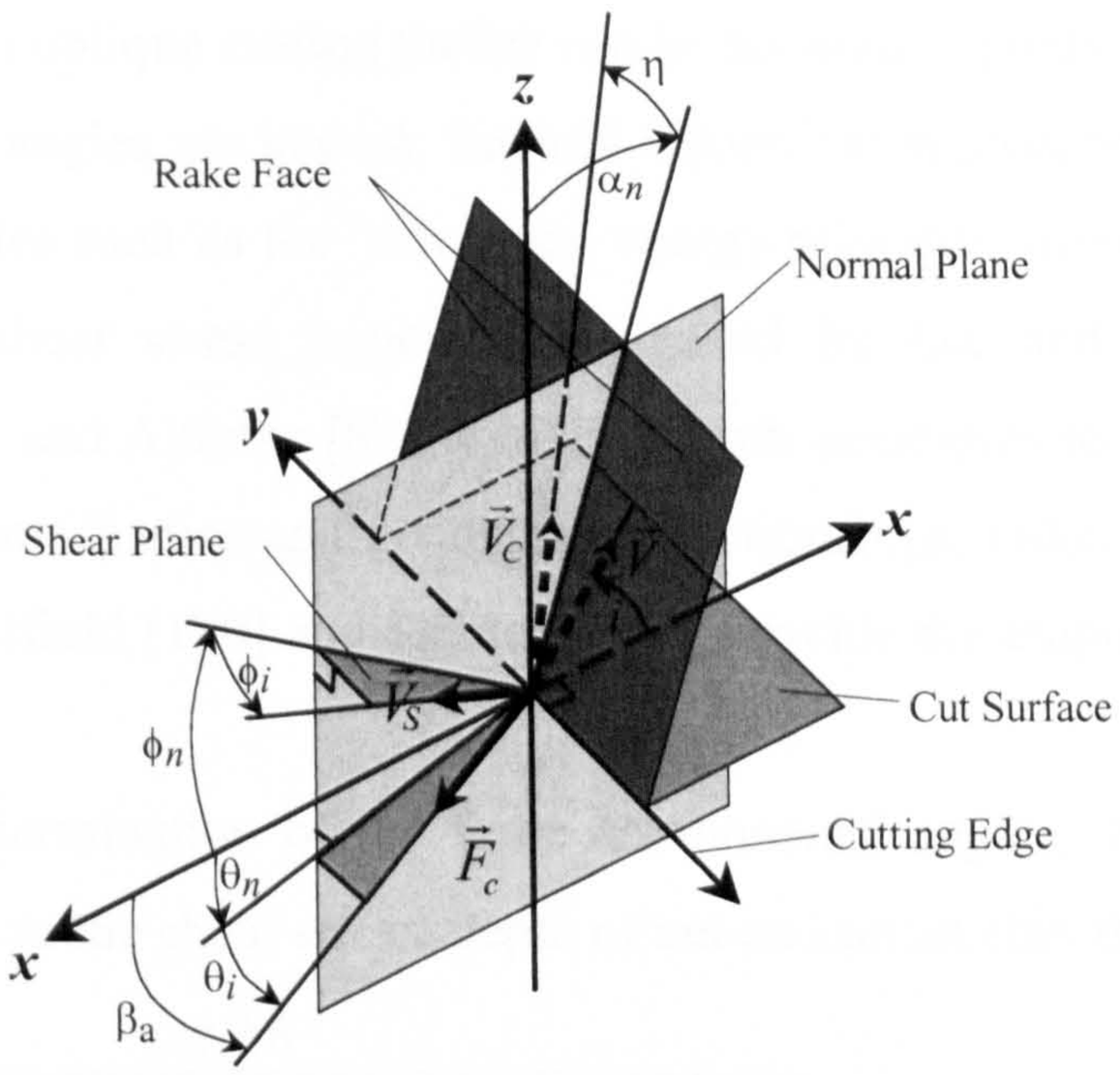

Figure 6.5. Geometry of oblique cutting process [94]

Using the above geometry, the cutting force vector components can be calculated as follows:

$$F_u = F\sin\beta_a = F\frac{\sin\theta_i}{\sin\eta} \tag{6.22}$$

$$F_v = \frac{F_u}{\tan\beta_a} = \frac{F_u\cos\eta}{\tan(\theta_n+\alpha_n)} \tag{6.23}$$

where

$$\sin\theta_i = \sin\beta_a\sin\eta \tag{6.24}$$

and

$$\tan(\theta_n+\alpha_n) = \tan\beta_a\cos\eta \tag{6.25}$$

The velocity vectors of the chip, shear and cutting, which form the velocity plane, can be defined by their Cartesian components as follows:

$$\vec{V} = (V\cos\iota, \quad V\sin\iota, \quad 0) \tag{6.26}$$

$$\vec{V}_c = (V_c\cos\eta\sin\alpha_n, \quad V_c\sin\eta, \quad V_c\cos\eta\cos\alpha_n) \tag{6.27}$$

$$\vec{V}_s = (-V_s\cos\phi_i\cos\phi_n, -V_s\sin\phi_i, V_s\cos\phi_i\sin\phi_n) \tag{6.28}$$

Using these coordinates and the velocity vector relationship of

$$\vec{V}_s = \vec{V}_c - \vec{V} \tag{6.29}$$

the following geometrical relationship between the shear and chip flow direction is obtained:

$$\tan\eta = \frac{\tan\iota\cos(\phi_n-\alpha_n)-\cos\alpha_n\tan\phi_i}{\sin\phi_n} \tag{6.30}$$

The cutting force of an oblique cutting theory can be accurately predicted when the values for the component vector angles are known. Several theoretical approaches have been developed to calculate these angles such as the 'minimum energy principle' proposed by Merchant [76] and the 'maximum shear stress principle' suggested by Lee and Shaffer [78]. Another approach by Shamoto and Altintas [82] combined both principles to predict the shear angle based on the laws of mechanics and geometrical relationships. Other theories, such as those by Armarego and Whitfield [190] and Stabler [191], provide the empirical methods to predict the values.

Following the determination of the force components' angles, the cutting force can be predicted with respect to the shear stress, depth of cut and uncut chip thickness as follows:

$$F_c = \frac{\tau_s bh}{\left[\cos(\theta_n + \phi_n)\cos\theta_i \cos\phi_i + \sin\theta_i \sin\phi_i\right]\cos\iota \sin\phi_n} \tag{6.31}$$

The cutting force components, *i.e.* the tangential, thrust and radial, can then respectively be derived as follows:

$$\begin{aligned} F_t &= F_c(\cos\theta_i \cos\theta_n \cos\iota + \sin\theta_i \sin\iota) \\ &= \frac{\tau_s bh(\cos\theta_n + \tan\theta_i \tan\iota)}{\left[\cos(\theta_n + \phi_n)\cos\phi_i + \tan\theta_i \sin\phi_i\right]\sin\phi_n} \end{aligned} \tag{6.32}$$

$$\begin{aligned} F_f &= F_c \cos\theta_i \sin\theta_n \\ &= \frac{\tau_s bh \sin\theta_n}{\left[\cos(\theta_n + \phi_n)\cos\phi_i + \tan\theta_i \sin\phi_i\right]\cos\iota \sin\phi_n} \end{aligned} \tag{6.33}$$

$$\begin{aligned} F_r &= F_c(\sin\theta_i \cos\iota - \cos\theta_i \cos\theta_n \sin\iota) \\ &= \frac{\tau_s bh(\tan\theta_i - \cos\theta_n \tan\iota)}{\left[\cos(\theta_n + \phi_n)\cos\phi_i + \tan\theta_i \sin\phi_i\right]\sin\phi_n} \end{aligned} \tag{6.34}$$

6.2. Improved dynamic cutting force model

This model is based on the oblique cutting theory and intended for a peripheral cutting process using helical end-mills and cutter run-out consideration. Figure 6.6.(a) shows the geometric model of the cutting tool which can be represented as a combination of a number of small segments along the z-axis. The cutting action of an individual tooth within each segment is modelled as a single point oblique cutting as illustrated in Figure 6.6.(b). The model considers the influence of the effective rake angle and un-deformed chip thickness, and adheres to the Stabler's principle [191], which states that when the normal rake angle is equal to or greater than 8°, the chip flow angle is approximately equal to the inclination angle.

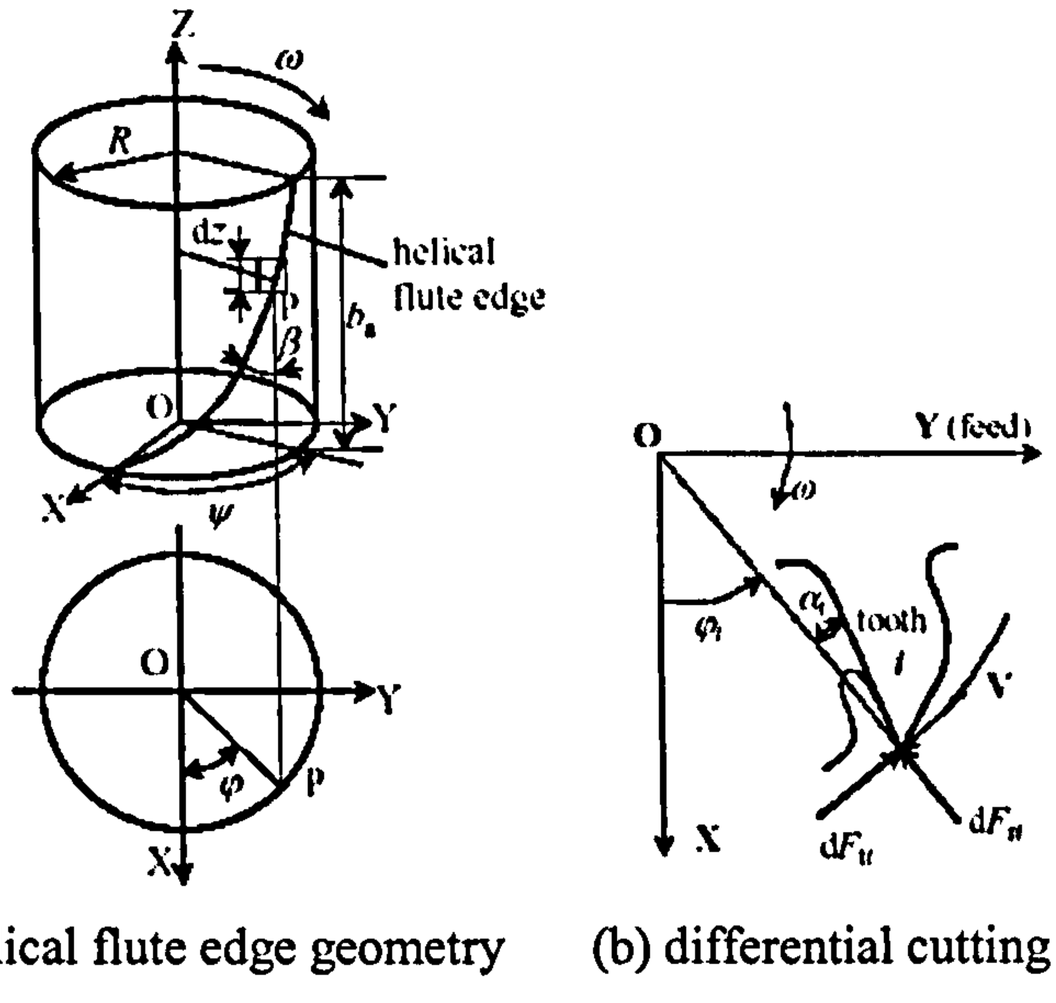

(a) Helical flute edge geometry (b) differential cutting forces

Figure 6.6. Diagram of the differential cutting force model of peripheral milling [84]

6.2.1. Analytical investigation

The differential tangential, normal and axial cutting force components at any point on the rake face can then be obtained as:

$$dF_{ti}(\varphi_i) = K_s t_i(\varphi_i) R \cot\beta d\varphi \tag{6.35}$$

$$dF_{ri}(\varphi_i) = c_1 dF_{ti}(\varphi_i) \tag{6.36}$$

$$dF_{ai}(\varphi_i) = c_2 dF_{ti}(\varphi_i) \tag{6.37}$$

The dynamic process of the model is given by rotating angular position of a point at the helical flute:

$$\varphi_i = \varphi - \omega t + (i-1)\frac{2\pi}{m} \quad (1 \le i \le m,\ 0 \le \varphi \le \psi) \tag{6.38}$$

where

$$\psi = \frac{b_a \tan\beta}{R} \tag{6.39}$$

The ***cutter run-out*** (see Figure 6.7) is taken into account and its effect on the actual cutting radius of the i^{th} tooth is represented by:

$$R_i'(\varphi_i') = \sqrt{R^2 + \delta_e^2 - 2R\delta_e \cos\left(\pi - \left|\varphi - \varphi_{e0} + \frac{2(i-1)\pi}{m}\right|\right)} \tag{6.40}$$

The un-deformed chip thickness removed by a point on the i^{th} helical flute for the down milling case (see Figure 6.8.(a)) can thus be calculated as follows:

$$t_i(\varphi_i') = \begin{cases} f_t \sin(\varphi_i') + (v_{ic(-T)} - v_{ic}) - (v_{iw(-T)} - v_{iw}) + \delta t_i(\varphi_i') & \text{for } 0 \le \varphi_i' \le \Omega \\ 0 & \text{otherwise} \end{cases} \tag{6.41}$$

Whereas for the up milling case (Figure 6.8.(b)):

$$t_i(\varphi_i') = \begin{cases} f_t \sin(-\varphi_i') + (v_{ic(-T)} - v_{ic}) - (v_{iw(-T)} - v_{iw}) + \delta t_i(\varphi_i') & \text{for } -\Omega \le \varphi_i' \le 0 \\ 0 & \text{otherwise} \end{cases} \tag{6.42}$$

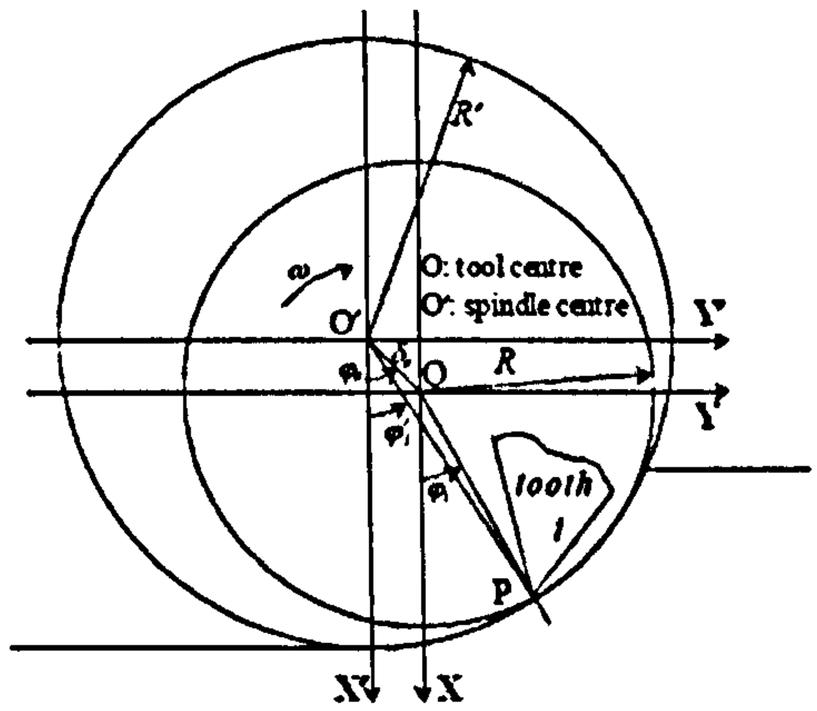

Figure 6.7. Diagram of the cutting tool run-out model relative to the spindle position [192]

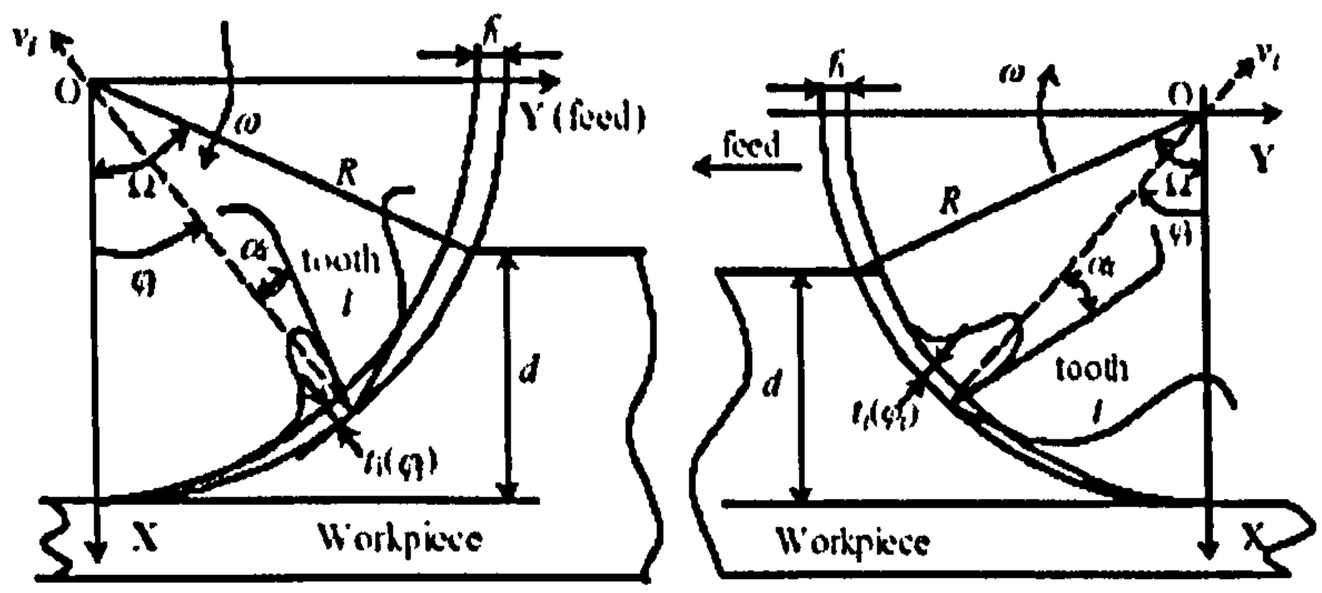

(a) Down milling (b) Up milling

Figure 6.8. Diagram of possible peripheral milling directions [192]

The differential cutting force components (equations(6.35)-(6.37)) can thus be resolved in the x, y, and z-directions by considering that cutter run-out is much less than the cutting radius:

$$R_i'(\varphi_i')\cot\beta \approx R\cot\beta \tag{6.43}$$

thus:

$$dF_{ix} = -K_s t_i(\varphi_i) R\cot\beta(\sin\varphi_i + c_1\cos\varphi_i)d\varphi \tag{6.44}$$

$$dF_{iy} = K_s t_i(\varphi_i) R\cot\beta(\cos\varphi_i - c_1\sin\varphi_i)d\varphi \tag{6.45}$$

$$dF_{iz} = -c_2 K_s t_i(\varphi_i) R\cot\beta d\varphi \tag{6.46}$$

where the tangential cutting force coefficient can be calculated as:

$$K_s = u_0\left(1 - \frac{\alpha_e - \alpha_{e0}}{100}\right)\left(\frac{t_0}{t_i(\varphi_i)}\right)^{0.2} \tag{6.47}$$

Furthermore, by assuming that

$$u' = u_0\left(1-\frac{\alpha_e-\alpha_{e0}}{100}\right)\left(\frac{t_0}{f_t}\right)^{0.2} \tag{6.48}$$

and only negligible variation of un-deformed chip thickness, the differential cutting force components for the down and up milling cases can be predicted as shown in appendices E.1 and E.2. The total force generated on the cutting tool edges can be obtained from by integrating the component equations across its length:

$$\begin{cases} F_{ix} \approx \int_{\varphi_s}^{\varphi_e} dF_{ix}\, d\varphi_i \\ F_{iy} \approx \int_{\varphi_s}^{\varphi_e} dF_{iy}\, d\varphi_i \end{cases} \tag{6.49}$$

where for down-milling case

$$\varphi_s = \max\left(0, -\omega t + (i-1)\frac{2\pi}{m}\right) \tag{6.50}$$

$$\varphi_e = \min\left(\Omega, \psi - \omega t + (i-1)\frac{2\pi}{m}\right) \tag{6.51}$$

and for up-milling case

$$\varphi_s = \max\left(-\Omega, -\omega t + (i-1)\frac{2\pi}{m}\right) \tag{6.52}$$

$$\varphi_e = \min\left(0, \psi - \omega t + (i-1)\frac{2\pi}{m}\right) \tag{6.53}$$

The total cutting force acting can be found by combining the force for each helical flute:

$$\begin{cases} F_x = \sum_{i=1}^{m} F_{ix} \\ F_y = \sum_{i=1}^{m} F_{iy} \\ F_z = \sum_{i=1}^{m} F_{iz} \end{cases} \tag{6.54}$$

6.2.2. Experimental calibration and prediction

The analytical model requires an experimental calibration of the radial and axial force ratios, as well as the initial total cutting energy per unit volume. The ratios for a cutting condition can be theoretically calculated from the cutting tool and workpiece material and geometry as presented by Shaw [193] and Oxley [194]. However, an experimental technique is normally necessary due to the inconsistency and manufacturer's tolerance of the calculated data.

The experimental investigation is performed using a single tooth helical solid carbide end mill to isolate the generated cutting force. The tool is fitted in a hydraulic chuck, mounted on

the spindle head of the machine tool and operated at a set of cutting conditions and parameters (see Table 6.1) to obtain a maximum radial immersion angle. A workpiece is fixed using the Microloc fixture system Kit-MD75 [163] attached on a Kistler table dynamometer 9255B [164], which itself is secured on the machine worktable (see Figure 6.9). The spindle and workpiece time vibration is measured using a pair of PCB industrial accelerometers and recorded using a Mobilyser Dataphysics dynamic signal analyser [160].

Cutting Tool	:	Single fluted solid carbide end-mill **Diameter** = 10 mm, **Helix angle** = 45°, **Radial rake angle** = 5°
Workpiece Material	:	Carbon steel EN8
Cutting Speed	:	1114 rpm (70 m/min)
Cutting condition	:	With coolant

Test Number	**1**	**2**	**3**	**4**	**5**	**6**	**7**	**8**
Feed rate (mm/tooth)	0.0197	0.0296	0.0395	0.0494	0.0592	0.0691	0.0790	0.0889
Axial depth of cut (mm)	10.545	10.545	10.545	10.45	10.39	10.45	10.39	10.39

Table 6.1. Cutting parameters and conditions for the experimental calibration

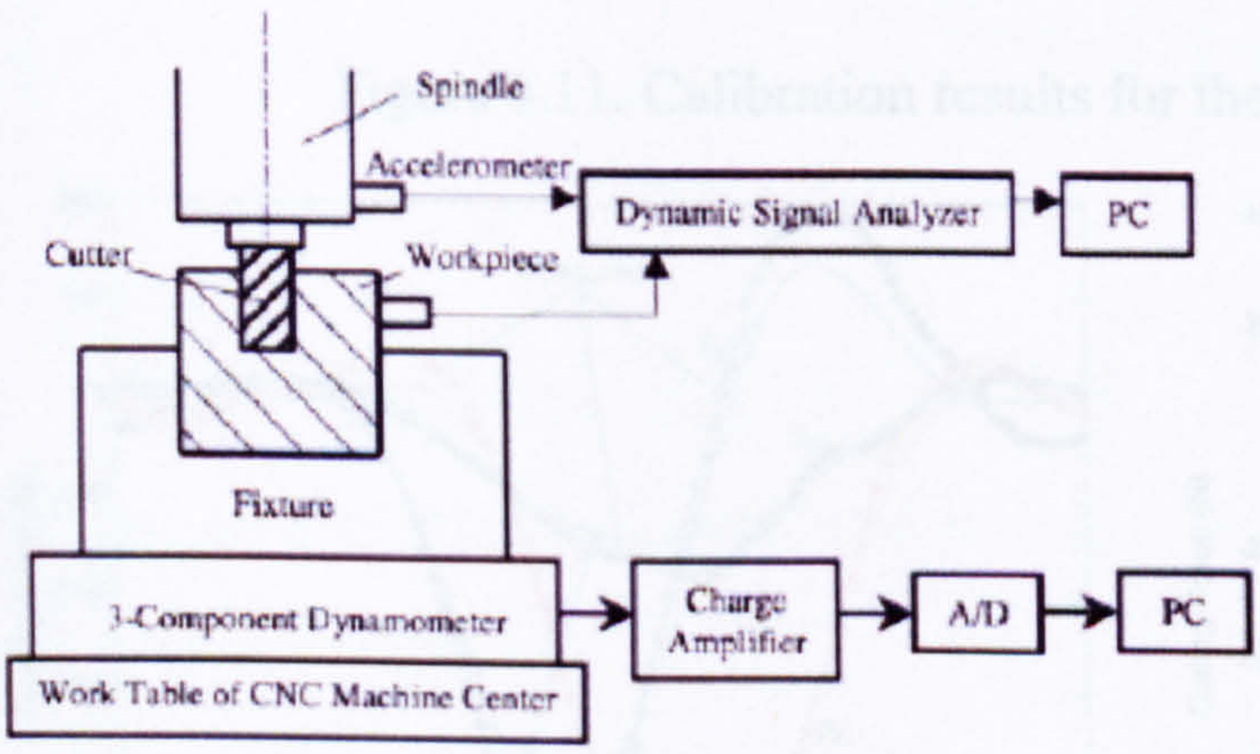

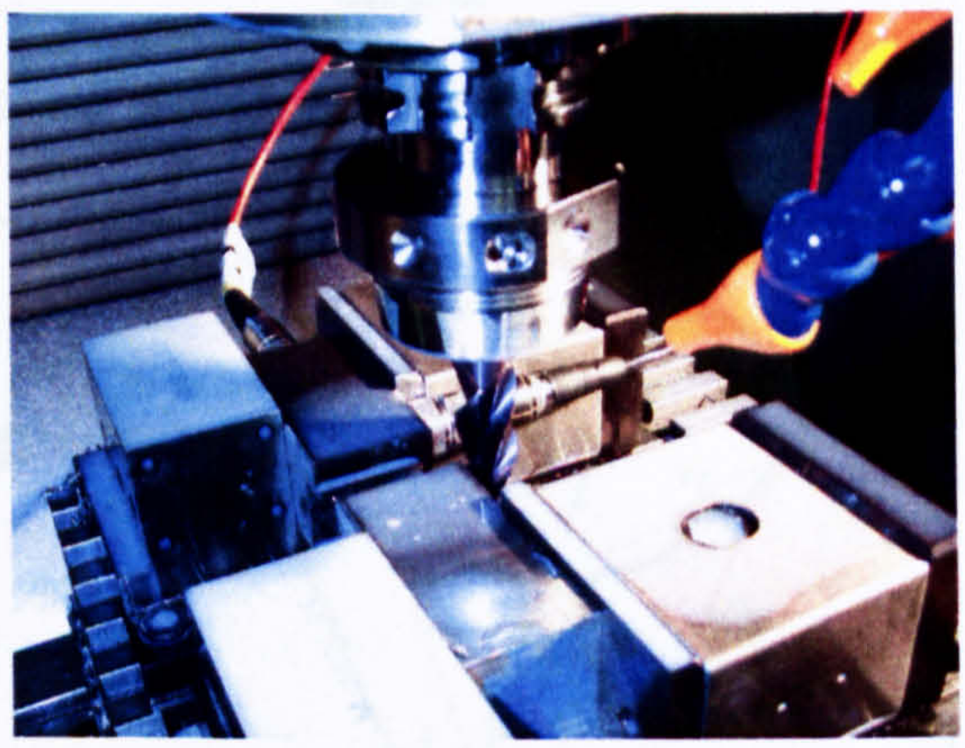

Figure 6.9. Diagram of the experimental investigation to calibrate the model coefficients

The calibration results are summarised in Table 6.2 and can be seen in Figure 6.10 and Figure 6.11. The predicted forces using the calibrated values for the same cutting conditions and parameters are shown in Figure 6.12 to Figure 6.19.

Test Number	**1**	**2**	**3**	**4**	**5**	**6**	**7**	**8**
f_t (mm/tooth)	0.0197	0.0296	0.0395	0.0494	0.0592	0.0691	0.0790	0.0889
u_0 (GJ/m^3)	2.4067	2.4433	2.3851	2.4532	2.3891	2.5146	2.4429	2.5184
c_1	0.5114	0.4832	0.4776	0.3889	0.3457	0.4052	0.3992	0.4171
c_2	0.2617	0.2871	0.3191	0.3529	0.3525	0.3596	0.3570	0.3599
Calculated c_2	0.2038	0.2413	0.2448	0.3667	0.4241	0.3540	0.3530	0.3292

Table 6.2. Calibrated and calculated values for cutting force coefficients

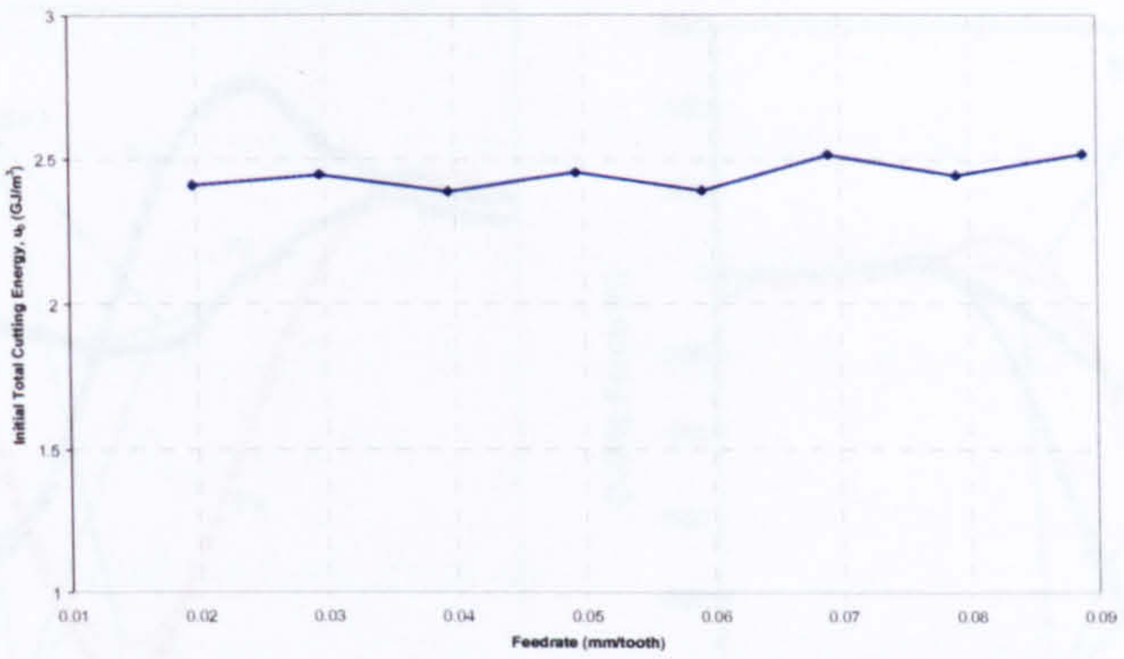

Figure 6.10.Calibration results for the initial total cutting energy per unit volume

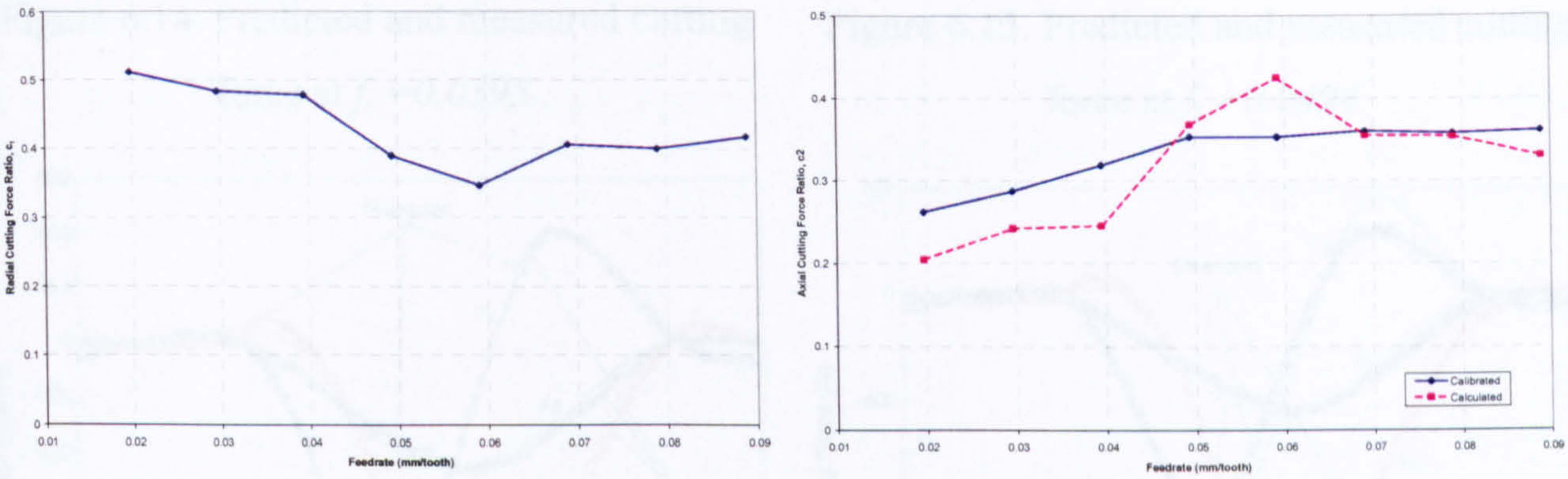

Figure 6.11. Calibration results for the radial and axial force ratios

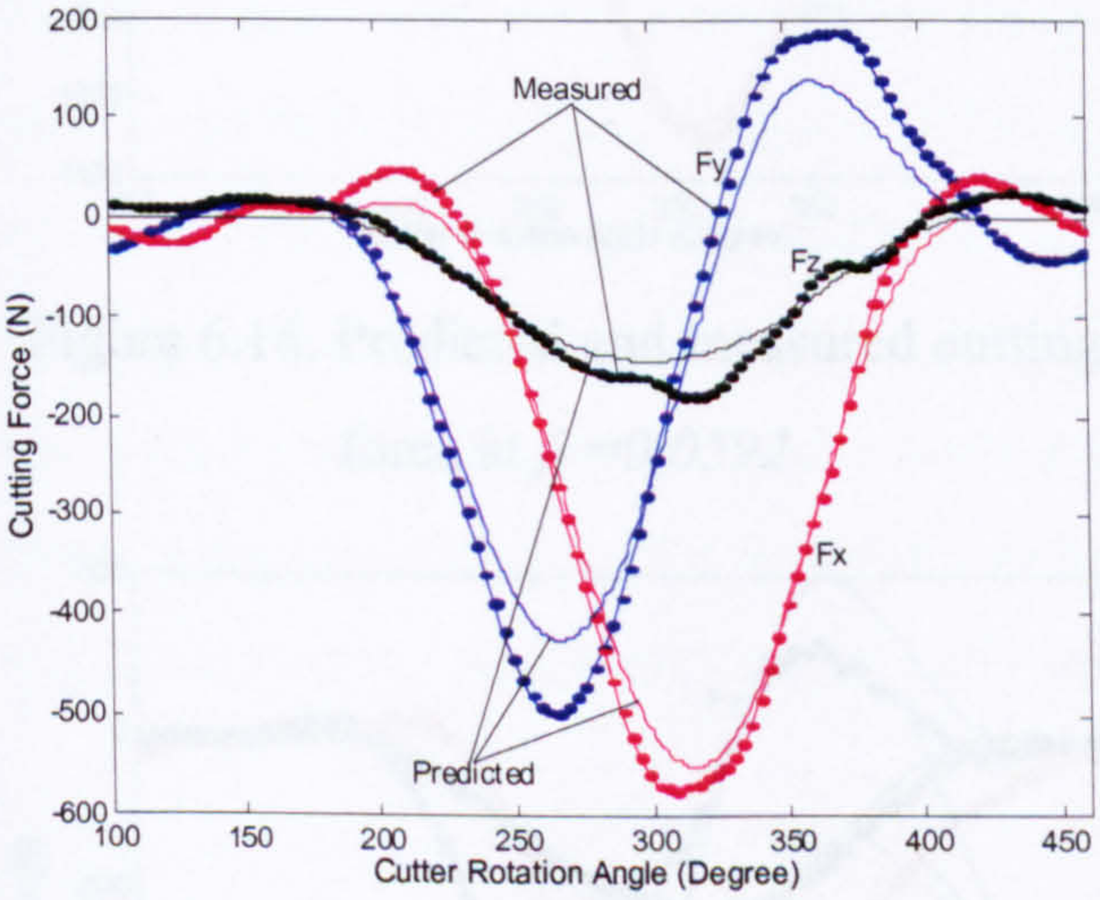

Figure 6.12. Predicted and measured cutting force at $f_t = 0.0197$

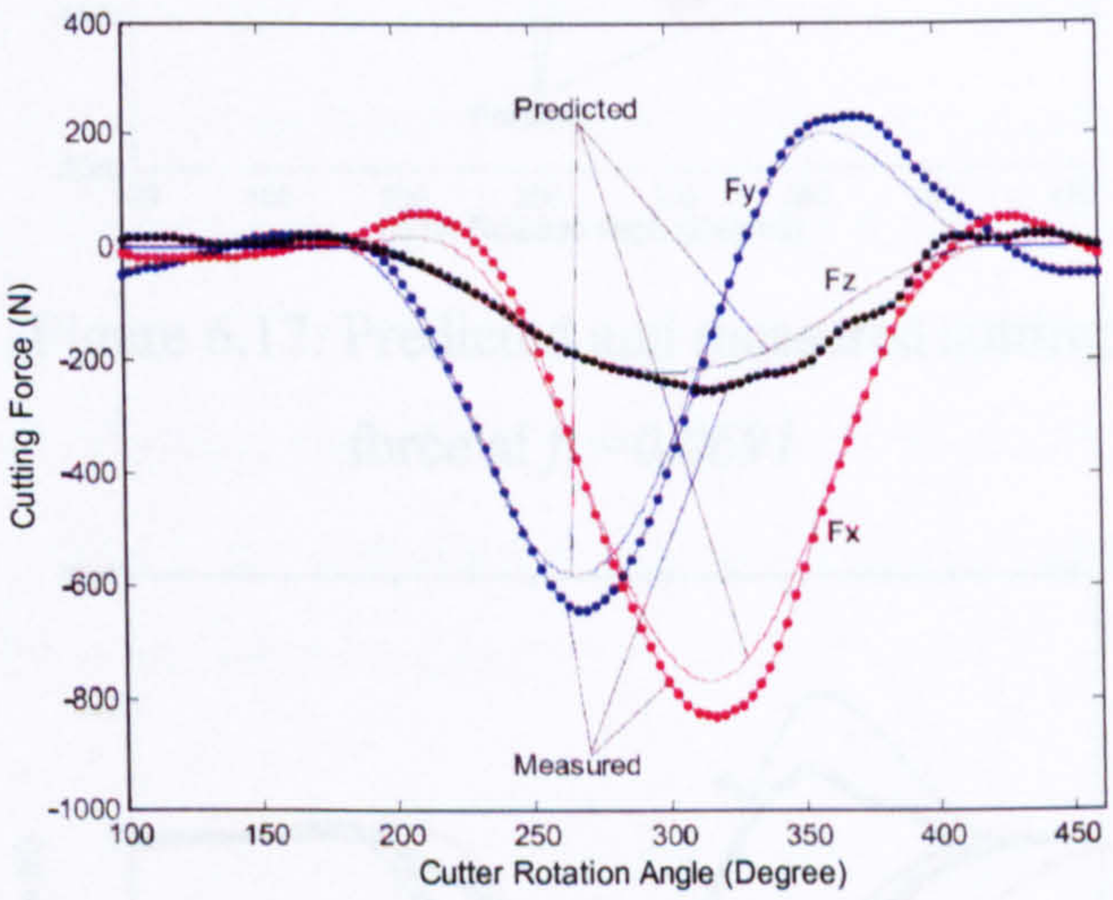

Figure 6.13. Predicted and measured cutting force at f_t =0.0296

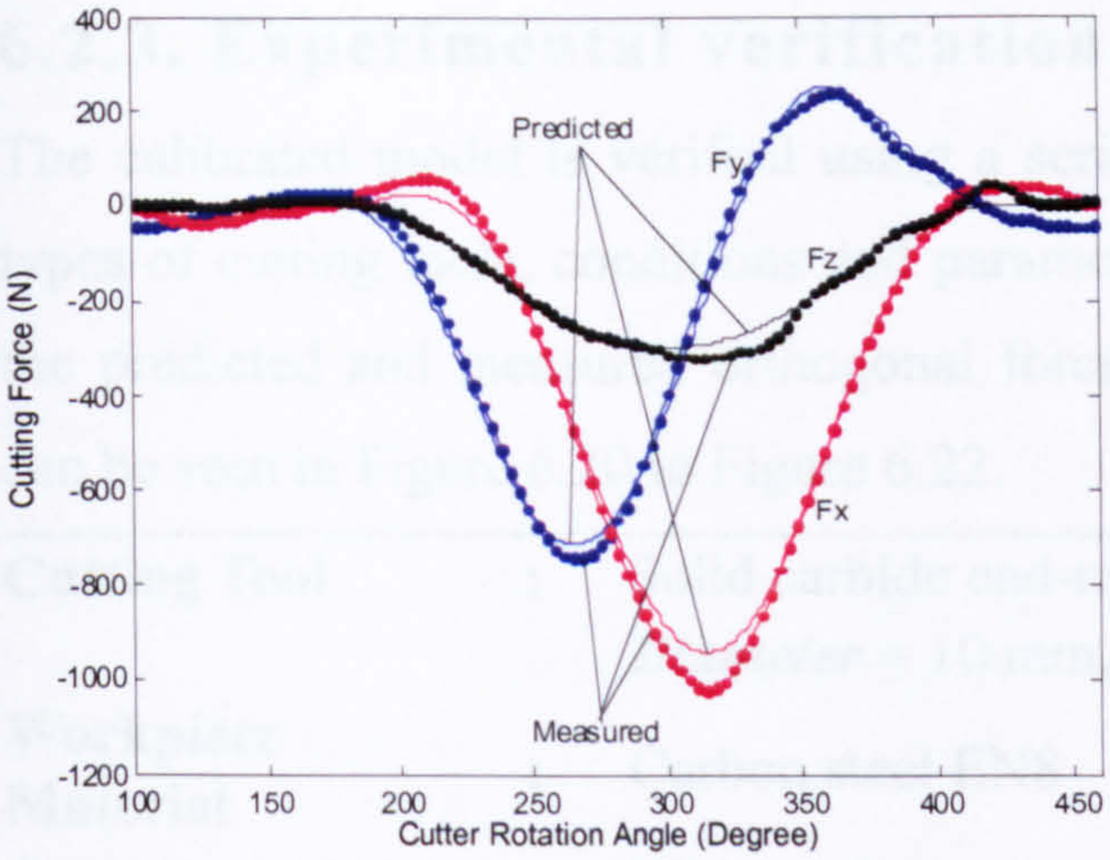

Figure 6.14. Predicted and measured cutting force at f_t =0.0395

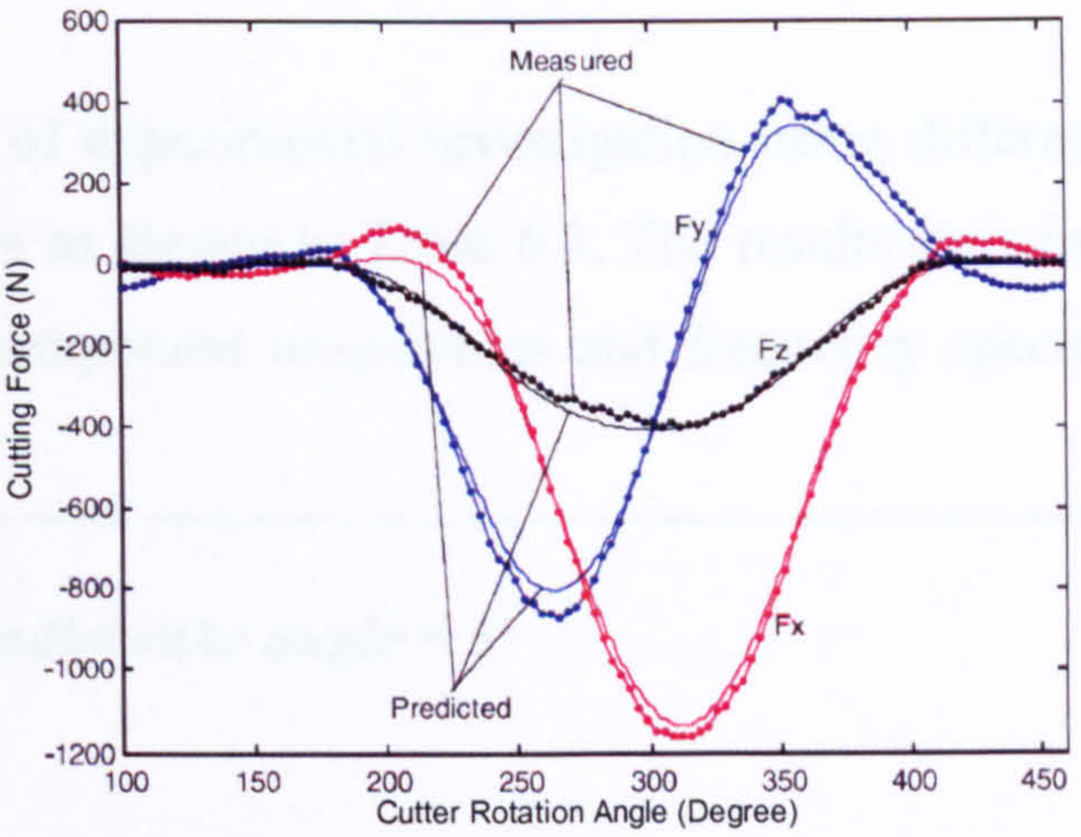

Figure 6.15. Predicted and measured cutting force at f_t =0.0494

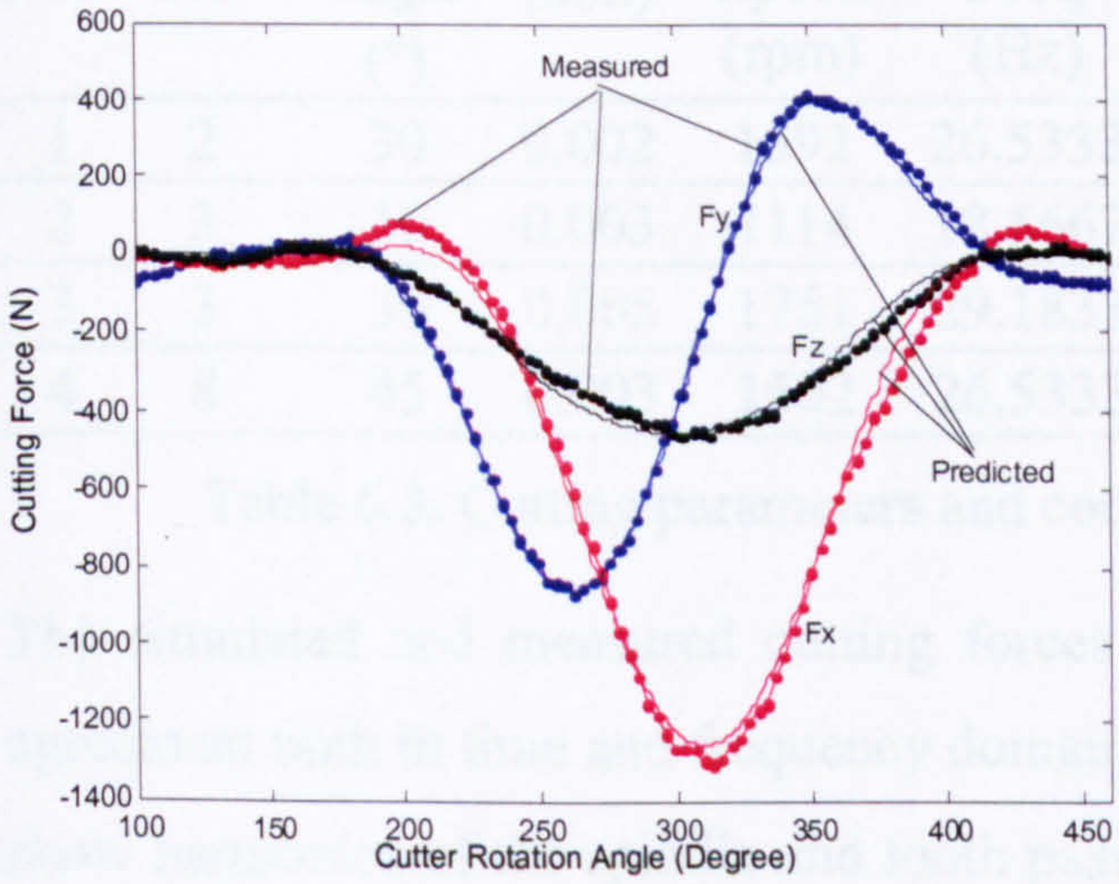

Figure 6.16. Predicted and measured cutting force at f_t =0.0592

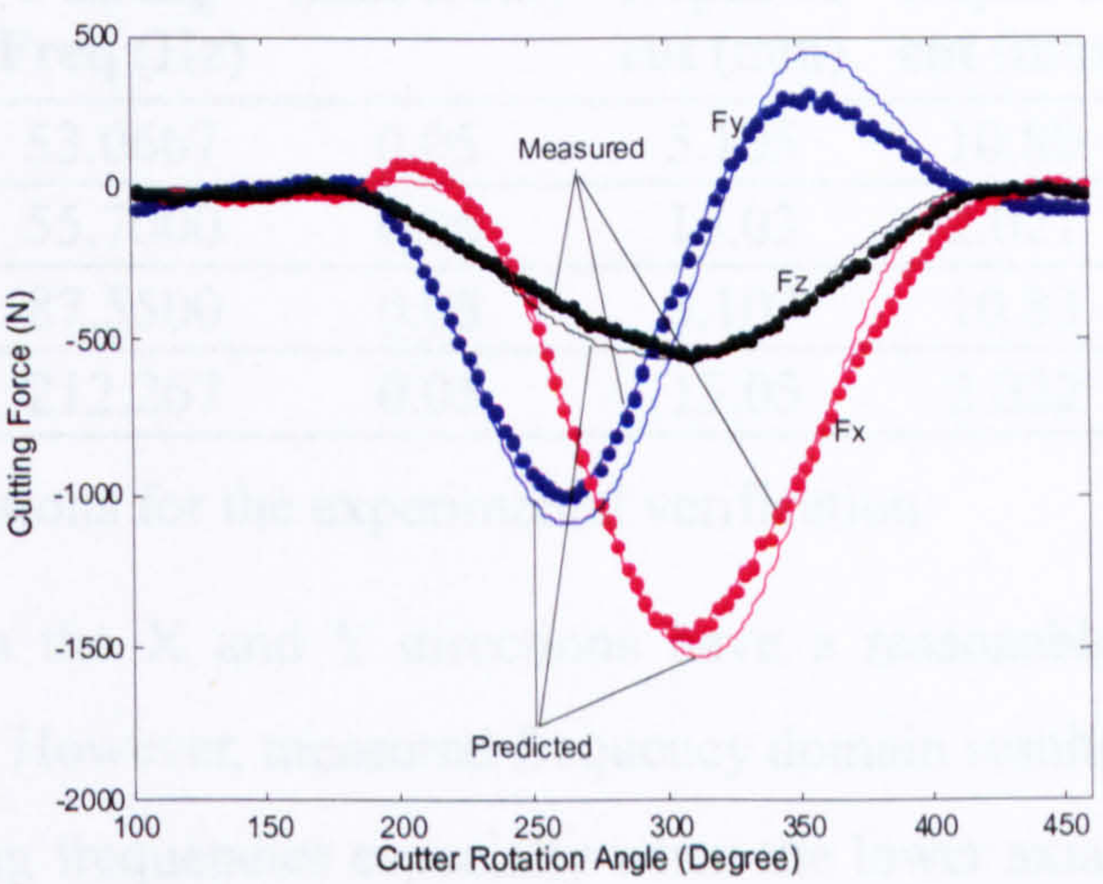

Figure 6.17. Predicted and measured cutting force at f_t =0.0691

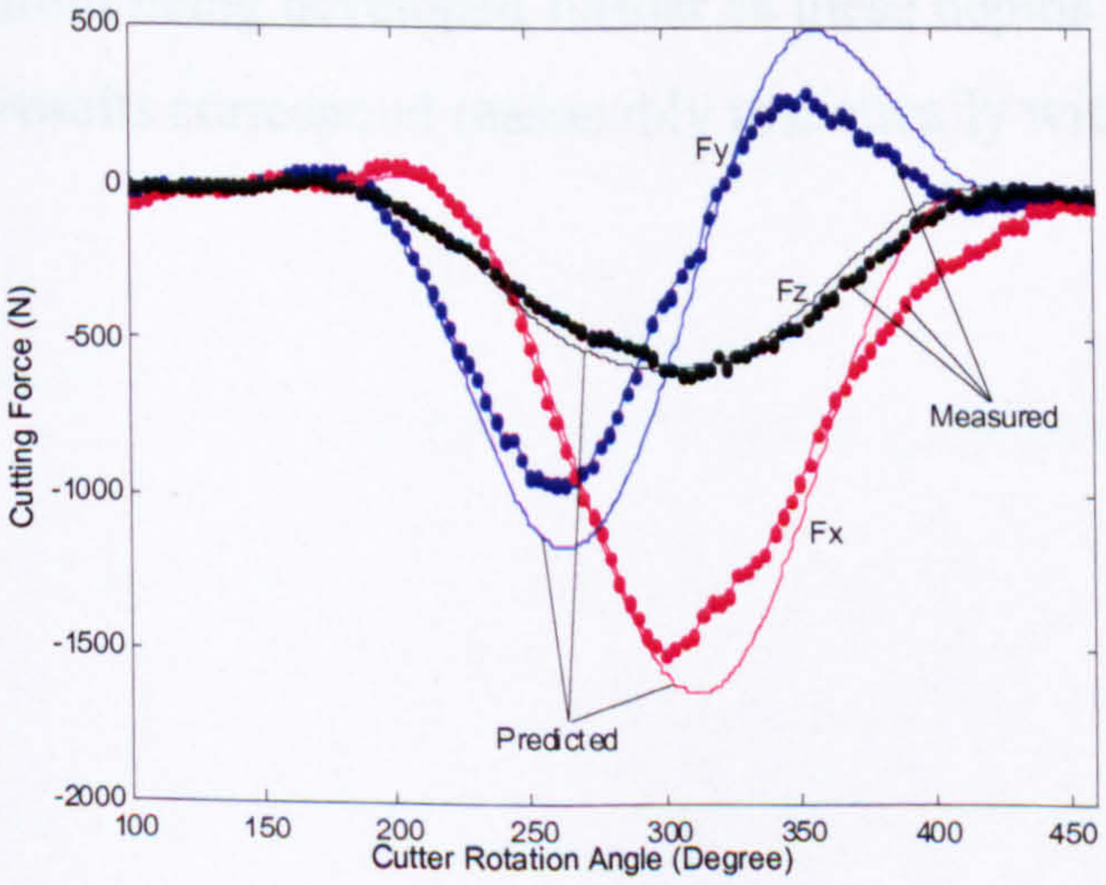

Figure 6.18. Predicted and measured cutting force at f_t =0.0790

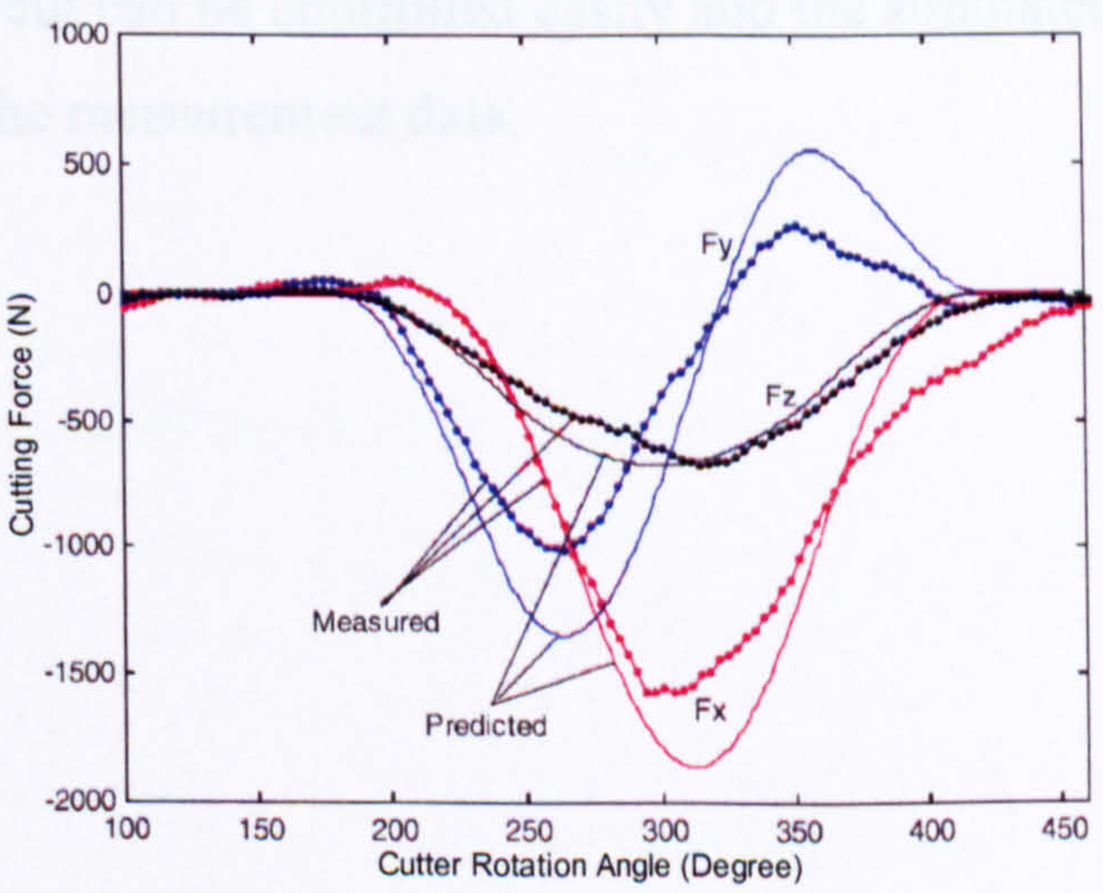

Figure 6.19. Predicted and measured cutting force at f_t =0.0889

6.2.3. Experimental verification

The calibrated model is verified using a series of experimental investigation using different types of cutting tools, conditions and parameters as shown in Table 6.3. The results showing the predicted and measured orthogonal force component magnitudes and frequency spectra can be seen in Figure 6.20 to Figure 6.22.

Cutting Tool	:	Solid carbide end-mill ***Diameter*** = 10 mm, ***Radial rake angle*** = 5°
Workpiece Material	:	Carbon steel EN8
Cutting condition	:	With coolant

Test No.	**Tooth No.**	**Helix angle (°)**	**δ_e (mm)**	**Angular Speed (rpm)**	**Spindle Freq (Hz)**	**Tooth Passing Freq (Hz)**	**Feed rate (mm/tooth)**	**Axial Depth of cut (mm)**	**Radial Depth of cut (mm)**
1	2	30	0.002	1592	26.5333	53.0667	0.05	5.105	10.80
2	3	30	0.003	1114	18.5667	55.7000	0.06	15.03	2.021
3	3	30	0.005	1751	29.1833	87.5500	0.05	5.107	10.83
4	8	45	0.003	1592	26.5333	212.267	0.05	15.05	2.022

Table 6.3. Cutting parameters and conditions for the experimental verification

The simulated and measured cutting forces in the X and Y directions have a reasonable agreement both in time and frequency domains. However, measured frequency domain results show harmonics of the spindle and tooth passing frequencies especially when the lower axial and higher radial depths of cut. This is believed to have come from the cutting tool run-out and amplified by the depth of cut selections. Nonetheless, this should not prevent the model from being developed further as these depths of cut can be controlled easily and the simulated results correspond reasonably realistically with the measurement data.

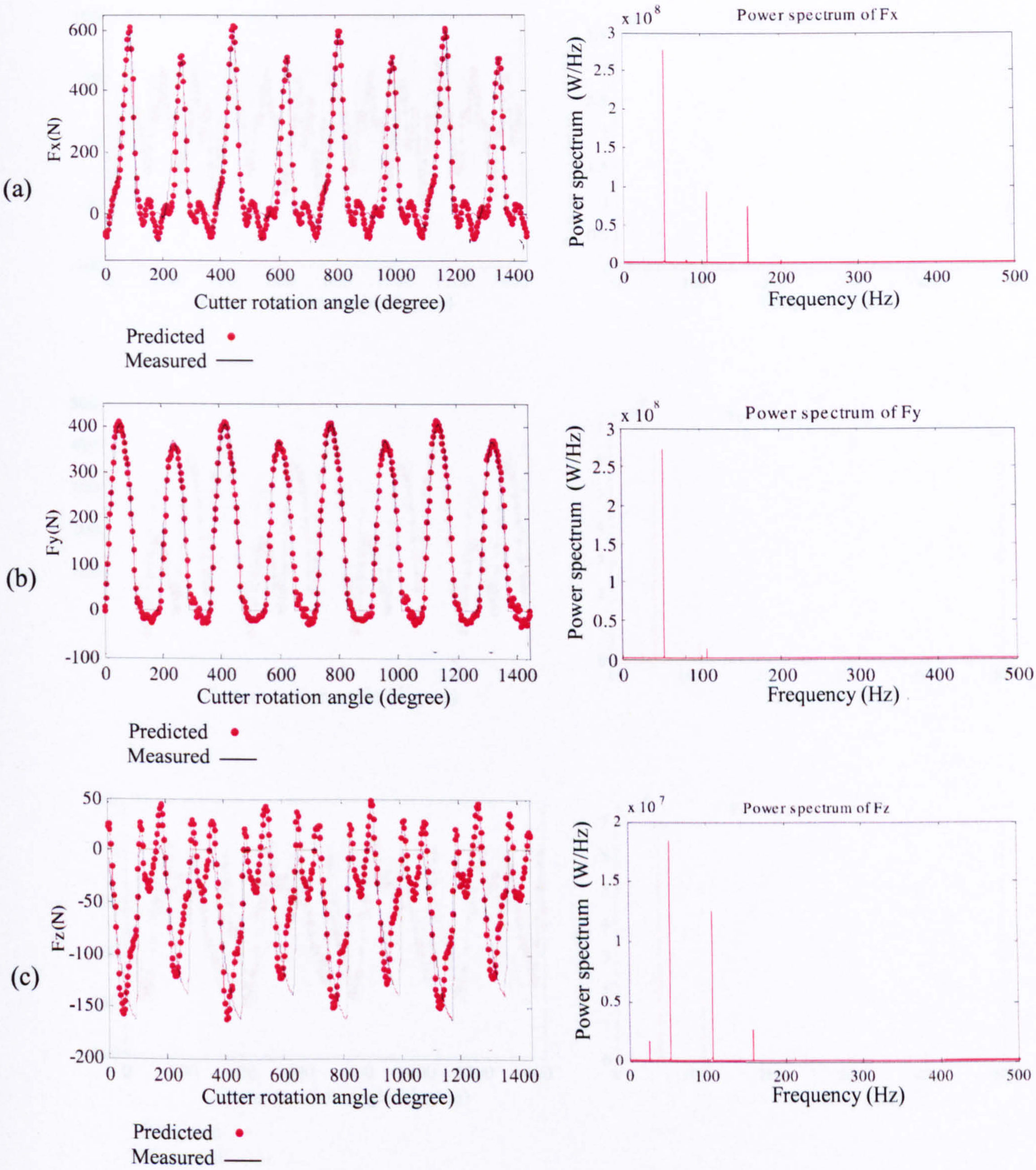

Figure 6.20. Predicted and measured cutting force for test no. 1

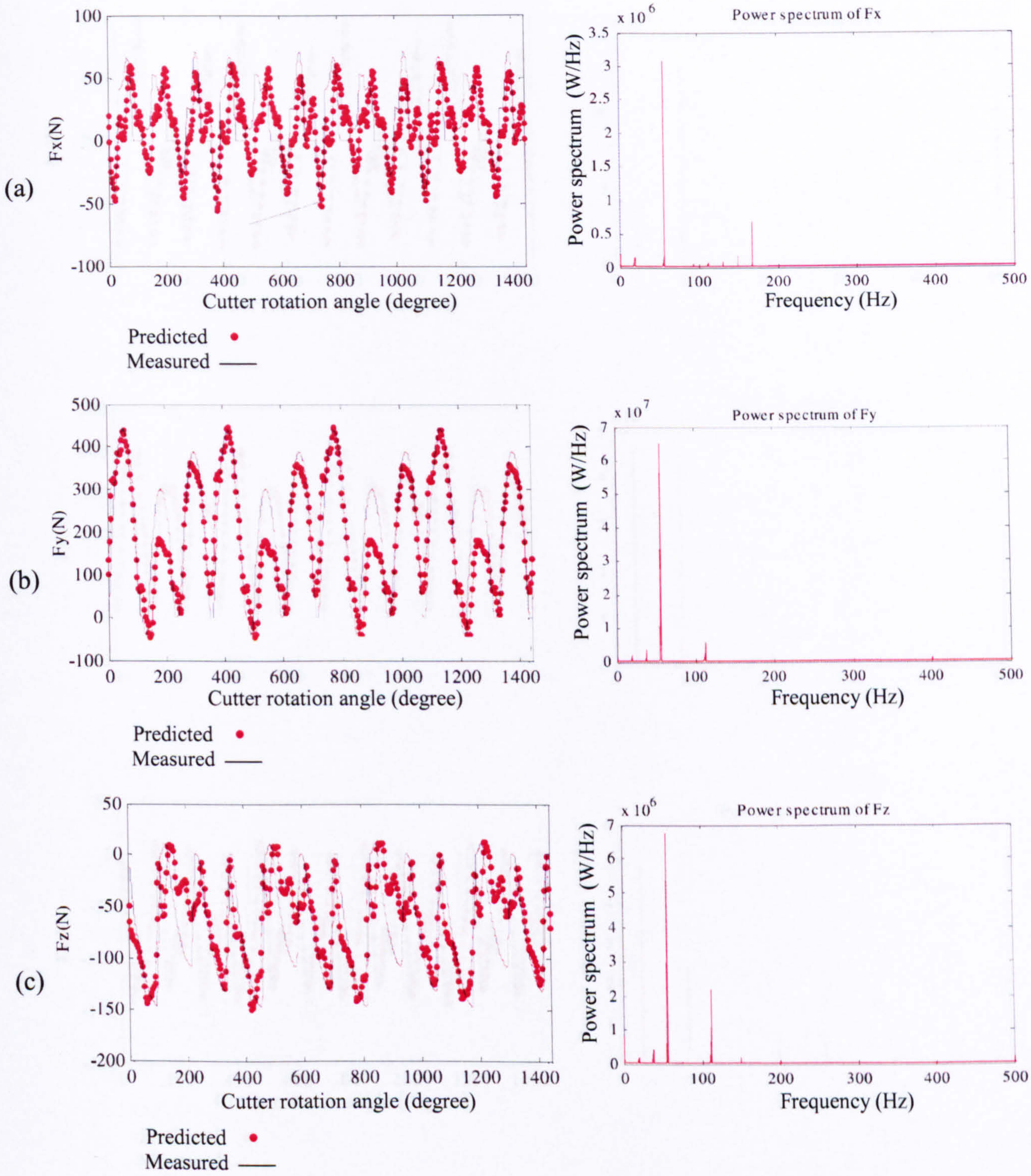

Figure 6.21. Predicted and measured cutting force for test no. 2

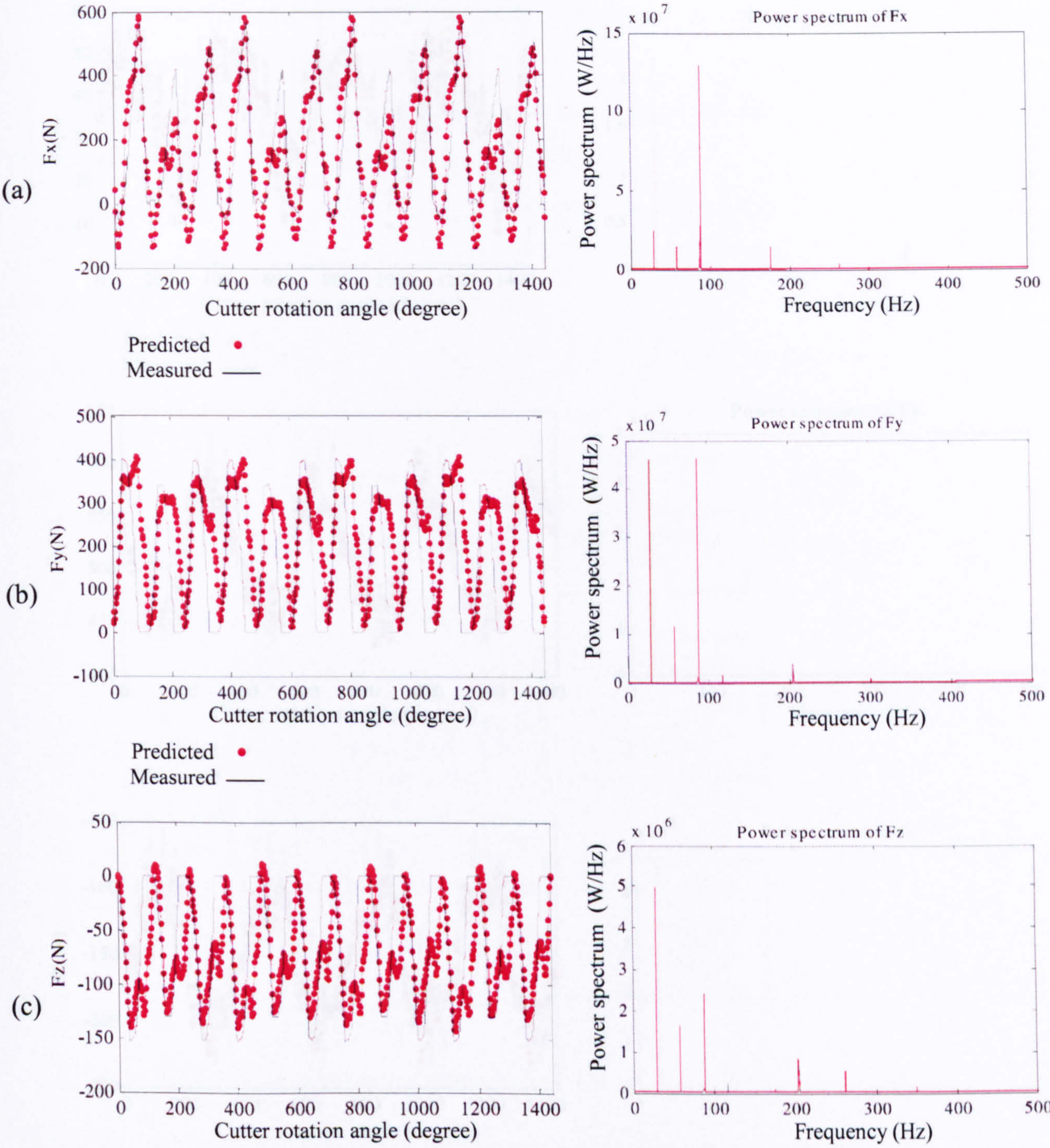

Figure 6.22. Predicted and measured cutting force for test no. 3

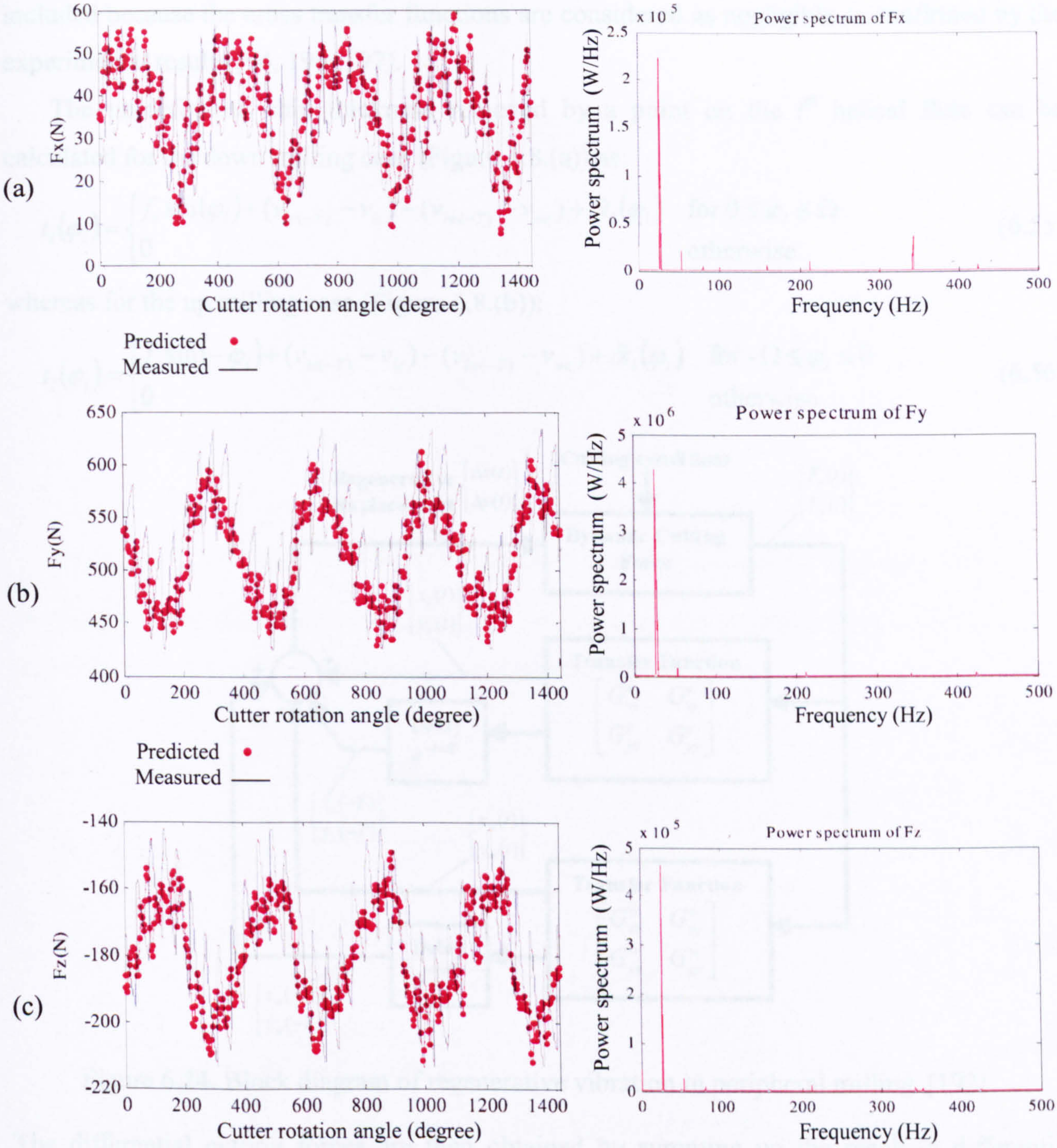

Figure 6.23. Predicted and measured cutting force for test no. 4

6.3. Machining dynamics model

The model consists of the validated dynamic cutting force model and the vibration model shown as the direct transfer function blocks in Figure 6.24. The cutting force model prediction is dependent on the un-cut chip thickness, the effect of the cutter-workpiece vibration and cutting tool run-out. Only the direct transfer functions of the workpiece and cutting tool are

included because the cross transfer functions are considered as negligible as confirmed by the experimental results [94, 196, 197].

The un-deformed chip thickness removed by a point on the i^{th} helical flute can be calculated for the down milling case (Figure 6.8.(a)) as:

$$t_i(\varphi_i)=\begin{cases} f_t \sin(\varphi_i)+(v_{ic(-T)}-v_{ic})-(v_{iw(-T)}-v_{wc})+\delta t_i(\varphi_i) & \text{for } 0\le\varphi_i\le\Omega \\ 0 & \text{otherwise} \end{cases} \tag{6.55}$$

whereas for the up milling case (Figure 6.8.(b)):

$$t_i(\varphi_i)=\begin{cases} f_t \sin(-\varphi_i)+(v_{ic(-T)}-v_{ic})-(v_{iw(-T)}-v_{wc})+\delta t_i(\varphi_i) & \text{for } -\Omega\le\varphi_i\le 0 \\ 0 & \text{otherwise} \end{cases} \tag{6.56}$$

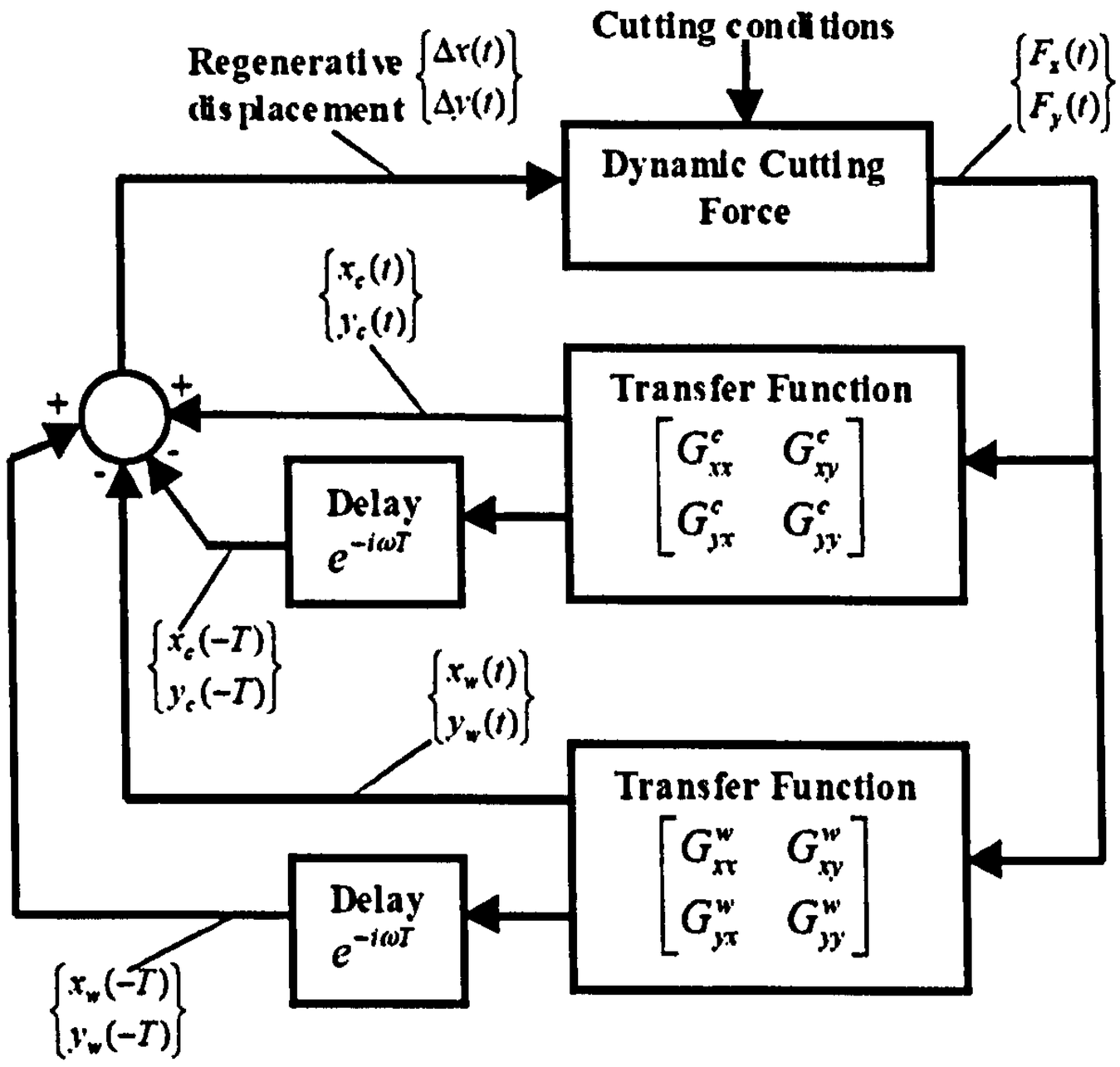

Figure 6.24. Block diagram of regenerative vibration in peripheral milling [192]

The differential cutting forces are then obtained by summing up the resolved differential cutting forces in the x and y components. Two separate sets of equations are produced for each type of the milling process (see appendices E.1 and E.2). The total cutting force applied on the whole cutting edge is, therefore, obtained by integrating the equations across its length (see equation (6.54)).

The cutter and workpiece vibration is modelled as a two degree-of-freedom spring-damper system, oscillating in the perpendicular directions of x and y as shown in Figure 6.25. The cutting forces excite the cutter and workpiece simultaneously in the normal and feed directions, causing the dynamic displacements which are carried to the un-deformed chip thickness direction with the following coordinate transformation:

$$v_{ic} = -x_c \cos(\varphi_i) - y_c \sin(\varphi_i) \tag{6.57}$$

$$v_{iw} = -x_w \cos(\varphi_i) - y_w \sin(\varphi_i) \tag{6.58}$$

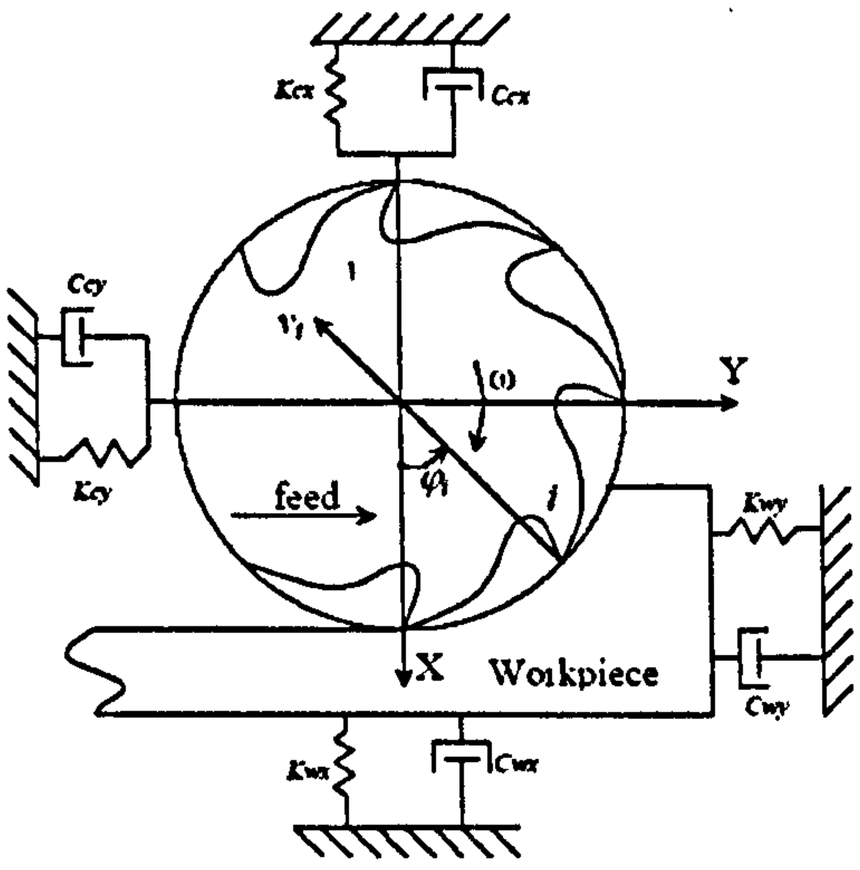

Figure 6.25. Two degree of freedom vibratory model of the milling operation [192]

The frequency domain response function of the cutter (*c*) and workpiece (*w*) in the X- and Y-directions for all modes (*k*) can be expressed respectively as follows:

$$G_{xx}^{c}(s) = \sum_{k=1}^{n} \frac{\alpha_{cxk} + \beta_{cxk}}{s^2 + 2\zeta_{cxk}\omega_{n\,cxk}s + \omega_{n\,cxk}^2} \tag{6.59}$$

$$G_{yy}^{c}(s) = \sum_{k=1}^{n} \frac{\alpha_{cyk} + \beta_{cyk}}{s^2 + 2\zeta_{cyk}\omega_{n\,cyk}s + \omega_{n\,cyk}^2} \tag{6.60}$$

$$G_{xx}^{w}(s) = \sum_{k=1}^{n} \frac{\alpha_{wxk} + \beta_{wxk}}{s^2 + 2\zeta_{wxk}\omega_{n\,wxk}s + \omega_{n\,wxk}^2} \tag{6.61}$$

$$G_{yy}^{w}(s) = \sum_{k=1}^{n} \frac{\alpha_{wyk} + \beta_{wyk}}{s^2 + 2\zeta_{wyk}\omega_{n\,wyk}s + \omega_{n\,wyk}^2} \tag{6.62}$$

An experimental modal analysis investigation is thus performed on the cutting tool and workpiece to identify their structural dynamic properties for machining dynamic model (Figure 6.24). A helical solid carbide end mill with 3 flutes, 20mm diameter, 30° helix angle and 5° radial rake angle, is fitted in a hydraulic chuck and mounted on the spindle head of the CNC machine centre. A workpiece of carbon steel EN8 is fixed to the Kistler table dynamometer 9255B [164] using the Microloc fixture system, Kit-MD75 [163]. The dynamometer is then secured on the worktable of the CNC machine centre.

A PCB impact hammer instrumented with a piezoelectric force transducer [198] is used to excite the cutter and the workpiece, and their responses are measured using the mounted ICP accelerometers [162] (see Figure 6.26). The accelerometers and the hammer are connected to the Data Physics SignalCalc Mobilyzer dynamic signal analyser [160] to calculate the transfer

functions. The results are processed by the modal analysis software, STAR*Struct* [124], to identify the modal parameters of the cutter and the workpiece.

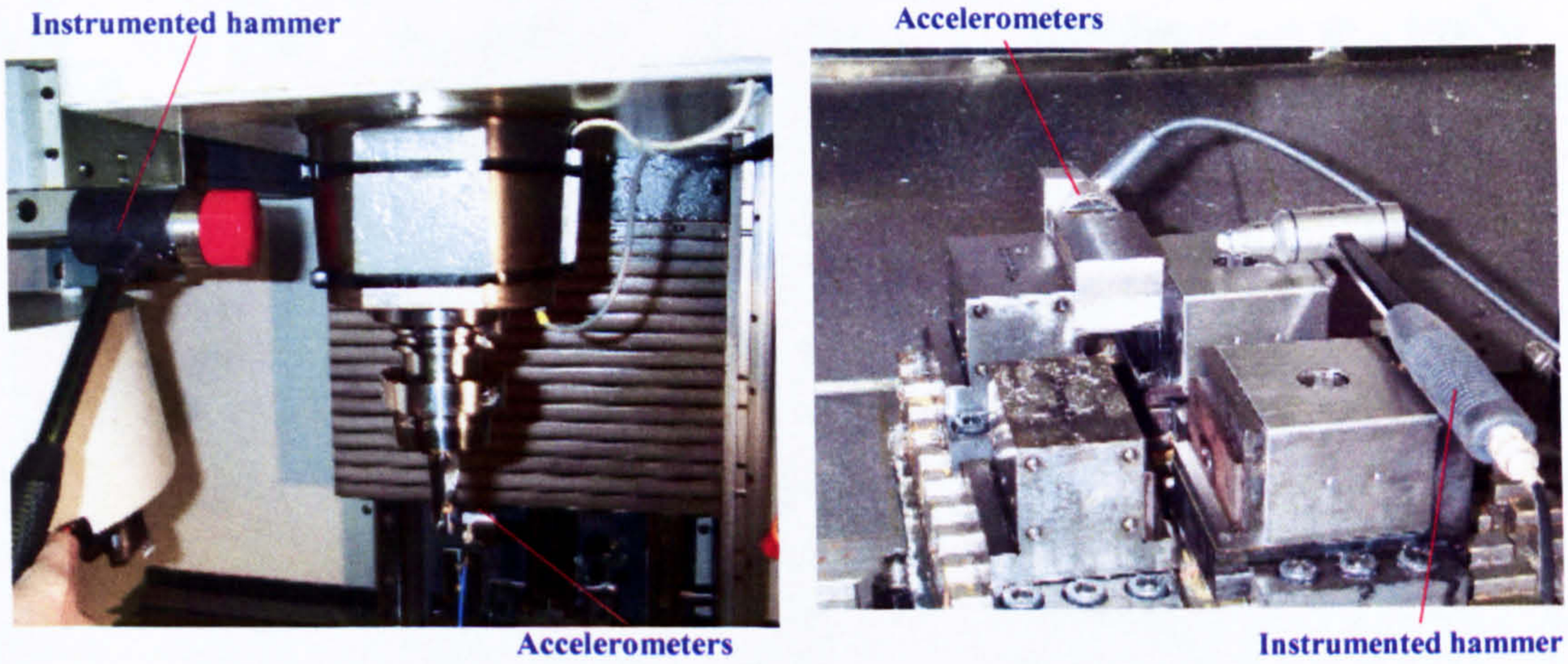

Figure 6.26. Experimental modal analysis configuration for the cutting tool and workpiece

Two direct transfer functions of the cutting tools are measured in the x and y direction by ***exciting the spindle*** and measuring the acceleration at ***the cutting tool***. This enables the translation of the measured spindle acceleration (or displacement) to that of the cutting tool. Figure 6.27 shows the measured transfer functions (black lines) and the curve-fit lines obtained by the STARStruct software (red lines).

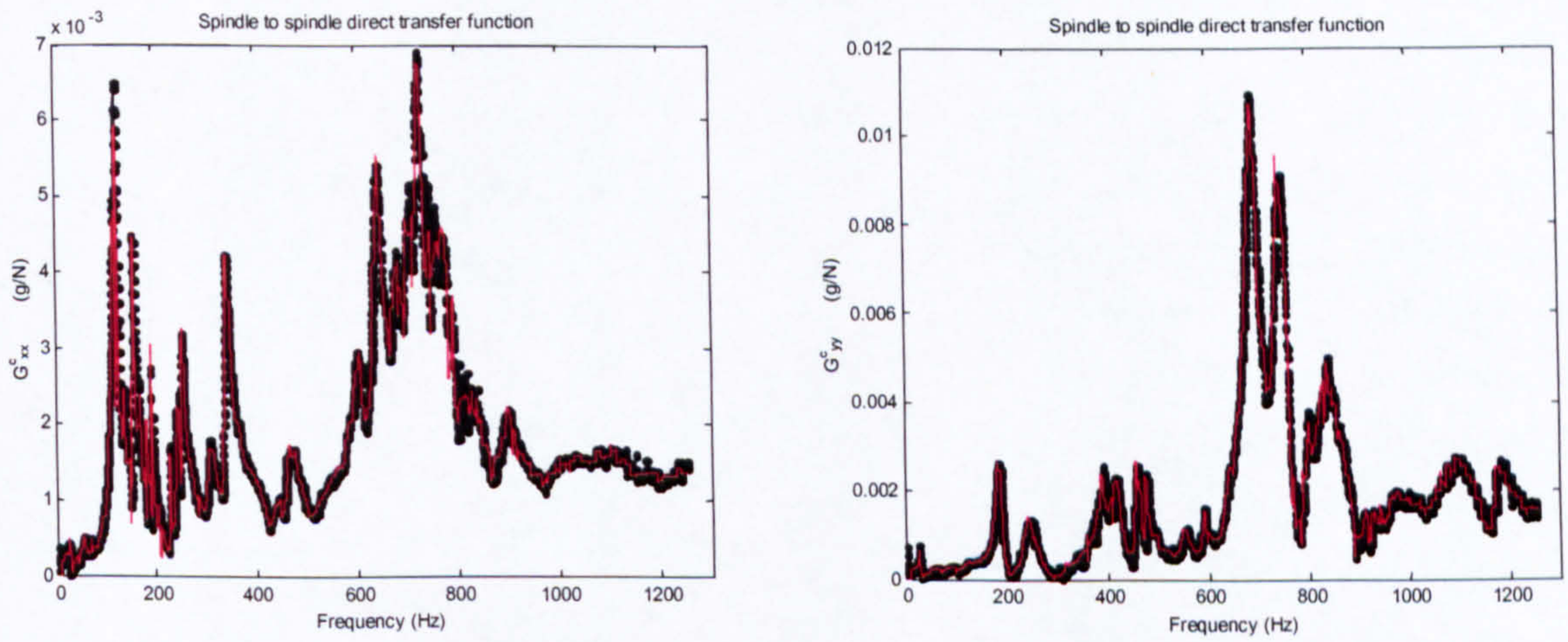

Figure 6.27. Transfer functions of the cutting tool w.r.t. the spindle in the X- and Y-directions

Table 6.4 and Table 6.5 show the extracted modal parameters of the cutting tool in the X- and Y-directions respectively. Similarly, two direct transfer functions of the workpiece are measured by ***the workpiece*** at the approximate cutting point and measuring the acceleration at the sensor location at ***the workpiece*** (see Figure 6.28). Table 6.6 and Table 6.7 show the extracted modal parameters of the workpiece in the X- and Y-directions respectively. The results indicated by the red characters in Table 6.7 contain negative damping values which

represent mathematical (virtual) modes used by the software to obtain the best curve-fit. The values are not utilised in the development of the model and only included for completeness.

Mode	ω_{dcx} (Hz)	ω_{ncx} (rad/s)	ζ_{cx} (%)	Residue $\sigma_{cx} + j\upsilon_{cx}$ (m/N)
3	120.5	757.7963	4.21	8.031267e-006+j1.830470e-006
8	247.05	1553.234	3.54	3.442107e-006+j5.209837e-007
9	341.65	2146.744	0.93693	9.108225e-006+j-1.908909e-006
12	645.48	4055.685	0.26558	8.633025e-007+j-7.830841e-007
13	715.39	4495.076	0.81218	-1.057337e-005+j-7.500871e-006
16	731.75	4597.741	0.29715	1.022476e-006+j-1.673413e-006
18	748.76	4704.604	0.16347	1.016291e-006+j-2.033546e-007
19	761.57	4785.126	0.41044	2.639827e-006+j2.095946e-007
20	811.46	5098.814	1.01	4.304769e-006+j4.423204e-007
22	987.15	6206.627	3.67	3.820509e-005+j3.567028e-006
23	1030	6471.883	0.789	9.331169e-007+j2.193275e-006
26	1160	7288.820	0.94237	-2.194058e-006+j-1.615678e-006
27	1200	7539.899	0.044894	-7.935642e-007+j2.950998e-007

Table 6.4. Identified modal parameters of the cutter in X-direction

Mode	ω_{dcy} (Hz)	ω_{ncy} (rad/s)	ζ_{cy} (%)	Residue $\sigma_{cy} + j\upsilon_{cy}$ (m/N)
1	49.21	309.1962	0.20605	-1.733888e-008+j1.712200e-008
2	94.72	595.1473	0.36509	2.465764e-008+j-6.332934e-008
4	160.38	1007.997	2.44	-4.392552e-007+j1.364358e-007
5	187.55	1178.641	1.97	2.269027e-006+j-1.301338e-006
8	238.66	1500.043	2.58	1.201795e-006+j-7.724067e-007
10	344.69	2166.074	1.72	3.348905e-006+j-5.251082e-006
11	439.92	2764.451	1.6	-7.110383e-007+j2.433423e-008
12	488.25	3067.772	0.218	-2.326689e-008+j8.504934e-008
15	586.86	3687.390	0.46732	1.274008e-007+j1.548505e-007
16	684.19	4299.626	1.85	2.273516e-005+j-9.893721e-006
18	751.8	4724.287	1.58	1.434414e-005+j-3.420460e-005
21	894.23	5620.215	2.39	-3.932861e-006+j-1.978372e-006

Table 6.5. Identified modal parameters of the cutter in Y-direction

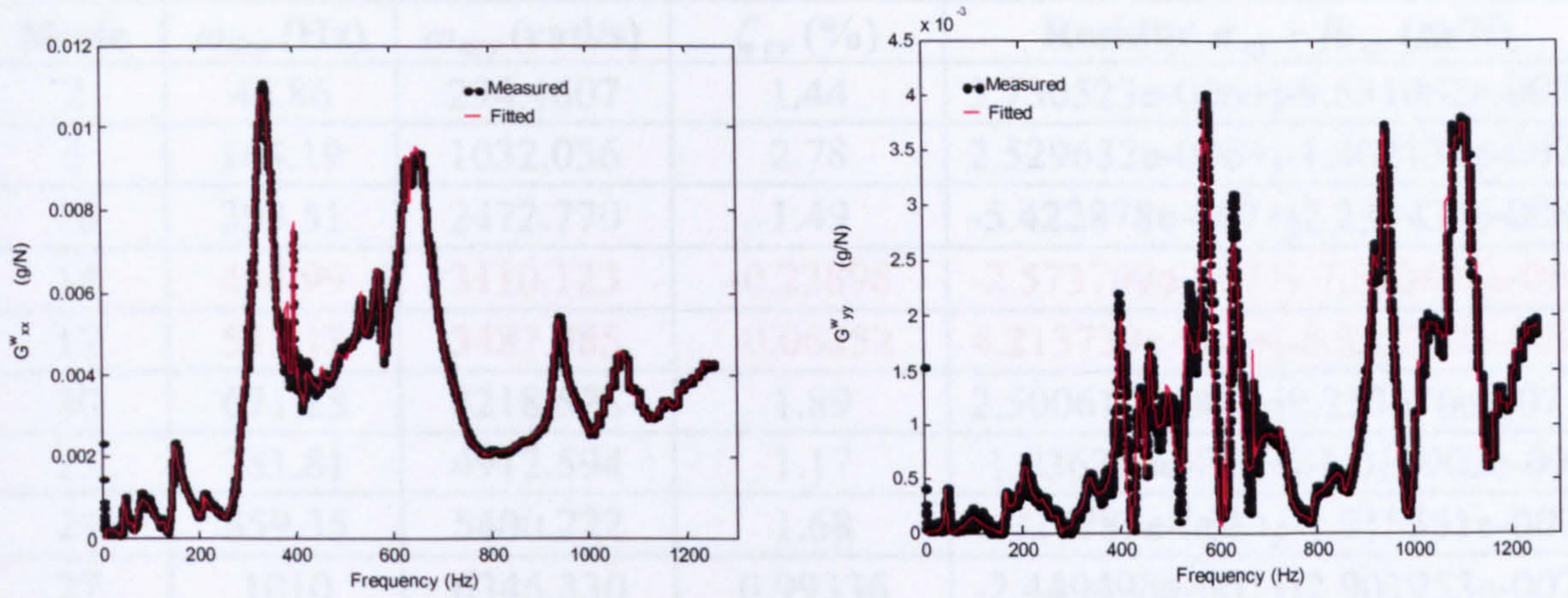

Figure 6.28. Transfer functions of the workpiece in the X- and Y-directions

Mode	ω_{dcy} (Hz)	ω_{ncy} (rad/s)	ζ_{cy} (%)	Residue $\sigma_{cy} + j\upsilon_{cy}$ (m/N)
1	43.44	273.0853	3.25	-1.258373e-006+j-5.699113e-008
3	79.39	506.8606	17.73	-3.764000e-006+j3.820564e-007
5	148.75	935.5075	4.34	-1.309762e-006+j-1.194027e-007
9	212.22	1333.515	1.21	-4.555126e-008+j1.650306e-008
12	330	2077.282	6.07	-3.609850e-006+j-1.209621e-006
14	383.6	2410.231	0.10927	-1.287093e-009+j9.626157e-009
15	398.76	2505.493	0.28086	-3.883548e-009+j5.595112e-008
17	419.8	2637.722	0.558	-2.171050e-008+j-6.944830e-009
18	454.45	2855.452	0.63879	-1.301600e-008+j7.290193e-009
19	484.83	3046.894	2.01	-4.375980e-008+j3.178899e-008
22	537.7	3378.544	0.6671	2.516786e-008+j1.832542e-008
23	575.21	3614.285	0.86247	6.845461e-008+j-2.399351e-008
24	637	4002.405	0.27934	4.345913e-009+j-1.189243e-008
25	654.58	4117.619	4.81	1.140337e-006+j1.759127e-007
26	703.16	4418.09	0.16402	2.009257e-011+j4.120233e-010
27	698.58	4401.554	7.45	5.674624e-007+j-6.033365e-007
28	839.54	5275.109	0.68471	-1.492584e-009+j-1.441823e-010
29	937.98	5893.982	1.28	6.224327e-008+j4.052831e-008

Table 6.6. Identified modal parameters of the workpiece in the X-direction

Mode	ω_{dcy} (Hz)	ω_{ncy} (rad/s)	ζ_{cy} (%)	Residue $\sigma_{cy} + j\upsilon_{cy}$ (m/N)
2	46.86	294.4607	1.44	3.730523e-006+j-9.531062e-007
5	164.19	1032.036	2.78	2.529632e-006+j-1.402137e-007
10	393.51	2472.770	1.49	-5.422878e-007+j2.234437e-008
14	494.99	3110.123	-0.23898	-2.573799e-007+j-7.380437e-008
17	555.13	3487.985	-0.06252	4.213739e-008+j-8.862332e-009
20	671.28	4218.528	1.89	2.500610e-006+j9.253670e-007
23	781.81	4912.594	1.17	-1.036336e-006+j-1.012902e-006
24	859.35	5400.222	1.68	4.027783e-008+j-1.915551e-007
27	1010	6346.330	0.99336	-2.449498e-007+j2.901953e-007
29	1090	6850.590	2.36	-8.814406e-007+j5.726684e-009
32	1200	7541.600	2.16	-8.919308e-007+j-6.399355e-007

Table 6.7. Identified modal parameters of the workpiece in the Y-direction

The experimental results are then integrated into the vibration sub-systems of the Simulink model for the machining dynamics process (see Figure 6.29 and the dotted shapes) containing the improved peripheral milling force model. The integration enables the simulations of the cutting tool and workpiece vibration in three orthogonal directions due to the cutting forces. The model also includes their respective frequency spectra obtained using the FFT to determine the frequency content of the vibration.

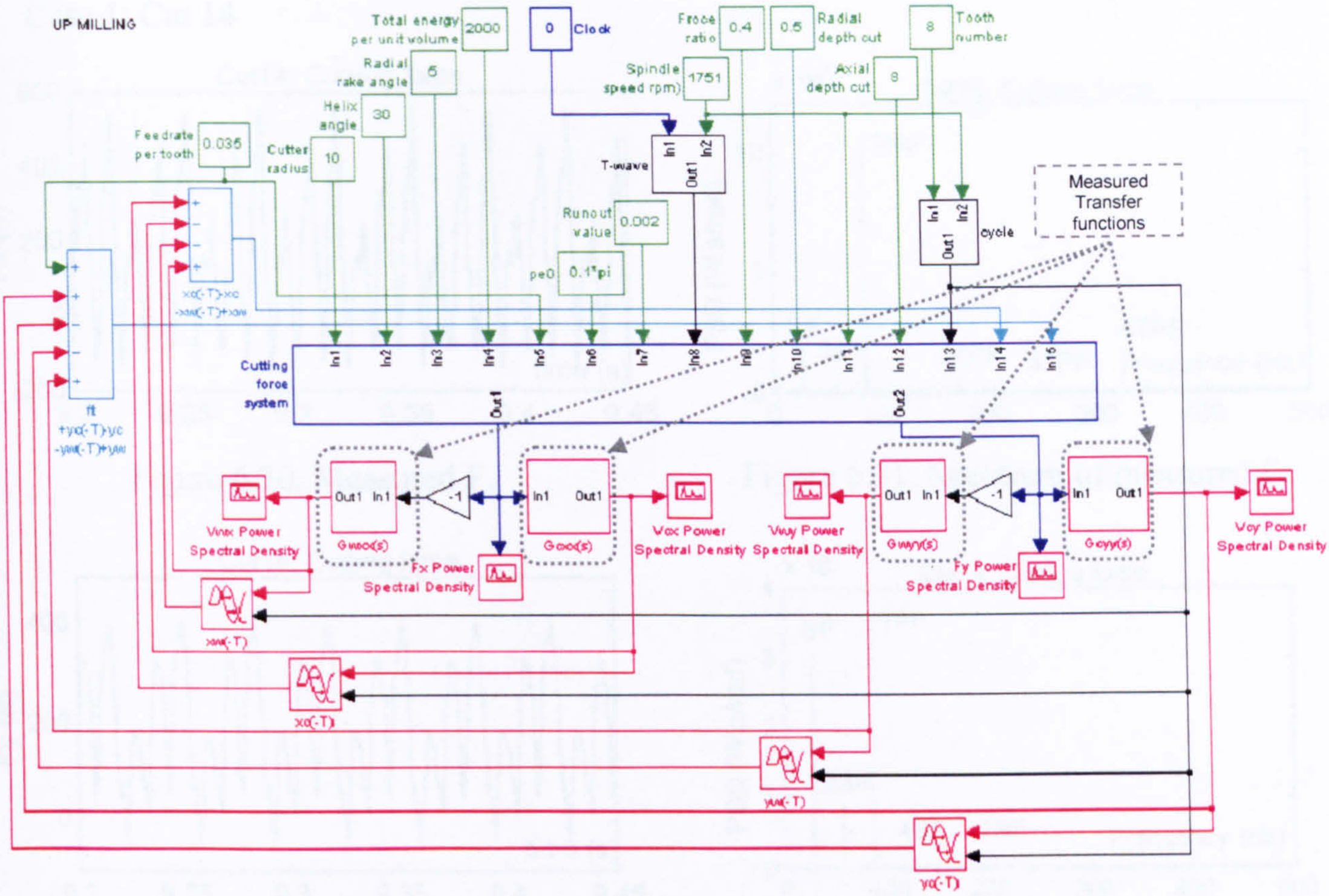

Figure 6.29. Simulink model of the machining dynamics [192]

6.4. Experimental validation and verification

The machining dynamics model is verified by two sets of cutting trials specified in Table 6.8.

Cutting Tool	:	Solid carbide end-mill ***Diameter*** = 10 mm, ***Radial rake angle*** = 5°
Workpiece Material	:	Carbon steel EN8
Cutting condition	:	With coolant

Test No.	**Tooth No.**	**Helix angle** (°)	δ_e (mm)	**Angular Speed** (rpm)	**Spindle Freq** (Hz)	**Tooth Passing Freq** (Hz)	**Feed rate** (mm/tooth)	**Axial Depth of cut** (mm)	**Radial Depth of cut** (mm)
14	3	30	0.005	1751	29.1833	87.55	0.05	4.92	11
13	2	30	0.002	1592	26.5300	53.07	0.06	5.03	11

Table 6.8. Machining parameters and conditions for the experimental verification

The measured and simulated results for both the cutting forces and displacements for each case are presented below:

- Case 1: Cut 14

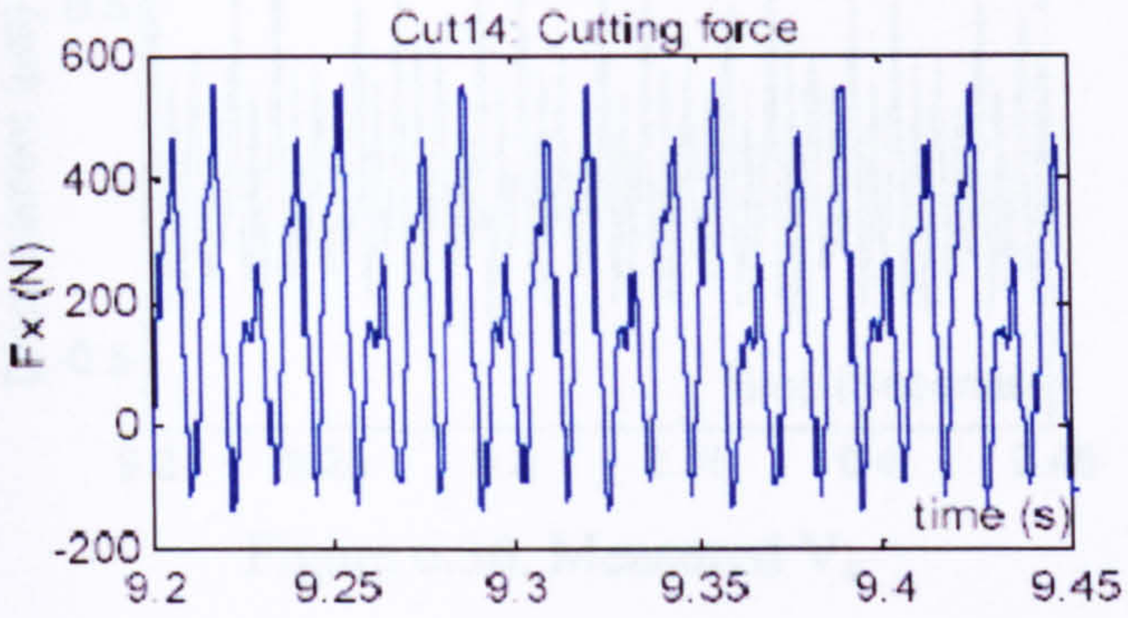

Figure 6.30. Measured F_x

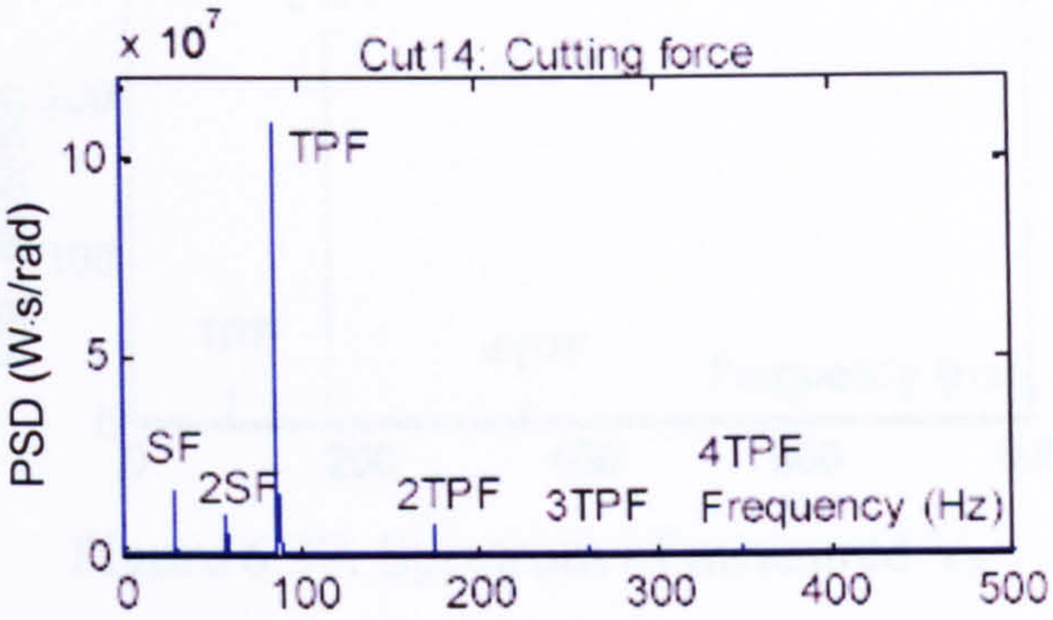

Figure 6.31. Spectrum of measured F_x

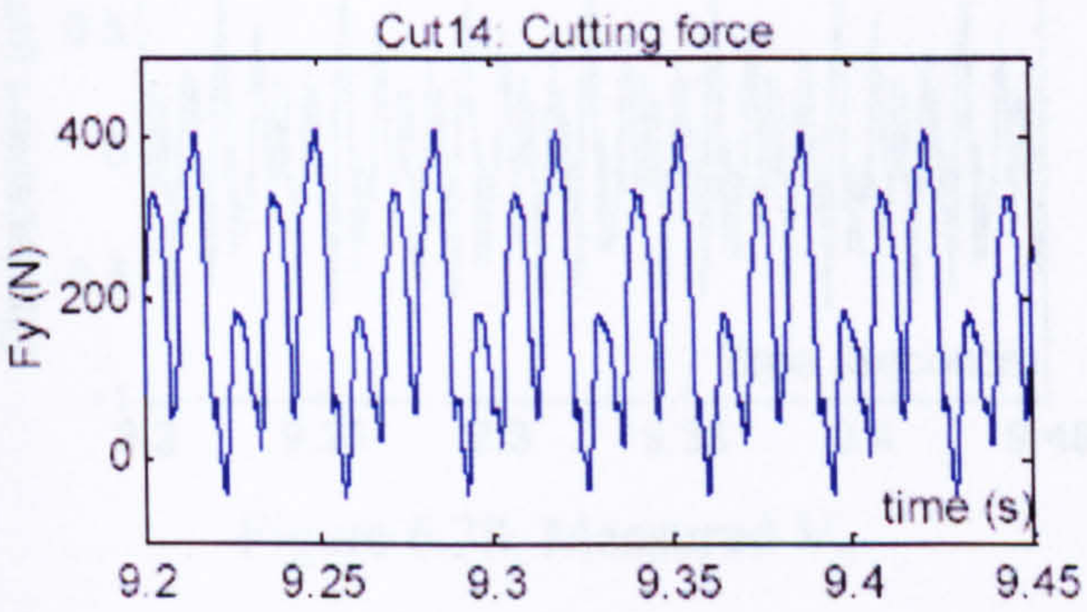

Figure 6.32. Measured F_y

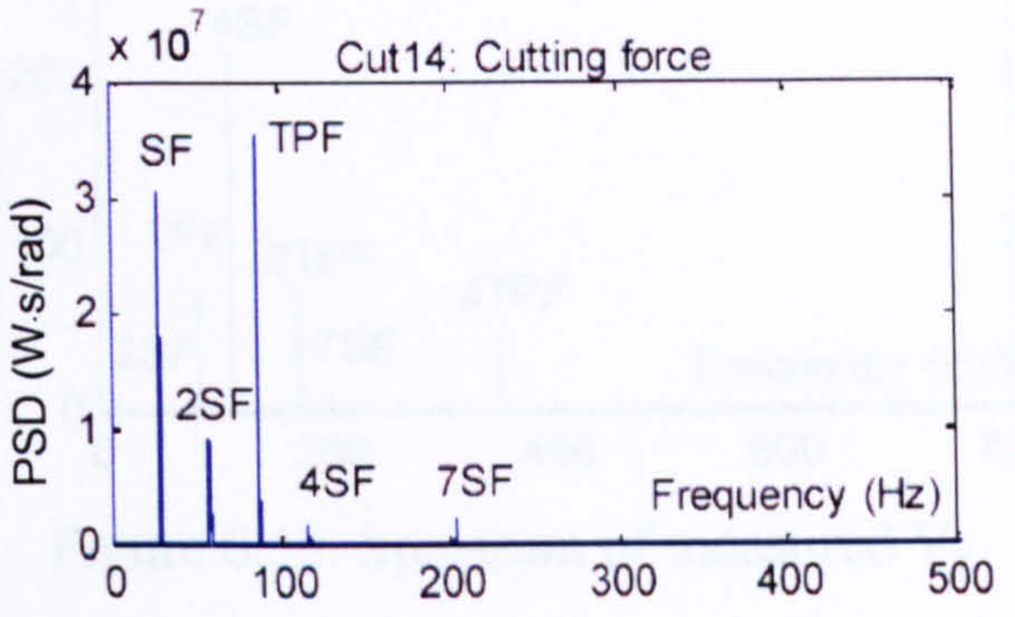

Figure 6.33. Spectrum of measured F_y

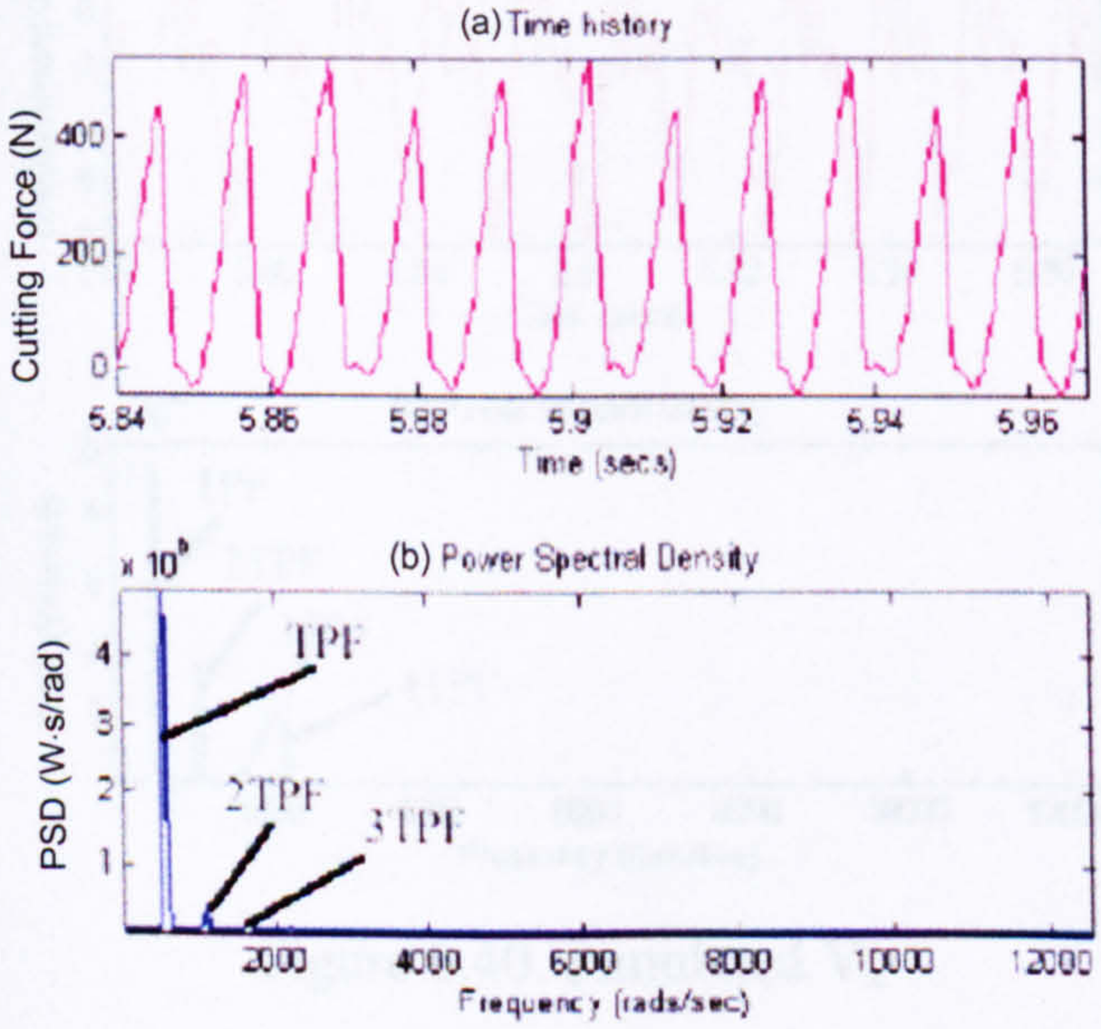

Figure 6.34. Simulated F_x

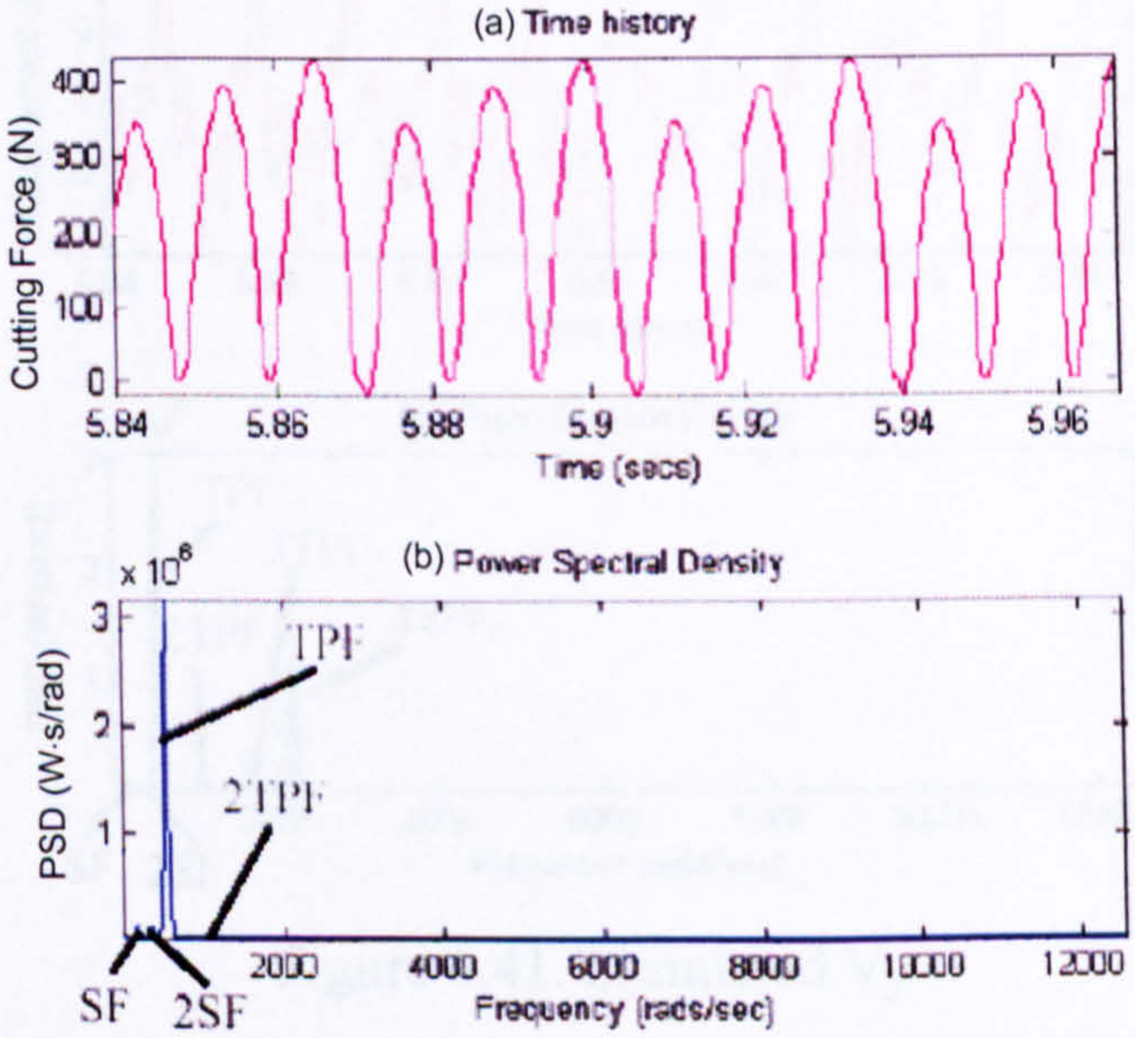

Figure 6.35. Simulated F_y

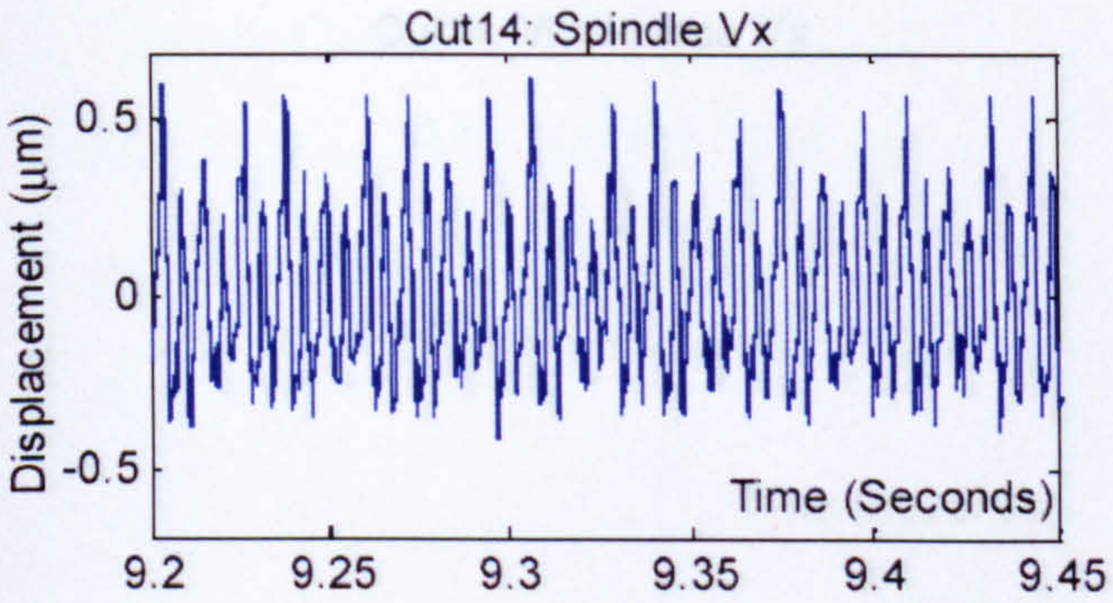

Figure 6.36. Measured V_x

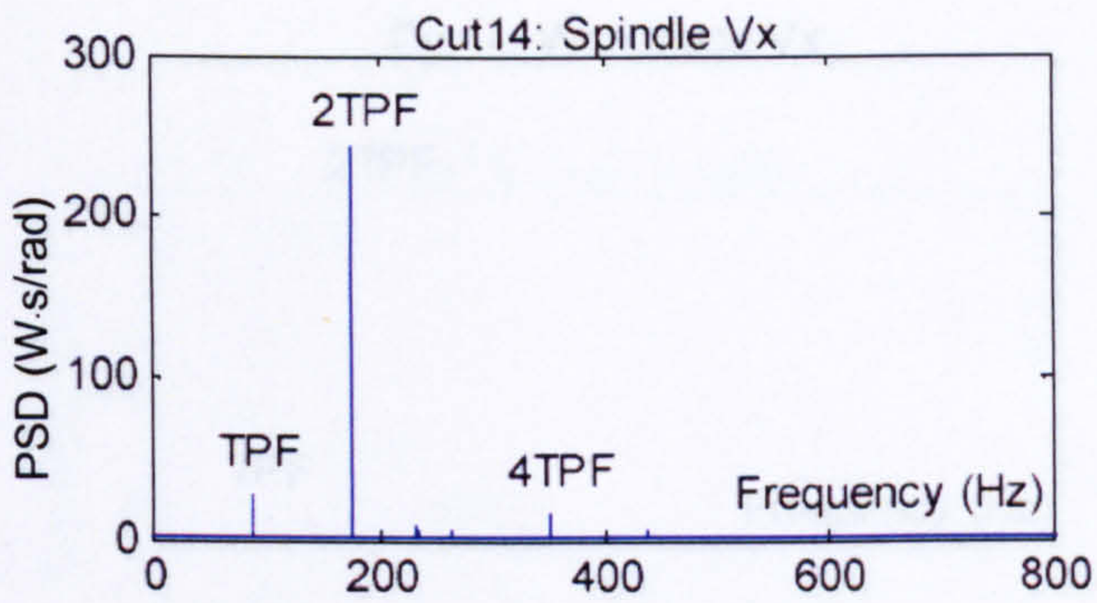

Figure 6.37. Spectrum of measured V_x

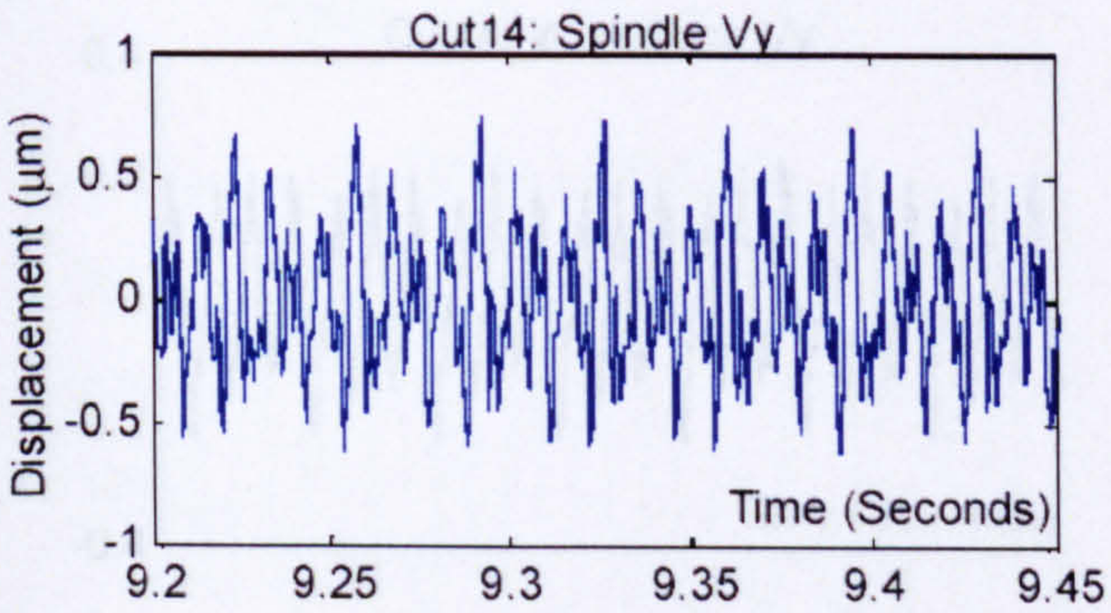

Figure 6.38. Measured V_y

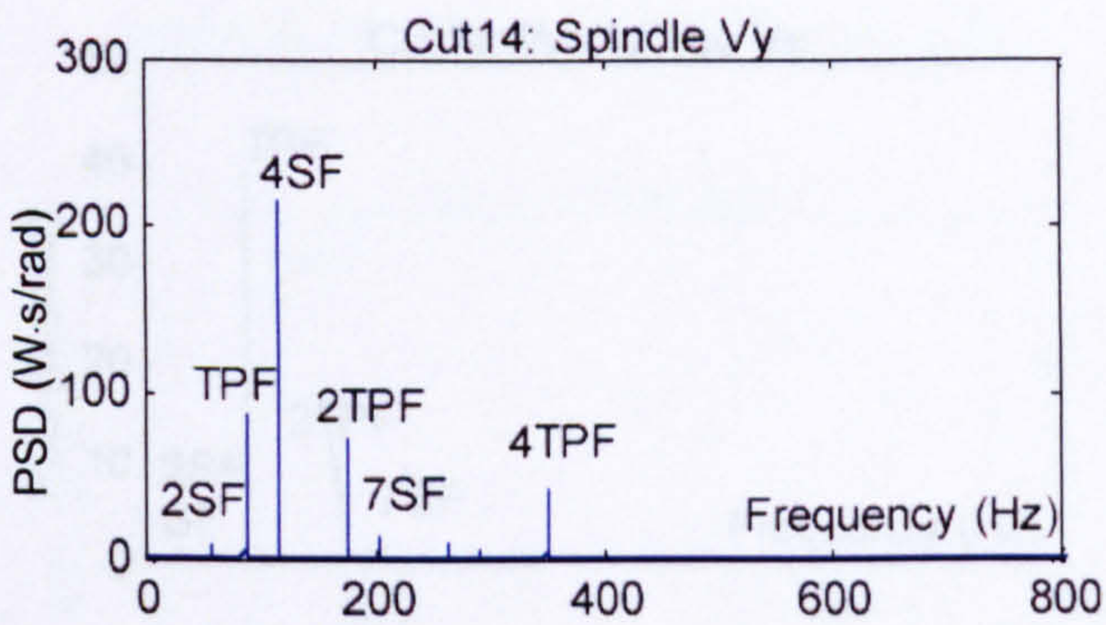

Figure 6.39. Spectrum of measured V_y

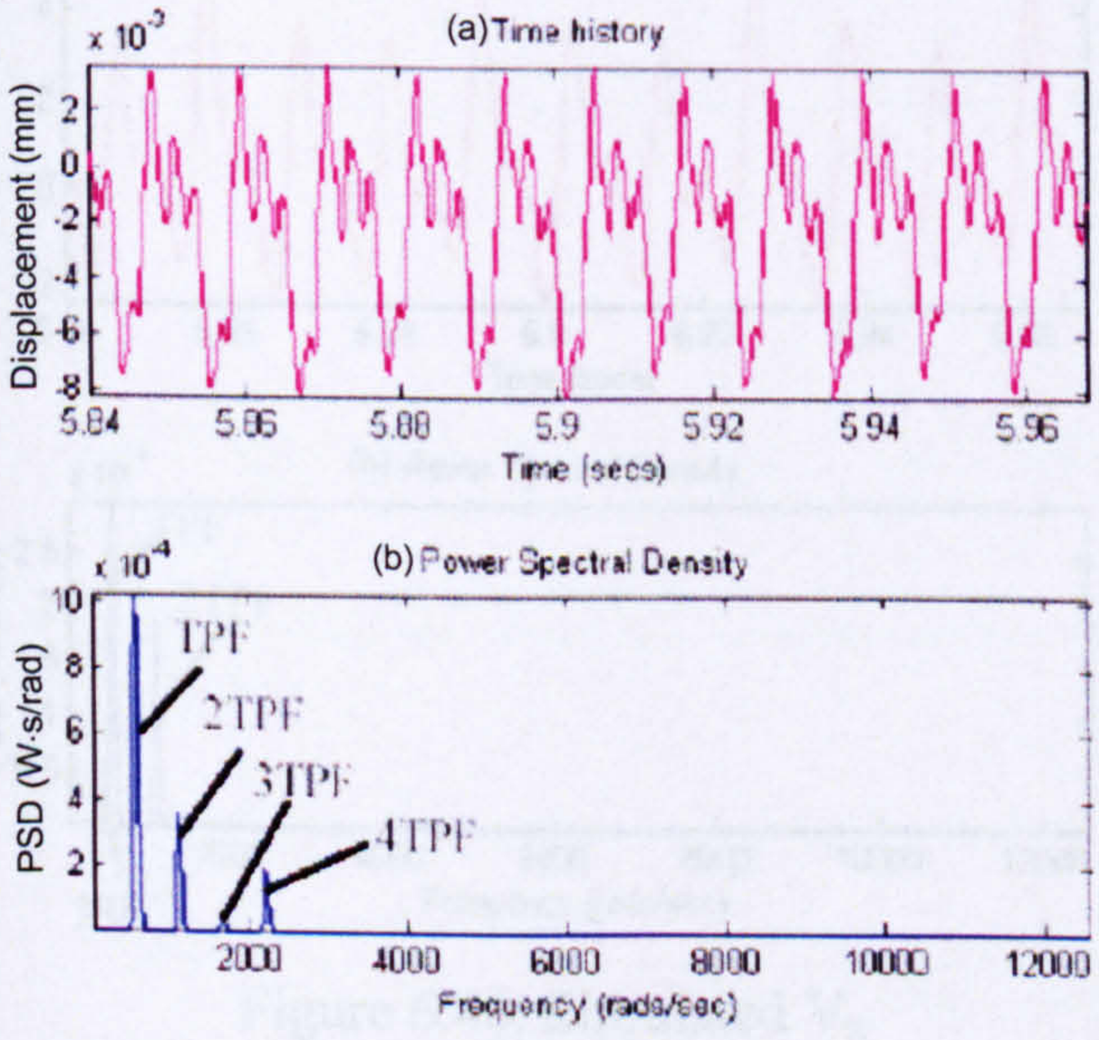

Figure 6.40. Simulated V_x

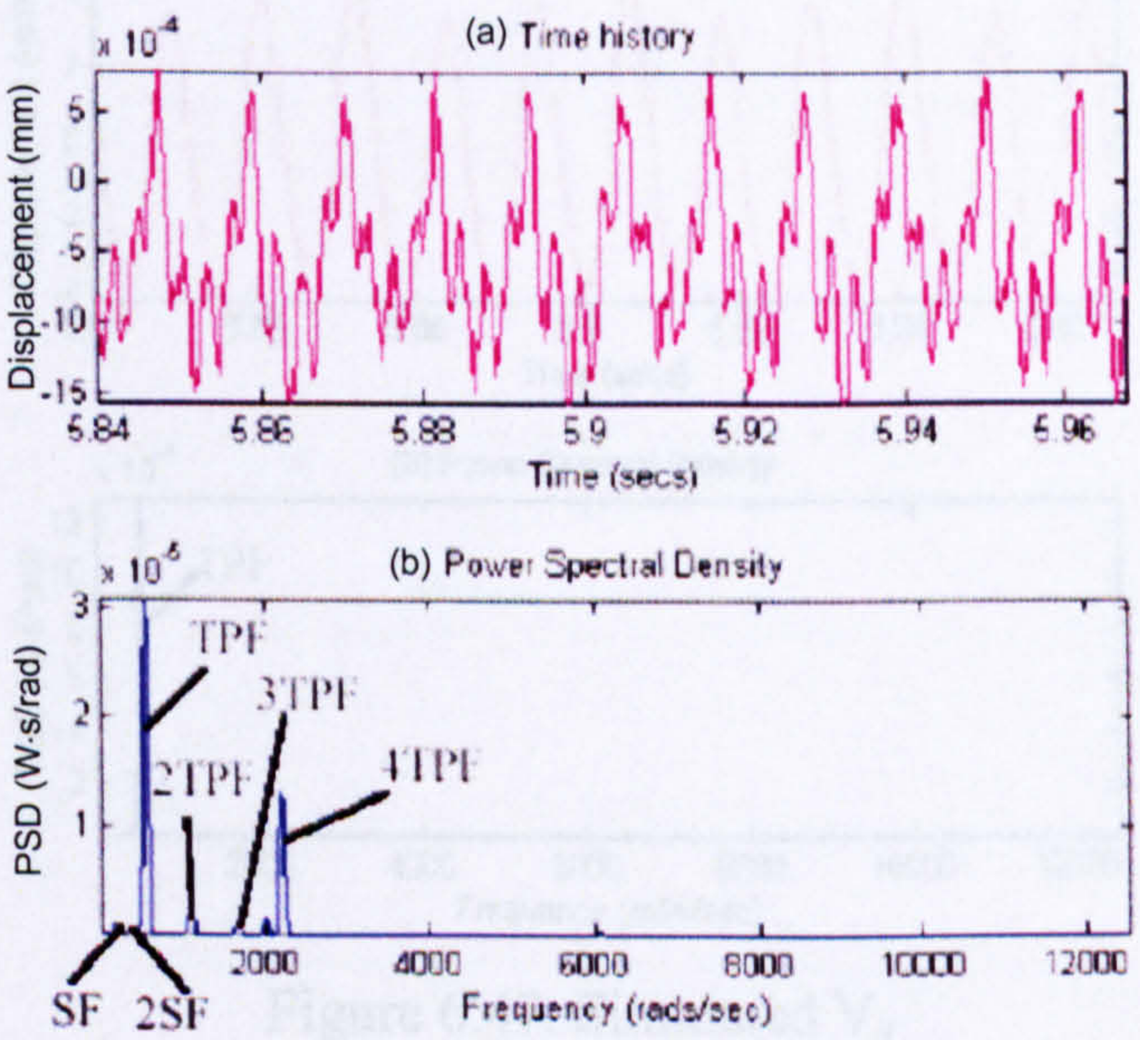

Figure 6.41. Simulated V_y

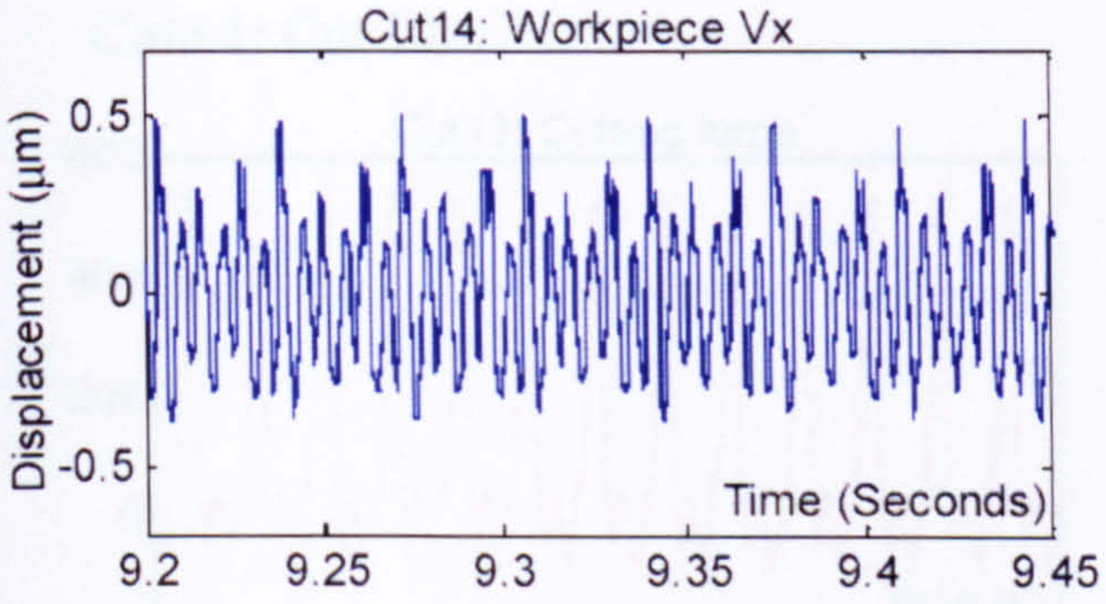

Figure 6.42. Measured V_x

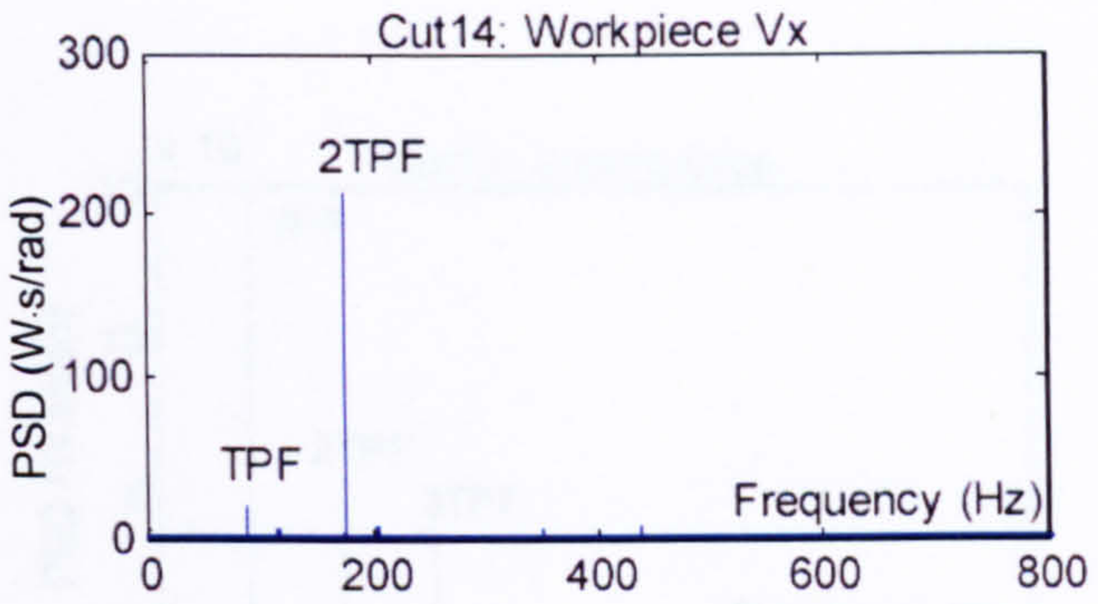

Figure 6.43. Spectrum of measured V_x

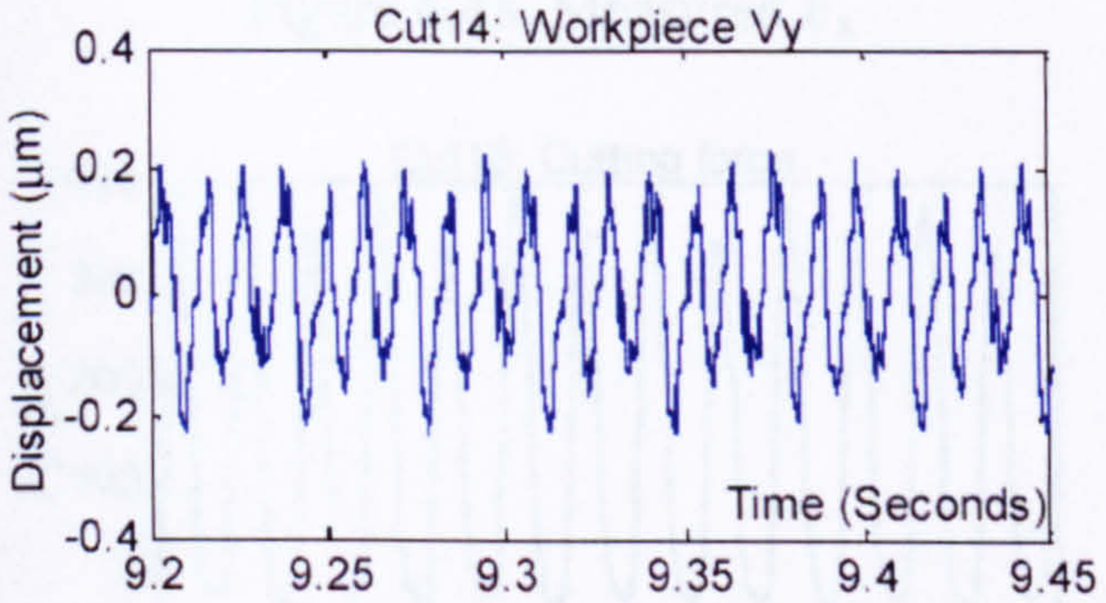

Figure 6.44. Measured V_y

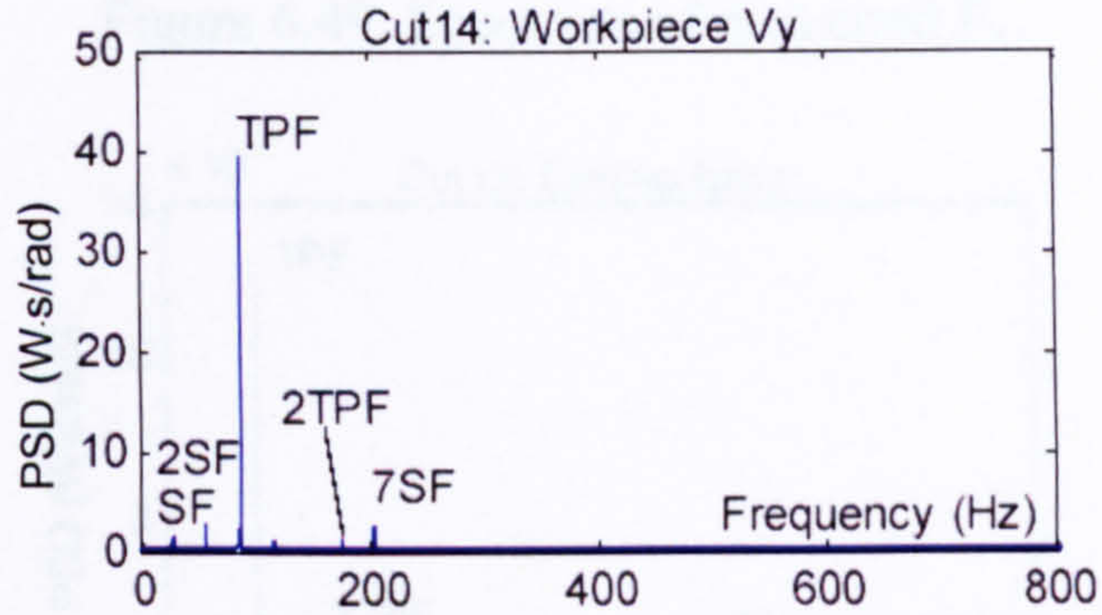

Figure 6.45. Spectrum of measured V_y

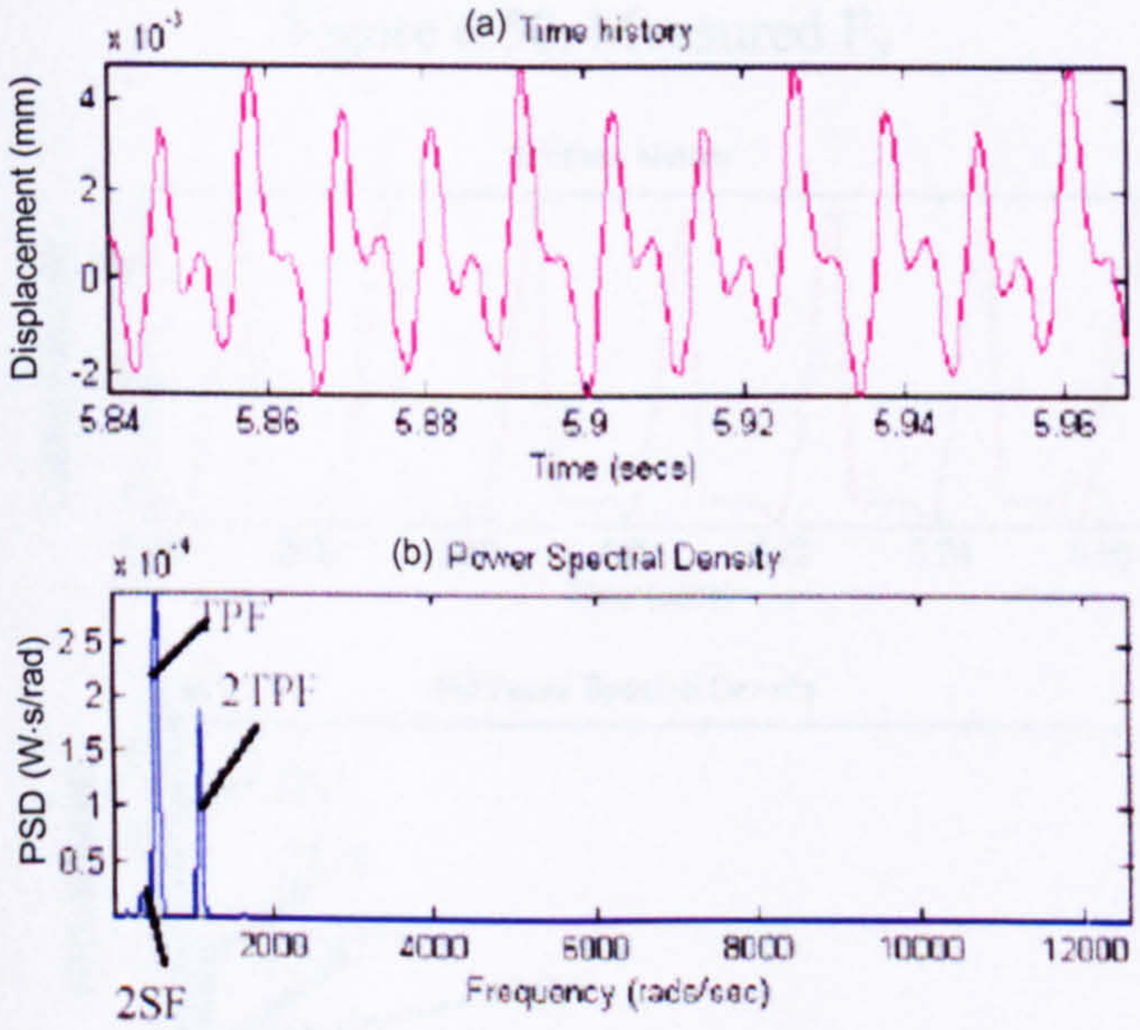

Figure 6.46. Simulated V_x

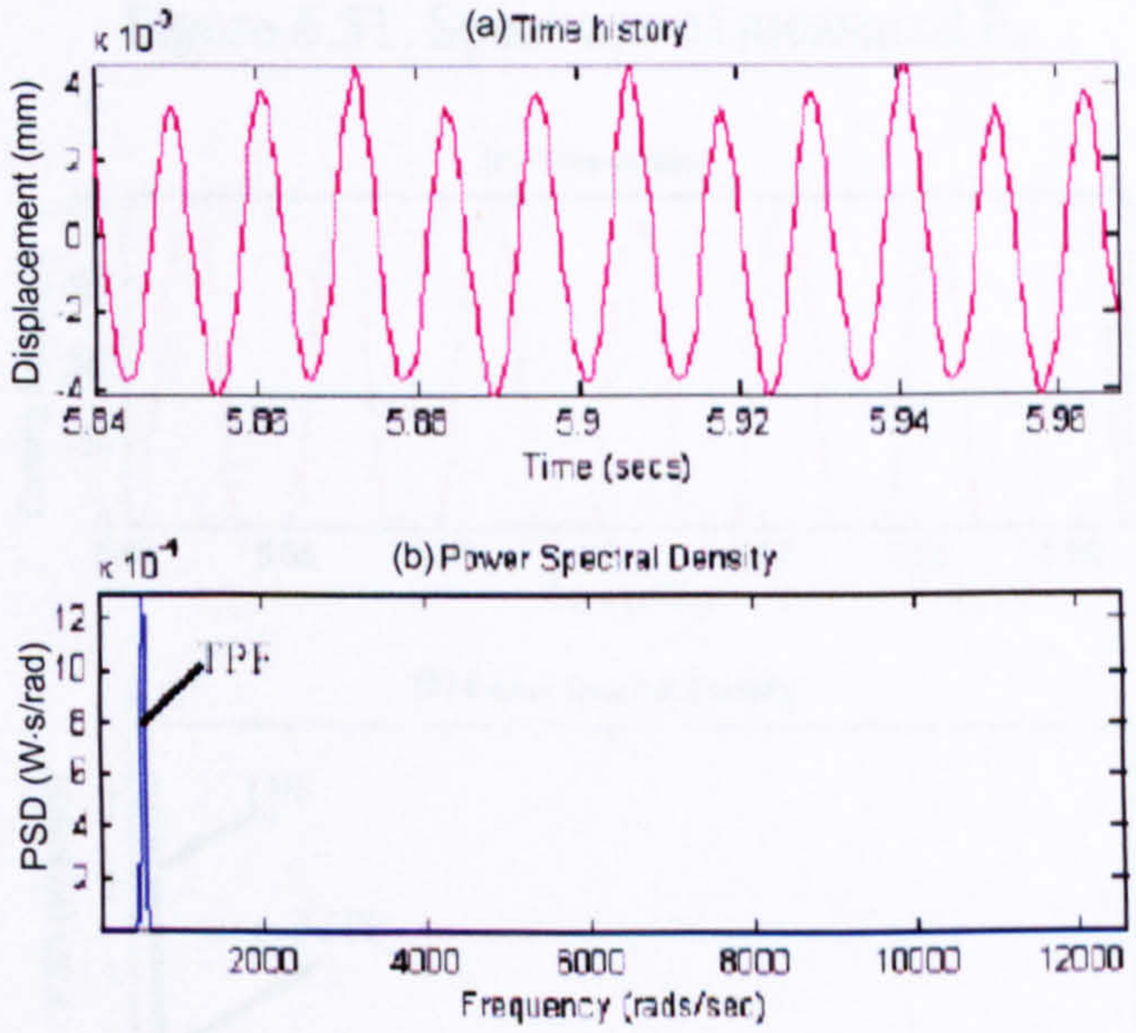

Figure 6.47. Simulated V_y

Case 1: Cut 13

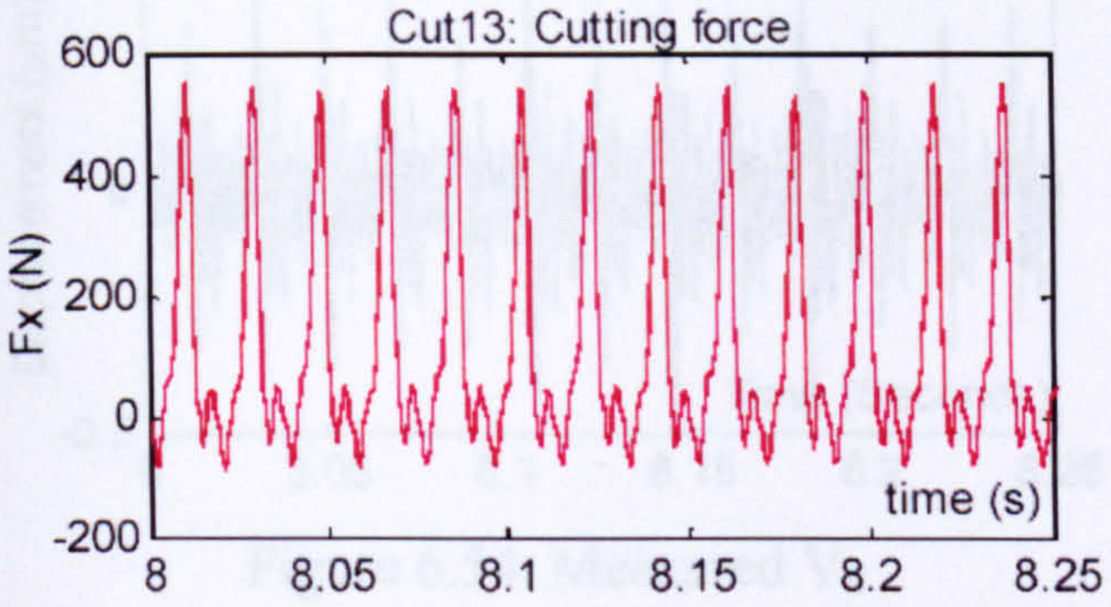

Figure 6.48. Measured F_x

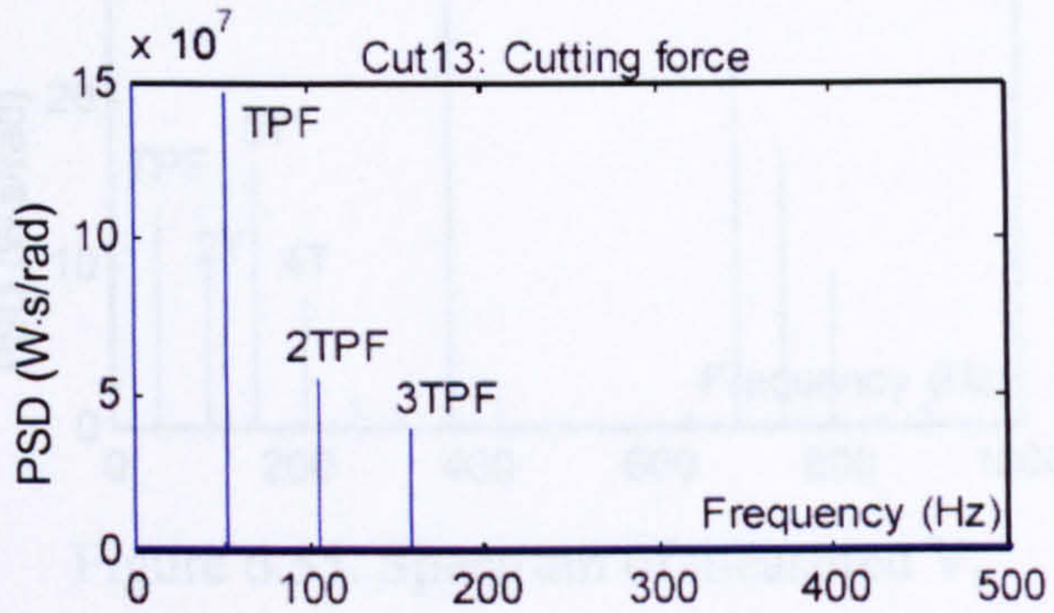

Figure 6.49. Spectrum of measured F_x

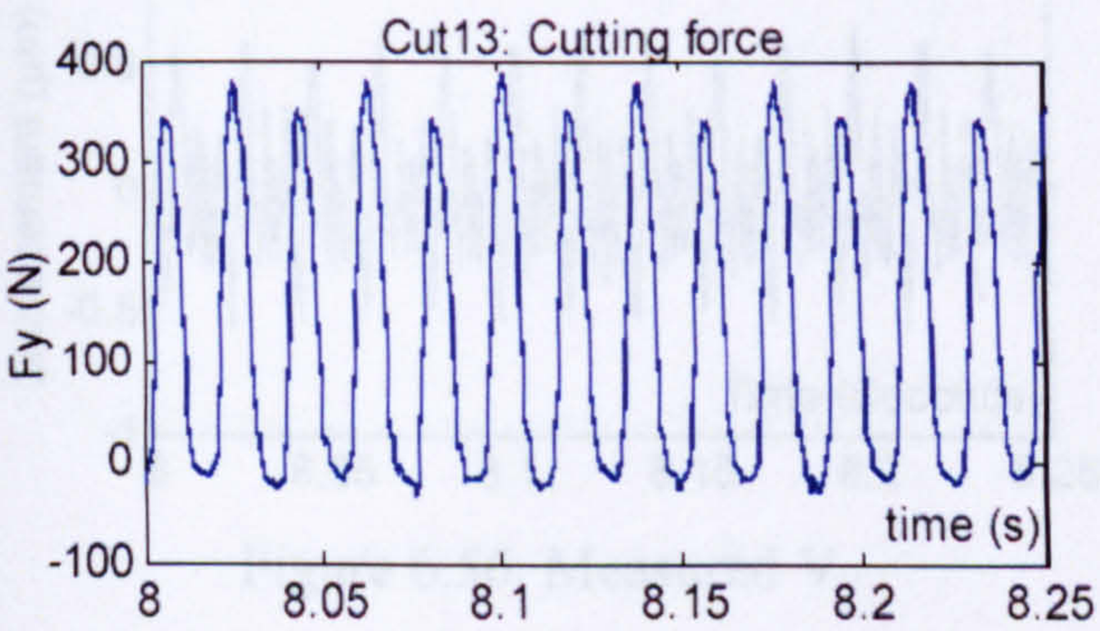

Figure 6.50. Measured F_y

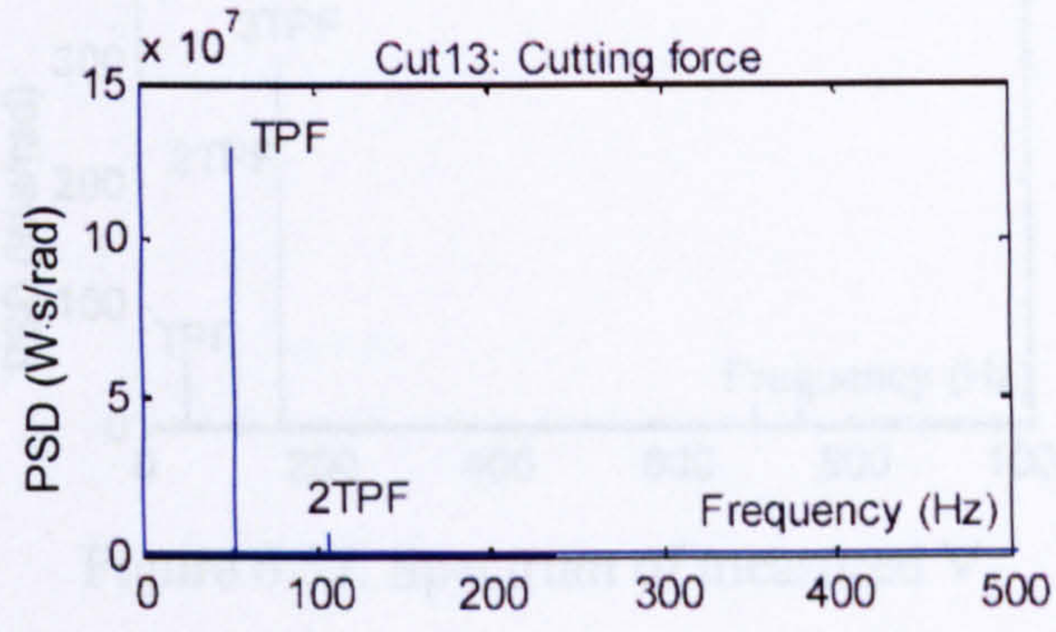

Figure 6.51. Spectrum of measured F_y

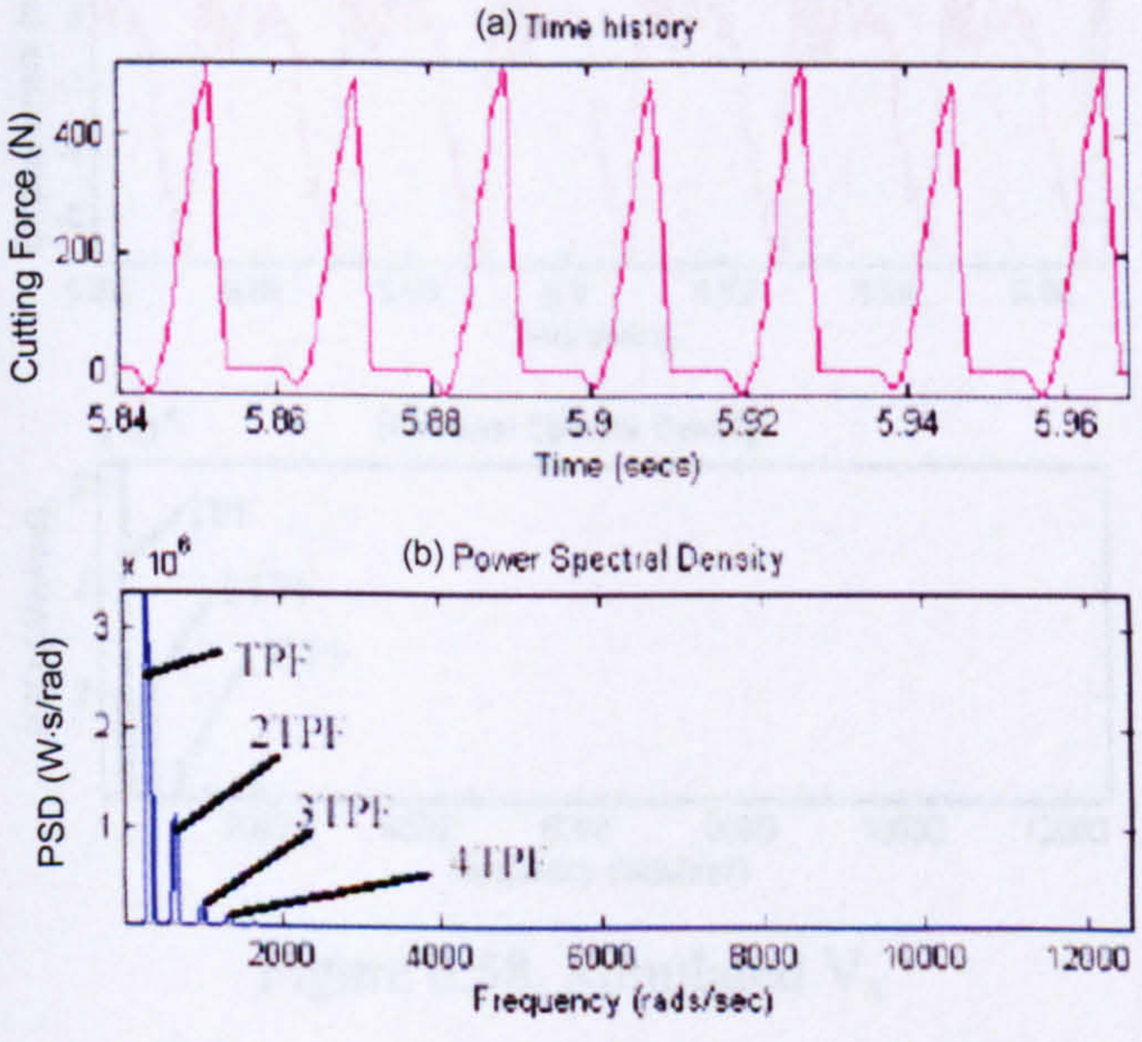

Figure 6.52. Simulated F_x

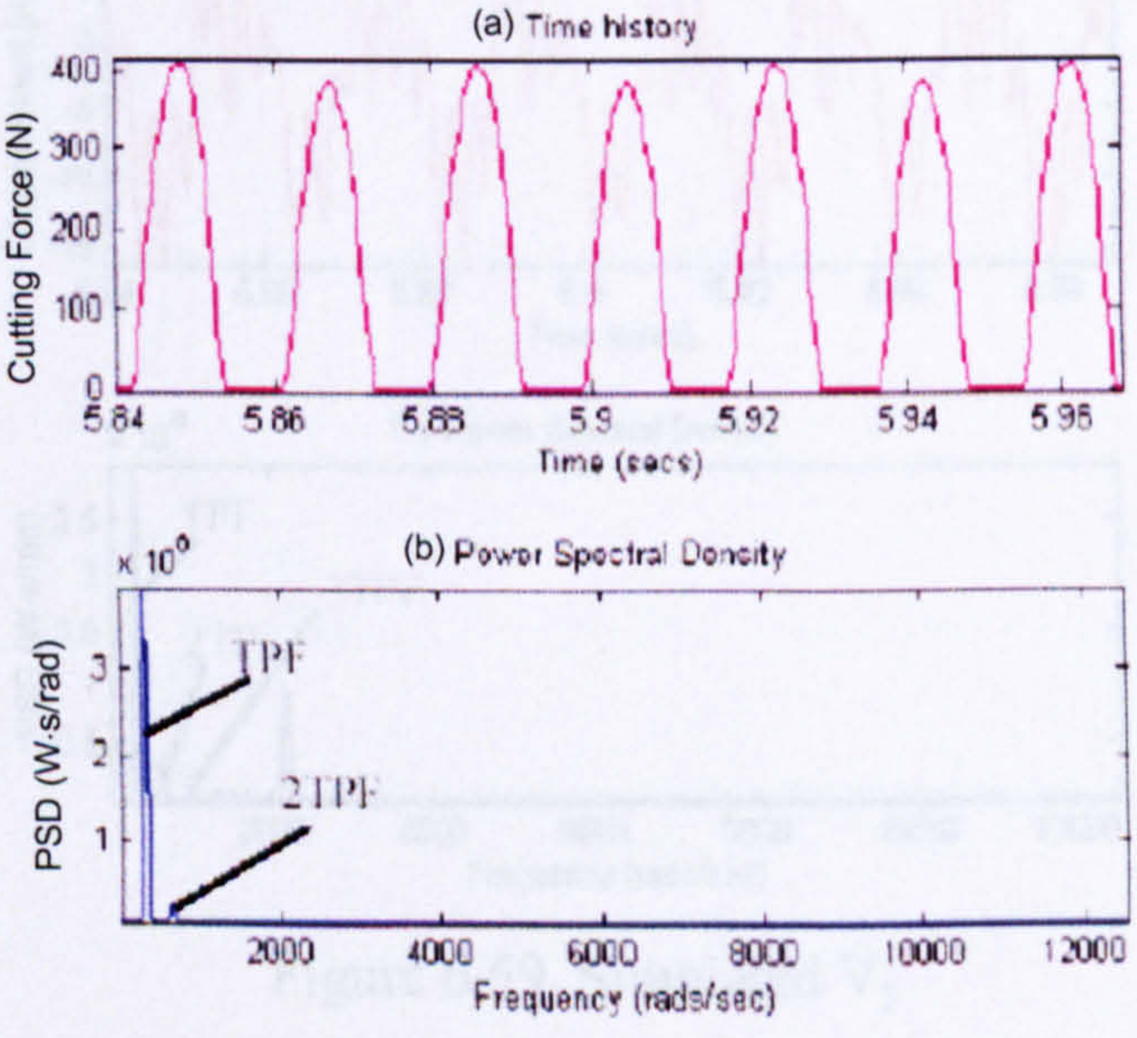

Figure 6.53. Simulated F_y

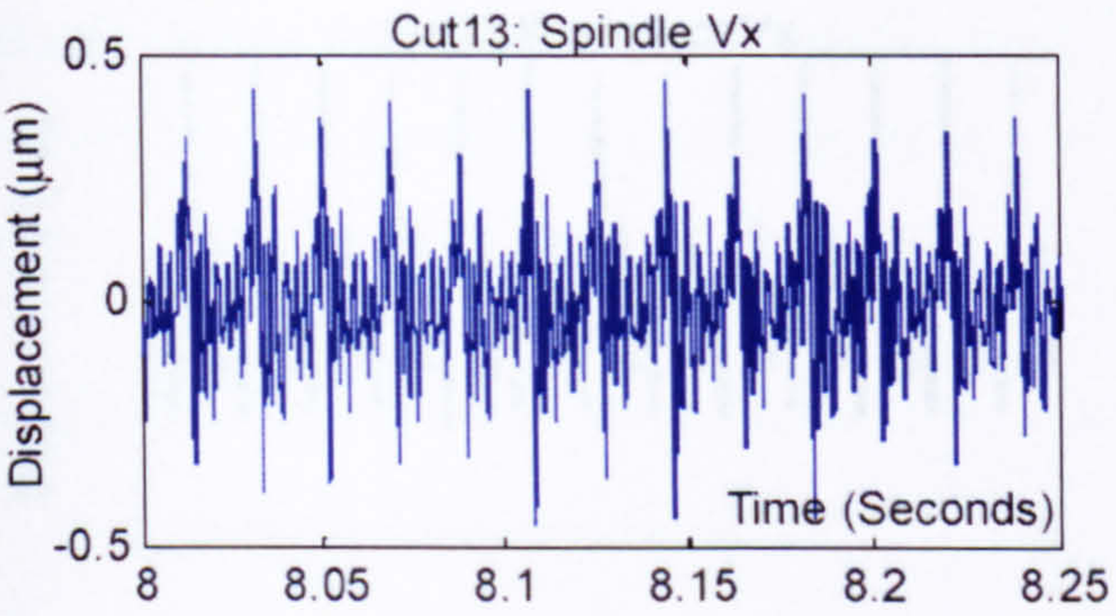

Figure 6.54. Measured V_x

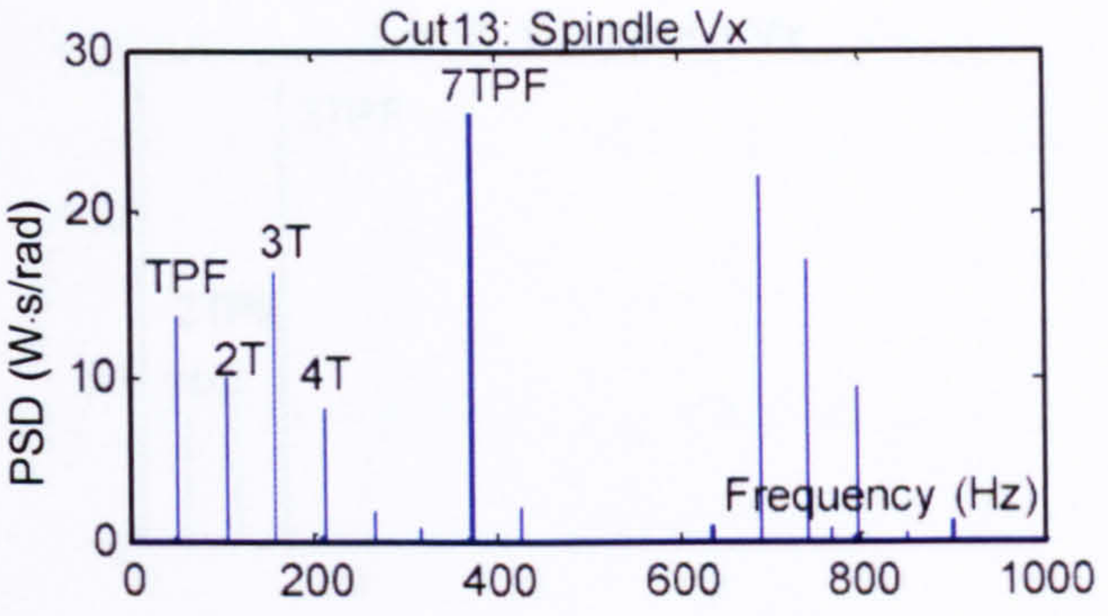

Figure 6.55. Spectrum of measured V_x

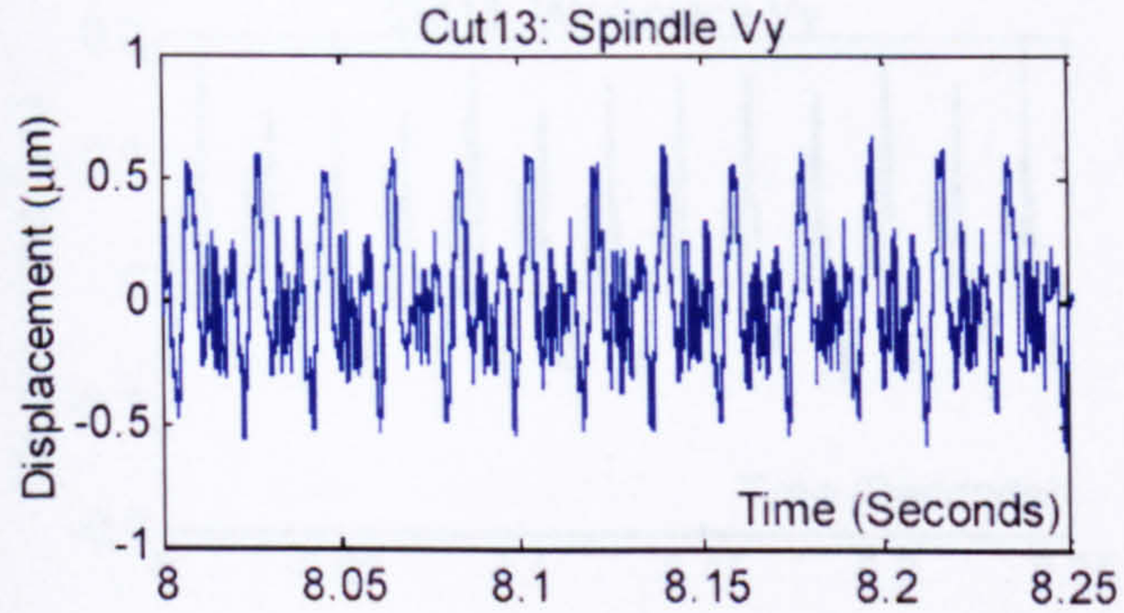

Figure 6.56. Measured V_y

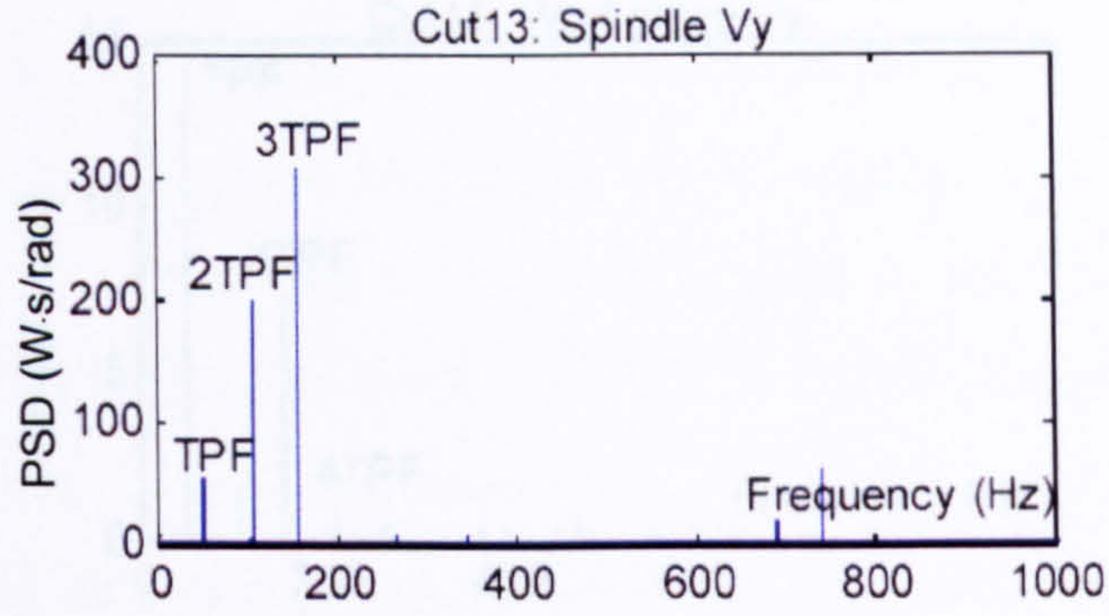

Figure 6.57. Spectrum of measured V_y

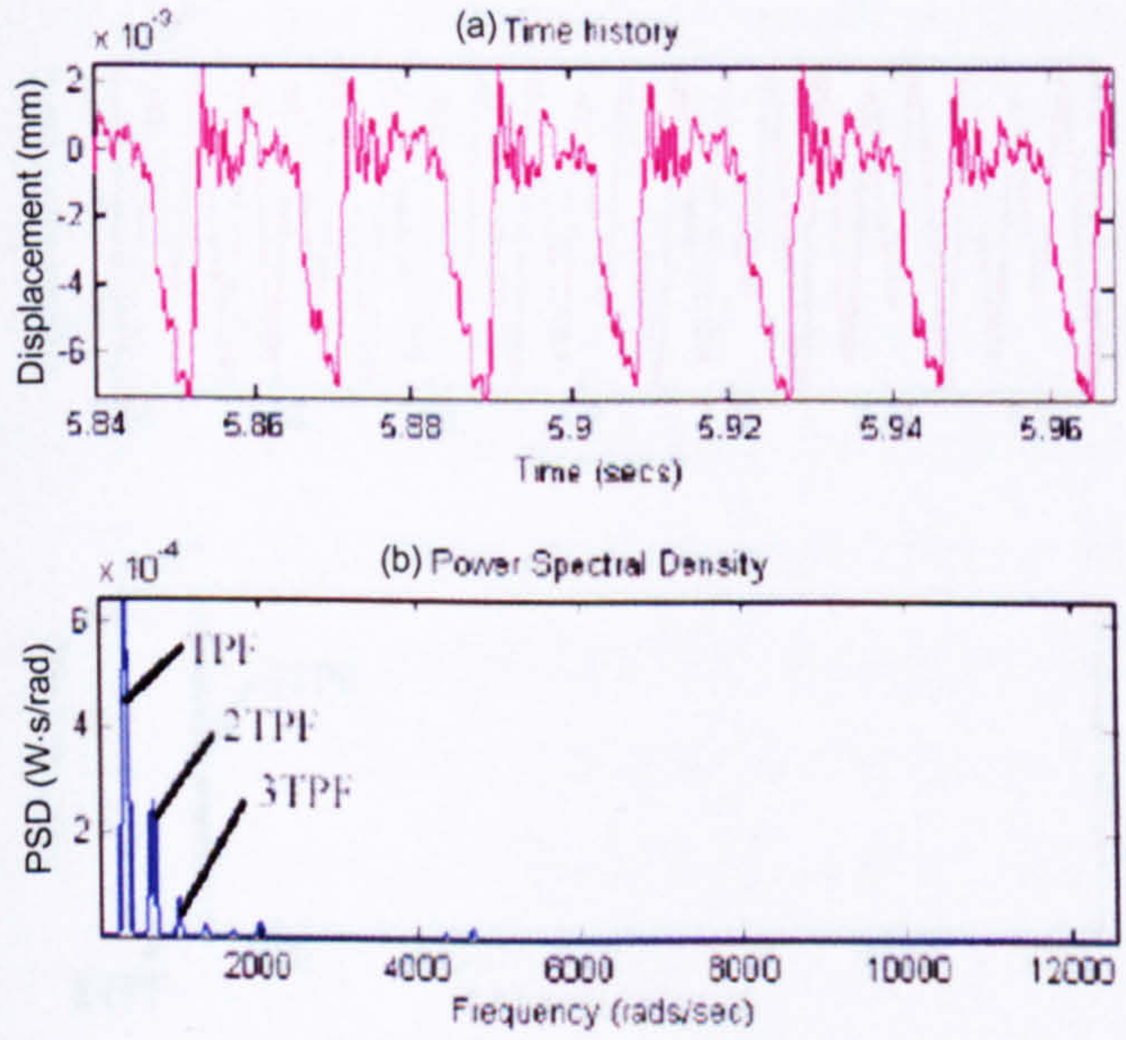

Figure 6.58. Simulated V_x

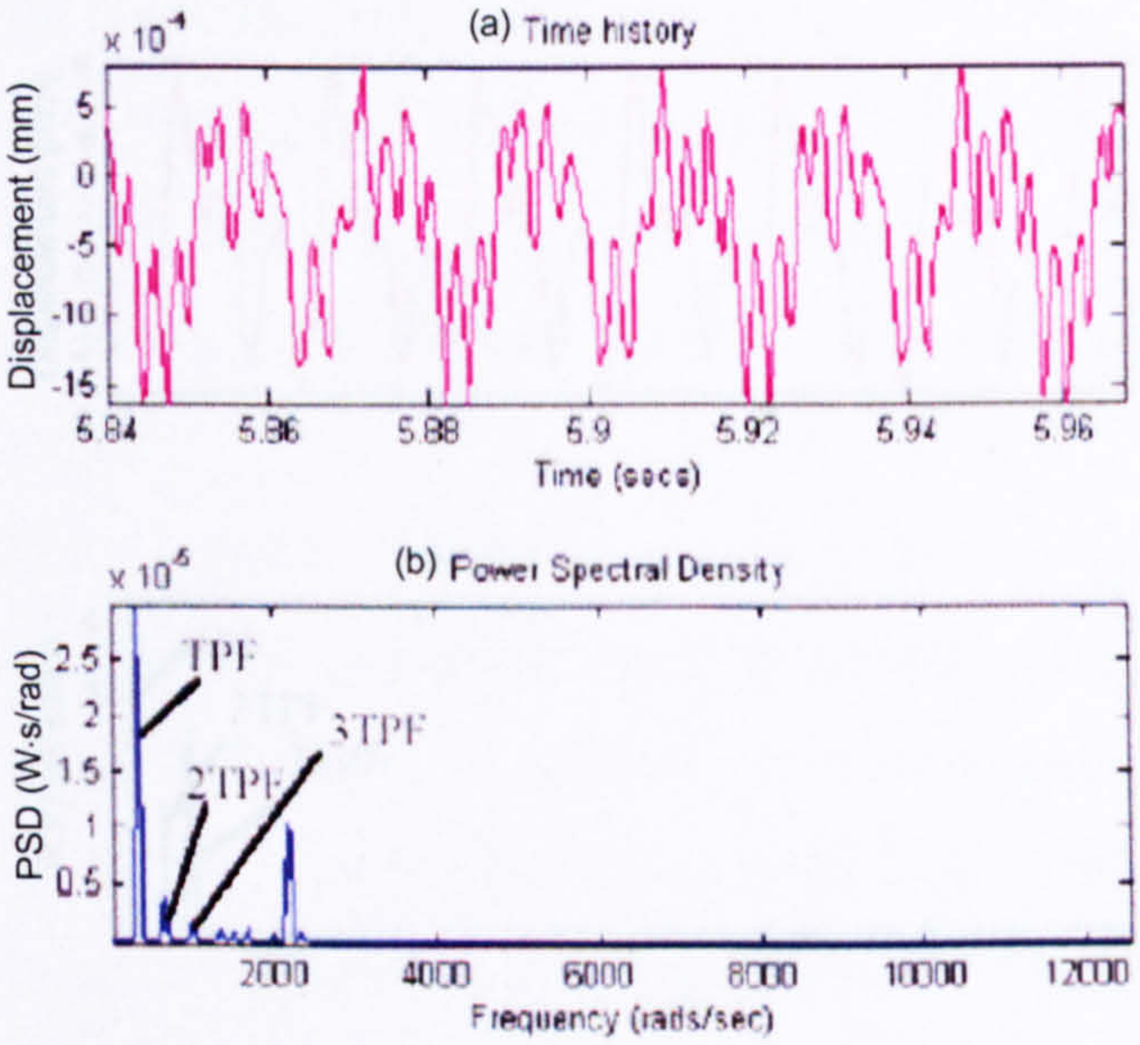

Figure 6.59. Simulated V_y

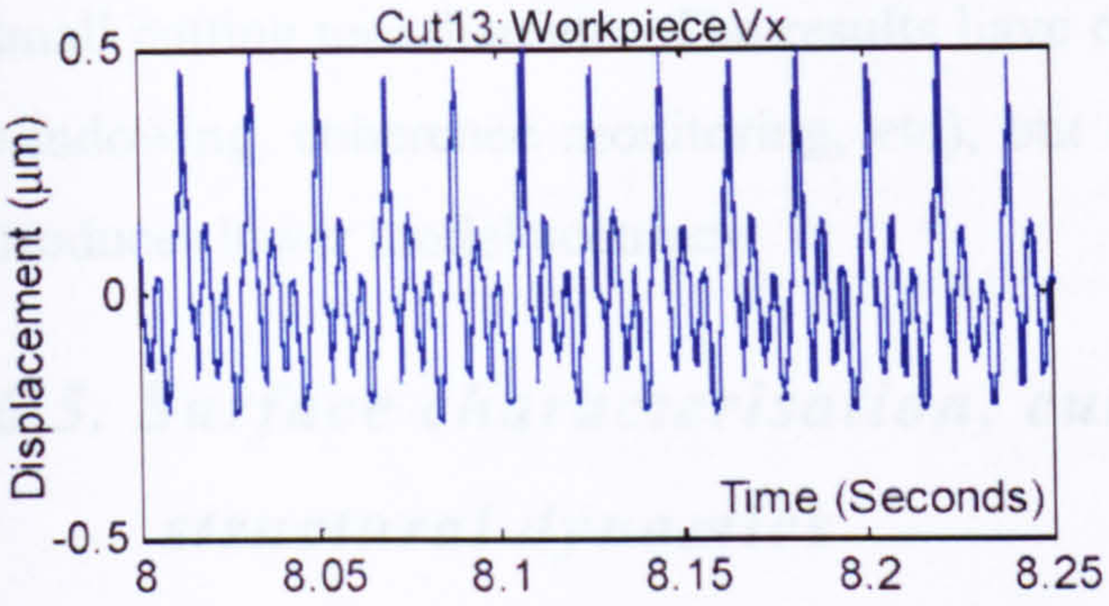

Figure 6.60. Measured V_x

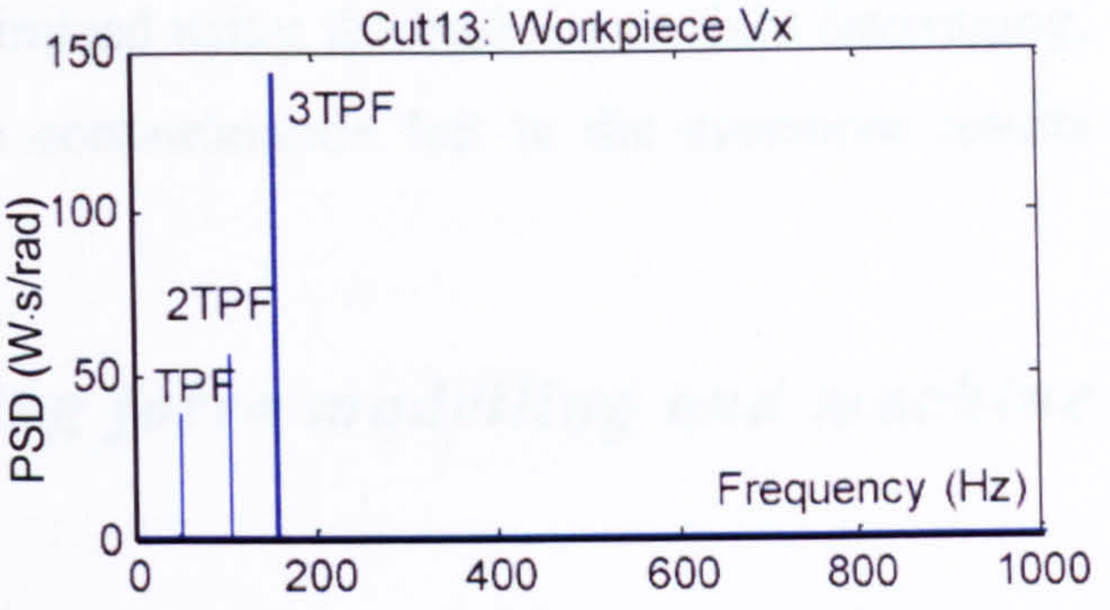

Figure 6.61. Spectrum of measured V_x

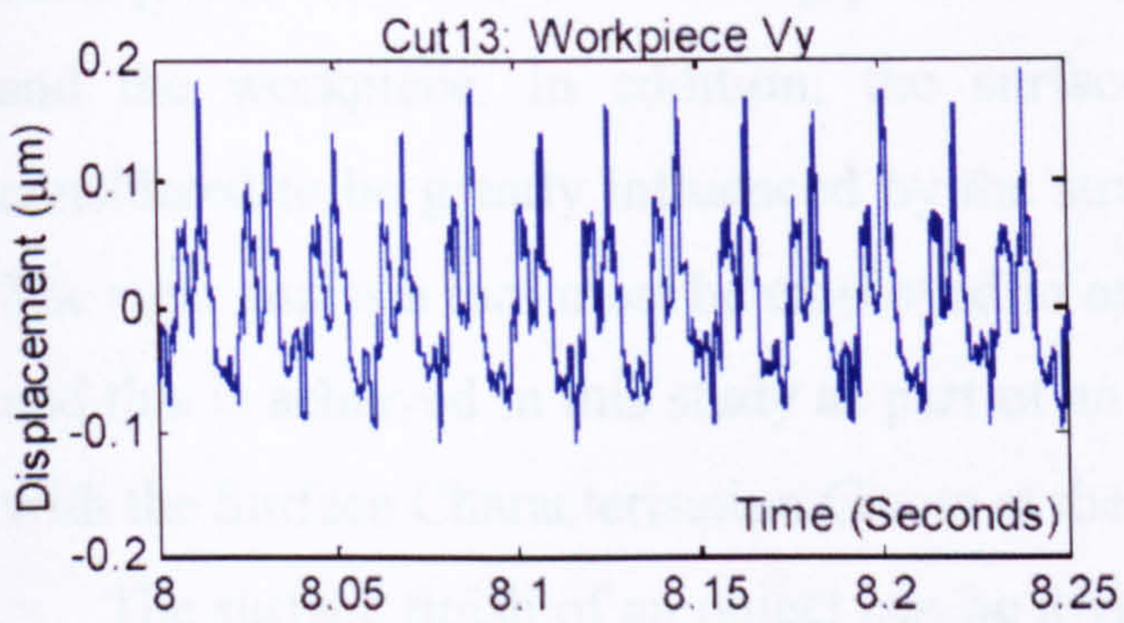

Figure 6.62. Measured V_y

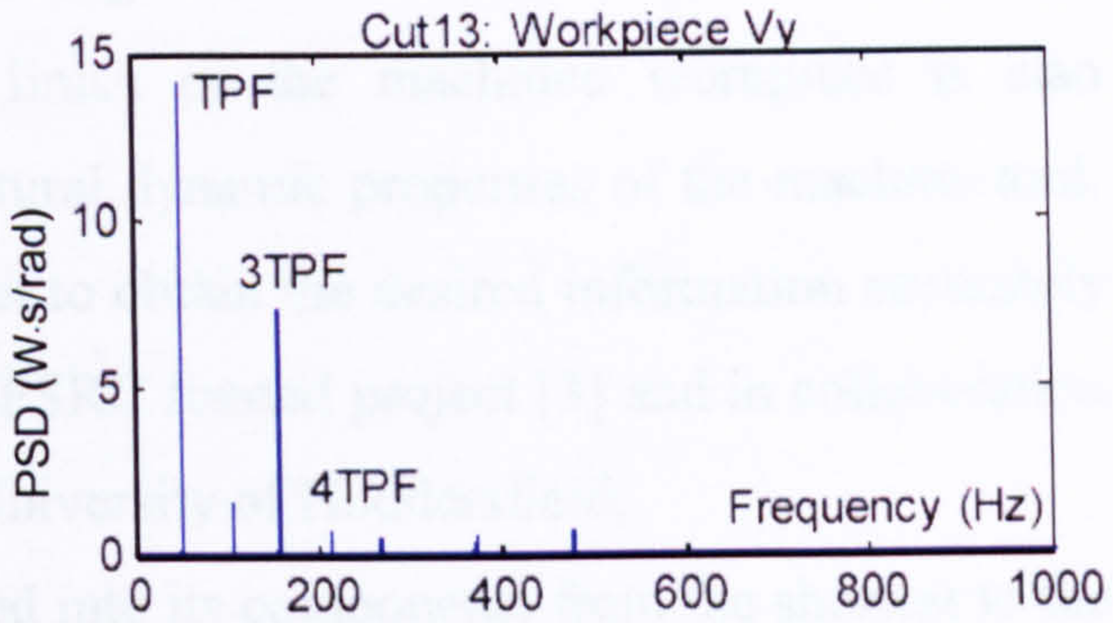

Figure 6.63. Spectrum of measured V_y

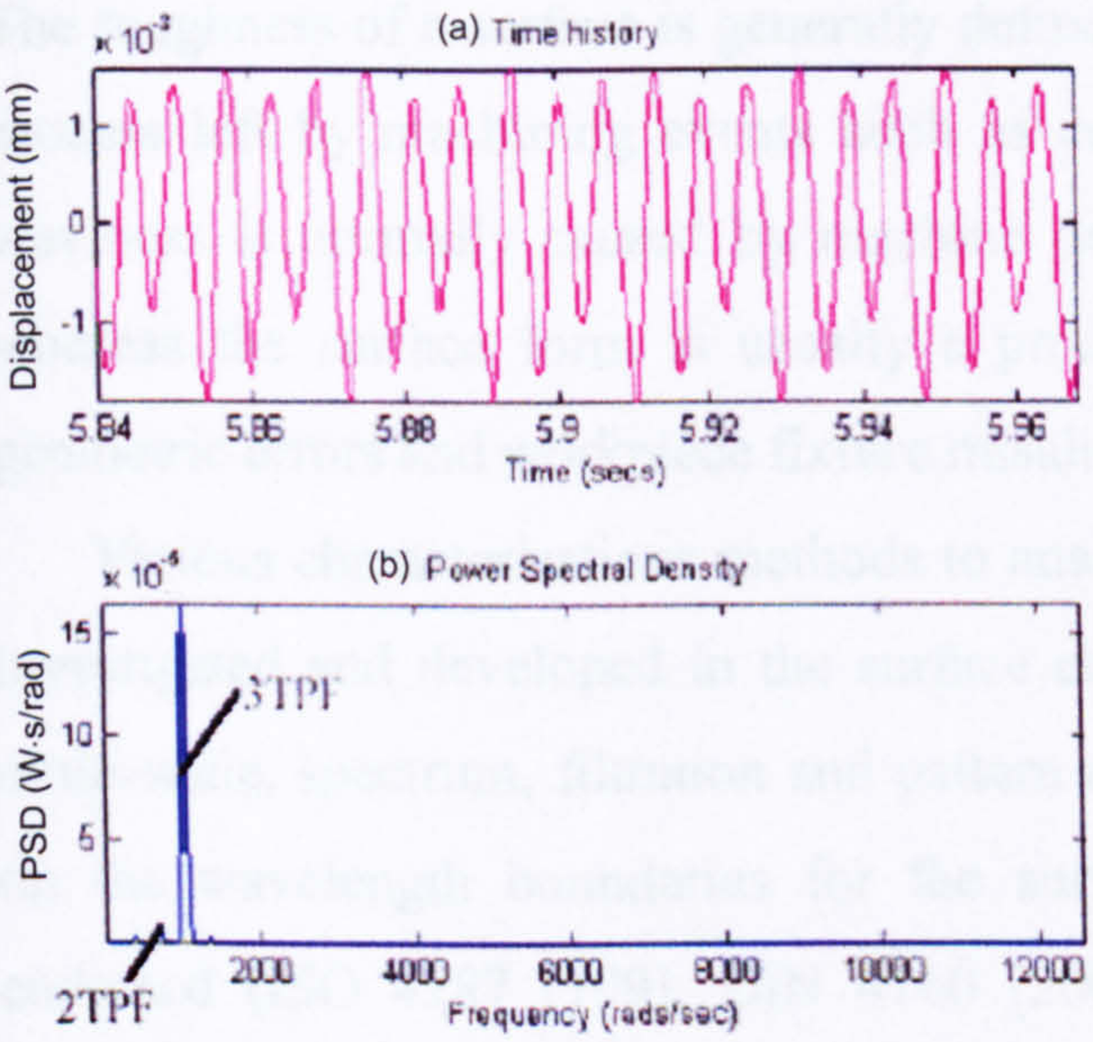

Figure 6.64. Simulated V_x

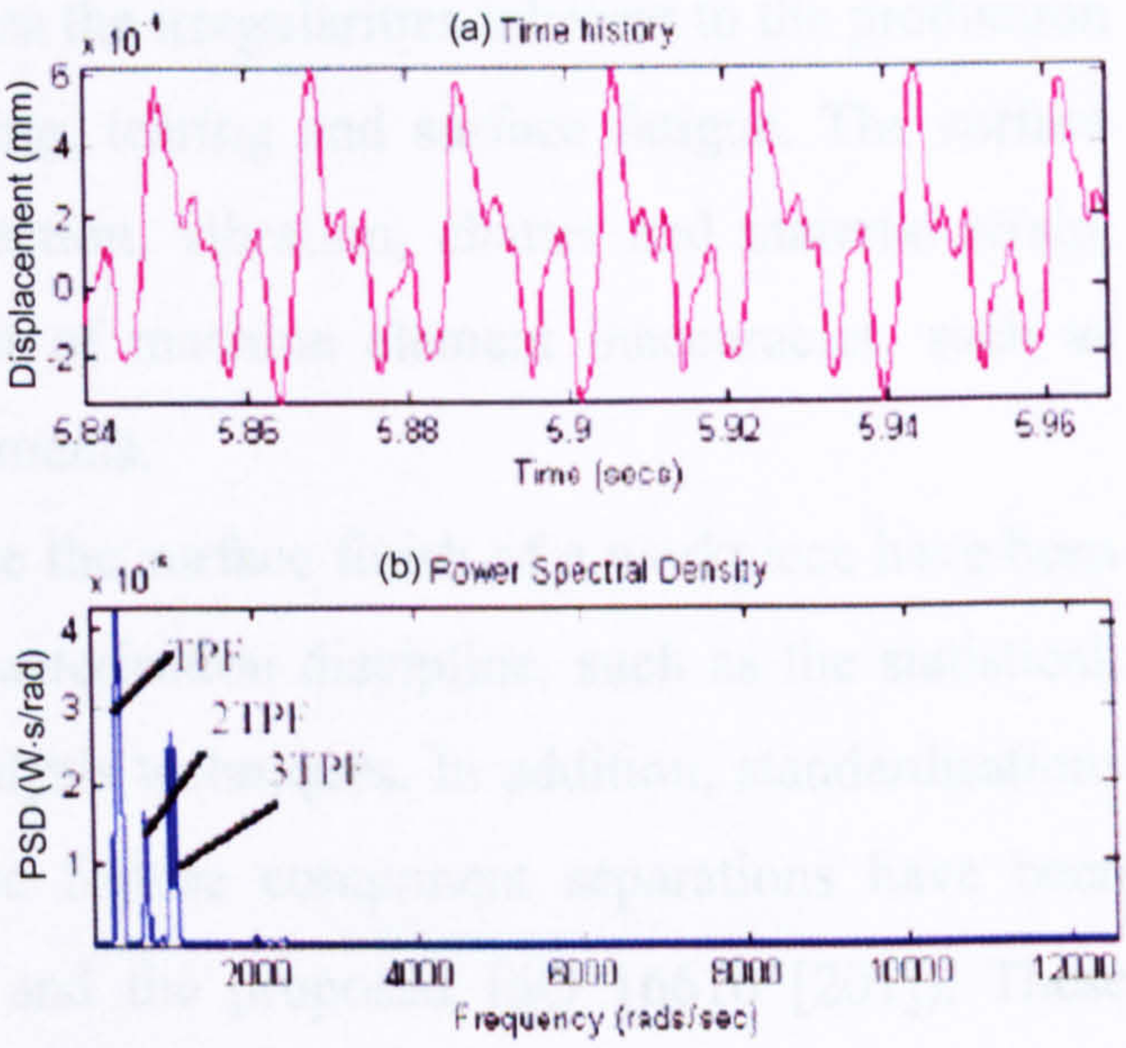

Figure 6.65. Simulated V_y

The simulated cutting forces and vibrations correspond reasonably well to the measured data, both in the time and frequency domains. Higher correlation is found in the amplitudes of the simulated and measured cutting forces and vibrations in the time domain. The simulated and measured frequency content is found to correspond well at the tooth passing frequencies but not at their multiples (harmonics). This is probably due to the limitation in the experimental modal analysis technique and the parameter extraction process. Difficulties were found during the experiments in attaching the accelerometers and performing the impact tests due to the

small cutting tool diameter. The results have optimised using the built-in routines (averaging, windowing, coherence monitoring, etc), but the contamination left in the measured results produces lower model accuracy.

6.5. Surface characterisation, cutting force modelling and machine structural dynamics

The characterisation of machined surface can reveal a wealth of information, such as the cutting tool conditions, machining parameters, cutting forces and vibration between the cutter and the workpiece. In addition, the surface finish of the machined workpiece is also considered to be greatly influenced by the structural dynamic properties of the machine tool. The right analysis tool must be employed in order to obtain the desired information accurately and this is achieved in this study as part of an EPSRC funded project [3] and in collaboration with the Surface Characterisation Group at the University of Huddersfield.

The surface finish of an object can be divided into its components from the shortest to the longest peak-to-peak spacing or wavelength as surface roughness, waviness and form error. The roughness of a surface is generally defined as the irregularities inherent to the production process left by machining events such as cutting, tearing and surface fatigue. The surface waviness is normally caused by machine deflection, vibration, chatter and material strain, whereas the surface form is usually a product of machine element inaccuracies, such as geometric errors and workpiece fixture misalignments.

Various characterisations methods to analyse the surface finish of a workpiece have been investigated and developed in the surface characterisation discipline, such as the statistical, multi-scale, spectrum, filtration and pattern analysis techniques. In addition, standardisations on the wavelength boundaries for the surface feature component separations have been endorsed (ISO 4287 [199], DIN 4760 [200] and the proposed ISO 16610 [201]). These separations are carried out on the measured data using different filtering techniques, such as 2CR, polynomial, phase-corrected [202] and valley suppression [203].

6.5.1. Surface generation model

The machine surface finish depends on various features including the geometry of the cutting tool, the cutter run-out, and the vibration between the cutting tool and the workpiece. The influence of the aforementioned parameters is implemented into the machining dynamics model following the diagram shown in Figure 6.66.

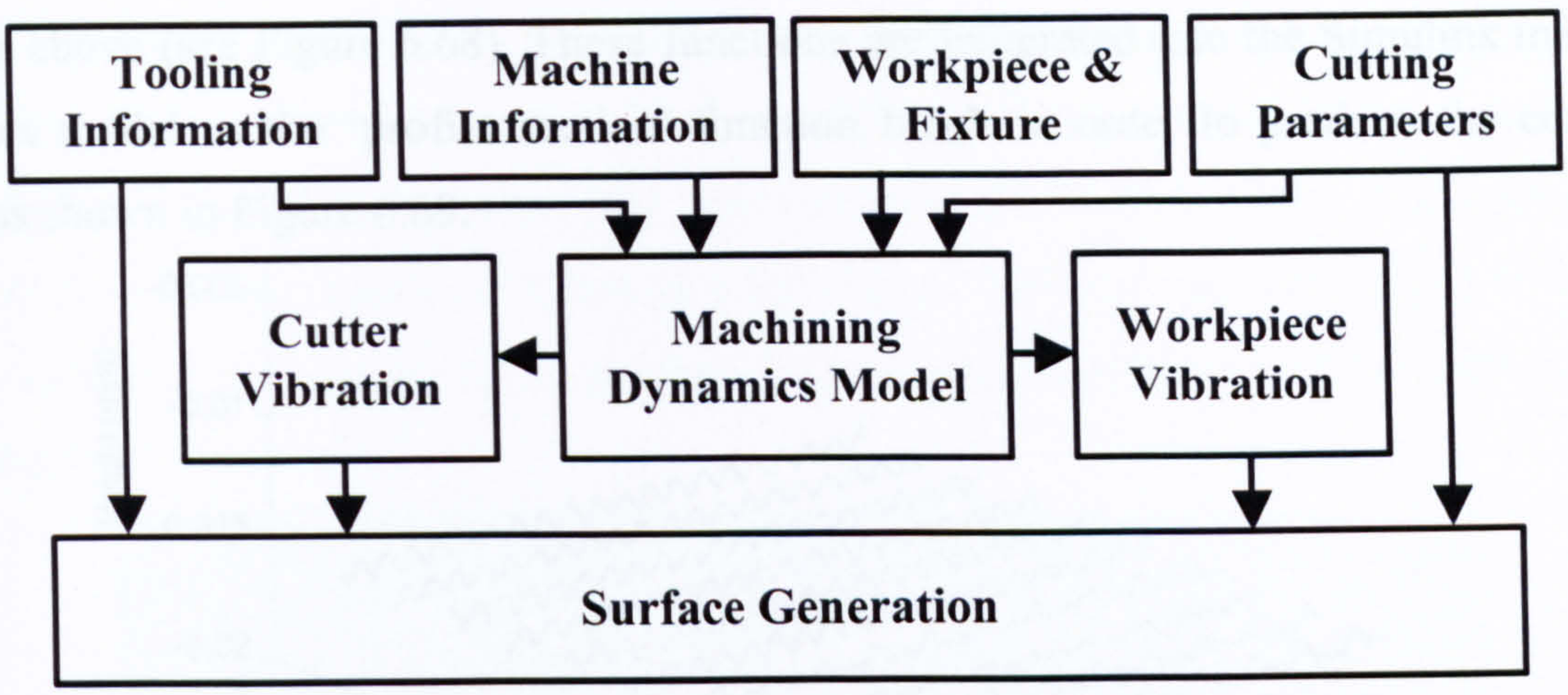

Figure 6.66. Diagram of surface generation principle

The simulated tooth trace geometry of the cutting tool generated by the model is calculated by equations (6.63) and (6.64), and illustrated in Figure 6.67.(a). The surface 2D profile on the surface finish left by the cutting operation is calculated using equations (6.65) and (6.66), and shown in Figure 6.67.(b).

$$\begin{cases} X_i(t) = R_i \cos(\varphi_i) + x_c - x_w \\ Y_i(t) = R_i \sin(\varphi_i) + \dfrac{f_t m}{2\pi}\omega t + y_c - y_w \end{cases} \qquad \begin{pmatrix} i = 1, 2, 3, \cdots, m \\ \varphi_i = \varphi - \omega t + (i-1)\dfrac{2\pi}{m} \end{pmatrix} \tag{6.63}$$

where

$$R_i = \left|\overline{O'P}\right| = \sqrt{R^2 + \delta_e^2 - 2R\delta_e \cos(\angle O'OP)} \tag{6.64}$$

The 2D profile is calculated by:

$$X = \min(Y_i(t)) \tag{6.65}$$

whereas the dimensional error can be found as:

$$\delta X(Y) = R - \min(Y_i(t)) \tag{6.66}$$

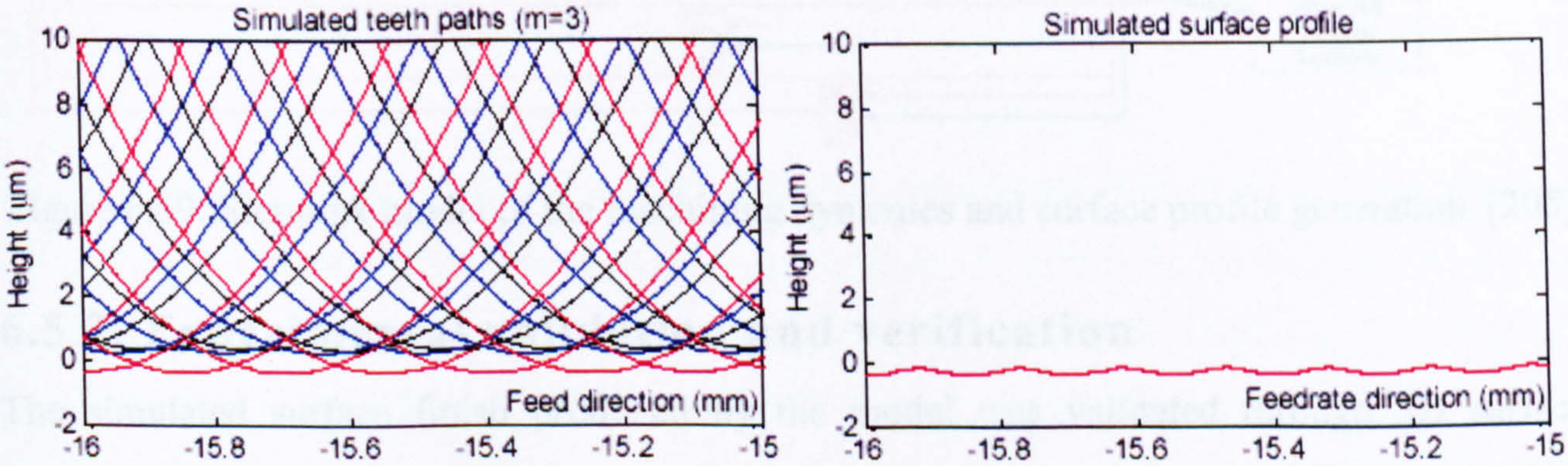

(a) Cutting tool tooth traces (b) 2D profile

Figure 6.67. Section profile of a machined surface [204]

The simulated 3D surface profile is produced by the model by the use of the Z-buffer scanning algorithm which accumulates the tooth traces produced by the 2D surface generation

function above (see Figure 6.68). These functions are integrated into the Simulink machining dynamics model as the 'profile section' function block in order to produce the completed model as shown in Figure 6.69.

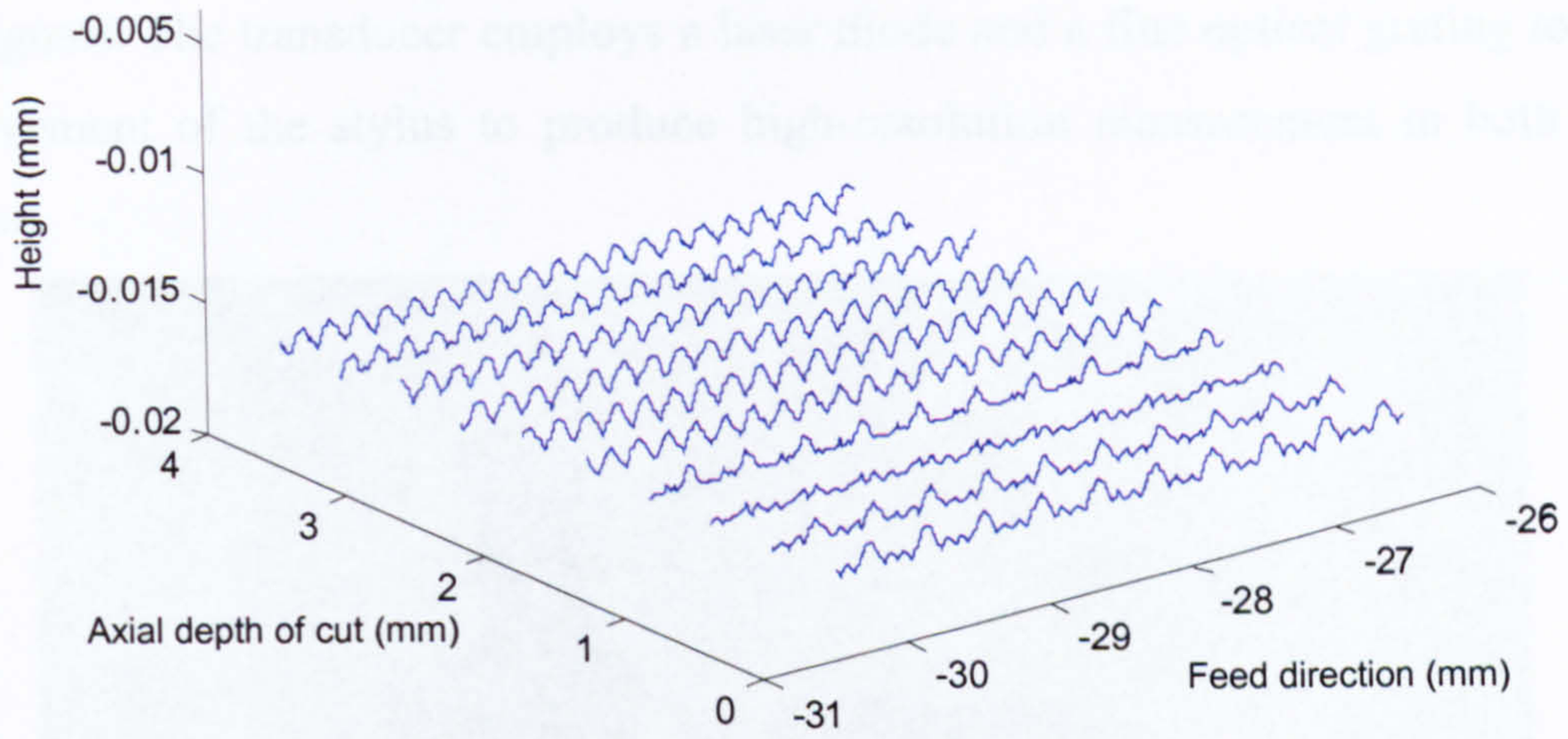

Figure 6.68. Simulated 3D profile of a machined surface [205]

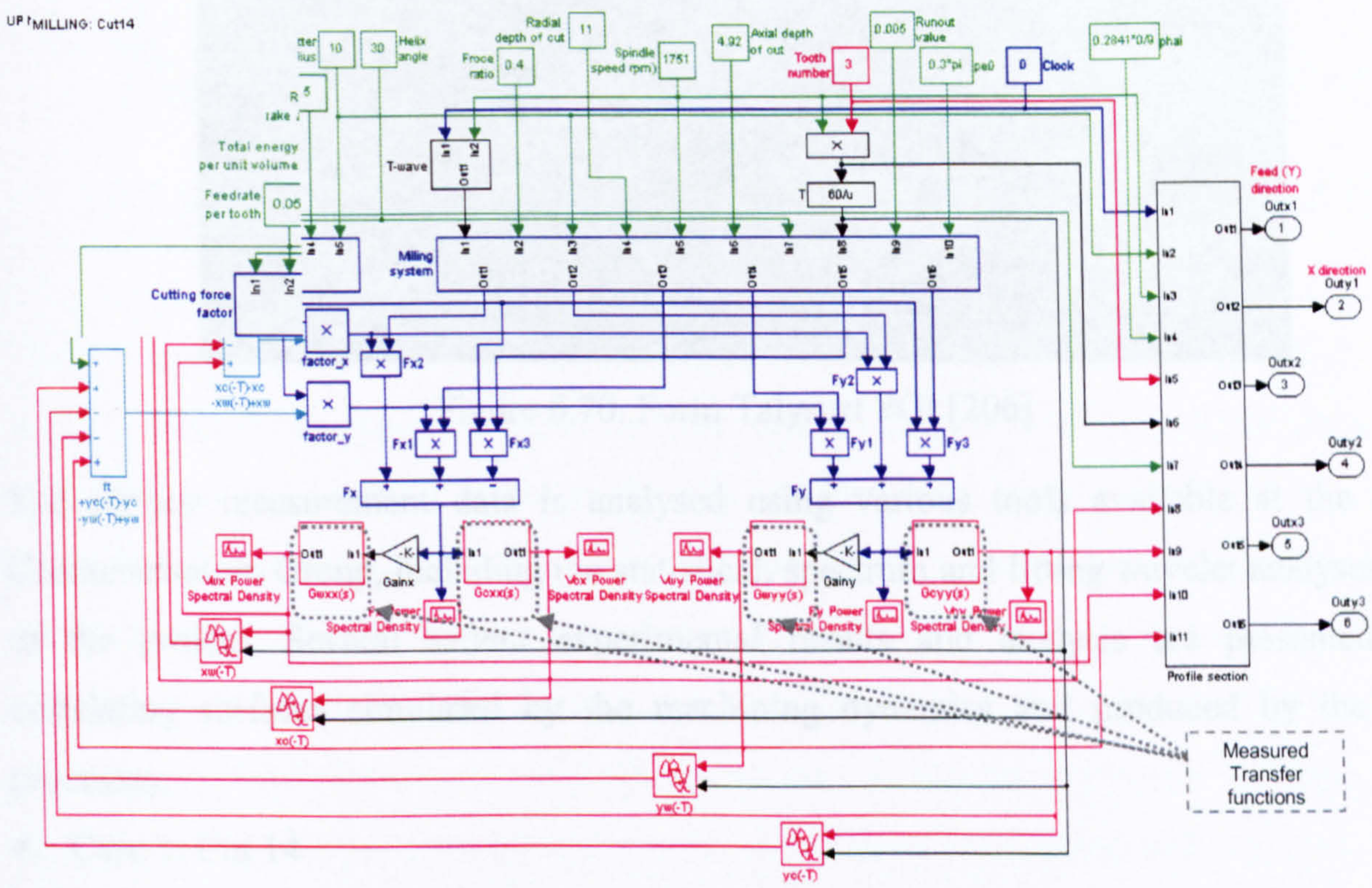

Figure 6.69. Simulink model of the machining dynamics and surface profile generation [205]

6.5.2. Experimental validation and verification

The simulated surface finish produced by the model was validated through 3D surface topography of the machined workpiece obtained from the experimental studies specified in Table 6.3. The validation and verification process includes the measurement of the surfaces well as the analysis on the simulated and measured surface parameters obtained using different surface characterisation techniques, including the lifting wavelet method.

The surface measurement is carried out on a sample area employing the Form Talysurf PGI (Phase Grating Interferometry) [206] as shown in Figure 6.70. It employs a contact measurement using a stylus and PGI transducer which converts the displacement into electrical signals. The transducer employs a laser diode and a fine optical grating to detect the minute movement of the stylus to produce high-resolution measurement in both amplitude and direction.

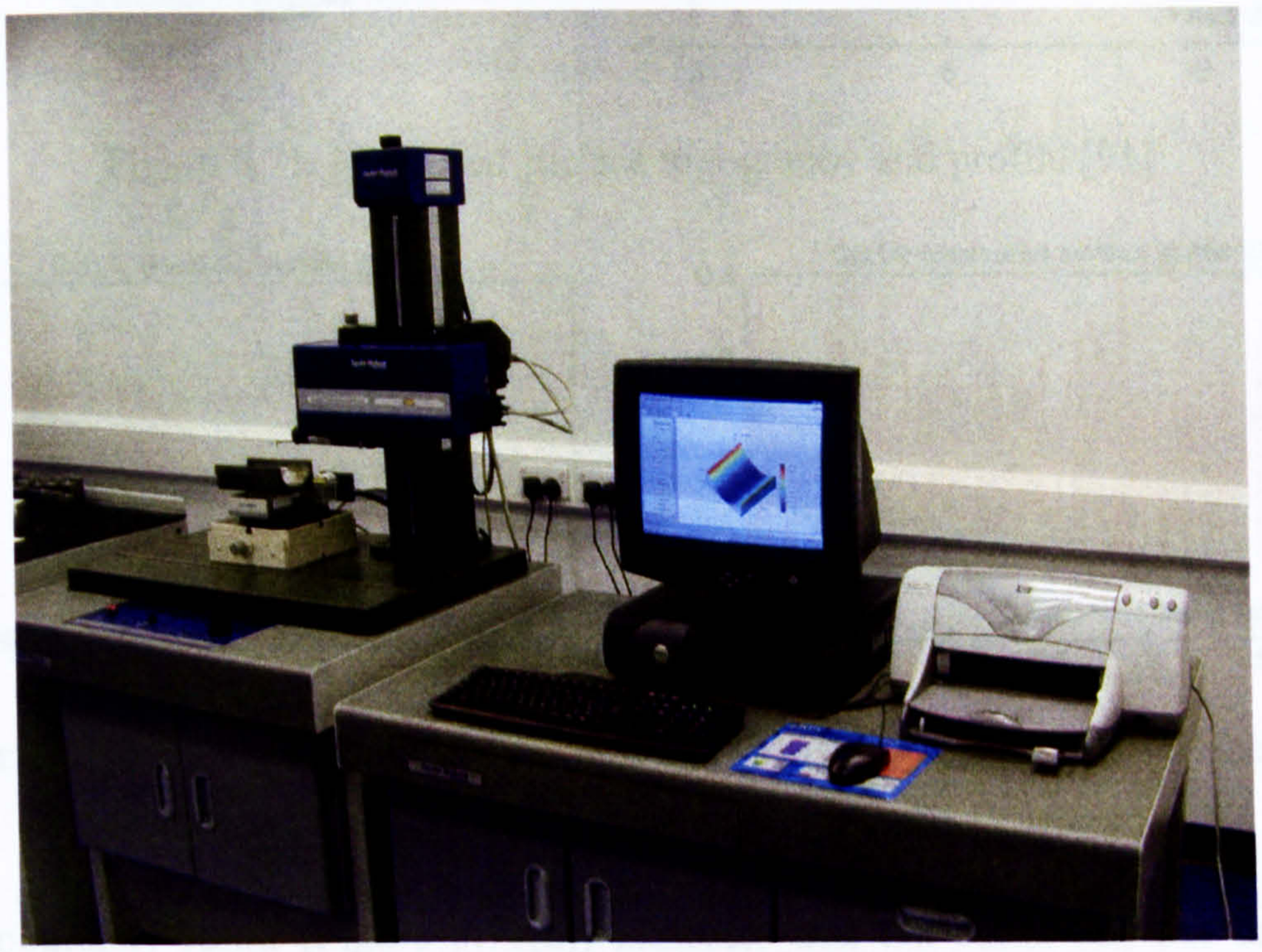

Figure 6.70. Form Talysurf PGI [206]

The surface measurement data is analysed using various tools available at the Surface Characterisation Group, including the statistical, spectrum and lifting wavelet analyses as part of the project. Several salient experimental results and analysis are presented below correlating surfaces simulated by the machining dynamics and produced by the cutting processes.

- Case 1: Cut 14

The machined workpiece surface produced in this experiment was measured and analysed using three- and two-dimensional surface topography. Figure 6.71 shows the 3D surface topography and the 2D surface profile along the feed rate path respectively. Frequency analysis of the 2D surface profile using the FFT was performed on the 2D surface profile producing the spectra of the surface seen in Figure 6.72(a). In addition, high pass filtering was carried out on the 2D surface profile results producing the high frequency surface profile representing the surface roughness (Figure 6.72(b)).

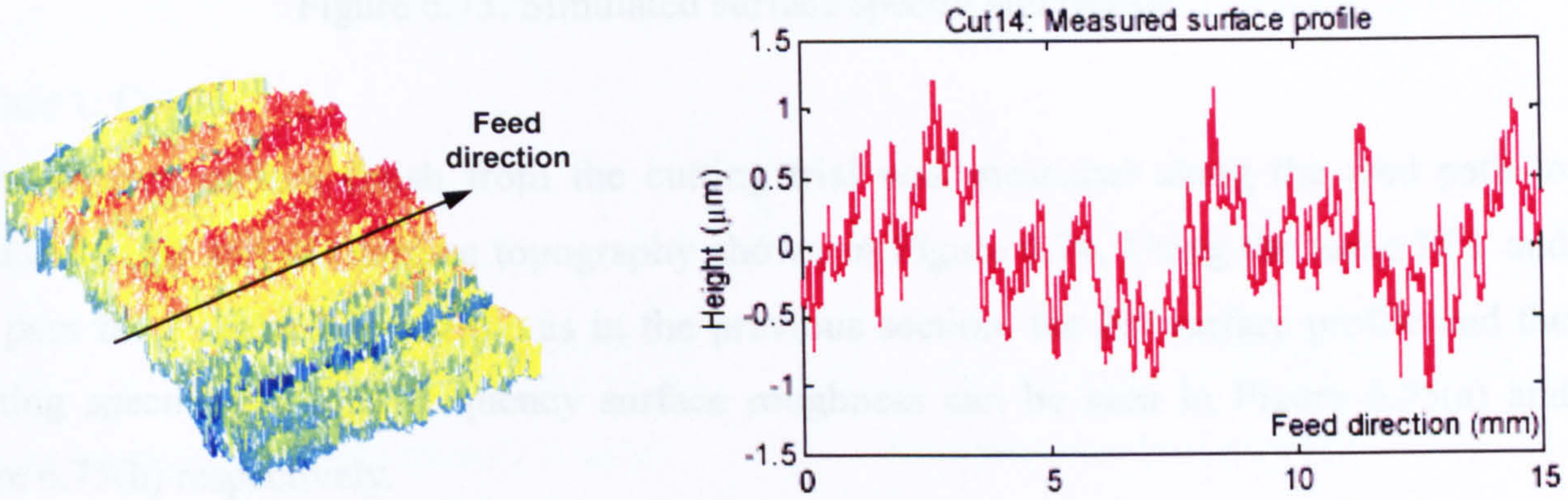

Figure 6.71. Measured surface topography and profile [93]

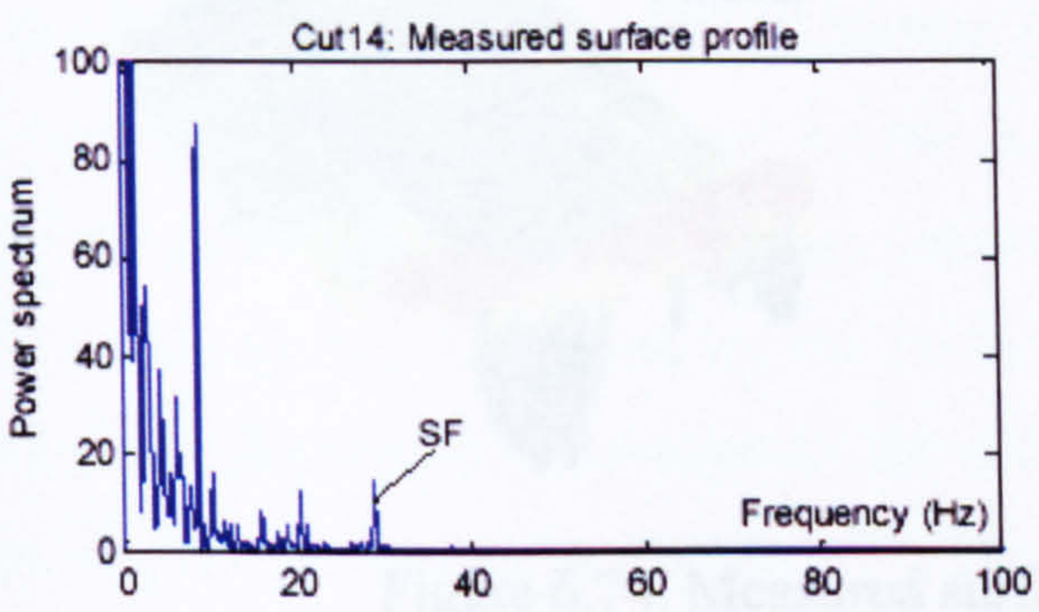

(a) Surface profile frequency spectra

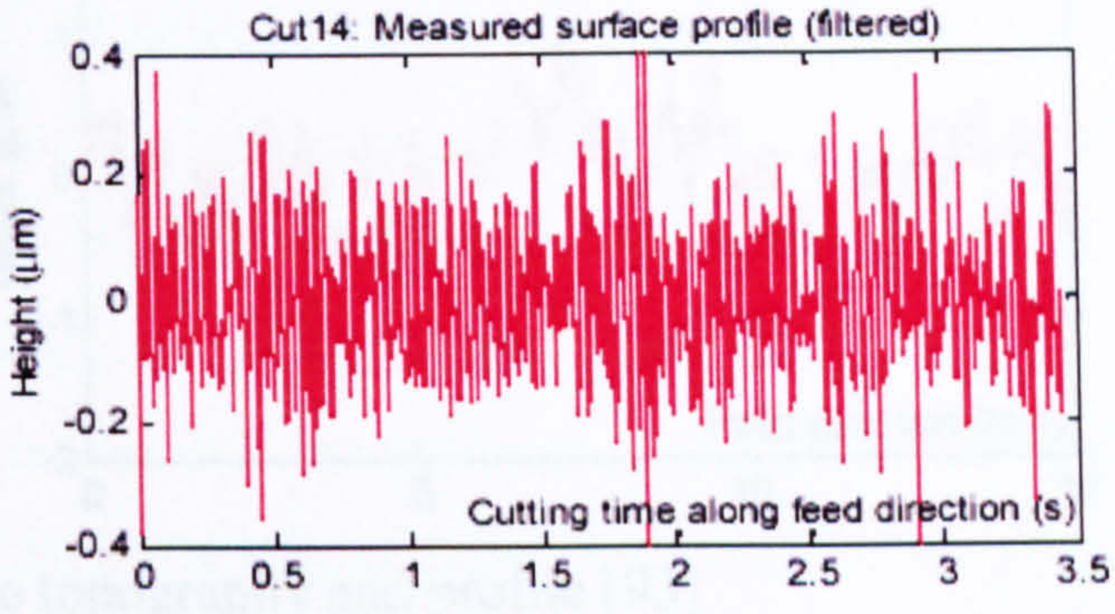

(b) High-pass filtered surface profile

Figure 6.72. Measured surface spectra and profile

The 3D topography result (Figure 6.71(a)) indicates that the cutter run out dominates the surface finish production as shown by the surface height variation perpendicular to the feedrate direction. Figure 6.73 shows the FFT and high pass filtering results of the simulated 2D surface finish respectively. The predicted spindle frequency (SF) agrees to the measured result, but the predicted higher harmonics are less observable in the measured results due to the dominance of the low frequency content (might be caused by cutting system structural modes, non-linear factors in the cutting process or non-homogeneous material property distribution). The high pass filtered results show better correlation although some further work is still required to better show the correlation.

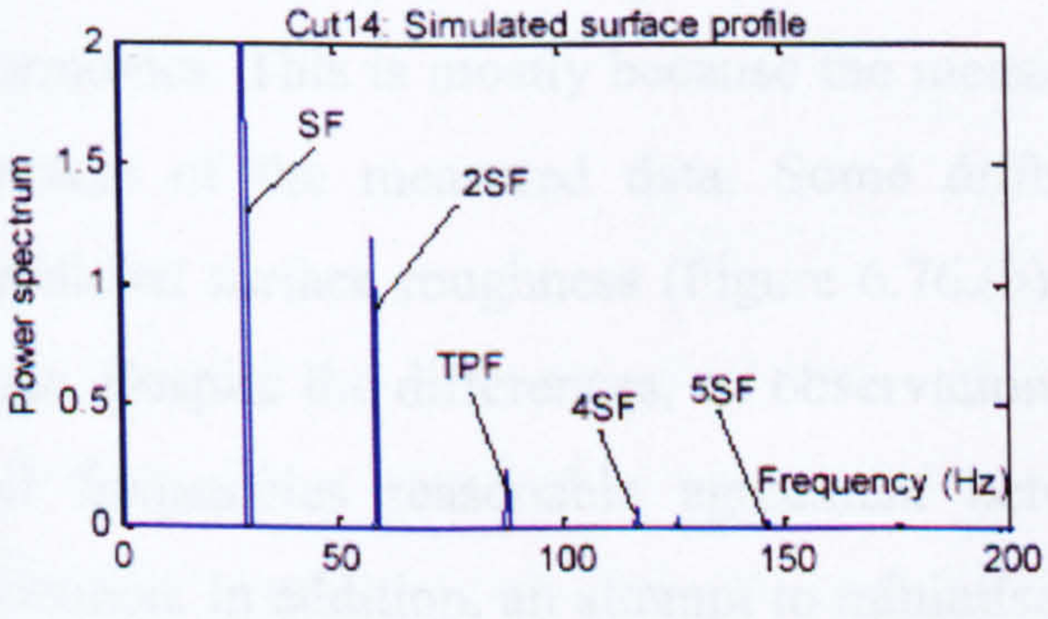

(a) Surface profile frequency spectra

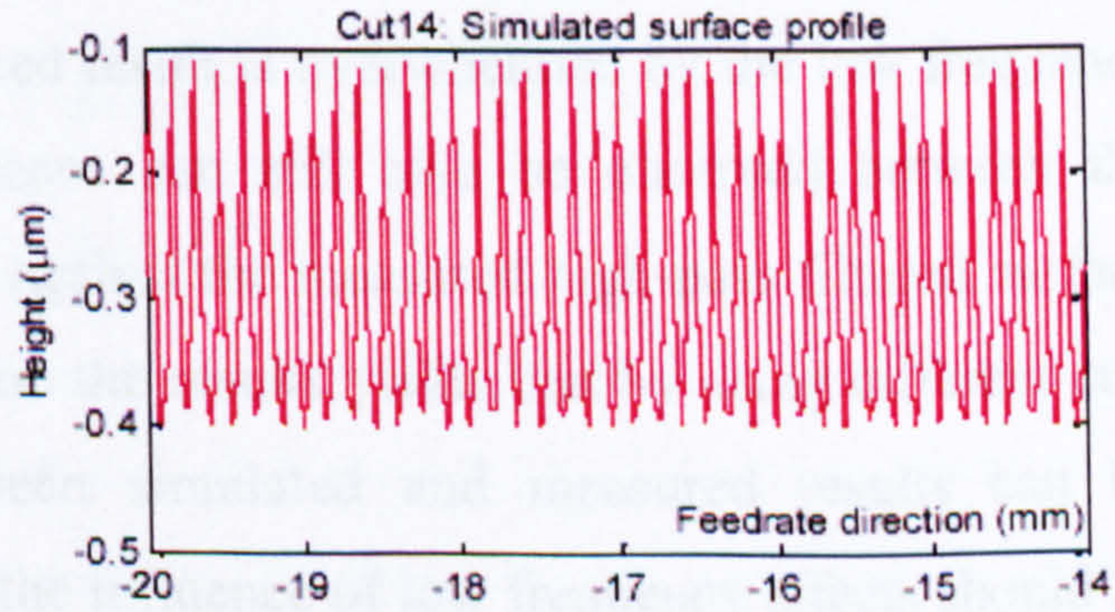

(b) Simulated surface profile

Figure 6.73. Simulated surface spectra and profile

- Case 1: Cut 13

The workpiece surface finish from the cutting trial was measured along the feed path to produce the 3D and 2D surface topography shown in Figure 6.74. Using the same FFT and high pass filter analysis technique as in the previous section, the 2D surface profile and the resulting spectra and high frequency surface roughness can be seen in Figure 6.75(a) and Figure 6.75(b) respectively.

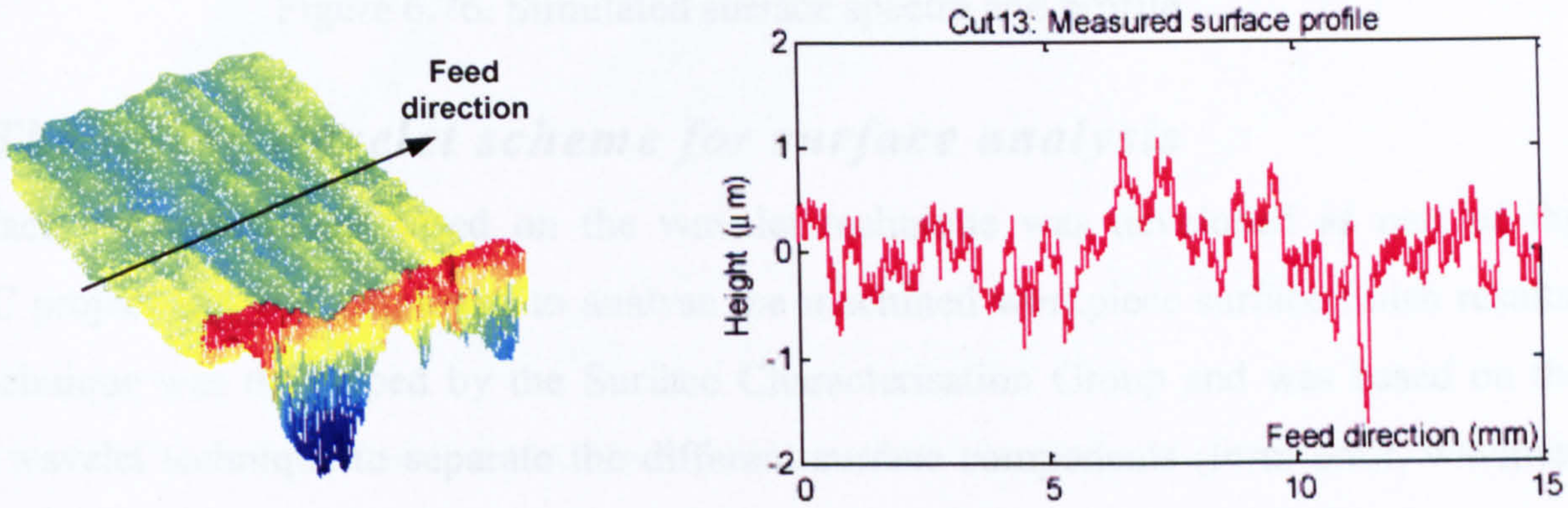

Figure 6.74. Measured surface topography and profile [93]

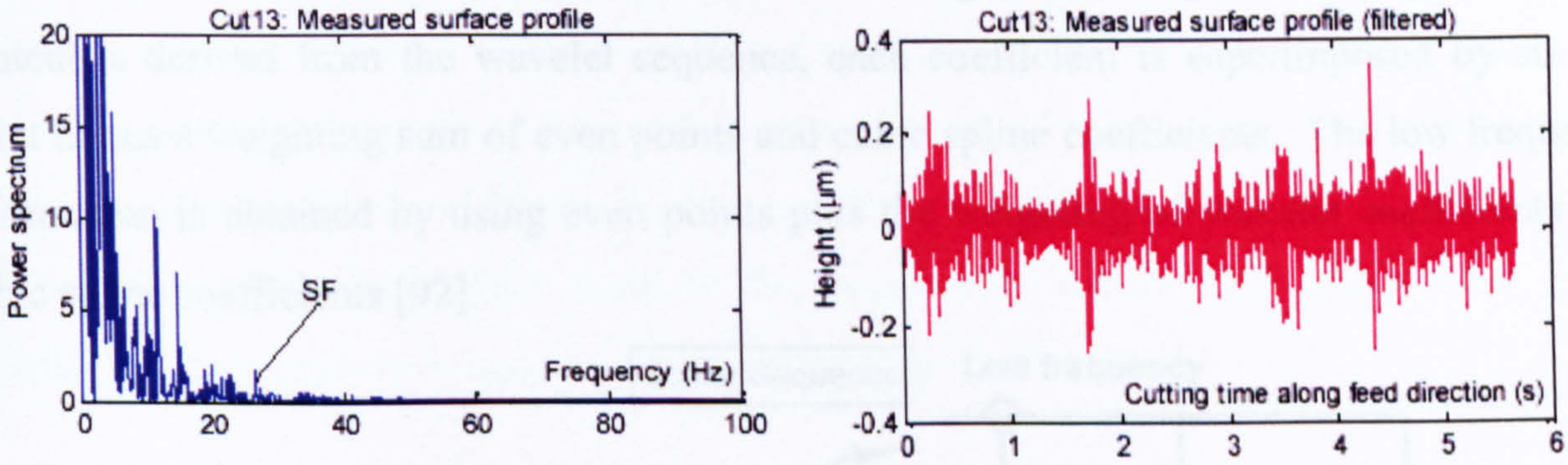

(a) Surface profile frequency spectra (b) High-pass filtered surface profile

Figure 6.75. Measured surface spectra and profile

Similar to the analysis results from the previous case ('Cut 14'), low frequency content still dominates the surface finish. The predicted spindle frequency (SF) shown in Figure 6.76.(b) agrees sufficiently accurately with the measured result but not the predicted higher frequency harmonics. This is mostly because the measured result is overwhelmed by the low frequency content of the measured data. Some difference can still also be observed between the predicted surface roughness (Figure 6.76.(b)) against the measured high-pass filtered surface data. Despite the differences, an observation on the results yields that by using different cut-off frequencies reasonable agreement between simulated and measured results can be obtained. In addition, an attempt to minimise the influence of low frequency effects should be carried out to improve the results further.

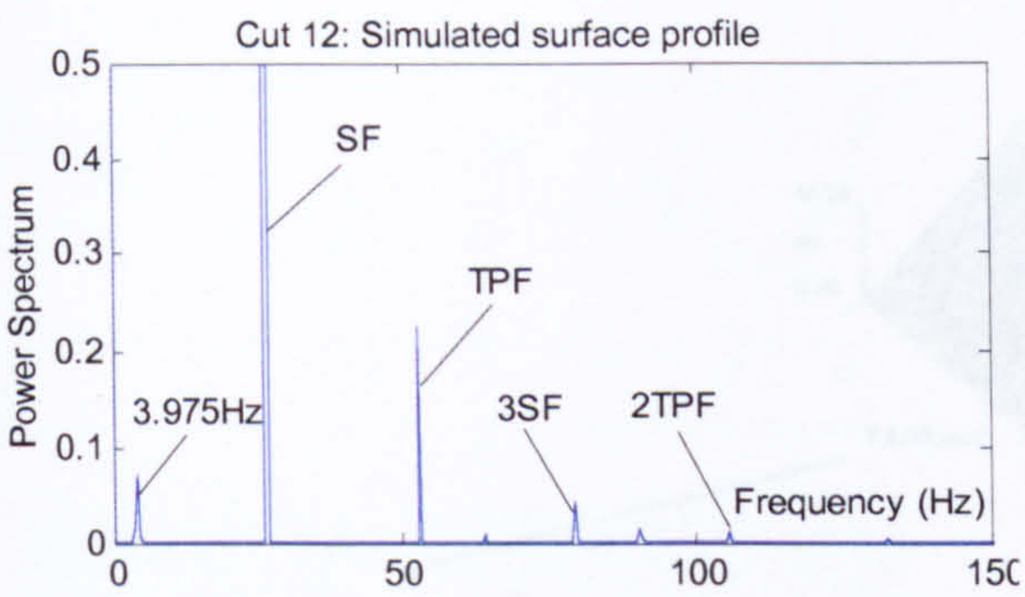

(a) Surface profile frequency spectra

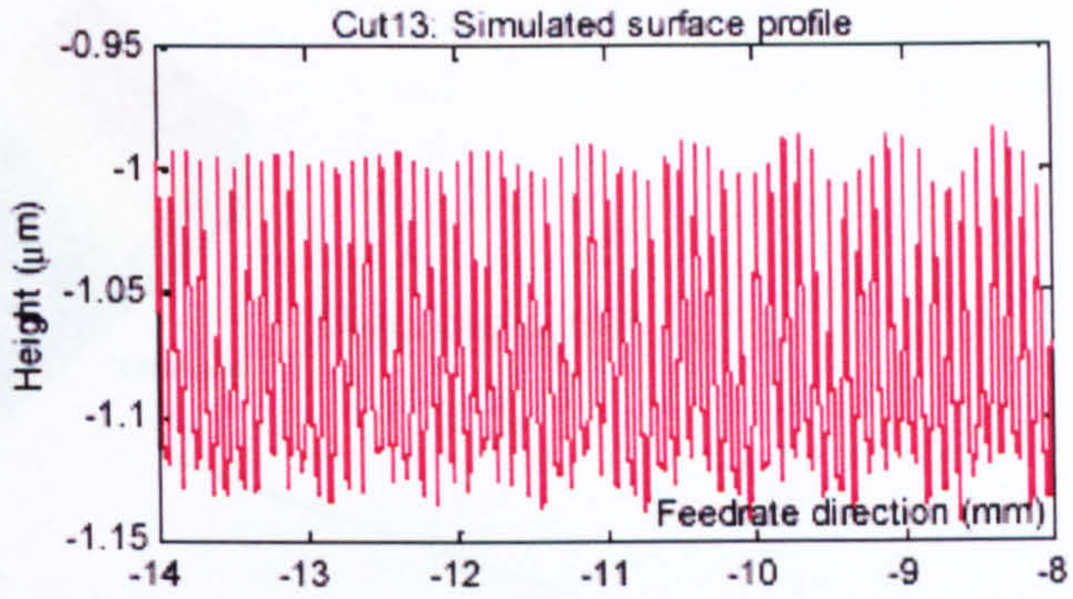

(b) Simulated surface profile

Figure 6.76. Simulated surface spectra and profile

6.6. The lifting wavelet scheme for surface analysis

A surface characterisation based on the wavelet technique was developed as part of the EPSRC project and was employed to analyse the machined workpiece surface finish results. The technique was developed by the Surface Characterisation Group and was based on the lifting wavelet technique to separate the different surface components (form error, waviness and roughness) as seen in Figure 6.77. The lifting wavelet transform divides the measured signal into two 'even' and 'odd' subsets, each containing half the signal. The high frequency content is derived from the wavelet sequence, each coefficient is superimposed by an odd point minus a weighting sum of even points and cubic spline coefficients. The low frequency information is obtained by using even points plus the weighting of Wavelet coefficients and cubic spline coefficients [92].

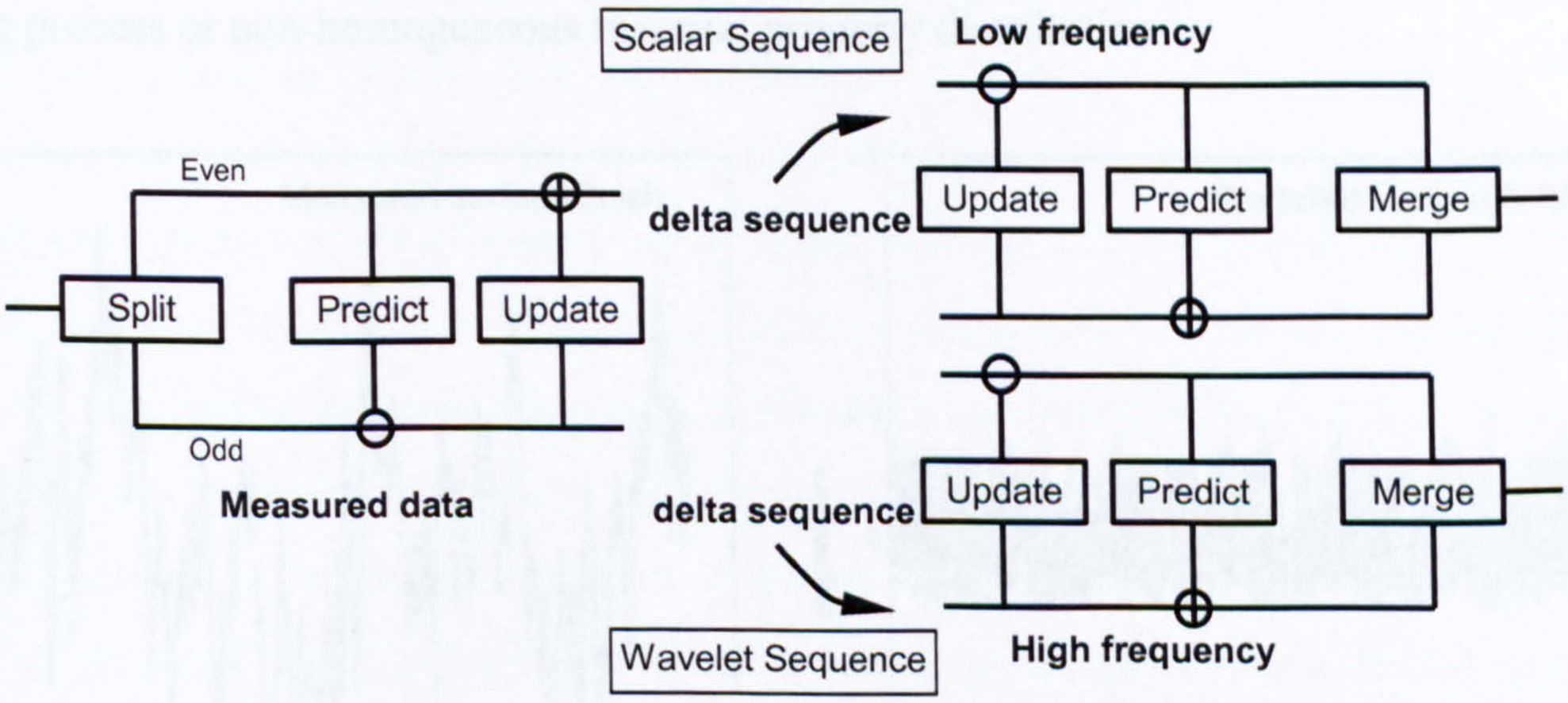

Figure 6.77. The lifting scheme [92]

Using this technique, the measured surface finish can be separated into the form error, waviness and roughness components as illustrated in Figure 6.78. The decomposition of machined surface finish into its components enables the identification and analysis of the factors affecting the machining process.

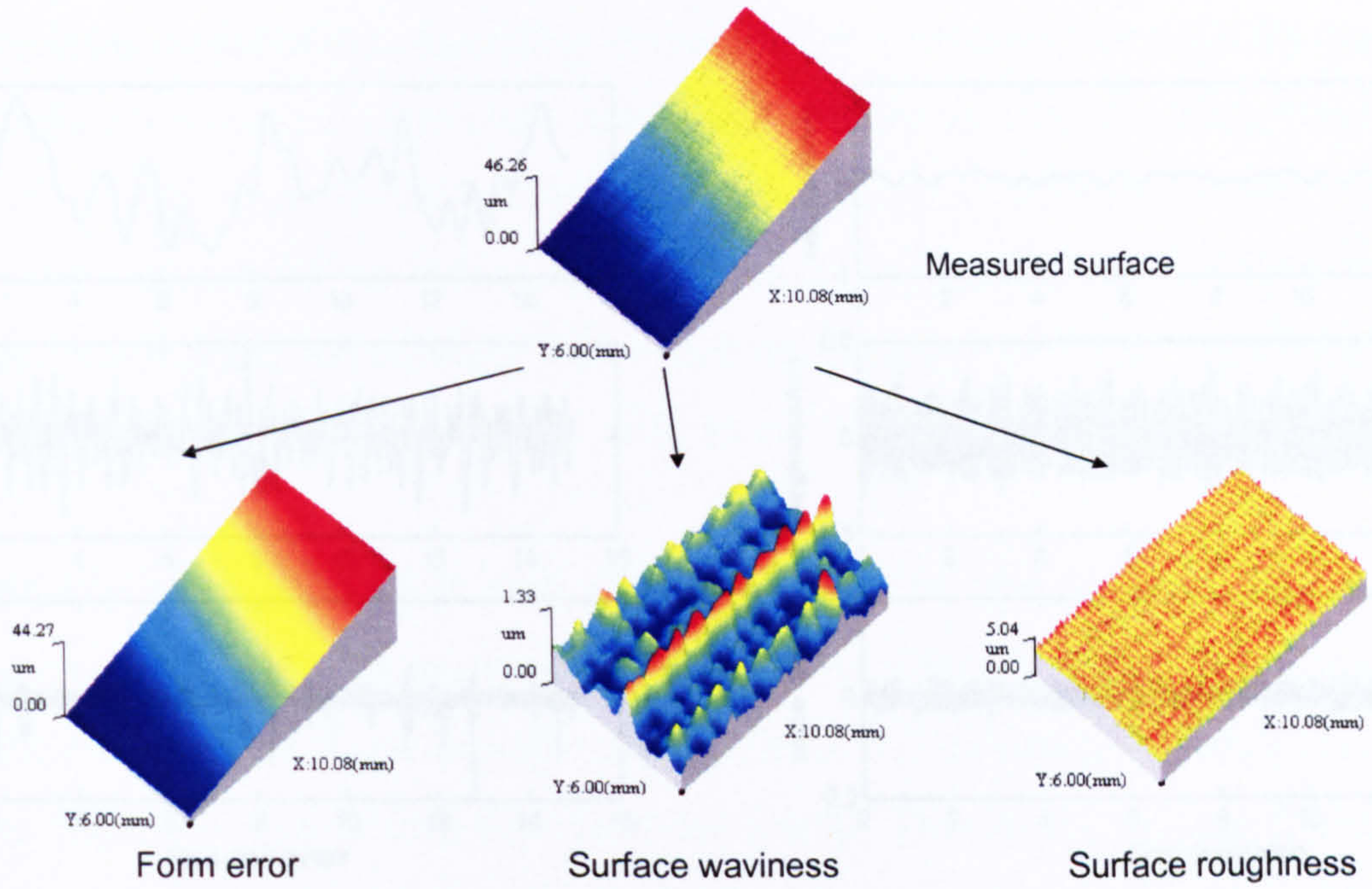

Figure 6.78. Surface component separation [93]

Figure 6.79 shows the measured surface profile against the predicted surface finish by the machining dynamics model for the 'Cut 14' case. The initial impression of the comparison between the two surfaces suggests that there is no or very low correlation between them. However, the application of the wavelet transform on both the measured and predicted data shows that better correlation is achieved in one or more of the surface wavelength band as shown in Figure 6.80. In addition, the low correlation is mainly attributed to the waviness component of the surface which could be due to structural modes, non-linear factors in the cutting process or non-homogeneous material property distribution

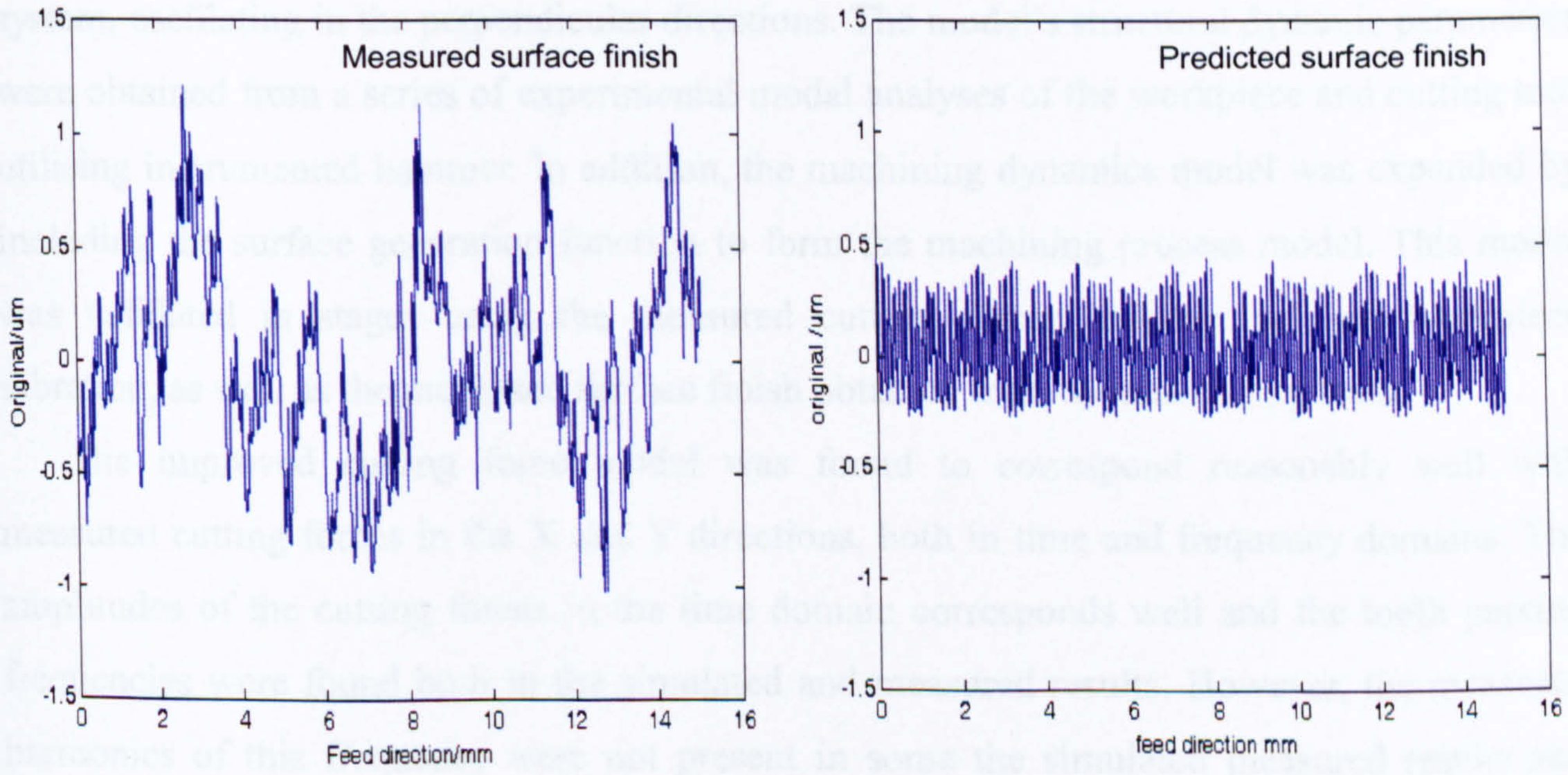

Figure 6.79. Measured against predicted surface finish of 'Cut 14'

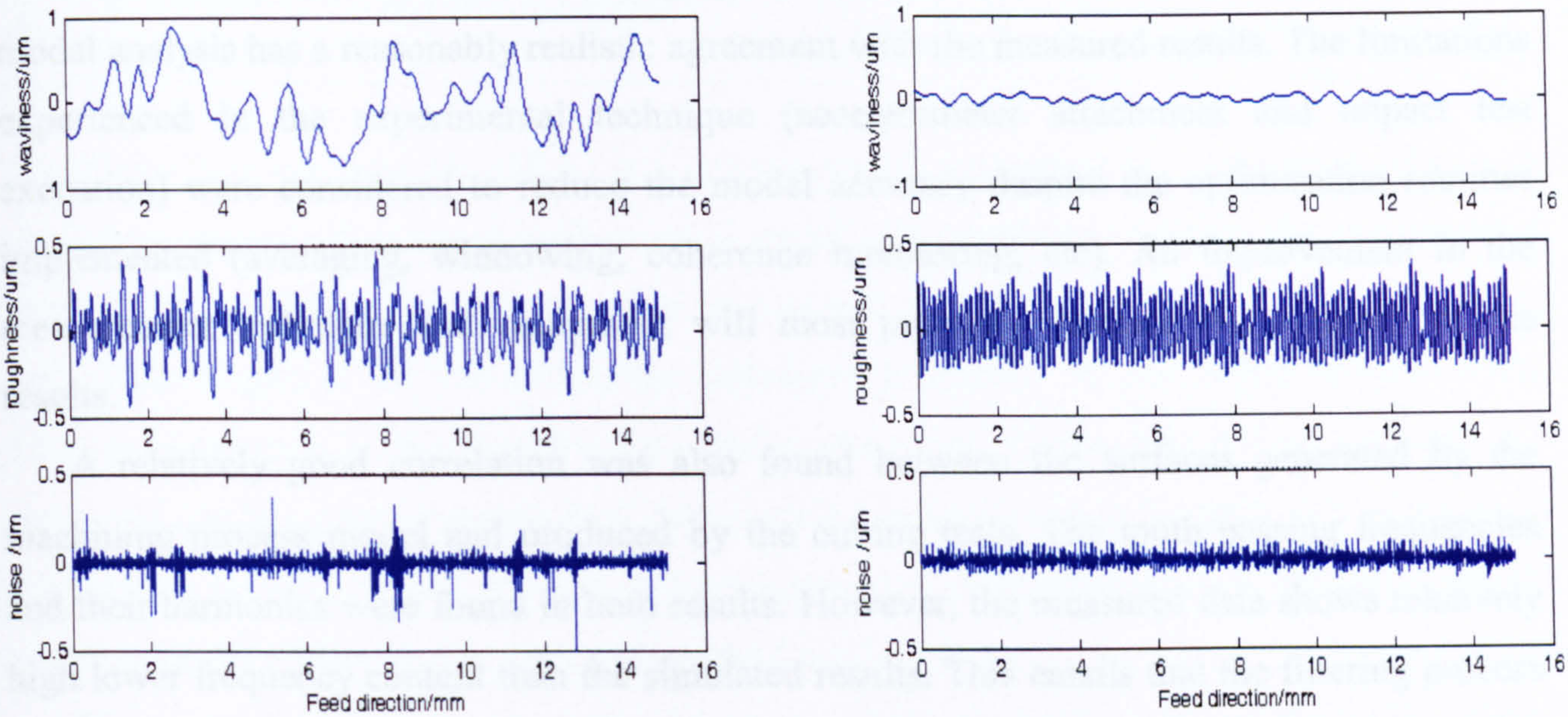

Figure 6.80. Decomposition of surface finish 'Cut 14' into its components

6.7. Conclusions

The development and validation of a machining dynamics model has been presented in this chapter. The model was developed as a combination of the improved dynamic cutting force and workpiece-cutting tool vibration models obtained through experimental modal analysis. The cutting force model was developed based on the oblique cutting theory of a peripheral milling process using helical end-mills and cutter run-out consideration. The workpiece-cutting tool vibration model was represented as two-degree-of-freedom spring-damper system, oscillating in the perpendicular directions. The model's structural dynamic parameters were obtained from a series of experimental modal analyses of the workpiece and cutting tool utilising instrumented hammer. In addition, the machining dynamics model was expanded by including the surface generation function to form the machining process model. This model was validated in stages using the measured cutting forces, cutting tool and workpiece vibration, as well as the machined surface finish obtained from several cutting tests.

The improved cutting force model was found to correspond reasonably well with measured cutting forces in the X and Y directions, both in time and frequency domains. The amplitudes of the cutting forces in the time domain corresponds well and the tooth passing frequencies were found both in the simulated and measured results. However, the measured harmonics of this frequency were not present in some the simulated measured results and further improvement is required.

The vibration model of the machining dynamics model obtained through the experimental modal analysis has a reasonably realistic agreement with the measured results. The limitations experienced in the experimental technique (accelerometer attachment and impact test execution) were considered to reduce the model accuracy despite the optimisation routines implemented (averaging, windowing, coherence monitoring, etc). An improvement in the measurement technique and equipment will most probably increase the accuracy of the results.

A relatively good correlation was also found between the surfaces generated by the machining process model and produced by the cutting tests. The tooth passing frequencies and their harmonics were found in both results. However, the measured data shows relatively high lower frequency content than the simulated results. This entails that the filtering process of the measured data did not remove these frequency contents significantly and further improvement on the algorithm is required.

The following chapter presents the development of the FEA model of the machine structure by interfacing CAE, FEM, and pre-/post-processing software in order to obtain detailed geometric representation whilst still producing accurate analytical results.

Chapter 7. STRUCTURAL DYNAMIC INVESTIGATION USING THE FINITE ELEMENT ANALYSIS

The Finite Element Analysis (FEA) is a computational mechanics technique to develop and simulate a spatially discretised mathematical model of a continuum system using a numerical method. The technique can be applied on various systems, including static, dynamic, thermal, and electromagnetic. In this study, the technique is applied to investigate the structural dynamic properties of the machine tool under study (see Figure 4.1) and to compare the simulated results against the measured data (detailed discussion is in Chapter 4). The resultant information is subsequently utilised to investigate the appropriate passive vibration control solution for the particular structure as discussed in Chapter 8.

The study combines the geometrical accuracy of the physical model developed by Myers [207] and the numerical accuracy of the analysis carried by Holmes [208] in order to develop an improved FEA model of the machine tool. The study extends the physical model (developed using the Pro/ENGINEER [209]) in order that a numerical analysis using the ABAQUS/Standard [210] can be performed accurately. It also includes a benchmark test of the method taken by the analysis of the machine base. Manufacturer-supplied data and direct measurements are both utilised for the development and numerical analysis of the model.

The use of solid modelling software to develop the physical model enables detailed machine geometries such as column and base ribbings to be represented. These elements are normally used to increase the machine's structural stiffness without having to considerably add more mass. The technique also allows non-structural elements with significant mass-effect, such as the Z-axis motor, to be modelled relatively easily.

The selection of ABAQUS/Standard software facilitates parametric studies of the FEA model to be carried out effectively. The software allows a variation in the damping properties of the machine structure, thus a more accurate model can be developed. The simulated results are validated using the modal model obtained using the experimental method (see Chapter 4). They are also compared to the data from the previous investigations to evaluate the accuracy, processing speed, and geometric requirements for obtaining sufficiently accurate data.

The validation process also includes model updating to improve the discrete model accuracy with respect to the measured dynamic properties by progressively reducing the error. One of the most important objectives of the exercise is to minimise the deviation between the actual and manufacturer supplied data of the mechanical elements. Furthermore, an accurate FEA model is required for the successful investigation of the vibration control using the

passive technique. The summary of the overall procedures undertaken in this structural dynamics study (including the system modelling, simulation result validation and model updating) is shown in Figure 7.1.

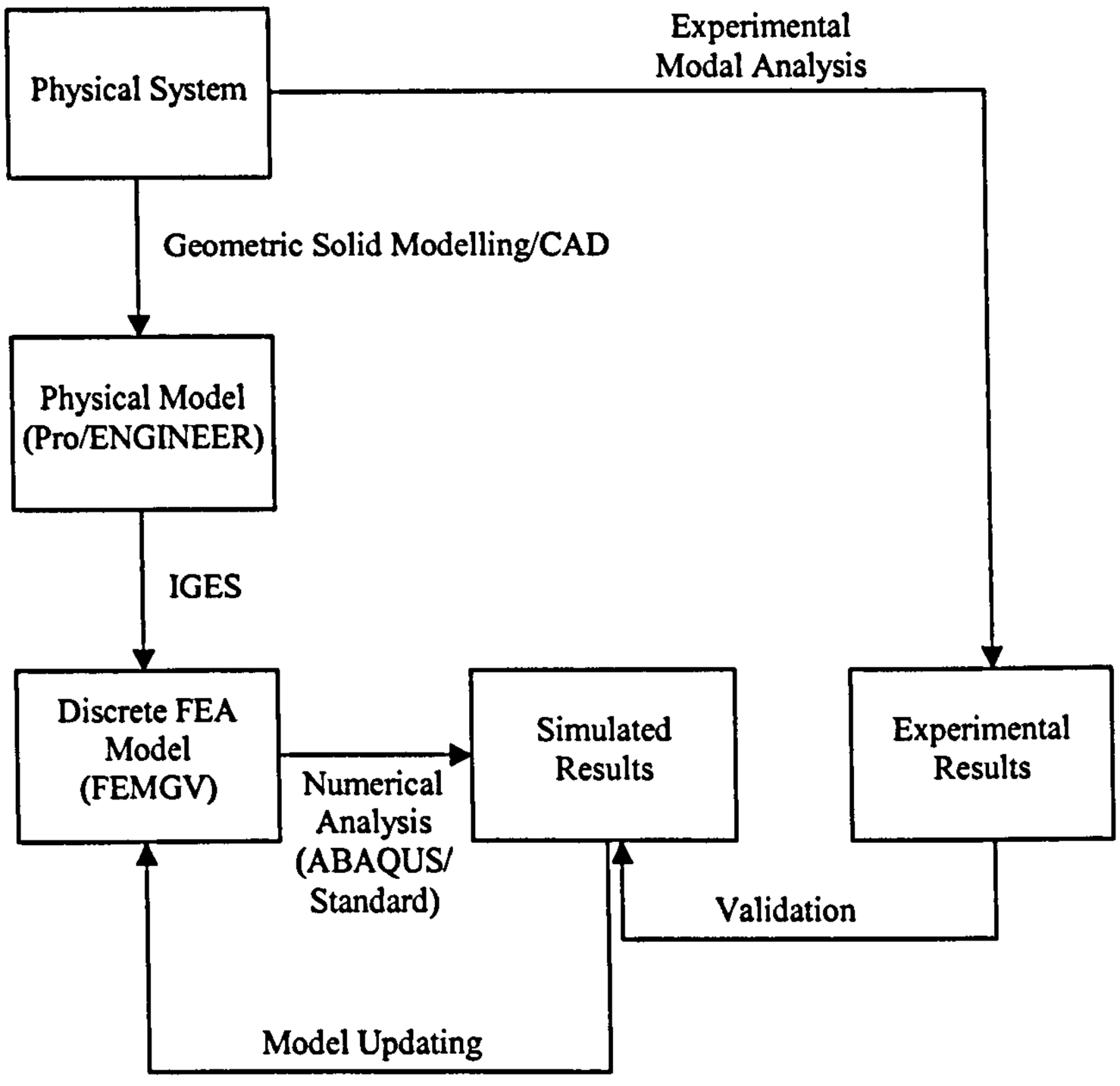

Figure 7.1. Diagram of the structural dynamic investigation through the FEA and experimental methods

7.1. Previous FEA structural dynamic investigation

Holmes [208] approached the physical modelling of the machine geometries by combining mostly two-dimensional finite elements with a small number of solid discrete elements using the FEMGV [211] package (a dedicated FEA pre- and post-processing software). The hollow machine base and column were modelled as second-order S85R plate elements (with eight nodes and five degree of freedom), normally utilised to represent conventional 3D stress/displacement shells. Thin depth and small strain characteristics were assumed, as the transverse shear flexibility was considered negligible. The element thickness variation due to deformation was thus considered insignificant and the in-surface rotation was ignored, resulting in the five degree of freedom. Lower-order reduced integration for the construction of the element stiffness matrix was implemented in the analysis in order to increase the simulation speed and accuracy. This was achieved by disregarding any element distortion and in-plane bending.

The investigation considered that the ballscrews were important due to their vibration transmissibility from one connected element to the other. Thus, the investigation modelled these elements as 2D mass-less beam elements with spring properties (BE2-SPRINGA) to sufficiently accurately represent the axial and radial stiffness between the connected points (nodes). The same technique (with different parameters) was applied to the bearings linking the linear guideways and the moving members (headstock, saddle and table).

The headstock and linear guideways were modelled as solid (continuum) 3D hexahedron (brick) elements with 20 nodes (HE20-C3D20) (see Figure 7.2). These second order elements were selected to model accurately the plasticity behaviour of the selected machine structural members considered to have bending-dominated behaviour. They were also able to represent the stress concentration more effectively and to model problems with simple contact conditions and small element distortion more accurately.

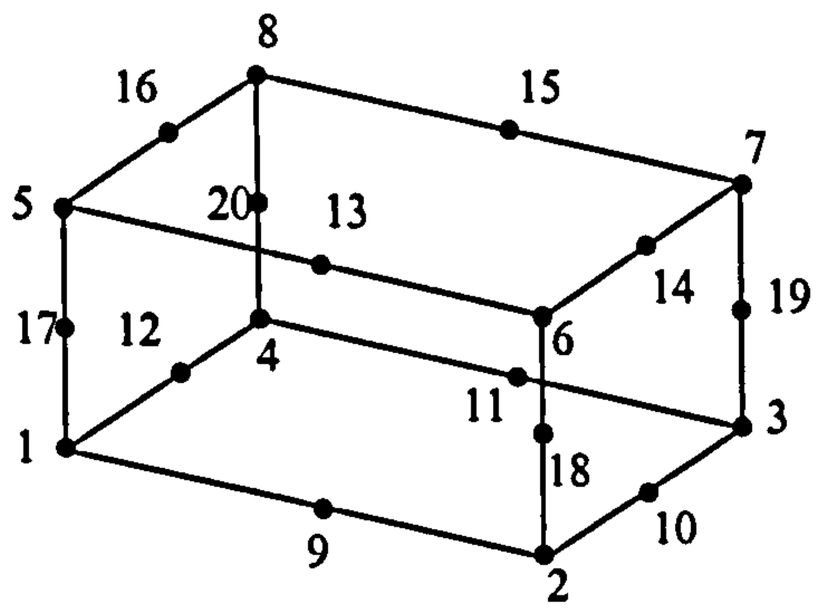

Figure 7.2. Physical representation of the C3D20 element

Figure 7.3.(a) shows the physical model of the machine structure, including the ballscrews, where colours are used to indicate the selected element types. This model was discretised (meshed) using a semi-automatic mode, where the segment number of the body edges was defined manually and then the mesh was generated automatically using the Paving algorithm as introduced by Blacker and Stephenson [212]. This algorithm, also called the advancing front or plastering techniques, initially created the outer mesh based on the edge segments and subsequently discretised the internal area using the density parameter. The process generated a quadrilateral and hexahedral free mesh for the 2D and 3D bodies respectively (see Figure 7.3.(b)).

The quality of the generated mesh influences the accuracy of the numerical analysis and is determined by the shape of the finite elements. It was calculated using the FEMGV's built-in function to measure and average the adherence values of the finite elements to the ideal criteria. These criteria vary from one element type to another and can include several geometric properties, such as the minimum angle, aspect ratio, inner-node positioning and

radius quotient. The built-in function can also produce tabulated results highlighting the non-compliant elements which are useful in assisting further work to improve the mesh quality. This can normally be performed by modifying the number of segments on each edge/line by generating finer and higher quality elements.

The input deck for the ABAQUS/Standard software was generated after the elements were assigned with the required structural properties and simulation conditions. The file generated contained the model definition and the numerical analysis method, which are represented by the model data (node geometric definitions, kinematic constraints, element types, material properties, etc.) and the history data (response type, loading, boundary conditions, etc.) respectively. The FEA numerical analysis of the model was performed using the subspace eigensolver numerical method. It took 8 minutes 19 seconds for the solutions to converge and the first five results are shown in Table 7.1

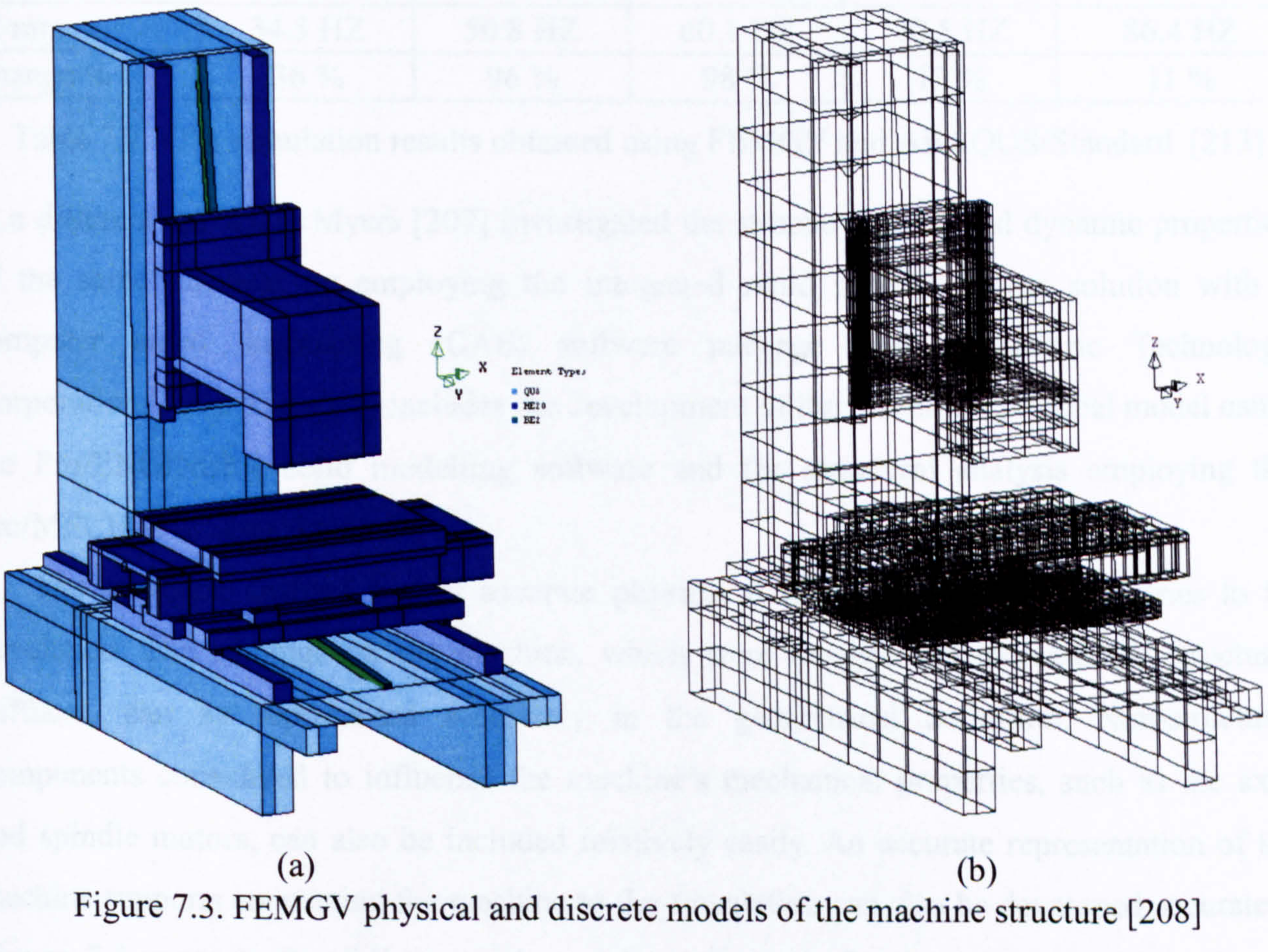

(a) (b)

Figure 7.3. FEMGV physical and discrete models of the machine structure [208]

Mode	**Natural Frequencies** (Hz)
1	19.1
2	20.7
3	24.5
4	46.3
5	59.7

Table 7.1. FEA simulation results for the machine structure [208]

The results of this investigation vary quite significantly with the measured results as presented in Chapter 4, especially in the suspended shaker configuration shown in Table 4.3.(a). The obtained results indicate that the lowest mode occurs at about 19 Hz, whereas the measurement results show that it occurs at a higher frequency of about 28 Hz.

To address this concern, Xu et. al [213] performed a parameter exercise to improve the FEA model by varying the machine column material and thickness. The column material was changed from cast iron to steel and the thickness was varied from 6 to 12 mm. Table 7.2 shows the results from the investigation indicating an better correlation between the new results and measured data.

	Natural Frequencies				
Wall Thickness	Mode 1	Mode 2	Mode 3	Mode 4	Mode 5
6 mm	25.4 HZ	25.9 HZ	30.4 HZ	62.3 HZ	77.6 HZ
9 mm	30.5 HZ	39.8 HZ	45.2 HZ	67.2 HZ	83.5 HZ
12 mm	34.5 HZ	50.8 HZ	60.1 HZ	70.5 HZ	86.4 HZ
Change %	36 %	96 %	98 %	13 %	11 %

Table 7.2. FEA simulation results obtained using FEMGV and ABAQUS/Standard [213]

In a different approach, Myers [207] investigated the structural static and dynamic properties of the same machine by employing the integrated rapid product design solution with a computer aided engineering (CAE) software package from Parametric Technology Corporation [209]. The study includes the development of the machine's physical model using the Pro/ENGINEER solid modelling software and the structural analysis employing the Pro/MECHANICA package.

The approach enabled a very accurate physical model of machine's geometries to be developed. The ribbings on the machine, which were designed to increase the structural stiffness, can be represented accurately in the geometrical definition. Non-structural components considered to influence the machine's mechanical properties, such as the axes and spindle motors, can also be included relatively easily. An accurate representation of the machine supports connecting the machine to the foundation can also be developed accurately. Figure 7.4 presents the full physical model constructed showing the very thorough and accurate representations of the machine structure.

The Pro/MECHANICA software utilised for the FEA analysis automatically determined the element type selection and the discretisation of the machine physical model. This feature minimises the user intervention during the numerical analysis process which means increased automation and faster analysis. The user is still required to specify the structural material

types and boundary conditions, although the time required for the solution converge is relatively longer from the previous method due to the large number of discrete elements generated from the fully automatic meshing process. The user does not have any control either over the structural damping properties resulting in less accurate simulation results.

The study assumed that the moving mechanical parts, i.e. the column, table and saddle, were attached rigidly onto the guideways. This affected the simulation results in which the stiffness of the structure were much higher than the actual values. Consequently, this resulted in higher than the actual values of the natural frequencies as indicated in Table 7.3. The investigation shows promising prospects for an accurate FEA analysis, although further improvements are required in order to more closely model the machine's behaviour.

Mode	**Natural Frequencies** (Hz)
1	47.8
2	53.2
3	81.8

Table 7.3. FEA simulation results obtained using the Pro/ENGINEER suite [207]

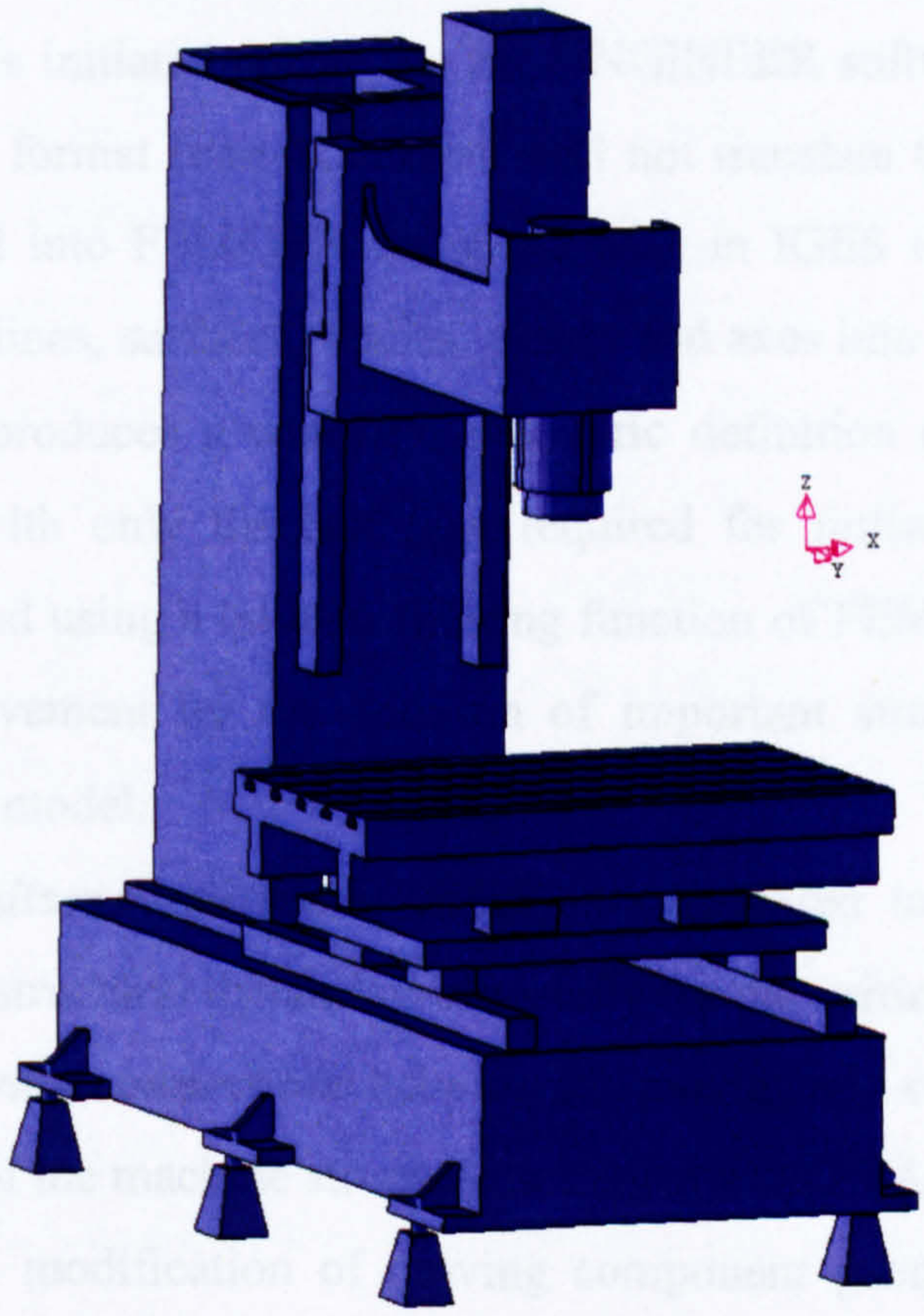

Figure 7.4. View of the complete Cincinnati machine structure

7.2. Physical model development

The previous studies show that the solid modelling software can offer very detailed geometries, whereas a dedicated FEA package is more flexible and can yield higher accuracy.

The lack of details in the connecting elements between the moving parts and the guideways of the FEA model developed using the CAE software package is considered as the major obstacles in achieving high accuracy simulation results. On the other hand, reasonably accurate simulation results can be achieved by dedicated FEA software using simplified physical models. Therefore, this investigation attempts to combine the aforementioned methods in order to obtain an optimum FEA solution on the machine's structural dynamic properties.

This particular part of the investigation carries the Pro/ENGINEER study further by transferring and refining the physical model into the FEMGV subroutine known as FEMGEN (Model Generator). The model is transferred via a common ASCII file format known as the Initial Graphics Exchange Specification (IGES) version 5.3 [214] enabling the translations of both geometrical and non-geometrical data, such as bodies, points, lines, surfaces and axes between the applications. The geometric model is then enhanced, pre-processed and conditioned within FEMGEN to provide a very accurate physical model while retaining the advantages of the FEA numerical method.

The transfer process is initiated within the Pro/ENGINEER software by selecting the 3D solid export to the IGES format (non-3D export will not translate the geometries properly). The file is then imported into FEMGEN using the built-in IGES translator to interpret the definitions of the points, lines, surfaces, bodies, planes and axes into the native binary format. The translation process produces a complex geometric definition of one-, two- and three-dimensional elements, with only the last type required for further processing. The extra elements are then removed using a built-in filtering function of FEMGEN. The filtered result is now ready for improvement by the addition of important structural elements and the adjustment of the current model:

- Modelling of the ***ballscrew stiffness***, which is considered to contribute significantly towards the machine structural dynamics, especially for the vertical axis
- Modelling of the ***bearing connections*** between the moving and static components
- ***Geometric changes*** of the machine structure to improve the FEA mesh quality
- Geometric definition modification of moving component geometries (headstock, table, saddle) to comply with the ***experimental configuration***

The modelling of the bearings and ballscrew elements are performed by using 2D mass-less beam FEA elements with spring properties to represent their vibration transmissibility from one connected element to the others. These FEA elements are also selected to produce an accurate representation of the axial and radial stiffness between the connected points. Each

connection/contact pair between one bearing unit and a guideway is represented by a beam element producing two beam elements per bearing unit (see Figure 7.5). The ballscrews are modelled as pair of beam elements between the nut and two points on the machine structure (see Figure 7.6).

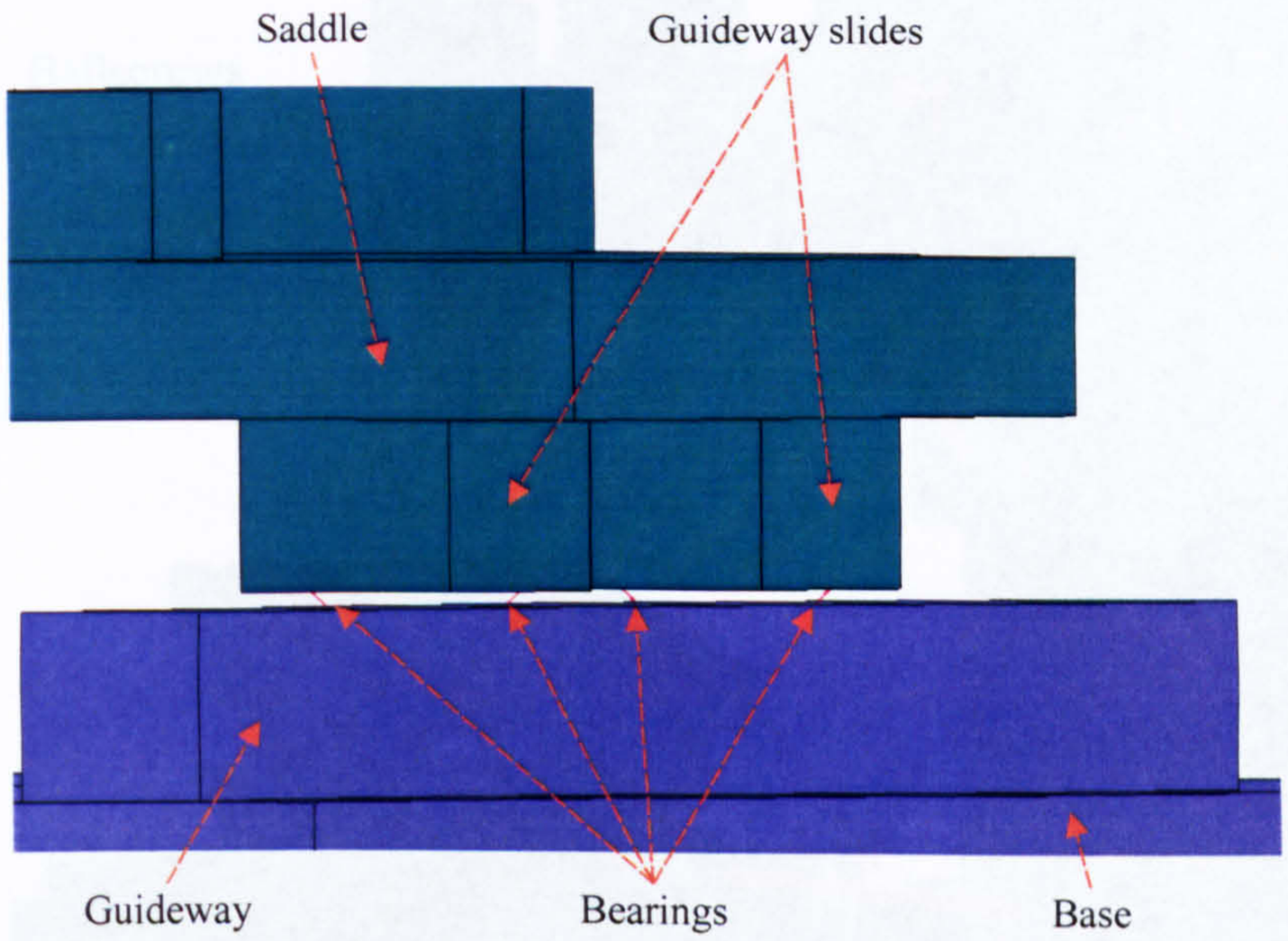

Figure 7.5. Physical modelling of the guideway bearings

The structural configuration of the machine column imported from Pro/ENGINEER has very small vertical gaps on the edges of the rear column surface (designed to be welded during the assembly process) (see Figure 7.7.(a)). These cavities generated problems in the discretisation process as the ratio between their heights and widths are very large, thus requires extremely fine mesh. With the default condition, the mesh quality is greatly degraded due to presence of a large numbers of skewed FEA elements. To overcome this, the gaps are filled up by extending and merging the neighbouring column materials (see Figure 7.7.(b)). This modification does not deviate the simulation process from representing the real system because these gaps are, in actual, filled in with welding material.

The geometric positions of some moving elements in the imported physical model are different from when the structural analysis was carried out experimentally (see Chapter 4). Hence, the physical model is modified to conform to the experimental geometric definitions in order to enable the FEA simulation result validation. For instance, the model's headstock position (measured between the worktable and spindle head base surfaces) is 250 mm compared to the experimental position of 300 mm. Thus, all points, lines and solids in the headstock are moved by 25 mm in the Z+ direction, including the guideway bearings, spindle assembly and motor geometries. Similar modifications are performed on positions of the table, saddle, and associated bearings.

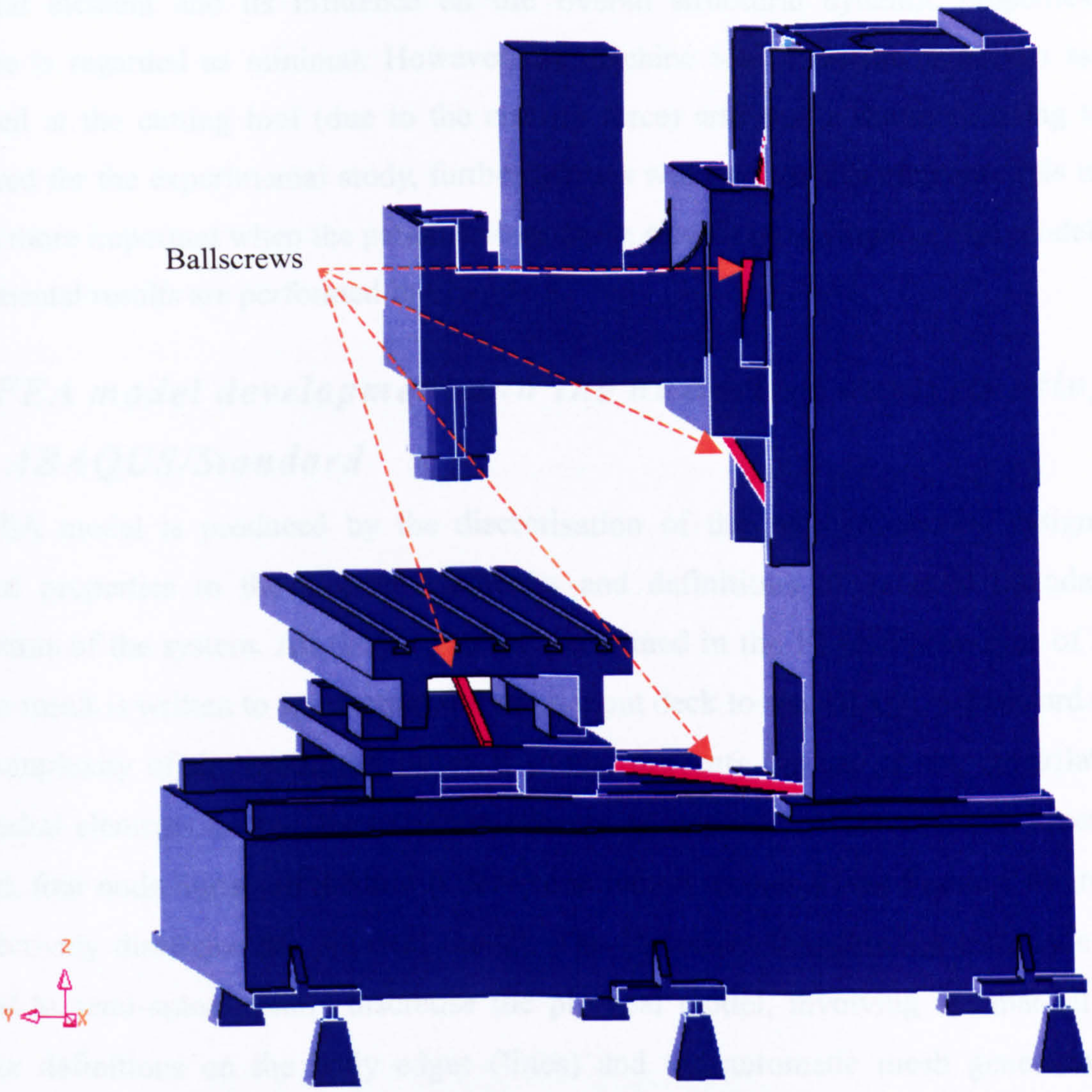

Figure 7.6. Physical modelling of the ballscrews

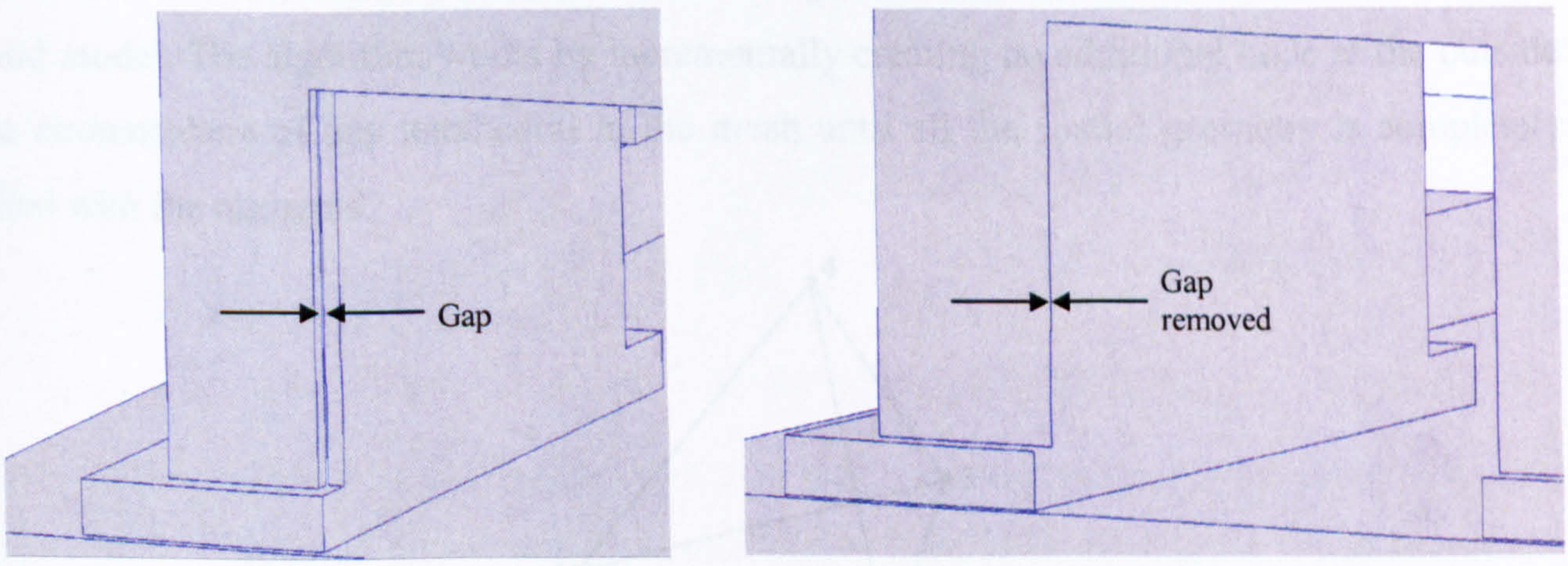

(a) (b)

Figure 7.7. Column gap modification on the physical model

The full physical model of the machine structure after all the factors mentioned above are implemented is shown on Figure 7.4 and employed as the basis for the development of the FEA model. The model does not include the cutting tool because it is considered as a non-

structural element and its influence on the overall structural dynamic properties of the machine is regarded as minimal. However, as machine tool vibration is known as mostly produced at the cutting tool (due to the cutting force) and that a dummy cutting tool was employed for the experimental study, further studies will include this element. This inclusion is even more important when the parametric exercise studies involving the FEA model and the experimental results are performed in Chapter 8.

7.3. FEA model development and the numerical analysis using ABAQUS/Standard

The FEA model is produced by the discretisation of the physical model, assignment of material properties to the discrete elements, and definitions of external boundaries and constraints of the system. All these steps are performed in the FEMGEN routine of FEMGV and the result is written to an external file as an input deck to the ABAQUS/Standard package. The complexity of the machine's physical model prevents the use of the quadrilateral and hexahedral elements for the discretisation process as employed in the previous investigation. Instead, four node linear tetrahedron (C3D4) continuum elements (see Figure 7.8) are utilised to effectively discretise the physical model. The Delaunay triangulation technique [215] is utilised to semi-automatically discretise the physical model, involving the manual segment number definitions on the body edges (lines) and the automatic mesh generation by the software. The automatic algorithm initially creates two-dimensional meshes on surrounding surfaces before three-dimensional mesh containing the tetrahedral elements are formed for the solid model. The algorithm works by incrementally creating an additional node at the outside the circumsphere of any tetrahedral in the mesh until all the spatial geometry is completely filled with the elements.

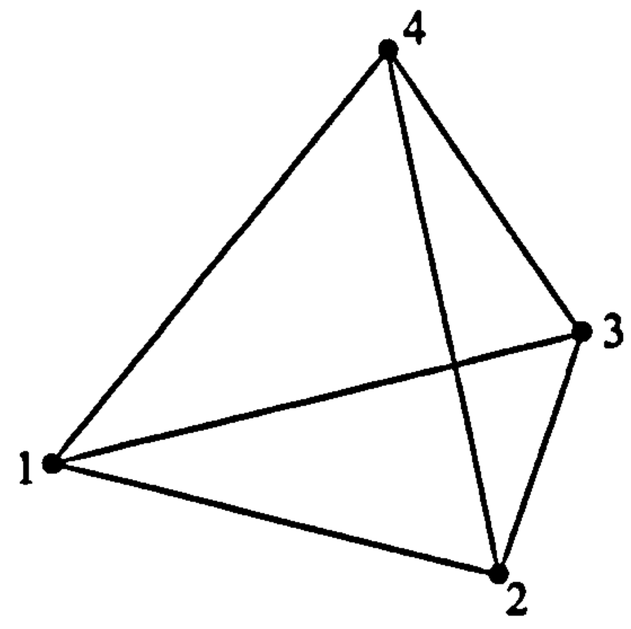

Figure 7.8. Physical representation of the C3D4 element

The ratio of the machine element's length and thickness is relatively high which entails that large numbers of divisions on the longer edges are required in order to obtain high quality

finite elements. This requirement consequently results in the generation of a large number of finite elements which necessitates longer computational time. However, this potential drawback is minimised by the use of high performance computing resources. The increased accuracy of the simulation results also outweighs heavily the time and resource costs. Nevertheless, an initial investigation is carried out to benchmark the analytical route taken by performing the FEA analysis on the machine base, where mixed element geometries are present but with less complexity (see Figure 7.9).

The discretisation of the benchmark physical model produces 126039 tetrahedral elements with 34280 nodes and 102840 variables. The overall quality of the generated finite elements (checked using the standard criteria: minimum angle, aspect ratio, inner-node positioning and radius quotient) is found to be within tolerable limit (97% of the elements satisfy the requirements). The base material is specified as carbon iron with Young's modulus of 100 kN/m, Poisson's ratio of 0.26 and density of 7×10^{-7} kg/m^3. The machine base's boundary conditions are defined such that it is considered as rigidly attached to the ground on all of the supporting legs. An input deck is then generated for the numerical analysis using the ABAQUS/Standard software.

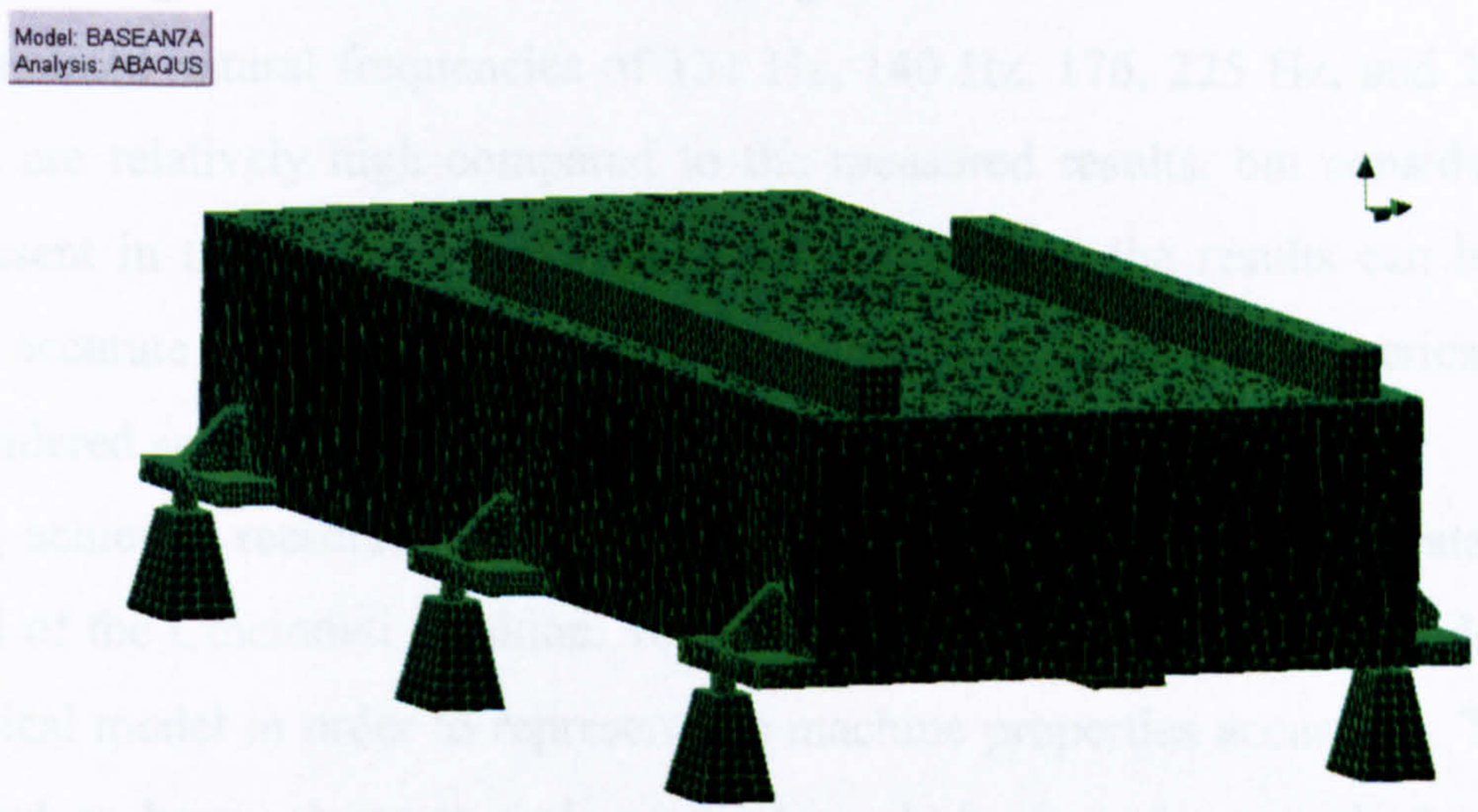

Figure 7.9. Discrete model for the machine base

The subspace eigensolver method is selected as the numerical method to solve the generated FEA model in order to obtain optimised use of the computational resources and reasonable tolerance to minor non-linearities. This solver presents the dynamics of the system as an eigenvalue problem and derives the solution from the linear perturbation of the equilibrium equation:

$$\left(\mu^2\mathbf{M} + \mu\mathbf{C} + \mathbf{K}\right)\boldsymbol{\psi} = 0 \tag{7.1}$$

The eigenvalues, and thus the natural frequencies, are calculated by assuming that the stiffness matrix is symmetric with negligible damping values. Equation (7.1) can therefore be represented in a simplified form as:

$$\left(-\omega^2\mathbf{M}+\mathbf{K}\right)\psi=0 \tag{7.2}$$

where

$$\mu=i\omega \tag{7.3}$$

Based on the aforementioned equations, a numerical iteration is carried out to find a solution for a small set of base vectors (a subspace). This solution is subsequently utilised to obtain the structural space containing the lowest eigenvectors which define the mode shapes. The default dimension of the subspace vectors (m) is defined using equation (7.4) where p is the number of eigenvectors requested.

$$m=\min(2p,\,p+8) \tag{7.4}$$

The numerical analysis is performed on a personal computer (PC) with a single Pentium 4 processor running at 1.5 GHz, 5 GB free hard drive space and 256 MB SDRAM, running Windows 2000 operating system service pack 4. Utilising the default ABAQUS/Standard environment configuration, a numerical convergence is obtained in 40 minutes 20 seconds yielding simulated natural frequencies of 131 Hz, 140 Hz, 176, 225 Hz, and 280 Hz. These frequencies are relatively high compared to the measured results, but considering that less mass is present in the structure and higher stiffness values, the results can be regarded as sufficiently accurate for the given structure. The time required for the numerical convergence is also considered as acceptable for the given model complexity.

Having achieved reasonable benchmark results, an input deck is generated for the full FEA model of the Cincinnati machine. Table 7.4 lists the structural property details attached to the physical model in order to represent the machine properties accurately. The ballscrews are modelled as beam elements and assumed as shafts in order to calculate the stiffness values. The bearing elements are modelled as spring connectors using the manufacturer-supplied stiffness values.

The boundary conditions for the FEA model are defined as the same as those for the benchmark test, i.e. rigid attachments of the machine leg surfaces to the infinitely stiff ground. The physical model discretisation using the semi-automatic method generates 469864 tetrahedral elements and 128554 nodes. These elements are also benchmarked against the ideal element criteria, but with an additional requirement for radius ratio (RADRAT), and approximately 96.1 % of them are found to fully satisfy the ideal conditions. Figure 7.10

shows the colour-coded discretised FEA model for the complete machine structure, illustrating the differing finite element qualities.

Machine Element	Material	Young's Modulus	Poisson's Ratio	Density
Base (inc. supports)	Cast Iron	1×10^{5} Nm^{-2}	0.26	7×10^{-9} kgm^{-3}
Table	Cast Iron	1×10^{5} Nm^{-2}	0.26	7×10^{-9} kgm^{-3}
Saddle	Cast Iron	1×10^{5} Nm^{-2}	0.26	7×10^{-9} kgm^{-3}
Column	Cast Iron	1×10^{5} Nm^{-2}	0.26	7×10^{-9} kgm^{-3}
Spindle Motor	Cast Iron	1×10^{5} Nm^{-2}	0.26	7×10^{-9} kgm^{-3}
Spindle Unit	Cast Iron	1×10^{5} Nm^{-2}	0.26	7×10^{-9} kgm^{-3}
Cutting Tool	Stainless Steel	2×10^{5} Nm^{-2}	0.29	7.9×10^{-9} kgm^{-3}
Ballscrews	Mass less spring	1.95×10^{5}		
X-Axis Bearings	Mass less spring	4.25×10^{5}		
Y-Axis Bearings	Mass less spring	4.91×10^{5}		
Z-Axis Bearings	Mass less spring	5.30×10^{5}		

Table 7.4. Material properties assigned for the machine tool elements

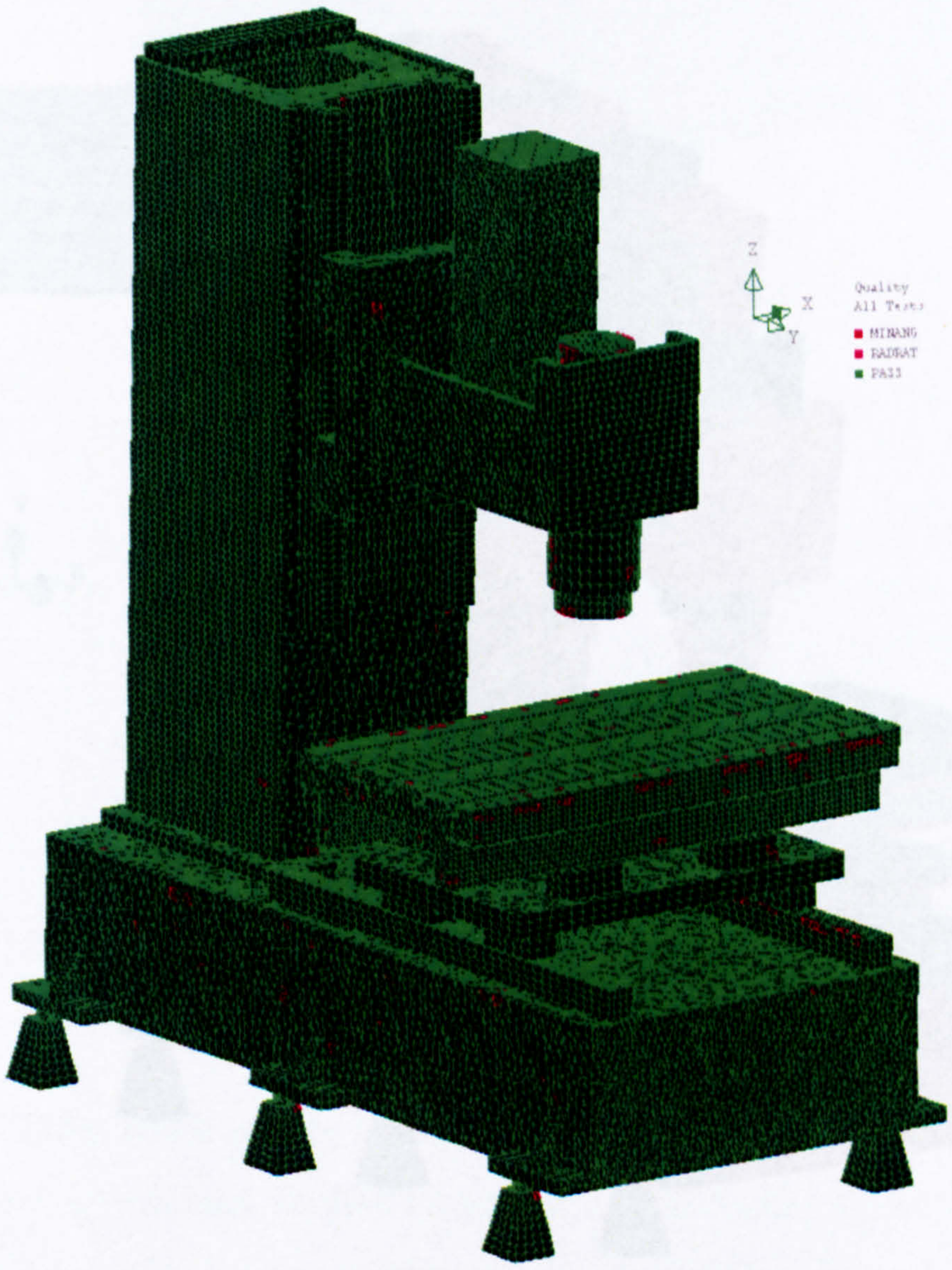

Figure 7.10. Discrete FEA model of the machine structure

The subspace eigensolver numerical analysis (the same as the benchmark test) is employed to find the solutions. The analysis is performed on a dedicated PC with a single Pentium IV processor running at 3 GHz supported by 1 GB of Dual Data Rate (DDR) SDRAM with 3 GB of free space. The ABAQUS/Standard environment configuration is modified in order to cope with the increased model complexity, both for the initial model check and the numerical analysis carried out by the software. The 'pre_memory' parameter is modified to 512 MB, whereas the 'standard_memory' value is increased to 931 MB.

The numerical convergence is reached after approximately 3.85 hours and the first ten simulated modes can be seen in Table 7.5. The first mode shape is represented by the column bending motion in the YZ plane as seen in Figure 7.11. Further analysis of the mode shape shows that the maximum displacement occurs at the spindle motor top (see Figure 7.12). The minimum displacement is also indicated in the figure (occurs at the bottom surface of the machine supports/legs) where the constraint boundaries are defined. The full results of the mode shape motions are summarised in Table 7.5.

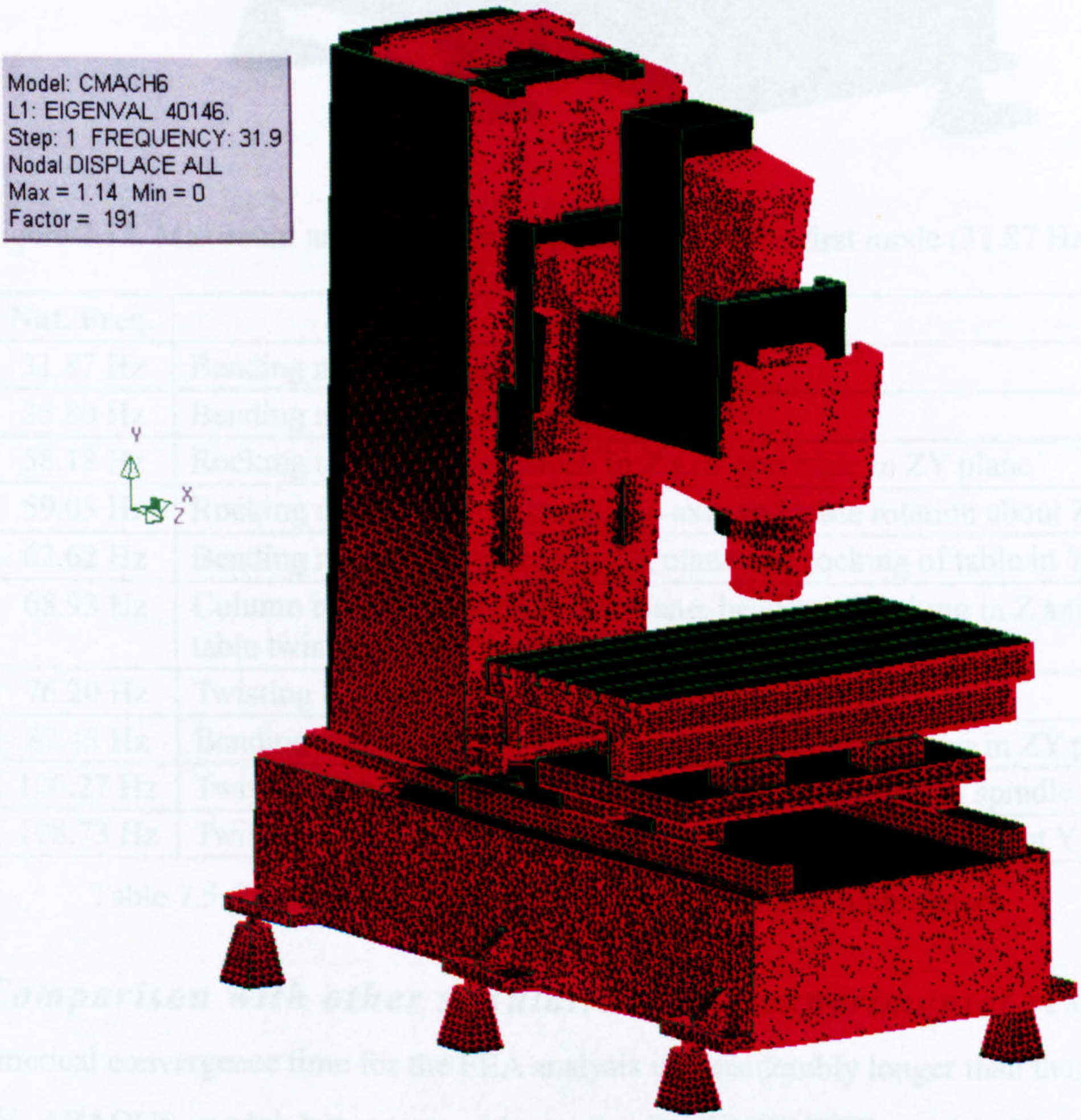

Figure 7.11. Mode shape of the first simulated natural frequency (31.87 Hz)

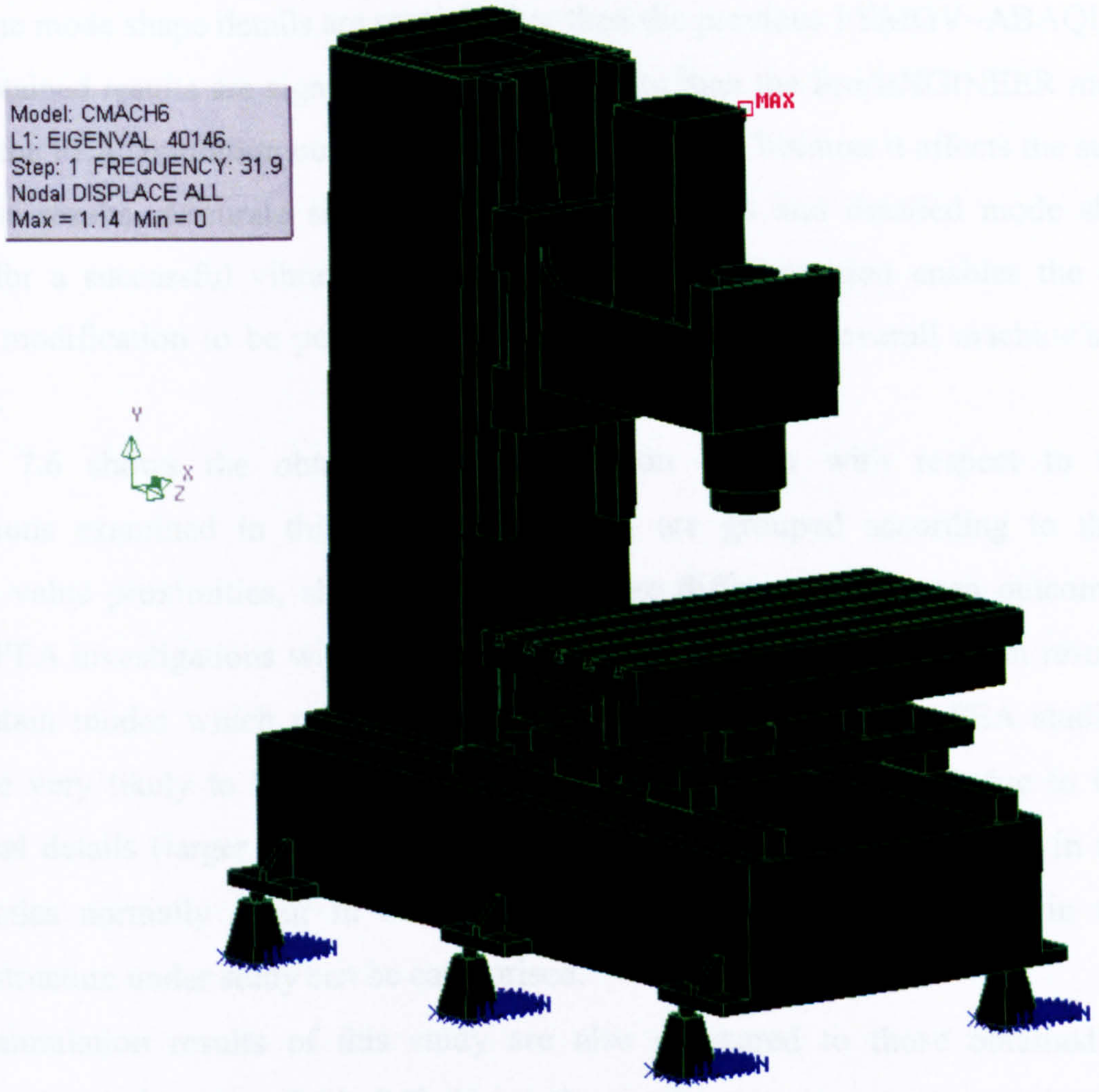

Figure 7.12. Maximum and minimum displacements of the first mode (31.87 Hz)

Mode	Nat. Freq.	Mode Shape
1	31.87 Hz	Bending motion of column in ZY plane
2	35.80 Hz	Bending motion of column in ZX plane
3	58.18 Hz	Rocking motion of headstock in Z axis and table in ZY plane
4	59.03 Hz	Rocking motion of headstock in Z axis and table rotation about Z axis
5	62.62 Hz	Bending motion of column in ZX plane and rocking of table in Y axis
6	68.93 Hz	Column bending motion in ZY plane, headstock rocking in Z axis, table twisting about Y axis
7	76.20 Hz	Twisting between column and headstock vertically
8	87.48 Hz	Bending motion of column and rocking of spindle motor in ZY plane
9	100.27 Hz	Twisting of headstock in ZY plane caused by rocking of spindle motor
10	108.73 Hz	Twisting of headstock in ZY plane and twisting of table about Y axis

Table 7.5. The first ten simulated natural frequencies mode shapes

7.4. Comparison with other simulations and experimental results

The numerical convergence time for the FEA analysis is considerably longer than the previous FEMGV–ABAQUS model but comparable to the Pro/ENGINEER model. However, the

levels of the mode shape details are much higher than the previous FEMGV–ABAQUS model and the obtained results are significantly more accurate than the Pro/ENGINEER model. The quality of the FEA simulation outcomes is an important issue because it affects the subsequent uses of the results. Accurate simulated natural frequencies and detailed mode shapes are essential for a successful vibration analysis study. This information enables the necessary structural modification to be performed in order to improve the overall machine's dynamic properties.

Table 7.6 shows the obtained FEA simulation results with respect to the other investigations examined in this study. The results are grouped according to the natural frequency value proximities, showing the percentage differences between outcomes of the previous FEA investigations with respect to the current study. The simulation results in this study contain modes which might have been missed by the previous FEA studies. These modes are very likely to be closely coupled, which can only be found due to the higher geometrical details (larger number of nodes and elements) of the FEA model in this study. These modes normally occur in non-linear and axis-symmetric structures, in which the machine structure under study can be categorised.

The simulation results of this study are also compared to those obtained from the experimental technique (see Table 7.7). Using the similar criteria as to the previous table, the simulation results are grouped with the closest measured natural frequencies. The simulation results reveal some modes which might have been missed during the measurements or the modal parameter extraction process. Several of the likely causes are the limited number of measured points during the experiment which lower the data resolution and the constrained excitation direction (only in Y-axis) causing only small movement in the perpendicular direction (X-axis). In addition, the detected motion in the perpendicular direction does not produce high coherence values resulting in the rejection of the data during the parameter extraction process.

FEMGV–ABAQUS			**Pro/ENGINEER**			**Current Model**	
Mode	Nat. Freq (Hz)	% Diff	Mode	Nat. Freq (Hz)	% Diff	Mode	Nat. Freq (Hz)
1	34.5	8.25	1	37	16.10	1	31.87
						2	35.80
2	50.8	12.68	2	42	27.81	3	58.18
						4	59.03
3	60.1	4.02	3	81	29.35	5	62.62
4	70.5	2.28	4	95	37.82	6	68.93

Table 7.6. Comparison of natural frequencies obtained by different FEA methods

Simulation Results			Corresponding Experimental Results	
Mode	Natural Freq. (Hz)	% Diff	Mode No	Natural Frequency (Hz)
1	31.87	12.69	1	28.28
2	35.80	26.59		
3	58.18	9.79	2	52.99
4	59.03	11.40		
5	62.62	18.17		
6	68.93	30.08		
7	76.20	19.01		
8	87.48	7.03	3	94.09
9	100.27	6.57		
10	108.73	6.82	4	116.69

Table 7.7. Comparison of natural frequencies from the simulation and experimental methods

The relatively high values of the simulated natural frequencies when compared to the measured data are believed as caused by the higher than actual stiffness values in the FEA model. The machine tool base is, in fact, not infinitely rigidly attached to the ground as the model suggest. The machine element connections, e.g. between the base and column, possess some flexibilities and are not infinitely stiff as suggested by the model. These flexibilities are due to the bolting and welding of the components, which are replaced in the simulation by the total merging of the elements' materials. In addition, the lower mass value in the model due to the ballscrew and bearing element representation contributes to a slight increase in the natural frequencies. Another assumption implemented in the FEA analysis performed is that no damping exists in the structure. This results in slightly higher simulated natural frequencies and the probable exposure of weak and hidden modes.

7.5. Conclusions

The development of the FEA model of the machine's structural dynamic properties has been presented in this chapter. The model was developed by closely interfacing a CAE (Pro/ENGINEER) and FEA (ABAQUS/Standard) software applications while employing FEMGV as the FEA pre- and post-processing application. This produced a very accurate representation of the machine structural geometry which enabled a more accurate identification of the vibration sources and the modes. However, the complexity of the model geometry required that tetrahedral elements were employed for the FEA analysis with Delaunay triangulation technique to generate the mesh. In addition, a relatively powerful computing power and resources were required in order to produce the more accurate siluation results.

The simulated results were compared to both measured results and simulation data obtained from a reduced FEA model and built-in CAE analysis. The comparison with the measured structural dynamic results was performed with those obtained from the experimental modal analysis using the suspended shaker configuration. A considerably good agreement was obtained for both the natural frequency and mode shape results. The simulated frequency analysis results also showed good correlation with the reduced FEA model and more detailed mode shapes were produced. The comparison of the simulated mode shapes with those from the CAE model produced good results but the frequencies were quite different. This is probably due to the less accurate representation of the material behaviour in the CAE software despite the very accurate representation of the machine geometry and mode shapes. Generally, the correlation results obtained between the higher modes were less accurate indicating that the mass parameters of the models vary considerably.

The simulated results also show closely coupled modes which were not detected by the experimental method. This was achieved because the machine geometry was modelled accurately, thus allowing detailed analysis of the vibration characteristics of the machine element to be performed. However, a more detailed experimental analysis is required to verify the existence of the coupled modes which also takes into account the machine structure's non-linearities and symmetries.

The next chapter presents the parametric investigation of the FEA Model to closely match the measured values and to devise a method in reducing the machine vibration through the passive method using the Structural Dynamic Modification technique.

Chapter 8. FEA Parametric Exercise and Vibration Control Analysis

The correlation between the FEA model and the experimental results discussed in Chapter 7 is considered as requiring further investigation for the successful derivation of a vibration reduction technique through the passive method. A detailed understanding of the contribution from the machine tool elements is required to develop the suitable vibration reduction technique, especially for the passive methods. The required additional investigation involves a correlation analysis, MIMO experimental modal analysis, a parametric exercise (sensitivity analysis) and structural dynamic modification studies of the FEA model.

The experimental results presented in Chapter 4 show that the dominant mode shape vectors are in the Y-axis direction. The simulation results (discussed in Chapter 7) demonstrate that the mode shape vectors are distributed in all three orthogonal directions. One of the most evident explanations for this is that the use of a single exciter in the Y-axis direction of the SIMO experimental configuration is not sufficient to excite the machine structure in the perpendicular directions (X- and Z- axes). The extent of this postulation is investigated in this study through the correlation analysis of the analytical and experimental models. The application of MIMO to improve the correlation of the analytical and experimental results (due to sufficient structural excitation in multiple directions) is also discussed.

The comparison of the simulation and experimental results (see Chapter 7) shows that the differences of the corresponding natural frequencies can be up to 12% (see Table 7.7). This investigation presents the method to reduce the margins through MIMO experimental modal analysis and to identify the influence of the element properties through parametric studies of the FEA model. The correlation and sensitivity analysis techniques using standard mathematical correlation benchmarking techniques, such as MAC (Modal Assurance Criterion), are employed to perform the parametric exercise. The techniques require that the FEA geometric model is modified slightly by including a cutting tool. The modification is carried out to match the geometric definition of the FEA model to that of the experimental configuration, where a dummy cutter is utilised as the excitation source in the measurement. This enables the spatial correlation of the analytical and experimental models to be performed, allowing a better comparison of the simulated and measured mode shapes.

The parametric studies carried out examine the influence of the Young's modulus property (stiffness) on the structural dynamic behaviour of the machine. A what-if analysis of this

property towards the dynamic behaviour is investigated to identify which parts of the structure can be stiffened or modified to improve the machine's dynamic properties. This study can be expanded to allow the influence of other material property types (mass, damping, shear modulus, etc.) to enable the determination of an optimum solution for the vibration control by allowing the accurate selection of the vibration absorbing material or structural modification. The study on the selection of various material types for the structural elements and their influence into the machine's dynamic properties can also be performed. The outcome of the study can be realised on the actual structure by performing a structural design adaptation, localised addition, increased stiffness, machinery isolation or combined methods.

This investigation employs FEMtools [216] software package from Dynamic Design Solutions in addition to the ABAQUS/Standard application. The FEMtools package is utilised for the correlation and sensitivity analysis, whereas ABAQUS/Standard is employed as the FEA solver. Data is interchanged between the applications seamlessly enabling the investigation process to be carried out efficiently.

8.1. FEA model modification to include the cutting tool

The FEA model discussed in the previous chapter was developed to represent only the structural elements affecting the dynamic/modal properties of the machine. Its geometric definition does not include the cutting tool because the element is not considered to affect the dynamic properties significantly. However, the omission creates difficulty for the correlation analysis in this study because it is different from the experimental method where a dummy cutting tool is employed as the source of excitation (see sections 4.3 and 4.4).

The correlation analysis produces spatially paired FEA nodes and measurement points (shown graphically as blue dots in Figure 8.1) by selecting the nearest FEA node to a measurement point in the three-dimensional space. It can also be seen from the figure that the missing FEA nodes of the cutting tool produce mismatched node-point pair of the experimental and FEA models. The measured point at the cutting tool is incorrectly matched to an FEA node on the machine table because there is none in the vicinity. This shows that the FEA model needs to be modified to include the cutting tool for a successful correlation analysis of the FEA and experimental models.

The cutting tool is modelled in the FEA as a solid cylinder assumed to be constructed from stainless steel material. This approach is considered as sufficient to enable the spatial correlation without compromising the structural dynamic properties of the FEA model. Table 8.1 shows the natural frequencies of both original and modified FEA models and confirms

that the modification changes the structural dynamic behaviour only insignificantly. In general, the modified FEA model tends to have lower natural frequencies due the extra mass of the cutting tool.

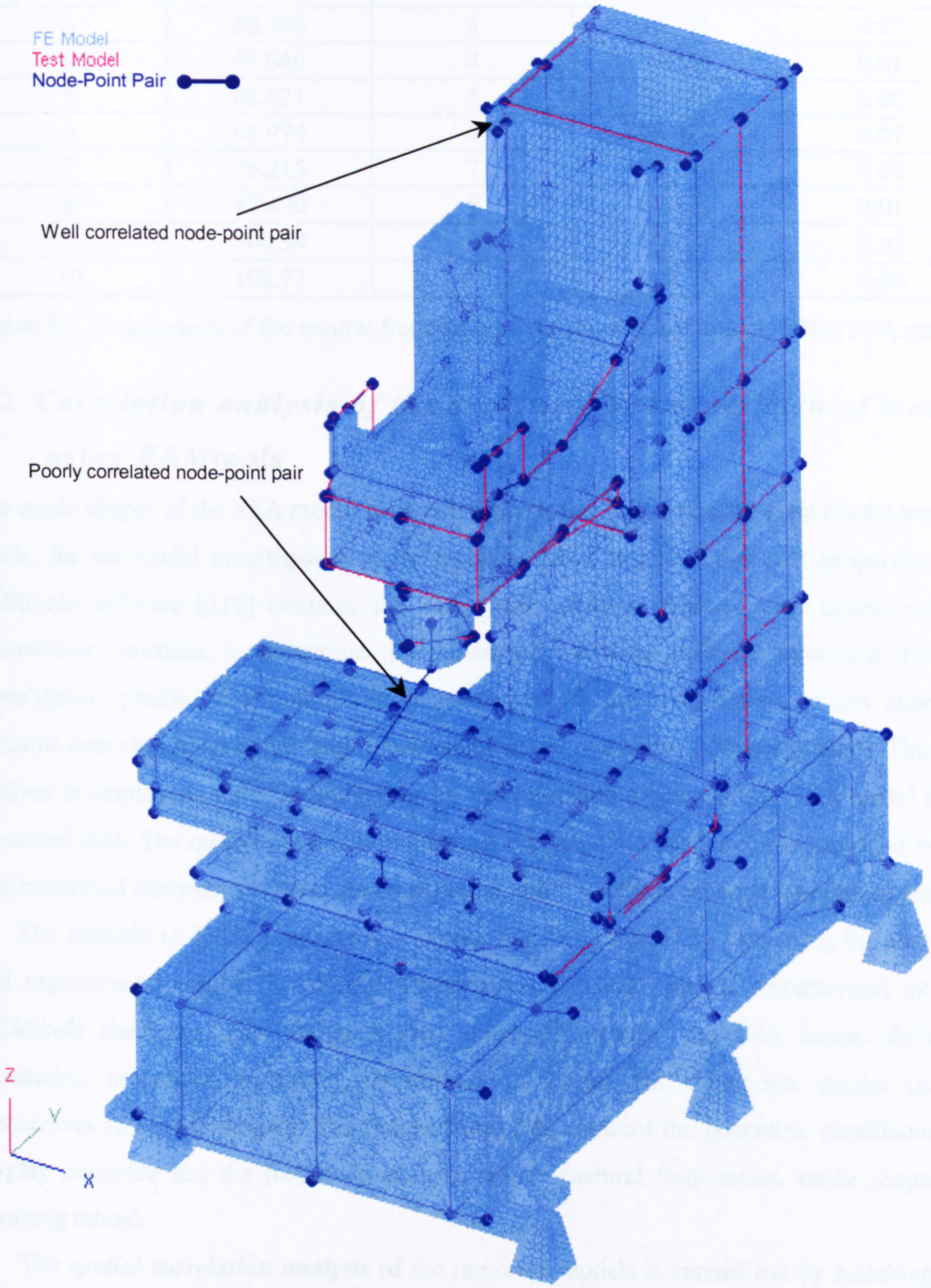

Figure 8.1. Spatial correlation result of the FEA model (no cutter) and the experimental data

Without Cutting Tool		With Cutting Tool		Difference (%)
Mode	Nat. Freq. (Hz)	Mode	Nat. Freq. (Hz)	
1	31.889	1	31.873	0.05
2	35.800	2	35.795	0.01
3	58.196	3	58.176	0.03
4	59.040	4	59.034	0.01
5	62.621	5	62.620	0.00
6	68.974	6	68.928	0.07
7	76.215	7	76.199	0.02
8	87.490	8	87.481	0.01
9	100.34	9	100.27	0.07
10	108.73	10	108.73	0.00

Table 8.1. Comparison of the natural frequencies from the original and modified FEA model

8.2. Correlation analysis of the analytical and experimental models using FEMtools

The mode shapes of the FEA model must correlate closely to the experimental modal analysis results for successful investigation of the machine tool's structural dynamic properties. The FEMtools software [216] contains the ***correlation analysis toolbox*** with qualitative and quantitative functions to determine the relationship between different structural dynamic investigation results. The toolbox can be employed for the investigation of any structural dynamic data regardless of the acquisition methods (i.e. analytical or experimental). Thus, the toolbox is employed in this investigation for the validation process of the FEA model to the measured data. The qualitative function (through the graphical interface) and quantitative tool (via numerical analysis) provided are employed in order to obtain accurate correlation results.

The analysis is divided into various phases and is initialised by importing the analytical and experimental results (in ABAQUS/Standard and STAR formats respectively) into the ***FEMtools database.*** The analytical data imported includes the FEA model definition (geometry, properties, materials, constraints, etc.) and the simulation results (natural frequencies and mode shapes). The experimental data contains the geometric coordinates, the display sequence and the frequency analysis results (natural frequencies, mode shapes and damping ratios).

The ***spatial correlation analysis*** of the imported models is carried out by matching their geometric data (using the built-in functions in FEMtools, including translation and rotation) to achieve the closest coordinate relationship in the three dimensional space. Figure 8.2 shows the raw geometric data of the experimental and analytical models and Figure 8.3 displays the

final spatial correlation result. The spatial correlation analysis also includes the pairing of the measured points to the nearest node on the FEA model and the results (***node-point pairs***) can be seen as the blue dot pairs in Figure 8.3. It can also be seen that the experimental model first point (point #1 = excitation location) is now correlated directly to the improved FEA model's cutting tool. The full node-point pair results of the spatial correlation are shown in Table 8.2.

This spatial correlation result provides a useful graphical qualitative tool to improve the correlation analysis accuracy. Utilising the static and dynamic graphical interfaces provided by the software, the general consistency of simulated and measured mode shapes can be determined. For instance, the visual representation of the first analytical and experimental mode shapes (see Figure 8.4.(a)) shows that they have higher correlation than the second mode shape pair (see Figure 8.4.(b)). It can be observed that the displacement deviation of the first mode shape pair is smaller than the second mode. Thus, it can be concluded that the first mode of the FEA model is sufficiently accurate in representing the first actual (measured) mode of the machine structure.

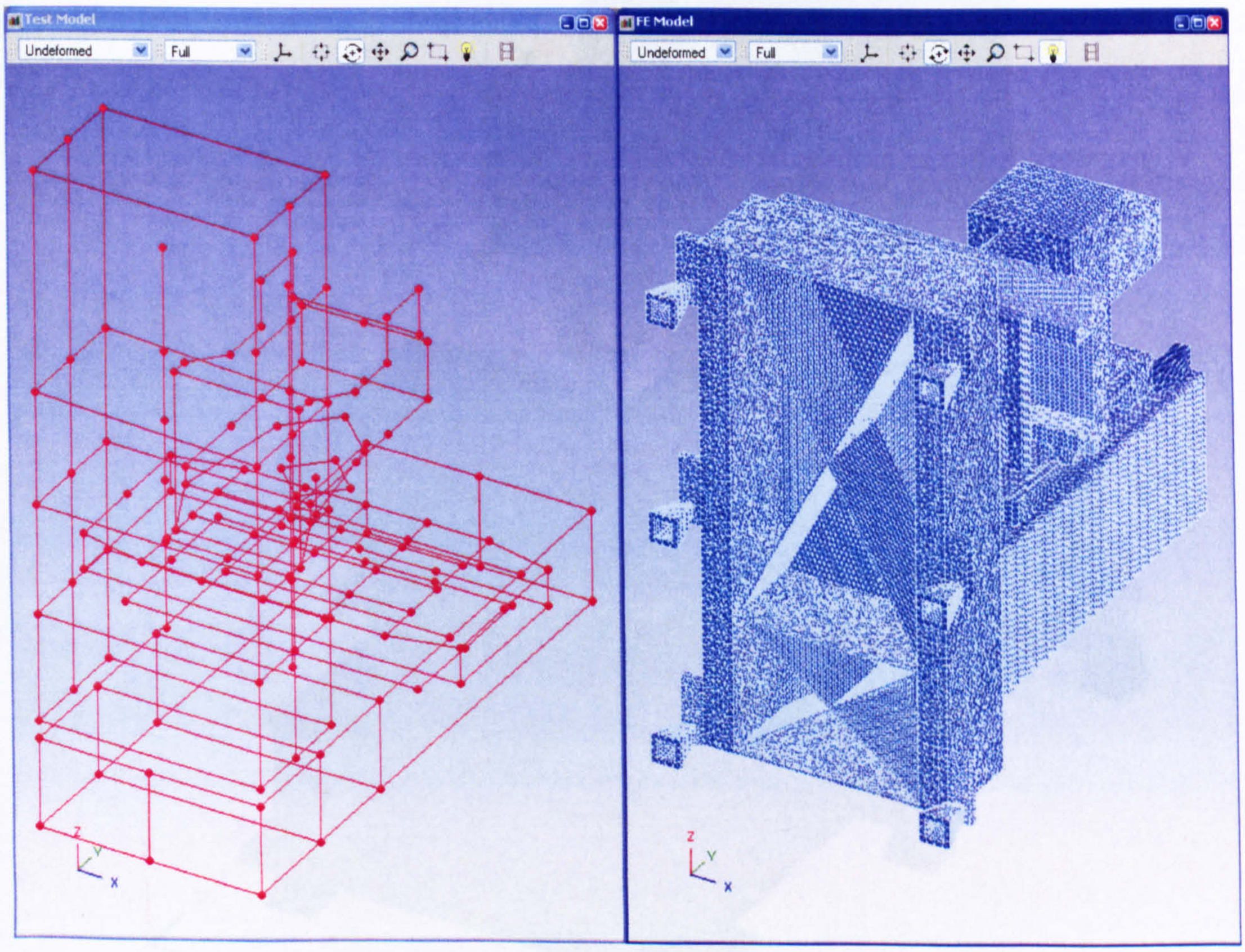

Figure 8.2. Raw experimental and analytical geometric data imported by FEMtools

The second stage of the correlation analysis explores the pairing of the analytical and experimental modes further by utilising the qualitative analysis tool provided by FEMtools. The study employs one of the most widely used techniques known as the MAC (Modal

Assurance Criterion) values, which lies between zero and one. The closer the MAC values to unity, the more identical the modes are. The MAC values are obtained through the mathematical manipulation of the mode shape's vectorial components. It is a measure of the squared cosine of the angle between two mode shape vectors (ψ_a , ψ_e) and is calculated using equation (8.1).

$$MAC(\psi_a, \psi_e) = \frac{\left[\psi_a^T \psi_e\right]^2}{\left(\psi_a^T \psi_a\right) \times \left(\psi_e^T \psi_e\right)} \tag{8.1}$$

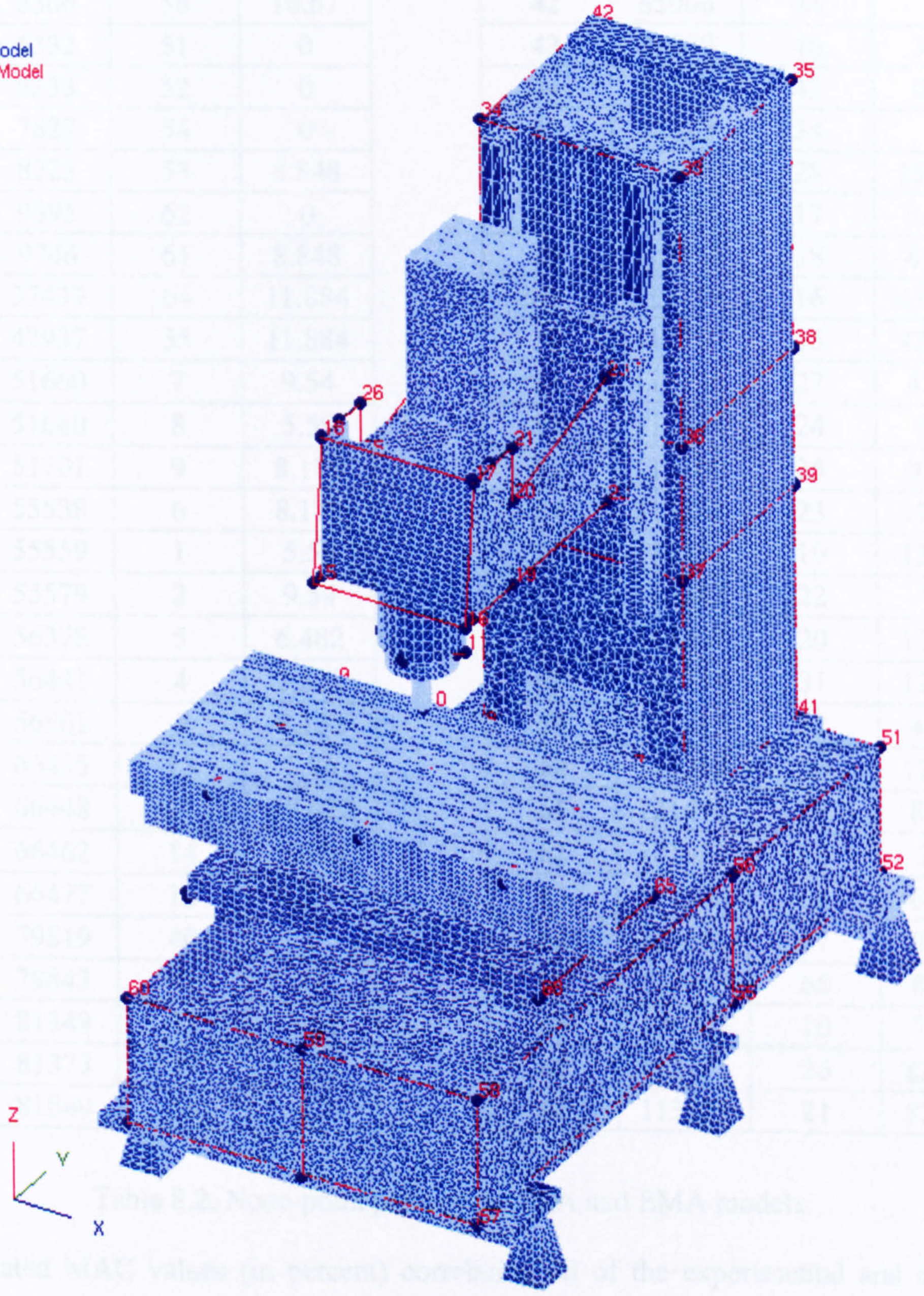

Figure 8.3. Spatial correlation result of analytical and experimental models showing the point numbers

Pair #	Node	Point	Distance (mm)
1	1	49	0
2	27	63	10.67
3	73	60	0
4	99	59	0
5	171	50	0
6	6051	57	0
7	6260	58	0
8	6306	56	10.67
9	6332	51	0
10	6333	52	0
11	7827	54	0
12	8223	53	8.848
13	9395	62	0
14	9746	61	8.848
15	37439	64	11.884
16	42937	55	11.884
17	51660	7	9.54
18	51680	8	5.59
19	51701	9	8.179
20	55538	6	8.179
21	55559	1	5.59
22	55579	2	9.54
23	56378	5	6.482
24	56441	4	2.522
25	56501	3	8.132
26	66435	13	5.86
27	66448	11	18.422
28	66462	14	5.364
29	66477	12	9.274
30	79819	40	0
31	79843	41	0
32	81349	37	3.51
33	81373	39	3.51
34	81849	36	4.2
35	81873	38	4.2
36	82874	33	0
37	82898	35	0
38	82950	42	0
39	82951	47	0
40	82986	45	3.51
41	83005	44	0.19
42	85906	48	0
43	86859	46	3.51
44	87315	43	0.19
45	88323	34	0
46	112395	28	15.347
47	112406	17	9.083
48	112426	18	4.743
49	112758	16	43.445
50	112770	15	42.749
51	112795	27	4.776
52	112811	24	9.89
53	113100	25	9.523
54	113242	23	17.191
55	113271	19	12.562
56	113287	22	9.1
57	113567	20	12.275
58	120230	31	12.768
59	121215	32	4.914
60	121259	30	12.423
61	121496	29	8.795
62	121913	68	7.89
63	121930	65	6.706
64	123661	67	9.605
65	123849	66	8.658
66	126511	10	7.489
67	112771	26	82.598
68	113225	21	82.961

Table 8.2. Node-point pairs of the FEA and EMA models

The calculated MAC values (in percent) correlating all of the experimental and analytical model mode shapes are listed in Table 8.3 and represented as 3D matrices in Figure 8.5. The

values also include experimental-experimental and analytical-analytical mode shape correlations results.

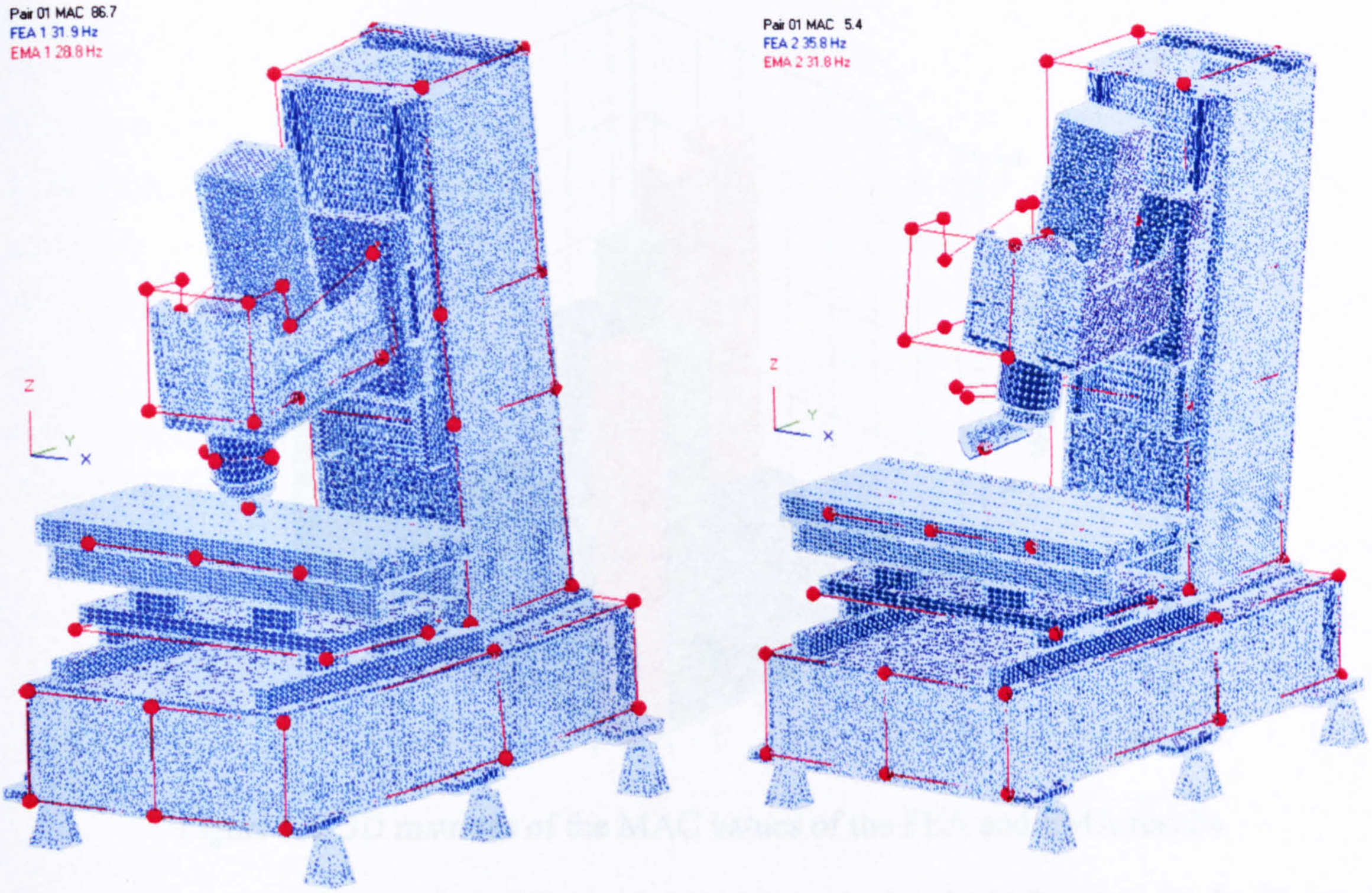

(a) Good correlation (1st mode, MAC=86.7%) (b) Poor correlation (2nd mode, MAC=5.4%)

Figure 8.4. Visual displays of the machine tool's mode shapes

FEA \ EMA	1	2	3	4	5	6	7
1	86.7	64.9	30.8	24.5	0	2.2	7.7
2	7.7	5.4	8.9	3.7	0	0	1.6
3	1	37.5	2.2	67.8	4.2	0.8	4.9
4	1.8	8.4	0.1	18	1.2	0.2	1.8
5	0.4	7.5	3.4	12.5	0.6	3.8	8.8
6	0.8	11	29.6	2.8	54.6	67.5	80.9
7	0.1	0	0.9	0	0.1	0	0.4

Table 8.3. MAC values (%) correlating the FEA and EMA models

When the simulated and measured mode shapes of a particular structure are identical (ideal condition), the MAC values in the diagonal cells of the correlation table (such as Table 8.3) will be unity. Similarly, the 3D bars positioned across the diagonal of the correlation matrices (such as Figure 8.5) should be at full heights (100%). The diagonal MAC values are of

importance because the mode orders of the analytical and experimental are the same at these points. The minimum MAC values for well-correlated mode shapes are about 0.6 (60%).

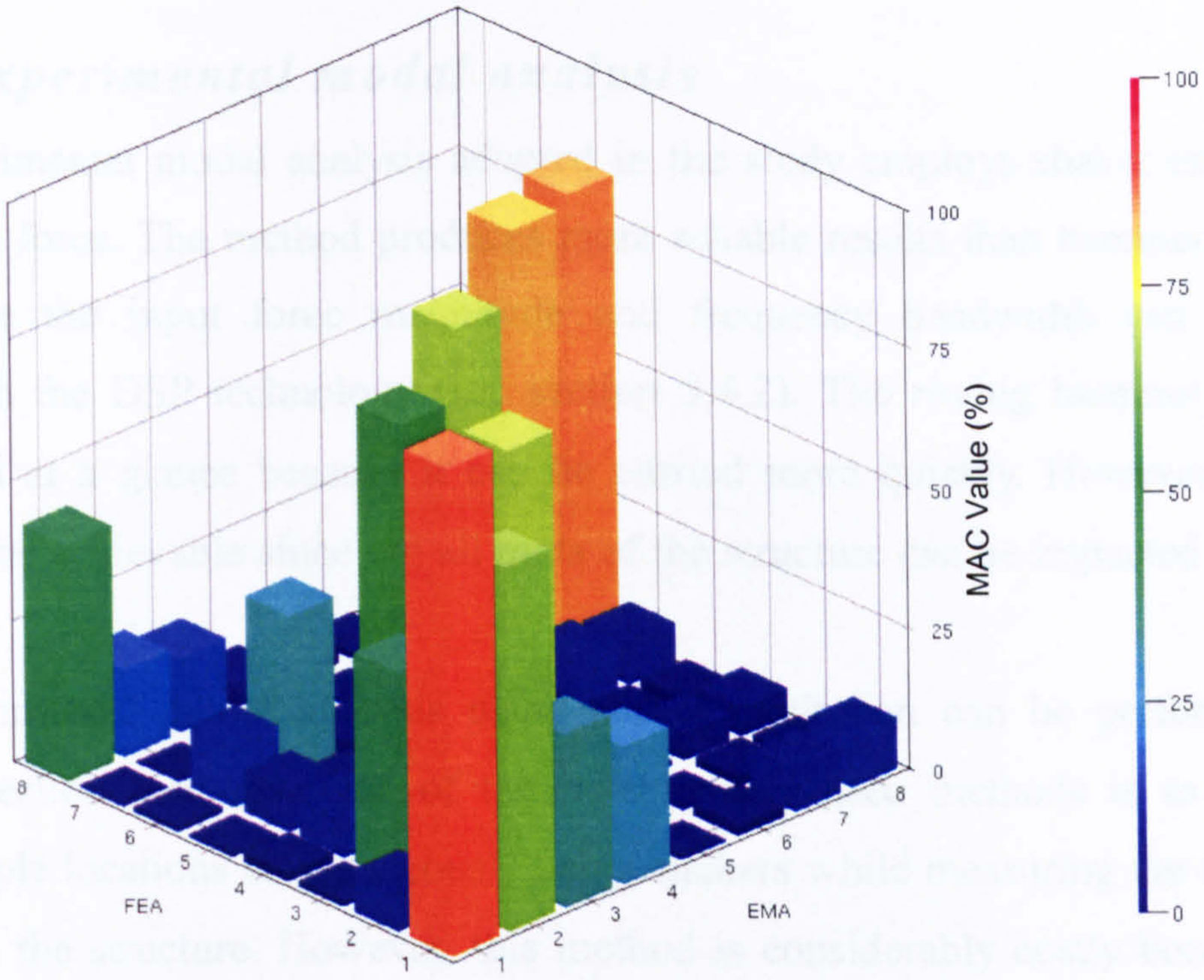

Figure 8.5. 3D matrices of the MAC values of the FEA and EMA results

It can be seen from Table 8.3 and Figure 8.5 that the calculated MAC values in the diagonal positions for the first and sixth modes are above 60% (out of eight mode shape correlation values). However, there are four other MAC values higher than 60% on the off-diagonal positions (i.e. not from the same FEA and EMA mode numbers). One of the most likely explanations for this is that there are missing (unidentified) modes, either on the analytical or experimental results. This results in the shifting of the whole mode shape data (in a column or row) for the particular modes, moving the acceptable MAC values to a non-diagonal position.

It can also be observed that three FEA rows contain more than one MAC value higher than 60% but this is not the case in the EMA columns. This can be interpreted as the amplitude of the FEA vector components being bigger than the EMA counterparts. One possible reason for this is that the experimental modal analysis does not excite the structure enough in one or more directions to produce the necessary vector magnitude. This argument is reinforced by a qualitative comparison of the natural frequencies and modes shapes of the simulation and experimental modal analysis results as shown in Table 7.5 and Table 7.7. The measured mode shapes show large vector amplitudes in the excitation direction in contrast to the perpendicular vectors. The assumption that the shaker excitation in the Y-axis direction would also excite the structure in the orthogonal (X-axis) direction is, thus, not completely

accurate in this case. A MIMO experimental modal analysis is considered as the technique to improve the correlation results.

8.3. MIMO experimental modal analysis

The MIMO experimental modal analysis adopted in the study employs shaker excitation to generate the input force. The method produces more reliable results than hammer excitation technique because the input force magnitude and frequency bandwidth can be tightly controlled through the DSP technology (see section 3.4.2). The roving hammer is a more attractive solution at a glance because it can be carried more quickly. However, full FRF results might not be achievable since not all parts of the structure can be impacted from three directions [56].

MIMO experimental modal analysis using shaker excitation can be performed using various data collection methods. One of the most widely used methods is to excite the structure at multiple locations simultaneously using shakers while measuring the response at various points on the structure. However, this method is considerably costly because of the multiple shaker units required and the customised software to resolve the response vectors in accordance to the excitation source.

A more cost effective method is to employ a single shaker with its excitation direction adjusted at an angle to the orthogonal axes (normally 45°). This approach employs the data acquisition software to vectorise the force into the orthogonal directions and to correlate the measured response to the force to calculate the FRF data. The use of customised software, however, can still be expensive and the magnitude of the shaker excitation force can be greatly reduced by the vectorisation.

This investigation employs an alternative method to acquire the MIMO modal analysis data by combining several SIMO results in a single parameter extraction process. This method does not require specialised experimental modal analysis software and only employs a single shaker. Thus, it is very cost effective to perform and there is no degradation in the excitation magnitude due the input force vectorisation. However, a longer measurement period is required since multiple SIMO experimental modal analysis must be performed to obtain the data. Thus, this method is suited long-term structural dynamics studies of a specific machine provided that no major structural change takes place on the machine. Uncertainty of measurement occurring with the technique is minimised by utilising 'averaging' statistical function on the FRF measurements.

An additional experiment is performed by exciting the machine at the cutting tool (where most of the vibration is likely to occur) using a shaker in the X-axis direction. A dummy tool is employed to enable a secure connection and is attached to the shaker via a stinger. The input force is measured by a force sensor placed between the stinger and the dummy cutting tool, and the machine responses are acquired using three industrial grade tri-axial accelerometers placed at various locations on the structure (see Figure 8.6). This measurement is to complement the SIMO experimental modal analysis in the Y-direction as shown in Figure 4.10.

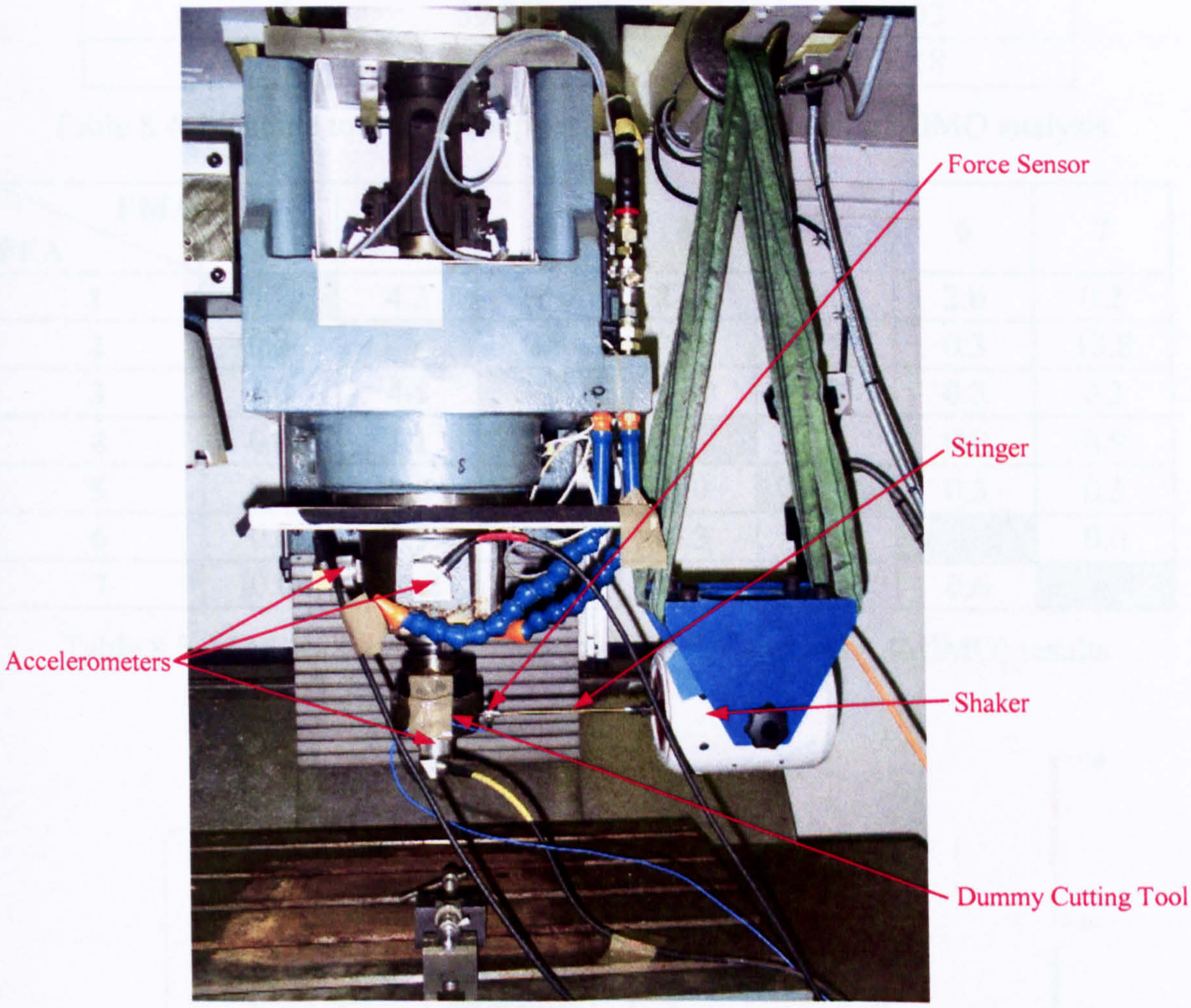

Figure 8.6. Test layout for tool tip excitation with no additional mass

The point numbers from both measurements are synchronised, so that they represent the response at the same locations on the structure. The modal parameter extraction from the MIMO measurement data is performed using the global curve fitting (see section 3.5(c) and 4.4). Two sets of analysis in the X- and Y-axis directions are carried out producing combined MIMO modal parameters for the machine structure as shown in Table 8.4.

The new MIMO experimental modal analysis results are then imported into FEMtools to replace the SIMO data and a correlation analysis against the FEA results is performed. Table 8.5 and Figure 8.7 show the updated results and it can be seen that the MAC values in the

diagonal position has been improved. Two MAC values are still above 60% (mode pairs 1 and 6), but two additional results are now close to or above 40% (mode pairs 2 and 3). The MAC values of mode pairs with very low previous correlation have also been improved.

Mode	Frequency (Hz)	Damping (%)
1	28.980	2.2013
2	29.879	4.4695
3	38.776	2.7620
4	50.075	1.3424
5	55.544	2.1354
6	59.957	1.1903
7	63.014	1.3718

Table 8.4. Machine tool's modal parameters obtained using MIMO analysis

FEA \ EMA	1	2	3	4	5	6	7
1	84.4	4.3	11.9	23.4	10.7	2.6	0.2
2	0.8	38.4	2.8	0.8	1.9	0.3	13.8
3	2.0	4.1	46.9	52.0	0.2	0.3	0.3
4	0.6	1.1	11.5	14.6	3.7	0.0	0.9
5	0.1	9.8	0.0	3.0	0.4	0.3	0.3
6	0.0	0.1	18.6	0.3	68.2	73.3	0.0
7	0.0	46.2	2.4	0.2	3.4	0.6	16.7

Table 8.5. MAC values (%) correlating the FEA and EMA (MIMO) results

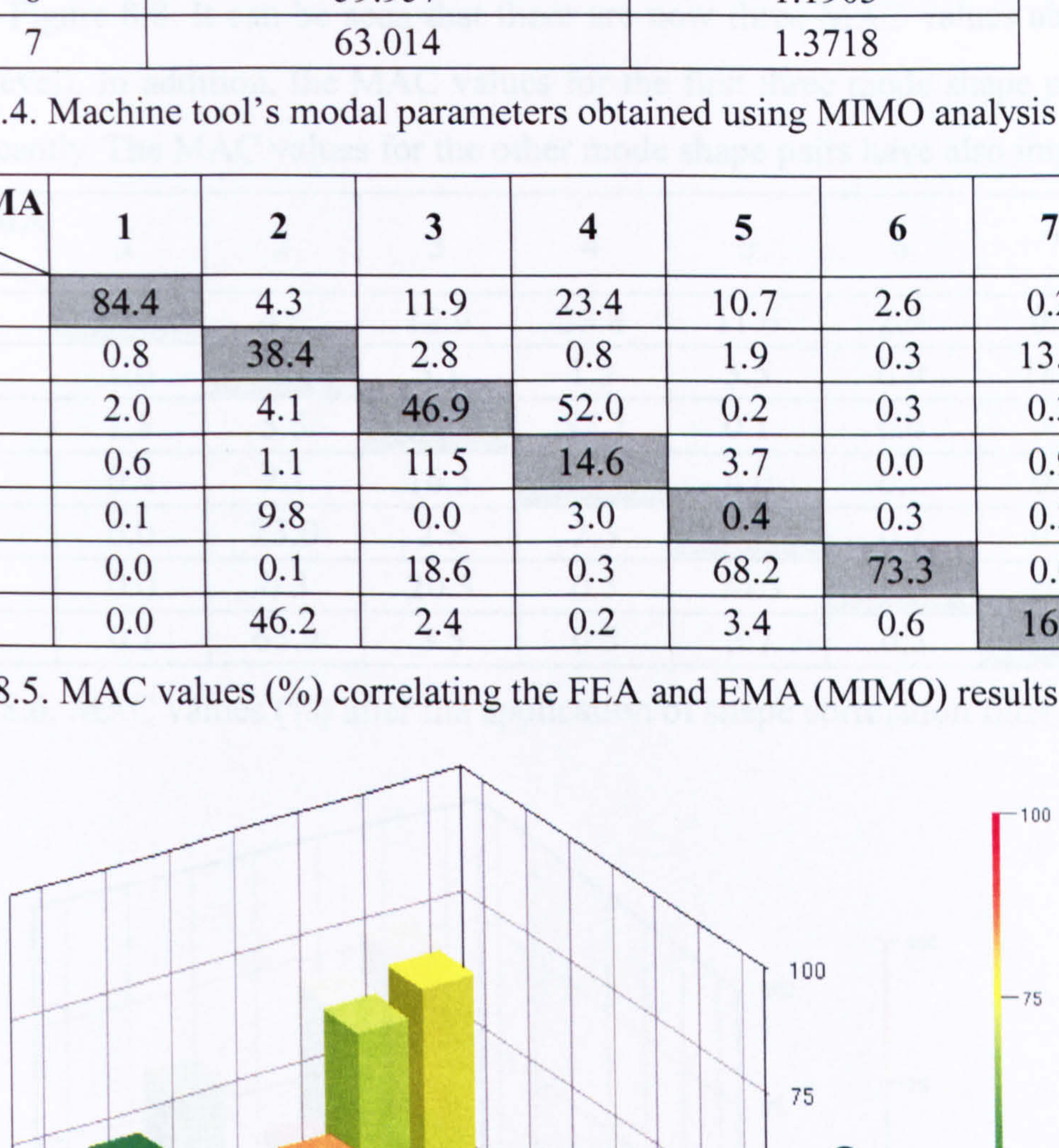

Figure 8.7. 3D matrices of the MAC values of the FEA and EMA results

The calculation of MAC values is based on the least squares based form of linear regression analysis [217]. Thus, the method is most sensitive to the largest displacement difference of the compared values (i.e. mode shape deflections). As the machine was not isolated from the environment during the experiment modal analysis, the ambient noise has some affect on the measured data (although it is minimal) as shown in section 4.4. Hence, the 'shape correlation filter' in FEMtools is investigated to minimise this effect in order to further improve the correlation. The minimum displacement value is increased from the default value of 1×10^{-6} to 0.5 as suggested by the manual [218] and the calculation results using the new data are shown in Table 8.6 and Figure 8.8. It can be seen that there are now three MAC values above 60% (the acceptable level). In addition, the MAC values for the first three mode shape pairs have increased significantly. The MAC values for the other mode shape pairs have also improved.

FEA \ EMA	1	2	3	4	5	6	7
1	88.4	4.8	12.9	25.8	11.6	2.9	0.1
2	1.0	78.2	5.1	1.3	3.5	0.9	18.2
3	1.5	5.5	50.8	57.7	0.1	0.4	0.3
4	0.4	2.1	16.5	20.7	4.0	0.1	0.5
5	0.0	23.0	2.5	2.3	1.6	0.2	0.3
6	0.0	0.3	20.5	0.5	74.3	77.6	0.0
7	0.1	65.9	3.5	0.5	3.7	0.3	31.7

Table 8.6. MAC values (%) after the application of shape correlation filter

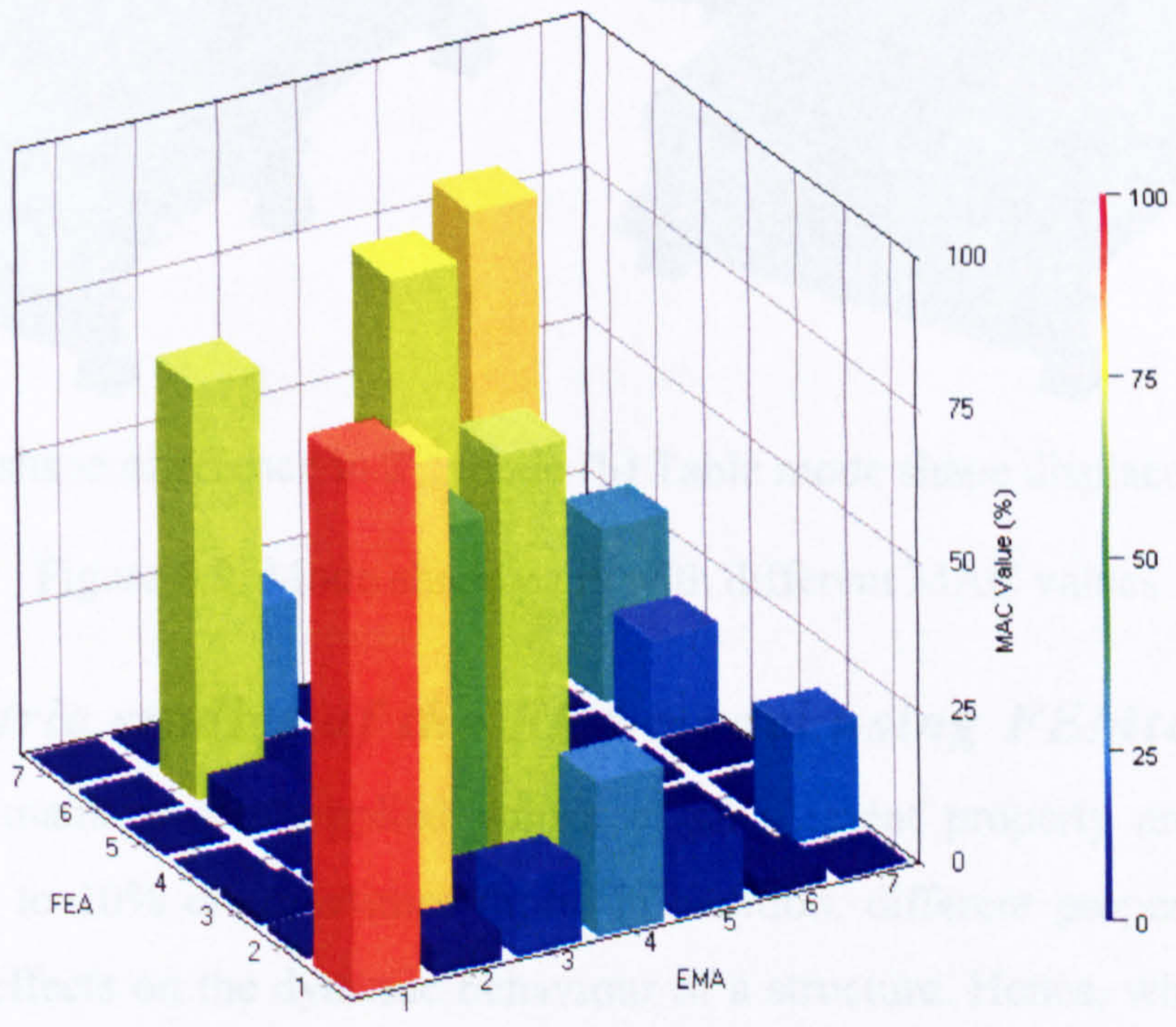

Figure 8.8. 3D matrices MAC values after the application of shape correlation filter

The MIMO experimental modal analysis has been shown to improve the correlation of the measured and analytical results. It was also shown that the 'shape correlation filter' could further improve the MAC values by removing the small differences of the mode shape pair deflections which might be caused by noise in the measured data. Visual checks using the graphical interface reveal that the mode shape pairs for low MAC values are caused by marked differences in column displacement (Figure 8.9(a)) and table movements (Figure 8.9(b)). Since the current correlation findings are considered acceptable, the experimental modal analysis results are considered sufficient and parametric studies of the FEA model in order to optimise the simulated structural dynamics will be discussed in the next section.

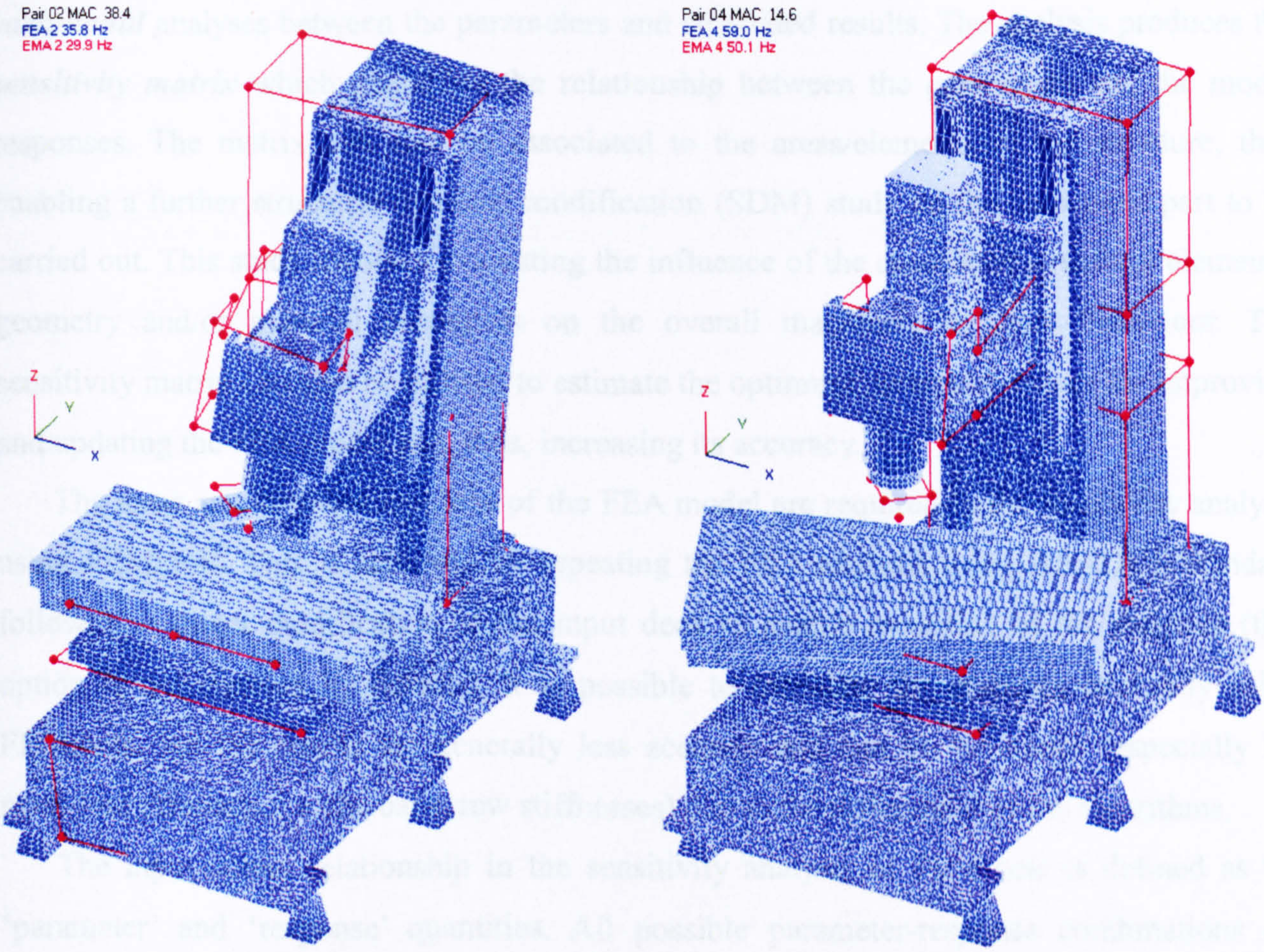

(b) Column mode shape difference in 2nd mode (b) Table mode shape displacement in 4th mode

Figure 8.9. Mode shape pairs with different MAC values

8.4. Parametric studies of the FEA model using FEMtools

The actual and manufacturer-supplied values of an element property are known to have tolerances of up to 10% or sometimes more. In addition, different properties of a material have dissimilar effects on the dynamic behaviour of a structure. Hence, when an FEA model is developed using such data, the simulated dynamic properties of a structure may vary to the

measured values to some degrees. The variation, however, must be minimised in order that a structural dynamic investigation of a particular machine can be performed successfully.

Various techniques can be performed to increase the simulation accuracy and one of the most widely employed approaches is the parametric study of the FEA model. The approach attempts to minimise the differences between the estimated and actual parametric values by varying the value of a certain parameter while keeping the others constant. In this way, the effect of certain parameters over the simulated behaviour can be determined.

The parametric studies in this investigation are performed using the ***sensitivity analysis toolbox*** of the FEMtools software package. The module provides a tool for ***what-if*** and ***variational*** analyses between the parameters and simulated results. The analysis produces the ***sensitivity matrix*** which quantifies the relationship between the parameters and the model responses. The matrix can also be associated to the areas/elements of the structure, thus enabling a further structural dynamic modification (SDM) study on the associated part to be carried out. This study involves evaluating the influence of the associated structural elements' geometry and/or material properties on the overall machine's dynamic behaviour. The sensitivity matrix can also be utilised to estimate the optimum parameter values for improving and updating the FEA model and, thus, increasing its accuracy.

The mass and stiffness matrices of the FEA model are required in the sensitivity analysis using FEMtools. This is achieved by repeating the FEA analysis using ABAQUS/Standard following a direct modification of the input deck to enable recording of the matrices (this option is not enabled by default). It is possible to calculate the matrices internally using FEMtools, but the results are generally less accurate and can be erroneous (especially for mass-less elements, i.e. the ballscrew stiffnesses) due to the differences in the algorithms.

The input-output relationship in the sensitivity analysis of FEMtools is defined as the 'parameter' and 'response' quantities. All possible parameter-response combinations are included in the analysis in order to determine which parameter has the biggest influence on a given response quantity. The parameters are assigned as 'local' quantities, which means that their values are varied for each element and not collectively as the whole body/structure. The response quantities are selected from the experimental modal analysis results (FEMtools 'test database') as the measured results are designated as the benchmarks/targets. The parameter-response combinations included in the analysis are presented in Table 8.7.

The sensitivity matrix is calculated using the 'normalised' method where the matrix elements are calculated as the ratios between the response and model parameter changes (see equation (8.2)) [219]. The method produces a dimensionless matrix and is suitable when the

analysed response and parameter quantities have different units. The element matrices (response and parameter) are analysed using the 'differential' approach (i.e., using their derivatives) to obtain the sensitivity matrix (see equation (8.3)). The sensitivity coefficient computations using the approach for the natural frequencies, mode shape and MAC values are shown in equations (8.4), (8.5) and (8.6) respectively. The normalised sensitivities are calculated by multiplying the result with the diagonal, square matrix of the response values as shown in equation (8.7). The coefficient of the sensitivity matrix represents the sensitivity of a certain response (e.g. a certain natural frequency) to a change in the parameter value of an FEA element.

Parameter	Response
Young's Modulus	Frequency
Mass Density	Mode
	MAC

Table 8.7. List of 'parameter-response' quantities for the sensitivity analysis

$$S_n = \left(\frac{dR}{R}\right) \Big/ \left(\frac{dP}{P}\right) \tag{8.2}$$

$$\mathbf{S} = S_{ij} = \frac{\delta R_i}{\delta P_j} \tag{8.3}$$

$$\frac{\delta f_i}{\delta P_j} = \frac{\psi_i^T \left(\frac{\delta \mathbf{K}}{\delta P_j} - 4\pi^2 f_i^2 \frac{\delta \mathbf{M}}{\delta P_j} \right) \psi_i}{8\pi^2 f_i \left(\psi_i^T [M] \psi_i \right)} \tag{8.4}$$

$$a_k^i = \frac{\psi_i^T \frac{\delta \mathbf{K}}{\delta P_j} \psi_i - \lambda_i \psi_i^T \frac{\delta \mathbf{M}}{\delta P_j} \psi_i}{\lambda_i - \lambda_k} \quad \text{for } i \neq k \tag{8.5.a}$$

$$a_k^i = -\frac{1}{2} \psi_i^T \frac{\delta \mathbf{M}}{\delta P_j} \psi_i \quad \text{for } i = k \tag{8.5.b}$$

$$\frac{\delta MAC}{\delta P} = 2 \left[\frac{\psi_e^T \psi_a \left\{ \frac{\psi_a}{\delta P} \right\}}{\psi_e^T \psi_e \psi_a^T \psi_a} - \frac{\left(\psi_e^T \psi_a \right)^2 \psi_a^T \left\{ \frac{\psi_a}{\delta P} \right\}}{\psi_e^T \psi_e \left(\psi_a^T \psi_a \right)^2} \right] \tag{8.6}$$

$$\mathbf{S}_n = \mathbf{S}_r \mathbf{R}_i^{-1} = \mathbf{R}_{ii}^{-1} \frac{\delta R_i}{\delta P_j} \mathbf{P}_{jj} \tag{8.7}$$

8.4.1. Sensitivity analysis result for Young's modulus parameter

The sensitivity matrix is created from M rows and N columns of response and parameter quantities respectively. The matrix elements contain the sensitivity values for each combination of response-parameter analysis result. This section presents the analysis outcomes for different response quantities as the result variation in the Young's modulus parameter. In addition, the sums of the sensitivity coefficient values are presented in order to determine the influence of different structural properties on the machine dynamic behaviour.

Figure 8.10 and Figure 8.11 show the sensitivity coefficients of the FEA model elements on the variation of the Young's modulus towards all of the machine's natural frequencies. The figures indicate that the increase in the Young's modulus of the spindle assembly, column and the headstock (elements 250,000 to 450,000) can increase the natural frequencies of the machine, especially the first two. On the other hand, increased stiffness in the machine base will not affect the natural frequencies significantly.

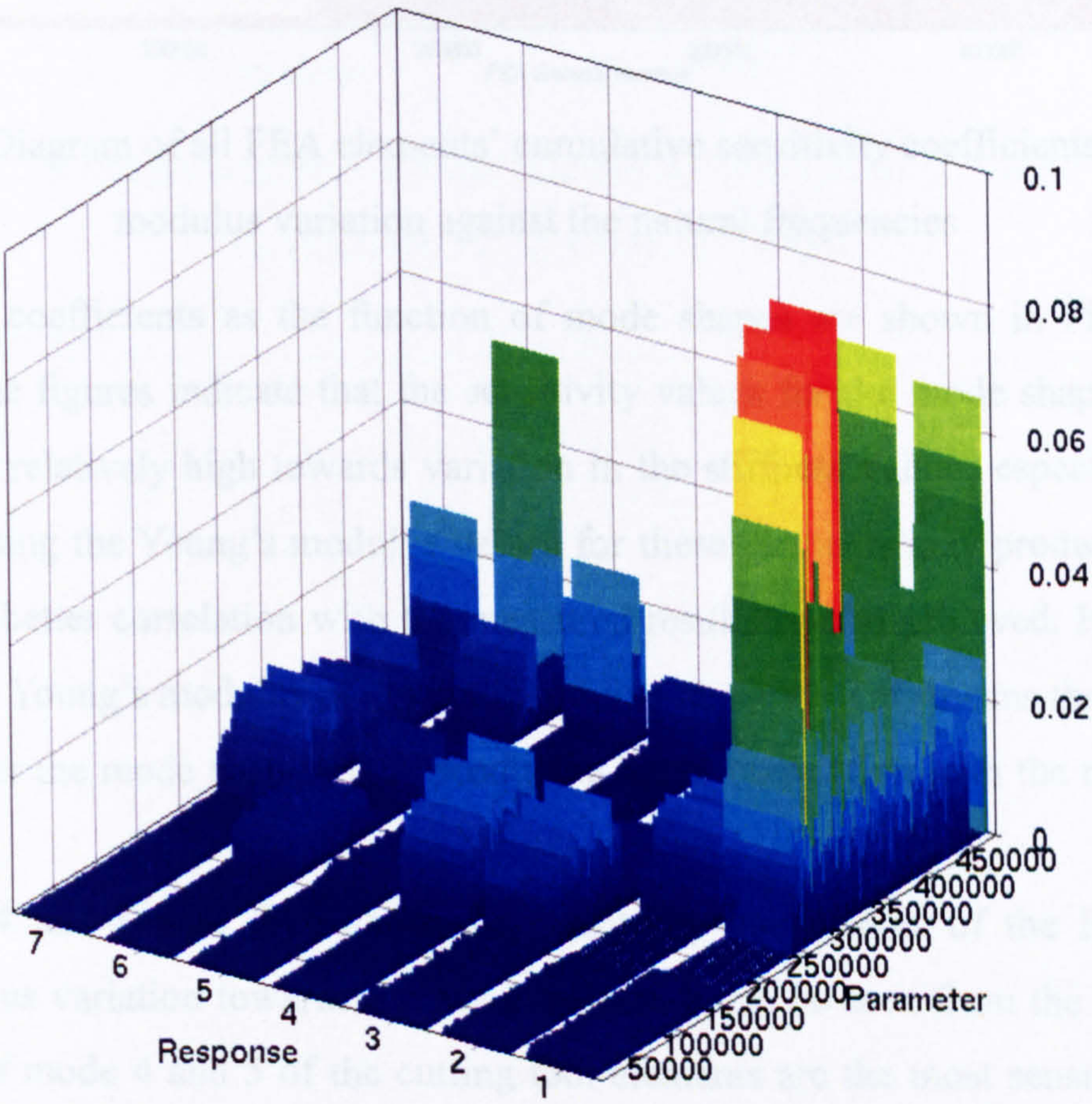

Figure 8.10. 3D Diagram of FEA element sensitivity coefficients of Young's modulus variation against the natural frequencies

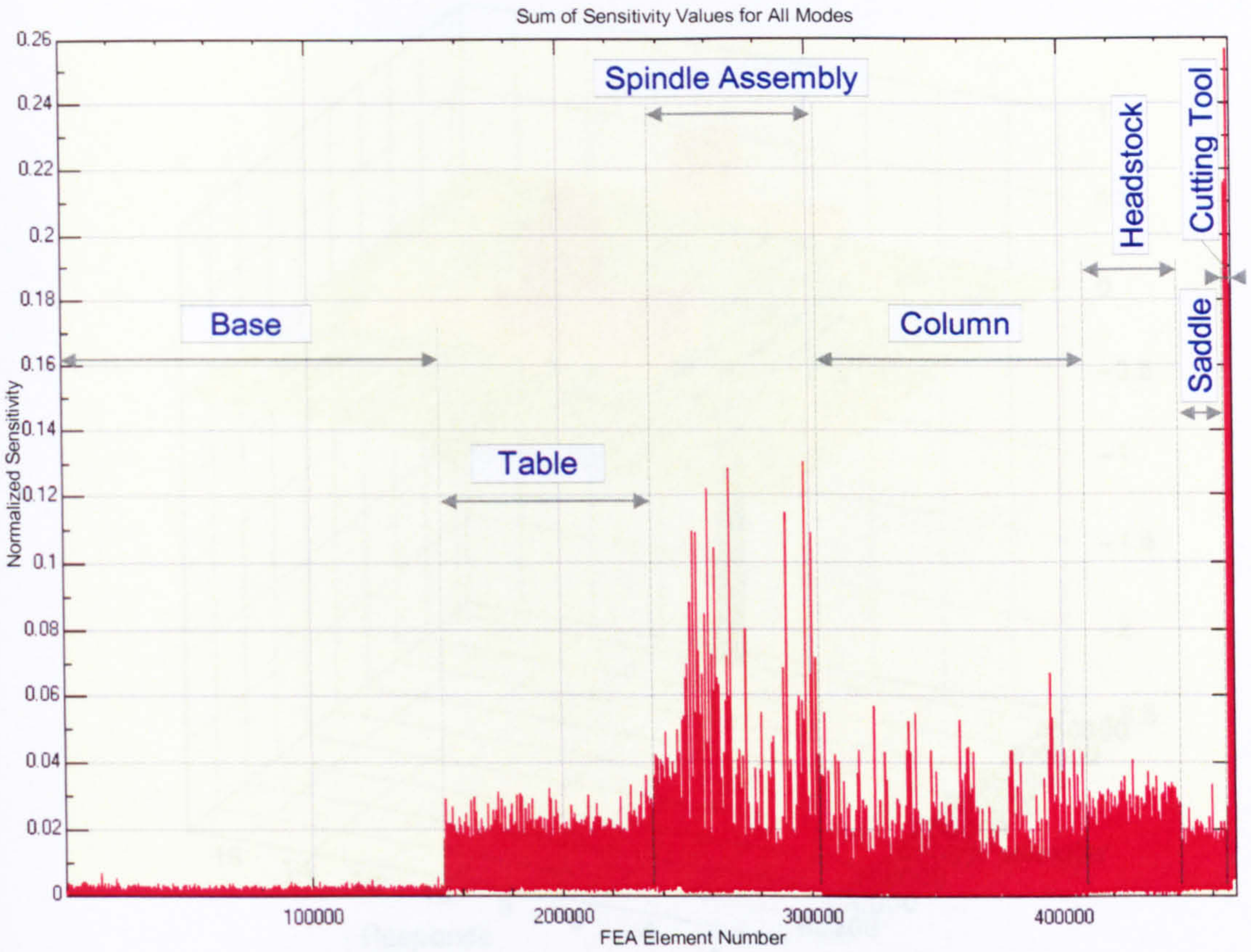

Figure 8.11. Diagram of all FEA elements' cumulative sensitivity coefficients of Young's modulus variation against the natural frequencies

The sensitivity coefficients as the function of mode shapes are shown in Figure 8.12 and Figure 8.13. The figures indicate that the sensitivity values for the mode shapes of the table and spindle are relatively high towards variation in the stiffness values, especially for higher modes. Decreasing the Young's modulus values for these elements may produce lower mode shapes, so that better correlation with the measured results can be achieved. However, it can be seen that the Young's modulus of the cutting tool is negative. This means that increasing its value may lower the mode shapes, thus producing better correlation with the measured mode shapes.

Figure 8.14 and Figure 8.15 show the sensitivity coefficients of the FEA model for Young's modulus variation towards the MAC values. It can be seen from the figures that the MAC values of mode 4 and 5 of the cutting tool elements are the most sensitive to Young's modulus variation. Increasing its values may raise the MAC values which means better correlation between the analytical and experimental results. The figures also show negative sensitivity values for the machine table. This can be interpreted that the Young's modulus for the table can be lowered in order to achieve better MAC values.

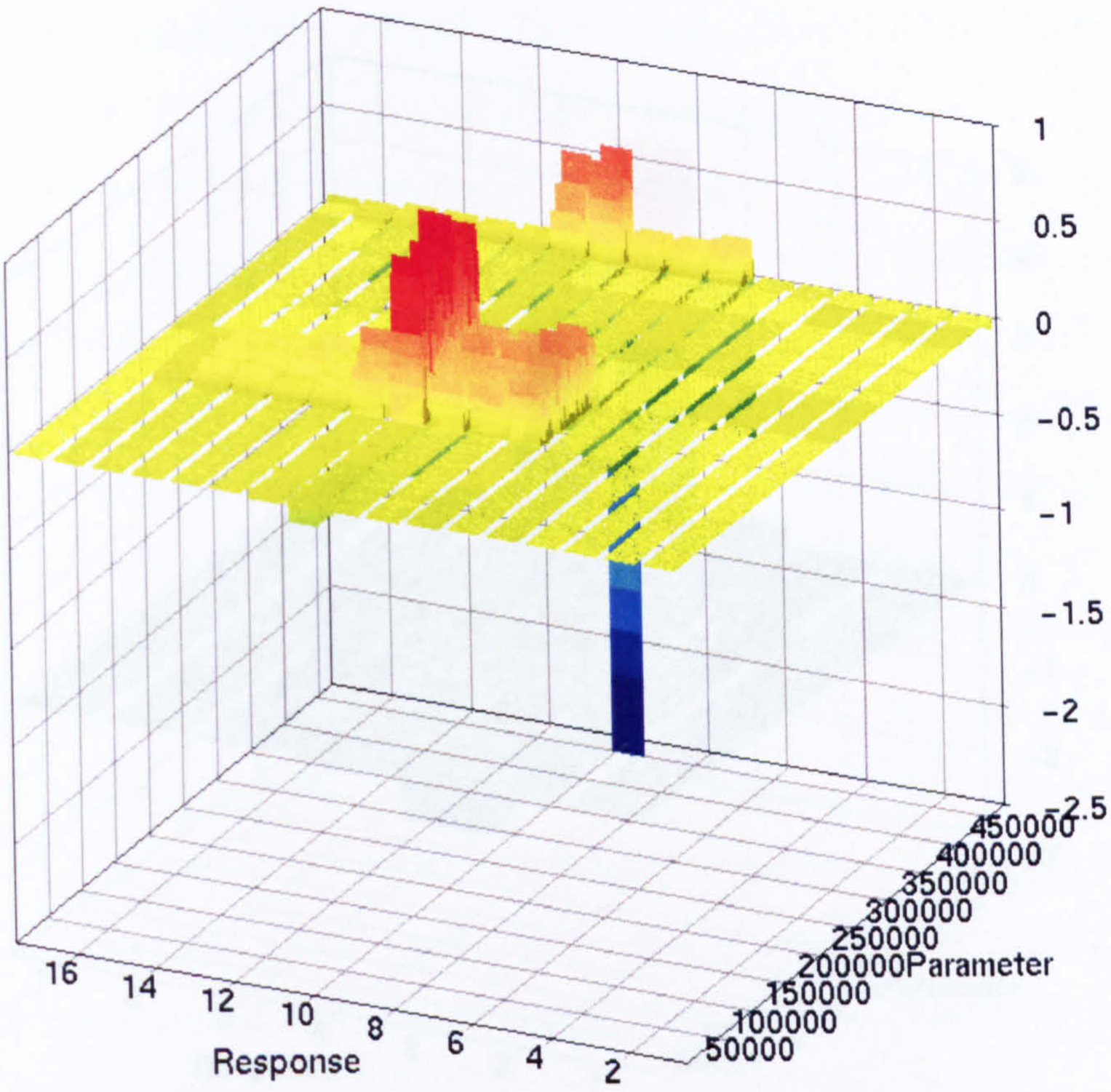

Figure 8.12. 3D Diagram of FEA element sensitivity coefficients of Young's modulus variation against of the mode shapes

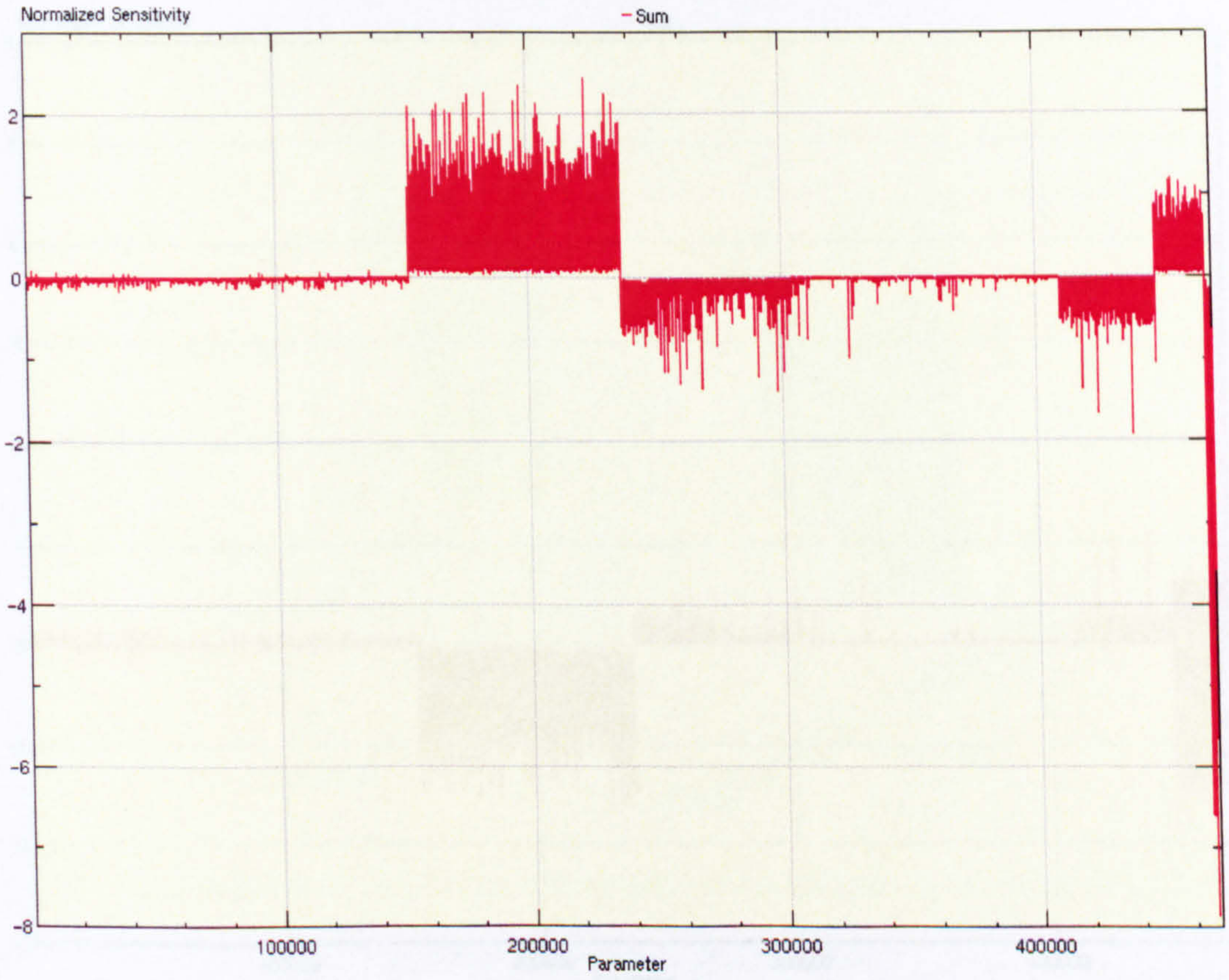

Figure 8.13. Diagram of all FEA elements' cumulative sensitivity coefficients of Young's modulus variation against the mode shapes

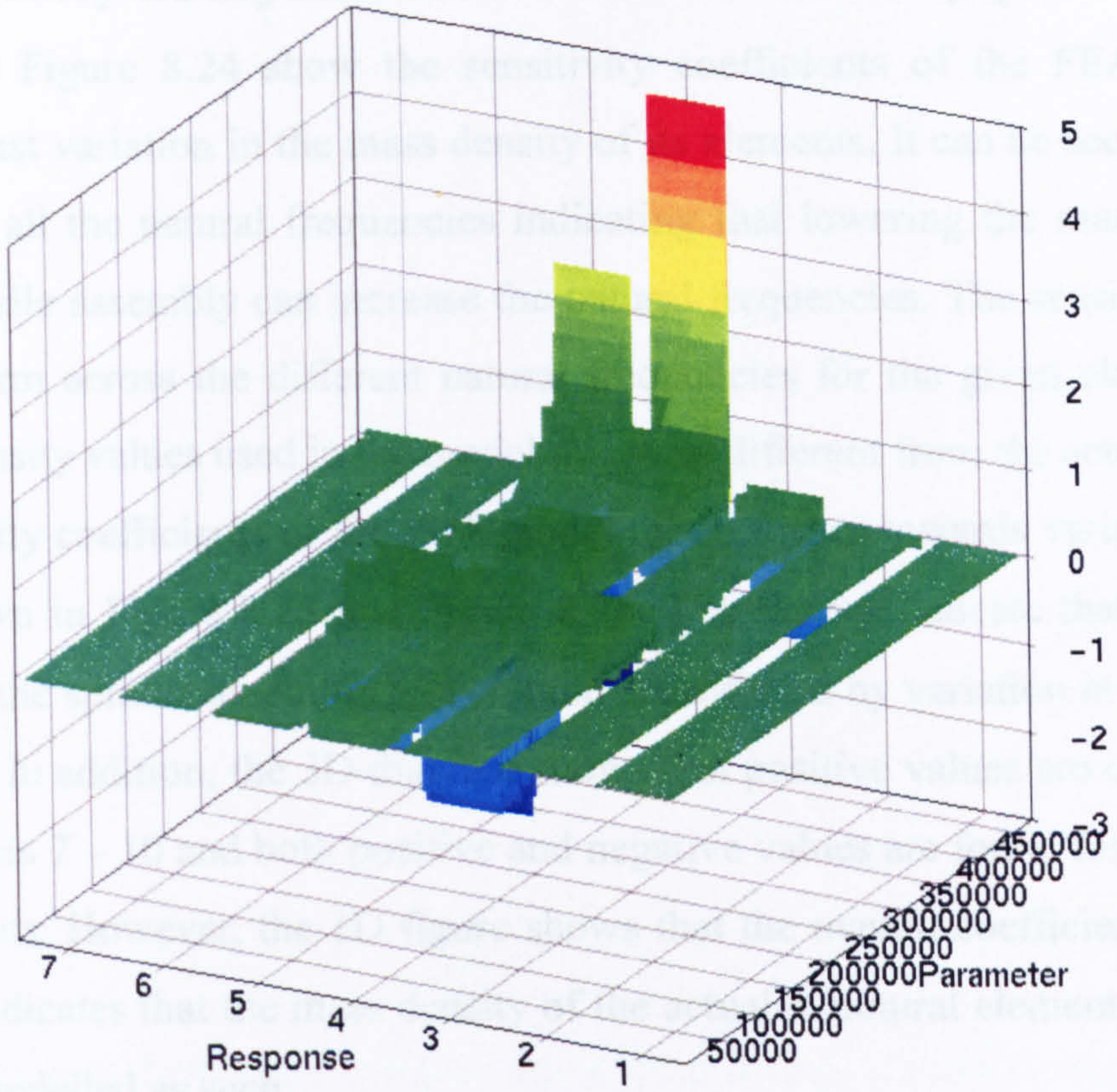

Figure 8.14. 3D Diagram of FEA element sensitivity coefficients of Young's modulus variation against the MAC values

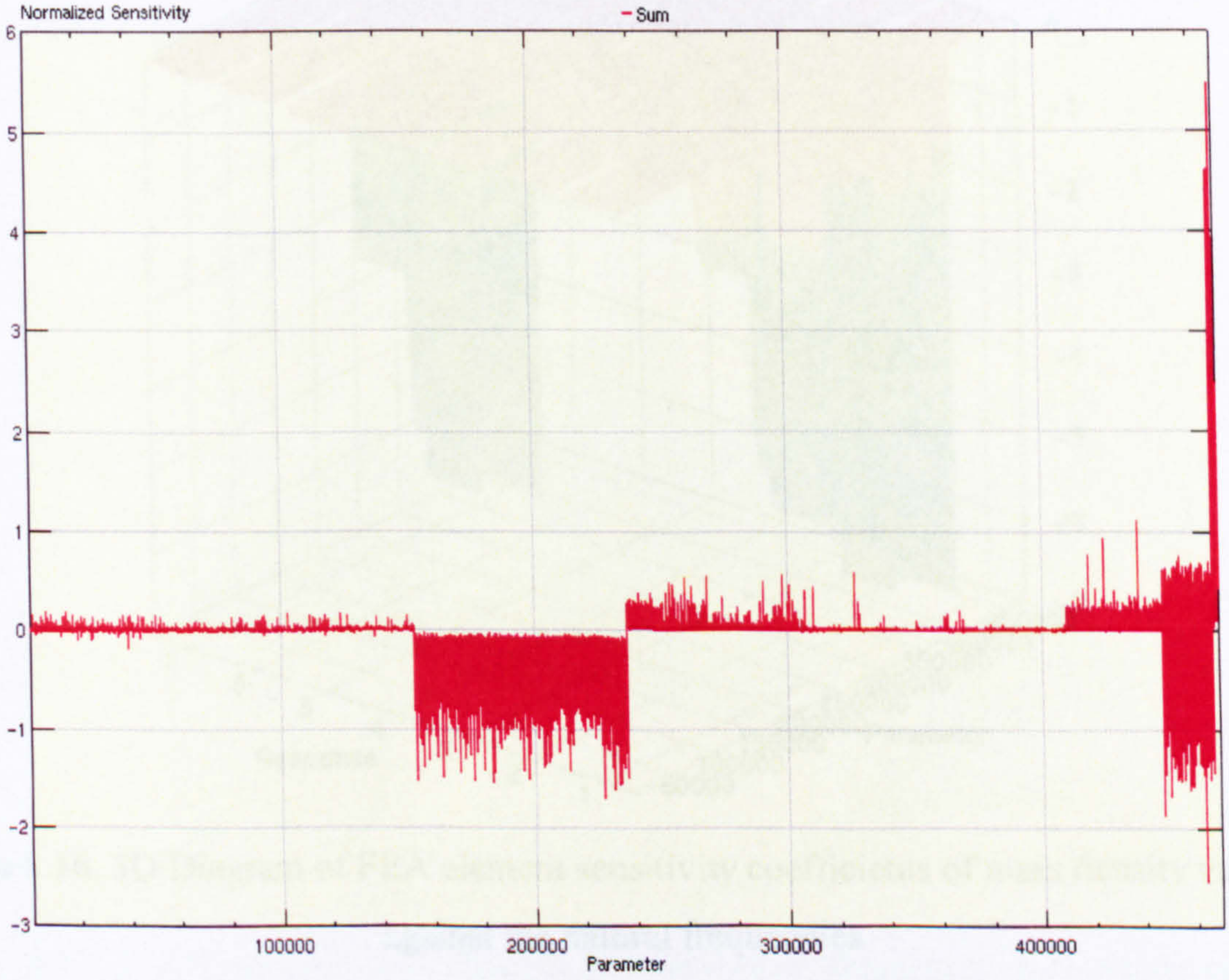

Figure 8.15. Diagram of all FEA elements' cumulative sensitivity coefficients of Young's modulus variation against the MAC values

8.4.2. Sensitivity analysis result for mass density parameter

Figure 8.23 and Figure 8.24 show the sensitivity coefficients of the FEA model natural frequencies against variation in the mass density of its elements. It can be seen that the values are negative for all the natural frequencies indicating that lowering the mass density of the column and spindle assembly can increase the natural frequencies. The sensitivity coefficient values are uniform across the different natural frequencies for the given elements, meaning that the mass density values used in the model might be different from the actual material.

The sensitivity coefficients of the FEA model mode shapes towards variation in the mass density are shown in Figure 8.25 and Figure 8.26. The figures indicate that only the higher mode shapes of the spindle assembly and column are affected by variation in the mass density of the elements. In addition, the 3D diagram shows that positive values are observed in mode shape components 7 – 10 and both positive and negative values are found for the higher mode shape components. However, the 1D figure shows that the overall coefficients are almost all positive. This indicates that the mass density of the actual structural elements are not uniform and should be modelled as such.

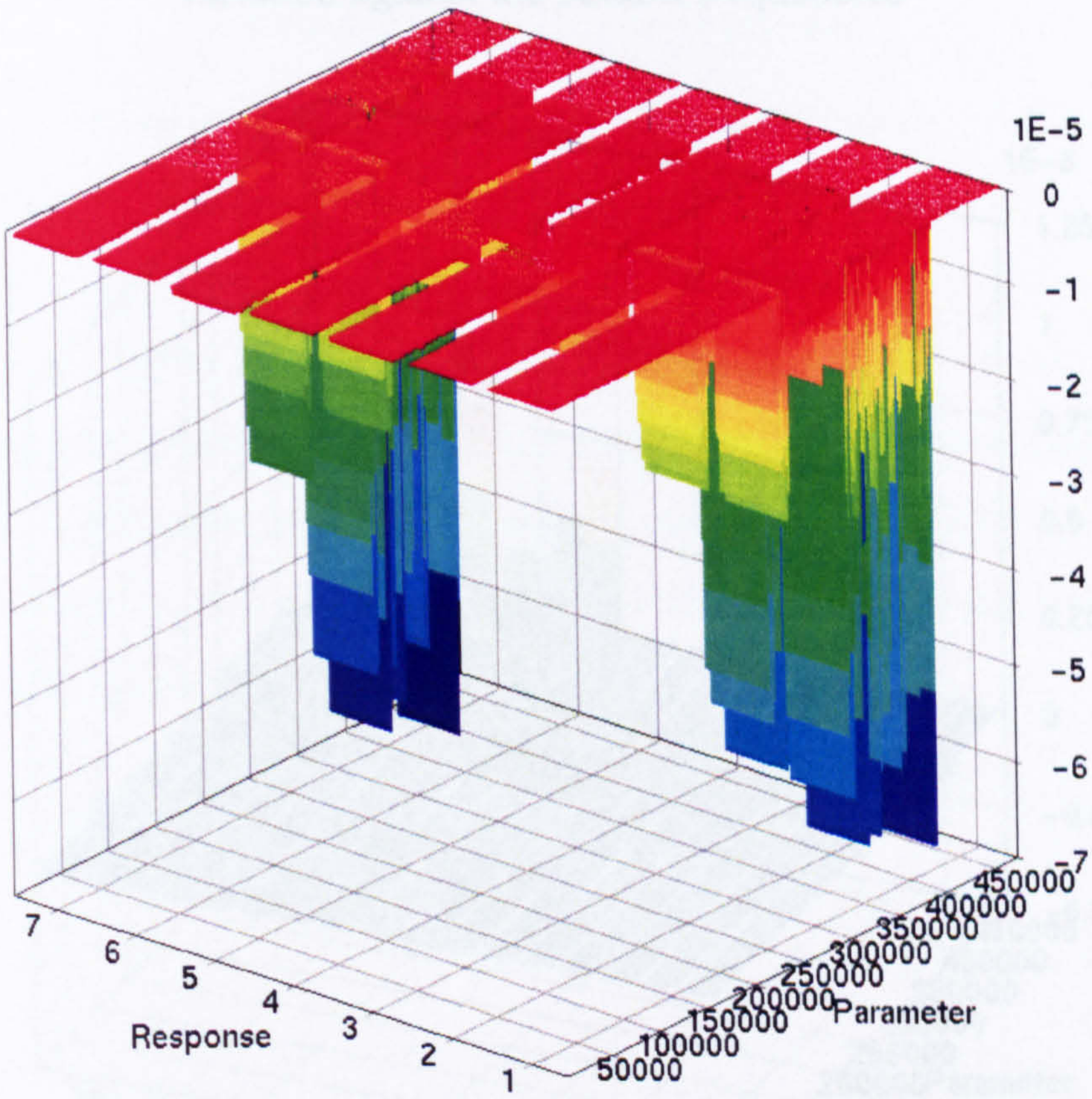

Figure 8.16. 3D Diagram of FEA element sensitivity coefficients of mass density variation against the natural frequencies

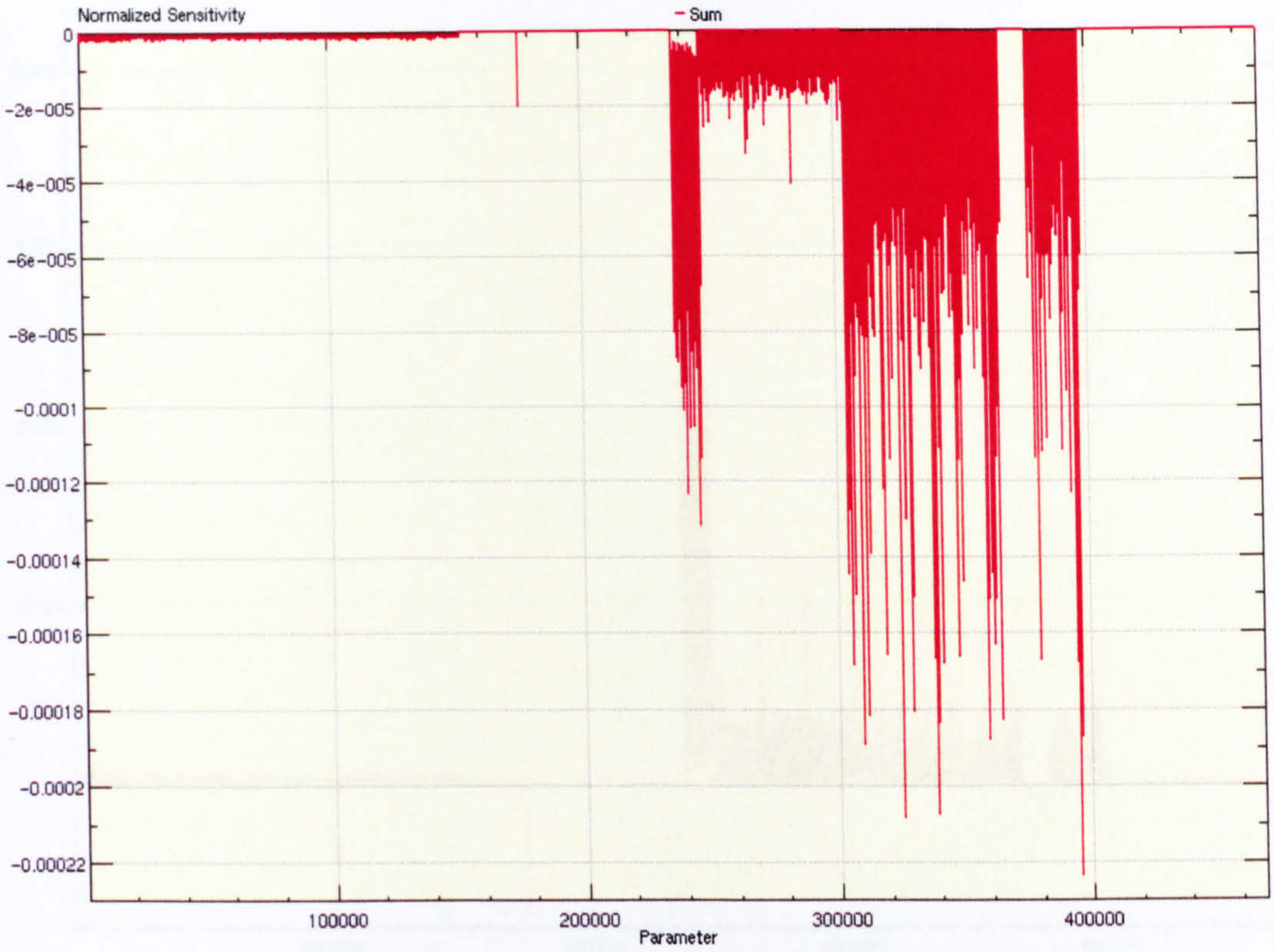

Figure 8.17. Diagram of all FEA elements' cumulative sensitivity coefficients of mass density variation against the natural frequencies

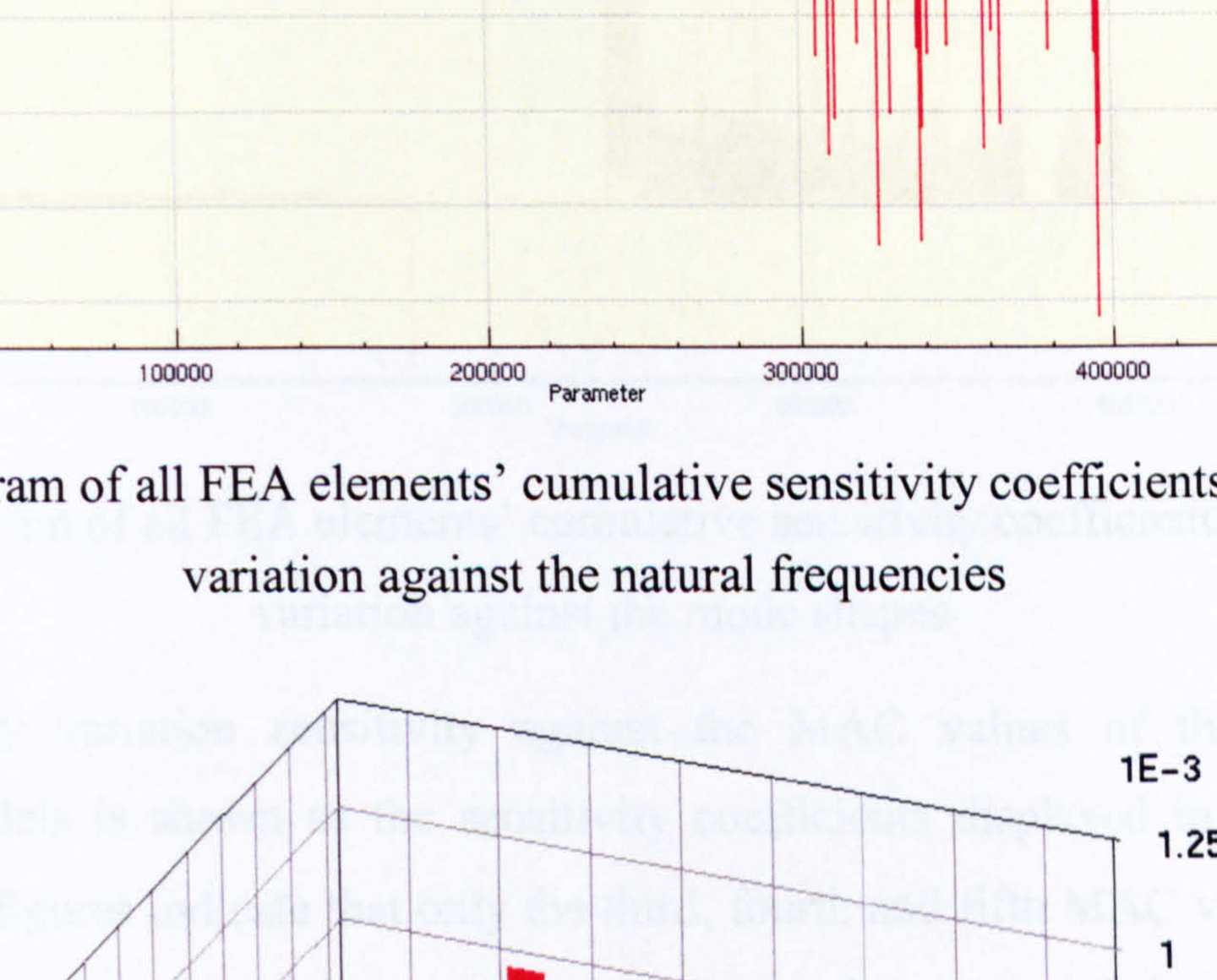

Figure 8.18. 3D Diagram of FEA element sensitivity coefficients of mass density variation against the mode shapes

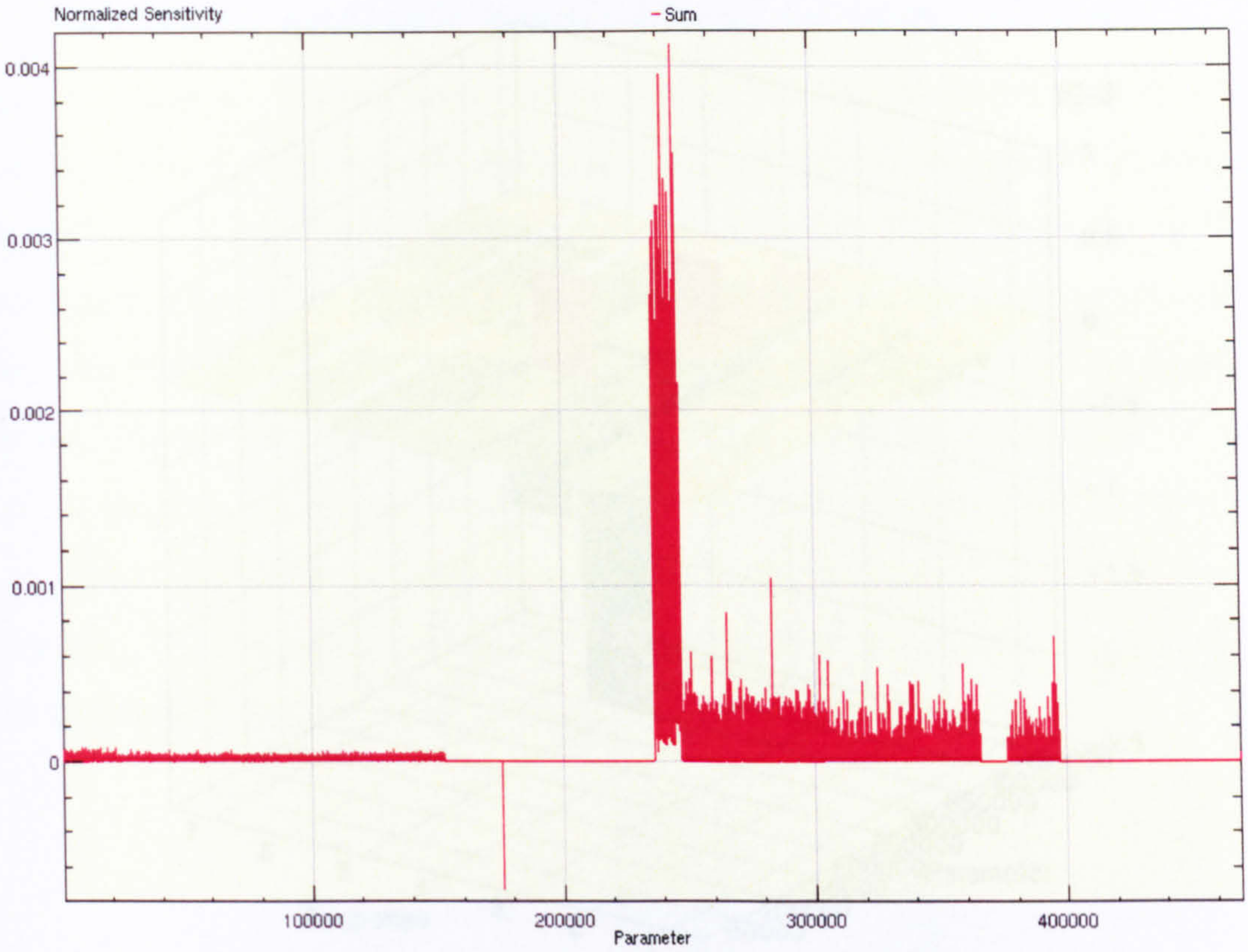

Figure 8.19. Diagram of all FEA elements' cumulative sensitivity coefficients of mass density variation against the mode shapes

The mass density variation sensitivity against the MAC values of the analytical and experimental models is shown as the sensitivity coefficients displayed in Figure 8.25 and Figure 8.26. The figures indicate that only the third, fourth and fifth MAC values are affected greatly by the mass density variations. It can be seen that some of the spindle assembly elements have negative coefficients indicating that lowering the mass density may increase the MAC values (correlation between measured and simulated results). This can also be interpreted that different mass densities are found in the spindle assembly, indicating that different materials are used to construct the element.

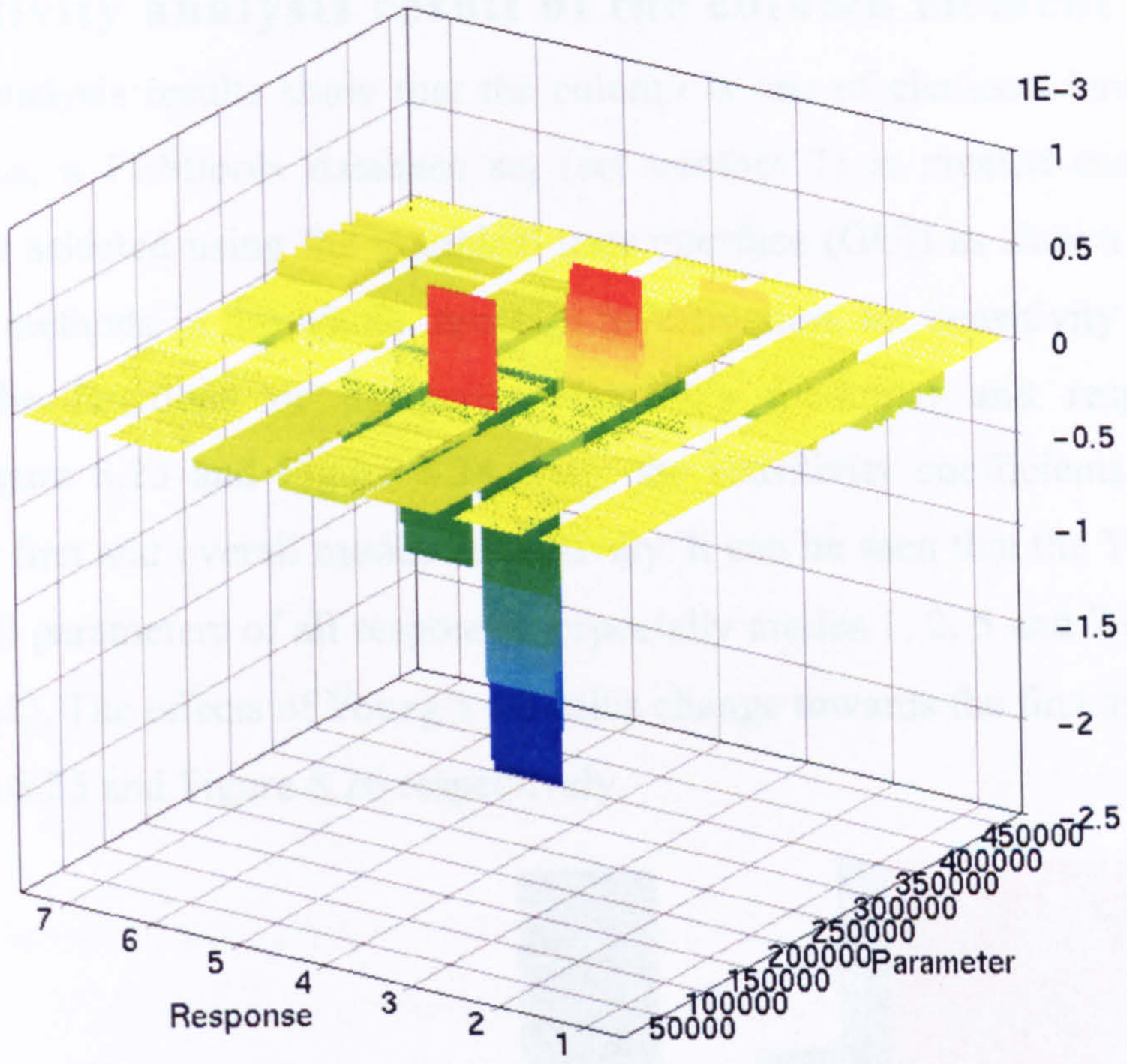

Figure 8.20. 3D Diagram of FEA element sensitivity coefficients of mass density variation against the MAC values

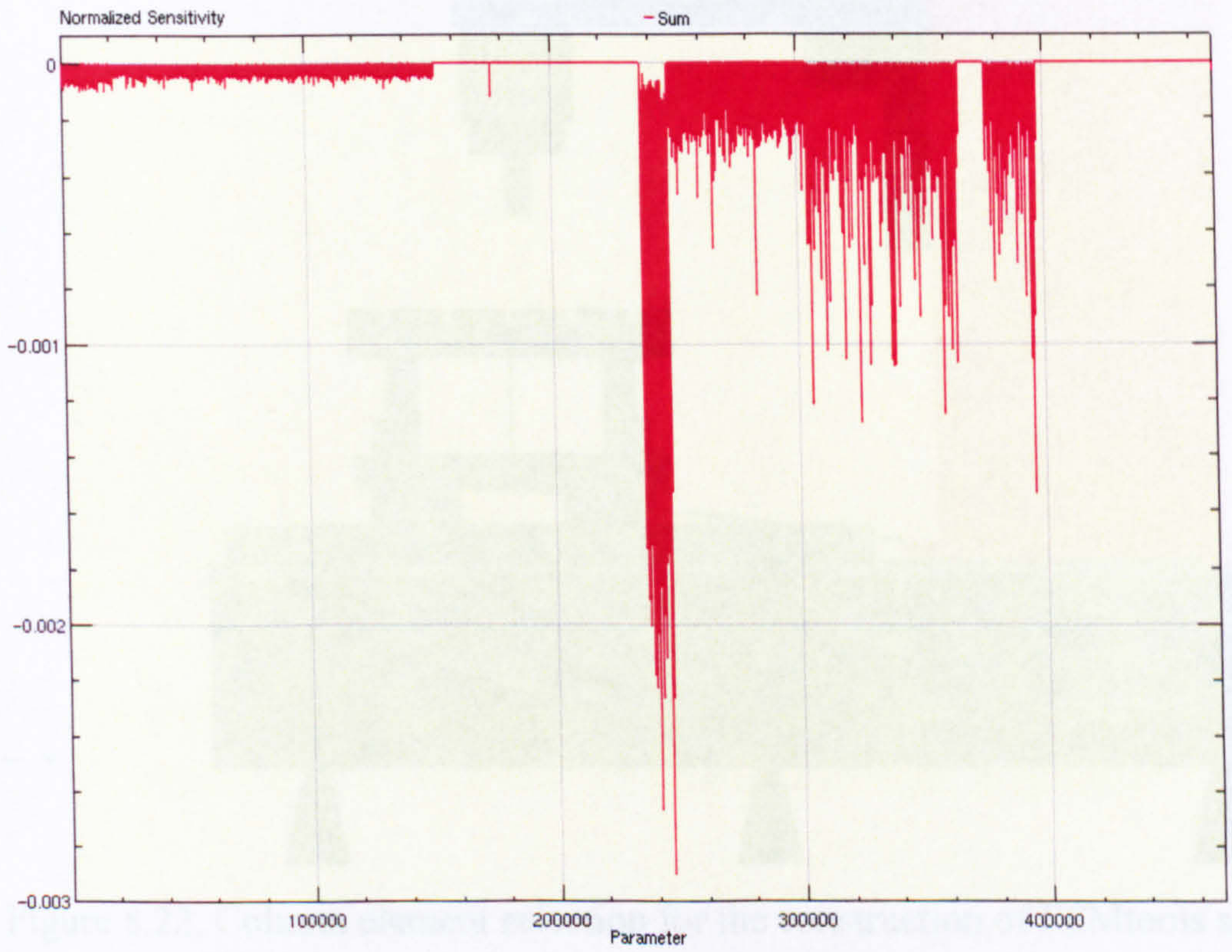

Figure 8.21. Diagram of all FEA elements' cumulative sensitivity coefficients of mass density variation against the MAC values

8.4.3. Sensitivity analysis result of the column element

The sensitivity analysis results show that the column is one of elements having the highest coefficients. Thus, a FEMtools database set (set number 7) is created containing all the column elements selected using the graphical user interface (GUI) as shown in Figure 8.22. Using the same methods in the whole structure investigation, the sensitivity coefficients are calculated as the functions of parameters (Young's modulus) and responses (natural frequencies). Figure 8.23 and Figure 8.24 show the sensitivity coefficients of the column elements for the first and overall modes respectively. It can be seen that the Young's modulus affects the modal parameters of all responses, especially modes 1, 2, 5 and 7 (see Figure 8.27 and Appendix F.2). The effects of Young's modulus change towards the first and all modes are shown in Figure 8.25 and Figure 8.26 respectively.

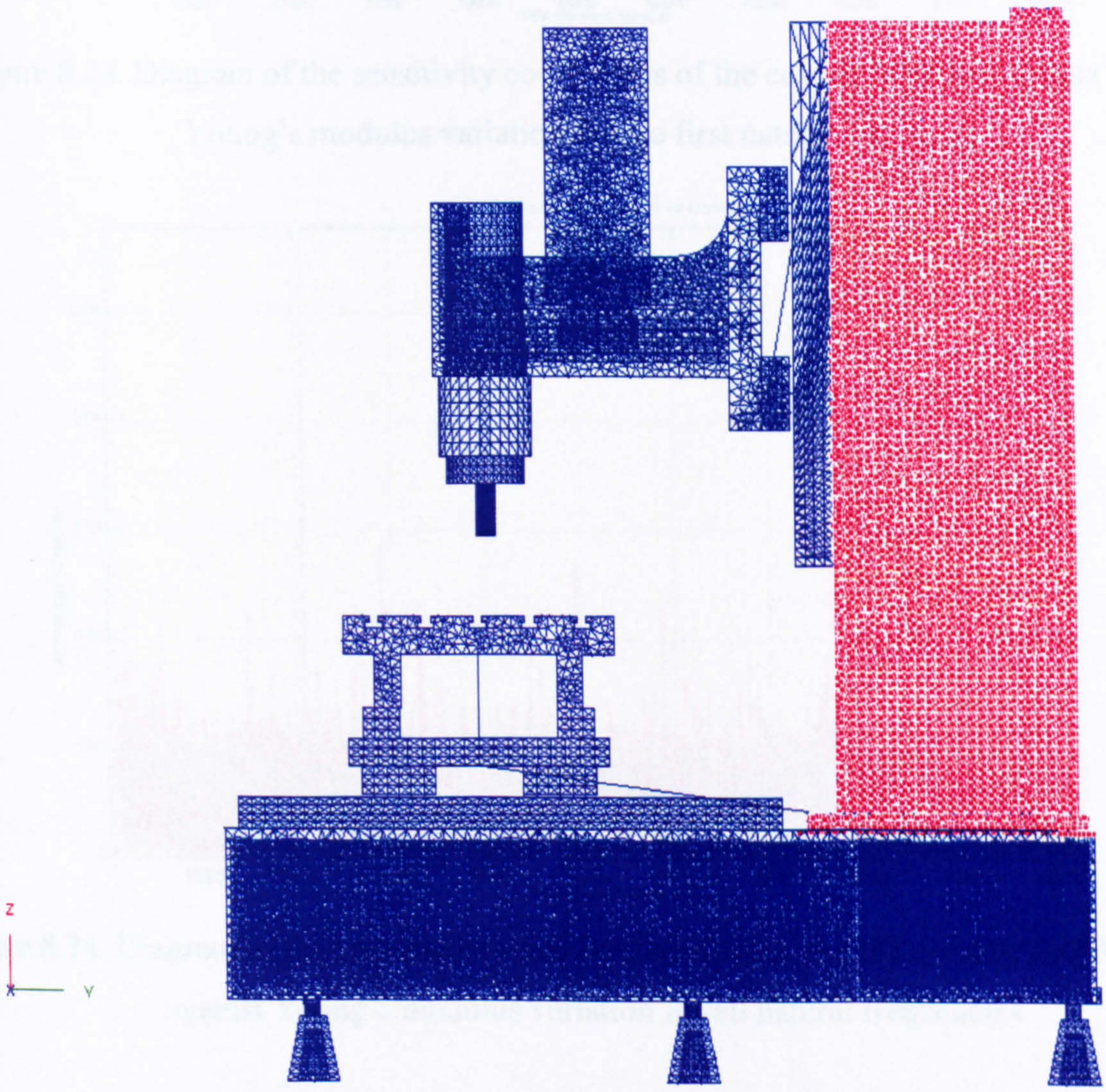

Figure 8.22. Column element selection for the construction of FEMtools set 7

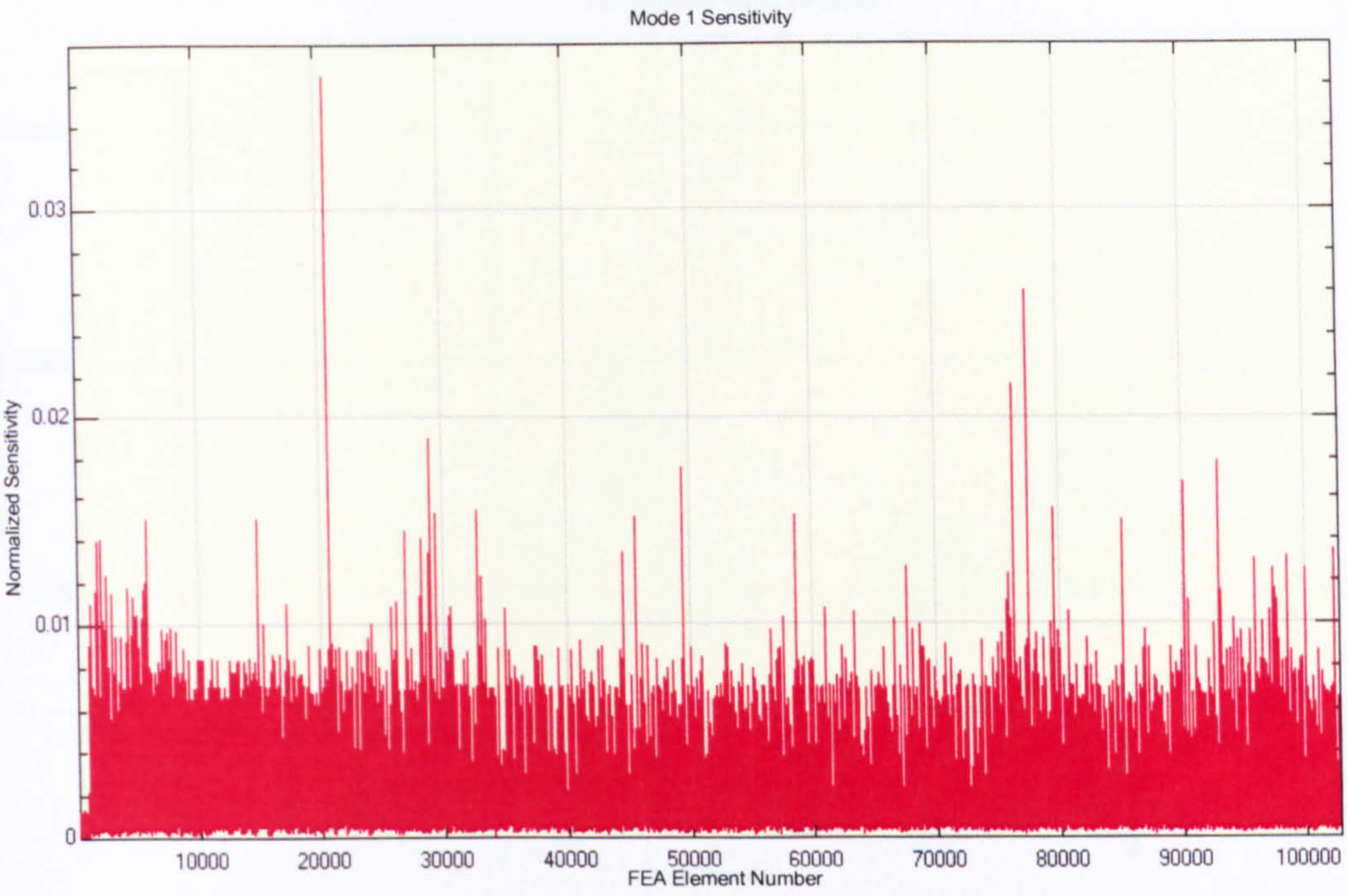

Figure 8.23. Diagram of the sensitivity coefficients of the column's FEA elements against Young's modulus variation for the first natural frequency

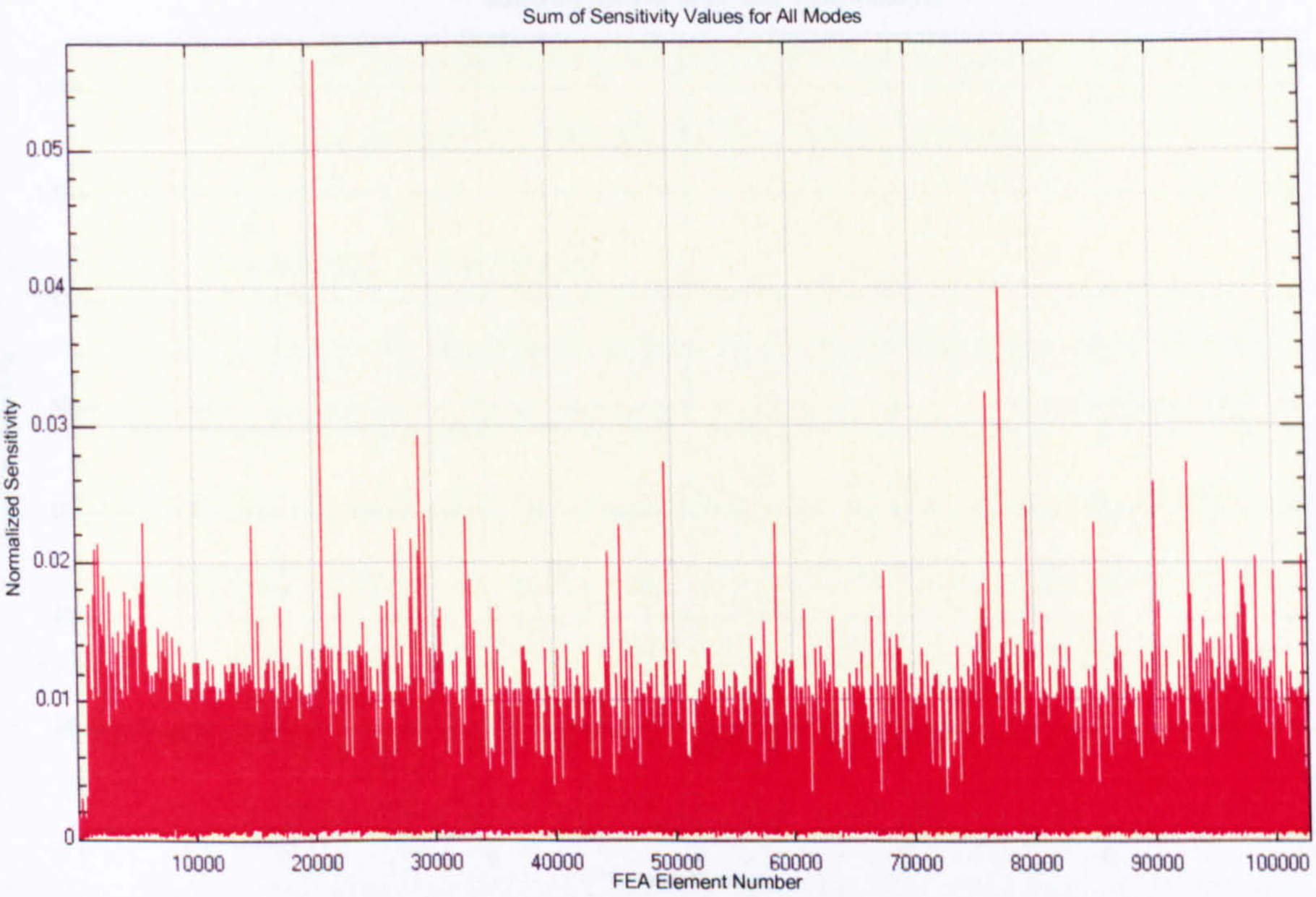

Figure 8.24. Diagram of the cumulative sensitivity coefficients of the column's FEA elements against Young's modulus variation for all natural frequencies

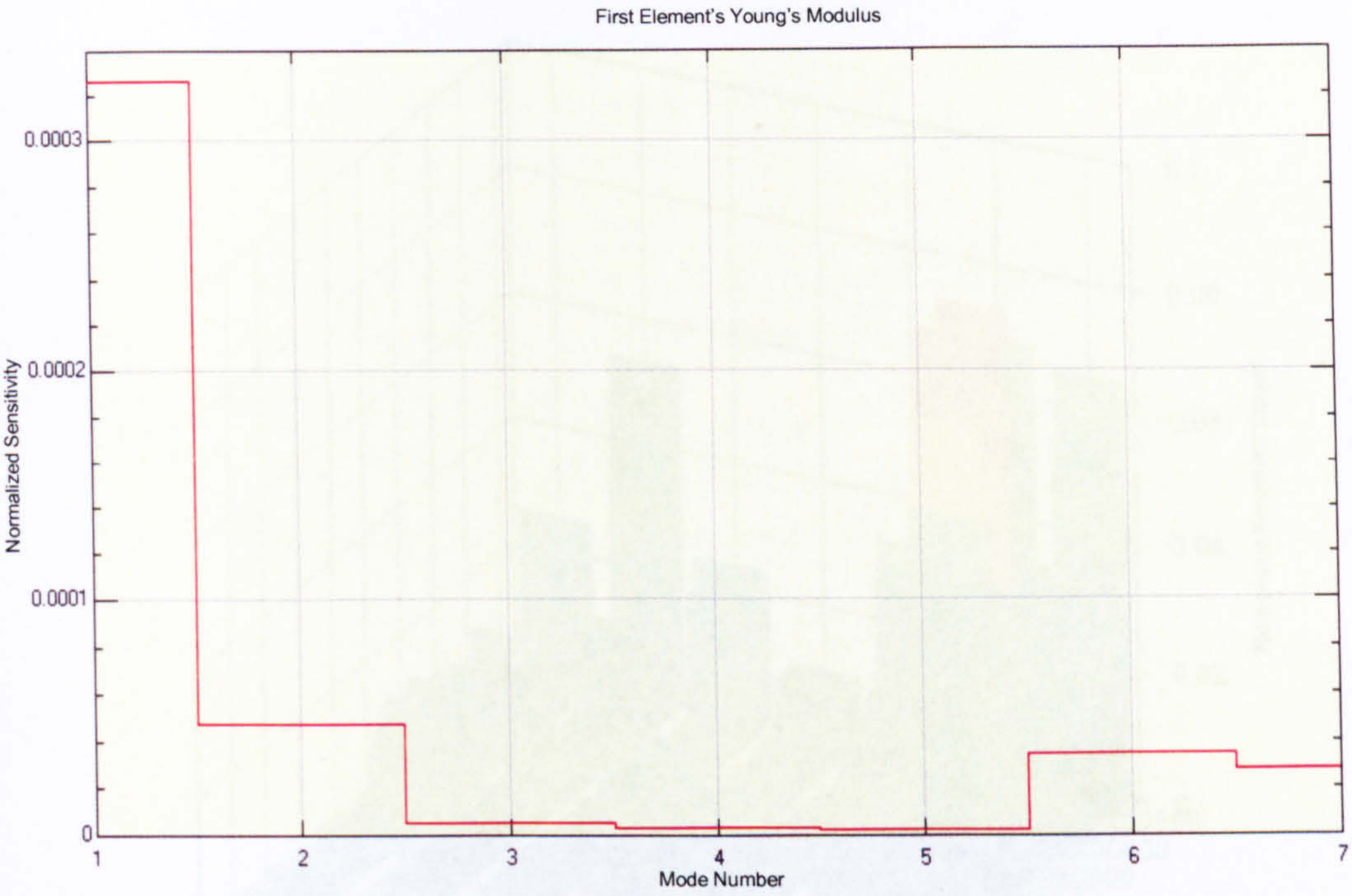

Figure 8.25. Diagram of the mode's sensitivity coefficients of the machine column against Young's modulus variation in FEA element 1

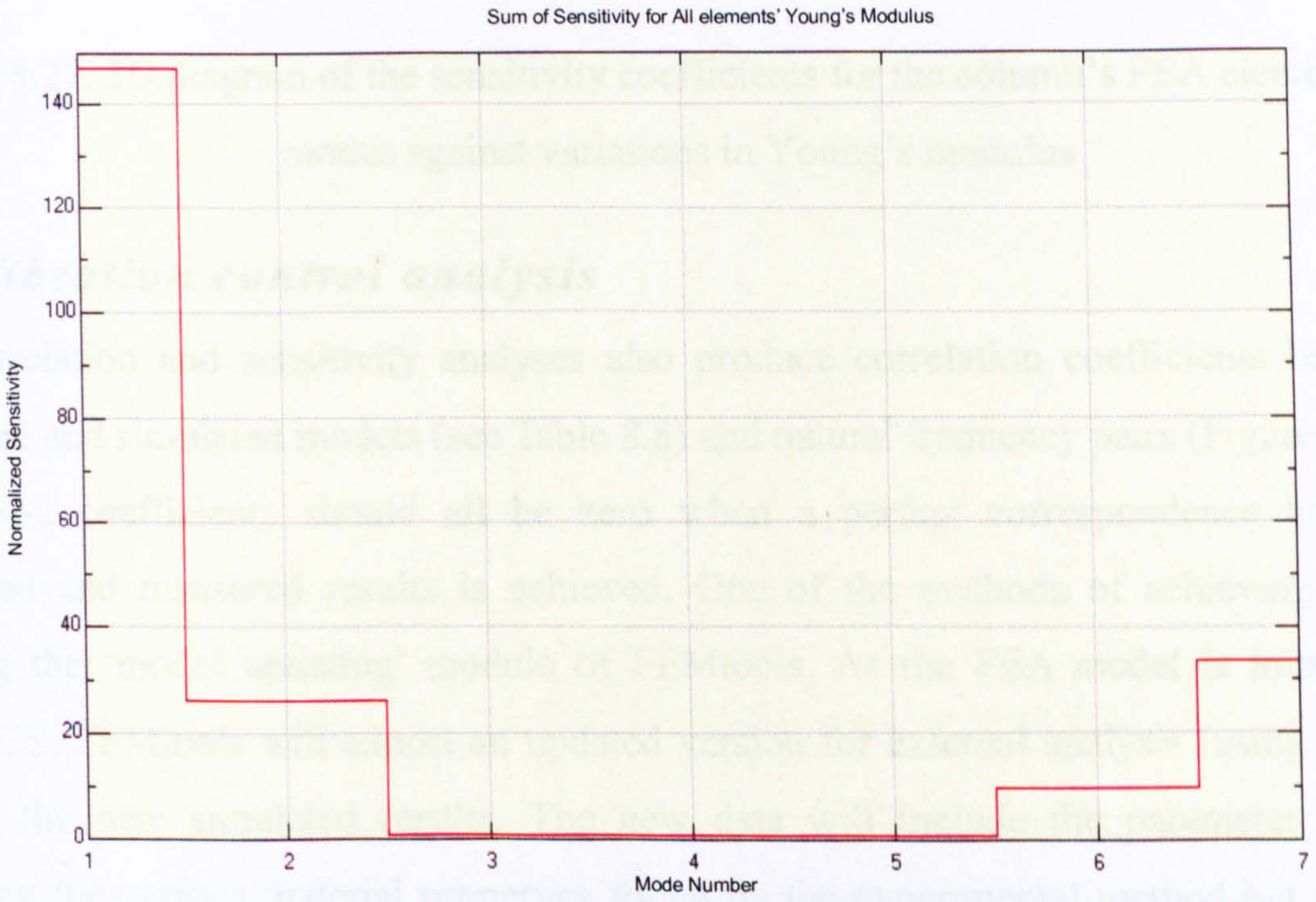

Figure 8.26. Diagram of the mode's cumulative sensitivity coefficients of the machine column against Young's modulus variation in all FEA elements

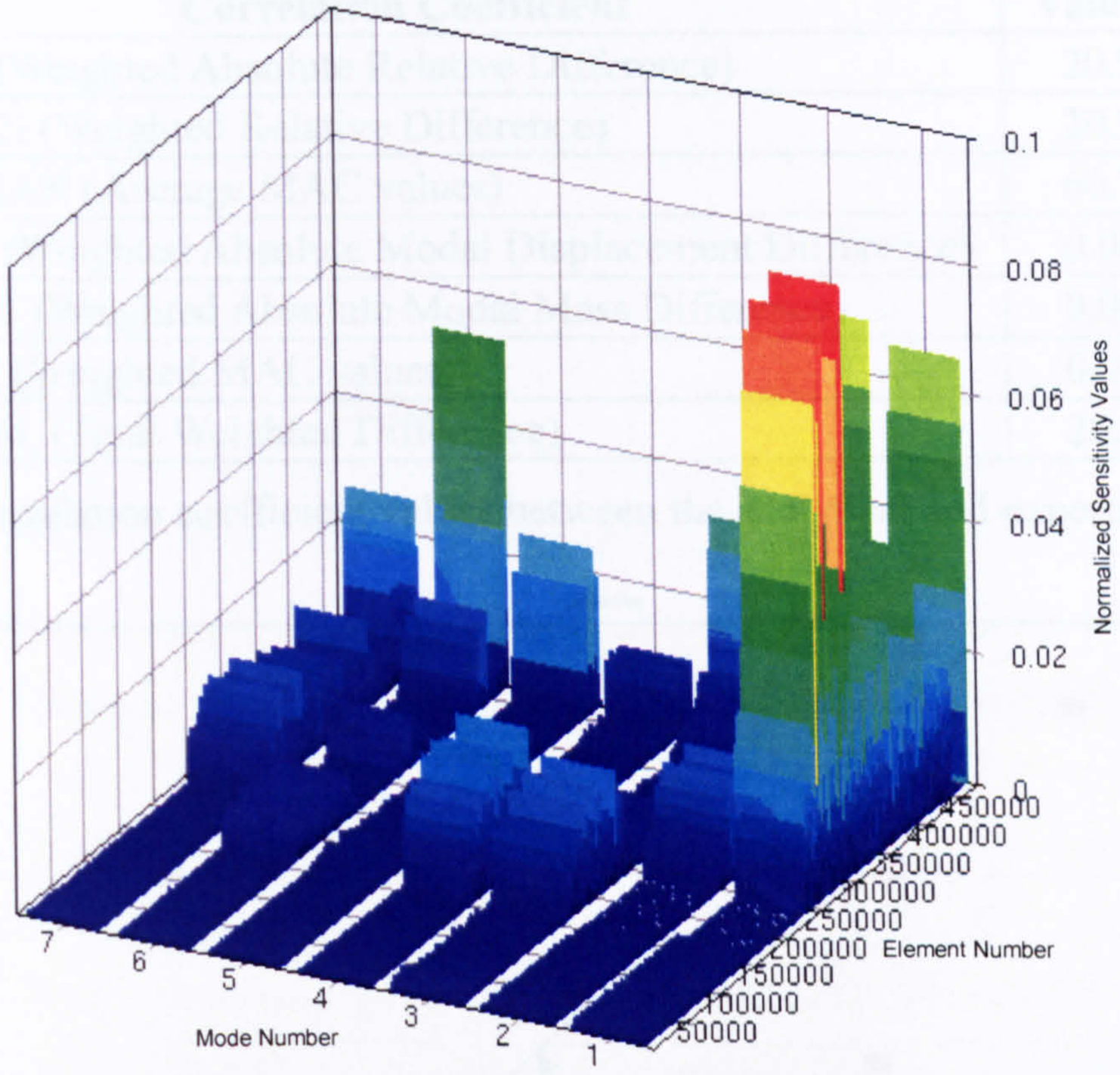

Figure 8.27. 3D diagram of the sensitivity coefficients for the column's FEA elements in all modes against variations in Young's modulus

8.5. Vibration control analysis

The correlation and sensitivity analyses also produce correlation coefficients between the measured and simulated models (see Table 8.8) and natural frequency pairs (Figure 8.28). The correlation coefficients should all be zero when a perfect correspondence between the simulated and measured results is achieved. One of the methods of achieving this is by utilising the 'model updating' module of FEMtools. As the FEA model is imported from ABAQUS, FEMtools will export an updated version for external analysis (using ABAQUS) to find the new simulated results. The new data will include the parameter differences reflecting the various material properties found by the experimental method but assumed as uniform by the analytical procedures. However, this cannot be achieved by the investigation at present because the version differences and interfacing constraint between the software. Thus, the next section will analyse the obtained results with respect to the current passive vibration control techniques researched in the field.

Correlation Coefficient	Value (%)
CCABS (Weighted Absolute Relative Difference)	20.9050
CCMEAN (Weighted Relative Difference)	20.9050
MACMEAN (Average MAC values)	60.7468
CCDISP (Weighted Absolute Modal Displacement Difference)	0.00000
CCMASS (Weighted Absolute Modal Mass Difference)	0.00000
CCMAC (Weighted MAC values)	0.00000
CCTOTAL (Total Weighted Difference)	20.9050

Table 8.8. Correlation coefficient values between the analytical and experimental data

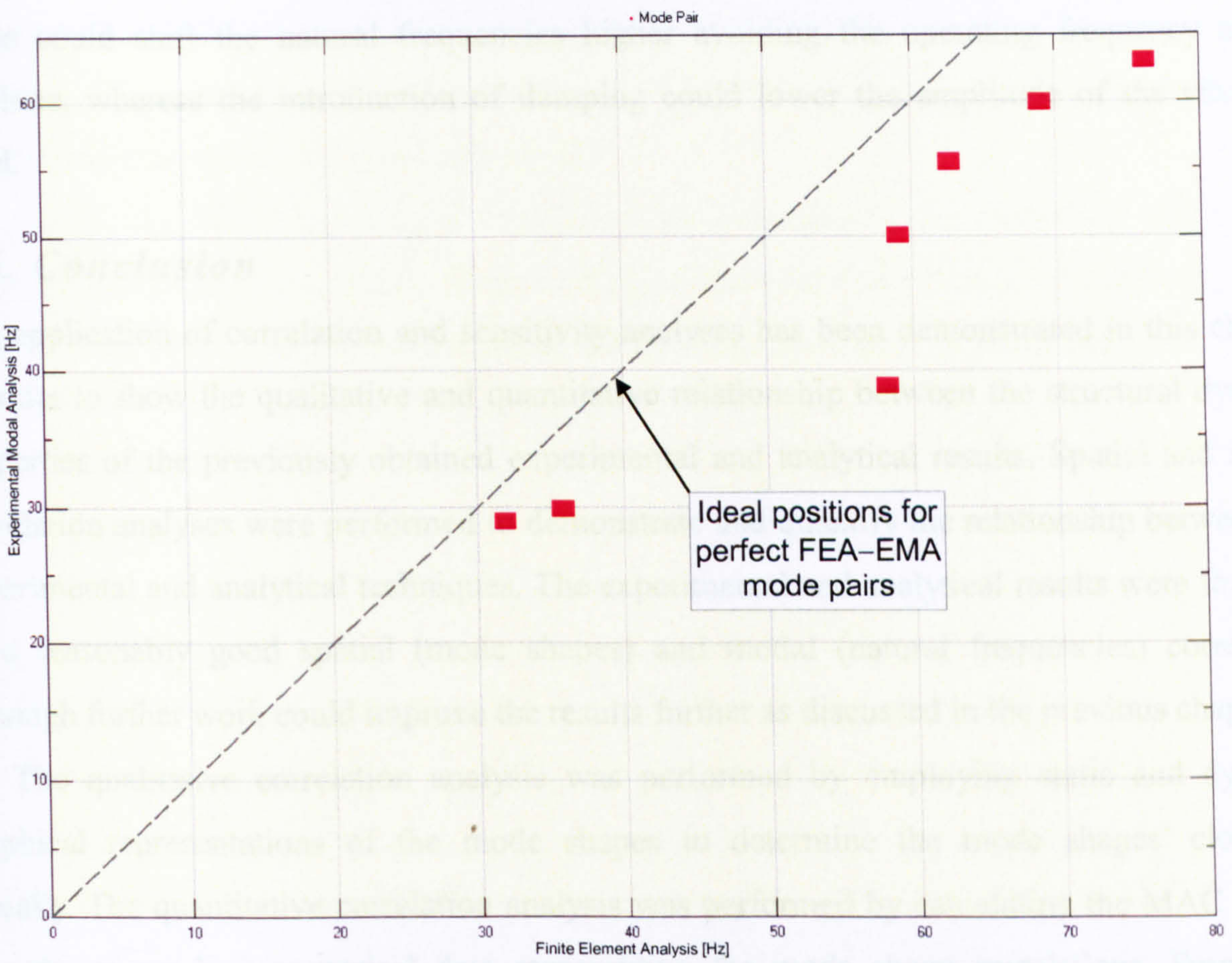

Figure 8.28. Map of experimental and analytical resonant frequency pairs

One of the most advanced techniques in vibration control involving the passive methods is by modifying the properties of the structure introducing smart materials (magneto- and electro-rheological fluid, magneto-strictive materials and visco-elastic polymer, etc.). These materials can change their properties by the application of magnetic or electric field, enabling the structural dynamic properties of the whole body to be altered. Petrone et. al. [220] presented an investigation into the dynamics behaviour (stiffness and damping properties) of rheological models simulating the various types elastomers. The study suggests that rheological materials can be utilised to model the behaviour of elastomer materials in order to modify the dynamic

behaviour of the structure. Thus, this knowledge provides information into the types of applications rheological materials can be implemented.

On the other hand, Rajoria and Jalili [221] presented a vibration control study through the passive method by the utilisation of carbon nanotube-epoxy reinforced composites. The study investigated the effect of the composite material introduction on the stiffness and damping properties of a structure. This and the previous investigations combined may produce the desired effect of using rheological materials for passive vibration control of a structure by modifying the stiffness and damping properties of the structure. The change in the stiffness value could shift the natural frequencies higher avoiding the operating frequency of the machine, whereas the introduction of damping could lower the amplitude of the vibration level.

8.6. Conclusion

The application of correlation and sensitivity analyses has been demonstrated in this chapter in order to show the qualitative and quantitative relationship between the structural dynamic properties of the previously obtained experimental and analytical results. Spatial and modal correlation analyses were performed to demonstrate and quantify the relationship between the experimental and analytical techniques. The experimental and analytical results were found to have reasonably good spatial (mode shapes) and modal (natural frequencies) correlation although further work could improve the results further as discussed in the previous chapters.

The qualitative correlation analysis was performed by employing static and dynamic graphical representations of the mode shapes to determine the mode shapes' closeness visually. The quantitative correlation analysis was performed by calculating the MAC values in order to produce numerical data representing the mode shape correlations. From both results, the study shows that the predicted machine column's behaviour in the Y-direction is close to the measured data, but not in the X-direction. This is confirmed by the sensitivity analysis study that changes in the column element stiffness will likely to change its modes and improve the correlation in the form of MAC values.

The sensitivity analysis technique has been demonstrated to determine the influence of the machine elements' Young's modulus and mass densities on the dynamic behaviour of the structure. The result shows that the column element is one of the most sensitive elements towards any change in the material property values. This means that modifying this element will change the natural frequencies and mode shapes of the machine structure significantly. In addition, it has been shown that the investigation was able to differentiate between the

different material types utilised in the machine structure. The simulated results were shown to produce acceptable correlation to the measured data, but further modification into the structural elements of the FEA model could improve it further.

In addition, the parametric studies performed using the sensitivity analysis produced sensitivity coefficients which can be employed as a 'parametric map' in order to improve the experimental and analytical model correlation. This 'map' can also be employed to develop a passive vibration control technique whereby the value of a given material property (stiffness or mass) is modified in order to shift the natural frequencies away from the operating frequency. Thus, the structural dynamic properties of the machine structure can be controlled passively to reduce its response towards the vibration generated, e.g. by the machining process, external forces and rapid axis travel.

Finally, the following chapter concludes and summarises the modelling and control investigations discussed in the thesis as well as produces several recommended investigations to carry the study further into the improvement and implementation of the results.

Chapter 9. CONCLUSIONS AND SUGGESTIONS FOR FURTHER WORK

It has been shown in the investigation that machine tool vibration is a complex function of structural dynamic properties, drive system performance, machining process operation, and machined surface finish. An accurate identification of a machine tool's structural dynamic properties is highly important because vibration introduced at or near its natural frequencies may grow exceedingly high and becomes uncontrollable. The machine drive performance is limited by its resonant frequencies, thus its analysis and modelling taking into account the contribution of its torsional and axial elements is essential. The production of accurate workpieces is of all importance in a machining operation. Thus, the modelling of the process to represent the mechanistic forces must be conducted in order to investigate its vibration characteristics. This can be assisted significantly with the recent progress in the 3D surface topography technology.

A machine tool structure is highly non-linear, hence a methodical experimental modal analysis is necessary in order to obtain the dynamics data accurately. SIMO and MIMO techniques using shaker excitation were employed to obtain the FRF data. The study outlines and validates various aspects of the experimental technique required to maintain the quality of the measured data using both SIMO and MIMO measurement methods. The study proposed that the suspended shaker technique be employed in modal analysis studies as opposed to the shaker on table method normally employed in the industry. The proposed technique showed that more accurate FRF data was produced because of less force contamination due to the removal of the force loop. However, it was also shown that the force introduced into the structure was reduced since the comparatively smaller and unclamped shaker cannot resist the opposing inertial force from the machine's mass.

Machine tool vibration is also influenced by its drive system as the positioning, velocity, acceleration and jerk of the drive's torsional and axial mechanical transmission system produces resonant frequencies, reducing its performance and the finished workpiece quality. The study has successfully developed and validated a single-axis drive system model based on the hybrid technique with explicit damping factors and non-linearities. The model includes both the torsional and axial elements as well as the viscous damping and coulomb friction to represent the energy dissipation effects. The model was validated in the time and frequency domains using deterministic and non-deterministic signals using the drive measured data generated as the response to the built-in signal generation functions. The model has been

utilised successfully as a proof of concept that a drive system's dynamic characteristics can be sufficiently simulated using such a technique, leading to the possibility of developing an active vibration control method through the drive system.

The investigation has contributed to the development of a machining dynamics model which represents the cutting force generation and machine vibration. The dynamic cutting force model was based on the oblique cutting theory and intended for a peripheral cutting process using helical end-mills and cutter run-out consideration. An experimental calibration was performed to determine the radial and axial force ratios, as well as the initial total cutting energy per unit volume. The results were utilised to validate and improve the initial values calculated from both the cutting tool, workpiece material and associated geometry as well as the cutting conditions. The machining dynamic model was completed by including a vibration model representing the workpiece and cutting tool motion as a two degree-of-freedom spring damper system. The parameter for the vibration model was obtained through an experimental modal analysis using instrumented hammer on both the workpiece and cutting tool. Several sets of cutting trials were carried out to validate the model by measuring the cutting forces and vibration of the cutting elements using a dynamometer and industrial accelerometers respectively. It has also been shown in the investigation that the surface finish of the machined workpiece contains information regarding the cutting tool condition, machining parameters, mechanistic forces and machine vibration. The measurement was taken using Form Talysurf PGI and the features were extracted using the 'lifting wavelet' scheme to separate the surface components.

An investigation into the structural modelling using the Finite Element Method (FEM) has become a viable solution in machine dynamics studies as the computing power has matured dramatically in recent years. A finite element model of the machine structure was constructed in the study and it was shown that close integration of different software could be employed to effectively develop and analyse the model. The geometric data for the machine was obtained by interfacing the physical model developed in a solid modelling software (Pro/ENGINEER) into the FEMGV pre-processing software. The geometric data was imported, manipulated and developed to produce the input deck for the ABAQUS/Standard FEA software. The analysis results were re-imported into FEMGV post-processing software and validated using the measured data obtained using the experimental modal analysis.

A vibration control analysis using the passive technique on the FE model has been demonstrated in the investigation. The investigation was carried out using the FEMtools software using the exported static and dynamics analysis data from ABAQUS. The

investigation included qualitative and quantitative correlation analysis of the simulated results of FEA model and the measured data from the experimental modal analysis. The difference between the manufacturer-supplied data and the actual values has been shown by the study to contribute to the variation between the analytical and experimental results. Parametric studies of the FEA model have shown that modifications on the values of the material properties have changed the structural properties of the machine (natural frequencies, mode shape vectors). Thus, by shifting the natural frequencies of the machine structure, a passive vibration control system can be implemented.

The ***PhD elements*** contained in this investigation are summarised as follows:

- Investigation into the use of suspended and worktable-supported shaker configurations in the investigation of machine tool's structural dynamic properties
- The development of a hybrid model with explicit damping factors and non-linearities for the digital drive system
- The development and structural dynamics investigation of the machine structure FE model employing Computer Aided Design (Pro/ENGINEER) and dedicated FEA (ABAQUS) software
- The validation and MAC (Modal Assurance Criterion) improvement of the FE model against the measured data from the experimental modal analysis using FEMtools correlation analysis

The ***contributions to knowledge*** of the study are summarised in the following:

- The development and validation of the cutting tool and workpiece vibration models for the integration into the machining dynamics model considering the dynamic cutting force model in collaboration with an academic partner as part of an EPSRC project.
- Characterisation of the machined surface by utilising 3D topography and investigation of the lifting wavelet scheme to separate the different surface parameters as a collaboration exercise with a research group partner as part of an EPSRC funded project.
- Investigation into the relationship between the surface parameters and measured cutting force, machine structural dynamics and workpiece-cutting tool vibration in collaboration with the academic partner and research group.
- Development of an FEA model for the machine tool structural dynamics using solid design, FEA pre- and post-processing, and FEA analysis software to combine geometric and numerical accuracies

- Improvement of the FEA model accuracy through incremental model validation against measured results obtained using SIMO and MIMO experimental modal analyses
- Parametric studies of FE model using FEMtools correlation and sensitivity analyses to find the relationship between machine's element property changes and the resulting structural dynamic behaviour in order to identify the machine structural components where passive vibration correction technique can be applied.

9.1. Further work

The parametric studies of the FEA model produced a list of suggested parameter changes to reduce the difference between the analytical and experimental data. The data produced from FEMtools 2.2.2 was found not to be compatible with ABAQUS/Standard version 6.4.1 and 6.5.1. An update to the interfacing capabilities data needs to be investigated to enable the complete development of passive vibration control system.

The results from the drive system modelling exercise also requires further investigations, especially in the area of active vibration control system. The limited frequency bandwidth of the velocity and position loop has been shown as insufficient to control the vibration normally experienced by the machine during cutting and non-cutting conditions. However, a more detailed investigation and modelling of the current control loop where the bandwidth is higher may provide an active vibration control solution through the drive system. This might involve the development of new compile cycles or the deployment of fully open–architecture (universal) drive systems in order to cater for the high frequency current control loop algorithm. In addition, the knowledge of the cutting process modelling can be taken into account and combined into the vibration compensation system since its frequency bandwidth coverage is sufficiently high.

References

1. **Metalworking Insiders' Report** – *The 2005 World Machine-Tool Output and Consumption Survey*, Gardner Publications, Inc., 2005

2. **British Standard, International Standard Organisation** – *Mechanical vibration - Evaluation of machine vibration by measurements on non-rotating parts – Part 1: General guidelines*, BS 7854-1: 1996, ISO 10816-1: 1995

3. **EPSRC Grant Award** – *Novel Metrology-Based Control Algorithms for Precision Manufacture (CAPM)*, EPSRC Grant No. GR/R13401/01, Universities of Huddersfield and Leeds Metropolitan, 2001 – 2004

4. **Ford D. G.** – *Machining to Microns – Error Avoidance or Compensation?*, Proceedings of International Conference on Laser Metrology and Machine Performance (LAMDAMAP'95), Southampton, 1995, (ISBN 1-85312-355-2), pp. 277 – 286

5. **AMTRI** – *Basic Structures for Machine Tools*, AMTRI Report, DTI Sponsored, 1992

6. **Furukawa Y., Moronuki N.** – *Contact deformation of a machine tool slideway and its effect on machining accuracy*, JSME International Journal, Vol. 30, Issue 263, 1987, pp. 868–874.

7. **Chatterjee S.** – *Spindle Deflections in High-speed Machine Tools – Modeling and Simulation*, International Journal of Advanced Manufacturing Technology, Vol. 11, 1996, pp. 232 – 239

8. **Bryan J. B.,** – *International status of thermal error research*, Annals of CIRP, Vol. 16(1), pp. 203, 1968

9. **Okafor A.C., Ertekin Y. M.** – *Derivation of machine tool error models and error compensation procedure for three axes vertical machining center using rigid body kinematics*, International Journal of Machine Tools and Manufacture, Vol. 40, Issue 8, June 2000, pp. 1199 – 1213

10. **Silva J. B. A., Burdekin M.** – *A modular space frame for assessing the performance of co-ordinate measuring machines (CMMs)*, Precision Engineering, vol. 26, Issue 1, January 2002, pp. 37-48

11. **Wang S. M., Ehmann, K. F.** – *Measurement Methods for the Position Errors of a Multi-Axis Machine. Part 1: Principles and Sensitivity Analysis*, International Journal of Machine Tools and Manufacture, vol. 39, Issue 6, June 1999, pp. 951–964

12. **Wang S. M., Ehmann, K. F.** – *Measurement Methods for the Position Errors of a Multi-Axis Machine. Part 2: Applications and Experimental Results*, International Journal of Machine Tools and Manufacture, vol. 39, Issue 9, September 1999, pp. 1485–1505

13. **Precision Engineering Centre** – *Error Simulation Program User's Guide*, School of Engineering, The University of Huddersfield, 1997

14. **European CRAFT Project:** SMS2-7854 – *An Investigation Into New Machine Tool Performance Standards For Dynamic, Thermal And Volumetric Calibration Of Machine Tools*, Precision Engineering Centre, The University of Huddersfield, 1999

15. **European CRAFT Project:** SMS2-7839 (SMT4-CT98-5517) – *Accuracy Verification Of Co-Ordinate Measuring Machines Of All Sizes, Types And Configurations Using*

Lasers And A Universal Artefact, Precision Engineering Centre, The University of Huddersfield, 1999

16. **Lei W. T., Hsu Y. Y.** – *Accuracy Test of five-axis CNC Machine Tool with 3D Probe–Ball. Part I: Design and Modeling*, International Journal of Machine Tools and Manufacture, vol. 42, Issue 10, August 2002, pp. 1153–1162

17. **Lei W. T., Hsu Y. Y.** – *Accuracy Test of Five-Axis CNC Machine Tool with 3D Probe-Ball. Part II: Errors Estimation*, International Journal of Machine Tools and Manufacture, Vol. 42, Issue 10, August 2002, pp. 1163–1170

18. **Carlisle K., Edson S. L.** – *Design of an Ultra Precision Machining Facility: ULTRA 350*, FY99 Technology Reports, Center for Precision Engineering, Lawrence Livermore National Laboratory, USA, 1999, pp. 3.11–3.15

19. **Fung E. H. K., Yang S. M.** – *An approach to on-machine motion error measurement of a linear slide*, Measurement, Volume 29, Issue 1, January 2001, pp. 51-62

20. **Ford D. G.** – *Electronic Accuracy Compensation*, JOWOG 39B (Machine Tools and Equipment) Meeting, Atomic Weapon Establishment (B), UK, October 1988

21. **Postlethwaite S. R.** – *Electronic Based Accuracy Enhancement of CNC Machine Tools*, PhD Thesis, Huddersfield Polytechnic in collaboration with Electronic Accuracy Systems Ltd, 1992

22. **Postlethwaite S. R., Allen J. P., Ford D. G.** – *The Use of Thermal Imaging, Temperature and Distortion Models for Machine Tool Thermal Error Reduction*, Proceedings Institution of Mechanical Engineers (IMechE), Journal of Engineering Manufacture, vol. 212, Part B, December 1998, pp. 671 – 679

23. **Allen J.** – *A General Approach to CNC Machine Tool Thermal Error Reduction*, PhD Thesis, The University of Huddersfield, 1997

24. **White A. J., Postlethwaite S. R., Ford D. G.** – *A General Purpose Thermal Compensation System for CNC Machine Tools*, Proceedings of International Conference LAMDAMAP 2001, Birmingham, 2001, (ISBN 1-85312-890-2), pp. 3 – 13.

25. **Blake M.D.** – *Investigation Into Load Effects On Machine Tool Accuracy*, MPhil Thesis, The University of Huddersfield, 1995

26. **Ford D. G., Postlethwaite S. R., Allen J. P., Blake M. D.** – *Compensation Algorithms for the Real-Time Correction of Time and Spatial Errors in a Vertical Machining Centre*, Proceedings of IMechE, Journal of Engineering Manufacture, vol. 214, Part B, 2000, pp. 221 – 234

27. **Yuan J., Ni J.** – *The Real-Time Error Compensation Technique for CNC Machining Systems*, Mechatronics, vol. 8, Issue 4, June 1998, pp. 359-380

28. **EPSRC Grant Award** – *Reduction of Errors in the Design and Integrated Manufacture of CNC Machine Tools (REDUCE)*, EPSRC Grant No. GR/R35186/01, Precision Engineering Centre, University of Huddersfield, 2001 – 2004

29. **Longstaff A., Fletcher S.** – *Compensation of Cincinnati Arrow 500 at The University of Huddersfield Using SinVCS*, Internal Report, Ultra Precision Engineering Centre, The University of Huddersfield, April 2004

30. **King R. I.** – *Handbook of High Speed Machining Technology*, Chapman and Hall, September 1985

31. **British Standard, International Standard Organisation** – *Mechanical vibration. Balance quality requirements for rotors in a constant (rigid) state. Specification and verification of balance tolerances – Part 1: Specification and verification of balance tolerances*, BS ISO 1940-1: 2003

32. **Inman D. J.** – *Engineering Vibration*, 2nd Edition, Prentice Hall, Prentice-Hall International, (ISBN 0-13-726142-X), 2001

33. **Fertis D. G.** – *Dynamics and Vibration of Structures*, Wiley-Interscience, (ISBN 0-471-25777-X), 1973

34. **Dimarogonas A. D.** – *Vibration For Engineers*, 2nd Edition, Upper Saddle River, Prentice Hall London, Prentice-Hall International, (ISBN 0-13-456229-1), 1996

35. **Adhikari S., Woodhouse J.** –*Identification Of Damping: Part 1, Viscous Damping*, Journal of Sound and Vibration, vol. 243, Issue 1, May 2001, pp. 43–61

36. **Adhikari S., Woodhouse J.** –*Identification Of Damping: Part 2, Non-Viscous Damping*, Journal of Sound and Vibration, vol. 243, Issue 1, May 2001, pp. 63–88

37. **Chen J. T., You D. W.** – *Hysteretic damping revisited*, Advances in Engineering Software, vol. 28, Issue 3, April 1997, pp. 165–171

38. **Chen L. Y., Chen J. T., Chen C. H., Hong H. K.** – *Free vibration of a SDOF system with hysteretic damping*, Mechanics Research Communications, vol. 21, Issue 6, 1994, pp. 599–604

39. **Kumabe J., Taniguchi O.** – *Dynamical Analysis of Vibration Cutting*, Bulletin of Japanese Society for Precision Engineering, vol. 5, Issue 3, 1971, pp. 73-74

40. **Ruud N. A., Karlsen R., Sørby K., Richt C.** – *Minimizing Vibration Tendencies in Machining*" [on-line], USA, available: http://www.mmsonline.com/articles/030406.html, accessed: 14 July 2004

41. **Lee K., Ibaraki S., Matsubara A., Kakino Y., Suzuki Y., Arai S., Braasch J.** – *A Servo Parameter tuning method for high-speed NC machine tools based on contouring error measurement*, Proceedings of the 6th International Conference LAMDAMAP 2003, Huddersfield, UK, 2003, (ISBN 1-85312-990-9), pp. 181 – 192

42. **Vafaei S., Rahnejat H. and Aini R.** – *Vibration Monitoring of High Speed Spindles Using Spectral Analysis Techniques*, International Journal of Machine Tools and Manufacture, vol. 42, Issue 11, September 2002, pp. 1223-1234.

43. **Schmitz T. L., Davies M. A., Medicus K. Snyder J.** – *Improving High-Speed Machining Material Removal Rates by Rapid Dynamic Analysis*, Annals of the CIRP, vol. 50, Issue 1, 2001, pp. 263 – 268

44. **Schmitz T. L.** – *Chatter Recognition by A Statistical Evaluation of The Synchronously Sampled Audio Signal*, Journal of Sound and Vibration, vol. 262, Issue 3, May 2003, pp. 721–730

45. **Jang D. Y., Choi Y., Kim H., Hsiao A.** – *Study of The Correlation Between Surface Roughness and Cutting Vibrations to Develop An On-Line Roughness Measuring Technique in Hard Turning*, International Journal of Machine Tools and Manufacture, vol. 36, Issue 4, April 1996, pp. 453–464

46. **Luo G. Y., Osypiw D., Irle M.** – *Surface Quality Monitoring for Process Control by On-Line Vibration Analysis Using An Adaptive Spline Wavelet Algorithm*, Journal of Sound and Vibration, vol. 263, Issue 1, May 2003, pp. 85–111

47. **Lee W.B., Cheung C.F., To S.** – *Materials Induced Vibration in Ultra-Precision Machining*, Journal of Materials Processing Technology, vols. 89–90, 1999, pp. 318–325

48. **Aglietti G. S., Stoustrup J., Langley R. S., Rogers E., Gabriel S. B.** – *Modelling and Feedback Control of Microvibrations*, Active Sound and Vibration Control, IEE Control Engineering Series 62, (ISBN 0-85296-0.38-7), 2002 .

49. **Tagawa Y., Nishiyama Y., Fujimura T., Yasuda M.** – *Control System Design for a 6DOF Micro Vibration Testing Device*, Proceeding of the 4th International Conference on Motion and Vibration Control, Zurich, Switzerland, 1998, pp. 175–185

50. **Ramsey, K. A.** – *Effective Measurements for Structural Dynamics Testing. Part I*, Sound and Vibration Magazine, vol. 9, no. 11, November 1975, pages 24-35

51. **Agilent Technologies** – *The Fundamentals of Modal Testing*, Application Note 243–3, 2000

52. **Lang G. F., Snyder D.** – *Understanding the Physics of Electrodynamic Shaker Performance, Sound and Vibration Magazine*, October 2001, pp. 2 – 10

53. **Lee M., Richardson M.** – *Determining the Accuracy of Modal Parameter Estimation Methods*, Proceedings of the International Modal Analysis Conference – IMAC X, San Diego, California, USA, 3–7 February 1992

54. **Schwarz B.J., Richardson M. H.** – *Experimental Modal Analysis*, CSI Reliability Week, Orlando Florida, US, October 1999

55. **Pavic A., Pimentel R., Waldron P.** – *Instrumented Sledge Hammer Impact Excitation: Worked Examples*, Proceedings of the International Modal Analysis Conference – IMAC XVI, Santa Barbara, California, USA, February 1998

56. **Avitabile P.** – *Modal Space: Back to Basics – Is there a difference between a roving hammer and a roving accelerometer modal test,* Experimental Techniques Magazine, September/October 1998, pp. 9–10

57. **Døssing O.** – *Structural Testing. Part II: Modal Analysis and Simulation*, Brüel & Kjær Application Note, March 1988

58. **Ramsey K. A.** – *Effective Measurements for Structural System Testing. Part II*, Sound and Vibration Magazine, vol. 10, no. 4, 1976, pp. 18–31

59. **Shye K., Van Karsen C., Richardson M.** – *Modal Testing using Multiple References*, Proceedings of the International Modal Analysis Conference – IMAC V, Imperial College, London, UK, February 1987, pp. 28 – 34.

60. **Phillips A. W., Allemang R. J.** – *An Overview Of MIMO-FRF Excitation / Averaging / Processing Techniques,* Journal of Sound and Vibration No. 262, pp. 651–675, 2003.

61. **Nessler G. L., Deel J. C.** – *Excitation Control for Consistent Modal Parameters When Testing Nonlinear Structures*, SAE Noise & Vibration Conference and Exhibition, Grand Traverse, MI, USA, May 2003

62. **Stanbridge A.B., Ewins D.J.** – *Modal Testing Using A Scanning Laser Doppler Vibrometer*, Mechanical Systems and Signal Processing, vol. 13, Issue 2, March 1999, pp. 255-270

63. **AMTRI** – *Vibration Measurements of A Vertical Milling Machine* , The University of Huddersfield, 24–25 February 1999

64. **Ewins D. J.** – *Modal Testing, Theory And Practice*, 2nd Edition, Baldock Research Studies Press, (ISBN 0-86-380218-4), 2000

65. **Hutin C.** – *Modal Analysis Using Appropriated Excitation Techniques*, Sound And Vibration Magazine, October 2000, pp. 2–9

66. **Stroud R.C.** – *Excitation, Measurement, and Analysis Methods for Modal Testing*, Sound and Vibration, August 1987, pp. 12 – 27

67. **Døssing O.** – *Structural Testing. Part I: Mechanical Mobility Measurements*, Brüel & Kjær Application Note, April 1988

68. **Formenti D.L., Richardson M.H.** – *Parameter Estimation from Frequency Response Measurements using Rational Fraction Polynomials (Twenty Years of Progress)*, Proceedings of the 20th International Modal Analysis Conference, Orlando, Florida, February 2002

69. **Richardson M.H., Formenti D.L.** – *Parameter Estimation from Frequency Response Measurements using Rational Fraction Polynomials*, Proceedings of the 1st International Modal Analysis Conference, Orlando, Florida, Nov. 1982, pp. 167–181

70. **Richardson M.H., Formenti D.L.** – *Global Curve Fitting of Frequency Response Measurements using the Rational Fraction Polynomial Method*, Proceedings of the 3rd International Modal Analysis Conference, Orlando, Florida, January 1985, pp. 390 – 397

71. **Peterson L. D., Alvin K. F.** – *Time and Frequency Domain Procedure for Identification of Structural Dynamic Models,* Journal of Sound and Vibration, vol. 201, Issue 1, 20 March 1997, pp. 137-144.

72. **Juang J. J.** – *Applied System Identification*, PTR Prentice Hall, Englewood Cliffs, New Jersey 07632, (ISBN 0-13-079211-X), 1994

73. **Van Der Auweraer H.** – *Structural Dynamics Modeling using Modal Analysis: Applications, Trends and Challenges*, IEEE Instrumentation and Measurement, Technology Conference Budapest, Hungary, May 2001

74. **Taleghani B. K., Pappa R. S.** – *Finite Element Vibration Analysis and Modal Testing of Graphite Epoxy Tubes and Correlation Between The Data*, NASA Technical Memorandum 110298, US Army Research Laboratory Technical Report 1288, Langley Research Center, Hampton, Virginia, USA, November 1996

75. **Kim H. S., Jeong K. S., Lee D. G.** – *Design and Manufacture of a Three-Axis Ultra-Precision CNC Grinding Machine*, Journal of Material Processing Technology, vol. 71, 1997, pp. 258 – 266.

76. **Merchant M.E.** – *Mechanics of the Metal Cutting Process, II. Plasticity conditions in Orthogonal Cutting*, Journal of Applied Physics, vol. 16, 1945, pp. 318–324

77. **Palmer W. B., Oxley P. L. B.** – *Mechanics of Orthogonal Machining*, Proceedings Institution of Mechanical Engineers, vol. 173, No. 24, 1959, pp. 623–654

78. **Lee E. H., Shaffer B. W.** – *Theory of Plasticity Applied to the Problem of Machining*, Journal of Applied Mechanics, vol. 18, 1951, pp. 405 – 413.

79. **Rubenstein C.** – *The application of force equilibrium criteria to orthogonal cutting*, International Journal of Machine Tool Design and Research, vol. 12, Issue 2, June 1972, pp. 121–126

80. **Rubenstein C.** – *The influence of strain rate in orthogonal cutting*, International Journal of Machine Tool Design and Research, vol. 12, Issue 2, June 1972, pp. 105–120

81. **Toropov A., Ko S. L.** – *Prediction of tool-chip contact length using a new slip-line solution for orthogonal cutting*, International Journal of Machine Tools and Manufacture, vol. 43, Issue 12, September 2003, pp. 1209–1215

82. **Shamoto E., Altintas Y.** – *Prediction of Shear Angle in Oblique Cutting with Maximum Shear Stress Principle and Minimum Energy Principle*, 1997 ASME International Mechanical Engineering Congress and Exposition, MED – vol. 6, Issue 1, 1997, pp. 121 – 128.

83. **Venuvinod P. K., Jin W. L.** – *Three-dimensional cutting force analysis based on the lower boundary of the shear zone. Part 1: Single edge oblique cutting*, International Journal of Machine Tools and Manufacture, Volume 36, Issue 3, March 1996, pp. 307–323

84. **Liu X. W., Cheng K., Webb D., Luo X. C.** – *Improved Dynamic Cutting Force Model in Peripheral Milling. Part I: Theoretical Model and Simulation*, International Journal of Advanced Manufacturing Technology, Issue 20, 2002, pp. 631 – 638

85. **Li X. P., Iynkaran K., Nee A. Y. C.** – *A Hybrid Machining Simulator Based on Predictive Machining Theory and Neural Network Modelling*, Journal of Materials Processing Technology, vol. 89, 1999, pp. pp. 224–230

86. **Cheng Y. M., Chin J. H.** – *Machining contour errors as ensembles of cutting, feeding and machine structure effects*, International Journal of Machine Tools and Manufacture, vol. 43, Issue 10, August 2003, pp. 1001–1014

87. **Shirase K., Altintas Y.** – *Cutting force and dimensional surface error generation in peripheral milling with variable pitch helical end mills*, International Journal of Machine Tools and Manufacture, vol. 36, Issue 5, May 1996, pp. 567–584

88. **Baek D. K., Ko T. J., Kim H. S.** – *A dynamic surface roughness model for face milling*, Precision Engineering, vol. 20, Issue 3, May 1997, pp. 171–178

89. **Yin L., Vancoille E. Y. J., Ramesh K., Huang H.** – *Surface characterization of 6H-SiC (0001) substrates in indentation and abrasive machining*, International Journal of Machine Tools and Manufacture, vol. 44, Issue 6, May 2004, pp. 607–615

90. **Cheung C. F., Chan K. C. , Lee W. B.** – *Surface characterization in ultra-precision machining of Al/SiC metal matrix composites using data dependent systems analysis*, Journal of Materials Processing Technology, vol. 140, Issues 1-3, 22 September 2003, pp. 141–146

91. **Jiang X. Q., Blunt L., Stout K. J.** – *Lifting wavelet for three-dimensional surface analysis*, International Journal of Machine Tools and Manufacture, vol. 41, Issues 13-14, October 2001, pp. 2163–2169

92. **Xiao S. J., Jiang X. Q., Blunt L., Scott P. J.** – *Comparison study of the biorthogonal spline wavelet filtering for areal rough surfaces*, International Journal of Machine Tools and Manufacture, vol. 41, Issues 13-14, October 2001, pp. 2103–2111

93. **Blunt L., Jiang X. Q., Zeng W.** – *3D Surface Metrology for the Machine Tool Diagnostics and Control*, CAPM Project Internal report, Surface Characterisation Group, University of Huddersfield, June 2004

94. **Altintas Y.** – *Manufacturing Automation – Metal Cutting Mechanics, Machine Tool Vibrations, and CNC Design*, Cambridge University Press, Cambridge, (ISBN 0-521-65029-1, 0-521-65973-6), 2000

95. **Ford D. G.** – *General Purpose CAD/CAE Aid to Design a Machine Tool System*, PhD Thesis, The University of Huddersfield, UK, December 1987

96. **Pislaru C., Ford D. G., Freeman J. M.** – *Improving CNC Machine Tools Performance by using Modular Approach*, Proceedings of the 5th International Conference LAMDAMAP 2001, Birmingham, UK, 2001, (ISBN 1-85312-890-2), pp. 301–311

97. **Pislaru C., Ford D. G., Holroyd G.** – *Hybrid Modelling and Simulation of a CNC Machine Tool Axis Drive*, Proceedings of the Institution of Mechanical Engineers (ImechE), Part I, Journals of Systems and Control Engineering, vol. 218 / I2, 2004, pp. 111–120

98. **Holroyd G., Pislaru C., Ford D. G.** – *Determination of Stiffness and Damping Sensitivity for Computer Numerically Controlled Machine Tool Drives*, Proceedings of the Institution Mechanical Engineers (IMechE), Part C, Journal of Mechanical Engineering Science, vol. 217, 2003, pp. 1165–1177

99. **Holroyd G., Pislaru C., Ford D. G.** – *Identification of Damping Elements in a CNC Machine Tool Drive*, Proceedings of LAMDAMAP 2001, Birmingham, UK, 17–20 July 2001, (ISBN 1-85312-890-2), pp. 289–301

100. **Bartlett H., Whalley R.** – *Power Transmission System Modelling*, Proceedings of IMechE, vol. 212, Part C, 1999, pp. 497 – 508.

101. **Moreno-Castaneda V. Y., Pislaru C., Freeman J. M., Ford D. G.** – *Modelling and Simulation of a Feed Drive Using Transmission Line Modelling Technique*, Proceedings of the 6th International Conference LAMDAMAP 2003, Huddersfield, UK, 2003, (ISBN 1-85312-990-9), pp. 193–204

102. **Holroyd G., Pislaru C., Ford D. G.** – *Modelling the Dynamic Behaviour of a Ball-Screw System Taking into Account the Changing Position of the Ball-Screw Nut*, Proceedings of the 6th International Conference LAMDAMAP 2003, Huddersfield, UK, 2003, (ISBN 1-85312-990-9), pp. 337–348

103. **Ebrahimi M., Whalley R.** – *Analysis, Modeling and Simulation of Stiffness in Machine Tool Drives*, Computers & Industrial Engineering, vol. 38, 2000, pp. 93 – 105.

104. **Erkorkmaz K., Altintas Y.** – *High Speed CNC System Design. Part II: Modeling and Identification of Feed Drives*, International Journal of Machine Tools & Manufacture, vol. 41, 2001, pp. 1487–1509

105. **Rober S. J., Shin Y. C.** – *Modeling And Control Of CNC Machines Using A PC-Based Open Architecture Controller*, Mechatronics, vol. 5, No. 4, 1995, pp. 401 – 420

106. **Blaszkowski M., Szafarczyk M., Al-Taleb M.**- *A New Technique For Identification Of Servo Drives Of Machine Tools And Robots*, Journal of Materials Processing Technology, vol. 76, 1998, pp. 36–41

107. **Pislaru C., Freeman J. M., Ford D. G.** – *Modal Parameter Identification for CNC Machine Tools Using Wavelet Transform*, International Journal of Machine Tools and Manufacture, vol. 43, No. 10, 2003, pp. 987–993

108. **Spencer B. F., Soong T. T.** – *New Application and Development of Active, Semi-Active and Hybrid Control Techniques for Seismic and Non-Seismic Vibration in The USA*, Proceedings of International Post-SMiRT Conference Seminar on Seismic Isolation, Passive Energy Dissipation and Active Control of Vibration of Structures, Cheju, Korea, 23–25 August 1999, pp. 113-125

109. **Garg D. P., Anderson G. L.** – *Structural vibration suppression viaactive/passive techniques*, Journal of Sound and Vibration: Letter to the Editor, vol. 262, 2003, pp. 739–751

110. **Stöbener U., Gaul L.** – *Active Vibration Control of a Car Body Based on Experimentally Evaluated Modal Parameters,* Mechanical Systems and Signal Processing, vol. 15, No. 1, 2001, pp. 173 – 188

111. **Ramsey K. A.** – *Experimental Modal Analysis, Structural Modifications and FEM Analysis on a Desktop Computer*, Sound and Vibration, February 1983, pp. 17–23

112. **Ismail F., Ziaei R.** – *Chatter Suppression in Five-Axis Machining of Flexible Parts*, International Journal of Machine Tools and Manufacture, vol. 42, Issue 1, January 2002, pp. 115-122.

113. **Martinez D. R., Hinnerichs T. D., Redmond J. M.** – *Vibration Control for Precision Manufacturing Using Piezoelectric Actuators, Precision Engineering,* vol. 20, Issue 2, April 1997, pp. 151

114. **Choudhury S. K., Goudimenko N. N., Kudinov V. A.** – *On-Line Control of Machine Tool Vibration in Turning*, International Journal of Machine Tools and Manufacture, vol. 37, Issue 6, June 1997, pp. 801-811

115. **Tarng Y. S., Li T. C.** – *On-Line Monitoring and Suppression of Self-Excited Vibration in End Milling,* Mechanical Systems and Signal Processing, vol. 8, Issue 5, September 1994, pp. 597-606

116. **Stammers C. W., Sireteanu T.** – *Vibration Control of Machines by Use of Semi-Active Dry Friction Damping*, Journal of Sound and Vibration, vol. 209, Issue 4, 29 January 1998, pp. 671-684

117. **Marsh E. R., Slocum A. H.** – *An Integrated Approach to Structural Damping*, Precision Engineering, vol. 18, Issues 2-3, April 1996, pp. 103-109.

118. **Orak S.** – *Investigation of Vibration Damping on Polymer Concrete with Polyester Resin, Cement and Concrete Research*, vol. 30, Issue 2, February 2000, pp. 171-174.

119. **Rivin E. I.** – *Vibration Isolation of Precision Equipment*, Precision Engineering, vol.17, Issue 1, January 1995, pp. 41–56

120. **Wilson E. L.** – *Damping and Energy Dissipation: Linear Viscous Damping Is A Property of The Computer Model And Is Not A Property of A Real Structure*, [on-line], USA, available: http://www.csiberkeley.com/Tech_Info/19.pdf, accessed: 30 October 2002

121. **Halim D., Moheimani S. O. R.** – *Reducing the Effect of Truncation Error in Spatial and Pointwise Models of Resonant Systems with Damping*, Mechanical Systems and Signal Processing, vol. 18, Issue 2, March 2004, pp 291–315

122. **Richardson M., Potter R.** – *Viscous vs. Structural Damping in Modal Analysis*, 46th Shock and Vibration Symposium, San Diego, California, USA, October 1975

123. **Institute of Sound and Vibration Research** – *Vibration Control Short Course*, Southampton Institute, 1–5 July 2002

124. **Spectral Dynamics Inc.** – *STAR System: Users Guide*, Part Number 3405-0113, Issue A, San Jose, November 1994

125. **Gloth G., Sinapius M.** – *Influence and Characterisation of Weak Non-Linearities in Swept-Sine Modal Testing,* Aerospace Science and Technology, vol. 8, Issue 2, March 2004, pp 111–120

126. **Schoukens J., Swevers J., Pintelon R., Van der Auweraer H.** – *Excitation Design for FRF Measurements in The Presence of Non-Linear Distortions,* Mechanical Systems and Signal Processing, July 2004, vol. 18, Issue 4, pp. 727–738

127. **Dimitriadis G., Cooper J. E.** – *A Method for Identification of Non-Linear Multi-Degree-Of-Freedom Systems*, Proceedings of the Institution of Mechanical Engineers (ImechE) Part G, Journal of Aerospace Engineering, 20 July 1998, vol. 212, no. 4, pp. 287-298

128. **Munsi A. S. M. Y., Waddell A. J., Walker C. A.** – *Modal Analysis of A Lightweight Structure – Investigation of The Effects of The Supports on The Structural Dynamics*, Mechanical Systems and Signal Processing, vol. 16, Issues 2–3, March 2002, pp. 273–284

129. **Avitabile P.** – *Modal Space: Back to Basics – Should I always use a hard tip for impact testing*, Experimental Techniques Magazine, November/December 1998, pp. 15–16

130. **Russel D. A.** – *Computational and Experimental Modal Analysis of a Clamped-Free Bar*, [on-line], USA, available: http://www.gmi.edu/~drussell/GMI-Acoustics/PostScript/Modal.ps, accessed: 12 November 2004

131. **Forest D.** – *Careful Planning Improves Impact testing*, Real-Time Update, Hewlett-Packard, Spring 1995

132. **Solartron Metrology** – *Product Catalogue C2002/01/E*, Bognor Regis, West Sussex, UK, 2002, pp. 60 – 77

133. **Wilcoxon Research Inc.** – *Vibration Instrumentation Catalogue*, Gaithersburg, MD 20878, USA, 2002, pp. 39 – 41

134. **Kistler Instrumente AG** – *The Piezoelectric Effect, Theory, Design, and Usage*, Special Print, 228.670, Winterthur, Switzerland, 2001, pp 105 – 112.

135. **Kistler Instrumente AG** – *The Piezotron Concept as a Practical Approach to Vibration Measurement,* Special Print, K20.250e, 2001

136. **PCB Piezotronics** – *Introduction to Signal Condition for ICP® & Charge Piezoelectric Sensors*, [on-line], USA, Available: http://www.pcb.com/techsupport/tech_signal.aspx, accessed: 8 June 2004

137. **Kistler Instrumente AG** – *Accelerometer Mounting Considerations*, Special Print, K20.305, Winterthur, Switzerland, 2002

138. **PCB Piezotronics: IMI Sensors** – *Model 629A11 Industrial ICP® Accelerometer: Installation and Operating Manual,* Depew, New York, USA, February 1999

139. **PCB Piezotronics: Force/Torque Division** – *Product Catalogue: Sensors for Load Torque, and Dynamic Force (FTQ-200D-0903)*, Depew, New York, USA, 2003

140. **Polytec GmbH** – *Laser Measurement Systems Start Page*, [on-line], USA, Available: http://www.polytec.com/int/_print/158_942.asp accessed: 28 July 2004

141. **Polytec GmbH** – *PSV-400-3D Scanning Vibrometer*, Catalogue Number LM_DS_PSV-400-3D, November 2003

142. **National Instruments** – *DSA Computer Based Instruments: NI 4551 and NI 4552 Technical Note : Analyser Fundamentals*, November 1999

143. **Cooley J. W., Tukey, J. W.** –*An Algorithm for the Machine Calculation of Complex Fourier Series*, Mathematics of Computation, vol. 19, Issue 90, 1965, pp. 297–301

144. **Welaratna R.** – *Effects of Sampling and Aliasing on the Conversion of Analogue Signals to Digital Format*, Data Physics Corporation, Sound and Vibration, December 2002.

145. **The Mathworks** – *Data Acquisition Toolbox. User's Guide Version 2*, The Mathworks Inc., September 2000

146. **Agilent Technologies** – *The Fundamentals of Signal Analysis*, Application Note 243, 2000

147. **Wickramarachi P.** – *Effects of Windowing on the Spectral Content of a Signal*, Data Physics Corporation, Sound and Vibration, January 2003.

148. **Brüel & Kjær** – *Windows to FFT Analysis – Part I*, Technical Review, No. 3, 1987.

149. **Brüel & Kjær** – *Windows to FFT Analysis (Part II)*, Technical Review, No. 4, 1987.

150. **Loewenstein E. B.** – *Reducing the Effects of Noise in a Data Acquisition System by Averaging*, Application Note 152, National Instruments Corp., April 2000

151. **Laney** J. – *Measurement Acquisition and Analysis Techniques with LabVIEW™*, NI Week, National Instruments Corp., DSP Measurement Group, 16–18 August 2000

152. **National Instruments Corp.** – Benefits of Deep Memory in High-Speed Digitizers, Application Note WP2264, National Instruments Corp., July 2002

153. **Avitabile P.** – *Modal Space: Back to Basics – Which shaker excitation is best*, Experimental Techniques Magazine, January/February 2001, pp. 11–13

154. **Gade S., Herlufsen H., Hansen H. K.** – *How to Determine the Modal Parameters of Simple Structures*, Application Note 3560, Brüel&Kjær, Denmark, May 1999

155. **Cincinnati Machine UK Ltd** – *Cincinnati Arrow 2 Series*, CD ROM, Document Number 91204263B001, Birmingham, UK, 2001.

156. **TIRA Maschinenbau GmbH** – *Technical Documentation: Vibration System TV51120-M*, Schalkau, Germany, 10 December 2001

157. **Brüel & Kjær** – *Product Catalogue: Vibration Exciter System – Types 4805, 4811 and 4815*, Naerum, Denmark, June 1996

158. **PCB Piezotronics: Force/Torque Division** – *Model 221B02 ICP® Quartz Force Sensor: Installation and Operating Manual*, Depew, New York, USA, August 2000

159. **The Modal Shop Inc.** – *Exciter Stingers 2100 Series*, Cincinnati, Ohio, USA, November 1997

160. **Dataphysics Corporation** – SignalCalc Mobilyzer User Manual, San Jose, California, USA, 2001

161. **Spectral Dynamics Inc.** – *STAR System: Reference Manual*, Part Number 3405-0114, Issue A, San Jose, November 1994

162. **PCB Piezotronics: Vibration Division** – *Model 353B03 ICP® Quartz Accelerometer: Installation and Operating Manual,* Depew, New York, USA, February 1999

163. **Micron Workholding Ltd** – *Microloc 75 Series*, [on-line], UK, Available: http://www.microloc.com, accessed: 25 June 2004

164. **Kistler Instrumente AG** – *3-Component Dynamometer F_x, F_y, F_z 9255B*, Datasheet DB06.9255Bm, Winterthur, Switzerland, February 1991.

165. **Siemens AG** – *SIMODRIVE 611 Digital SINUMERIK 840D/810D Description of Functions: Drive Functions* (FBA), Manufacturer/Service Documentation, October 2000

166. **Texas Instruments** – *Field Orientated Control of 3-Phase AC-Motors*, Application Note, Literature No. BPRA073, 1998

167. **Siemens AG** – *Siemens Technical Education Program (STEP) 2000 self-study courses*, [on-line], USA, Available: http://www.sea.siemens.com/step/default.html, Accessed: 11 May 2004

168. **Leonhard W.** – *Control of Electrical Drives*, 2nd Edition, Springer-Verlag, ISBN 3-540-59380-2, 1997

169. **The Mathworks** – *Power System Blockset. User's Guide Version 2*, The Mathworks Inc., September 2000

170. **Texas Instruments** – Digital Signal Processing Solution for Permanent Magnet Synchronous Motor, Application Note, Literature No. BPRA044, 1997

171. **The Mathworks** – *Simulink Reference Version 5*, The Mathworks Inc., July 2002

172. **Dr. Johannes Heidenhain GmbH** – *Rotary Encoders*, Catalogue No. 349-529-24-70, January 2004

173. **Spetzer J., Ekhaml B.** – *Resolvers: Things you need to know about sizing and applying*, Motion System Design, March 2001, pp. 61–64

174. **Braasch J.** – *Position Measurement on Machine Tools: by Linear Encoder or Ballscrew and Rotary Encoder?*, [on-line], Germany, Available: http://www.heidenhain.com/posmeas.html, accessed: 26 October 2004

175. **Siemens AG** – *SIMODRIVE 611 Digital SINUMERIK 840D/810D Description of Functions: Extended Functions* (FB2), Manufacturer/Service Documentation, October 2000

176. **Industrial Devices Corporation** – *Linear Technology Comparison: Mechanical Drive Comparison*, [on-line], Available: http://www.idcmotion.com/pdf/9003.pdf, Accessed: 5 August 2004

177. **Lingafelter T.** – *How To Pick A Feed Unit*, [on-line], USA, Available: http://www.mmsonline.com/articles/ 069702.html, accessed: 5 August 2004

178. **Banemann R., Deister J.** – *Couplings For Servo Drives: Press Report*, KTR Kupplungstechnik, Germany, 20 November 2003

179. **KTR** – *ROTEX GS, Backlash-free shaft couplings*, KTR Kupplungstechnik GmbH, Germany, 2003

180. **Rexroth Star** – *Precision Ball Screw Assemblies End Bearings and Ho*usings, Catalogue No. RA 83 301/07.99, Deutsche Star GmbH, Schweinfurt, Germany, 1998

181. **Eschmann P., Hasbargen L., Weigand K.** – *Ball and Roller Bearings: Theory, Design and Application, Chapter 4: Friction, Temperature and Lubrication*, John Wiley and Sons, 1985, pp. 201–247

182. **THK** – *LM System General Catalog*, Catalogue No. 300-E, THK Co. Ltd, Tokyo, Japan, 2002

183. **Pislaru C.** – *Parameter Identification and Hybrid Mathematical Modelling Techniques Applied to Non-Linear Control Systems*, PhD Thesis, University of Huddersfield in Collaboration with Micrometalsmith Ltd. and Renishaw Ltd., October 2001

184. **Siemens AG** – *Cincinnati Machine Servo Optimisation Course Documentation*, Manufacturer/Service Documentation, 6 November 2002

185. **Holroyd G., Pislaru C., Ford D. G.** – *Determination of Stiffness and Damping Sensitivity for Computer Numerically Controlled Machine Tool Drives*, Proceedings of the Inst. Mech. Engineers (IMechE), Part C, Journal of Mechanical Engineering Science, vol. 217, 2003, pp. 1165 – 1177

186. **Haase F., Lockwood S., Ford D. G.** – *Active vibration control of machine tool structures - Part 2: An experimental active-vibration control system*, Proceedings of LAMDAMAP 2003, Huddersfield, UK, 17 July 2003, (ISBN 1-85312-990-9), pp. 451 – 460

187. **Hashemi J., Tseng A.A., Chou P.C.** – *Finite element modeling of continuous and segmental chip formation in high speed orthogonal machining*, Journal of Materials Engineering and Performance, vol. 3, No. 6, 1994, pp. 712–721

188. **Shih A.J., Yang H.T.Y.** – *Experimental and finite element predictions of residual stresses due to orthogonal metal cutting*, International Journal of Numerical Methods in Engineering, vol. 36, 1993, pp. 1487–1507

189. **Ceretti E., Fallbohmer P., Wu W.T., Altan T.** – *Application of 2D FEM to chip formation in orthogonal cutting*, Journal of Materials Processing Technology, vol. 59, 1996, pp. 169–180

190. **Armarego E. J. A.,Whitfield R. C.** – *Computer Based Modelling of Popular Machining Operations for Force and Power Predictions*, CIRP Annals, vol. 34, 1985, pp. 59–65

191. **Stabler G. V.** – *The Chip Flow Law and Its Consequences*, Advances in Machine Tool Design and Research, 1964, pp. 243 – 251

192. **Liu X. W., Cheng K., Webb D., Longstaff A. P., Widiyarto M. H.** – *Improved dynamic cutting force model in peripheral milling. Part II: experimental verification and prediction*, International Journal of Advanced Manufacturing Technology, vol. 24, no. 11/12, 2004, pp. 794–805

193. **Shaw M. C.** – *Metal Cutting Principles*, Oxford University Press, ISBN 0-19-514206-3, Oxford, 1984

194. **Oxley P. L. B.** – *The Mechanics of Machining: An Analytical Approach to Assessing Machinability (2nd edition)*, Ellis Horwood Ltd, ISBN 0-7458-0007-6, Chichester, 1989

195. **Kistler Instrumente AG** – *Systems for Multicomponent Measurements with Type 9255B/9257B/9265B*, Datasheet IN06.9255m, Winterthur, Switzerland, May 1997.

196. **Altintas Y., Budak E.** – *Analytical Prediction Of Stability Lobes In Milling*, Annals of the CIRP, 44: 1, pp. 357-362, 1995

197. **Budak E., Altintas Y.** – *Analytical Prediction Of Chatter Stability In Milling; Part 1: General Formulation, Part 2: Application Of The General Formulation To Common Milling Systems,* ASME Transactions, Journal of Dynamic Systems, Measurement and Control, vol. 120, issue 1, 1998, pp. 22-36.

198. **PCB Piezotronics: Vibration Division** – *Model 086C02 Modally Tuned® ICP® Impulse Hammer With Force Sensor And Tips: Installation And Operating Manual,* Depew, New York, USA, February 1999

199. **International Organization for Standardization,** "ISO 4287 – Geometrical Product Specifications (GPS) – Surface texture: Profile method – Terms, definitions and surface texture parameters", 2000

200. **Deutsches Institut für Normung e.V.,** "DIN 4760 Form deviations; Concepts; Classification system, translation, English", June 1982

201. **International Organization for Standardization,** "ISO/TC 213 N", Warsaw, Poland June 2003

202. **International Organization for Standardization,** "ISO 11562 – Geometrical Product Specifications (GPS) – Surface texture: Profile method – Metrological characteristics of phase correct filters", 1996

203. **International Organization for Standardization,** *Geometrical Product Specification (GPS) – Surface texture: Profile method; Surfaces having stratified functional properties – Part 1: Filtering and general measurement conditions*, 1996

204. **Liu X. W., Cheng K., Webb D., Longstaff A. P., Widiyarto M. H. N., Jiang X. Q., Ford D. G.** – *Investigation Of The Cutting Force Coefficients In Ball-End Milling*, Proceedings of LAMDAMAP 2003, Huddersfield, UK, 17 July 2003, (ISBN 1-85312-990-9), pp. 45 – 54

205. **Liu X. W., Cheng K., Webb D., Jiang X. Q., Xiao S. J., Blunt L.** – *Modelling the machining dynamics of peripheral milling -- Part 3: Prediction and verification of machined surface topography and roughness*, Proceedings of the IMechE, Part B: Journal of Engineering Manufacture, to be published

206. **Taylor Hobson Ltd,** *Form Talysurf PGI*, [on-line], UK, available: http://www.taylor-hobson.com/talysurfpgi.htm

207. **Myers A., Ford D. G., Xu Q.** – *Finite Element Analysis of the Structural Dynamics of a Vertical Milling Machine*, Proceedings of International Conference LAMDAMAP 2003, Huddersfield, 2003, (ISBN 1-85312-990-9), pp. 431 – 440.

208. **Holmes A.** – *Dynamic Analysis of A Machine Tool Cincinnati Arrow Series 2 500 VMC*, Advanced Mechanical Analysis NHA 2436 Internal Report, University of Huddersfield, August 2003

209. **Parametric Technology Corporation** – *Pro/ENGINEER Wildfire*, 367 – PRO/E WILDFIRE – BRO – 0204, 2004

210. **Hibbitt, Karlsson and Sorensen, Inc.** – *Getting Started with ABAQUS/Standard*, Pawtucket, USA, 2000.

211. **Femsys Limited** – *FEMGV User Manual for Version 6.4-01*, Leicester, UK, March 2003

212. **Blacker T. D., Stephenson M. B.** – *Paving: A New Approach To Automated Quadrilateral Mesh Generation*, International Journal For Numerical Methods in Engineering, vol. 32, 1991, pp.811–847

213. **Xu Q., Barrans S., Holmes A., Ford D.** – *Understanding the Dynamic Response of a Machine Tool Structure by Finite Element Analysis*, EUSPEN's 4th International Conference, Glasgow, UK, 30 May – 3 June 2004

214. **American National Standard Institute (ANSI)** – *Initial Graphics Exchange Specification IGES 5.3*, ANSI/US PRO/IPO 100, 1996

215. **Bern M., Eppstein D., Gilbert J.R.** – *Provably good mesh generation*, Proceedings of the 31st Annual Symposium on Foundations of Computer Science, IEEE, 1990, pp. 231–241

216. **Dynamic Design Solutions** – *FEMtools Analysis Integration Tools and Application Development: User Guide version 2.2*, Part No. FTUG–222–0305, Leuven, Belgium, May 2003

217. **Allemang R. J.** – *The modal assurance criterion – twenty years of use and abuse*, Sound and Vibration, pp. 14-21, August 2003

218. **Dynamic Design Solutions** – *FEMtools Analysis Integration Tools and Application Development: Example Manual version 2.2*, Part No. FTEM–222–0305, Leuven, Belgium, May 2003

219. **Dynamic Design Solutions** – *FEMtools Analysis Integration Tools and Application Development: Theoretical Manual version 2.2*, Part No. FTTM–222–0305, Leuven, Belgium, May 2003

220. **Petrone F., Lacagnina M., Sionti M.** – *Dynamic characterization of elastomers and identification with rheological models*, Journal of Sound and Vibration, Vol. 271, 2004, pp. 339-363

221. **Rajoria H., Jalili N.** – *Passive vibration damping enhancement using carbon nanotube-epoxy reinforced composites*, Composites Science and Technology, in press, 2005.

Appendix A. Experimental Modal Analysis Data

A.1. Equipment

- ***Shaker***

Type : TIRAvib S514 electro-mechanical type

Operating Range : 2 – 7000 Hz with 200N rated force

Up to 13 mm constant displacement from 0 to about 30 Hz

Constant velocity from ± 30 Hz to 100 Hz at up to 1.5 m/s

Constant acceleration from 100 Hz to 7000 kHz at up to 87 g

Power Amplifier : TIRA BAA 500

Stinger : Modal Shop 2125G12

Performance :

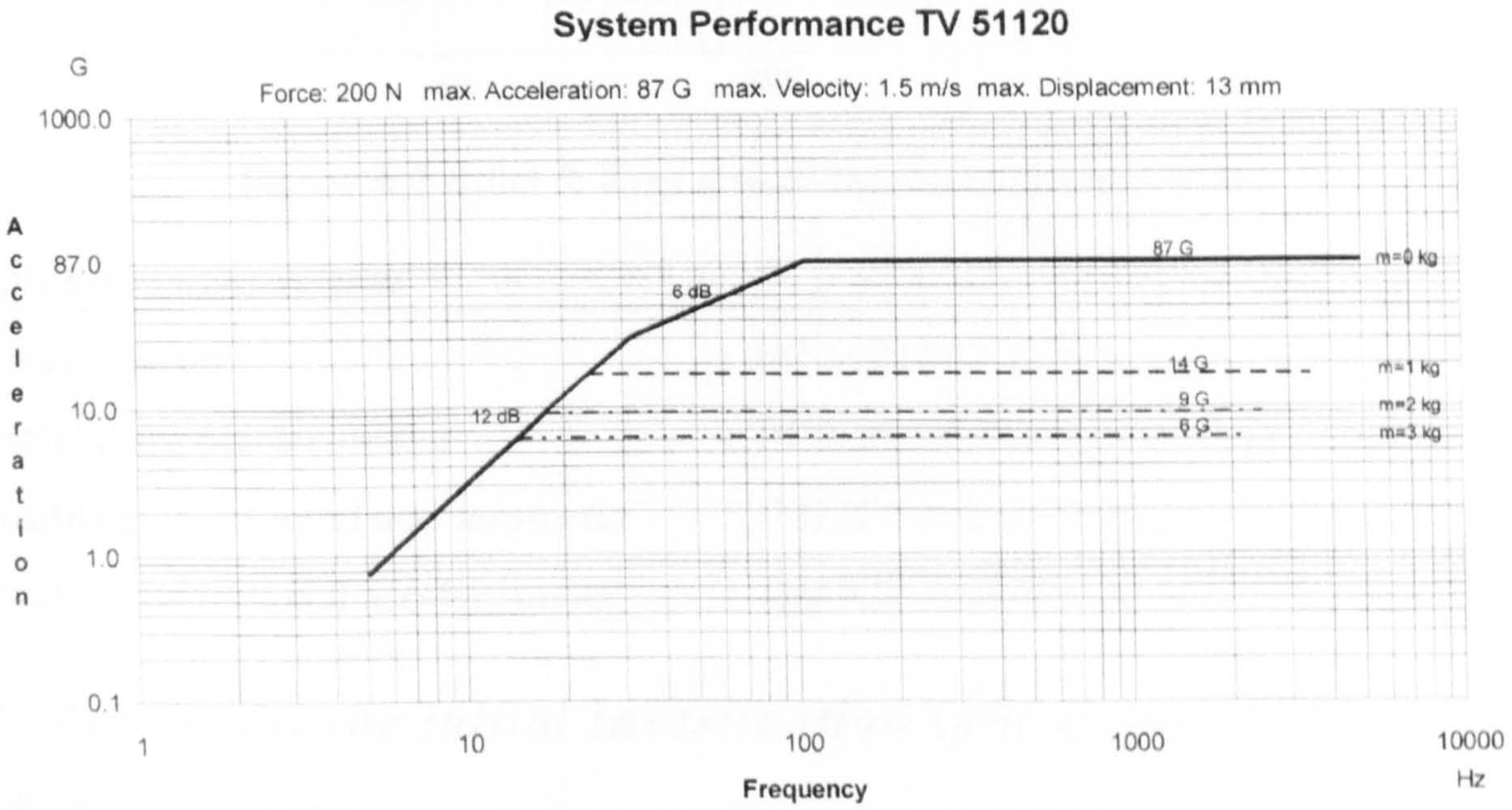

Figure A.1. TIRAvib shaker excitation characteristics

Type : Brüel & Kjær permanent magnet electro-mechanical exciter body type 4805 with high g head type 4811

Operating Range : 0 – 8500 Hz with 230N rated force

12.7 mm maximum constant displacement

1.27 maximum constant velocity

130 g maximum constant acceleration

Power Amplifier : Brüel & Kjær 2707 and pre-amplifier

Performance :

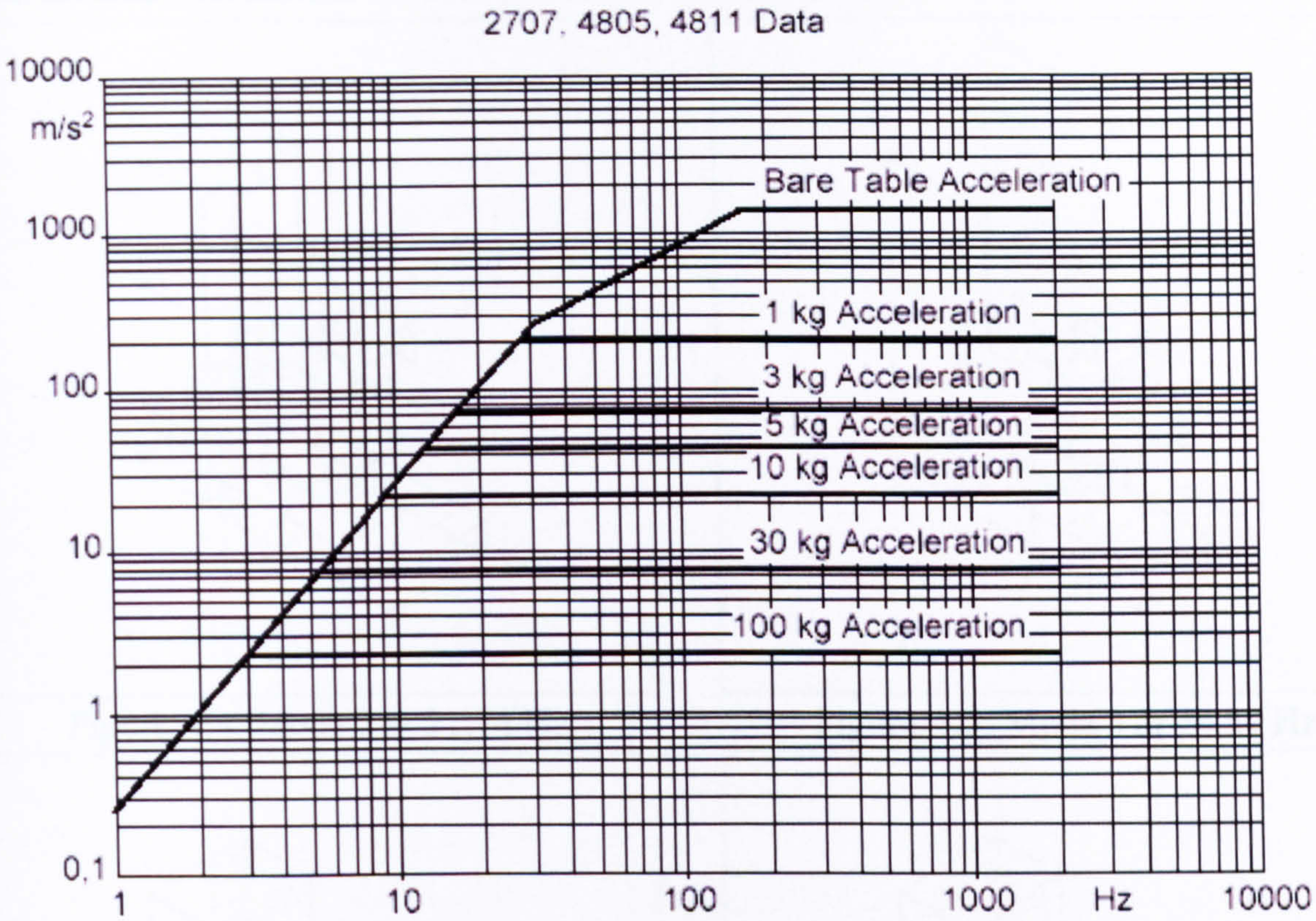

Figure A.2 Brüel & Kjær shaker excitation characteristics

- ***Measurement system***

Force sensor	: PCB 221B02 ICP Quartz
Miniature accelerometer	: PCB ICP quartz sensors model 353B03
Industrial uni-axial accelerometer	: IMI ICP sensors model 629A11
Industrial tri-axial accelerometer	: IMI ICP sensors model 623C21

A.2. Results for the initial investigation (uni-directional)

- ***Stability diagrams***

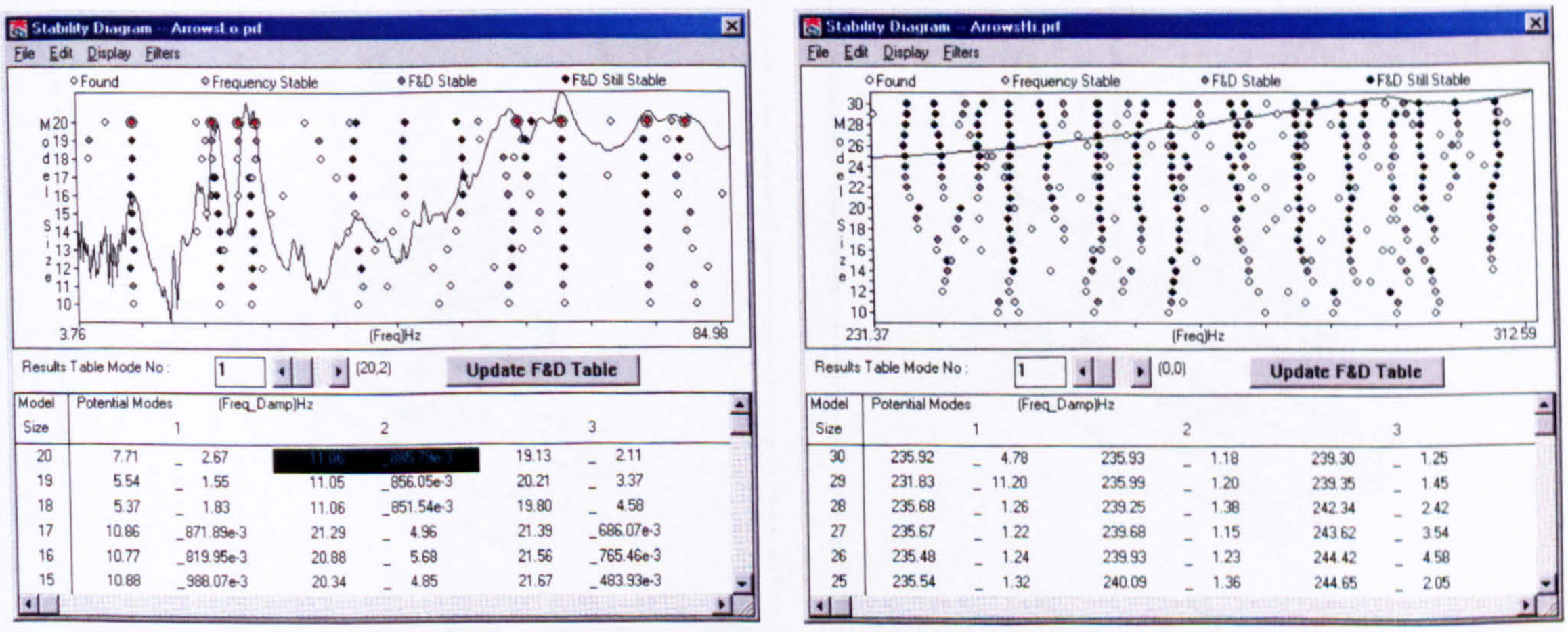

Figure A.3 STAR Modal stability diagram for the lower and upper frequency ranges

■ *Mode shapes*

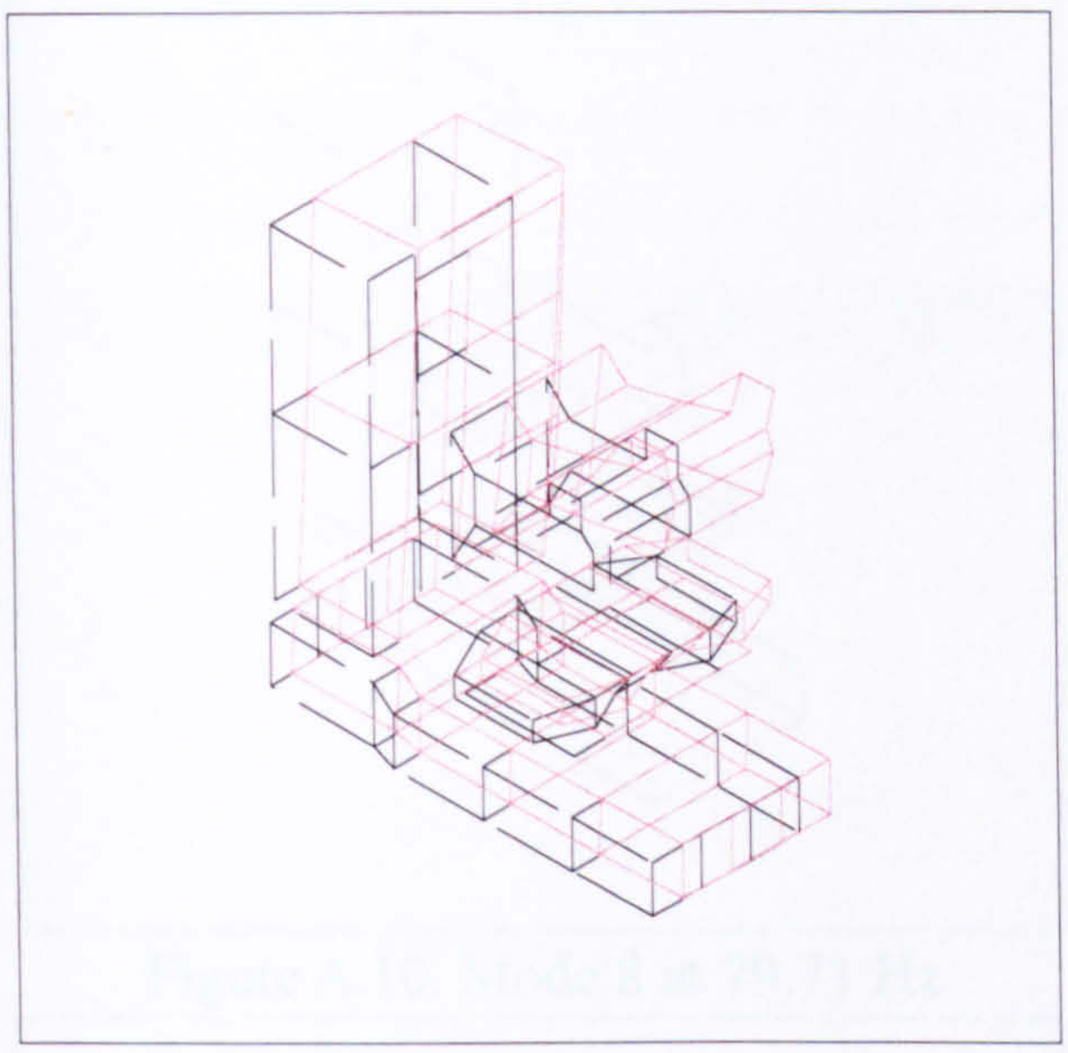

Figure A.4. Mode 2 at 21.14 Hz

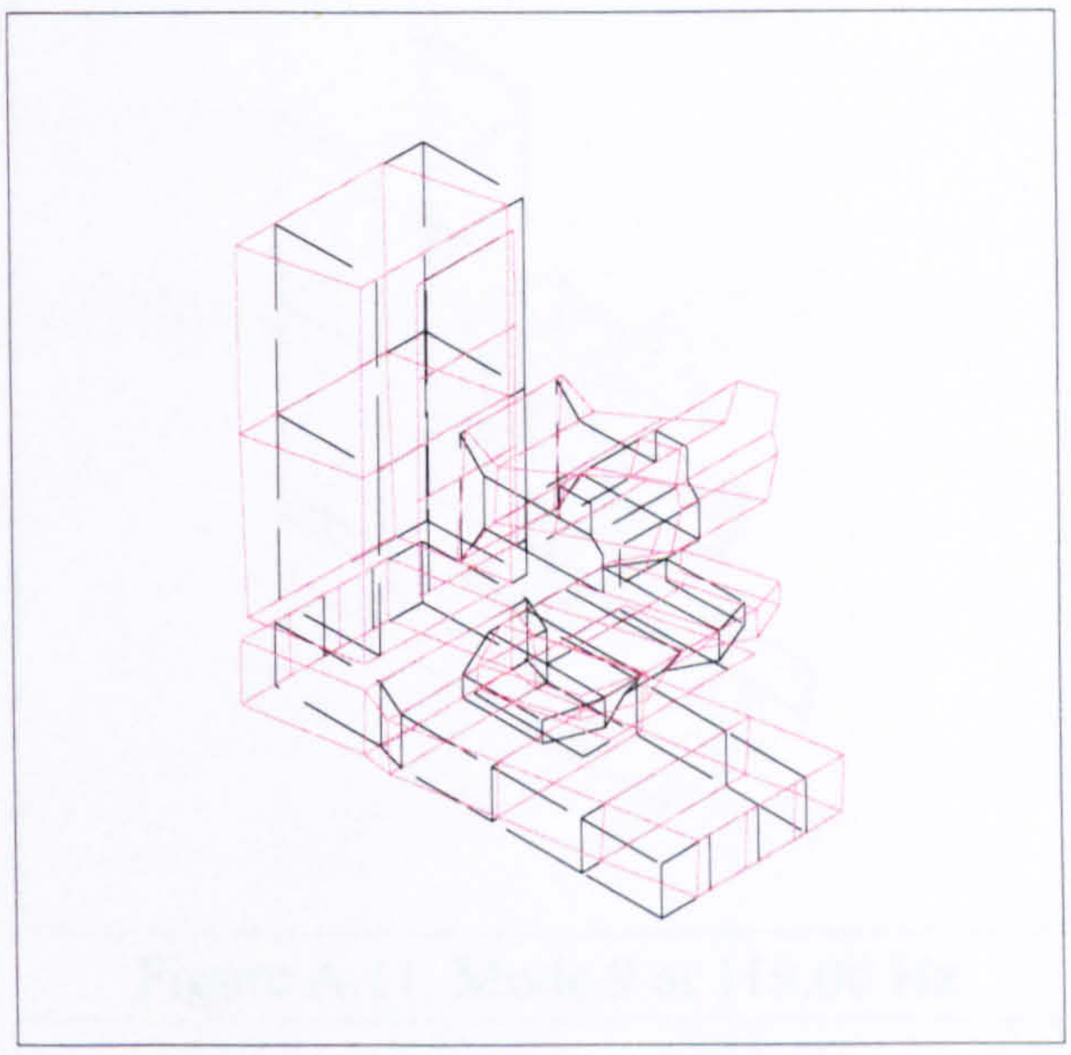

Figure A.5. Mode 3 at 24.39 Hz

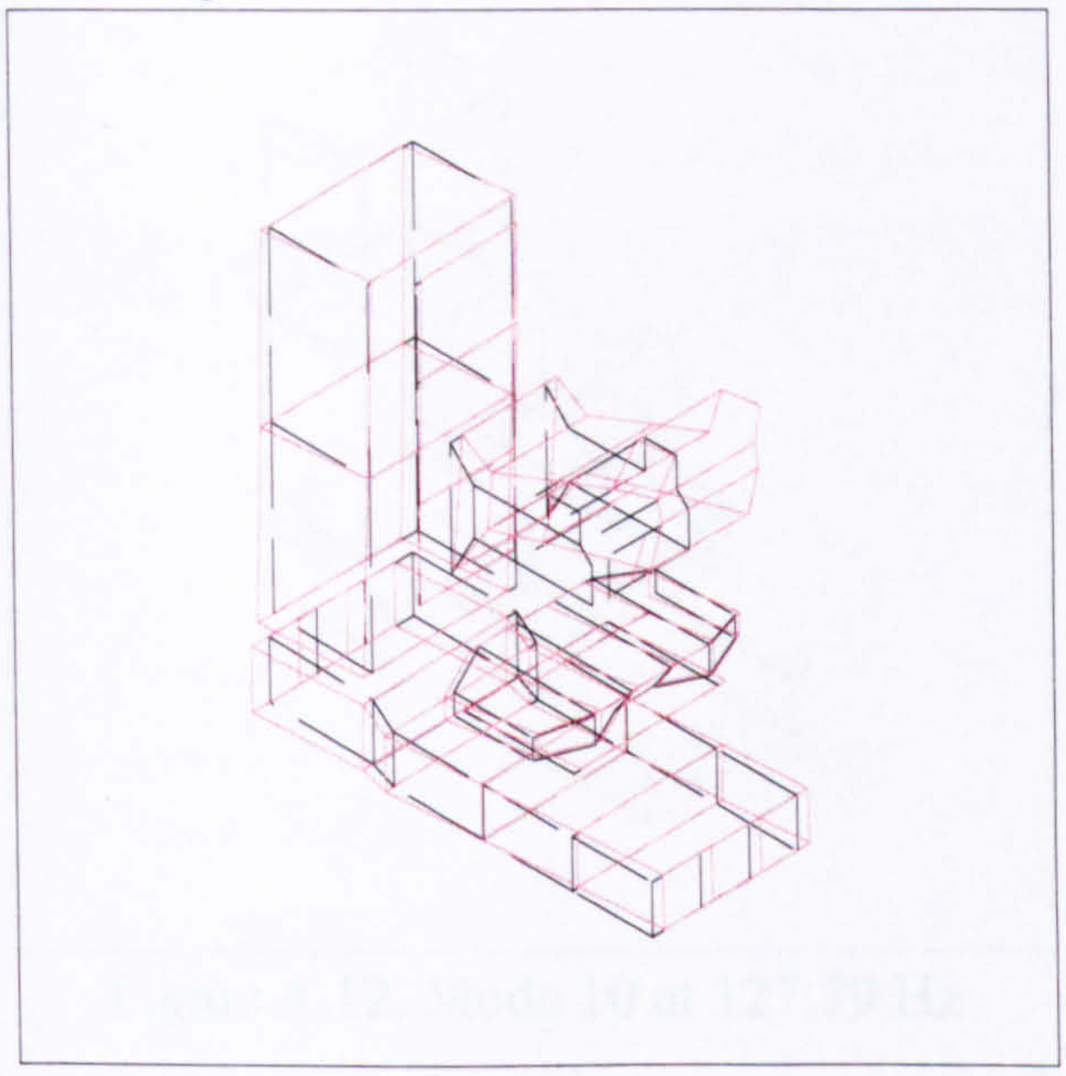

Figure A.6. Mode 4 at 26.49 Hz

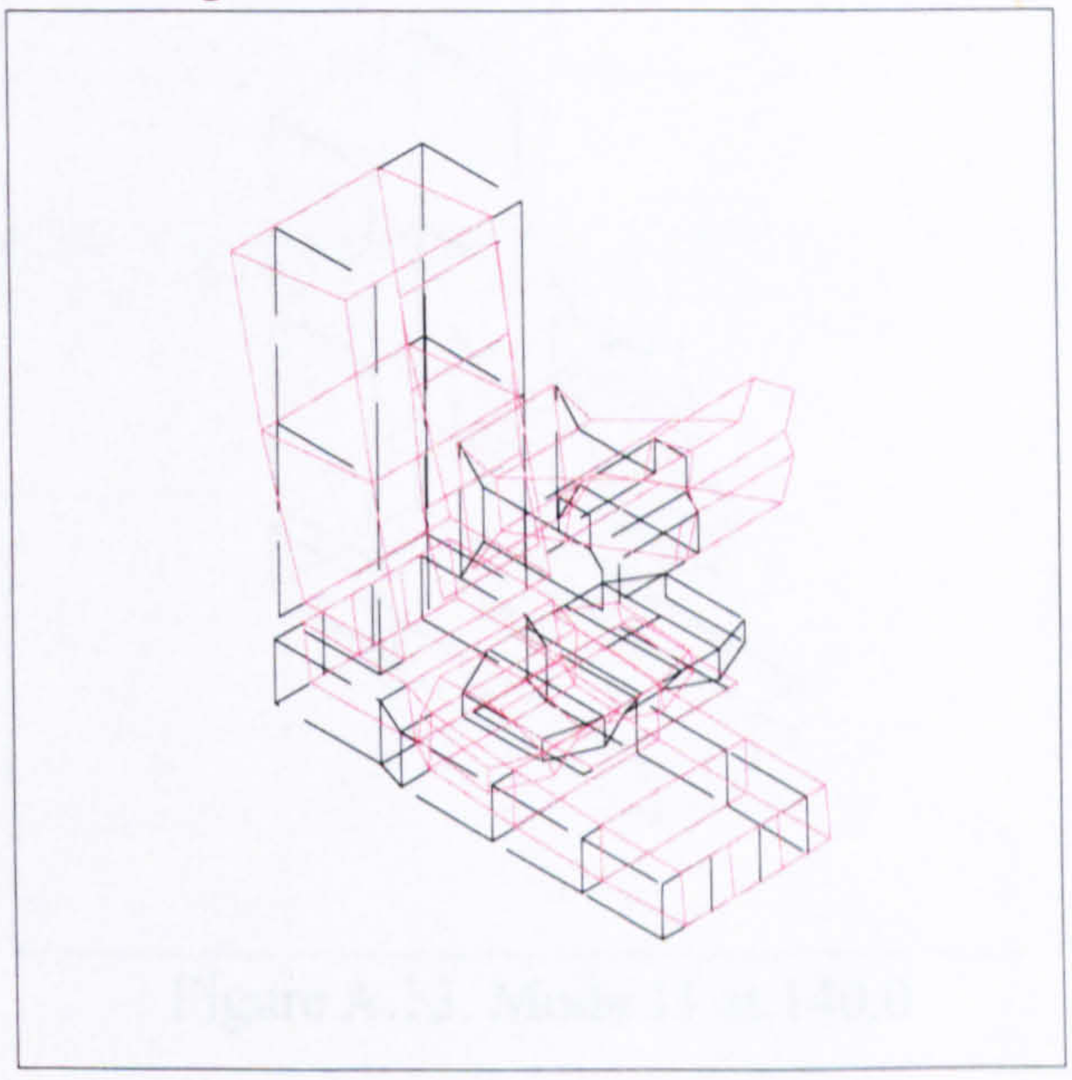

Figure A.7. Mode 5 at 59.03 Hz

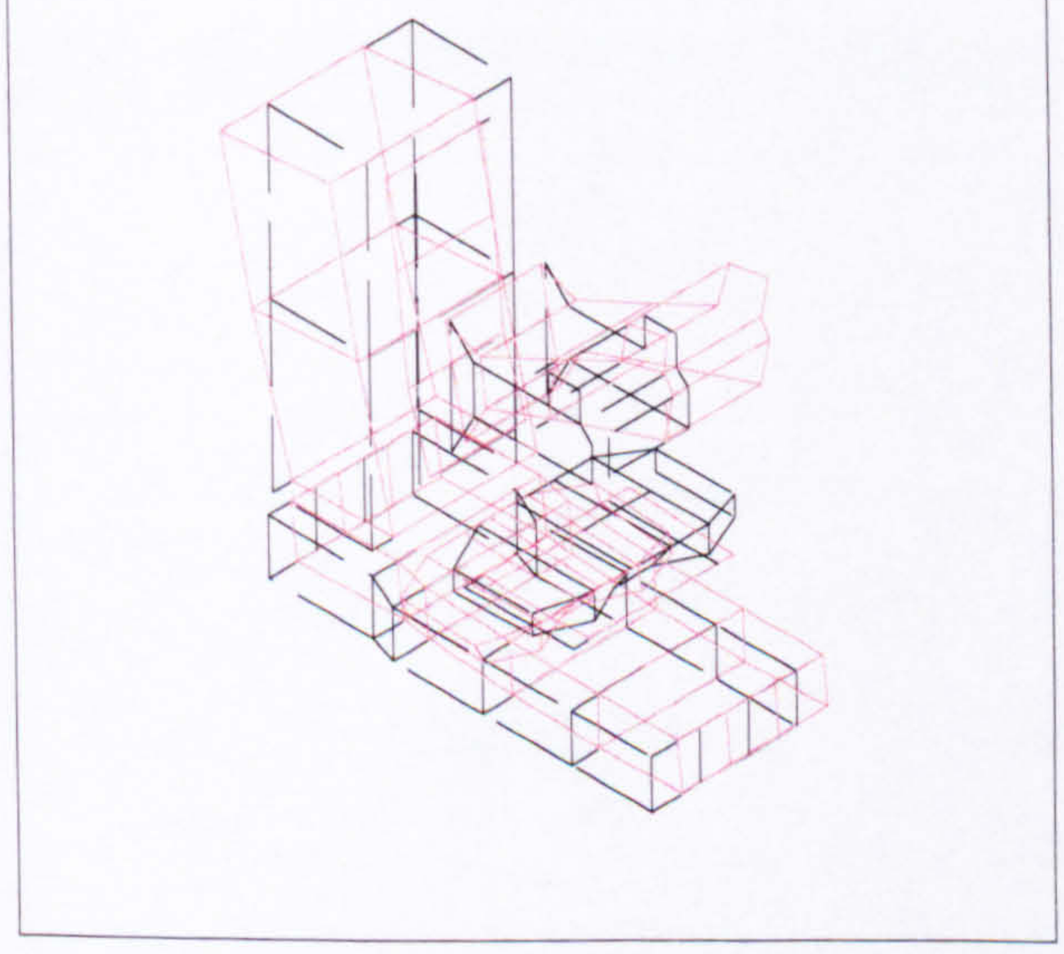

Figure A.8. Mode 6 at 64.44 Hz

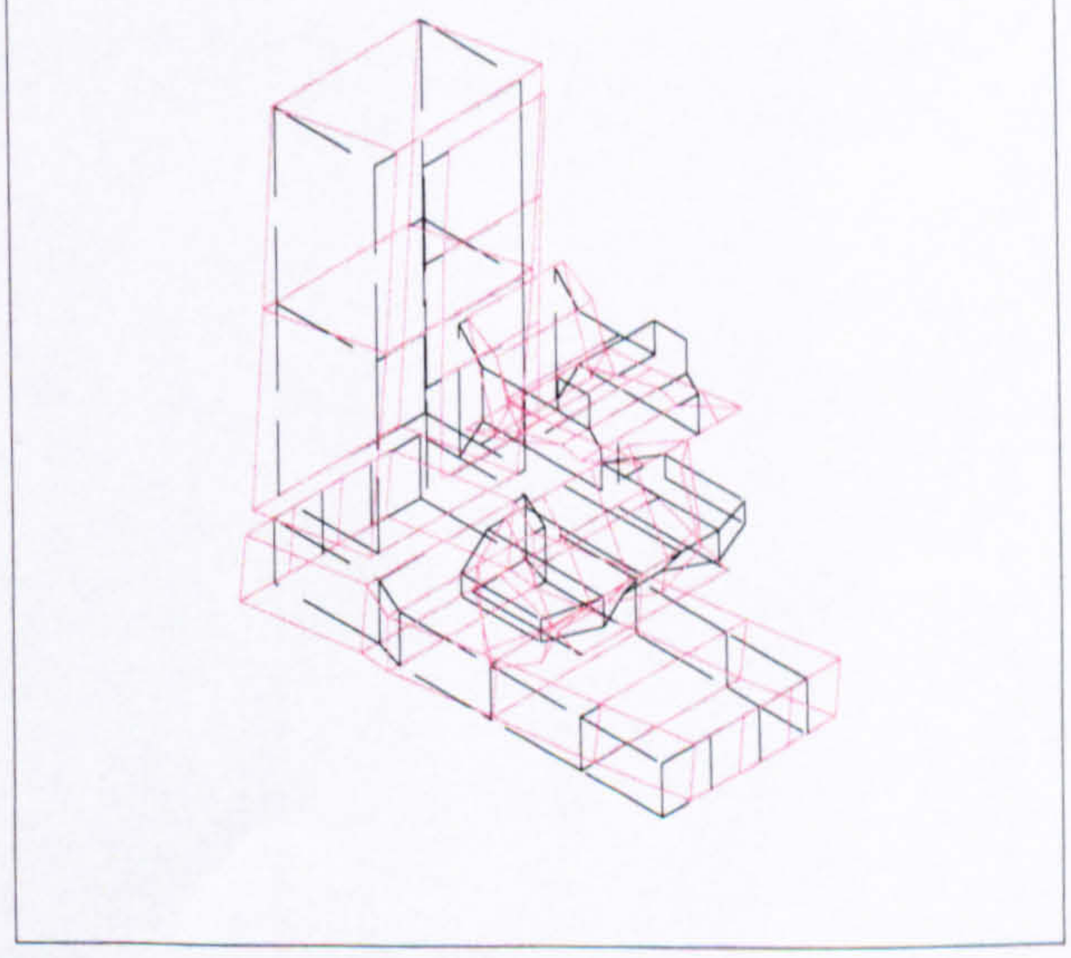

Figure A.9. Mode 7 at 74.96 Hz

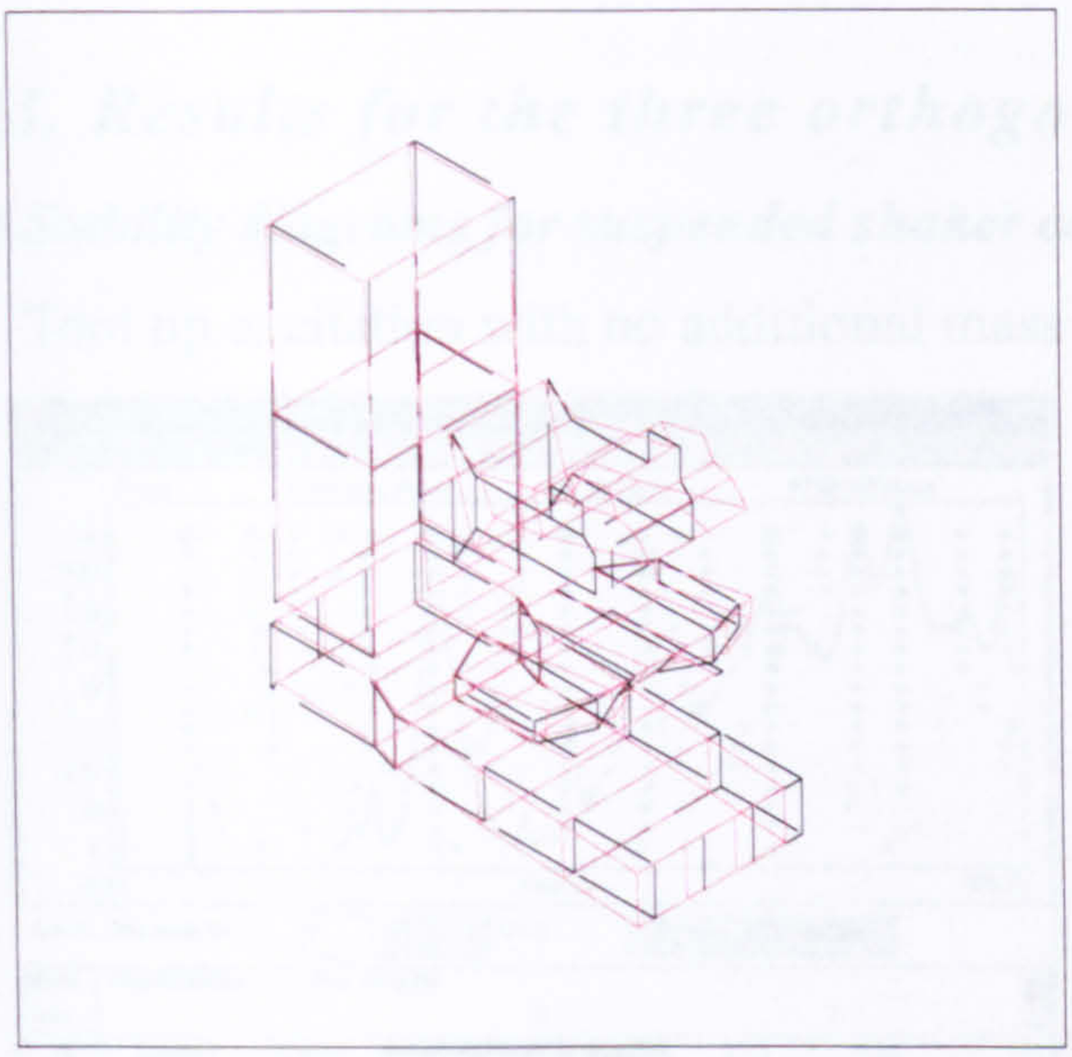

Figure A.10. Mode 8 at 79.71 Hz

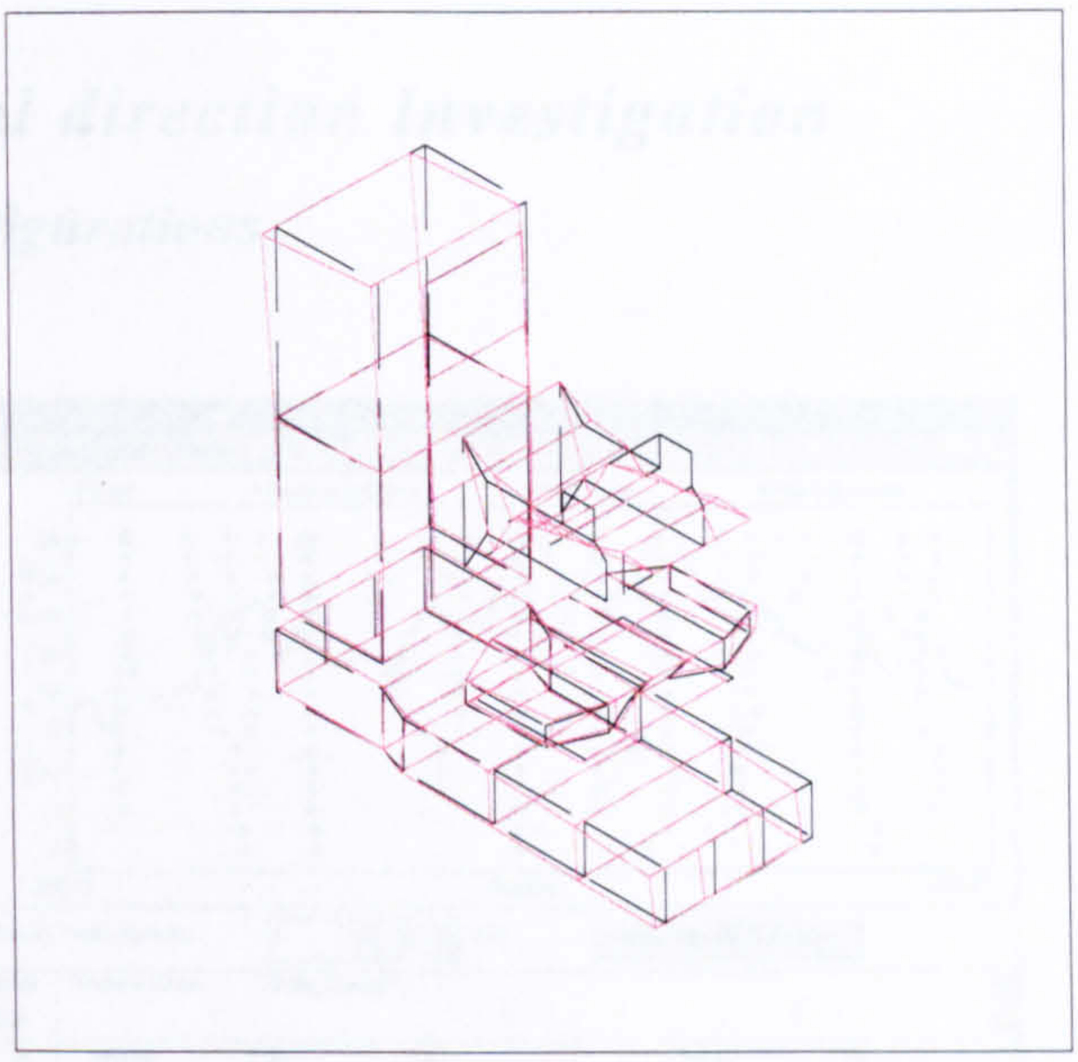

Figure A.11. Mode 9 at 119.06 Hz

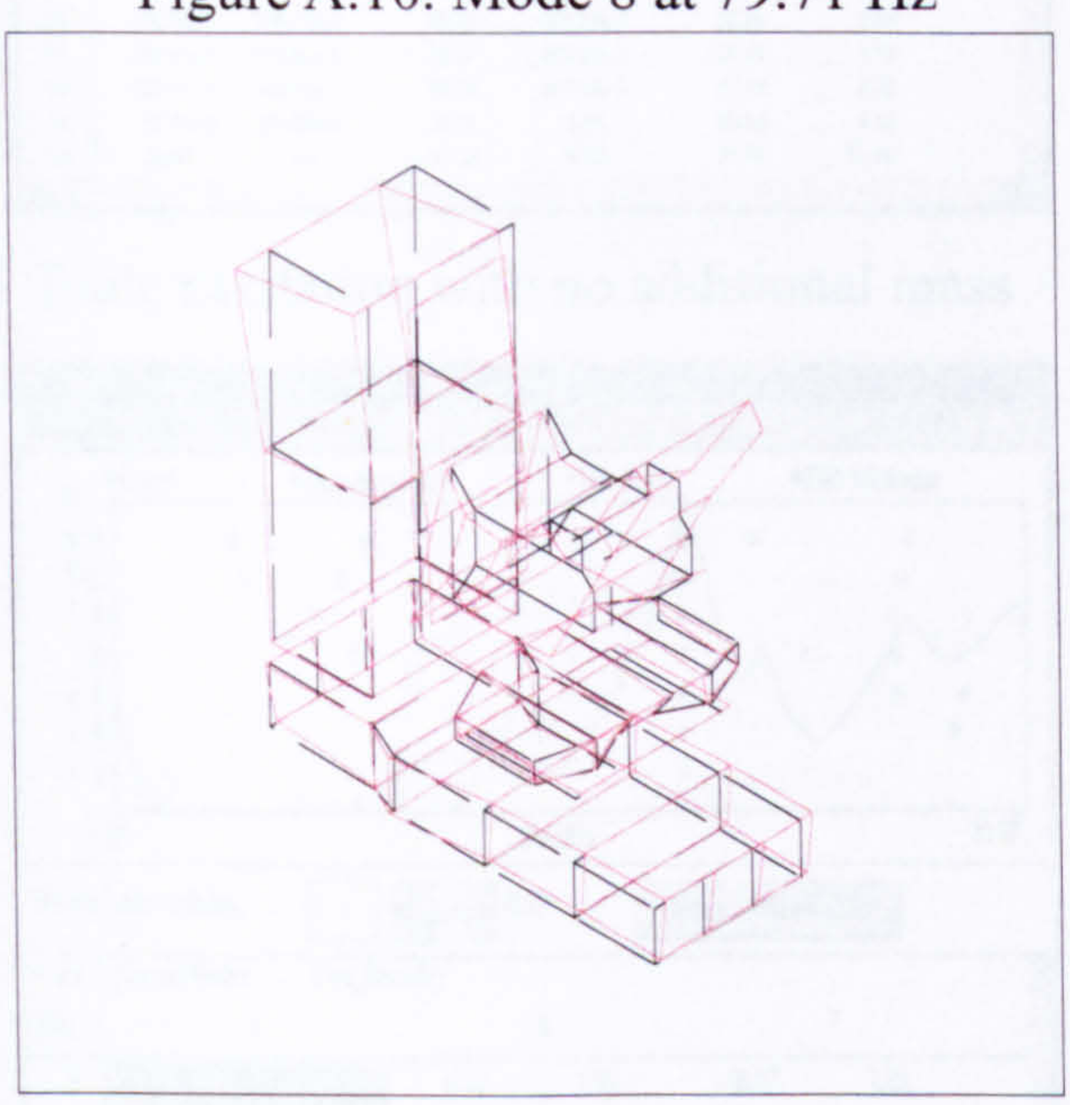

Figure A.12. Mode 10 at 127.79 Hz

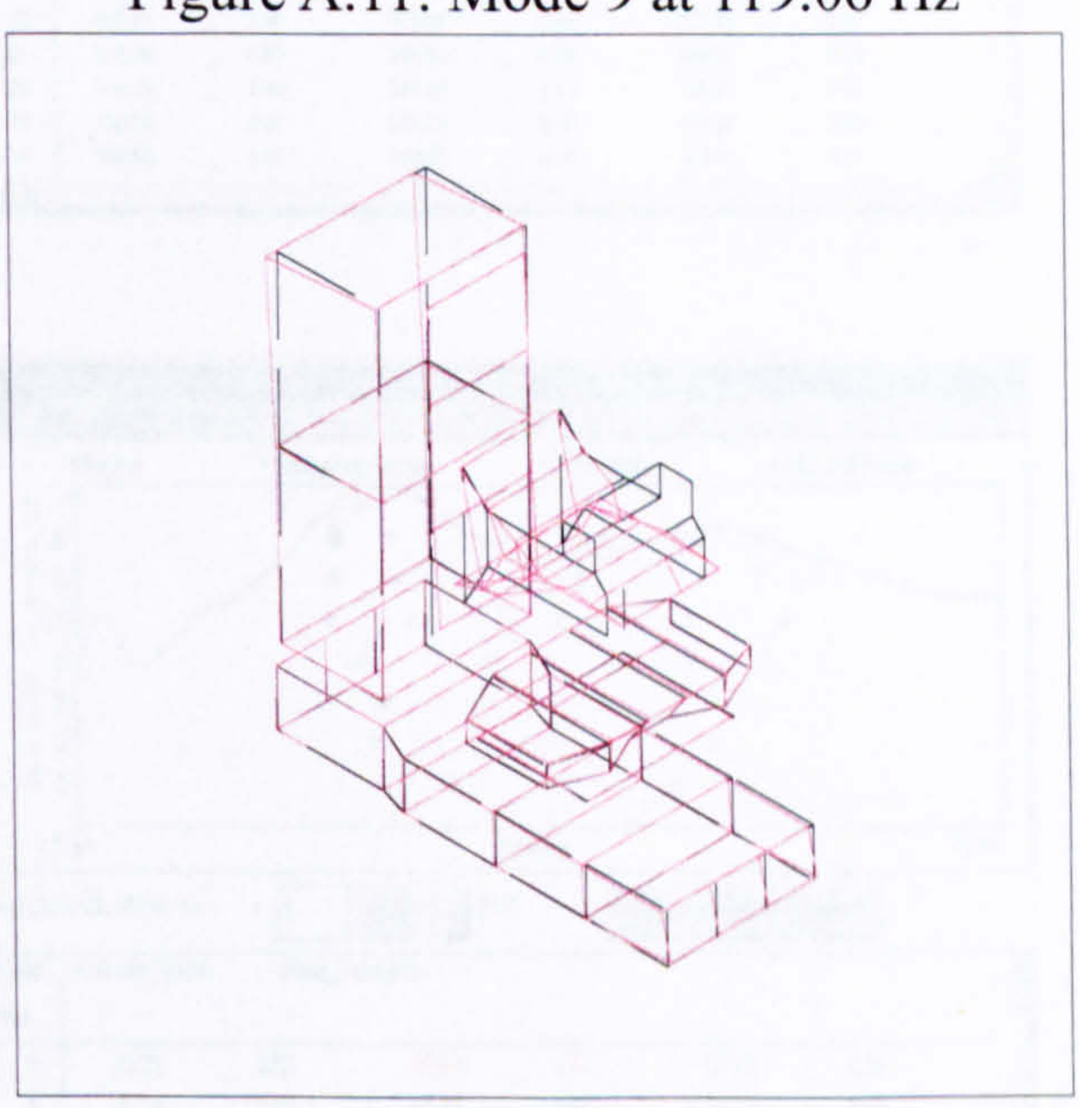

Figure A.13. Mode 11 at 140.0

A.3. Results for the three orthogonal direction investigation

(a) Stability diagrams for suspended shaker configurations

- Tool tip excitation with no additional mass

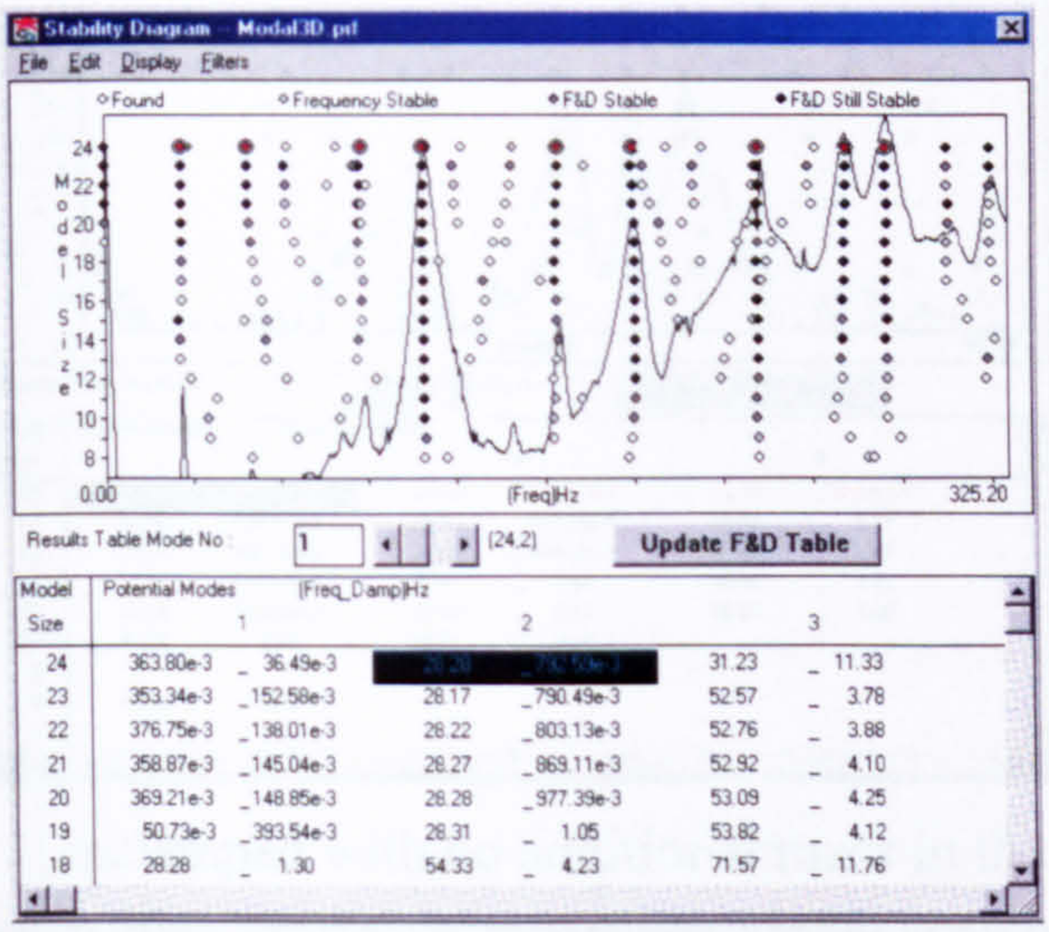

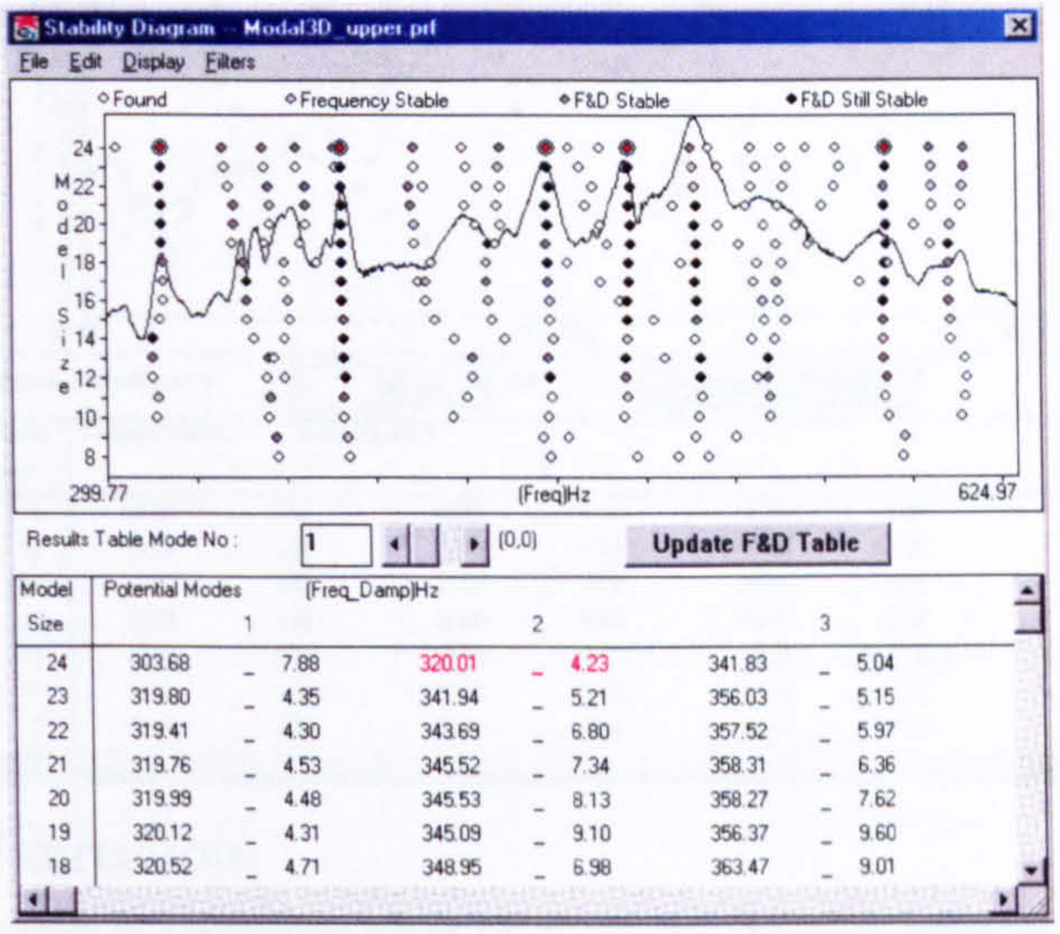

- Table excitation with no additional mass

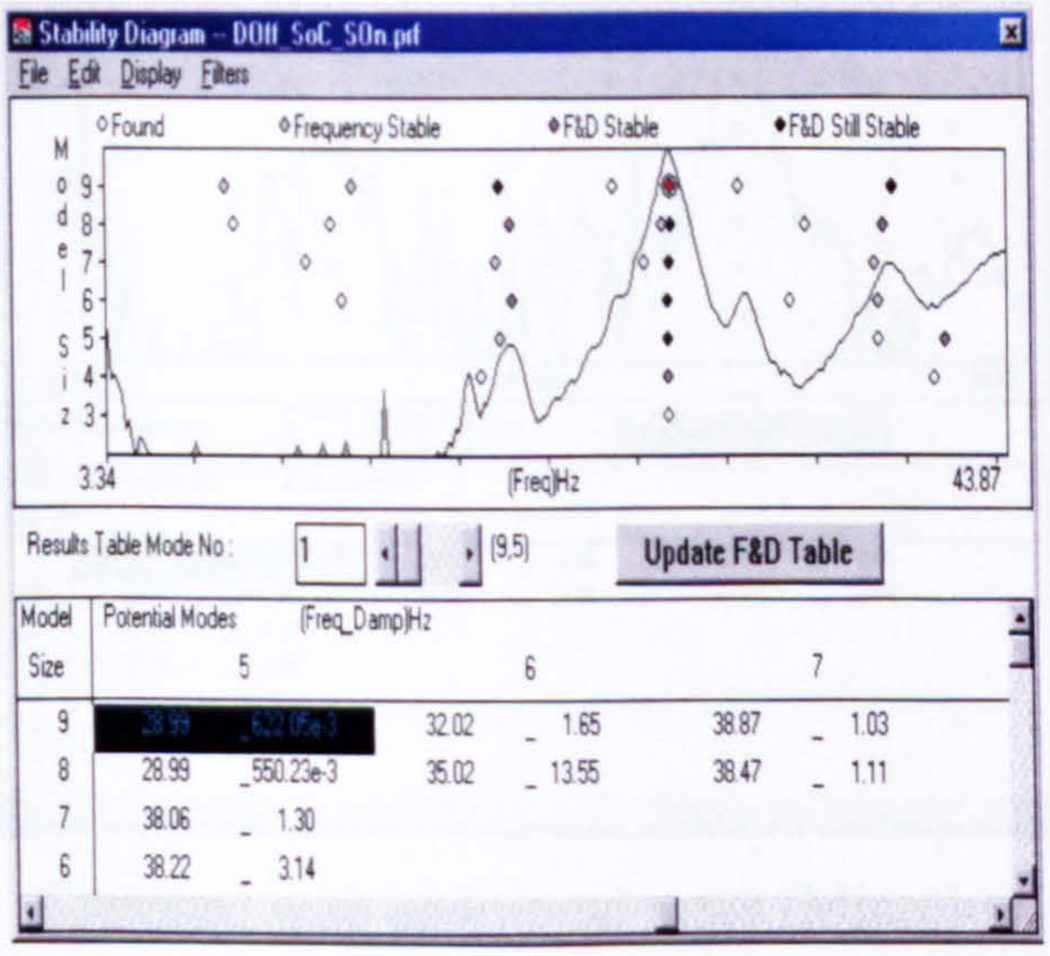

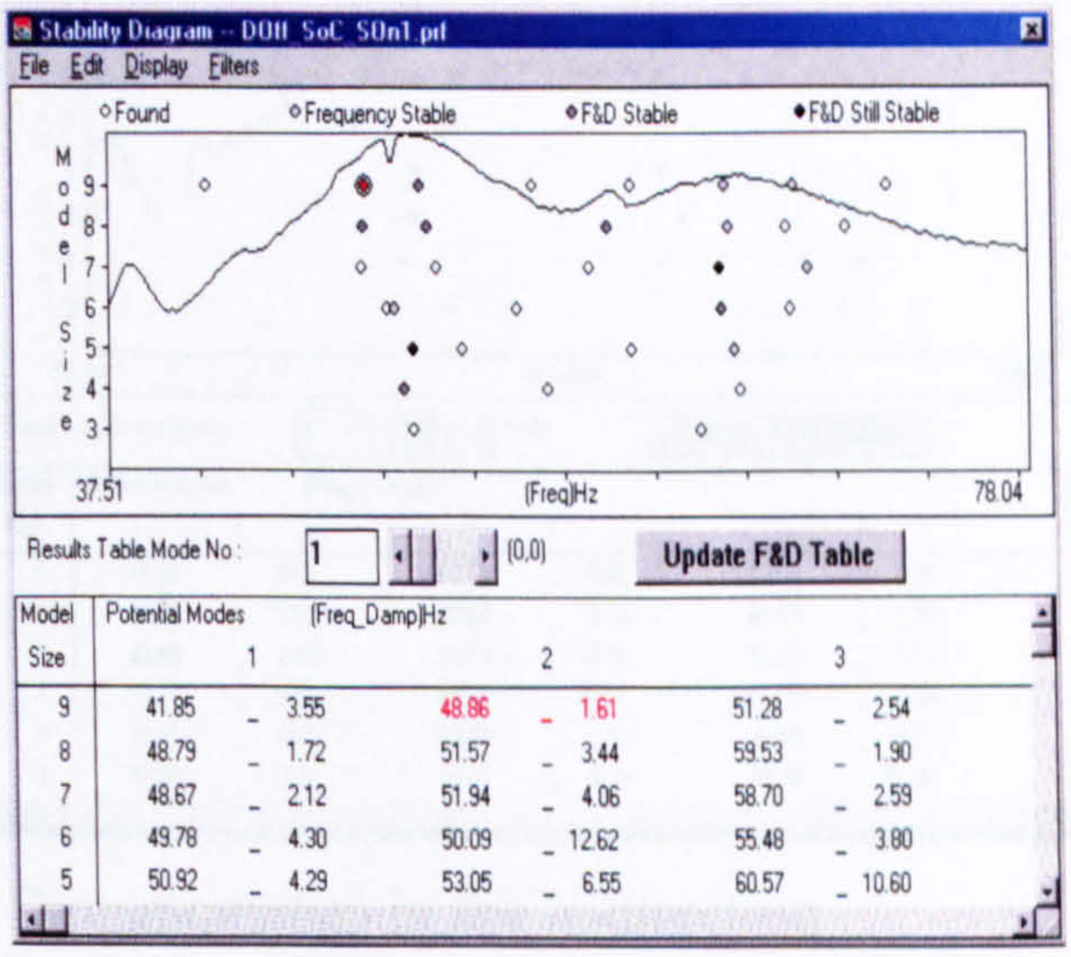

- Table excitation with additional mass (Microloc & Dynamometer)

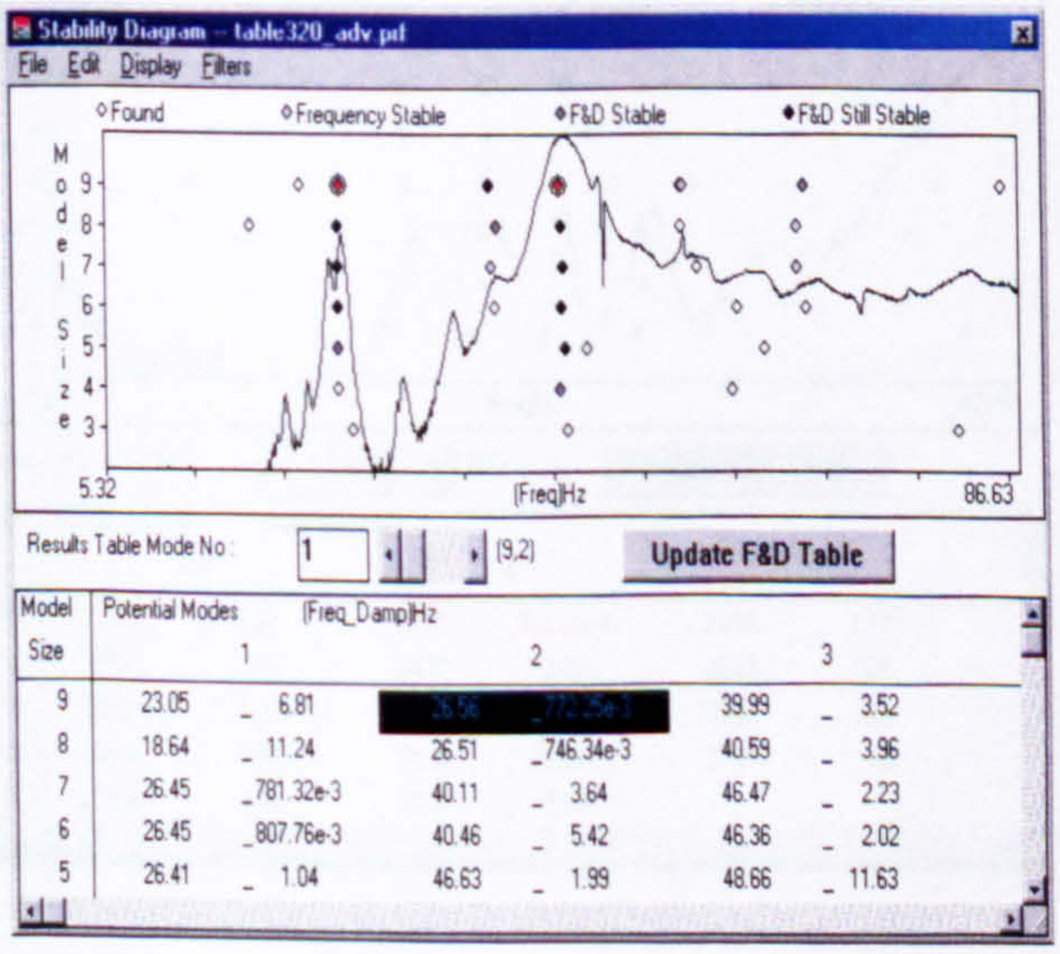

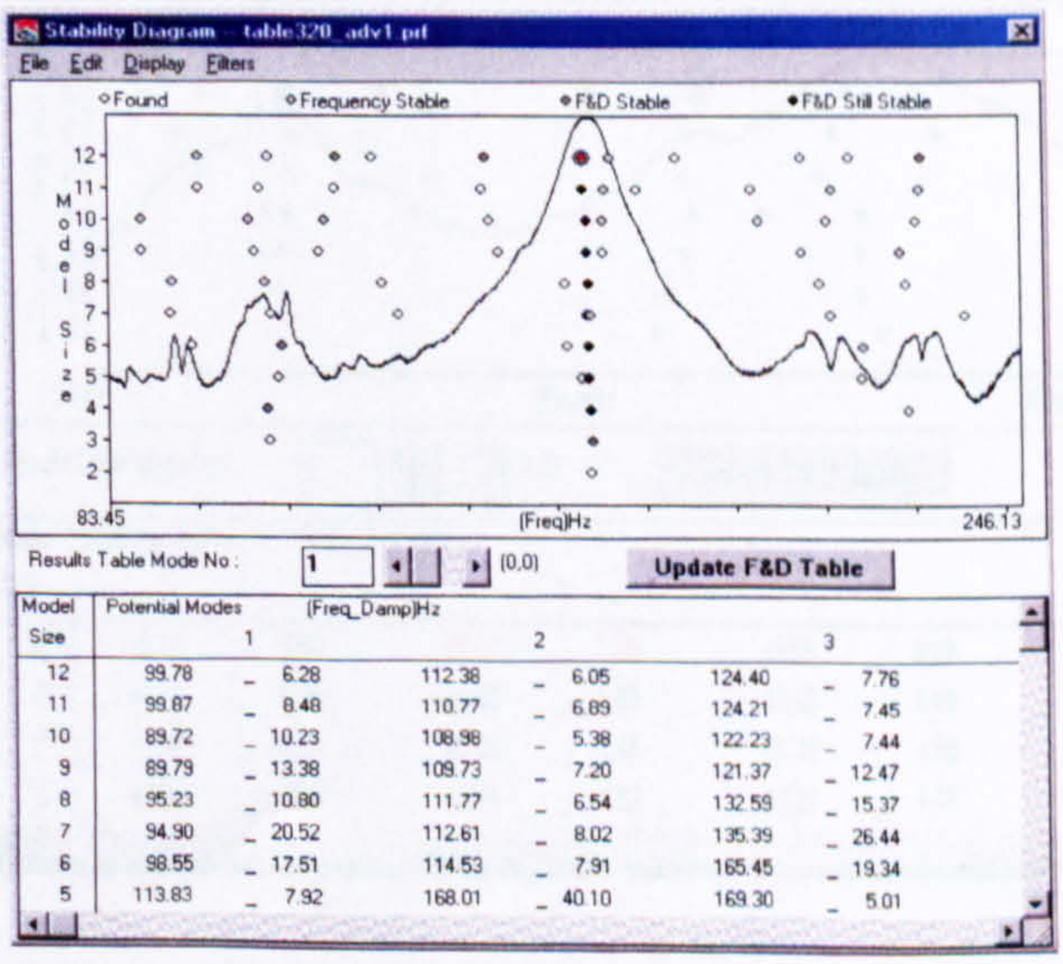

(b) Stability diagrams for shaker-on-worktable configurations

- Unclamped with no additional mass in the X-direction

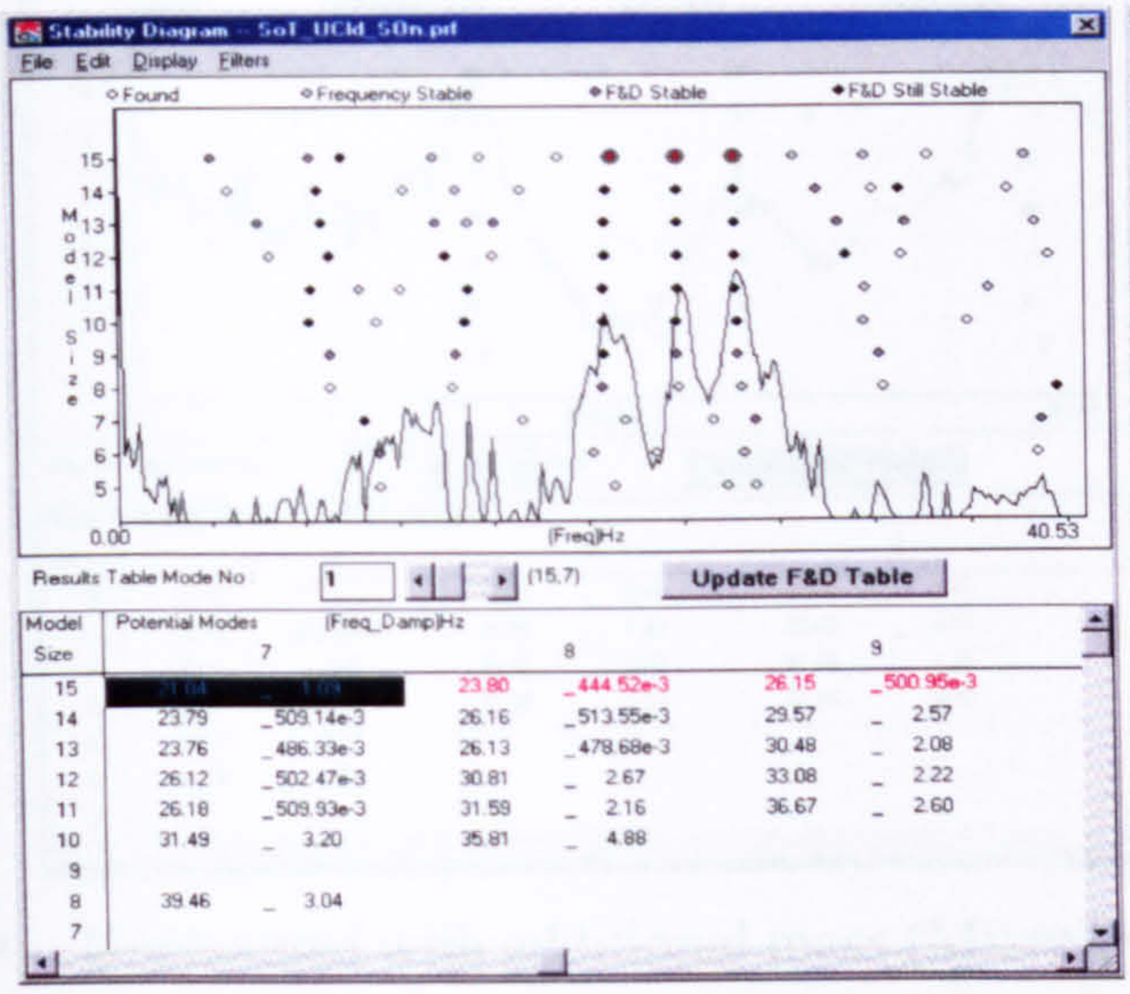

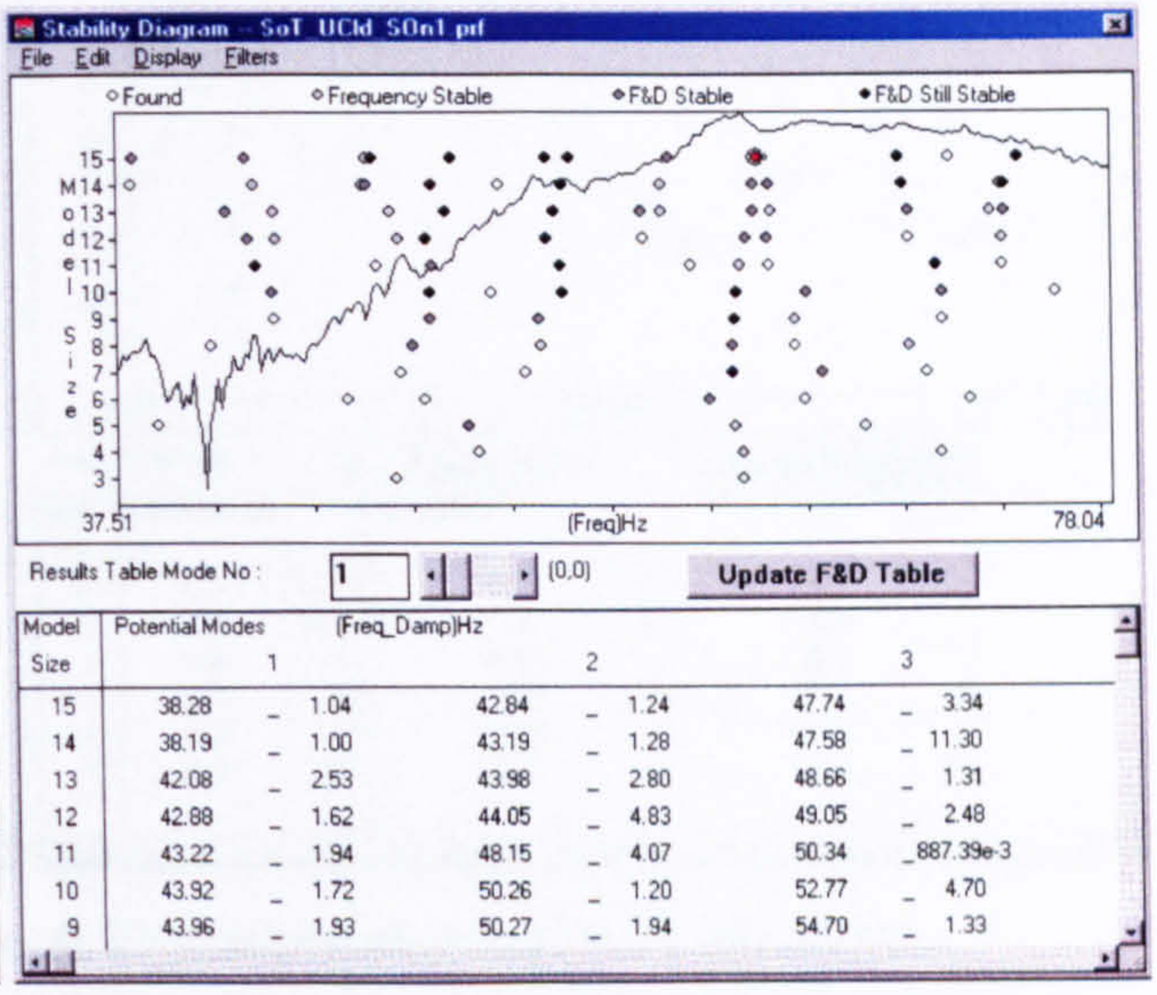

- Unclamped with no additional mass in the Y-direction

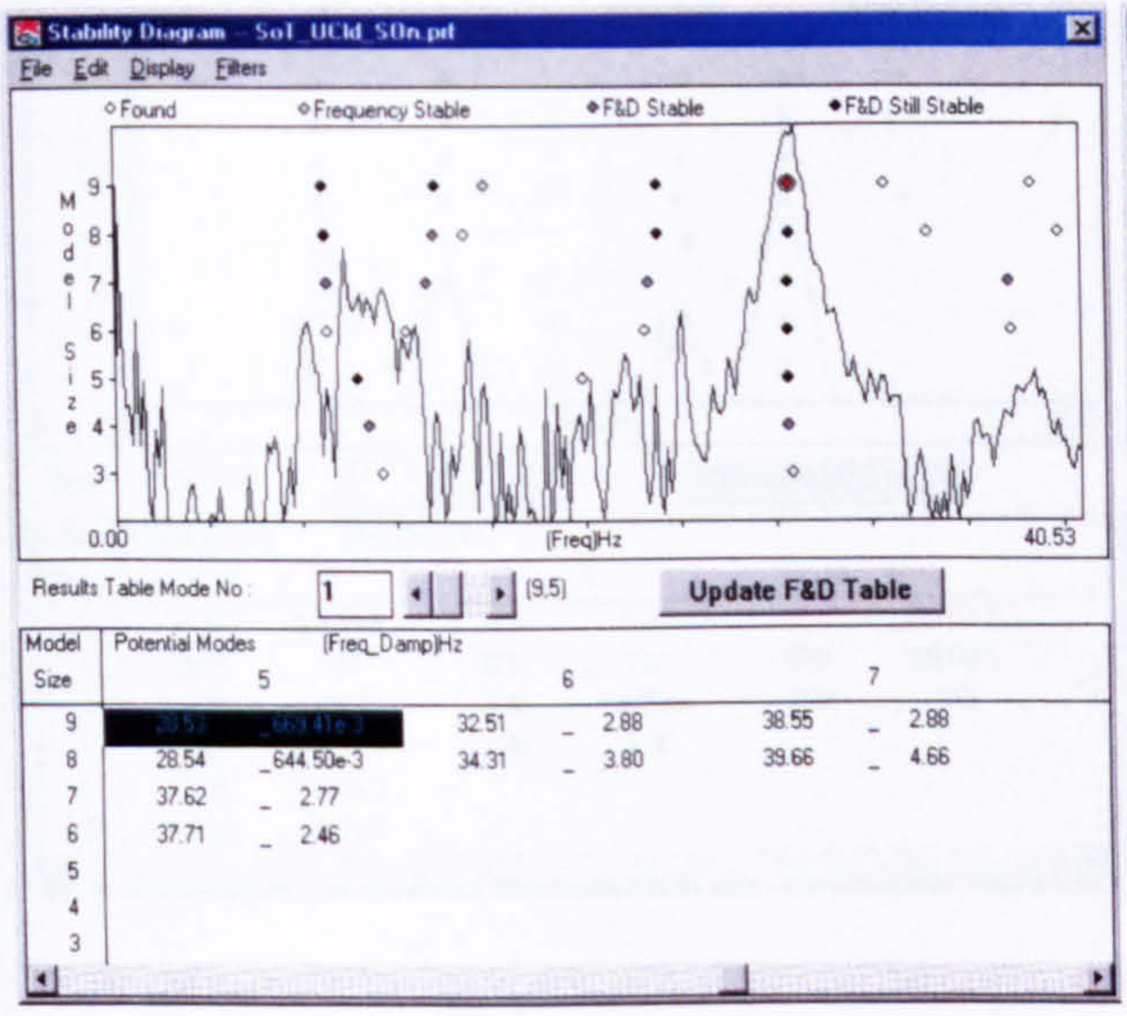

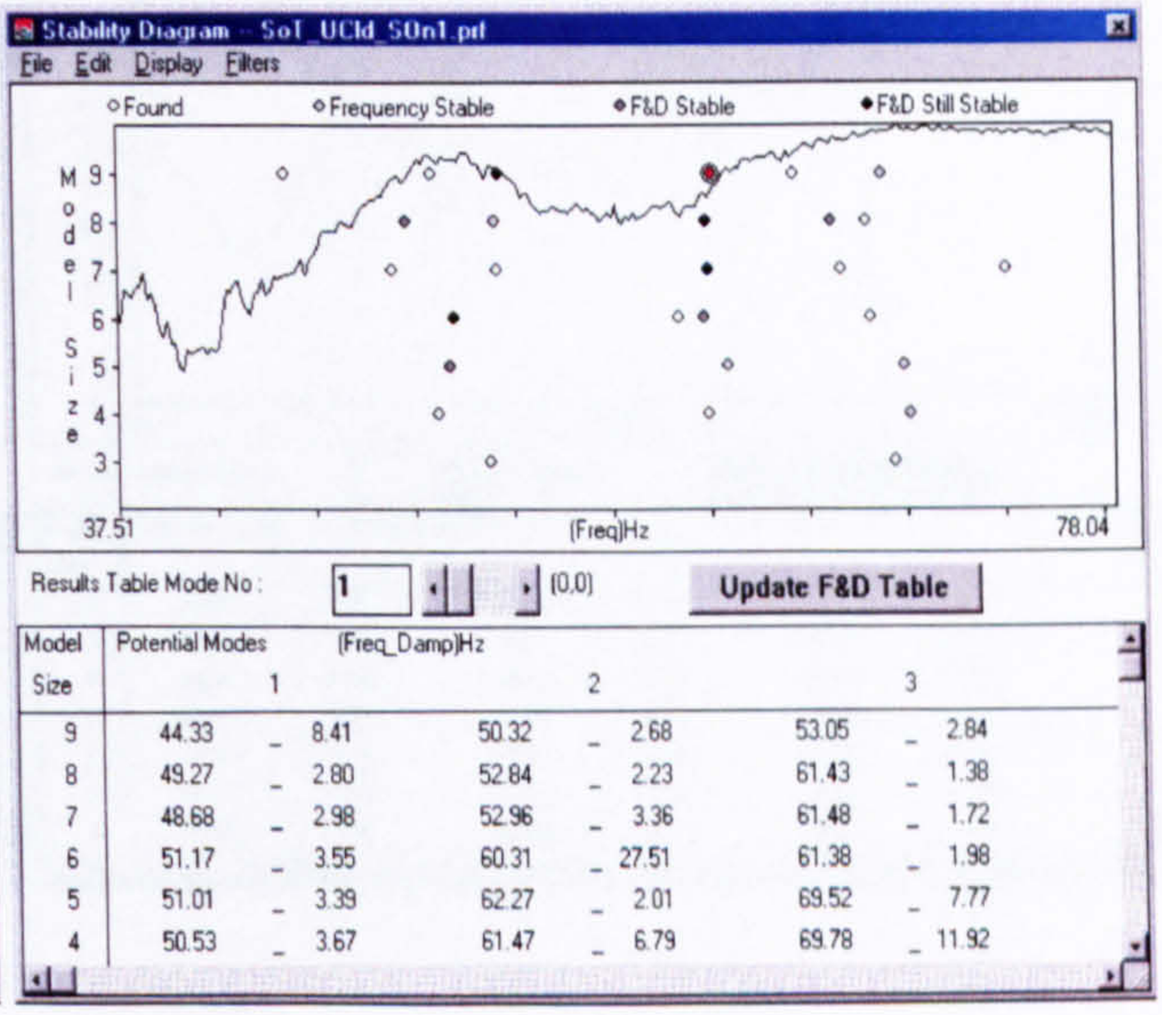

- Clamped with additional mass (Microloc & Dynamometer) in the X-direction

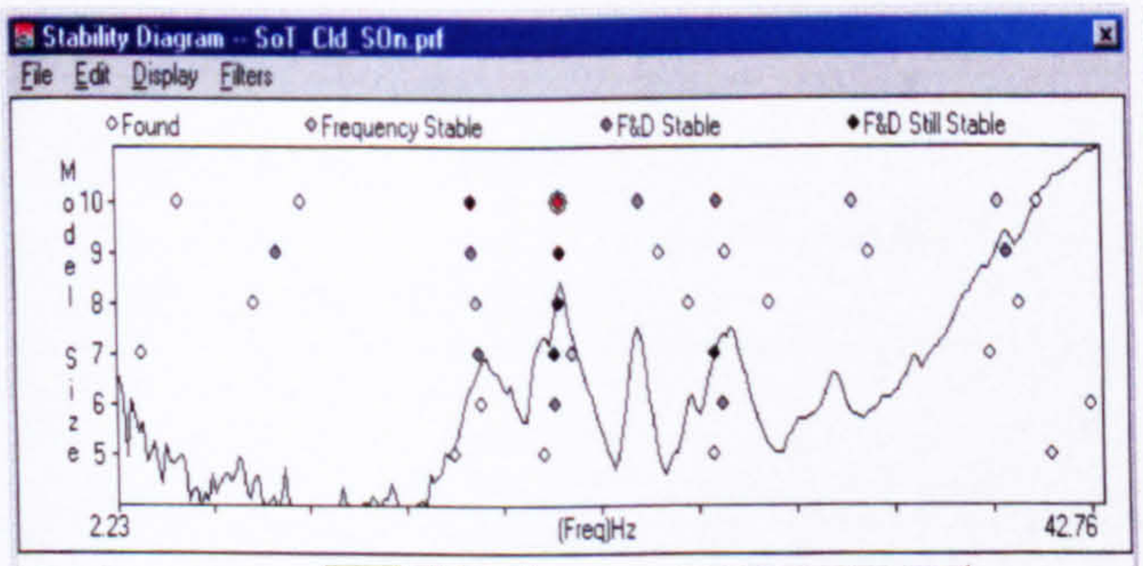

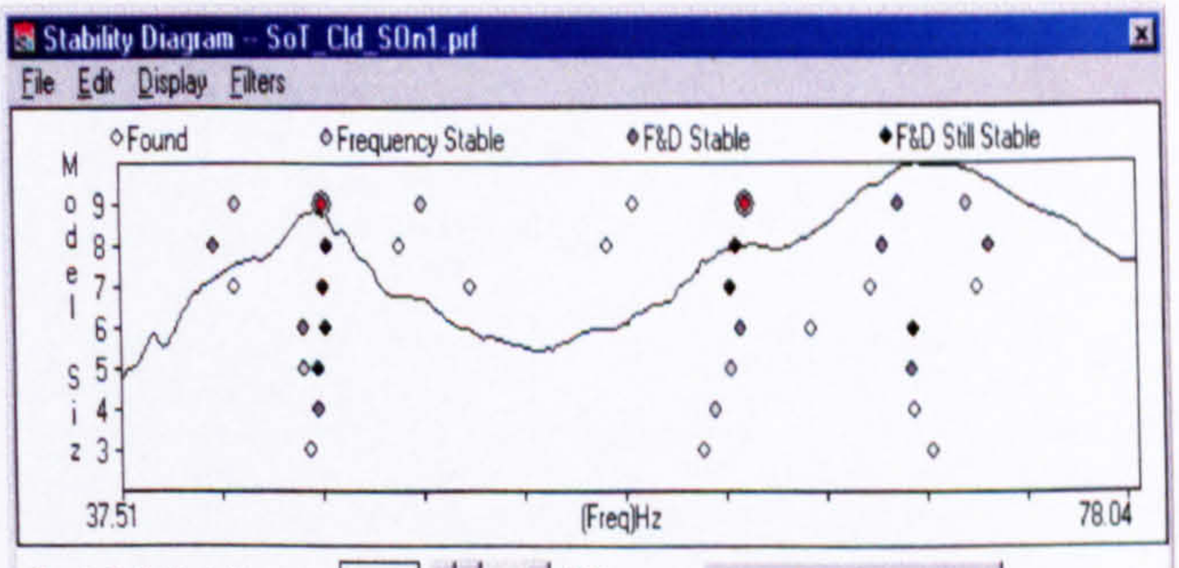

- Unclamped with additional mass (Microloc & Dynamometer) in the X-direction

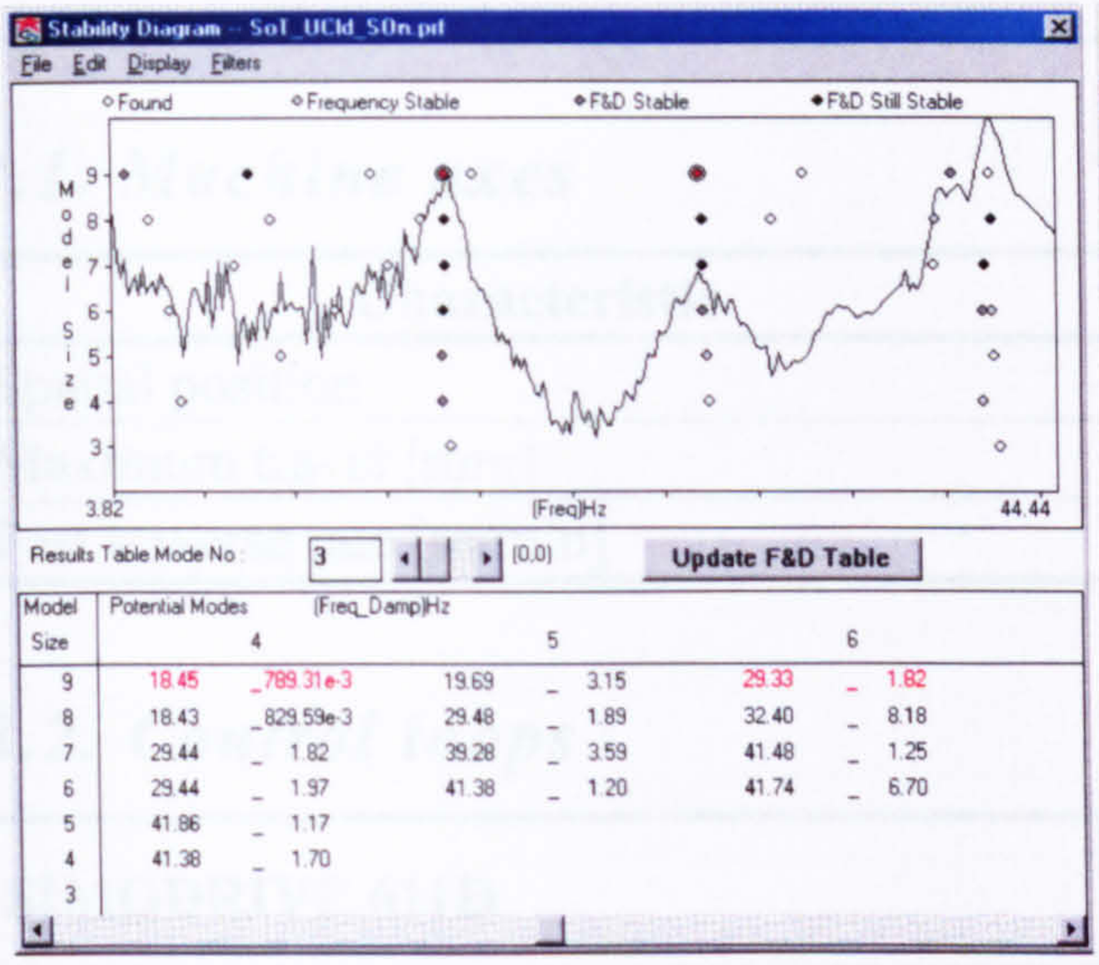

Model Size	Potential Modes (Freq_Damp)Hz 4		5		6	
9	18.45	_789.31e-3	19.69	_ 3.15	29.33	_ 1.82
8	18.43	_829.59e-3	29.48	_ 1.89	32.40	_ 8.18
7	29.44	_ 1.82	39.28	_ 3.59	41.48	_ 1.25
6	29.44	_ 1.97	41.38	_ 1.20	41.74	_ 6.70
5	41.86	_ 1.17				
4	41.38	_ 1.70				
3						

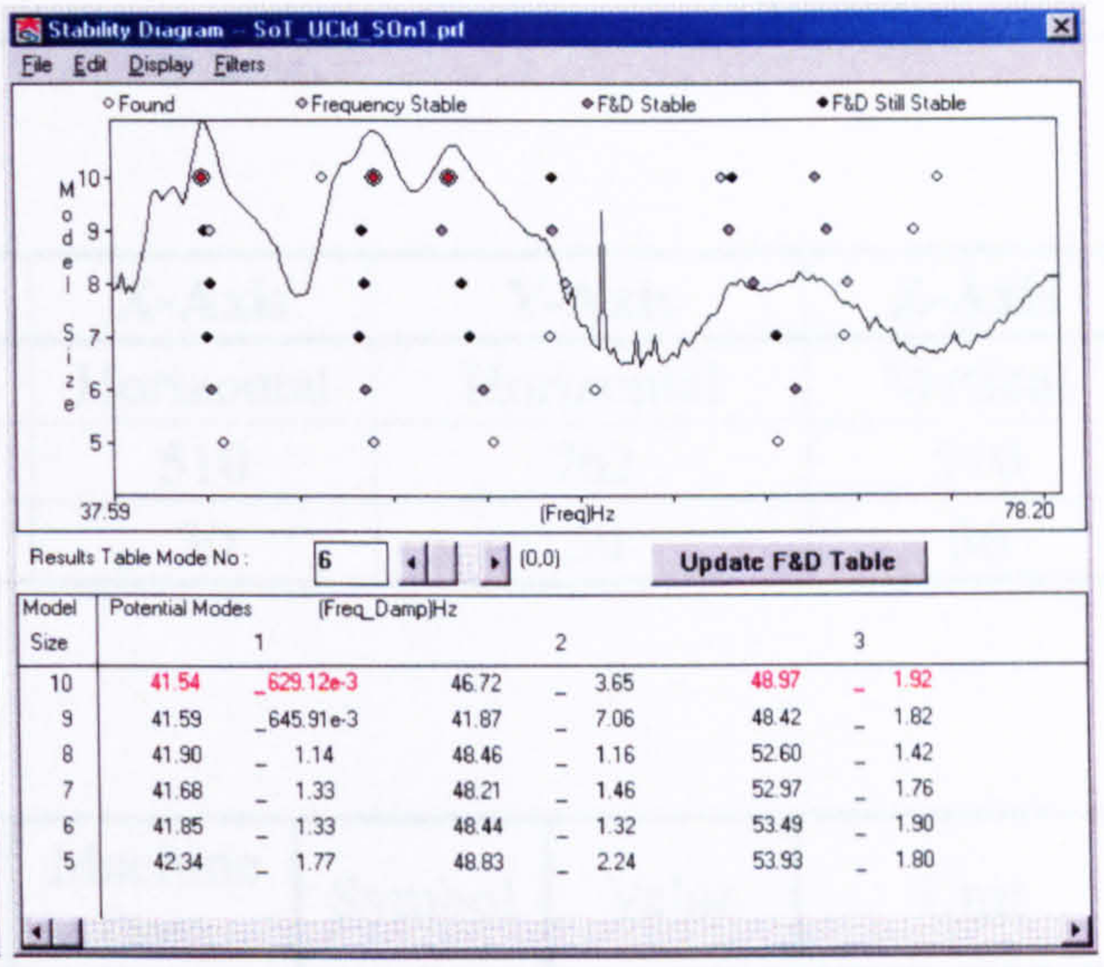

Model Size	Potential Modes (Freq_Damp)Hz 1		2		3	
10	41.54	_629.12e-3	46.72	_ 3.65	48.97	_ 1.92
9	41.59	_645.91e-3	41.87	_ 7.06	48.42	_ 1.82
8	41.90	_ 1.14	48.46	_ 1.16	52.60	_ 1.42
7	41.68	_ 1.33	48.21	_ 1.46	52.97	_ 1.76
6	41.85	_ 1.33	48.44	_ 1.32	53.49	_ 1.90
5	42.34	_ 1.77	48.83	_ 2.24	53.93	_ 1.80

- Unclamped with additional mass (Microloc & Dynamometer) in the Y-direction

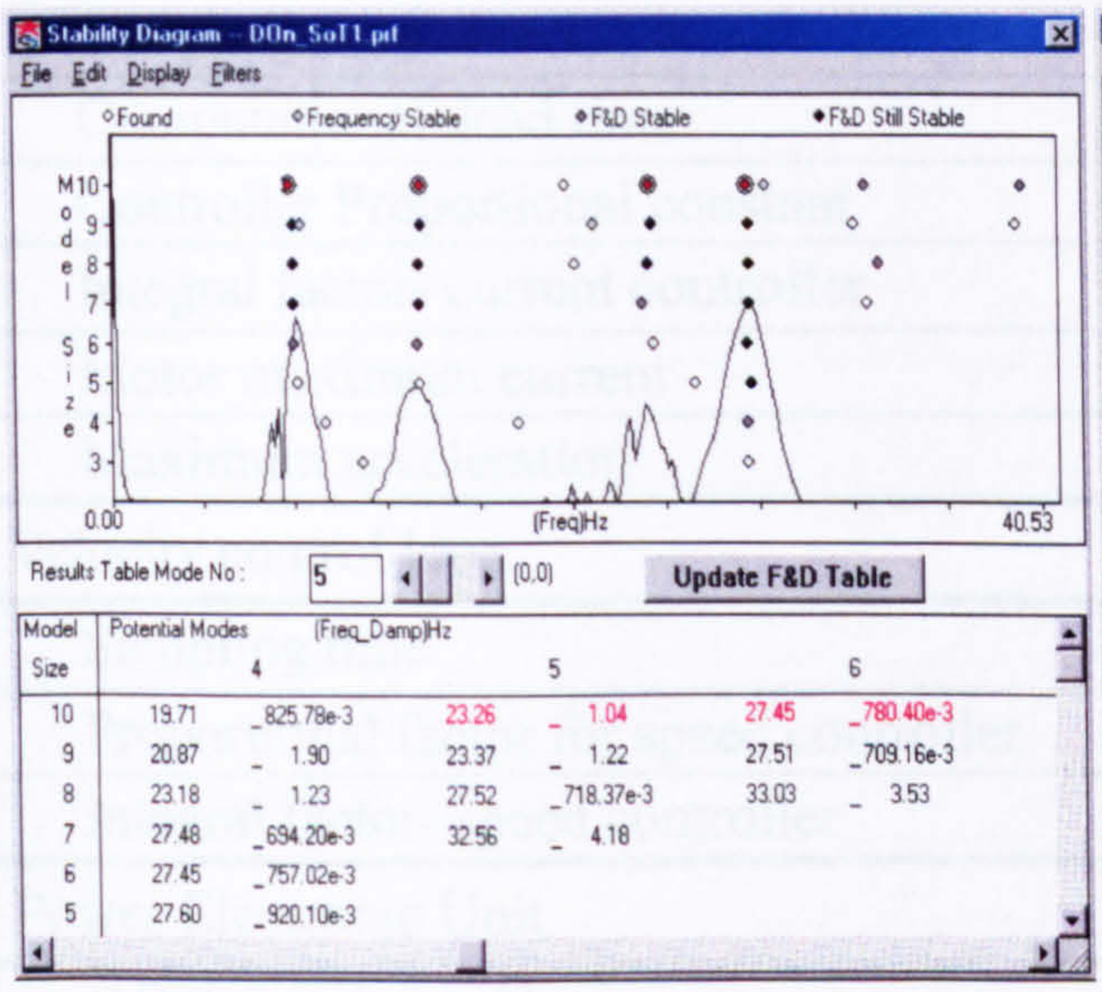

Model Size	Potential Modes (Freq_Damp)Hz 4		5		6	
10	19.71	_825.78e-3	23.26	_ 1.04	27.45	_780.40e-3
9	20.87	_ 1.90	23.37	_ 1.22	27.51	_709.16e-3
8	23.18	_ 1.23	27.52	_718.37e-3	33.03	_ 3.53
7	27.48	_694.20e-3	32.56	_ 4.18		
6	27.45	_757.02e-3				
5	27.60	_920.10e-3				

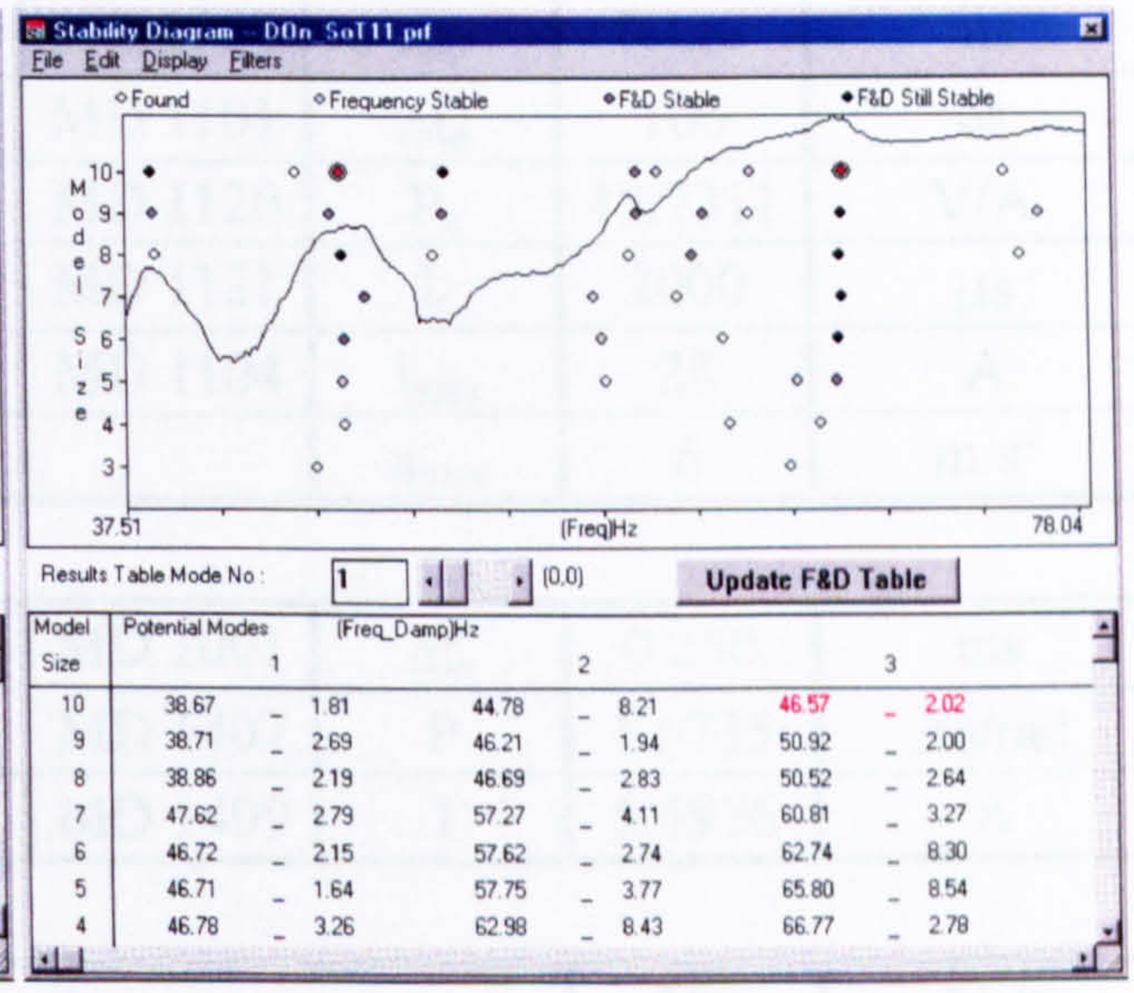

Model Size	Potential Modes (Freq_Damp)Hz 1		2		3	
10	38.67	_ 1.81	44.78	_ 8.21	46.57	_ 2.02
9	38.71	_ 2.69	46.21	_ 1.94	50.92	_ 2.00
8	38.86	_ 2.19	46.69	_ 2.83	50.52	_ 2.64
7	47.62	_ 2.79	57.27	_ 4.11	60.81	_ 3.27
6	46.72	_ 2.15	57.62	_ 2.74	62.74	_ 8.30
5	46.71	_ 1.64	57.75	_ 3.77	65.80	_ 8.54
4	46.78	_ 3.26	62.98	_ 8.43	66.77	_ 2.78

B.1. Machine axes

Characteristic	X-Axis	Y-Axis	Z-Axis
Spatial position	Horizontal	Horizontal	Vertical
Maximum travel [mm]	510	762	510
Fast traverse rate [m/min]	30	30	30

B.2. Control loops

SIMODRIVE 611D	Machine Data	Symbol	Value	Unit
Current control loop				
Sampling time	MD 1000	Δt_c	0.125	ms
Computational dead time	MD 1101	Δt_d	100	us
Controller Proportional constant	MD 1120	P_c	15.7311	V/A
Integral factor- current controller	MD 1121	I_c	2000	µs
Motor maximum current	MD 1104	I_{max}	28	A
Maximum acceleration		a_{max}	6	m/s^2
Velocity control loop				
Sampling time	MD 1001	Δt_v	0.250	ms
Proportional factor for speed controller	MD 1407	P	1.5735	As/rad
Integral factor- speed controller	MD 1409	I	5.4976	A
Power Electronic Unit				
DC link voltage, V_{DC}			300	Volt
Switching frequency, f_{pwm}			8000	Hz
PWM period, t_{pwm}			125	µs

SINUMERIK 840D	Machine Data	Symbol	Value	Unit
Position control loop				
Sampling time	MD 10050	Δt_v	4	ms
Proportional factor for position controller	MD 32200	K_v	3	(m/min)/mm
Linear encoder (Heidenhain LS186C)				
Feedback pulses			1000	pulse/mm
Length			640	mm

B.3. Permanent magnet synchronous motors (Siemens)

	X- and Y-axis	Z-axis
Order designation number	1FK6063-6AF71-1AG2	1FT6064-6AH71-4AB1
Phase inductance, L [mH]	6.5	6
Phase resistance, R [Ω]	0.83	0.63
Back emf constant, λ [V/1000 rpm]	92	65
DC Link voltage, V_{DC} [V]	600	600
Maximum current, I_{max} [A]	28	49
Maximum torque, M_{max} [Nm]	36	38
Rated torque, M_{rated} [Nm]	6	4.8
Torque constant, K_t [Nm/A]	1.39	1.04
Number of pole pairs, p	3	3
Maximum speed, ω_{max} [rpm]	5300	6800
Rated speed, ω_{rated} [rpm]	3000	4500
Electrical time constant, T_e [ms]	7.8	9.5
Mechanical time constant, T_m [ms]	2.1	2.2
Motor inertia, J_{mot} [kg·m^2]	1.61×10^{-3}	1.62×10^{-3}
Encoder	Optical incremental encoders, 2048 pulse/cycle	

B.4. Mechanical transmission system

- ***Ballscrews (published and calculated parameter values)***

Characteristic	X-axis	Y-axis	Z-axis
Manufacturer/Type	PGM THK/Unique		
Diameter, *D* [mm]	32	32	32
Root diameter, d_1 [mm]	25	25	25
Ball diameter [mm]	6.35	6.35	6.35
Length, *l* [mm]	813.5	996	974
Distance between bearings, ℓ_a [mm]	706.5	894	867
Screw pitch, ℓ_p [mm]	12	12	12
Ballscrew assembly mass [kg]	16		
Efficiency coefficient	0.9		
Maximum speed [rpm]	2500	2500	2500
Buckling strength, P_1 [1] [N]	78,259	48,875	51,966
Inertia, J_{BS} [2] [kg m^2]	6.58×10^{-4}	8.06×10^{-4}	7.88×10^{-4}
Preload [N]	1560	1560	1560
Drag Torque [Nm]	0.422	0.422	0.422
Axial Rigidity of Nut (*) [N/μm]	727	727	727
Ratio [3] [ms^{-1}/rpm]	0.00191	0.00191	0.00191
Radial Rigidity, k_{rot} [4] [Nm/rad]	10,123.5	12,394.6	12,120.9
Axial Rigidity, k_{ax} [5] [N/m]	1.207×10^8	9.857×10^7	1.008×10^8

(*) Preloaded nut rigidity under an axial force of 9440 N

Equations for the calculated parameters (in brackets):

[1] $P_1 = \eta_2 \frac{{d_1}^4 \times 10^4}{{\ell_a}^2}$, where η_2 = mounting method coefficient (fixed/supported = 10)

[2] $J_{BS} = \frac{\pi}{32} \times D^4 \times l \times \rho$, where ρ: specific density (steel = 7860 kg/m^3)

[3] $Ratio = \frac{\ell_p}{2 \times \pi}$

[4] $k_{rot} = \frac{GJ_P}{l}$, where G = shear modulus (N/m^2)

J_P = polar moment of inertia (m^4), $J_P = \frac{\pi}{32} D^4$ (tube)

[5] $k_{ax} = \frac{EA}{l}$, where A = axial area (m^2), tubular, using the root diameter

E = Young's modulus (N/m^2) = 2×10^{11} (steel)

- ***Bearings***

Thrust bearings (NSK-RHP) XYZ (1st set) – BSB025062DBHP3 – back-to-back	
Contact angle, α [°]	60
Bore diameter, d_b [mm]	25
Pitch circle diameter, d_{bl} [mm]	15
Outer diameter, D_b [mm]	62
Basic static load rating, C_o [kN]	47.5
Axial rigidity, k_b [N/μm]	650
Moment of inertia (rotating inner ring), J_b [Kg cm^2]	
Mass, m_b [kg]	
Limiting speed, n_{bmax} [rpm]	2300

Radial support bearings (NSK-RHP) X (2nd set) – 6305-2RSJ RE AV2S5	
Contact angle, α [°]	0
Bore diameter, d_b [mm]	25
Pitch circle diameter, d_{bl} [mm]	17
Outer diameter, D_b [mm]	62
Basic static load rating, C_o [kN]	11.7
Dynamic load rating, C_o [kN]	20.6
Axial rigidity, k_b [N/μm]	0
Moment of inertia (rotating inner ring), J_b [Kg cm^2]	
Mass, m_b [kg]	0.220
Limiting speed, n_{bmax} [rpm]	8500

Radial support bearings (NSK-RHP) Y (2nd set) – 6005-2RSJ RE AV2S5	
Contact angle, α [°]	0
Bore diameter, d_b [mm]	25
Pitch circle diameter, d_{bl} [mm]	12
Outer diameter, D_b [mm]	47
Basic static load rating, C_o [kN]	6.5
Dynamic load rating, C_o [kN]	10.7
Axial rigidity, k_b [N/μm]	0
Moment of inertia (rotating inner ring), J_b [Kg cm^2]	
Mass, m_b [kg]	0.08
Limiting speed, n_{bmax} [rpm]	10200

Radial support bearings (NSK-RHP) Z (2nd set) – 6305-2RSJ RE AV2S5	
Contact angle, α [°]	0
Bore diameter, d_b [mm]	25
Pitch circle diameter, d_{bl} [mm]	17
Outer diameter, D_b [mm]	62
Basic static load rating, C_o [kN]	11.7
Dynamic load rating, C_o [kN]	20.6
Axial rigidity, k_b [N/μm]	0
Moment of inertia (rotating inner ring), J_b [Kg cm^2]	
Mass, m_b [kg]	0.220
Limiting speed, n_{bmax} [rpm]	8500

- ***Motor shaft (calculated parameter values)***

Diameter = 24 mm Length = 50 mm

Assuming material is steel:

$$J_{shaft} = \frac{m \times r^2}{2} = \frac{\pi}{32} \times D^4 \times L \times \rho = 1.28 \times 10^{-5}\ kg\ m^2$$

$$k_{ax\ shaft} = \frac{E \times A}{l} = \frac{E \pi D^2}{4l} = \frac{2 \times 10^{11} \times \pi \times 0.024^2}{4 \times 0.050} = 1.810 \times 10^9\ Nm^{-1}$$

$$k_{rad\ shaft} = \frac{G \times J_P}{l} = \frac{G \times \pi \times D^4}{l \times 32} = \frac{8 \times 10^{10} \times \pi \times 0.024^4}{0.050 \times 32} = 52.115 \times 10^3\ Nmrad^{-1}$$

$$c_{cr\ shaft} = 2\sqrt{k_{rad} J} = 2\sqrt{52115 \times 1.28 \times 10^{-5}} = 1.633\ Nm(rads^{-1})^{-1}$$

- ***Ballscrew nuts***

Nut	X-axis	Y-axis	Z-axis
Axial rigidity [N/m]	727	727	727
Ball circle diameter [mm]	6.35	6.35	6.35
Mass [kg]	1.34	1.34	1.34
Material	Steel		

B.5. Mechanical load

- ***Mechanical element mass***

Component	X-Axis [kg]	Y-Axis [kg]	Z-Axis [kg]
X-axis table	327		
X-axis covers telescopic (pair)	14		
X-axis table screw bracket	4		
X-axis ball-screw assembly	16		
X-axis THK guideways	18		
X-axis linear scale	3		
X-axis motor	13		
X-axis total mass	345		
Y-axis saddle		160	
Y-axis covers front telescopic		20	
Y-axis cover rear sliding		19	
Harness and power track		4	
Y-axis table		327	
Y-axis Mass		598	
Z-axis motor			152
z-axis carrier without motor			212
Z-axis complete carrier			364

- ***Inertia of the load referred to the ball-screw***

$$J_L = m_{tot}\frac{\ell_p{}^2}{(2\times\pi)^2}$$ where m_{TOT} = total mass (kg) and ℓ_p = pitch length (m)

$$\text{X-Axis}: J_{Lx} = 345\frac{0.012^2}{(2\times\pi)^2} = 1.26\times10^{-3}\,kg\,m^2$$

$$\text{Y-Axis}: J_{Ly} = 598\frac{0.012^2}{(2\times\pi)^2} = 2.18\times10^{-3}\,kg\,m^2$$

$$\text{Z-Axis}: J_{Lz} = 364\frac{0.012^2}{(2\times\pi)^2} = 1.33\times10^{-3}\,kg\,m^2$$

- ***Total inertia at the motor***

$J = J_m + J_{shaft} + J_L$

X-Axis : $J_x = 1.61\times10^{-3} + 1.28\times10^{-5} + 1.26\times10^{-3} = 2.8828\times10^{-3}\, kg\ m^2$

Y-Axis : $J_y = 1.61\times10^{-3} + 1.28\times10^{-5} + 2.18\times10^{-3} = 3.8028\times10^{-3}\ kg\ m^2$

Z-Axis : $J_z = 1.62\times10^{-3} + 1.28\times10^{-5} + 1.33\times10^{-3} = 2.9628\times10^{-3}\ kg\ m^2$

B.6. Guideways

PGM-THK linear guideway Type : HSR35A2SSCOQZ+1090L H II	
Basic static load rating, C_o [kN]	61.1
Basic dynamic load rating, C [kN]	37.3
Radial rigidity (downward/upward), k_{rl} [N/μm]	1066
LM block mass, m_{bl} [kg]	1.6
LM rail mass, m_{rl} [kg/m]	6.6
LM rail length, l_{rl} [m]	1.09

Appendix C. Simulink model of the mechanical transmission

C.1. Motor shaft and coupling system

The transmission of the motor rotational position and velocity to the ballscrew by these mechanical elements is modelled by the subsystem '*motor_shaft_and_coupling*' (see Figure C. 1). The motor shaft (located inside and outside the motor body) is considered as a separate element because it is not included in the motor model equations. It is modelled in the '*motor_shaft*' subsystem using torsional spring and viscous damping elements to represent the mechanical torque opposing and driving the motor and coupling hub respectively.

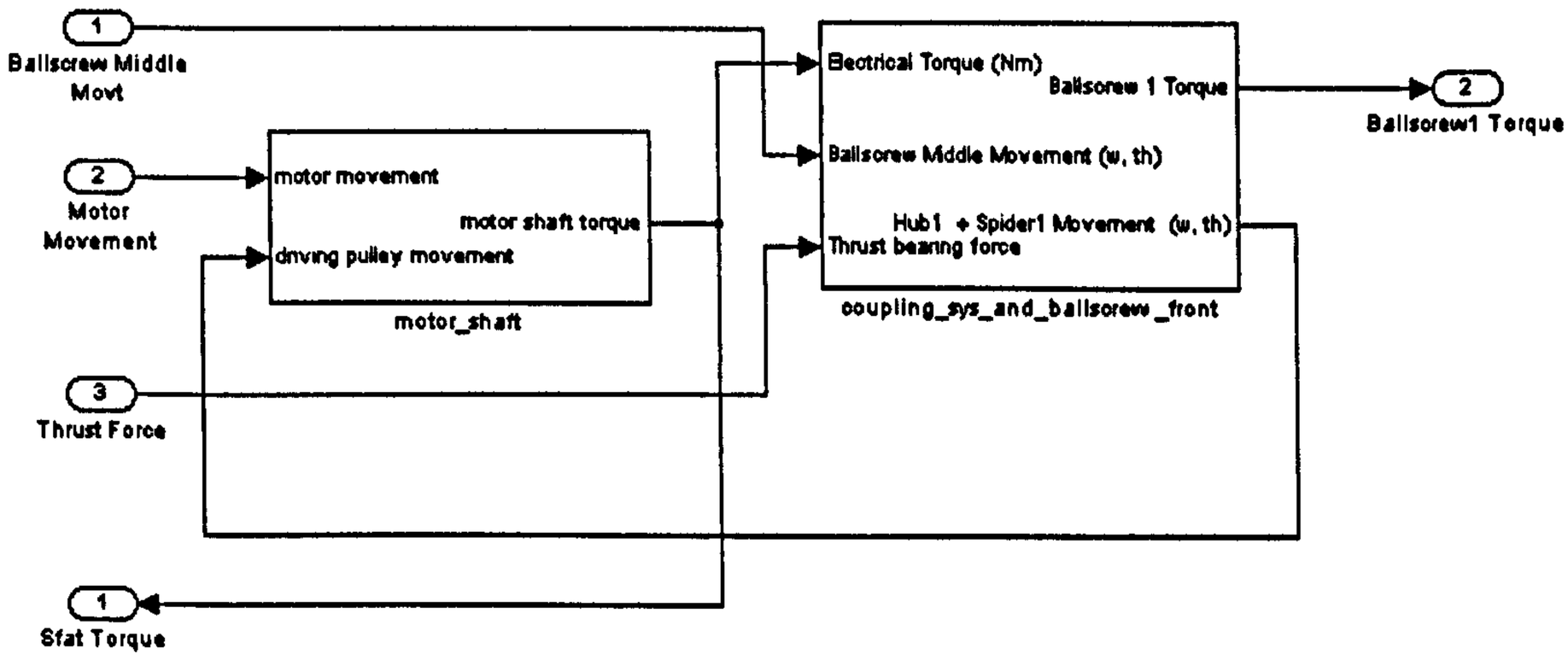

Figure C. 1. Subsystem '*motor_shaft_and_coupling*'

Motor shaft calculation (assumed as steel)

Length = 50 mm (outside the body) Diameter = 24 mm Material = steel

Length = 338 mm (outside + inside the body) $\rho = 7.8 \times 10^3$ kg/m^3 G= 8.0×10^{10} N/m^2

Shaft outside + inside the body

Inertia $= J_{shaft} = \frac{m \times r^2}{2} = \frac{\pi}{32} \times D^4 \times L \times \rho = 8.59 \times 10^{-5}\ kg\ m^2$

Torsional stiffness $= k_{rot} = \frac{GJ_\tau}{l} = \frac{8.0 \times 10^{10} \times \pi \times 0.024^4}{32 \times 0.338} = 7709$ Nm/rad

where, $J_\tau = \frac{\pi}{32} D^4$ (assumed to be rod)

Critical damping $= c_{cr\ shaft} = 2\sqrt{k_{rot} J} = 2\sqrt{7709 \times 8.59 \times 10^{-5}} = 1.63\ Nmsrad^{-1}$

Damping coefficient = c = Damping ratio × Radial critical Damping/$\sqrt{2}$

$= 0.00696 \times 1.63 / \sqrt{2} = 0.008$

Shaft outside the body

Inertia $= J_{shaft} = \frac{m \times r^2}{2} = \frac{\pi}{32} \times D^4 \times L \times \rho = 1.27 \times 10^{-5}\ kg\ m^2$

$$\text{Torsional stiffness} = k_{rot} = \frac{GJ_P}{l} = \frac{8.0\times10^{10}\times\pi\times0.024^4}{32\times0.05} = 52115 \text{ Nm/rad}$$

$$\text{Critical damping} = c_{cr\ shaft} = 2\sqrt{52115\times1.27\times10^{-5}} = 1.63\ Nmsrad^{-1}$$

$$\text{Damping coefficient} = c = 0.00696 \times 1.63 / \sqrt{2} = 0.008$$

The coupling system is modelled according to their assembly, i.e. two hubs and one polymer element (spider) in the '*coupling_sys_and_ballscrew_front*' subsystem (see Figure C. 2). The spider (polymer material) is considered as two parts to enable the torque distribution modelling and because its material is considered much less rigid than the rest of the system. Its inertia is apportioned to the adjacent hubs, whereas its torsional rigidity is represented as a spring damper subsystem '*hubs coupling*'.

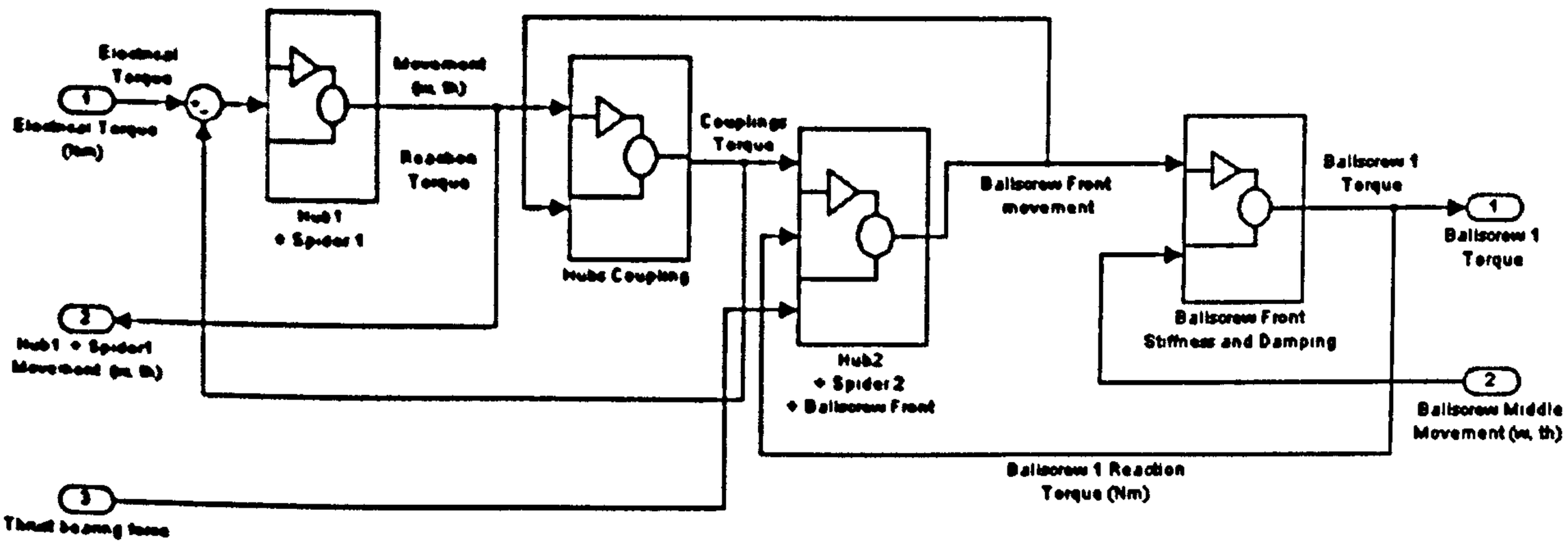

Figure C. 2. Subsystem '*coupling_sys_and_ballscrew_front*'

C.2. Front ballscrew and ballscrew support bearing

The '*coupling_sys_and_ballscrew_front*' subsystem also includes the models of the front (first quarter) of the ballscrew and the back-to-back ballscrew support bearings. The front ballscrew inertia model is included in the '*Hub2 + Spider2 + Ballscrew Front*' subsystem, whereas the stiffness and damping model is in the '*Ballscrew Front Stiffness and Damping*'. The axial and radial characteristics of the bearing inertia, friction and axial stiffness are modelled in the '*Hub2 + Spider2 + Ballscrew Front*' subsystem. The subsystem (see Figure C. 3) represents the ballscrew support bearing stiffness and friction in the '*bearing-radial*' and '*bearing-axial*' lower subsystems. The '*Torque acting on ballscrew front inertia*' calculates the rotational velocity and displacement due to the coupling torque output.

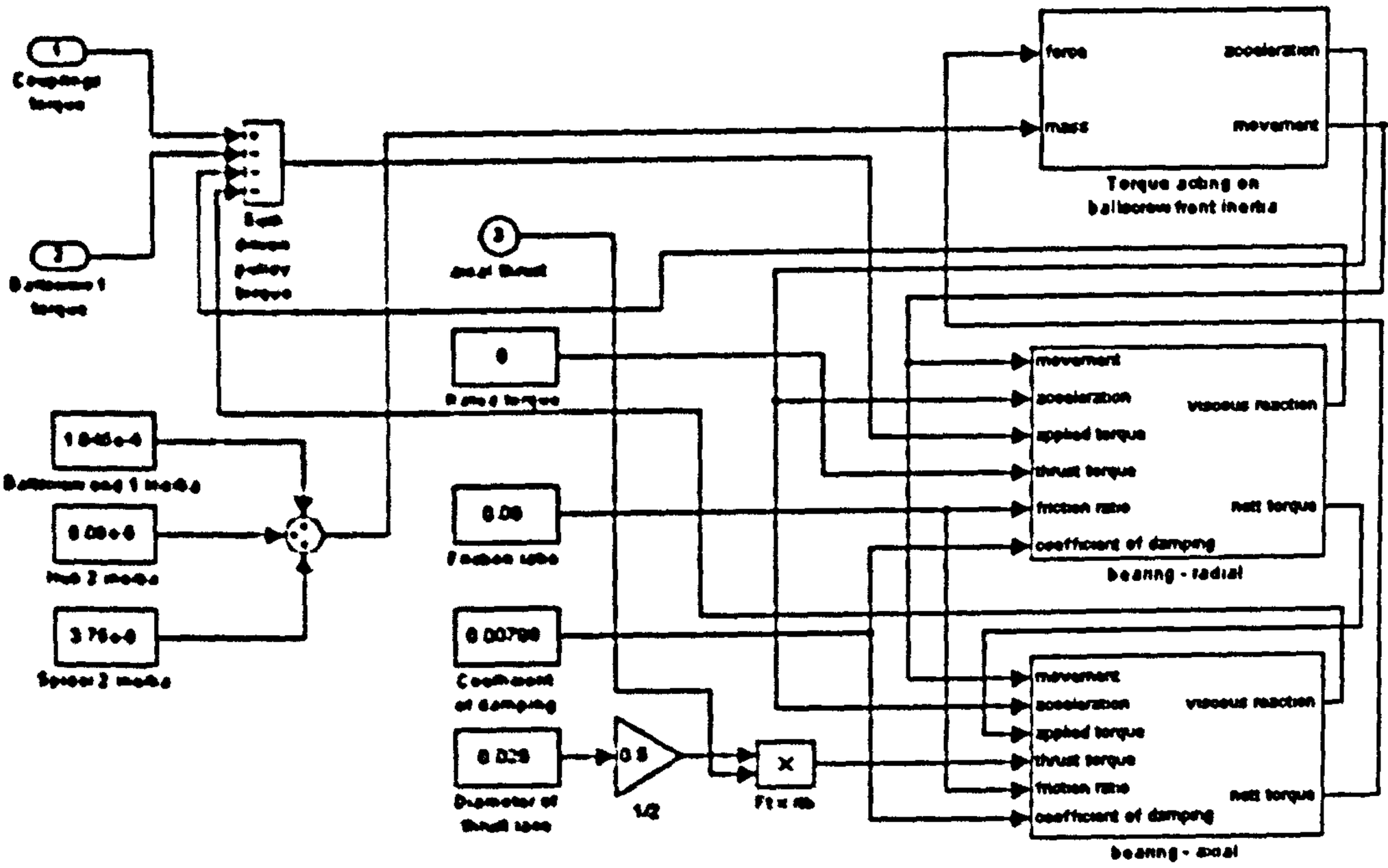

Figure C. 3. Subsystem '*Hub2 + Spider2 + Ballscrew Front*

Coupling System + Ballscrew 1 Front End

Hub 1 + Spider 1

Inertia, J_{HUB1} $= 5.08 \times 10^{-5}$ kg·m^2

Spider 1 Inertia, J_{SPDR_1} = Spider 1 Inertia/2 = 7.5×10^{-6} /2 = 3.75×10^{-6} kg·m^2

Hubs coupling

Torsional Rigidity, k_{HUB_1} = 6189 Nm/rad

Damping coefficient = relative damping × damping power = 0.8 × 6.6 = 5.28 Watt

Hub 2 + Spider2 + Ballscrew 1 front end

Coupling Hub 2 Inertia, J_{HUB2} $= 5.08 \times 10^{-5}$ kg·m^2

Ballscrew end 1 Inertia, J_{BS_1} (½ ballscrew in series) = $\frac{J_{BS}}{2} = \frac{0.000658}{2} = 3.29 \times 10^{-4}$ kg m^2

Spider 2 Inertia, J_{SPDR_1} = Spider 1 inertia/2 = 7.5×10^{-6} /2 = 3.75×10^{-6} kg·m^2

Rated torque = 6 Nm

Friction ratio = 0.06

Coefficient of damping = Damping ratio × Radial critical damping/$\sqrt{2}$

= 0.00696 × 5.162 / $\sqrt{2}$ = 0.0147

Fixed end bearing

Rated torque = 6 Nm

Friction ratio = 0.06

Coefficient of damping = 0.0147

Friction

Default velocity tolerance = 5e-5

Default cycle time = 1e-6

Ballscrew 1 stiffness and damping

Torsional rigidity, k_{BS_1} = Torsional rigidity × 2 = 10,123.5 × 2 = 20247 Nm/rad

Rotary critical damping = $2\sqrt{J_{BS\_1} \cdot k_{BS\_1}}$ $= 2\sqrt{1.1\times10^{-4} \times 20{,}247} = 2.985$ Nms/rad

Coefficient of damping = damping ratio × Radial critical damping/$\sqrt{2}$

$= 0.00696 \times 5.162 / \sqrt{2} = 0.0147$

Ballscrew front stiffness and damping

The torsional rigidity and damping of the front ballscrew is modelled separated in the subsystem '*ballscrew front stiffness and damping*' (see Figure C. 4). The subsystem models the torsional rigidity of the first front quarter length of the ballscrew shaft by calculating the output torque from the relative movement of the ballscrew 1 inertial element. The output torque drives the '*ballscrew_middle*' subsystem and opposes the torque output from the coupling system.

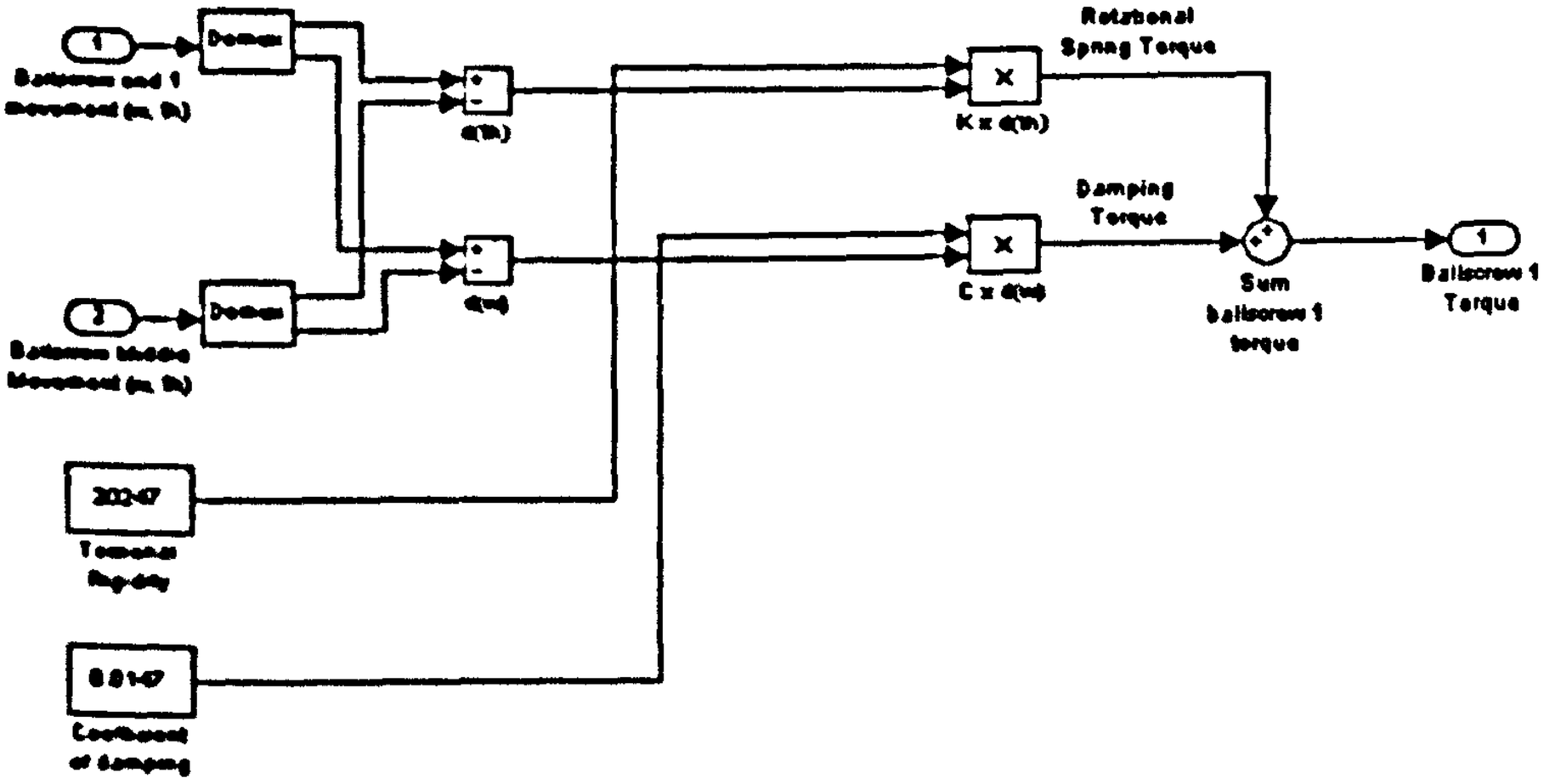

Figure C. 4. Subsystem '*ballscrew front stiffness and damping*'

C.3. Ballscrew middle

The '*ballscrew_middle*' subsystem (see Figure C. 6) represents the dynamic behaviour of the ballscrew centre portion where the ballscrew nut (and the table) is assumed to rest. The subsystem models the dynamic interaction between the ballscrew shaft and the nut, the conversion of rotational to linear movement, and the axial force dynamics of the ballscrew shaft. The technique assumes that the ballscrew nut rests and oscillates about the centre of the ballscrew shaft.

The '*ballscrew_middle*' subsystem includes the '*torque_on_inertia*' sub-subsystem which represents the torsional dynamic behaviour of the ballscrew middle when subjected to the input torque from the neighbouring elements. The driving torque is received from the ballscrew front and opposed by both the ballscrew end and ballscrew nut elements. The resulting ballscrew middle rotational movement is converted into linear form through the multiplication with the ballscrew ratio.

The axial dynamic behaviour of the ballscrew middle is modelled by the '*force_on_mass*' and '*axial_stiffness*' sub-subsystems. The axial force produced from the ballscrew middle movement is resisted by the tangential and normal forces in the '*ballscrew_nut*' sub-subsystem. The ballscrew axial stiffness is represented by the '*axial_stiffness*' sub-subsystem using a linear spring damper system.

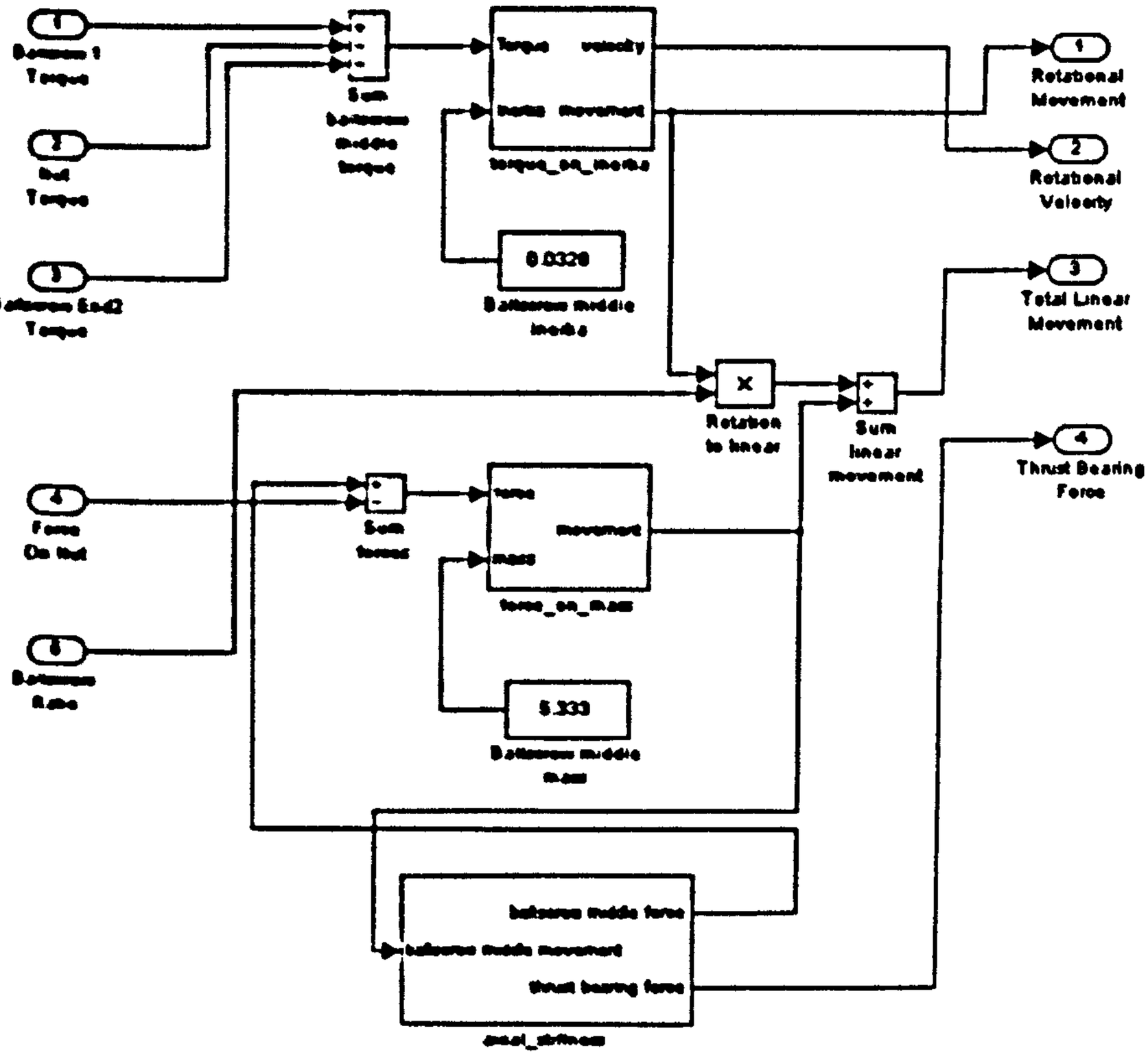

Figure C. 5. Subsystem '*ballscrew_middle*'

C.4. Ballscrew nut

Figure C. 7 illustrates the '*ballscrew_nut*' subsystem which models the force and torque interaction between the ballscrew nut, shaft and the worktable (including the workpiece load). The '*axial_stiffness*' block in the subsystem represents the axial force model interaction in the ballscrew nut due to the relative movement between the nut and the table. The axial and

rotational forces are entered into the '*nut_forces*' sub-subsystem to calculate the torsional interaction between the nut and the rotating element.

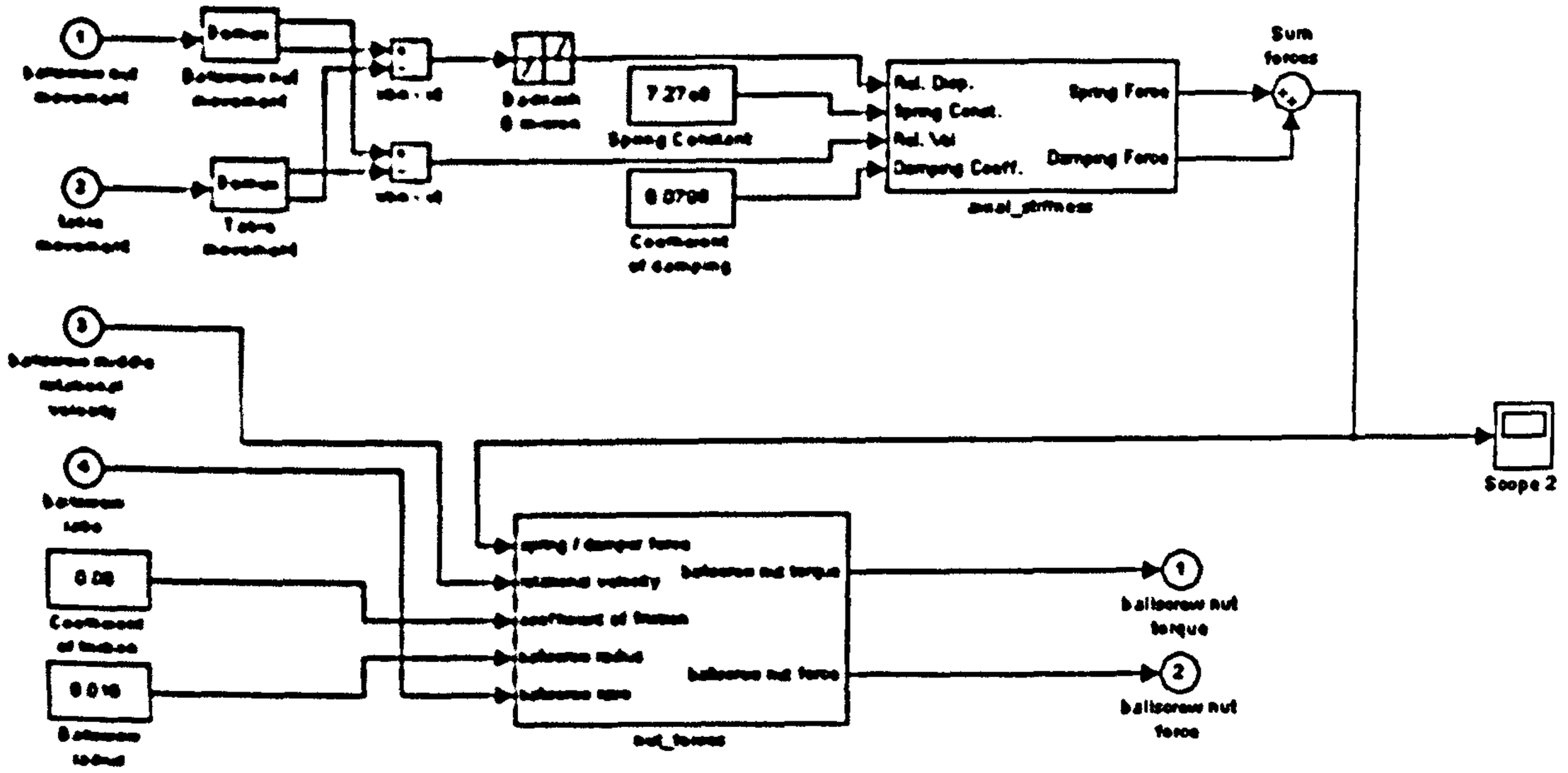

Figure C. 6. Subsystem '*ballscrew_nut*'

The '*nut_forces*' sub-subsystem (see Figure C. 7) represents combines the normal and tangential force elements due to the friction of both the ballscrew shaft and the nut against the rolling ball elements. The sub-subsystem '*set_sign*' is employed to determine the direction and scaling of the friction force due to the non-linear nature of the friction model.

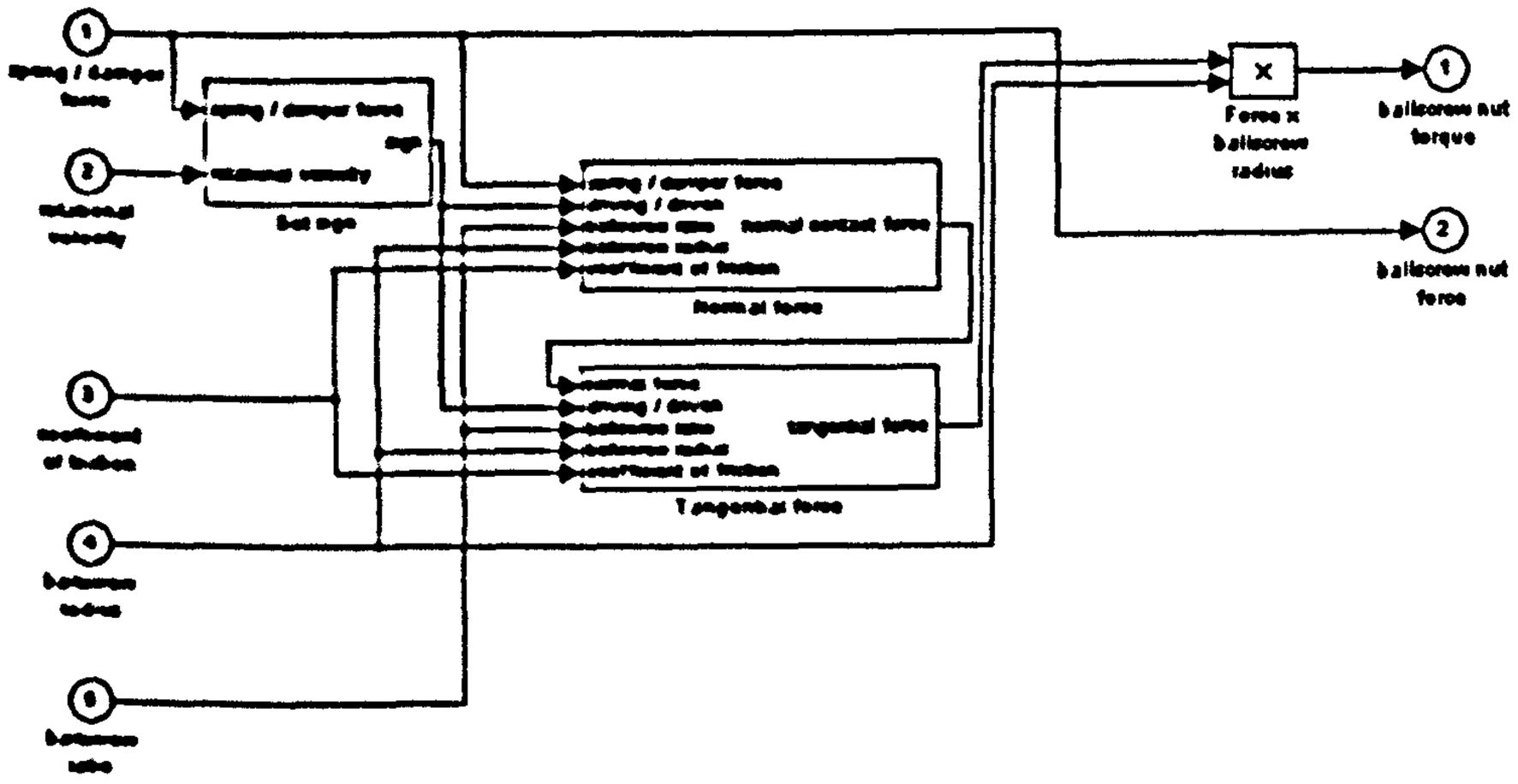

Figure C. 7. Subsystem '*nut forces*'

C.5. Ballscrew end

The '*ballscrew_end*' subsystem models the mechanical dynamic behaviour of the last quarter of the ballscrew shaft as shown in Figure C. 8. The '*ballscrew_end*' and '*radial_bearing*' sub-

subsystems represent the torsional rigidity and friction at to the radial support bearing of the ballscrew end element respectively.

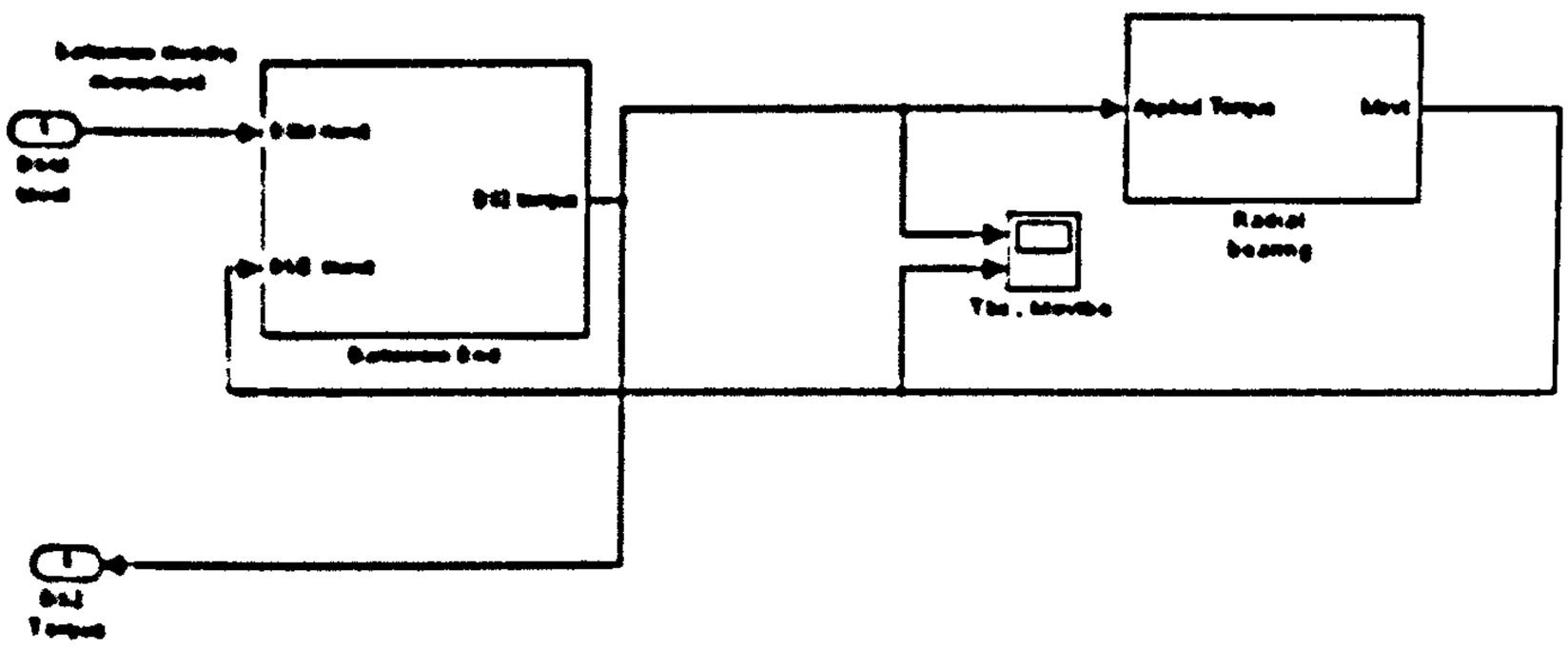

Figure C. 8. Subsystem '*ballscrew2*'

The '*ballscrew_end*' sub-subsystem models the torque as the result of the relative movement of the ballscrew middle and end elements. The ballscrew end movement is calculated in the '*radial bearing*' block by applying Newton's 2nd law on the output torque of the ballscrew end inertia as shown in Figure C. 9. The calculation in the '*radial bearing*' sub-subsystem also considers the frictional and torsional force generated by the radial support bearings involving the reaction force to both the axial force from the '*ballscrew_middle*' subsystem and the torque applied by the '*ballscrew_end*' subsystem.

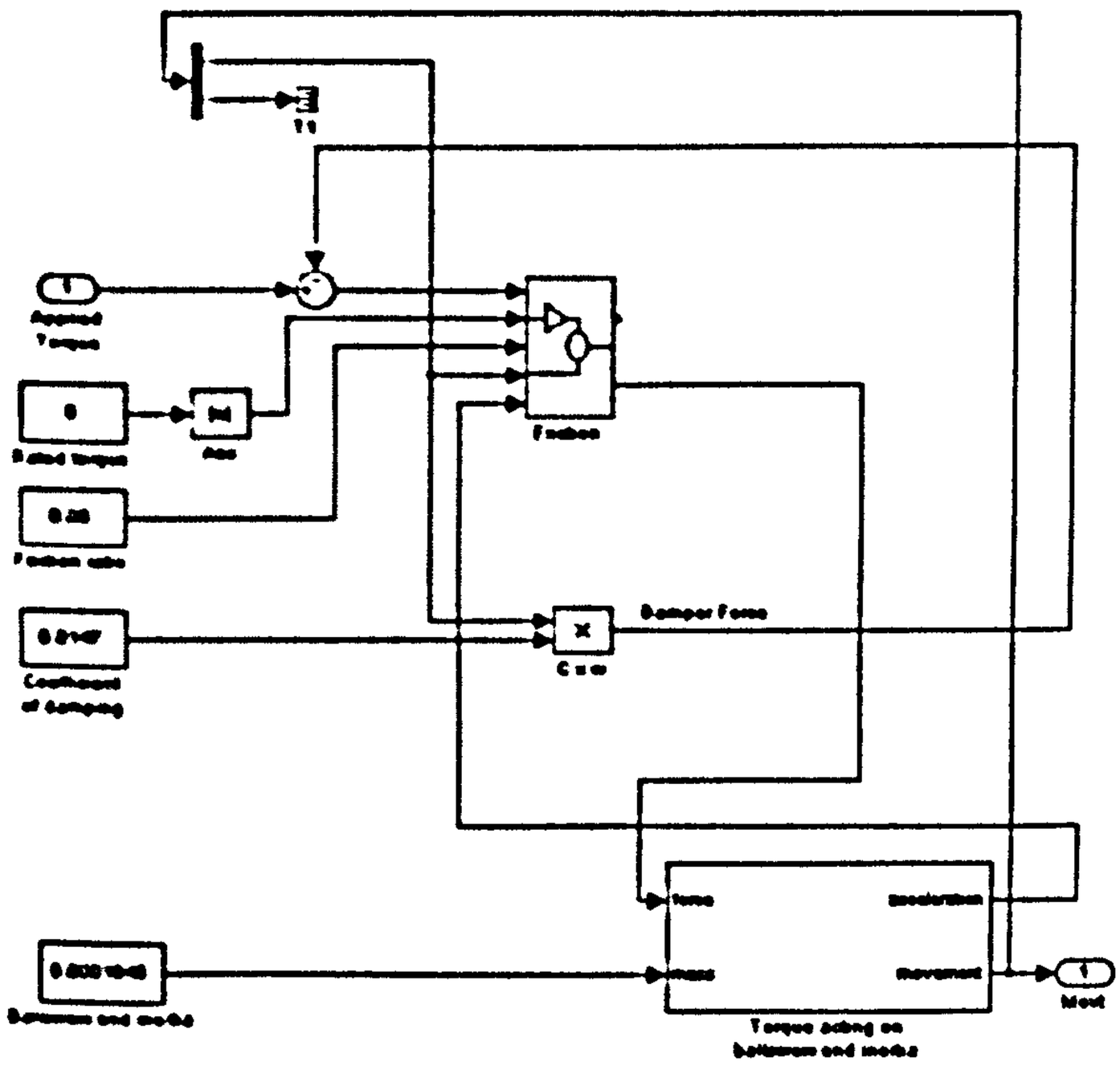

Figure C. 9. Subsystem '*radial bearing*'

Ballscrew element calculation

Preload = 1560 N

Ballscrew Rotational critical damping = $2\sqrt{J_{BS} \cdot k}$ = $2\sqrt{6.58\times10^{-4}\times10{,}123.5}$ = 5.162 Nms/rad

Ballscrew Axial critical damping = $\sqrt{2km}$ = $\sqrt{2\times1.207\times10^{8}\times16}$ = 62148.210 Nms

Nut critical damping = $\sqrt{2km}$ = $\sqrt{2\times7.27\times10^{8}\times16}$ = 152524.892 Nms

Ballscrew Ratio = 0.00191 m/rad

Ballscrew Radius = 0.016 m

Ballscrew Middle

Inertia = Ballscrew Inertia / 2 = 0.000658 / 2 = 0.000329 kg·m^2

Mass = Ballscrew Assembly Mass / 3 = 16 / 3 = 5.333 kg

Ballscrew Axial Stiffness

Axial Stiffness = 1.207×10^8 N/m

Coefficient of damping = Modal test result × critical damping / $\sqrt{2}$

= 0.0798 × 62148.210 / $\sqrt{2}$ = 8606.541

Ballscrew Nut

Backlash = 0 m

Coefficient of Friction = as supplied by Cincinnati = 0.06

Spring Constant = Nut axial rigidity as supplied by Cincinnati = 7.27×10^8 N/m

Coefficient of damping = Modal test result × critical damping / $\sqrt{2}$

= 0.0798 × 62148.210 / $\sqrt{2}$ = 8606.541

Ballscrew End

Spring Constant = Radial Rigidity × 2 = 10,123.5 × 2 = 20247

Coefficient of damping = Modal test result × critical damping / $\sqrt{2}$

= 0.0798 × 62148.210 / $\sqrt{2}$ = 3506.845

Ballscrew End Inertia = Ballscrew Inertia / 4 = 0.000658 / 4 = 0.0001645

Rated Torque = 6

Coefficient of damping = Modal test result = 0.0798

Thrust Race Diameter = 0.025

Drag Torque = 0.422

Friction Ratio = as supplied by manufacturer = 0.06

C.6. Table

The '*table*' subsystem describes the table mechanical dynamic behaviour in terms of the friction force with the guideways, the reaction force to the nut and the table movement. The static loading of the machine also considers the worktable load mass which in the form of a dynamometer weighing 80 kg (including the clamping device). This load plus the mass of the table and the associated load form the X-axis mass. The model of this subsystem is shown in Figure C. 10 below.

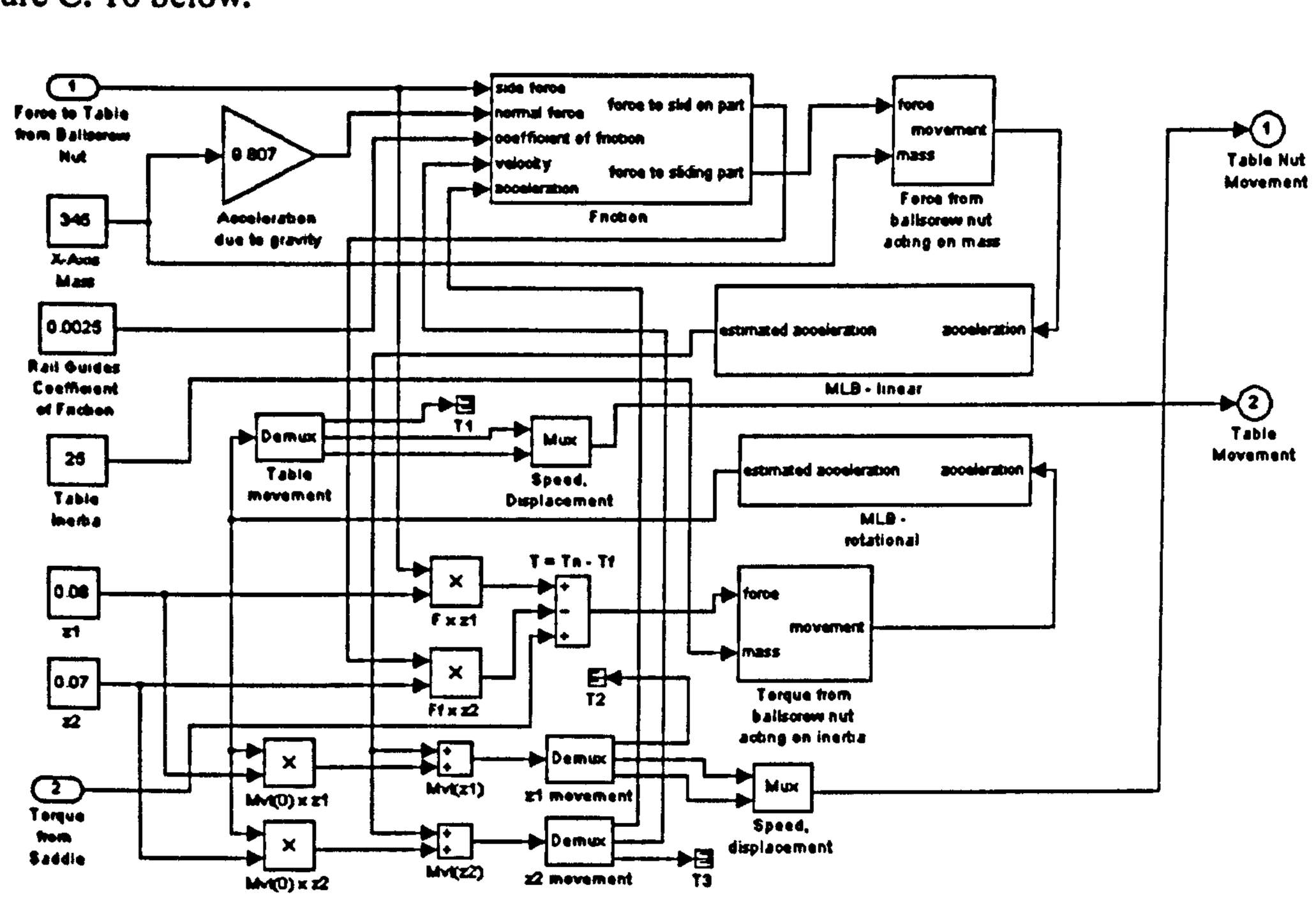

Figure C. 10. Simulink model of the '*table*' subsystem

Table

X-Axis Mass (Table Plus)	= 345 kg		
Table Inertia	= $m \times r^2 = 345 \times 0.102^2 = 1.104$ kg m^2		(distance measured)
Coefficient of Friction	= 0.0025		(supplied by manufacturer)
z1	= 0.35	m	(table c.o.g. to nut – estimated from drawing)
z2	= 0.3	m	(table c.o.g. to rail – estimated from drawing)

C.7. Saddle stiffness

This subsystem (see Figure C. 11) describes the generation of reaction torque of the saddle element opposing movement of the table. It is a spring damper element with the parameter constants obtained from the manufacturer's catalogue.

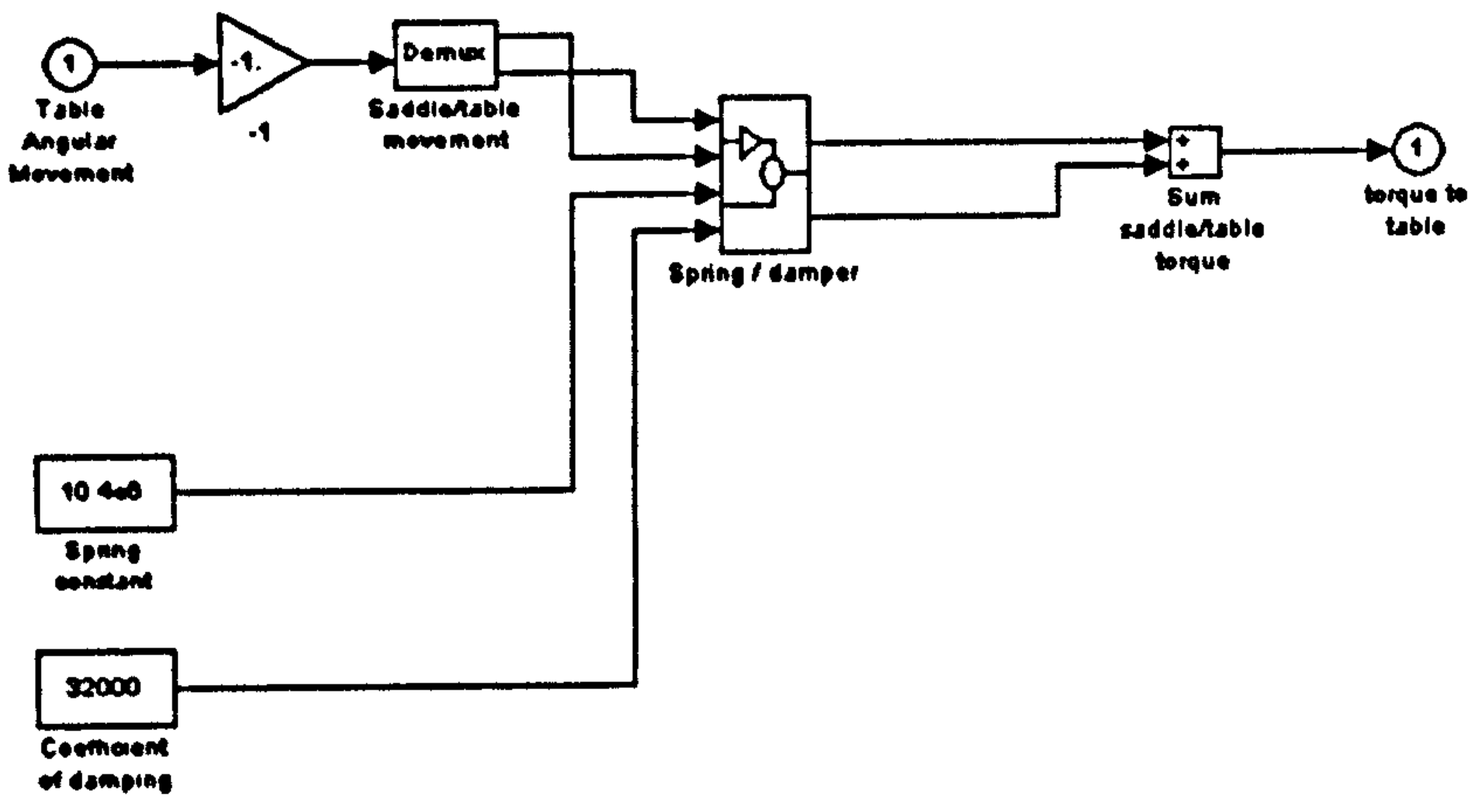

Figure C. 11. Subsystem '*Saddle stiffness*'

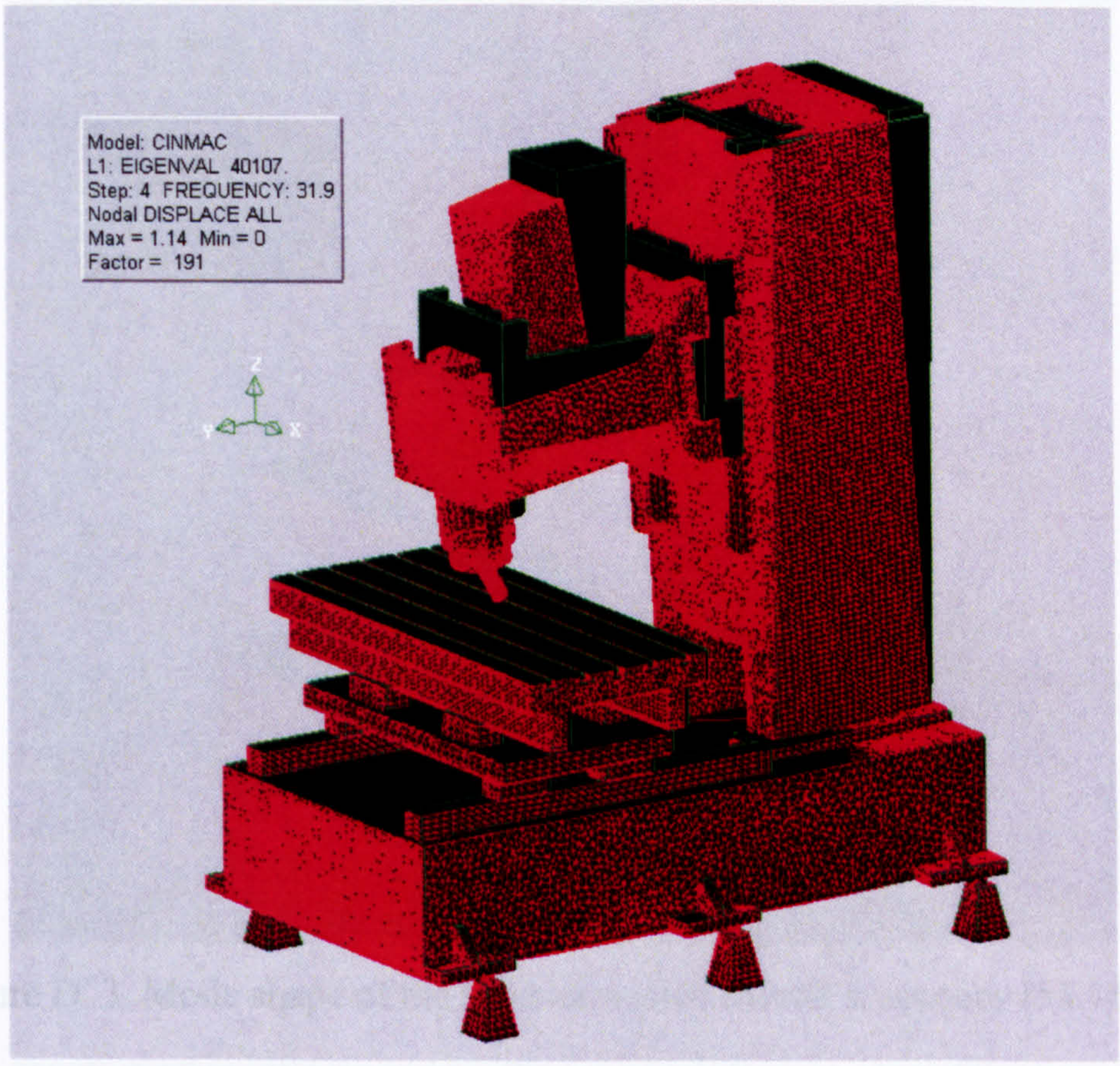

Figure D. 1. Mode shape of the first simulated natural frequency (31.87 Hz)

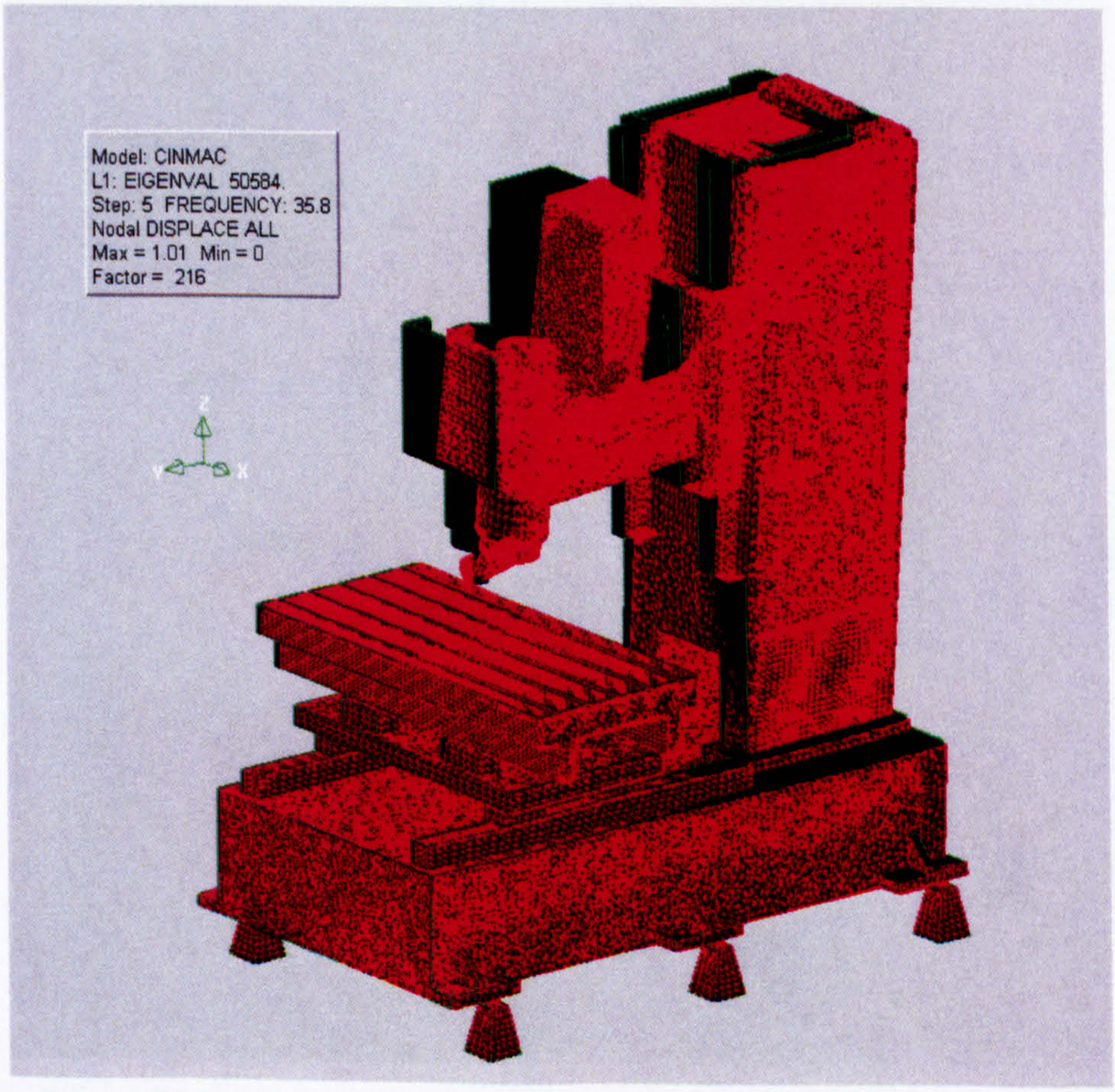

Figure D. 2. Mode shape of the second simulated natural frequency (35.80 Hz)

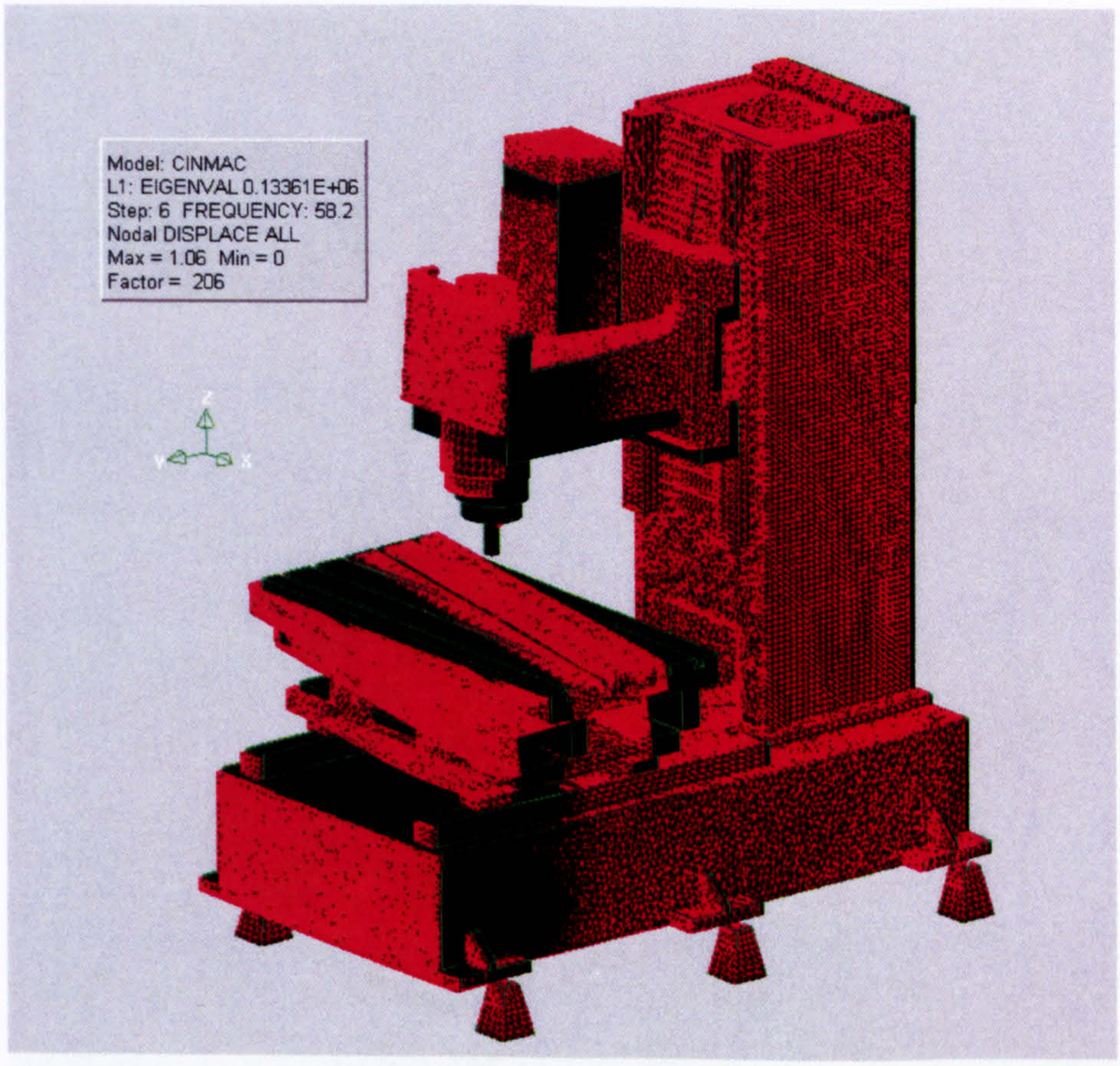

Figure D. 3. Mode shape of the third simulated natural frequency (58.18 Hz)

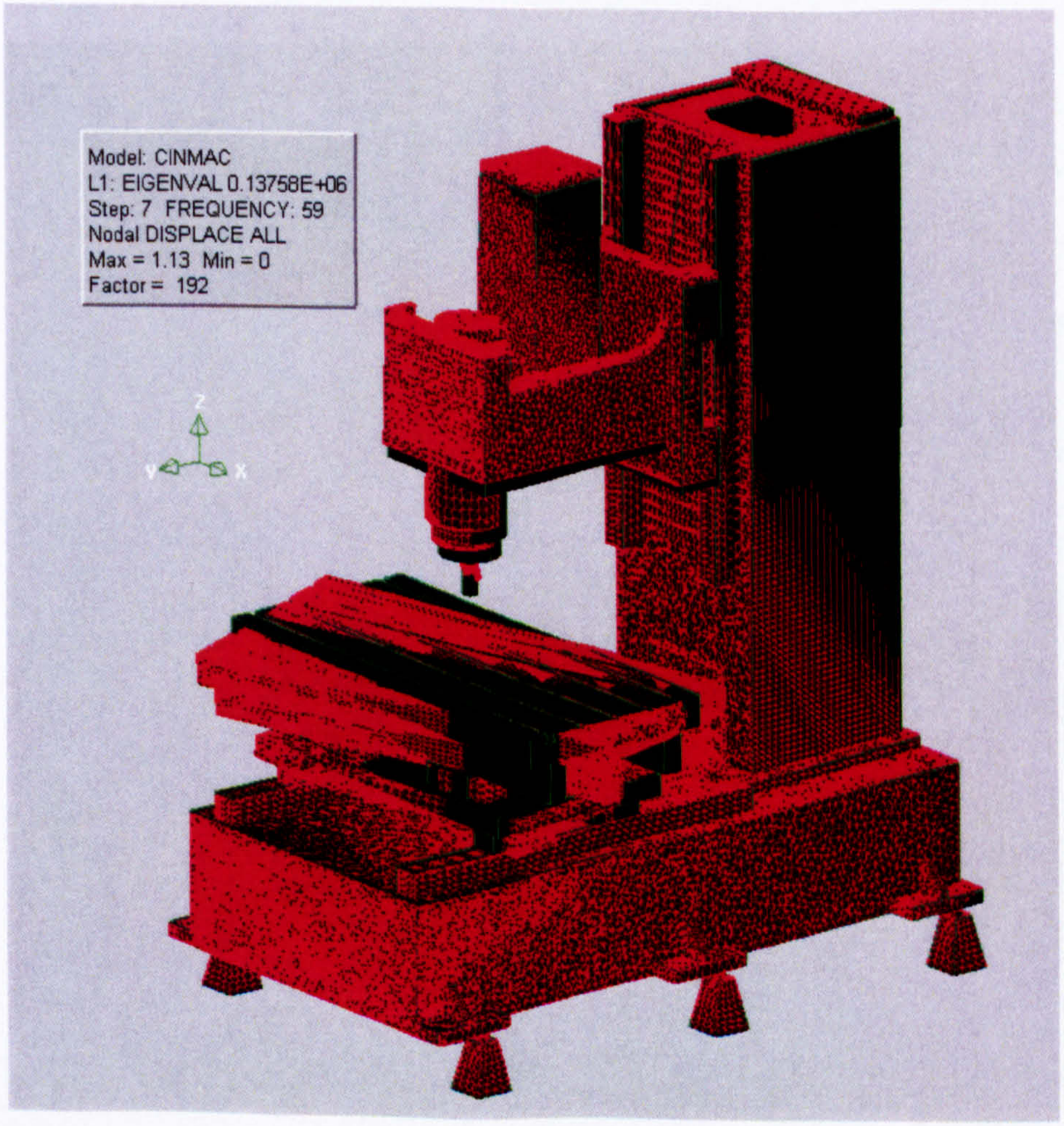

Figure D. 4. Mode shape of the fourth simulated natural frequency (59.03 Hz)

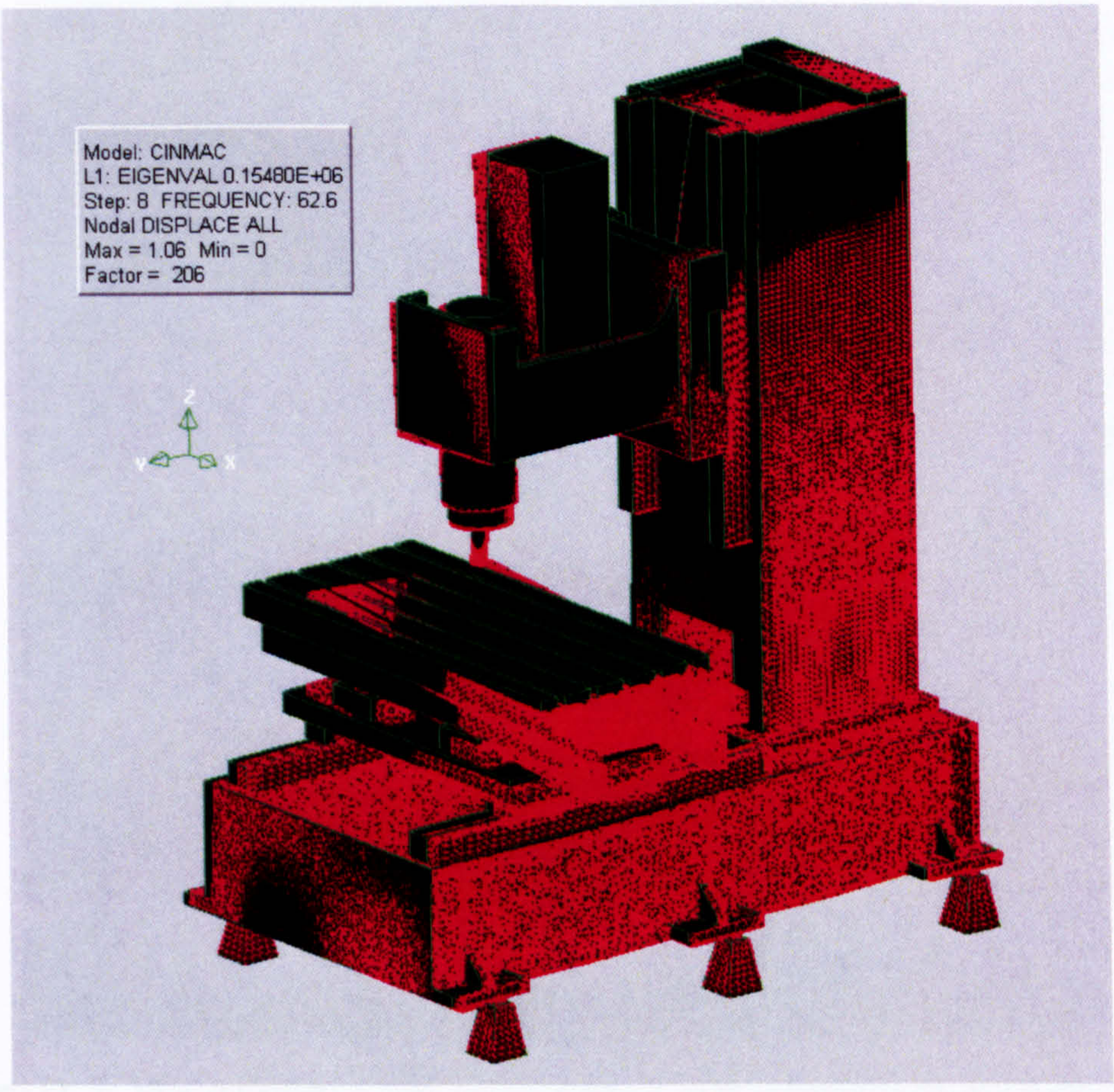

Figure D. 5. Mode shape of the fifth simulated natural frequency (62.62 Hz)

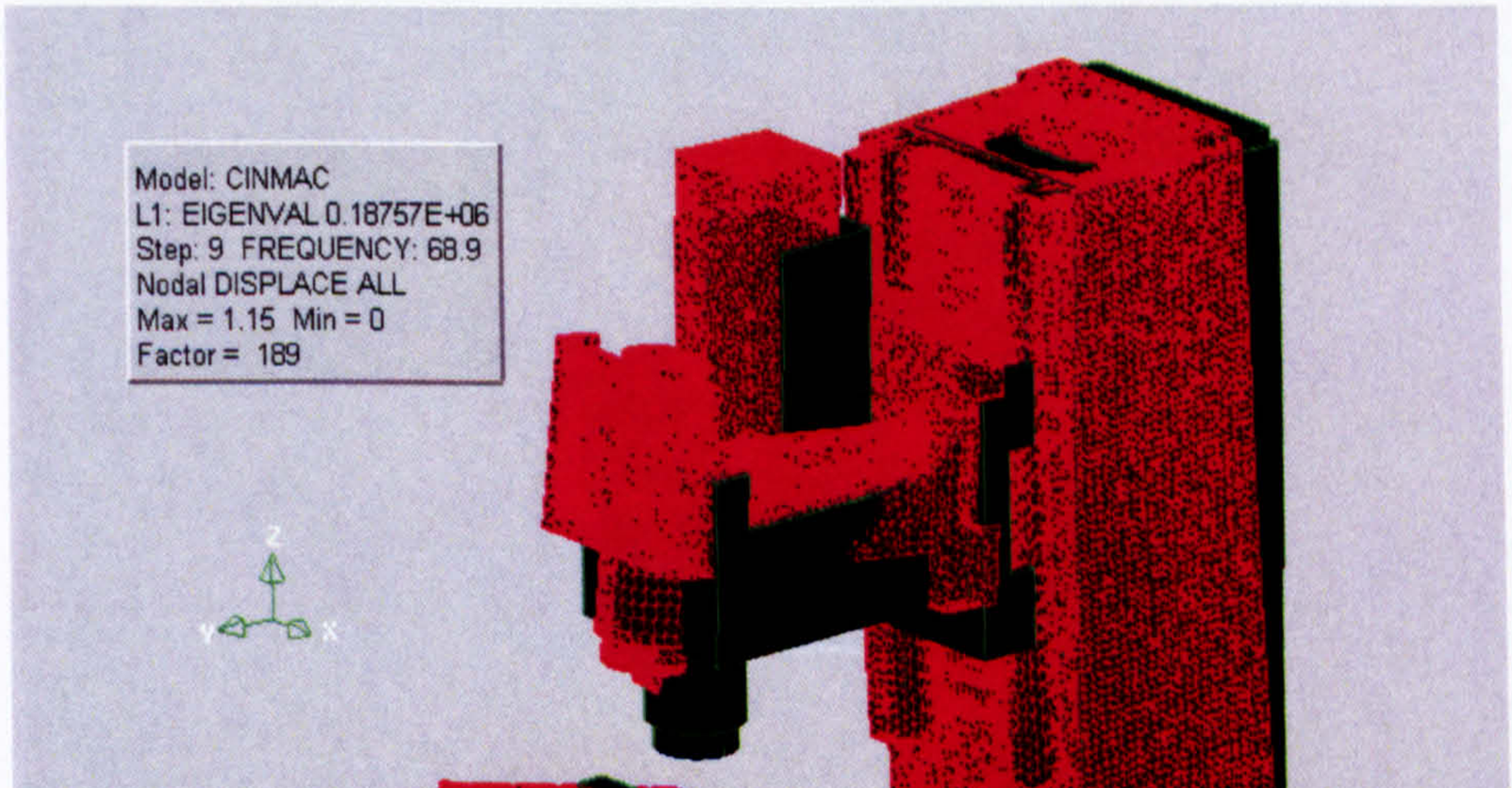

Figure D. 6. Mode shape of the sixth simulated natural frequency (68.93 Hz)

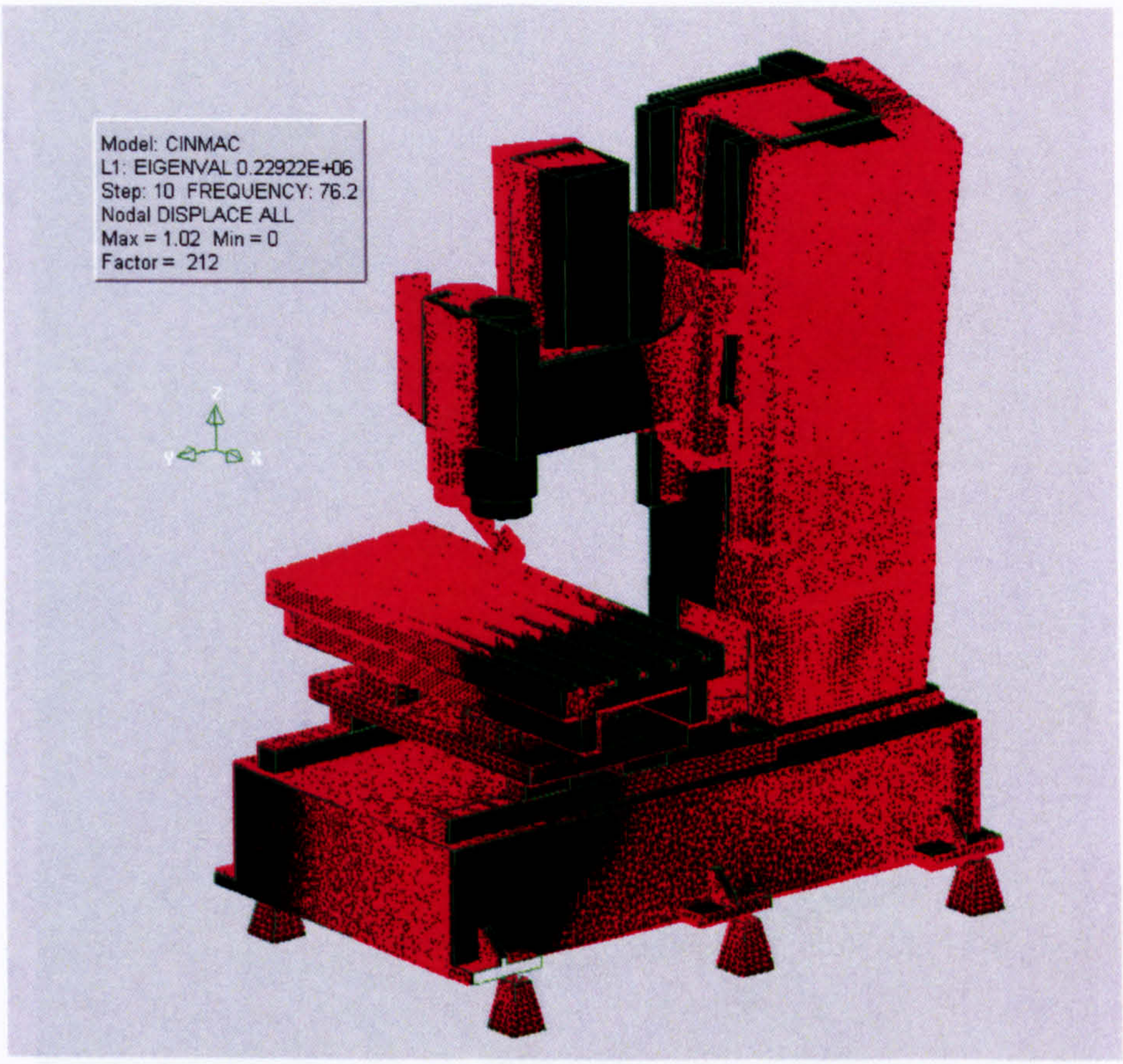

Figure D. 7. Mode shape of the seventh simulated natural frequency (76.20 Hz)

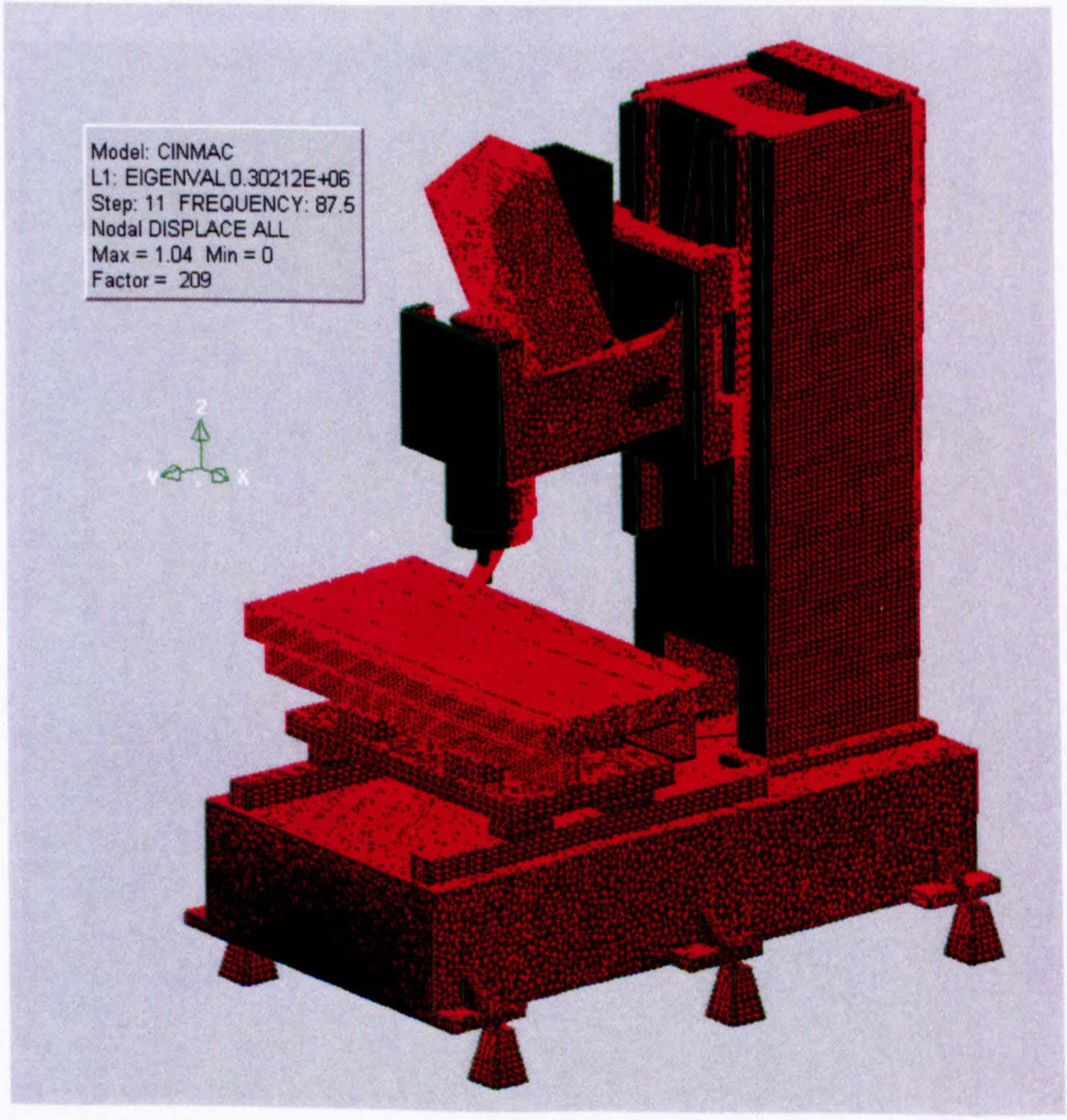

Figure D. 8. Mode shape of the eighth simulated natural frequency (87.48 Hz)

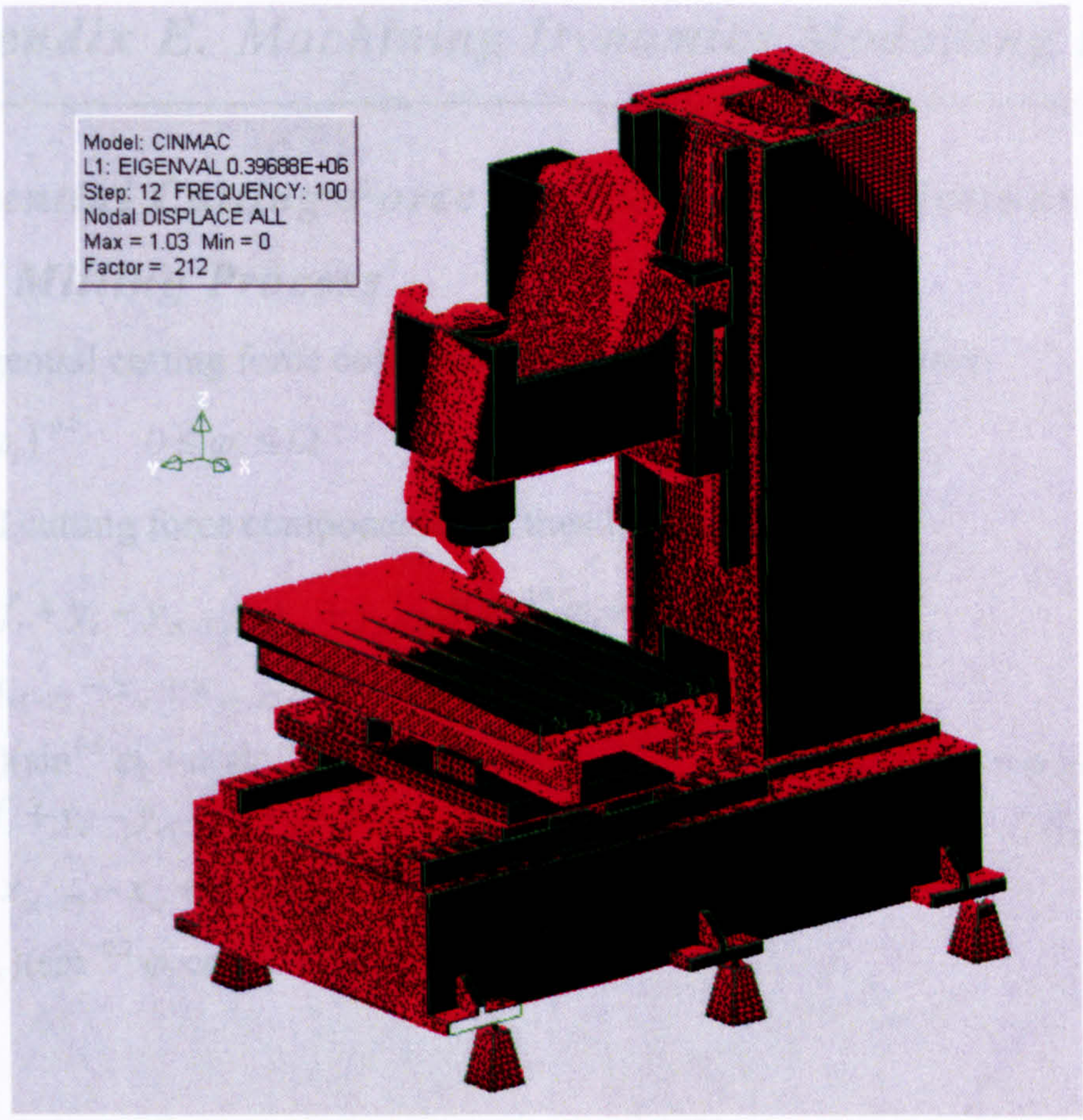

Figure D. 9. Mode shape of the ninth simulated natural frequency (100.27 Hz)

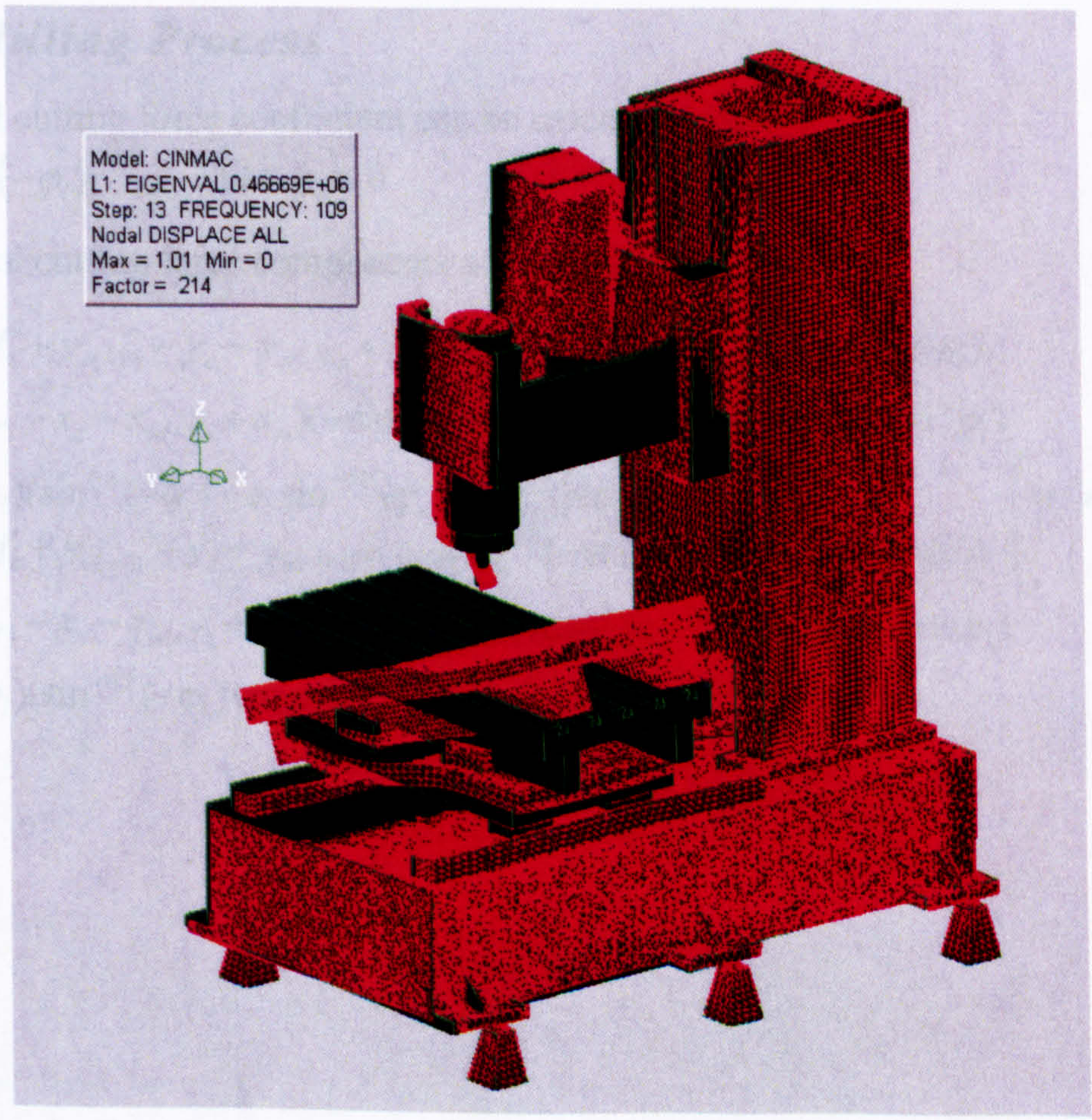

Figure D. 10. Mode shape of the tenth simulated natural frequency (108.73 Hz)

Appendix E. Machining Dynamics Modelling Equations

E.1. Differential Cutting Force Component Calculations for The Down Milling Process

The actual tangential cutting force coefficient can be predicted as follows:

$$K_s \approx u'(\sin\varphi_i)^{-0.2} \qquad 0 \le \varphi_i \le \Omega \tag{9.1}$$

The differential cutting force components can thus be obtained as:

$$\begin{cases} dF_{ix} = -K'_s[(f_t + y_c - y_{c(-T)} - y_w + y_{w(-T)})(\sin^{1.8}\varphi_i + c_1\sin^{0.8}\varphi_i\cos\varphi_i) \\ \quad + (x_c - x_{c(-T)} - x_w + x_{w(-T)})(\sin^{0.8}\varphi_i\cos\varphi_i + c_1\sin^{-0.2}\varphi_i\cos^2\varphi_i) \\ \quad + \delta t_i(\varphi_i)(\sin^{0.8}\varphi_i + c_1\sin^{-0.2}\varphi_i\cos\varphi_i)]d\varphi_i \\ dF_{iy} = K'_s[(f_t + y_c - y_{c(-T)} - y_w + y_{w(-T)})(\sin^{0.8}\varphi_i\cos\varphi_i - c_1\sin^{1.8}\varphi_i) \\ \quad + (x_c - x_{c(-T)} - x_w + x_{w(-T)})(\sin^{-0.2}\varphi_i\cos^2\varphi_i - c_1\sin^{1.8}\varphi_i) \\ \quad + \delta t_i(\varphi_i)(\sin^{-0.2}\varphi_i\cos\varphi_i - c_1\sin^{0.8}\varphi_i)]d\varphi_i \end{cases} \begin{pmatrix} \varphi_i = \varphi - \omega t + (i-1)\dfrac{2\pi}{m} \\ 0 \le \varphi_i \le \Omega \end{pmatrix} \tag{9.2}$$

E.2. Differential Cutting Force Component Calculations for The Up Milling Process

The tangential cutting force coefficient can be calculated by:

$$K_s \approx u'[\sin(-\varphi_i)]^{-0.2} \qquad -\Omega \le \varphi_i \le 0 \tag{9.3}$$

The differential cutting force components are calculated as follows:

$$\begin{cases} dF_{ix} = K'_s[(f_t + y_{c(-T)} - y_c - y_{w(-T)} + y_w)(\sin^{1.8}(-\varphi_i) - c_1\sin^{0.8}(-\varphi_i)\cos\varphi_i) \\ \quad + (x_{c(-T)} - x_c - x_{w(-T)} + x_w)(-\sin^{0.8}(-\varphi_i)\cos\varphi_i + c_1\sin^{-0.2}(-\varphi_i)\cos^2\varphi_i) \\ \quad + \delta t_i(\varphi_i)(\sin^{0.8}(-\varphi_i) - c_1\sin^{-0.2}(\varphi_i)\cos\varphi_i)]d\varphi_i \\ dF_{iy} = K'_s[(f_t + y_{c(-T)} - y_c - y_{w(-T)} + y_w)(\sin^{0.8}(-\varphi_i)\cos\varphi_i + c_1\sin^{1.8}(-\varphi_i)) \\ \quad + (x_{c(-T)} - x_c - x_{w(-T)} + x_w)(-\sin^{-0.2}(-\varphi_i)\cos^2\varphi_i - c_1\sin^{0.8}(-\varphi_i)\cos\varphi_i) \\ \quad + \delta t_i(\varphi_i)(\sin^{-0.2}(-\varphi_i)\cos\varphi_i + c_1\sin^{0.8}(-\varphi_i))]d\varphi_i \end{cases} \begin{pmatrix} \varphi_i = \varphi - \omega t + (i-1)\dfrac{2\pi}{m} \\ -\Omega \le \varphi_i \le 0 \end{pmatrix} \tag{9.4}$$

F.1. Sensitivity coefficients for the whole structure

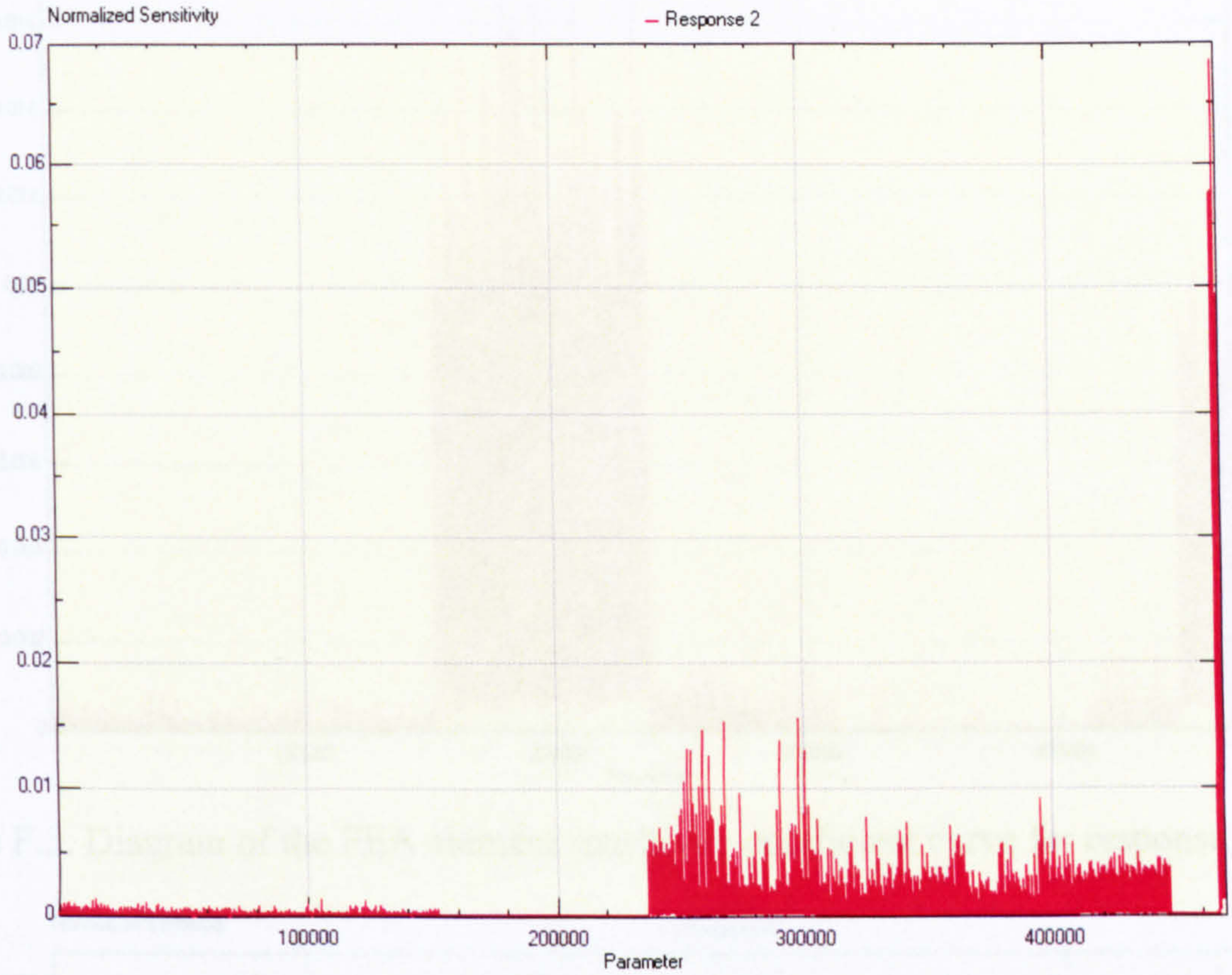

Figure F.1. Diagram of the FEA element sensitivity coefficient curve for response (mode) 2

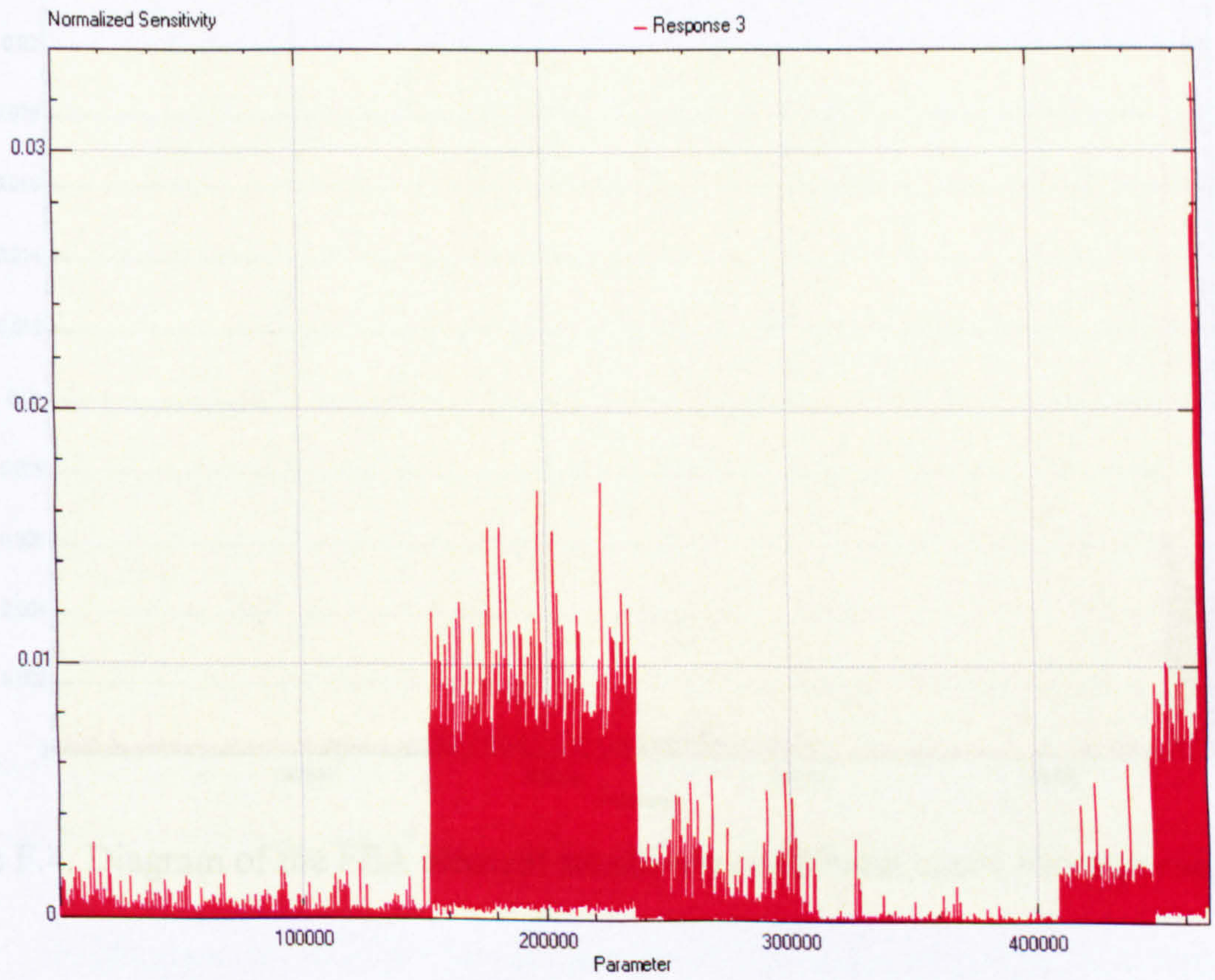

Figure F.2. Diagram of the FEA element sensitivity coefficient curve for response (mode) 3

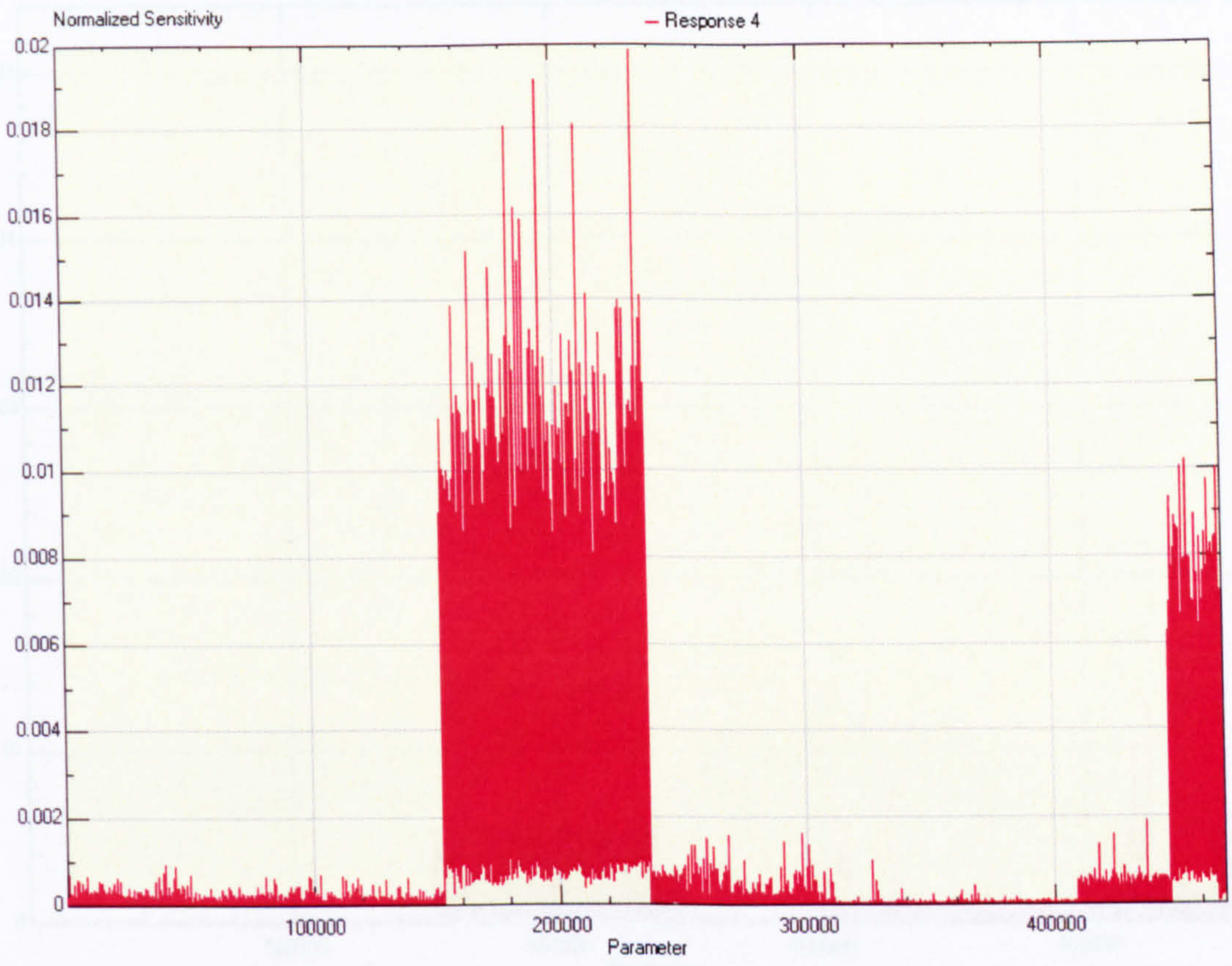

Figure F.3. Diagram of the FEA element sensitivity coefficient curve for response (mode) 4

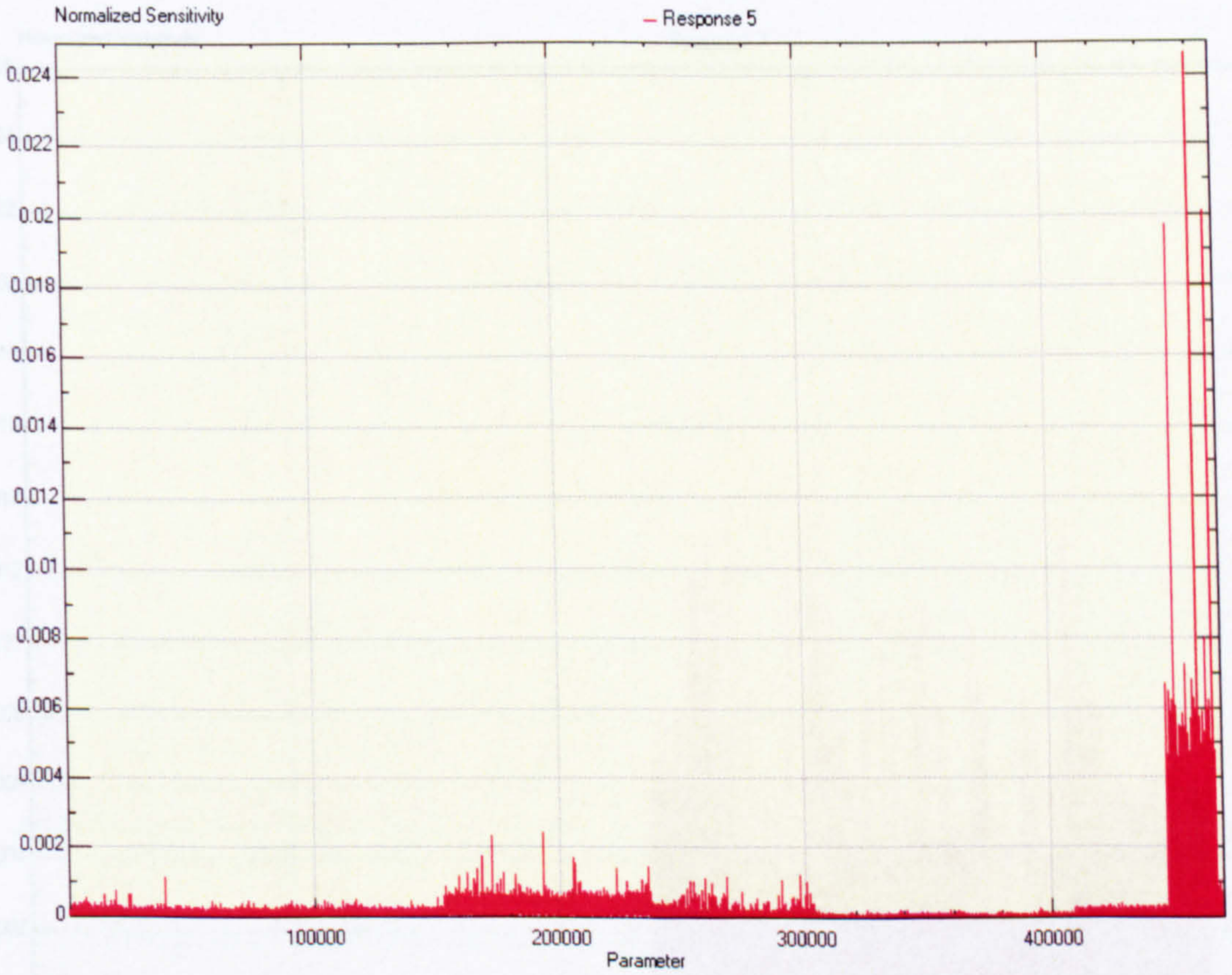

Figure F.4. Diagram of the FEA element sensitivity coefficient curve for response (mode) 5

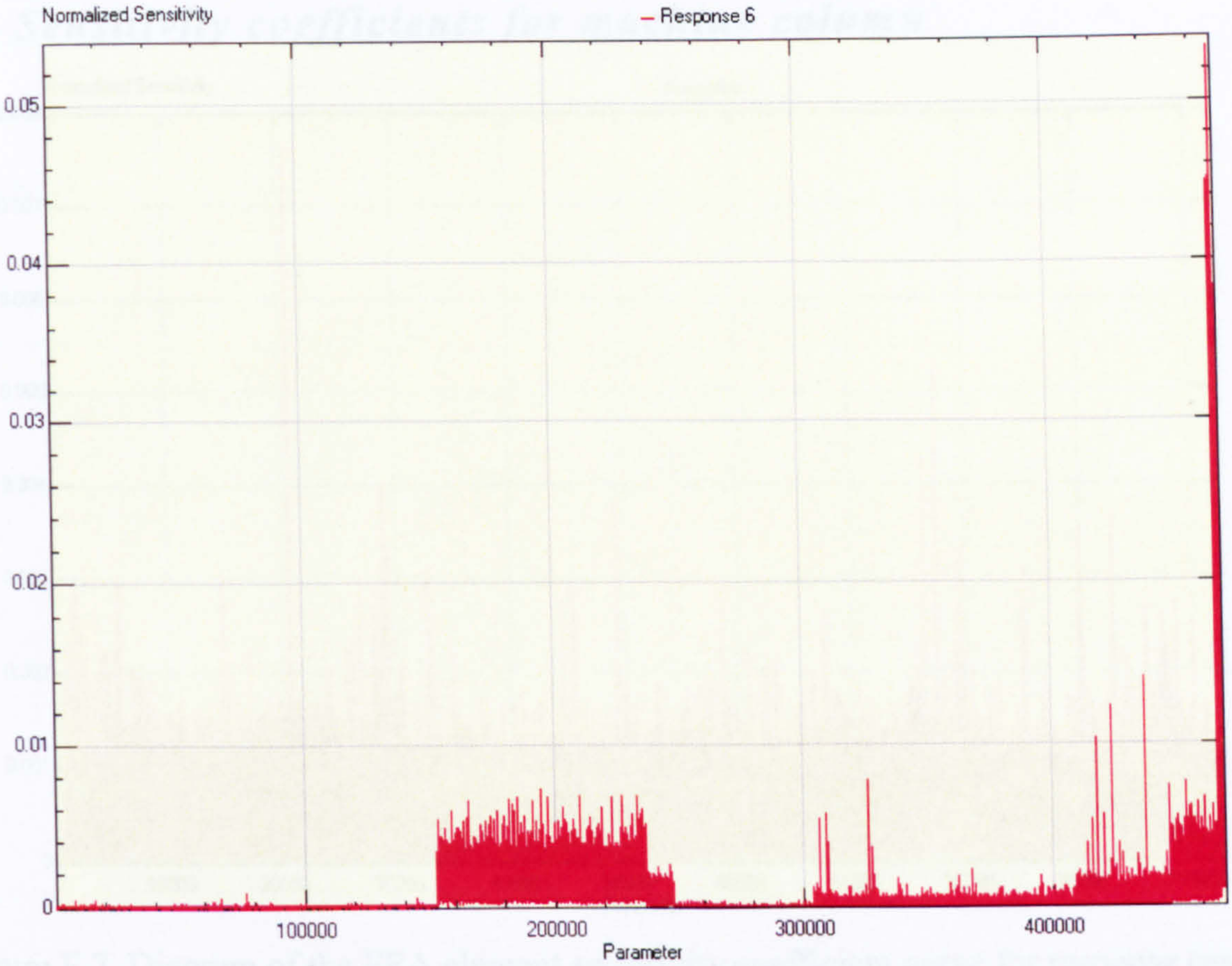

Figure F.5. Diagram of the FEA element sensitivity coefficient curve for response (mode) 6

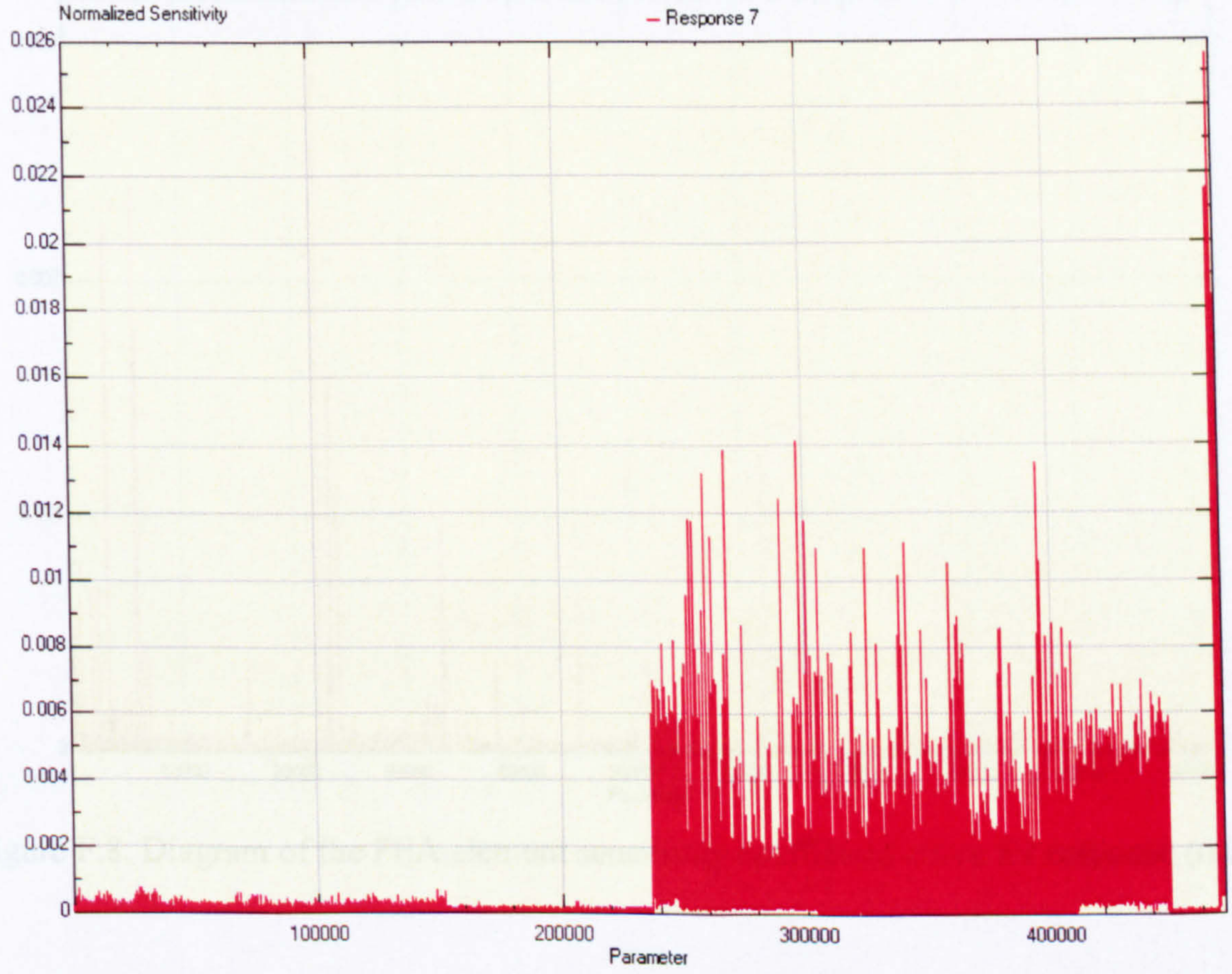

Figure F.6. Diagram of the FEA element sensitivity coefficient curve for response (mode) 7

F.2. Sensitivity coefficients for machine column

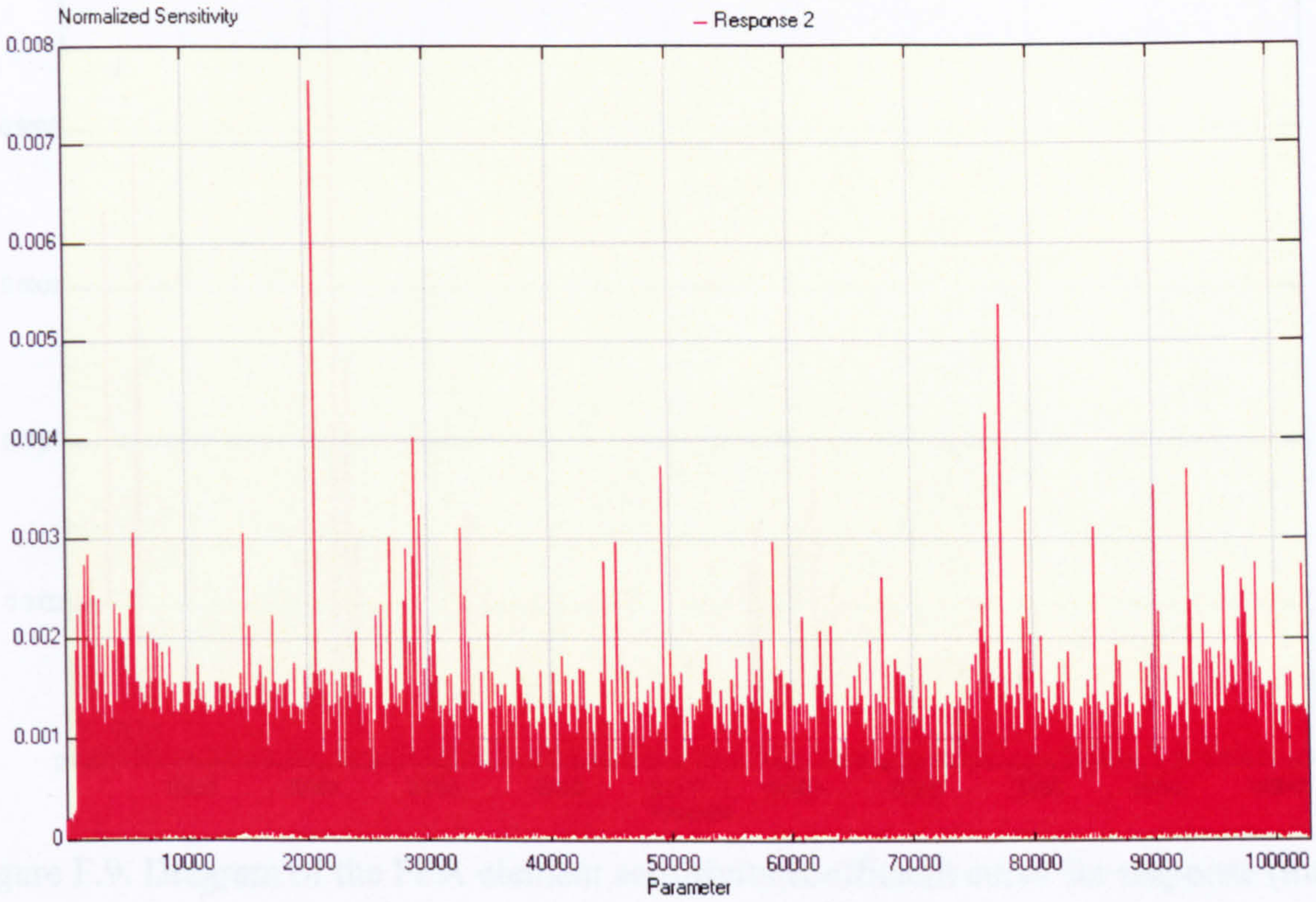

Figure F.7. Diagram of the FEA element sensitivity coefficient curve for response (mode) 2

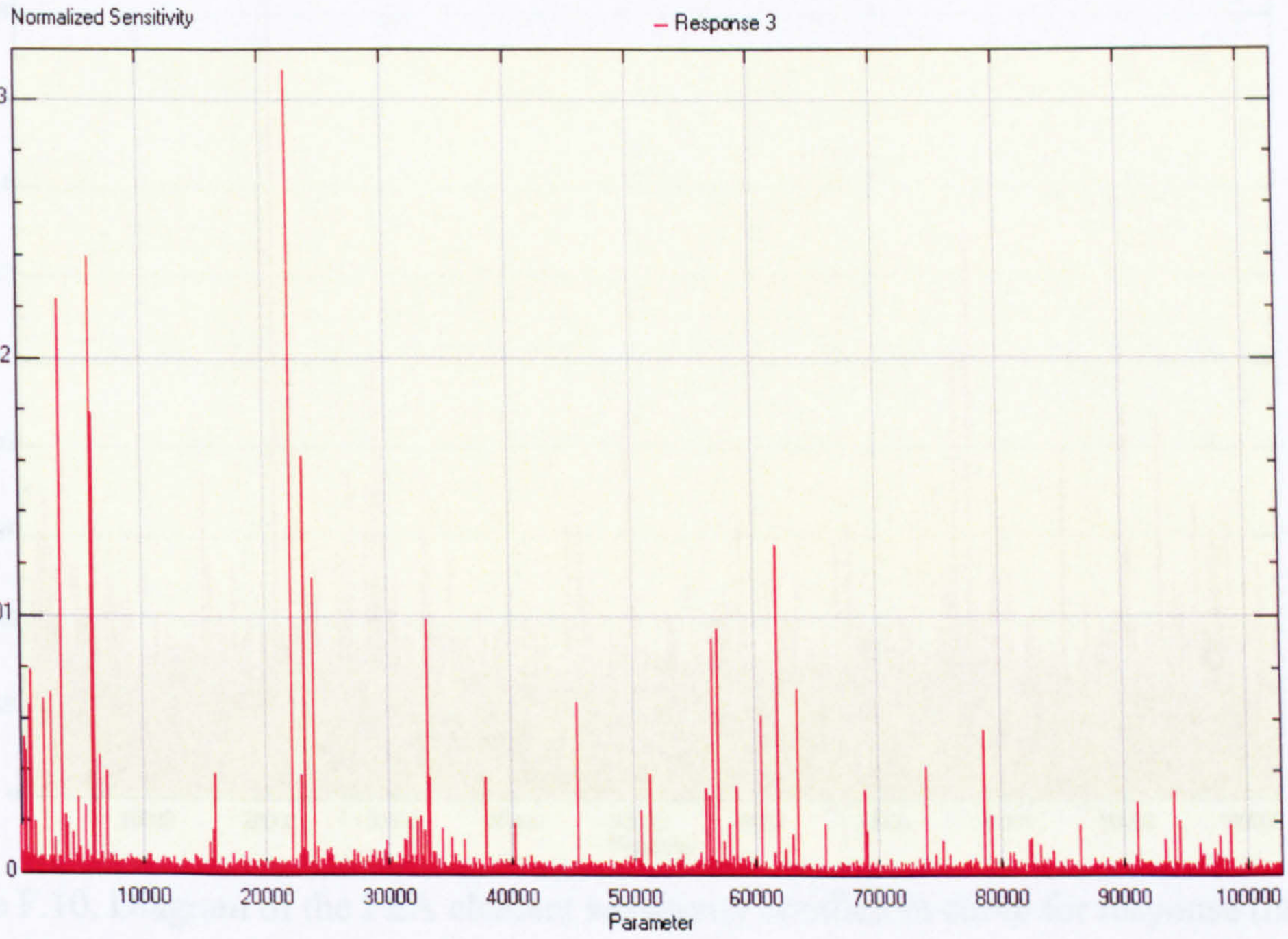

Figure F.8. Diagram of the FEA element sensitivity coefficient curve for response (mode) 3

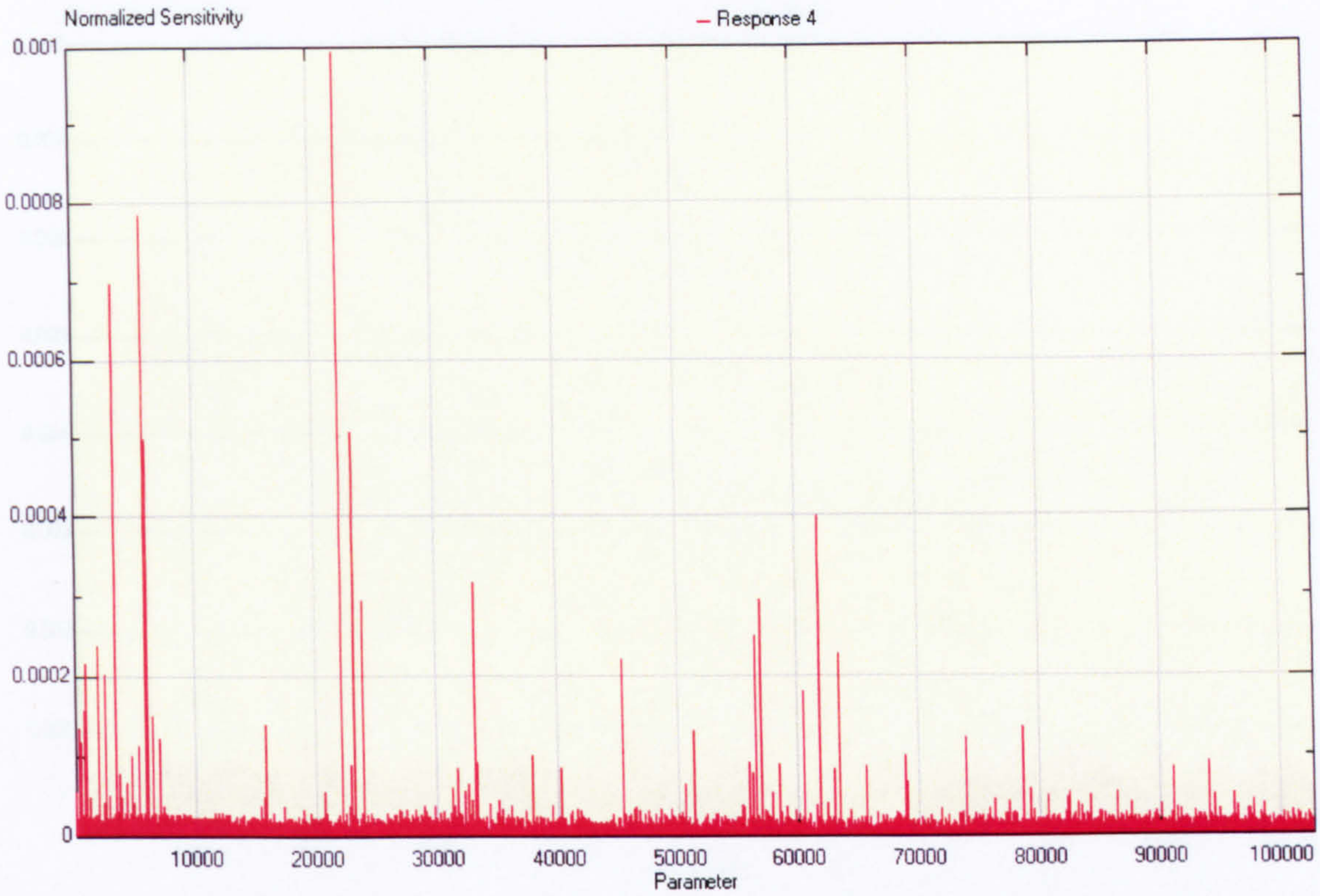

Figure F.9. Diagram of the FEA element sensitivity coefficient curve for response (mode) 4

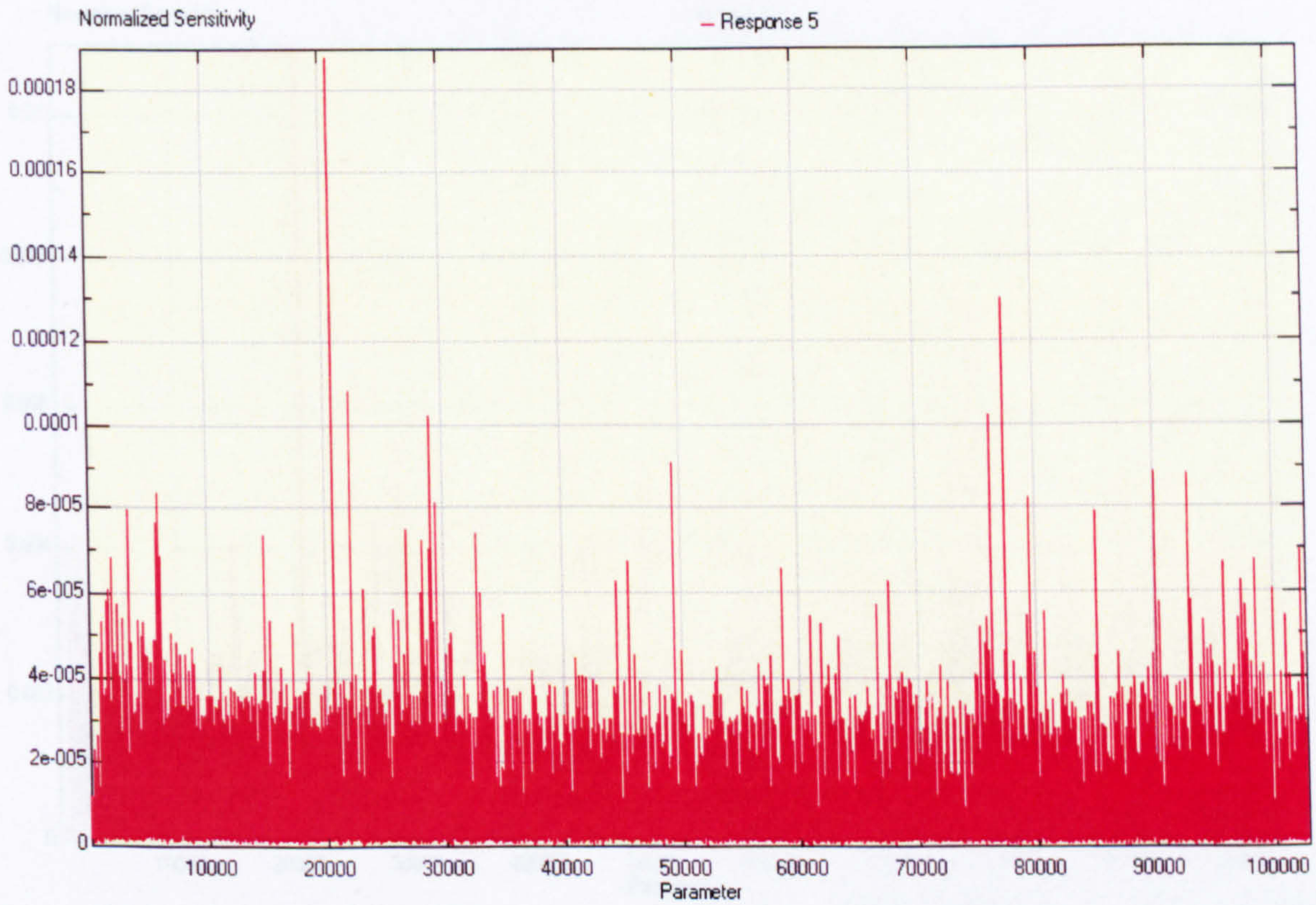

Figure F.10. Diagram of the FEA element sensitivity coefficient curve for response (mode) 5

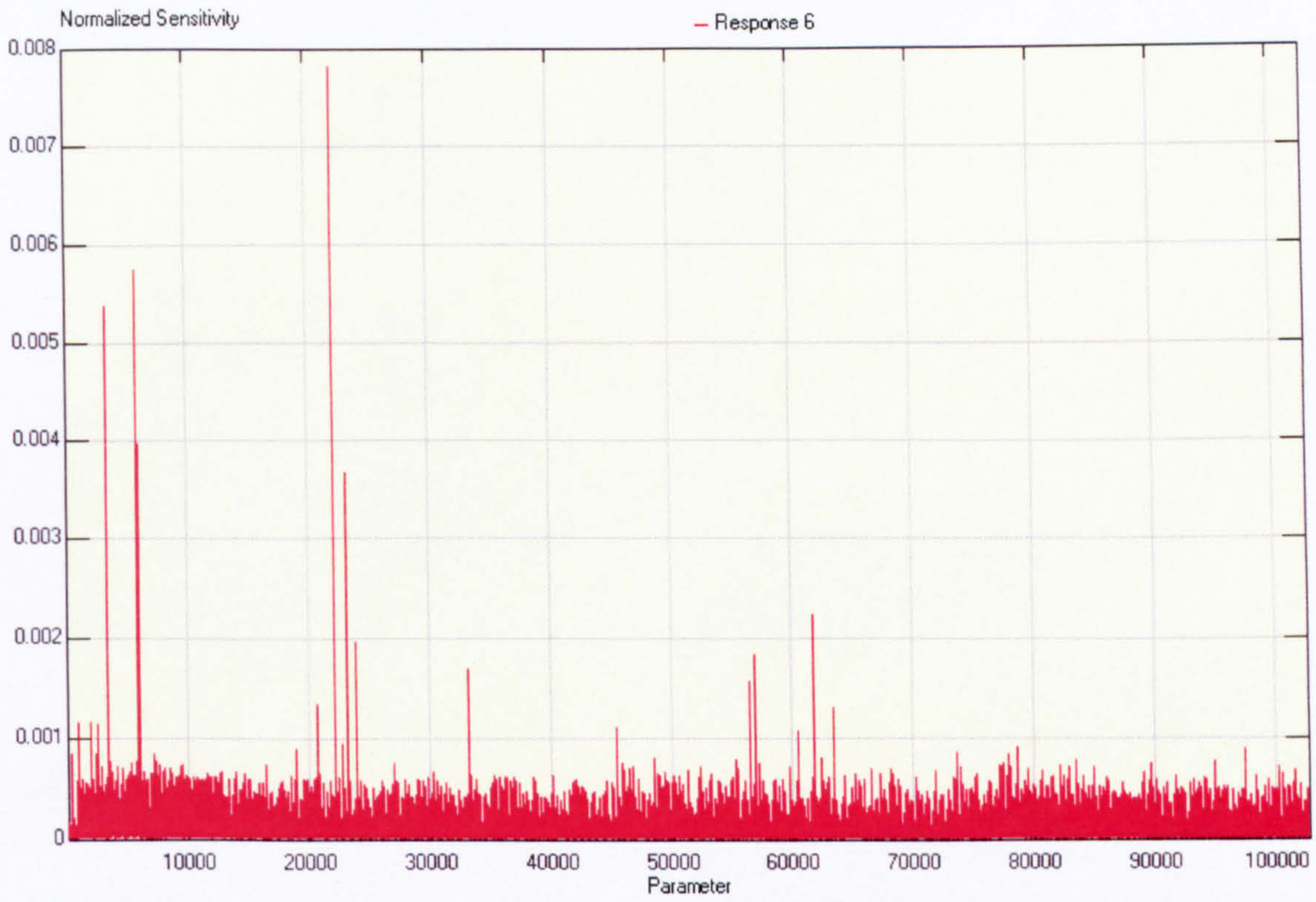

Figure F.11. Diagram of the FEA element sensitivity coefficient curve for response (mode) 6

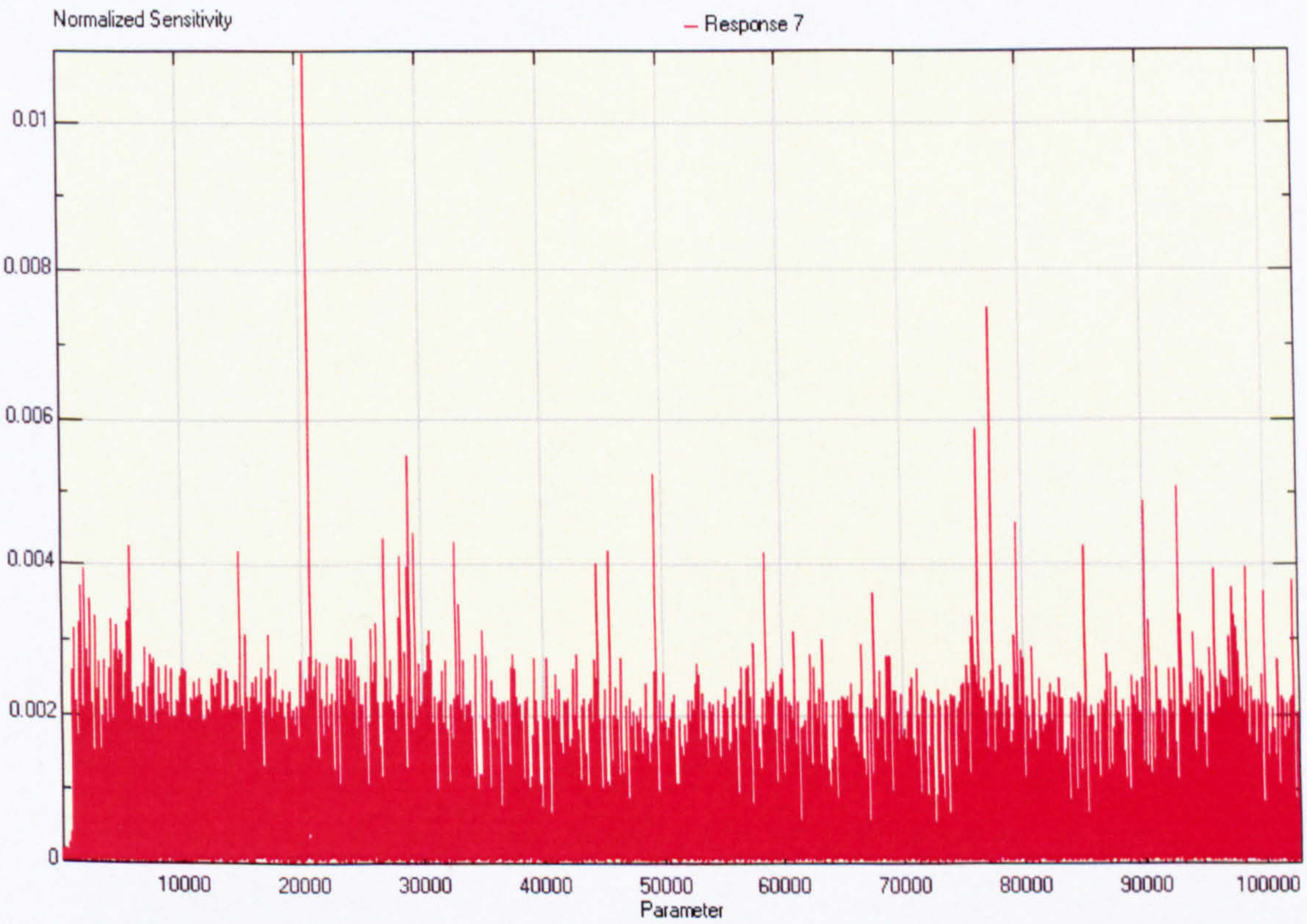

Figure F.12. Diagram of the FEA element sensitivity coefficient curve for response (mode) 7